NASA Conference Publication

24th Aerospace Mechanisms Symposium

Compiled by
Kenneth J. Frantz
Kennedy Space Center

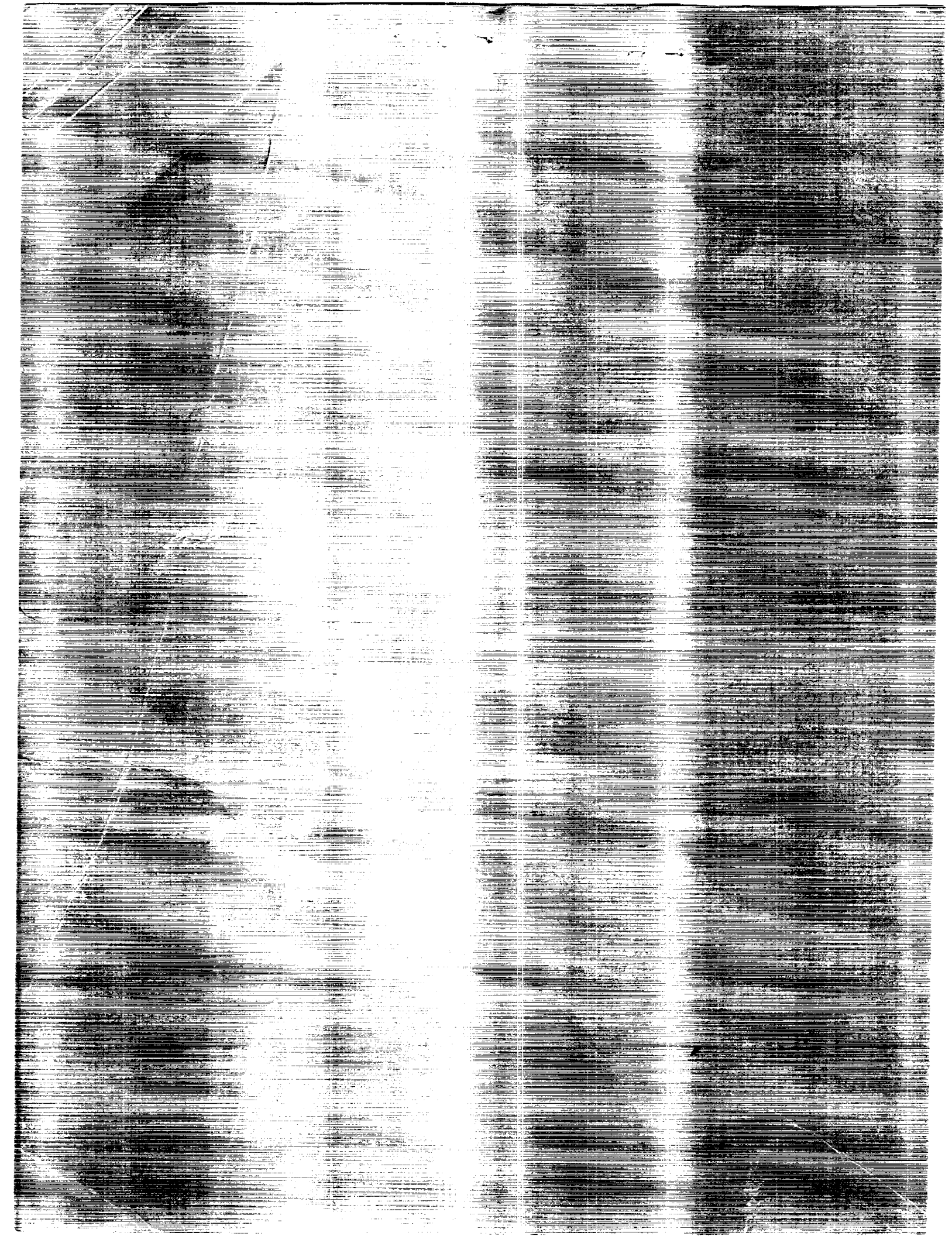

PREFACE

The proceedings of the 24th Aerospace Mechanisms Symposium, which was hosted by the John F. Kennedy Space Center, Kennedy Space Center, Florida, on April 18 to 20, 1990, are reported in this NASA Conference Publication. The symposium was sponsored by the National Aeronautics and Space Administration, the California Institute of Technology, and Lockheed Missiles and Space Company, Inc.

The purpose of the symposium was to provide a forum for the interchange of information among those active in the field of mechanisms technology. To that end 26 papers were presented on aeronautics and space flight, with special emphasis on actuators, aerospace mechanism applications for ground support equipment, lubricants, latches, connectors, and other mechanisms for large space structures. The papers were prepared by authors from a broad aerospace background, including the U.S. aerospace industry, NASA, and European and Asian participants.

The efforts of the review committee, session chairmen, and speakers contributing to the technical excellence and professional character of the conference are especially appreciated.

The use of trade names or names of manufacturers in this publication does not constitute an official endorsement of such products or manufacturers, either expressed or implied, by the National Aeronautics and Space Administration.

TABLE OF CONTENTS

TABLE OF CONTENTS (cont)

SESSION III

SESSION IV

SESSION V

TABLE OF CONTENTS (cont)

SESSION VI

SESSION VIII

SYMPOSIUM SCHEDULE

TUESDAY, 17 APRIL 1990

4:30-8:00pm Pre-registration and Social Hour
(Lobby, Hilton Hotel)

WEDNESDAY, 18 APRIL 1990

8:00 Wednesday Authors Breakfast
(Board Room II, Hilton Hotel)

8:00 REGISTRATION AND COFFEE
(Lobby, Hilton Hotel)

10:00 INTRODUCTORY REMARKS
Mr. James D. Phillips, Host Chairman
NASA Kennedy Space Center

CENTER WELCOME
Lt. General Forrest McCartney (USAF, Ret), Center Director
NASA Kennedy Space Center

10:30 SESSION I
Mr. John F. Rogers, Session Chairman
NASA Langley Research Center, Hampton, VA

- *Cycle Life Machine for AX-5 Space Suit*
  Deborah S. Schenberger
  NASA AMES Research Center, Moffett Field , CA
- *Development of Shape Memory Metal as the Actuator of a Failsafe Mechanism*
  V. G. Ford, M. R. Johnson
  Jet Propulsion Laboratory, Pasadena, CA
  S. D. Orlosky
  TiNi Alloy Co., Oakland, CA
- *SPOT4 Space Magnetic Recorder Mechanisms*
  A. Borrien, E. Vialatoux, J. L. Lhermet, and A. Didier
  Centre Nationale d'Etudes Spatiales, Toulouse, France

11:50 LUNCH

1:00 SESSION II

Mr. Peter Pawlowski, Session Chairman
DLR, Koln, West Germany

- *Development of the CLAES Instrument Aperture Door System*
  David M. Stubbs
  Lockheed Palo Alto Research Laboratory, Palo Alto, CA
- *A Soft Actuation System for Segmented Reflector Articulation and Isolation*
  Michael L. Agronin and Louise Jandura
  Jet Propulsion Laboratory, Pasadena, CA
- *A Dynamic Motion Simulator for Future European Docking Systems*
  Georges Brondino and Ph. Marchal
  Centre National d'Etudes Spatiales, Toulouse, France
  D. Grimbert and P. Noirault
  MATRA, Velizy, France
- *The Development of an Expendable Launch Vehicle Interface for an STS Deployable Payload*
  Ed Eubanks and John Gibb
  Lockheed Missiles & Space Company, Sunnyvale, CA

2:45 COFFEE BREAK

3:00 SESSION III

Mr. Russell P. Hacker, Session Chairman
Stanford University, Stanford, CA

- *Development of a Multipurpose Hand Controller for JEMRMS*
  N. Matsuhira, S. Iikura, M. Asakura, and Y. Shinomiya
  Toshiba Corp., Kawasaki, Japan
- *A Robot End Effector Exchange Mechanism for Space Applications*
  Barney F. Gorin, Fairchild Space Co., Germantown, MD
- *A New Six Degree-of-Freedom, Force-Reflecting Hand Controller for Space Telerobotics*
  D. McAffee, E. Snow, W. Townsend, L. Robinson and J. Hanson,
  Jet Propulsion Laboratory, Pasadena, CA
- *The Resupply Interface Mechanism RMS Compatibility Test*
  Stewart W. Jackson and Frank G. Gallo
  Fairchild Space Co., Germantown, MD

6:30 RECEPTION

THURSDAY, 19 APRIL 1990

7:00 Thursday Authors Breakfast
(Board Room II, Hilton Hotel)

8:30 SESSION IV
Mr. Robert Crawford, Session Chairman
AEC-Able Engineering Co., Goleta, CA

- *Relatchable Launch Restraint Mechanism for Deployable Booms*
  Robert M. Warden
  AEC-Able Engineering Co., Goleta, CA
- *The Connector Space Reduction Mechanism*
  M. Bruce Milam
  NASA/Goddard Space Flight Center, Greenbelt, MD
- *Driving and Latching of the Starlab Pointing Mirror Doors*
  Herbert R. Beaven, Jr., and Raymond R. Avina
  Lockheed Missiles & Space Company, Sunnyvale, CA
- *Orbital Maneuvering Vehicle (OMV), Three-Point Docking Latch*
  W. Neill Myers, John C. Forbes, and Wayne L. Barnes
  NASA Marshall Space Flight Center, Huntsville, AL

10:15 COFFEE BREAK

10:30 SESSION V
Mr. Douglas A. Rohn, Session Chairman
NASA Lewis Research Center, Cleveland, OH

- *Experience With Synthetic Fluorinated Fluid Lubricants*
  Peter L. Conley and John J. Bohner
  Hughes Aircraft Co., Los Angeles, CA
- *Tribomaterial Factors in Space Mechanism Brake Performance*
  Dr. Howard M. Hawthorne
  National Research Council of Canada
  Vancouver, BC, Canada
- *Positive Lubrication System*
  Dennis W. Smith and Fred L. Hooper
  Honeywell, Phoenix, AZ

11:50 LUNCH

1:00 SESSION VI
Dr. J. W. Kennel, Session Chairman
Battelle Memorial Institute, Columbus, OH

- *Active Control of Bearing Preload Using Piezoelectric Translators*
  Ted W. Nye, TRW Space & Technology Group, Redondo Beach, CA

- *Test Results and Flight Experience of Ball Bearing Momentum and Reaction Wheels*
  Dr. Werner Auer, TELDIX GmbH, Heidelberg, Germany
- On the Design and Development of a Miniature Ceramic Gimbal Bearing
  R. A. Hanson, B. O'Dwyer, K. M. Gordon, and E. W. Jarvis
  MPB Corp., Keene, NH
- *AX-5 Space Suit Bearing Torque Investigation*
  S. Loewenthal, Bearing Consultant, San Jose, CA
  V. Vykukal, Air-Lock, Inc., Milford, CT
  R. MacKendrick and P. Culbertson, Jr
  Sterling Federal Systems, Palo Alto, CA

2:45 COFFEE BREAK

3:00 SESSION VII
Mr. Sterling W. Walker, Session Chairman
NASA Kennedy Space Center
- *Report From Europe*
  David Wyn-Roberts
  European Space Technology Center
  Noordwijk, The Netherlands
- *Space Shuttle Operations - Considerations and Experience*
  Jay F. Honeycutt
  NASA Kennedy Space Center

6:00 EVENING SOCIAL ACTIVITIES

FRIDAY, 20 APRIL 1990

7:30 Friday Authors Breakfast
(Upper Seashells Room, Hilton Hotel)

9:00 SESSION VIII
Mr. William L. Cowart, Session Chairman
Lockheed Space Operations Co., Titusville, FL
- *Design of a Telescoping Tube System for Access & Handling Equipment*
  Alan C. Littlefield
  NASA Kennedy Space Center, FL
- *Clean Access Platform for Orbiter*
  Harold R. Morrison and Jesse L. Harris
  Lockheed Space Operations Co., Titusville, FL
- *Circularity Measuring System*
  Gary R. RohrKaste
  Thiokol Corp, Cape Canaveral AF Station, FL

- *Development of Cable Drive Systems for an Automated Assembly Project*
  Charles A. Monroe, Jr.
  NASA Langley Research Center, Hampton, VA

10:45 COFFEE BREAK

11:00 NASA KENNEDY SPACE CENTER OVERVIEW
Mr. James D. Phillips, Host Chairman
NASA Kennedy Space Center

PRESENTATION OF THE HERZL AWARD
Mr. Aleck C. Bond
NASA Johnson Space Center (Ret.), Houston, TX

CLOSING REMARKS
Dr. Charles W. Coale, General Chairman
Lockheed Missiles & Space Co., Sunnyvale, CA

12:00 LUNCH

1:00 TOUR OF NASA KENNEDY FACILITIES
Mr. Larry Schultz, Tour Coordinator
NASA Kennedy Space Center

Because of processing of the Space Shuttle for launch, the itinerary is uncertain and will be planned with regard both to safety and non-interference with work in progress.

SYMPOSIUM ORGANIZING COMMITTEE

Charles W. Coale	General Chairman	LMSC
Joel Burdick	Administrative Chairman	CIT
Joseph F. Wilson	Operations Chairman	LMSC
James D. Phillips	Host Chairman	NASA KSC
Sterling W. Walker	Host Vice-Chairman	NASA KSC
Charles S. Cornelius		NASA MSFC
David F. Engelbert		NASA ARC
Harvey H. Horiuchi		JPL
Stuart H. Loewenthal		LMSC
Ronald E. Mancini		NASA ARC
Jerry E. McCullough		NASA JSC
John W. Redmon, Sr.		NASA MSFC
John F. Rogers		NASA LaRC
Douglas A. Rohn		NASA LeRC
Gordon Rysavy		NASA JSC
William C. Schneider		NASA JSC
Donald Sevilla		JPL
Jesse D. Timmons		NASA HQ
Bowden W. Ward		NASA GSFC
Nathan D. Watson		NASA LaRC
David Wyn-Roberts		ESTeC

SYMPOSIUM ADVISORY COMMITTEE

Paul W. Bomke	JPL
Aleck C. Bond	NASA JSC (Ret)
H. Mervyn Briscoe	ESTeC (Ret)
Kenneth C. Curry	JPL
Otto H. Fedor	LSOC (Ret)
Frank T. Martin	NASA GSFC (Ret)
Peter A. Minderman	NASA KSC (Ret)
Alfred L. Rinaldo	LMSC (Ret)

Cycle Life Machine for AX-5 Space Suit

Deborah S. Schenberger
NASA-Ames Research Center

ABSTRACT

The need to complete cycle life testing of the new AX-5 space suit joints provided a unique opportunity for mechanism design. To test the joints, a complex series of motions needed to be performed with a high degree of accuracy. According to research on previous space missions, the elbow and knee joints of a suit could see up to 120° of oscillation. These oscillations could occur every second in the elbow and knee joints for approximately 70,000 and 17,000 cycles respectively. Coupled with this movement could be man induced loads of up to 150 lbs. in the elbow and 350 lbs. in the knee which could occur as often as every ten cycles. In trying to design a mechanism to meet these and other criteria, an interesting phenomenon was discovered in the motion of the joint itself. Contrary to what had been expected, as the top of the elbow or knee joint rotated through a fixed arc, the center of rotation of the joint moved several inches both horizontally and vertically. This was discovered after failing to find the center of rotation easily and resorting to using a three-dimensional model of the entire joint on a CAD system. Using the CAD system allowed each joint to be rotated incrementally in space so that the motion could be modeled accurately. Because of the motion discovered, the base of the joint had to be allowed to move as the joint was oscillated and yet be restrained in some manner so that the joint would follow an arc as it rotated on its bearings. The solution was a crank-rocker mechanism. A stepper motor was chosen to obtain the complex motion envelope within the accuracy range required. Using the CAD system again, the crank-rocker mechanism was laid out so that the link connecting the flywheel to the joint produced one oscillation of the joint for each rotation of the flywheel (Figure 1). The base of the joint would be free to move, but would withstand high torques imposed by a lever arm attached to the base of the joint with a small mass suspended from the end. After each ten cycles, an actuator would be activated by a programmable logic controller and a downward force would be applied, taking the slack out of a cable attached to the mass, and applying the necessary man induced loads. The final design performed as expected with no modification required in the mechanism. This project is currently ready for testing to begin.

INTRODUCTION

When the space station is being constructed, an advanced space suit will be needed by astronauts which will be more durable as well as more comfortable. One of two main prototypes for that new suit is the AX-5 space suit developed at NASA-Ames Research Center. One of the main advantages of the AX-5 suit is that it can be pressurized to 8.3 psi, which is twice the pressure of current space suits. Another advantage is its hard aluminum shell which maintains a

constant volume, thus making the suit more comfortable to work in since it will not bind. The suit is made up of 15 parts connected mainly by rotary bearings which allow almost a full range of motion. These features provide ease of movement, and the hard shell provides protection from space debris.

The criteria for testing the advanced suits was developed from extensive videotapes of previous space suit use during space shuttle missions, as well as from research done on prototype suits at Johnson Space Center (JSC). According to the data collected, the elbow and knee joints of the advanced suit would see a maximum of 70,720 and 16,474 cycles respectively for a typical mission in space. A joint cycle, as defined by JSC, was 80% of the full range of motion a joint could withstand. For both the elbow and the knee, the full range of motion was 120°. Eighty percent of this motion was therefore 96° in both cases. Coupled with these joint cycles would be man induced loads caused by the astronaut pushing from within the suit, which could occur ten percent of the time. Further research by JSC showed that an astronaut could exert a maximum of 20.8N (150 lbs.) on the elbow and 48.4N (350 lbs.) on the knee. Most of the testing was to be performed with the joint pressurized to 8.3 psi because the internal pressure would effect the movement of the balls inside the rotary bearings; however, after a set number of cycles, the joint was to stop in the vertical position, depressurize, cycle twice, and re-pressurize. The purpose of this depress repress cycle was to model the astronaut entering and exiting the suit.

A cycle life machine needed to be developed to perform testing on both the knee and elbow joints for the cycles and loads specified above. Other important testing criteria the machine needed to meet were to complete one joint cycle in one second, to insure that the joint was within one degree of vertical when the man induced load was applied, and to sequence the test so that a man induced load occurred every ten cycles.

DESIGN

In designing a mechanism to meet these and other criteria, an interesting phenomenon was discovered in the motion of the joint itself. Since the center point of the elbow and knee joint's top bearing surface (Figure 3), shown as the top circular disk, followed an exact circular arc, no problems were expected in designing a mechanism to cycle the joints through an arc of 96° measured from the center of rotation. What was not considered was the fact that the entire top face of the joint would be secured to a bracket, thus the top face created a plane which did not follow any type of fixed arc. This was discovered after failing to find the center of rotation for the joint by inspection and resorting to using a three dimensional CAD (computer aided design) model (Figures 2&3). Each segment of the joint was rotated incrementally through a series of angles, specifically 45°, 90°, 135°, and 180°. Having the multiple views in three dimensions showed that the center of rotation for the top face was indeed moving and that to compensate the base of the joints would have to move several inches both vertically and horizontally in order for the top face of the joint to follow a fixed arc. Figure 3 shows an average center of rotation which was chosen to illustrate the amount the joint would need to moye in a typical case. The testing criteria therefore altered so that the 96° would be measured by the amount of inclination of the top surface relative to the base.

Free movement of the base, shown as the bottom circular disk, was an unacceptable solution because there would be no insurance that the rotary bearing in the base of the joint would turn and keep the base of the joint vertical. In order for the joint to be properly tested, the rotary bearing at the base had to be forced to turn rather than be allowed to move out of vertical as the joint cycled because this vertical position was the only way to insure that an arc of 96° had been completed. Several designs for controlling the position of the base were discussed before it was decided that a long tube with a small weight attached to the end would greatly increase the torque the joint would have to overcome to move out of vertical (Figure 1). The weight was only one pound in order to not load the joint. This rod-weight combination was used in conjunction with a guide (not shown in Figure 1) which inhibited horizontal movement as well as movement out of the plane. The end of the rod-weight combination was then connected to a flexible steel cable with enough slack to allow the necessary range of motion. After ten joint cycles, the joint stopped in the vertical position and an air cylinder attached to the opposite end of the cable would remove the cable slack, applying the necessary load.

Design of the mechanism to oscillate the joint went through a similar design process. Oscillation, although it could have been accomplished by continual reversals with a stepper motor or AC motor, was not used because of the extreme wear on the motor from the constant reversals of direction occurring every second, the overhung load and the inherent fatigue of the mechanical components being compounded by the high speed and complete reversal of the inertial weight. In order to avoid these problems, a mechanism which used purely rotational motion from a motor was decided upon. Using a crank-rocker mechanism became an obvious choice after deciding upon rotational motion. A crank-rocker four bar linkage mechanism depends on the relative lengths of each of the links to determine its range of motion. Using the CAD system once again, several linkage configurations were tried until the exact configuration to give an arc sweep of 96° on the output link was determined with no singularities. This method was extremely visual and helped convey the concept of the design to the customer. Also, the effect of changing any one parameter could instantly be seen in the overall design. Once the layout of the linkages was known, the physical appearance and design of each of the linkages was developed (Figure 1). The most critical linkage, the bracket to which the joint attached, was designed in double shear and gusseted to prevent any flexure of the bracket when the man induced load of 48.4N (350 lbs.) was applied.

PNEUMATIC AND ELECTRICAL CONTROL DESIGN

The man induced load was just one part of the pneumatic control system (Figure 4) that had to be developed for the cycle life machine. The sequence began with the joint being pressurized, cycling ten times, stopping in the vertical position for a man induced load, and continuing with this routine for 16 sets of cycles. After 16 sets, the joint had to depressurize, cycle twice, re-pressurize, and continue with the original sequence. This entire sequencing needed to continue until the required number of test cycles were completed. During normal operation, air would flow continually into the joint through a flow meter, which also greatly constricted the flow. During the depress/repress cycle, this flow meter would increase the length of the test

by a factor of ten or more and was unacceptable; therefore, the flow meter needed to be bypassed so that the joint could be rapidly depressurized and re-pressurized. This was solved pneumatically by using two three-way valves rather than the obvious choice of one four-way valve (Figure 4). The first valve controlled whether air was received from the source or vented to the atmosphere. The second valve controlled whether the flow went through the flow meter or around the flow meter. This allowed depressurization and re-pressurization of the suit in less than two seconds.

Most of the components of the pneumatic system were determined by the needs of the electrical control system. To insure the integrity of the test, each step of the cycle had to be verified in some manner. Most of this was accomplished through the use of pressure switches which served as flags to the control system. For instance, the joint would not continue cycling if a certain pressure was not reached within the joint or if the cylinder pressure was not fully released on one side of the piston and fully activated on the other.

In order to control all of these criteria and still use the stepper motor and indexer for position control, the indexer was integrated with a PLC (programmable logic controller) which controlled and operated all of the peripheral hardware, such as the solenoid valves and pressure switches. The communication between these devices was accomplished using software provided with the PLC.

CONCLUSIONS

In order to accurately test the AX-5 space suit a complex series of motions needed to be performed which provided a unique opportunity for mechanism design. The cycle life machine design showed how three dimensional computer images can enhance mechanical design as well as help in visualizing mechanisms before manufacturing them. In the early stages of the design, potential problems in the motion of the joint and in the four bar linkage system were resolved using CAD. Since these problems would have been very difficult and tedious to solve on a drawing board, they would probably not have been addressed prior to fabrication, thus limiting the final design or requiring design modification after fabrication.

PROJECT STATUS

The AX-5 Space Suit Cycle Life Machine is currently manufactured, installed, and preliminarily testing has begun. Testing is expected to last for one month.

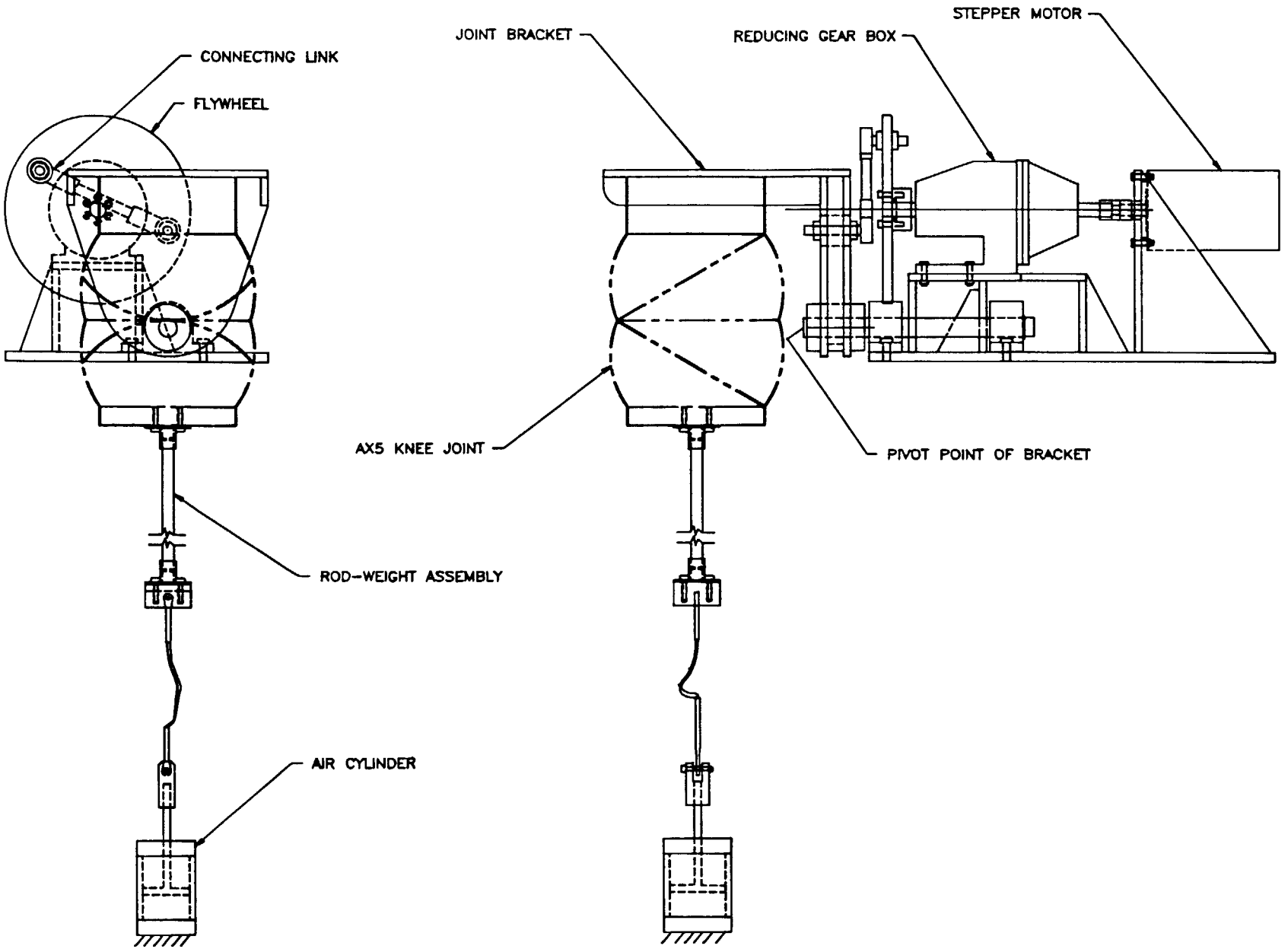

AX5 SPACE SUIT CYCLE LIFE MACHINE ASSEMBLY DRAWING

FIGURE 1

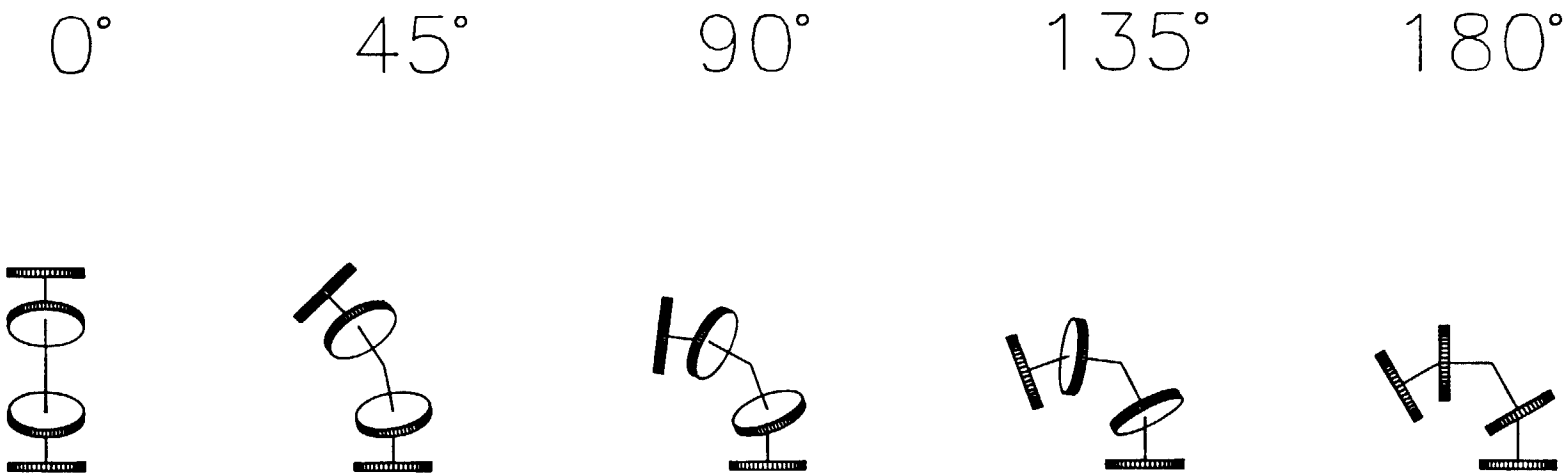

THREE–DIMENSIONAL MODEL OF AX5 ELBOW JOINT

FIGURE 2

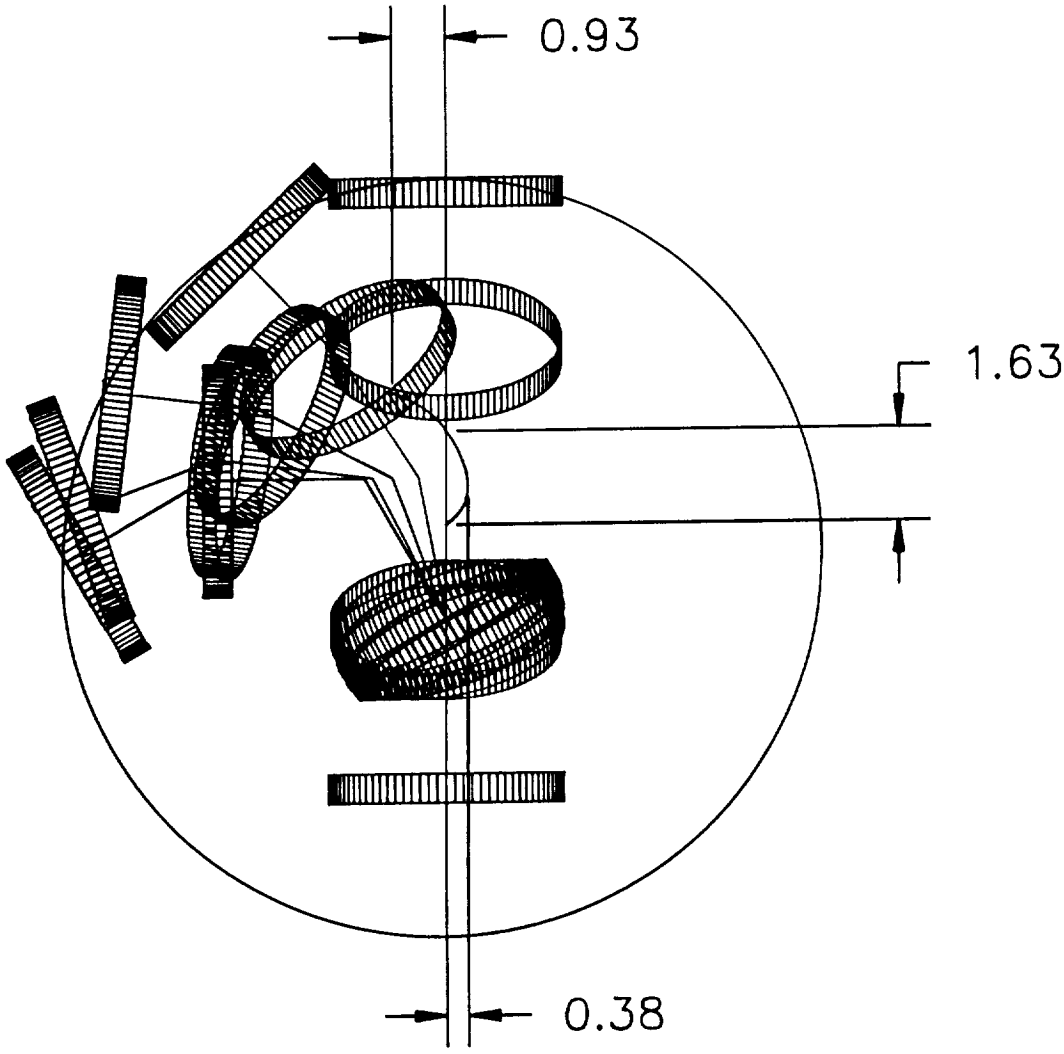

OVERLAY OF SEVERAL ANGLES OF ROTATION SHOWING MOTION OF AX5 SPACE SUIT KNEE JOINT

FIGURE 3

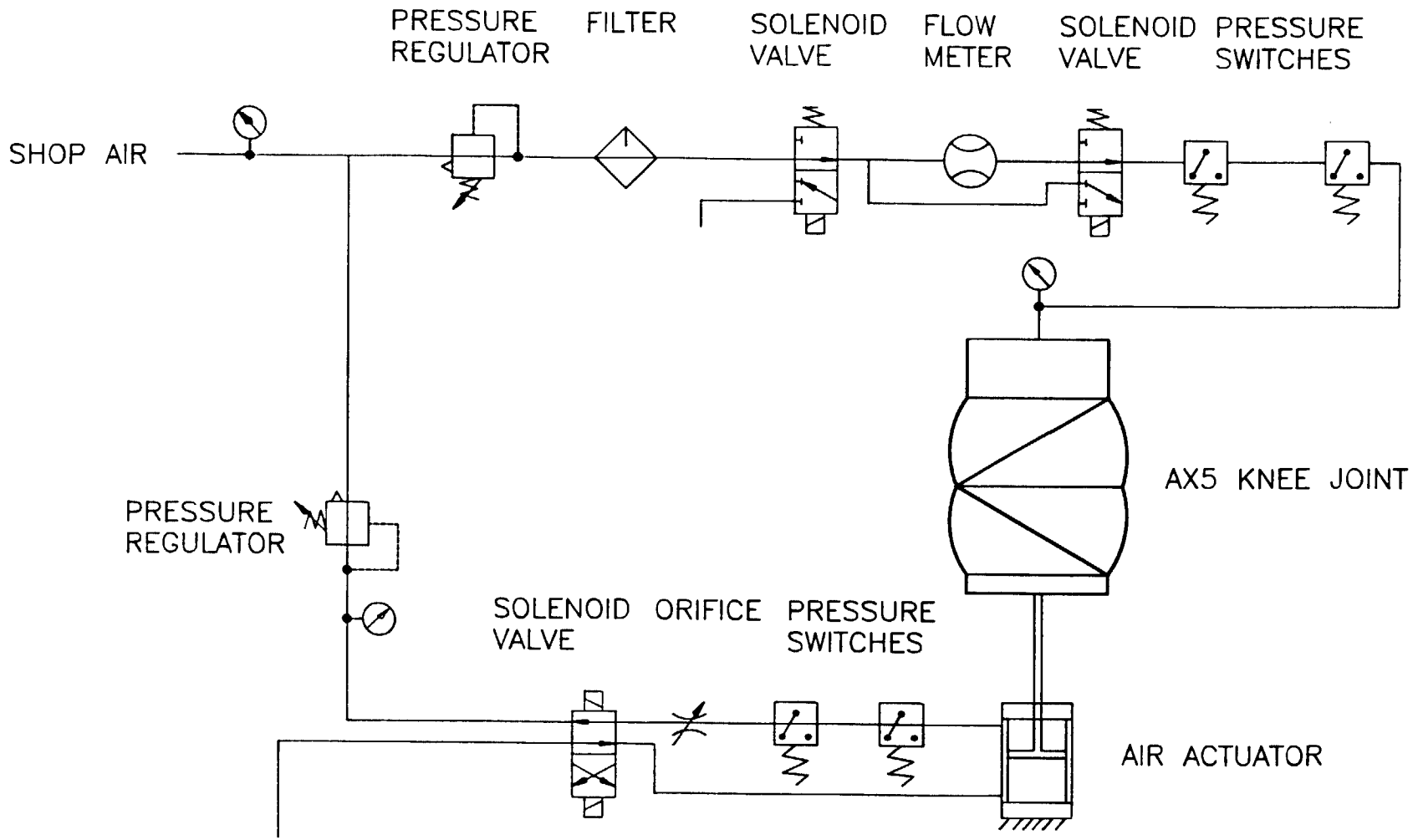

AX5 SPACE SUIT PNEUMATIC CONTROL DIAGRAM

FIGURE 4

DEVELOPMENT OF SHAPE MEMORY METAL AS THE ACTUATOR OF A FAIL SAFE MECHANISM

V. G. Ford*, M. R. Johnson*, and S. D. Orlosky**

ABSTRACT

A small, compact, lightweight device has been developed using shape memory alloy (SMA) in wire form to actuate a pin-puller that decouples the flanges of two shafts. When the SMA is heated it contracts producing a useful force and stroke. As it cools, it can be reset (elongated in this case) by applying a relatively small force. Resistive heating is accomplished by running a current through the SMA wire for a controlled length of time. The electronics to drive the device are not elaborate or complicated - consisting of a timed current source. The total available contraction is 3% of the length of the wire. This paper describes this device, the engineering properties of the SMA, and the tests performed to verify the design concept.

INTRODUCTION

The Wide Field Planetary Camera (WFPC) on the Hubble Space Telescope detects electromagnetic radiation in a broad wavelength range from infrared to ultraviolet. There are two WFPC units - the first (WFPC I) is expected to be launched in March 1990, and the second (WFPC II) is a replacement unit expected to replace WFPC I on a follow-up mission. During the qualification test cycle for WFPC I, it was observed that contaminant deposition on the lens surfaces and on the detector blocked short wavelength radiation, preventing the desired transmission and reception of ultraviolet light. Additionally, a window that seals the aperture of the optical path of WFPC I from the outside environment also reduced the transmission of ultraviolet radiation by more than 80%.

Several refinements have been adopted for WFPC II to improve the transmission of ultraviolet. More stringent controls on materials used in the instrument have been maintained. Additionally, a new detector with more sensitivity in the ultraviolet was developed. Finally, the aperture window was mechanized for WFPC II to swing out of the optical path after the satellite and its payload have been exposed to space long enough to have outgassed sufficiently.

* Jet Propulsion Laboratory, California Institute of Technology, 4800 Oak Grove Drive, Pasadena, California 91109

**TiNi Alloy Company, 1144 65th Street, Unit A, Oakland, California 94608

The Aperture Window Mechanism had to fit within a small available volume and to use existing electronics with as little modification as possible. If a failure occurs in the motor or electronics of the window drive, the mechanism was required to have an override system that moves the window to the open position. The override is known as a fail-safe function.

The SMA device that will be described in this paper is the component of the Aperture Window Mechanism that actuates the fail-safe function. If the motor or drive train of the window fails, this component releases a preloaded torsion spring that will drive the window to the open position. A design goal of this component was to have low mass and volume, to require little modification to existing electronic controls, and to be as simple as possible.

Figure 1 shows the Aperture Window Mechanism assembled in the mechanisms housing of WFPC II. A four-bar linkage has an over-center position that spring-loads and latches the frame of the window against a machined surface of the housing in the closed position. Figure 2 shows a cross-section of the mechanism actuator. A motor drives the wave generator of a harmonic drive that turns an output shaft. The coupling flange on the shaft houses the SMA fail-safe actuator to be described in this paper. The coupling flange also

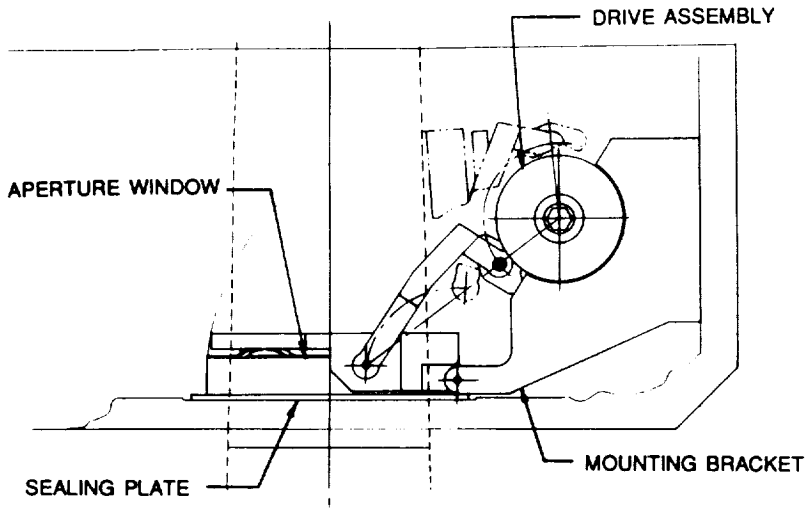

Figure 1. The Aperture Window Mechanism of WFPC II

has a feature that engages one end of the torsion spring. During normal operation, the torque from the drive shaft is transmitted through the coupling flange to the fail-safe actuator, through its plunger to the drive link of the four-bar. The drive link is flanged to retain the plunger in a slot and has a

feature to preload the other end of the torsion spring. When fail-safe action is required, the plunger is pulled, the torsion spring preload is released, and the drive link is forced to the open position.

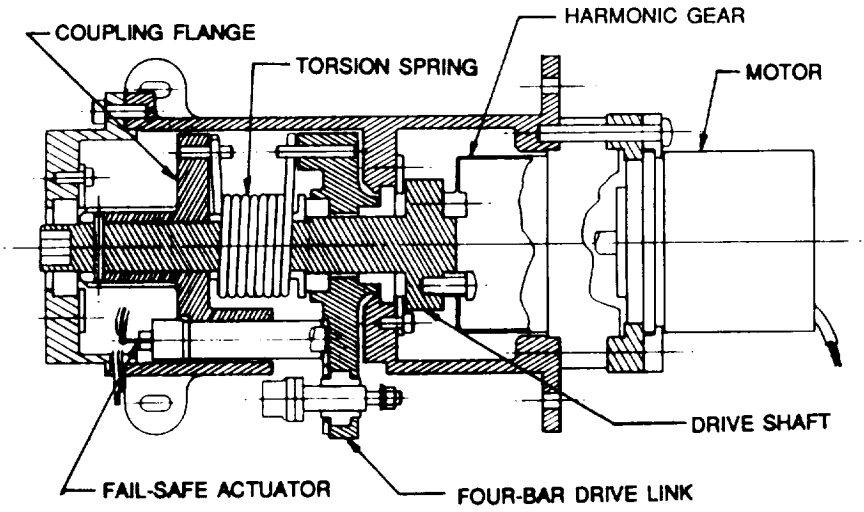

Figure 2. Cross-Section of the Aperture Window Mechanism Actuator

FAIL-SAFE ACTUATOR DESIGN

The fail-safe actuator is a pin puller device as shown in Figure 3. It consists of a preloaded plunger that engages a slot. A compression spring presses against a spring retainer that pushes the plunger causing it to be forced into the slot. Redundant SMA wires loop around the end of an insulated core which engages the plunger. When current passes through the wires they are heated and contract, pulling the core against the spring load and the friction load of the sliding plunger.

Figure 4 shows an exploded isometric of the actuator with its parts labeled. The interface to the Aperture Window Mechanism is the plunger, which is made of Nitronic 60 CRES. This material was chosen for its hardness of approximately R_c43 and gall resistance. The applied force is 31 pounds in shear across the face of the plunger. The hard material, combined with a fine surface finish, provides a low coefficient of friction when sliding is required against the coupling flange of the Aperture Window Mechanism. This flange is hard anodized aluminum with a surface infusion of molybdenum disulfide. The low coefficient of friction minimizes the required output

force from the actuator.

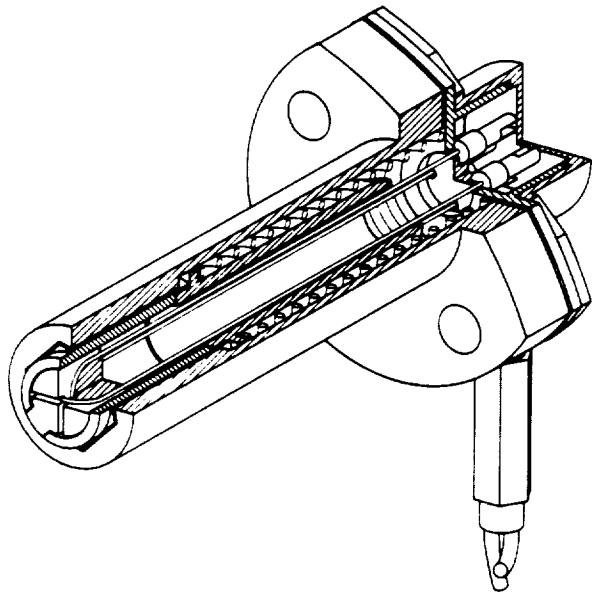

Figure 3. Cut-Away Isometric of the Fail-Safe Actuator

Since the SMA wires actuate by resistance heating, they must be insulated from each other and the rest of the mechanism. The core performs this function. It is constructed of a polyimide resin, Vespel SP-1, to provide the necessary insulation, heat transfer resistance, and force transmission from the wires to the plunger. The details of the cruciform shape in the end of the core guides and insulates the two SMA wires, allowing them to cross perpendicularly without contacting each other.

The spring in the actuator performs a dual function. It preloads the moving mass of the plunger assembly in the extended position. This provides resistance to unlatching during the expected vibration and shock environment and raises the natural frequency of the moving components. The spring also provides the force necessary to extend the SMA wires during their transition to the martensitic state by exceeding the chosen martensitic plateau stress of 5000 psi. This will be discussed further in the next section.

The spring insulator is made of Vespel SP-1 and prevents electrical contact between the SMA wire and the BeCu spring. It forms the mandrel for the spring locating it between the spring insulator and the bore of the device housing. The spring insulator also limits the stroke of the plunger assembly, preventing excessive strain in the wire.

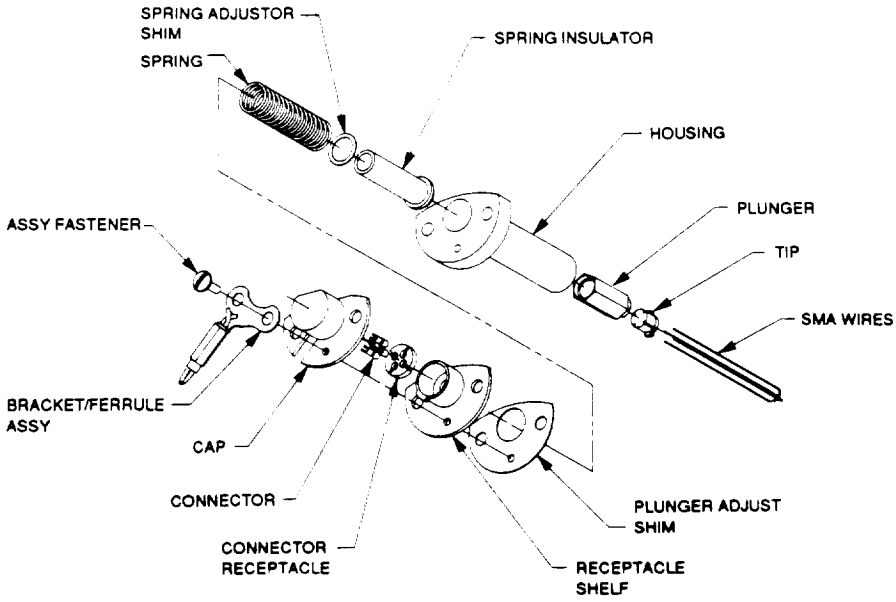

Figure 4. Exploded-View Isometric of the Fail-Safe Actuator

The housing is made of titanium 6Al-4V. This material was chosen for its ability to carry the bending stresses induced by the loading of the fail-safe actuator. A portion of the bore is hexagonal to prevent any rotation of the plunger that would twist the SMA wires. The hexagonal portion is anodized with a surface infusion of molybdenum disulfide that lowers the coefficient of friction and forms a non-galling surface in contact with the plunger.

Electrical contact and mechanical retention of the SMA wire is accomplished with special connectors. The connectors mechanically prevent the wire from slipping, thus are essential for maintaining the tension in the wires. The connectors are purchased from Raychem Corporation of Menlo Park and are shown in Figure 5. They consist of a beryllium copper socket that is slit like a tuning fork, forming tangs that are then bent outward. A ring made of a proprietary SMA alloy called Tinel is used to squeeze the tangs to grip a wire that passes through the socket. The Tinel ring is slipped over the outside diameter of the socket, forcing the tangs to return elastically to their unbent position. When the connector is cooled to -90 C (below the transition temperature of Tinel) the ring material transforms to low strength martensite. The stored spring energy of the tangs deforms the ring into a larger oval shape. The SMA wire is inserted through the connector at this lowered temperature. As the connector warms toward ambient temperature, the ring goes through transition to Austenite and returns to its original smaller round shape, pulling in the tangs and clamping the wire tightly. The

retention capability is high, typically above 22 Newtons (5 lb). For assembly, the connector is dipped into liquid nitrogen, the wire is slipped through the connector, then as the connector warms up, the wire is squeezed into place. The connector body is radiused to eliminate possible stress concentrations in the SMA wire that might reduce the life of the actuator. The high compressive force on the wire creates a gas-tight joint resulting in a low electrical resistance and a high corrosion resistance.

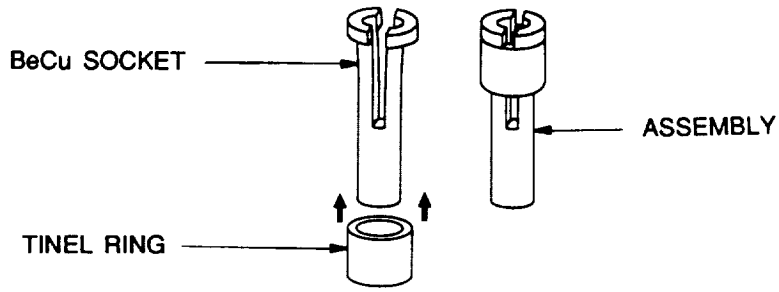

Figure 5. Connector Made of Beryllium Copper and Tinel

The actuator is assembled by first installing the connectors on the SMA wires, then sliding the looped wires through the plunger and the housing. The plunger core is inserted by looping the SMA wires around its two grooves. The spring insulator, the spring adjustor shim, and the spring are next inserted in order into the housing. The plunger shim and the receptacle shelf are placed on the housing flange. The spring is compressed and the connectors are slipped through slots onto their receptacle, which is guided into the receptacle shelf to form the preloaded assembly.

Pigtails are then soldered onto the connectors, after which the cap is installed with the assembly fastener. The wires slip over the lip on the receptacle shelf through a slot on the cap to be clamped in the bracket/ferrule assembly that is also attached to the housing with the assembly fastener. When the actuator is mounted to the coupling flange of the Aperture Window Mechanism, the mounting hardware redundantly retains the bracket/ferrule assembly and the cap against the flange. Figure 6 shows orthographic projections of the actuator with overall dimensions labeled.

Due to contamination concerns, all polymers in the fail-safe actuator were limited to be Vespel SP-1. This material meets the stringent outgassing requirements of WFPC II and has good engineering properties.

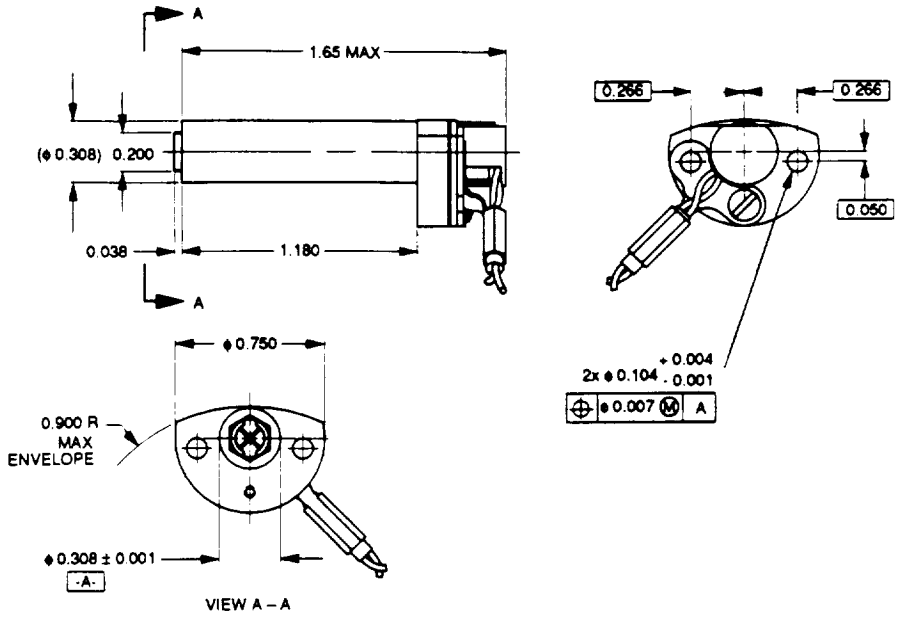

Figure 6. Orthographic Views of the Fail-Safe Actuator

PROPERTIES OF TITANIUM-NICKEL SHAPE-MEMORY ALLOY

Shape-memory alloy designates a class of materials which exhibit a pronounced change in stress-strain characteristics over a narrow temperature range. The most common of these, an alloy of nickel and titanium commonly referred to as Nitinol, was the material chosen for use in the fail-safe actuator.

The advantages of nickel-titanium shape memory alloy for this application are its large work output per unit volume (a typical value is 10 joules/cm^3 [1]), electrical resistivity which makes it suitable for direct Joule heating, a long fatigue lifetime, and a non-reactive chemistry. The disadvantages of TiNi are: thermal energy conversion efficiency is low (of the order of one or two percent), and the cycle rate is slow because of the need to dissipate heat. These are not serious disadvantages in the present application.

Good design practice in using shape-memory alloy wire includes careful handling and retention to prevent creation of surface defects which can propagate as cracks, limiting current so that the actuator is not overheated, and limiting strain to about three percent. Failure to observe these limitations can lead to unstable behavior in which the wire changes length from one cycle to the next, and to premature failure. A correctly installed and operated SMA wire actuator can be expected to operate for millions of

cycles with a high degree of repeatability.

There is no convenient method of soldering wires made of nickel-titanium. Swaged or crimped electrical connections which have sufficient mechanical strength to function as mechanical attachments, and which have long useful lifetimes, have been developed. For the purposes of this design, the beryllium copper-Tinel connector was chosen to enable easier inspection of the contact area.

Power requirements for driving an SMA wire are a function of the wire diameter chosen to produce the necessary forces, the length of material needed to perform the required movement, and the speed with which the actuation takes place. The physical size of the SMA actuator is chosen to meet mechanical requirements of the system. A relationship exists between the speed of actuation for an SMA element and the current density (amps/mm^2) through the material. Based on this relationship and the current available to perform the actuation, the speed of performance is determined.

Use of shape-memory materials for actuation requires an understanding of how the stress-strain properties of the metal change with temperature and how this change can be used to extract work. For most practical applications an SMA actuator can be treated as a two state device: in its low-temperature state, it is pliable and easily deformed while in its high-temperature state it is rigid and very strong. Referring to Figure 7, these two states have been illustrated on a stress-strain diagram. The high-temperature (austenite) state shows a rather conventional elastic curve. The low temperature (martensite) state, however, exhibits a pronounced plateau of plastic

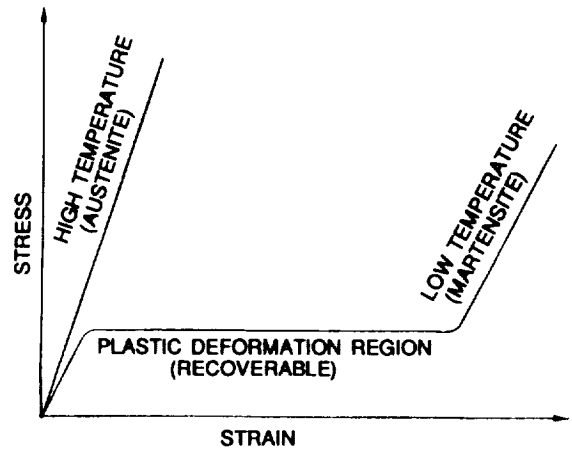

Figure 7. Stress-Strain Diagram of Austenitic and Martensitic States of Nitinol

deformation at a specific stress level. This plastic deformation is recovered (the material "remembers" its high temperature state) when heated above its transition temperature. A plot of length versus temperature illustrates this in Figure 8, in which a typical hysteresis loop appears. Depending on the processing of the material the plateau can occur anywhere in the range of from 0 to about 104 MPa (15,000 psi) [2]. Furthemore the maximum stress in the material was limited to 208 MPa (30,000 psi). This latter limit, based on operational experience [3], produces designs which are reliable over many cycles of operation. Much higher recovery stresses are possible, but cycle lifetime is thereby reduced.

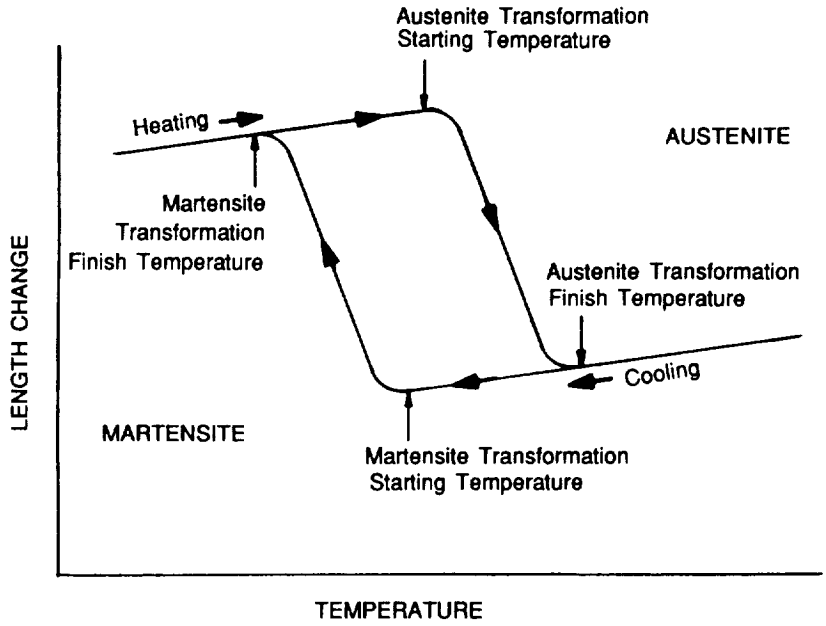

Figure 8. Length Change Versus Temperature of SMA Wire Under Constant Stress

Actuators take advantage of these changes in properties to produce useful work. In operation of the actuator, loading on the SMA wire comes from two sources: the return spring exerts a linearly increasing force during actuation, and a friction load is exerted when the pin moves. For test purposes, the friction load is assumed constant over the entire stroke length of the actuator. These two loads are shown in Figure 9. The entire actuation cycle is illustrated in this figure. As the cold wire is heated, the stress rises from point A to B before movement begins. When the friction load is overcome, the wire starts to pull the plunger, compressing the spring and increasing the stress to point C as the SMA completes the transition to austenite. When power is discontinued, the wire cools and reverts to the ductile low-temperature phase. The spring then overcomes the force of the SMA, and it elongates as the plunger returns to its original position.

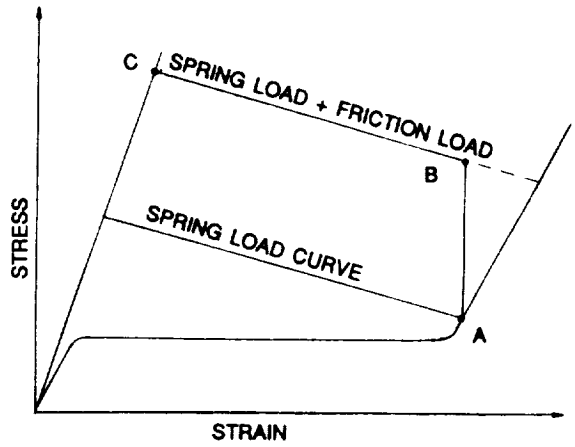

Figure 9. The Force Recovery Cycle of the Nitinol Wire Actuator

ACTUATOR PERFORMANCE TESTING

A simplified version of the flight component was developed by TiNi Alloy Company to test and demonstrate the concept of the SMA actuator. Figure 10 shows this breadboard set-up. SMA (Nitinol) wire 0.203 mm (0.008 in.) in diameter was looped around a grooved Vespel pin. The groove in the pin retained, guided and insulated the SMA wire. The Vespel pin slid through an aluminum flange mounted to a steel shaft. The pin was loaded with a compression spring to tension the SMA and to reach into a slot machined in an adjacent retaining flange. In the back of the pin, a rod was pressed axially into a small hole, then extended to carry the core of a Linear Variable Differential Transducer (LVDT) that measured displacement of the pin. The retaining flange was mounted on bearings that rotated around the steel shaft. A cable wound around the retaining flange at a radius of one inch. Torque loads were applied to the system by hanging weights from the cable to duplicate the torque load of the torsion spring of the Aperture Window Mechanism. The weights were removed and changed to alter the test load. The pin was placed at a radius of 19 mm (0.75 in.), thus the SMA wire had to pull against the friction generated by forces on the pin against the slots in the aluminum flanges. Thin aluminum tubes were crimped to the ends of the SMA wire to mechanically retain the wire and to provide an electrical contact surface where current-carrying wires were soldered. In this case, the crimping was considered for breadboard purposes only - not for aerospace applications.

As the device was actuated, force, current, displacement, resistance and temperature were monitored. The device was powered by a square wave current pulse generator controlled to deliver one pulse. The duration and amplitude

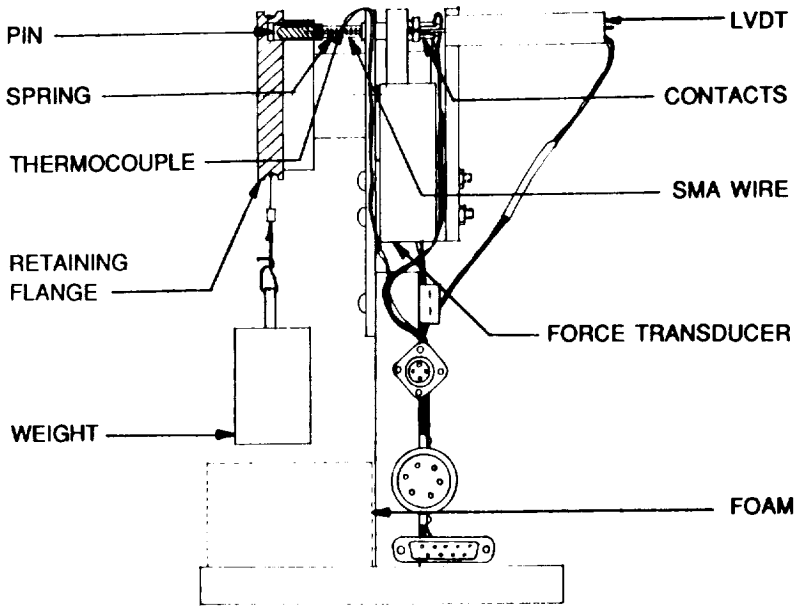

Figure 10. Breadboard Set-Up to Test the SMA Actuator Concept

were variable, with the current to the SMA monitored by measuring the voltage across a 1 ohm resistor and the pulse length read off the screen of a memory oscilloscope. A force transducer measured the force on the pin. Displacement was monitored using the calibrated LVDT voltage output. Resistance was measured by monitoring the voltage across the SMA wire. A thermocouple was epoxied onto the surface of the SMA wire to measure its temperature. Force versus stroke testing was done at TiNi Alloy Company, using a PC-based testing system that monitored the LVDT and force transducer outputs. At JPL, a memory oscilloscope was used to plot resistance, current, displacement and temperature versus time.

TEST RESULTS

Figure 11 shows a plot of TiNi Alloy Company test results comparing force delivered by the SMA wire versus distance moved by the pin. In this plot, a peak force of 12.1 Newtons (2.7 pounds) was reached, and the pin moved a total distance of .72 millimeters (.028 inches). The torque load applied to the flange was 497 Newton-mm (4.4 in-lbs) and the current was constant at 1.2 amps during this actuation. This peak force is equivalent to a peak stress of 187 MPa (26,900 psi) which is 90% of the stress limit of 208 MPa (30,000 psi) that was adopted to prevent elongation during cycling. During testing at JPL, the torque load on the flange was varied from zero to 565 N-mm (5.0 in-lb).

Current was also varied to demonstrate the device sensitivity to current stability.

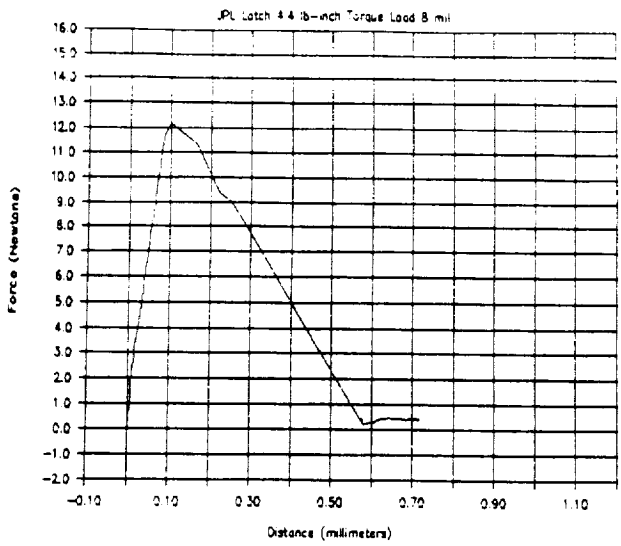

Figure 11. Force Versus Distance Plot of 0.008 Inch Nitinol Wire

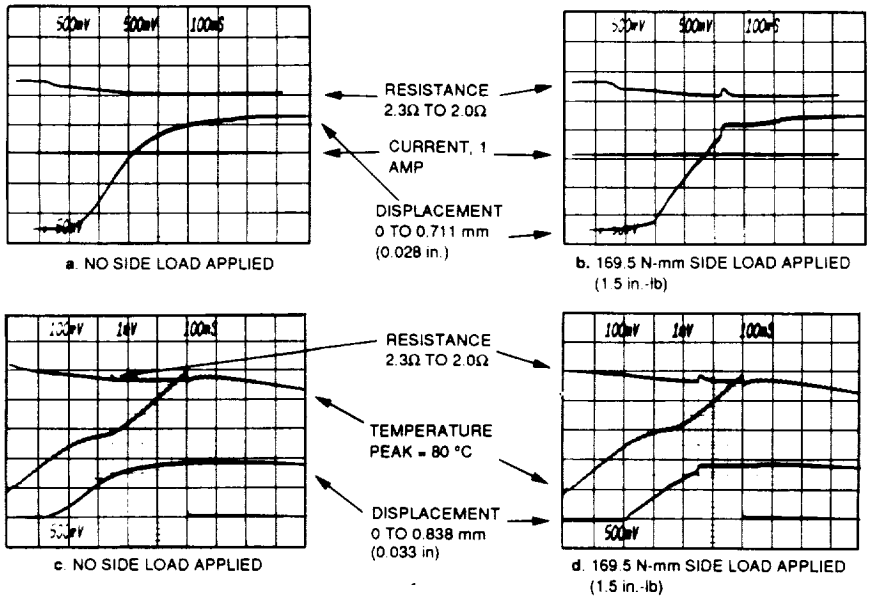

Figure 12. Oscilloscope plots showing device actuation under no-load and load conditions using one ampere current pulse through 0.203 mm (0.008 in.) diameter SMA wire.

Figure 12 shows oscilloscope plots where resistance, current, displacement and temperature were monitored. In Figure 12a, no torque load was applied, the resistance of the SMA wire went from 2.3 to 2.0 ohms as it heated, the current applied was 1 amp for a duration of 900 milliseconds, and the displacement of the pin was 0.86 millimeters (0.034 inches). Figure 12b shows a plot of the same conditions, except that a 1.5 inch-pound load is applied. The total displacement of the pin is identical to the unloaded condition, though the side load created a more pronounced step when the pin began moving and when it broke loose from the retaining slot. Figures 12c and d are plots of the identical conditions as 12a and b respectively, except that displacement, resistance and temperature were monitored.

In Figure 13, the displacement, resistance and temperature were monitored with an applied torque load of 1.5 in-lb with varying current conditions. The table at the bottom of the figure summarizes the four

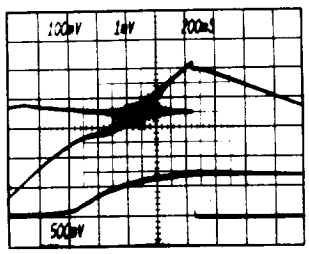
a. 0.75 AMPERE FOR 1.25 sec

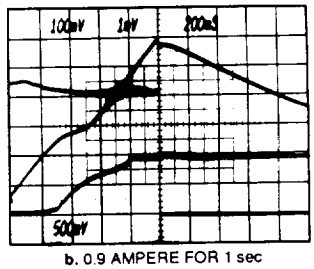
b. 0.9 AMPERE FOR 1 sec

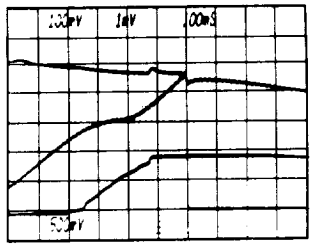
c. 1.0 AMPERE FOR 0.6 sec

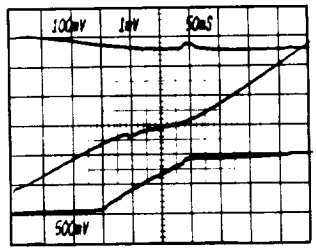
d. 1.25 AMPERES FOR 0.5 sec

	Current (amp)	Pulse Length (sec)	Peak Temp (C)	Movement Threshold Temp. (C)	Actuation Temp. (C)	Maximum Displace-ment (mm)	Actuation Time (sec)
a	0.75	1.25	80	47	N/A	0.55	N/A
b	0.9	1.0	112	48	91	0.91	0.80
c	1.0	0.9	122	48	72	0.89	0.54
d	1.2	0.5	122	49	65	0.89	0.28

Figure 13. Oscilloscope plots showing performance against a side load of 169.5 N-mm (1.5 in-lb) with varying currents.

conditions and the resulting data. At the lowest current shown, 0.75 Amps, actuation did not occur though the transition had begun. The difference in actuation temperatures is due to the time lag of heat transferred through the epoxy to the thermocouple. The peak temperatures achieved are a function of current level, pulse length, and heat transfer from the SMA wire.

In Figure 14, the torque load was increased to 5 inch-pounds and the current was 1.2 amperes with a pulse length of 0.5 seconds. This configuration was cycled over 200 times until failure. The failure occurred at one of the crimp contacts which started slipping, emphasizing the need for more careful anchoring.

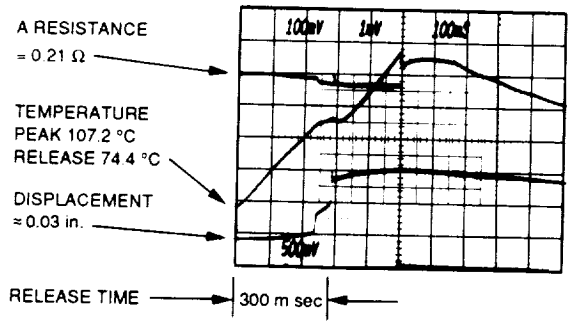

Figure 14. Plot of actuation with a side-load of 565 N-mm (5 in-lb) with an applied current of 1.2 amps for 0.5 seconds.

At the time of writing this paper, no further testing has been done. Full qualification testing is expected on an engineering model and on protoflight units to be built. Some of this testing is expected to be finished by the time the paper is to be presented, and will be included in the presentation.

CONCLUSIONS

The goal of the testing done was to establish the flexibility of this device to the varying environments it could potentially encounter. Testing in thermal-vacuum conditions was not funded at the time, so the tests performed concentrated on current variations and time variations in the laboratory environment. The testing was to establish minimum limits of current and time that would actuate the device, and to test the maximum limits to ensure that the device would not overheat within the expected times for actuation. Because life cycling and demonstration of the device was planned, the testing did not try to establish maximum conditions that would cause failure of the SMA wire. The minimum limits established were that actuation would occur

reliably with a current of 0.9 amps for a duration of greater than 0.8 seconds. The actuator performed well with a current of 1.2 amps for 0.5 seconds, reaching a peak temperature measured at 109 C. At the current level of 1.2 amps for 0.5 seconds, no degradation was observed during cycling. Figure 15 shows a plot of the data points collected at JPL superimposed on the

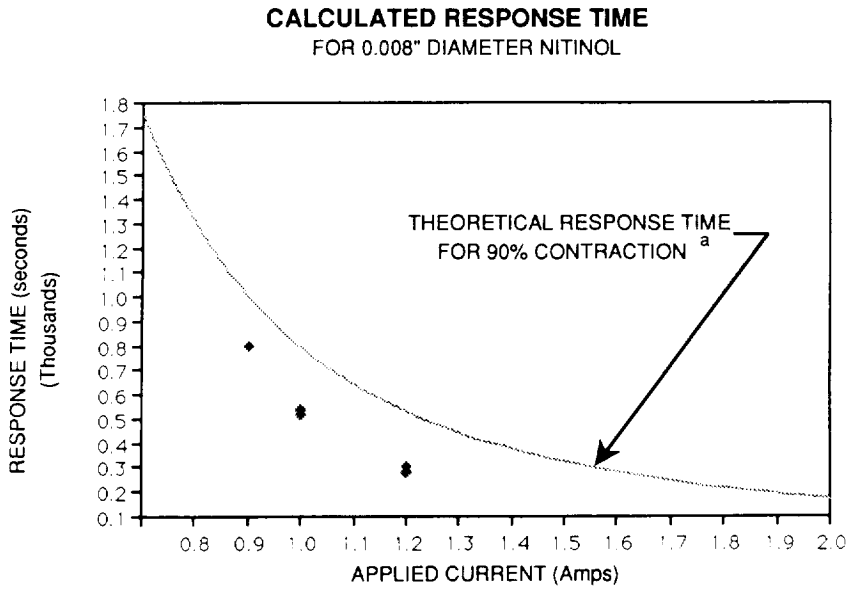

Figure 15. Response time versus current for 0.203 mm (0.008 in.) diameter Nitinol in still air.

calculated theoretical response curve for 90% contraction of the SMA wire. The curve represents the response time versus applied current of Nitinol wire in still air at 20 C. The breadboard device appears to be actuating at less than 90% contraction, and to follow the theoretical curve very closely.

To characterize this device adequately for aerospace applications, thermal-vacuum testing must be done. All the testing described above was done in a laboratory environment with an ambient temperature of 21 C. The heat transfer conditions in a vacuum will greatly affect current level and duration required for actuation. It is expected that actuation will occur at lower current levels, with shorter response times. The wire may overheat more readily. The testing that is planned will help establish response curves for the wire in a vacuum. The wire currently planned for the engineering model will have a larger diameter which will affect the current, response time and temperature relationship. This also will be characterized by further testing.

a. Based on empirical studies performed at TiNi Alloy Company.

STATUS OF THE ACTUATOR

Several design changes were required after the breadboard testing phase was completed. The required preload on the aperture window was raised which increased the friction load on the plunger. Because of this, the diameter of the SMA wire was increased to provide more force when actuated. Hardware development of the flight version of the fail-safe actuator is currently through the detail drawing stage. The fail-safe actuator is scheduled for design review in January 1990. Development and component testing are scheduled to take place from January through May of 1990. The procurement of the SMA connectors to be used in the design is already in process. The flight testing of the Aperture Window Mechanism is scheduled for November 1990 with assembly in the WFPC II to begin in January of 1991. The assembled WFPC II is scheduled to be sent to Goddard in August of 1992 for preparation for launch on the replacement mission.

REFERENCES

[1] A. D. Johnson, A. D. "Experimental Results on a Continuous Band Nitinol Engine," Proceedings of the Nitinol Heat Engine Conference, NSWC MP 79-441, Sept. 1978

[2] A. D. Johnson, "Training Phenomena in Nitinol," (IBID, Nitinol Heat Engine Conference)

[3] A. D. Johnson and S. D. Orlosky, "Electronic Braille Page Output Device Using Nitinol SMA," Phase II Grant Application Dept. of Health and Human Services, Dec. 1986

The research described in this paper was carried out by the Jet Propulsion Laboratory, California Institute of Technology, under a contract with the National Aeronautics and Space Administration.

SPOT 4 SPACE MAGNETIC RECORDER MECHANISMS

A. BORRIEN* and E. VIALATOUX*
J. L. LHERMET** and A. DIDIER**

ABSTRACT

The French National Earth observation program "SPOT" will enter into a new phase with the SPOT 4 satellite.

The design of this satellite will be quite different from the previous ones. One of the main new parts is the magnetic tape recorder that has been developed by Schlumberger Industries for the French Administration.

This paper presents the design of the magnetic tape recorder, which was derived from industrial knowledge and mission requirements; the main technical characteristics of this recorder; and the mechanical subsystems of the recorder and their locations and contributions to the final performance. The philosophy of the development program, required to achieve the desired performance and reliability for each flight model, is described, and information on the schedule and current development is presented. The components of the tape plate system, which are subjected to heavy mechanical operation, fatigue, and wear in the thermal environment of the mission, are discussed. These three specific system components are described:

- transmission belts
- tape rollers of the recorder
- reel hub ball bearings

For each of these components, a description of its function in the recorder is given, as well as the mechanical stress imposed during the various operational phases. These aspects directed the technical approaches taken during the detail design.

The qualification testing program, which was used to verify the design safety margins, is described. Finally, the first test results of a functioning model of the flight system are presented. These results demonstrate the operation of the mechanical systems under simulated mission environmental conditions.

*Centre National d'Etudes Spatiales Toulouse, France
**Schlumberger Industries Velizy, France

INTRODUCTION

Obviously, an earth observation satellite must be able to fly over any part of the world. However, it only can transmit its pictures when in the visibility of a ground station. Because of the number of stations and their geographical locations, the satellite needs to store these data and restore them later. The storage of high quality pictures requires a large memory capacity and, therefore, the use of a numeric recorder.

Schlumberger Industries has worked for many years in the field of magnetic recorders and has built machines with a tape density of 33,000 bits per inch, magnetic heads with 42 tracks in one inch, and a bit error rate better than 10^{-7}. These recorders are very often used in European industrial centers, in satellite ground stations, and in mathematical centers. Schlumberger has designed different prototypes for avionics, marine, and submarine applications in the United States and Europe. This great competence, acquired from laboratory experience and on-board machines, has allowed this company to study and design a space magnetic recorder for French programs. A version of this recorder has been adapted for use in the SPOT 4 program satellite under a CNES contract. This equipment is composed of two boxes. The first box contains the signal treatment electronics, the electrical interfaces, and the detection and error correction code. The second box, which is pressurized and sealed, contains the mechanical system (see fig. 2). As for all satellite mechanisms, the Space Magnetic Recorder (SMR) has to satisfy the reliability requirements of the satellite mission.

THE SMR CONCEPT

The SPOT 4 mission is characterized by its life duration in orbit of four years, associated with an 1800-hour recorder operation life time. The actual earth-imaging is achieved by a sequence of very short frames, which leads to a great number of start-stop sequences for the recorder (in the order of 45,000 cycles). The SMR design reflects the need to survive the severe vibration constraints imposed by the launch phase.

The quantity of information to be stored requires a digital recording in the order of 50 Mbps and a total capacity greater than 100 gigabits. The quality of the images obtained is directly related to the bit error rate (BER). The use of the high-density digital record mode, in the order of 20,000 bits per inch, is associated with an error correction code permitting the achievement of BER performance better than 10^{-6} during the recorder's life cycle.

This advanced performance is obtained for recording and playback by means of linear magnetic heads with very narrow track width (280 microns) on a magnetic tape 3300 meters long (on a reel 380 millimeters in diameter) winding at a constant speed and tension with very high stability. The magnetic tape consists of a polyethlene terephtalate (mylar) base, a polyester urethane and carbon backing, and a front surface of an oxide iron pigment (F_2O_3).

Due to its nature, exposure in a vacuum is forbidden. Moreover, the performance of the recorder is directly related to the friction of the turning mechanisms (ball bearings). The

current technique of lubrication with an Andok C type grease is a proven technique. The use of a solid lubricant, such as MoS2, would be incompatible with the performance objectives and with the life cycle of the mission. It is therefore necessary to enclose the magnetic tape and the transport mechanisms in hermetically sealed enclosures, pressurized with nitrogen (about one bar). The magnetic tape and head interface possess an optimal temperature range and humidity level that requires active thermal control within the container.

This enclosure must guarantee a perfect leakproof condition during storage on the ground and during the mission in order to ensure the mechanical interface between the tapedeck and the satellite platform and to provide for thermal exchanges in orbit.

The principal part of the recorder tape deck is a mono-block transport with coaxial, counter-rotating reels supplied with a double capstan loop in which the magnetic heads are situated. This configuration responds to the need to minimize the variations of the kinetic moment in orbit and to guarantee a very weak winding error (flutter), while creating a zone of high tape stability in the vicinity of the magnetic heads.

THE MECHANICAL FUNCTIONS

The mechanisms required to reel and wind the magnetic tape must accomplish three main functions, specifically, the guidance of the tape during its winding, the tape tension servo, an the tape speed servo. The guidance is an essential function of the recorder. In fact, the performance of the recorder depends on the transversal stability support and on the position accuracy between the forward operation used while recording and the reverse used in reading. The selected coaxial reel's geometry necessitates two parallel reeling planes and requires an inclined plane to allow the magnetic tape to pass from the low plane to the upper plane. This plane change generates some threading constraints that are minimized by the geometry of the tape path. On these reference planes are mounted the winding rollers that guide the magnetic tape in a very precise manner. The capstans have an essential role in the winding. Their geometric precision must be excellent and the pairing of their diameter must be better than 2.5 μm. The pollution coming from the magnetic heads in contact with the oxide and from the rolling friction is a source of errors. The elimination of this pollution is achieved by two cleaners placed on both sides of the heads. The oxide from the magnetic tape is continuously rubbed towards the twisted fibers of a cleaning tape driven by a motorized device programmed in advance.

The tension servo, maintained by the reel motors, guarantees a constant tape tension as the tape passes from one reel plane to the other. This servo is established by coaxial reel holders driven by a synchronous belt and direct current servo motors.

The tape tension at the reel input and output is regulated by the means of spring sensors which provide a tension reference. A braking mechanism of metallic strapping, associated with the tension spring/sensor system, is activated at each stopping of the recorder and the emergency condition of an accidental power loss. This device avoids the creation of

tape loops that would jeopardize the mission. Finally, a mechanism locks the two reels at launch.

The speed servo is implemented by means of a double capstan loop that helps change the plane of the tape path. Each capstan is driven by a servo motor of the same type as those of the reels. These motors are equipped with a disk encoder and an optical electronic unit, providing the tachometer function. The capstans also serve to ensure magnetic tape guidance and winding at a constant speed (flutter less than 0.5 percent). They also provide a local increase in tape tension, which helps eliminate any external mechanical disturbances from this zone.

MAIN CHARACTERISTICS AND DESCRIPTION

The main characteristics of the machine are listed in Table 1. The mechanical packaging is composed of an airtight box, the tape plate with all mechanisms, the power supply, and the control loops electronics. This packaging weighs 95 kg and is 700 mm in length, 600 mm in width, and 410 mm in height. The power consumption is 180 W-hrs and occurs in the reproducing mode. The SMR can be operated over a small range of temperature (+10 °C, + 40 °C).

There are numerous mechanical components throughout the machine. There are more than 100 ball bearings of different sizes, 8 electrical motors, 2 synchronous belts, 2 optical encoders, 12 tape rollers, 10 angular position sensors, springs, and a wide range of precision-machined parts. For a reliable design and the best mechanical performance, numerous materials are used. Common materials such as aluminum, magnesium, and titanium alloys are used. However, also incorporated are unusual space mechanism materials such as "numetal" (iron-nickel), cast steel, copper, polymers, and elastomers. Some of these materials are covered with a surface treatment of molybdenium disulfide, anodic oxidation, passivation, nickel plating, or chromium plating. New manufacturing and assembly techniques have been studied and space qualified for this program; for example, chromic anodic oxidation on magnesium.

MAIN STEPS OF THE DEVELOPMENT PLAN

The development of SMR proceeded along the following steps:

Concept Development of All Mechanical Functions and Associated Components

This phase consisted of technology validation programs for the manufacture and assembly of parts that require the use of special materials, often unknown to the European space industry. This was the case, for example, for the reading heads and the capstan motors.

Some components, such as belts, are mass produced for ground applications; manufacturers have only incomplete technical data on them. This situation led to numerous evaluation tests with many samples.

This phase ended with a functional analysis and FMECA on the whole mechanical architecture of the machine. These analyses allow the identification of critical components.

Qualification of Critical Components and Functions

This key phase gives the knowledge of safety margins in accordance with mission requirements. Before the beginning of qualification tests, is is important to ensure that the flight components are exactly the same as the test components, and that the same manufacturing and assembly procedures are used.

It is also important that each component be tested in the same environment (mechanical, thermal, electrical, atmospheric) as it will see in flight. Several functions are distributed in different parts of the machine and only a test with a representative model gives significant performance and lifetime results. That is the case for the rollers, the tape-head interface, and the emergency braking mechanism.

These components are tested on a model very close to the flight machine. Software and hardware installations around the test machine must also be very close to flight standards.

Identification Step

The objective of this step is to demonstrate that, in space conditions (vibrations + orbital lifetime + mission cycles), the BER is less than 10^{-6} for the entire mission life. These tests also validate the control loops of tape tension and tape speed, the cleaning of the tape and, the braking and the locking mechanism.

CNES has decided to conduct three global tests on three machines. With these tests we can, experimentally, check theoretical studies and investigate reliability. This is necessary due to the relative inaccuracy of theoretically calculated results in the field of mechanics.

Manufacture and Acceptance Tests

Flight models have to undergo acceptance tests in order to avoid "premature breakdown" and to be declared "fit-for-flight."

Philosophy of Development Steps

To follow the whole development cycle step by step, will require too much time and will be incompatible with the SPOT 4 program schedule. On the other hand, to conduct phases in parallel will inevitably result in premature decisions and tends to expose the program to dramatic consequences. The aim, then, is to find the best overlap between phases and to put

in place some technical "go aheads." For example, to begin the parts qualification, it is necessary to have the knowledge of the following documents:

- calculation notes and definition plans
- mission profile
- FMECA (failure mode effects and criticality analysis)

The analysis of these documents involves results which are combined to define critical elements and to stipulate corrective actions. Critical mechanical aspects are gathered in nine categories:

- vibrations during launch
- thermal stresses
- in-orbit lifetime
- ground storage
- aging
- pollution sensitivity or emission
- technology sensitivity
- manufacturing divergencies
- assembly and adjustment procedures

Qualification plans have to demonstrate the good behaviour of components for all identified critical aspects. Manufacturing criticality analysis leads sometimes to procedural improvements and to define key points for sensitive operations. The beginning of the identification step occurs necessarily before the end of qualification because the storage and aging tests are incompressible. Decisions are based on partial results, knowing that the final results could impact the design of flight models. The decision to start manufacturing flight models requires the careful conclusions of all the qualification test experts.

State of Development

Today, seven flight models have been ordered for planned French earth observation missions. Qualification tests on component lots are still going on. Tests on representative models have been done and have validated:

- tape-head interface
- vibrations behaviour
- BER performance over the thermal range
- control loops for speed and tape tension
- mechanisms lifetime

The first test on an identification model began in 1989. Vibration qualification was accomplished in July 1989. The electronic cards acceptance tests are currently in progress. These tests will be followed by life cycle endurance tests. All mechanical components for all the flight units have been almost fully procured.

TRANSMISSION BELTS

The Role of Belts

The first function of the drive belt is to allow the electric motor to drive the reel hub shaft, through a speed reduction, allowing the use of a smaller motor. When the machine is in the reading or recording mode, the belt has to guarantee a smooth takeup of the tape and a constant tape tension. When the machine is in the stop or startup mode, the belt must resist the transient stresses due to the kinetic momentum variation and not disturb the control loop (see fig. 2). In case of an electrical power failure, the emergency braking device introduces a high friction torque to avoid unrolling of the tape, and puts a high traction to the belt. The second function of the belt occurs during launch. To lock the reel hub and avoid tape destacking, a steel strap is taut on the toothed pinion belt, and the friction between strap and belt must prevent any rotation of the reels.

Design Requirements

The mission imposes a high reliability for any component for which a single failure leads to the loss of the recorder. Mission requirements are:

- emergency braking : 24 ground activations + 8 flight activations
- locking activations : 8 ground activations + 1 launch activation
- ON/OFF cycles : 45,000
- lifetime operation : 200 hours on ground + 1,800 hours in orbit

Other requirements are derived from the actual mechanical design:

- belt sliding is forbidden, thus a synchronous belt is used
- motor size and tape speed require a high transmission ratio
- the compact requirements necessitate a nonstandard transmission size
- the belts directly affect the final performance of the tension control loop

Therefore, the dynamic disturbances generated by the transmission have to be low and the belt must have good rigidity and damping behaviour. To satisfy all these requirements, polyurethane synchronous belts (SYNCHRO FLEX), reinforced with a steel wire manufactured by Continental, were chosen. These belts have the following qualities:

- synchronous drive
- no relaxation
- good wear resistance
- small size
- high power transmission
- low pre-tension; thus, low load on bearings
- high transmission ratio

- high resistance to overloads
- small pitch; thus, smooth transmission

Evaluation Program

The belt design development described above led to the identification of sensitive parameters and performance of elementary tests. These tests give us the knowledge of functional limits and a first estimation of safety margin. Moreover they help to determine the critical parameters list for the hardware and to optimize the preparation of the qualification program, especially for the definition of a representative mechanical environment, the choice of sensors and measurements, and identification of acceptance criteria. This approach led to the identification of the following tests:

- static characterization
- traction on the belt
- traction on the steel wire
- shearing of belt teeth
- cycle fatigue testing
- alternate overload cycles up to rupture

Results

Belt tests have pointed out the following critical parameters:

- pollution : scraps of polyurethane and aluminum dust coming from belt and pinion are scattered throughout the mechanism at the completion of the life mission time.

- steel wire hooking in the polyurethane matrix : the external turn of the reinforcing wire may get outside the polyurethane matrix.

- failure mode of belt : tearing of tooth belt due to crack progression on tooth root.

- failure mode of pinion : indentation and wear of the tooth tip due to friction on steel wire after erosion of the polyurethane matrix.

- life time : experimental margin seems to be comfortable for mission requirements.

- static characteristics are not crucial.

The evaluation program has confirmed the belt design obtained by analysis: (see fig. 3)

belt length : 500 mm
belt width : 6 mm
belt pitch : 2.5 mm
pinion teeth : 24

wheel teeth : 151
ratio : 6.29

Manufacturing Improvements

Manufacturing of the belt qualification lot began after the end of the evaluation program and the expert analysis assessment. To avoid the protrusion of the wire from the polyurethane matrix during life, the following actions have been proposed to the manufacturer:

- winding the wire around the mold at reduced speed in order to have a regular wire turn pitch
- final quality control using X-ray inspection

To minimize manufacturing variations, it was decided to always use the same mold for all belts. To this end, a new mold has been constructed for this application. All the wire is taken from the same reel and is tested at regular intervals. To prevent from mixing evolution, all the belts have to be manufactured from the same polyurethane batch material. Samples of the polyurethane are cut off after polymerization to check the chemical characteristics. The final acceptance of the belt lot is given after mechanical tests have been completed on several belts, as mentioned in the evaluation program. The whole lot can be rejected if the results are not consistent.

Qualification Plan

The reliability required for this component and the dramatic consequences of a failure required the test evaluation of a larger sample of belts. As the lot contains only about 80 belts, the number of destructive tests must obviously be limited. The following summarizes the qualification programs:

- 28 belts are randomly selected for qualification. Both visual and binocular inspection and weighing are done to have a reference condition .
- 10 belts are destroyed with:
    - teeth shearing
    - chemical analysis
    - wire and belt traction
    - fatigue
- 2 belts are mounted on a demonstration model of the recorder mechanisms for vibration testing.
- 10 belts (8 + two previous ones) are mounted on simplified models to expose them to a representative mechanical environment : reel and tape inertia, braking loads, speed variation.

- 8 belts are used for storage : 4 of them are stored under tension and the other 4 are stored in a relaxed state. The storage lasts at least 4 years.

TAPE ROLLERS

Tape Roller Function

The tape rollers are used for transition of the tape from one reel to the other and guarantee the transverse stability of the tape during reading and recording sessions. There are 12 rollers on a machine and each of them has a specific role (see fig. 1). Two rollers guide the tape at the reel entrance or exit. Four rollers allow the transition between the two reels planes and are, for that reason, slightly tilted. Two other rollers guide the tape towards the capstans. Just before the reading heads, two identical rollers located on the capstans motor axis provide a constant drag on the tape. Lastly, two rollers are mounted on the tape tension sensors. They are movable and are part of the tape tension control.

Tape Roller Requirements

The rollers present some critical design constraints. They must rotate during more than 2,000 hours of operation at 1,000 rpm and endure 45,000 start/stop cycles, without damaging the tape by wear pollution, lubrication pollution, or adhesion while the recorder is in stand by mode. The mission life cycle for each roller is approximately 1.5×10^8 revolutions (see fig. 4). A primary concern is the problem of sliding between the roller and the tape when the recorder starts and stops. This sliding increases the wear. It is very difficult to avoid sliding on every roller because of the contact angle, which can vary from 18° to 210° depending on the location of the roller on the tape plate. Additionally, some rollers are in contact with the oxide side of the tape while others are in contact with the back side. Thus, two different tribology and wear mechanisms act on the roller coating.

Rollers Design

To define the best roller geometry, material, and coatings, a test program was implemented. Delrin and aluminum alloy were tested. Aluminum was better for machining accuracy. The wear volume was measured by superposition of the roller profile before and after the test, and by calculation of the area between the two curves. Worn surfaces analysis gives the shape of profile accommodation. Three shapes can be achieved : bi-conical shape, cylindrical shape, and barrel shape. Tests show that the cylindrical shape gives the best results. After a literature search, two surface coatings were selected for evaluation; specifically, a chromic oxidation coating with a 5-μm depth and a hard anodic oxidation coating with a 25-μm depth. Two similar endurance tests on two recorders have been conducted. The choice criterion is based on transverse stability performance of the tape, wear volume generated by the rollers, and pollution analysis. An optical monitoring technique was employed to check the stability of the tape and detect local substrate appearance. The test was divided into three stages with intermediate wear measurements obtained without hardware disassembly. An

evaluation was made after 70,000 start/stop cycles and 2,200 hours. The two coatings demonstrated good performance for transverse stability, while wear volume was less with the chromic anodic oxidation coating.

Based on these test results and the fact that the thermal characteristics of the anodic coating are more well known to Schlumberger, the chromic anodic oxidation coating was chosen for the roller coating.

Manufacturing Improvements

Consistent manufacturing results for both the qualification and flight rollers must be achieved. Material uniformity is obtained by tooling every roller from the same bar of metal. Chemical and ultrasonic checks are conducted on the raw material. The machining process includes thermal treatment, and several samples are preserved for coating analysis. These samples are cut into sections and, then, the depth and the adhesion of the coatings is inspected under a light microscope. The diameter, the profile accuracy, and the roughness are carefully measured on each roller to detect any geometrical variation or distorsion due to thermal surface treatment. The assembly and adjustment procedures have been developed to allow precise reproducibility of the tape transverse stability on each recorder.

CONCLUSION

Schlumberger Industries has manufactured the first European Space Magnetic Recorder, with the collaboration of Sextant Avionics and to CNES requirements. Due to the complexity of the tape plate mechanisms, many single-point failure modes exist. To provide more assurance of mission success, through redundancy, two recorders shall be placed on the satellite. The success of this enterprise is dependent on good coordination between various professions : mechanics, electronics, magnetic science, and thermal and computer science. The first in-orbit operation is scheduled for 1993.

CHARACTERISTICS OF THE SPOT 4 RECORDER

RECORDING CAPABILITIES	
Two channels at	25Mbits
Total capacity	> 100 Gbit
REPRODUCE PERFORMANCE	
Reverse direction only	
Bit error rate	$< 10^{-6}$
PHYSICAL PARAMETERS	
Operating temperature	10°C < 40°C
Mass	130 kg
Power requirements	160w (record) 220w (reproduce)
LIFE TIME	
Life time in orbit	> 4 years
Tape running hours	> 1800 hours
Head life	> 8500 km
Start/stop	> 45 000
RECORDER CHARACTERISTICS	
Tape width	1 inch
Reel diameter	15 inch
Tape length	3200 m
Record/repro speed	1,35 m/s

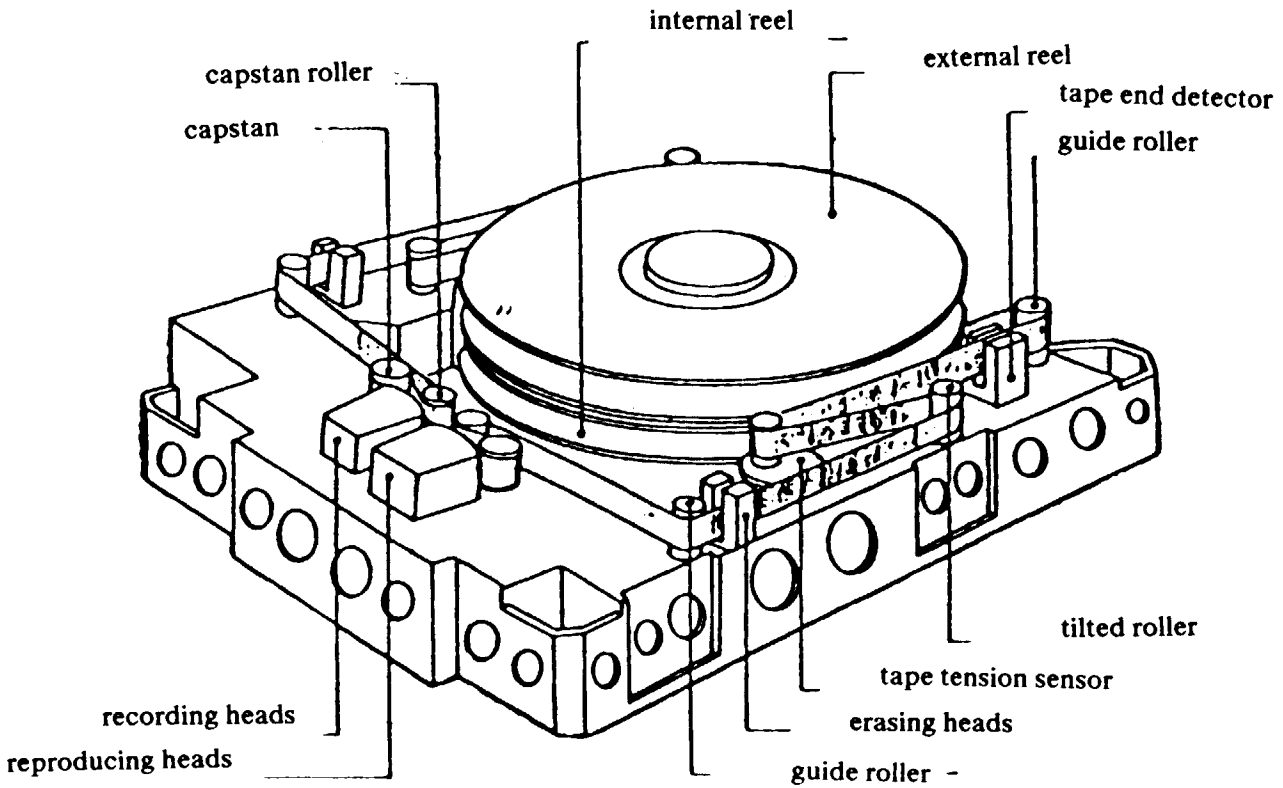

FIGURE 1 : Space Magnetic Recorder (S.M.R.) - Mechanical part

FIGURE 2 : Internal view of the running tape mechanical part

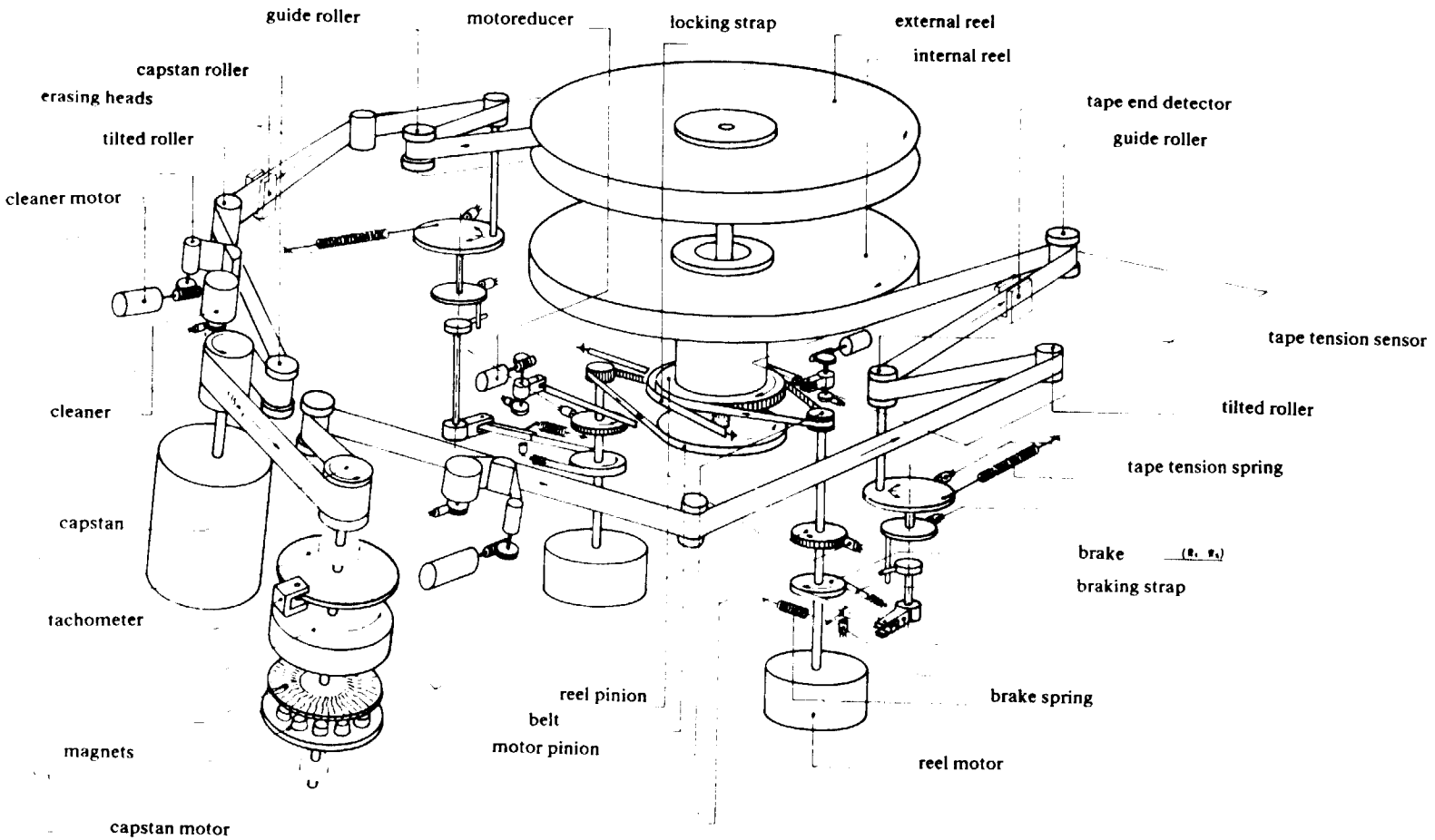

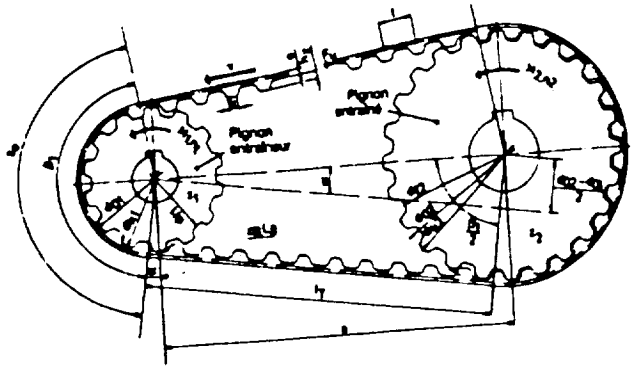

FIGURE 3 : Synchronous belt transmission

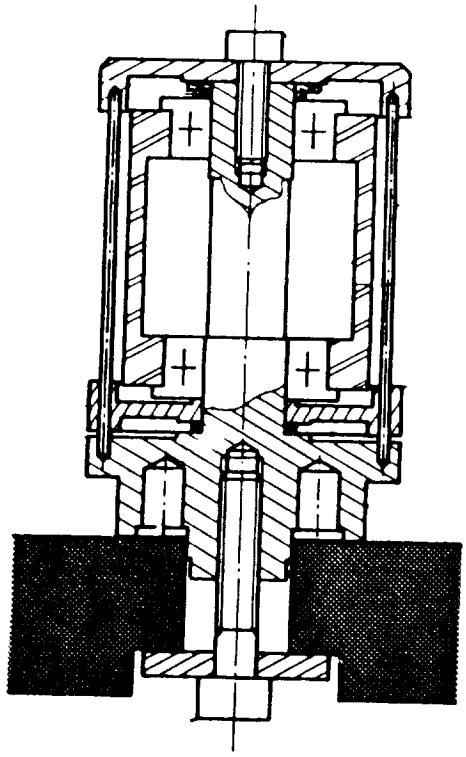

FIGURE 4 : Tape roller sideview

DEVELOPMENT OF THE CLAES INSTRUMENT APERTURE DOOR SYSTEM

D. M. STUBBS*

ABSTRACT

This paper describes the design, assembly, and test processes followed in developing a space-qualified aperture door system. A blackbody calibration source is mounted inside the door, requiring the assembly to open and close a minimum of 150 cycles for instrument recalibration. Within the door system are four separate mechanisms, three of which are redundant; a pyro launch latch, a hinge bearing assembly, and a pair of pivot mechanisms. Decoupling devices within the pivot mechanisms allow an active drive unit to automatically overdrive a failed drive unit. The door is also stowable for possible Shuttle retrieval and re-entry.

Throughout the paper, illustrations and photographs of the flight hardware help acquaint the reader with the design. The aim of this paper is to pass on lessons learned in all phases of developing this spaceflight mechanism.

INTRODUCTION

The Lockheed Palo Alto Research Laboratory has designed a space-qualified, Cryogenic Limb-Array Etalon Spectrometer (CLAES). It will be flown on the NASA Upper Atmospheric Research Satellite (UARS) scheduled for launch aboard the Space Shuttle in 1991. The satellite mission is to collect stratospheric sciences data, while the CLAES instrument specifically measures infrared signatures of 13 trace gases 10 to 60 kilometers above the Earth. The instrument is 1.22 meters in diameter, 2.74 meters long, weighs 1200 kg, and has an 18 month operational lifetime.

This paper focuses on the CLAES aperture door and all related structures and mechanisms. The requirements are addressed with discussions relating to safety issues and redundancy definition. Descriptions of the door system's six subassemblies are given with insights into their selection process. Manufacturing, assembly, and testing phases of the door system are also presented.

The aperture door system has passed all tests and is mounted to the CLAES instrument presently undergoing top-level instrument testing.

---

*Lockheed Palo Alto Research Laboratory, 3251 Hanover Street, Palo Alto, CA 94304-1187.

DOOR SYSTEM DESIGN REQUIREMENTS

Safety is the primary design requirement of the door system, since the CLAES instrument will be launched aboard the manned Space Shuttle.

The instrument is an assembly of two major components; the instrument package and the cryostat. Refer to Figure 1. The instrument package consists of a vacuum shell, telescope, Fabry-Perot Etalon Spectrometer, focal plane array, and pressure sealing aperture door. The cryostat is a solid cryogen containment system that maintains the instrument package at cryogenic temperatures. The cryostat and instrument package share a common vacuum. This internal vacuum thermally isolates the cryogens from the outside environment and maintains cleanliness standards within the instrument package. It is critical that the door maintains a vacuum seal at all times. Should there be a sudden loss of vacuum from any source within the CLAES instrument, the cryogens will sublimate causing the pressure within the entire instrument to rise at a rapid rate. Burst disks are designed to release this pressure, venting the gases overboard.

With an operational lifetime of 18 months, reliability is crucial to the success of the mission. The aperture door must open and close at least 150 cycles making its reliability a key element in the instrument design. Even though doors are only one of many critical hardware elements in spaceflight systems, they seem to get more than their fair share of management's attention.

List of Door System Requirements

1) Aperture dimensions: 24.4 cm high by 22.7 cm wide oval.
2) Door vacuum seal integrity must be maintained throughout launch. Margin of safety: 2.5
3) Operating environment: vacuum, 185 K minimum.
4) Pivot mechanism drive units: redundant stepper motors.
5) Door hinge assembly: redundant bearings.
6) Open positions: 135 degrees, 200 degrees.
7) Door location feedback: redundant limit switches, 3.0 degree repeatability.
8) Expected duty cycle: opened 48 hours, closed 48 hours.
9) 150 open/close cycles (minimum) over 18 months.
10) Max door closure time from 200 degrees: 60 sec.
11) Launch latch: redundant pyro actuated device utilizing a NASA Standard Initiator.
12) Relatch mechanism for recovery and re-entry. No redundancy requirement. Added late in the program.
13) Door must house a blackbody calibration source - 1.5 Kg.
14) A door stop shall provide protection for the vacuum shell.
15) Door must fit within the envelope of an external earthshade.
16) Maximum door system weight - 10.0 Kg.

DESIGN SELECTION PROCESS

The CLAES door system had many restrictions placed on it prior to the actual design phase. The most definitive restriction was that the door pivots, for lack of a better description, like a toilet seat. Refer to Figure 2. This pivot motion requirement came from the need for the internally mounted blackbody calibration source to view the relatively hot Earth as a heat source when the door was in the fully open position. The pivoting requirement preempted any trade studies of possibly more compact and reliable methods of opening such as translation or swivel motion.

The design requirements also specified the type of actuators and feedback in two of the door system mechanisms negating trade studies in these areas as well. The launch latch required a redundant pyro actuated device. Pyro devices were singled out due to their highly reliable performance record. The pivot drive mechanism requirement mandated redundant stepper motor drive units with redundant limit switch feedback. The CLAES electrical engineering staff chose steppers and limit switches due to the ease in which such devices can be interfaced and controlled with electronics.

An actual design trade study was only performed on the door pivot mechanism. It will be presented in this section.

Reliability

The UARS satellite is to be lifted into orbit by the Space Shuttle. When all satellite bus equipment has been activated to the satisfaction of the launch crew, UARS will be released. No instrument doors will be opened for a period of two weeks due to the anticipated contamination caused by the outgassing of the satellite's predominantly graphite epoxy structure. Without the luxury of an astronaut to aid a failed door opening mechanism, reliability is a major concern.

Reliability is determined by the quantity and type of moving parts in any mechanism. The design thrust was to create elegantly simple mechanisms with redundant elements that allowed for uncomplicated solutions.

Pivot Mechanism

The requirements placed on the pivot mechanism were that it be driven by redundant stepper motors with redundant limit switch feedback. NASA added the constraint that two separate mechanisms drive the door. Single point failures were unacceptable. It was clear that two highly reliable clutching mechanisms were necessary; one to disengage the failed stepper drive while another engaged the healthy drive.

Of the ten clutching mechanisms investigated, all had one common disadvantage; they required an actuator. These actuators were deemed single point failures and could not be tolerated. A mechanism was sought which automatically performed the needed clutching action.

After searching through mechanisms literature for many weeks, the solution presented itself during an inspirational moment at a weekly design meeting. By placing a simple torsion spring device between the door shaft and each drive unit, a soft-coupling will exist that can effectively perform the needed automatic function. The required spring rate and applied loads dictated a helical torsion spring design. A complete description of this device can be found in the following section.

DOOR SYSTEM DESCRIPTION

The door system is located on the outer radial surface of the instrument package vacuum shell. The door boss is integrally machined to the 1.22 meter diameter shell. Analysis showed that bonding or welding the boss to the shell would not have given a sufficient load carrying safety margin.

The door seals to the door boss by way of a Viton O-ring. The O-ring seal has a 2.62 mm cross-sectional diameter and is retained to the shell boss by a dovetail gland.

The door system contains six subassemblies; the door/blackbody calibration source assembly, hinge bearing assembly, pivot mechanism, launch latch mechanism, door stop assembly, and relatch mechanism. Refer to Figure 3. Descriptions of each subassembly will be given in this section.

Door/Blackbody Calibration Source Assembly

The door is machined out of a solid block of 6061-T651 aluminum. External ribs stiffen the door to pressure loads. A special coating, Magnaplate HCR, is applied to the sealing surface of the door flange to prevent stiction of the O-ring seal. The surface treatment hardens and lubricates aluminum surfaces. General Magnaplate performs this proprietary process on many different materials at its plant in Ventura, California.

The blackbody calibration source is an aluminum plate mounted to the door by four insulating, fiberglass posts. Radial grooves machined into the top surface of the clear anodized plate help create a high emissivity blackbody source. The back surface of the plate is instrumented with platinum resistance thermometers (PRTs) and flat element heaters for fine temperature control. Multi-layered insulation and an outer aluminum shield surround all but the front surface of the plate. The blackbody electrical harness ends at a hermetically sealed connector affixed to the top, inner surface of the door.

There was concern that the external mating harness would fail under bending loads after many door cycles in the cold space environment. It was decided to have the harness twist during the door cycles since the kinematics of twisting are less stressful to wires than bending. The Kapton wrapped electrical harness is routed from the door through a cable mount and retainer. The mount supports the harness to the door while the retainer guides the bundle through its twisting motion. An 11.0 cm diameter loop was

used to distribute the twisting over a reasonable length and to lower the spring rate of the cable. With this cabling arrangement the door is free to pivot with negligible resistance.

Hinge Bearing Assembly

A bearing assembly is mounted on either side of the door hinge shaft. Coaxially mounted, deep-groove ball bearings are attached through a "Z" arrangement within each assembly. Refer to Figure 4. A stainless steel mount links the outer race of one bearing to the inner race of the other. If one bearing seizes, the linking element allows the good bearing to spin the entire subassembly. Deep groove ball bearings were chosen for this assembly due to their low friction, small size, and ample load rating. Barden Bartemp bearings were singled out from other manufacturers due to their low temperature operating capability. Two wave washers preload each assembly 178 newtons to ensure all of the balls in the bearings are immobilized during the launch environment. Otherwise, the balls would be free to peen the races.

The "Z" mount configuration was chosen due to its compact size and high reliability. A disadvantage of this arrangement is that a moment can be applied to the bearings when under a radial load. This was minimized by mounting the bearings as close together as possible.

Pivot Mechanism

The heart of the door system design is the redundant pivot mechanism. It consists of duplicate drive trains connected to opposing ends of the door hinge shaft. Both drive trains are composed of a drive unit (integral two degree stepper/100:1 harmonic drive) and a helical spring decoupler. Each drive unit generates 6.78 N-m energized torque and 2.26 N-m detent torque at the splined output shaft. The drive units are manufactured by Schaeffer Magnetics in Chatsworth, California; a professional outfit that delivered excellent flight hardware on schedule.

Each decoupler consists of a helical torsion spring, rod center, sleeve bearing, bearing mount, and a pair of cam plates. Refer to Figure 4. Both decouplers are identical except for oppositely wound springs. Each spring is wound in the direction that increases coils when opening the door since applied stresses are lowest in this arrangement. Each decoupler is capable of 1.56 N-m torque at their 370 degree yield deflection.

The sleeve bearing is manufactured out of DuPont Vespel SP-3; a 15% molybdenum-filled polyimide resin composition with low outgassing and friction coefficient properties. Both the stainless steel rod center and bearing mount have splined ends for attachment to the door hinge shaft and drive unit. Each decoupler is secured to the door hinge shaft with a cotter pin. The cam plates trigger the limit switches at the 0, 135, and 200 degree door locations.

As a redundant feature of the mechanism, it is planned to have both drive units wind the decouplers 251 degrees in the open direction before

launch. If a total failure of the redundant door drive electronics occurs prior to the initial door open command, firing the pyro launch latch will allow the spring decouplers to automatically open the door.

Pyro Launch Latch Mechanism

The launch latch is a slight modification of a mechanism previously designed by the Lockheed Missiles and Space Company (LMSC). Refer to Figure 5. An aluminum bracket mounts two LMSC developed pyrotechnic pinpullers to the vacuum shell boss. Each pinpuller contains one NASA Standard Initiator and can actuate under a 3380 newton double shear load at 185 K. An aluminum threaded rod with spherical end fits between the pinpuller shafts and up through the door into a spring tensioning device. The tensioning device consists of a compression spring, housing, spherical washer, thirty spring washers and a castellated nut. This device performs two functions. If only one pinpuller actuates, the threaded rod will be free to pivot around the failed pinpuller shaft while being pulled up into the door by the compression spring. The thirty spring washers allow for an accurate application of 667 newtons tensile preload to the load carrying rod.

Door Stop Assembly

If a complete failure of the door drive electronics occurs prior to the initial door open command, the pyro launch latch will be fired allowing the prewound spring decouplers to open the door. A pair of door stop assemblies decelerate the door ten degrees past the 200 degree position.

These simple devices mount to the vacuum shell. Each stop device consists of a compression spring, stud, and plunger. The springs are sized to compress to half of their stroke capability. The door will impact the stop assemblies near its center of gravity.

Relatch Mechanism

The requirement that the door be stowable for Shuttle retrieval and re-entry came from the customer after most of the door system drawings had been completed. Waiving a redundancy requirement on this device allowed for an inexpensive solution.

A TRW Globe D.C. motor/gearhead/brake assembly was chosen as the drive unit. This stock catalog item was originally designed for operation in a one atmosphere environment. The supplier made minor material modifications in the unit for vacuum compatibility. A load carrying cam with a 19 mm moment arm slides onto the splined output shaft of the drive and is secured with a cotter pin. The entire assembly mounts to a bracket on the vacuum shell boss. A 6.3 mm diameter dowel pin is pressed into the door side wall to carry the 14 g Shuttle landing loads. A limit switch assembly is placed at the cam open location for position feedback. When the door is closed, the drive unit cam pivots over the pin and presses the door to the vacuum shell boss. The drive electronics automatically de-activate the D.C. motor through a current limiting circuit. When the unit is de-energized, the brake clamps down on the motor shaft allowing the cam to secure the door in the closed position with a preload of 593 newtons.

The relatch drive actually has a dual role. The drive cam will be positioned under the door relatch pin at launch. Should the vacuum O-ring seal stick to the door, the relatch drive will push up on the pin with 1779 newtons to overcome the seal stiction.

A simple backup to the cam relatch design was added due to the negligible cost of implementation. A 1.0 cm diameter hole is located in the door flange near the pivot hinge shaft with a threaded hole in the vacuum shell boss. An astronaut EVA will be required to thread a bolt through the door and into the vacuum shell boss.

TEST PERFORMANCE

Six separate qualification tests were performed on the door system. An aluminum mounting plate was used in the tests for accurate duplication of all vacuum shell interfaces. The mounting plate also provided a void behind the door for pressure testing. All tests were performed in an ambient environment unless otherwise stated. The tests were performed in the order in which they are listed in this section.

Manufacturing, assembly, and testing difficulties will be addressed in the following section.

Relatch Drive Unit Torque Test

The relatch drive unit was mounted with a pulley, cable, and weight bucket attached to the output shaft. To determine the stall torque, successive weights were added to the weight bucket until the drive stalled. The brake torque was acquire by adding weights to the weight bucket until backdriving of the deactivated unit commenced. The drive unit torque measurements were; 34.0 N-m (stall), 11.3 N-m (brake).

Door Pressure Test - Figure 6.

A vacuum was pulled on the door and a helium leak detector found no leaks. Nitrogen gas was then used to backfill and positively pressurize the door. The door was found to vent at 10.34 kPa. This was 27 percent below the pressure requirement. After replacing the O-ring seal with one of a lower durometer, the test was repeated with more favorable results. The door vent pressure was determined to be 13.10 kPa.

Blackbody Electrical Harness Life Test - Figure 7.

A representative harness and test fixture simulating the harness interfaces were placed in a styrofoam container with dry ice to achieve the 185 K space environment. An insulated shaft passing through the container wall allowed personnel to cycle the harness assembly through a 200 degree arc. The harness was cycled 600 times (four times the anticipated lifetime cycles) while an ongoing continuity check confirmed a successful test.

Door System Functional Test

The entire door system was assembled to the test mounting plate. This assembly was in turn mounted to a holding fixture that oriented the door pivot axis along the gravity vector to simulate a zero gravity environment. A comprehensive functional test was then performed on all subsystems including; the door pivot mechanism, pyro launch latch, and relatch mechanism. Anomalies were found and corrected during the pivot drive microswitch actuation. The microswitch and pivot mechanism problems will be addressed in the next section.

Door System Vibration Test

The complete door system test assembly was mounted to a three axis vibration fixture. Random vibration exposures were performed on all three axes per the NASA Shuttle launch specification. The door maintained a vacuum throughout the test with no measurable leakage. After the test, an abbreviated functional test of the pivot drive units was performed while the pyro launch latch remained engaged. No anomalies were found.

Pyro Launch Latch Actuation/Cold Functional Test - Figure 8.

The door test assembly was mounted to the holding fixture and placed in a cryogenically cooled vacuum chamber. While in a vacuum at 185 K, one of the two pyro pinpullers was fired. This single pinpuller actuation successfully tested the redundant feature of the launch latch mechanism. The pivot drives and relatch mechanisms were then fully function tested with no abnormalities.

MANUFACTURING, ASSEMBLY AND OPERATIONAL DIFFICULTIES

The CLAES instrument is a protoflight design; no funding was allocated for a development test unit. With this requirement, the tested door system hardware was also to be flown.

There are always countless annoying little problems to overcome when building new hardware. The major difficulties in developing the aperture door system will be addressed in this section. Problems arose in three areas; decoupler spring creep, limit switch actuation, and door stiffness.

Decoupler Spring Creep

The most compliant members in the door pivot mechanisms are the two decoupler torsion springs. Under normal operating conditions the decoupler springs must only overcome the spring forces in the door location feedback microswitches. The decoupler spring rate is designed as high as practical to insure repeatable angular displacements at the decoupler ends. Otherwise, the orientation of the door with respect to the pivot drive steppers will change continually over the life of the mechanism. This can create major problems for the control electronics.

Each spring is heat treated and shot peened to reduce undesirable residual stresses in the 304L stainless steel material. Under a stepper drive unit failure, the worst case deflection of either decoupler will be 251 degrees; 200 degrees to rotate the door and 51 degrees to actuate the microswitches. The springs yield after a deflection of 370 degrees.

During the pivot mechanism functional testing, orientation of the decoupler ends shifted up to 15 degrees for any combination of loading conditions. Angular displacement commands sent to the stepper motors did not correlate consistently with the displacement of the door.

During a spring design literature search it was discovered that a crucial step was left out of the spring manufacturing process. Helical torsion springs tend to creep at stress values less than those in the plastic region unless they are "stress set". Displacing a spring to its highest working stress level will place a memory into the material. The spring will then deflect consistently at stresses less than the "set" level. Each decoupler spring was set at the plastic yield stress level. The springs now register consistently throughout the door pivot operations.

Limit Switch Actuation

Four limit switch assemblies provide orientation feedback for the door pivot mechanism. Two switch assemblies are mounted on either side of the door hinge for redundancy while the remaining two are located at the stepper drive units. A complete switch assembly consists of three microswitches, three actuators, and a mounting bracket. In this design, the actuator is a cantilevered strip of stainless steel that transfers the actuation force from the decoupler cam to the delicate switch. Each assembly has switches oriented at 0, 135, and 200 degrees.

During functional testing, the switches did not operate in a repeatable manner to the three degree location tolerance. The switch actuator's cantilever slope angle was found to be too shallow for close tolerance feedback. The solution was simple. By locally bending the switch actuator into a sharp "V", the cam displaces it over a much smaller deflection angle. Refer to Figure 9. With this feature, the switch feedback tolerance is easily met.

Door Stiffness

As the Shuttle passes through the max Q launch condition, the door external pressure is one-tenth of an atmosphere while the random vibrations are at their peak. To ground test the door sealing capability for this worst case condition, a relationship between g-level and internal pressure was created; equivalent inertial load pressure. This internal pressure was determined to be 4.83 kPa. The door seal margin of safety requirement dictated a minimum pressure of 12.07 kPa. During pressure testing, the door vented at a differential pressure of 10.34 kPa.

The door is machined out of a solid piece of 6061-T651 aluminum. The cost of redesigning the door structure would be high. It could be machined out of a stronger material such as a 300 series stainless steel but the increased weight would have been prohibitive. Alternate solutions were sought.

The solution was found in the door O-ring seal. The seal material, cross-sectional diameter, and contact length determine the door sealing force. Lowering this force would allow the door to seal with less deflection, raising the venting pressure. The contact length and cross-sectional diameter could not be changed since the dovetail gland was already machined in the vacuum shell. A search to replace the original 70 durometer Viton material was enacted. We located a moldable, 60 durometer Viton material manufactured by Parker Seal Company in Lexington, Kentucky. With this new seal material, the door vents at 13.10 kPa.

SUMMARY

This paper has described the design, assembly, and test processes followed in developing the CLAES aperture door system. All operational tests have been successfully completed, demonstrating the door system meets all of the original performance requirements. The CLAES instrument will be flown on NASA's Upper Atmospheric Research Satellite (UARS) scheduled for launch aboard the Space Shuttle in 1991.

ACKNOWLEDGEMENTS

The development of the CLAES instrument was performed by the Lockheed Palo Alto Research Laboratory under contract to NASA Goddard Space Flight Center. The author wishes to express his gratitude to the CLAES Program office for the opportunity to work on this challenging assignment. Special thanks goes to Bruce Steakley, the CLAES opto-mechanical group leader, for his ideas, patience, and continued support.

ORIGINAL PAGE
BLACK AND WHITE PHOTOGRAPH

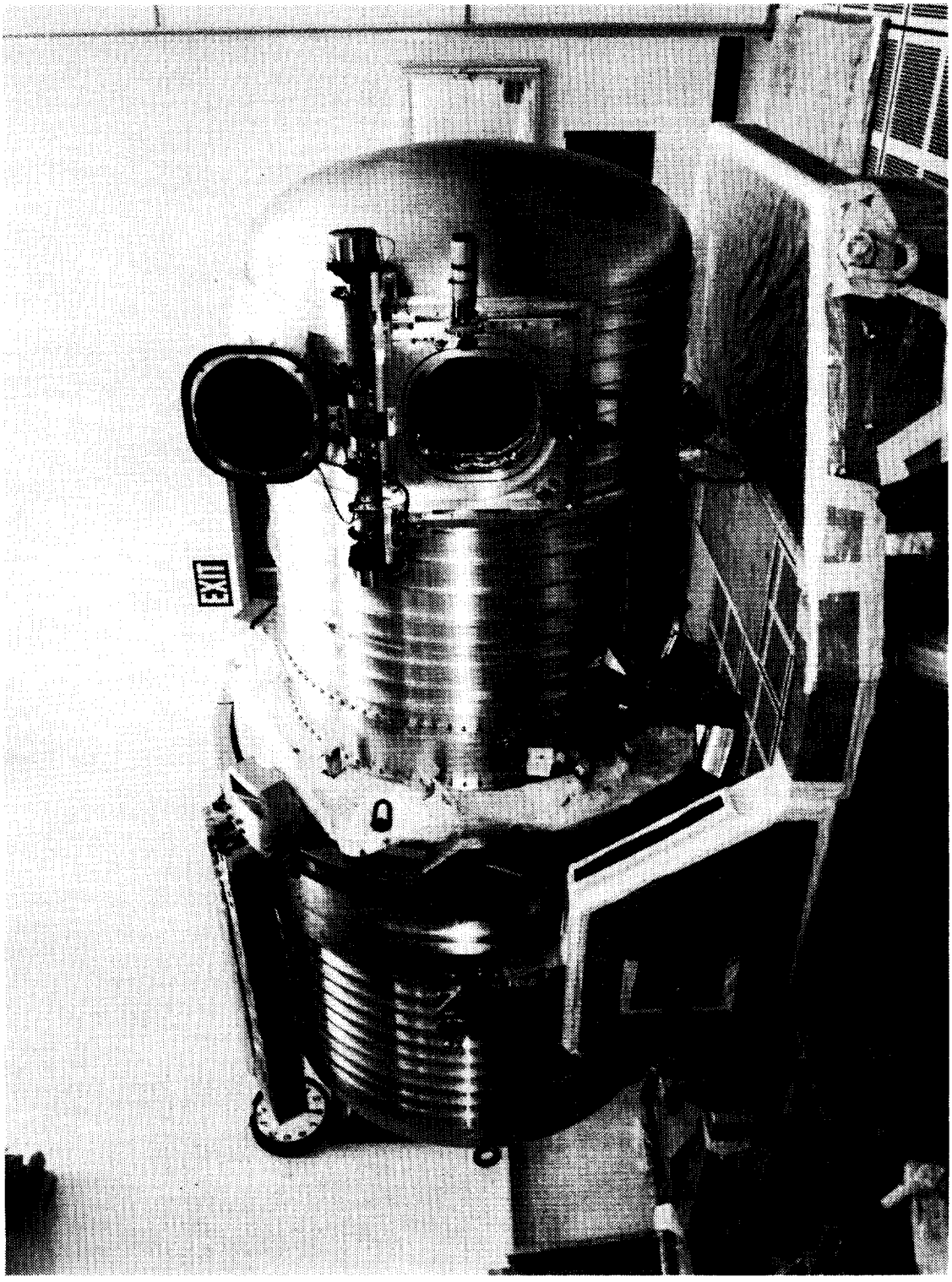

Fig. 1 CLAES Instrument Mounted to Ground Handling Dolly

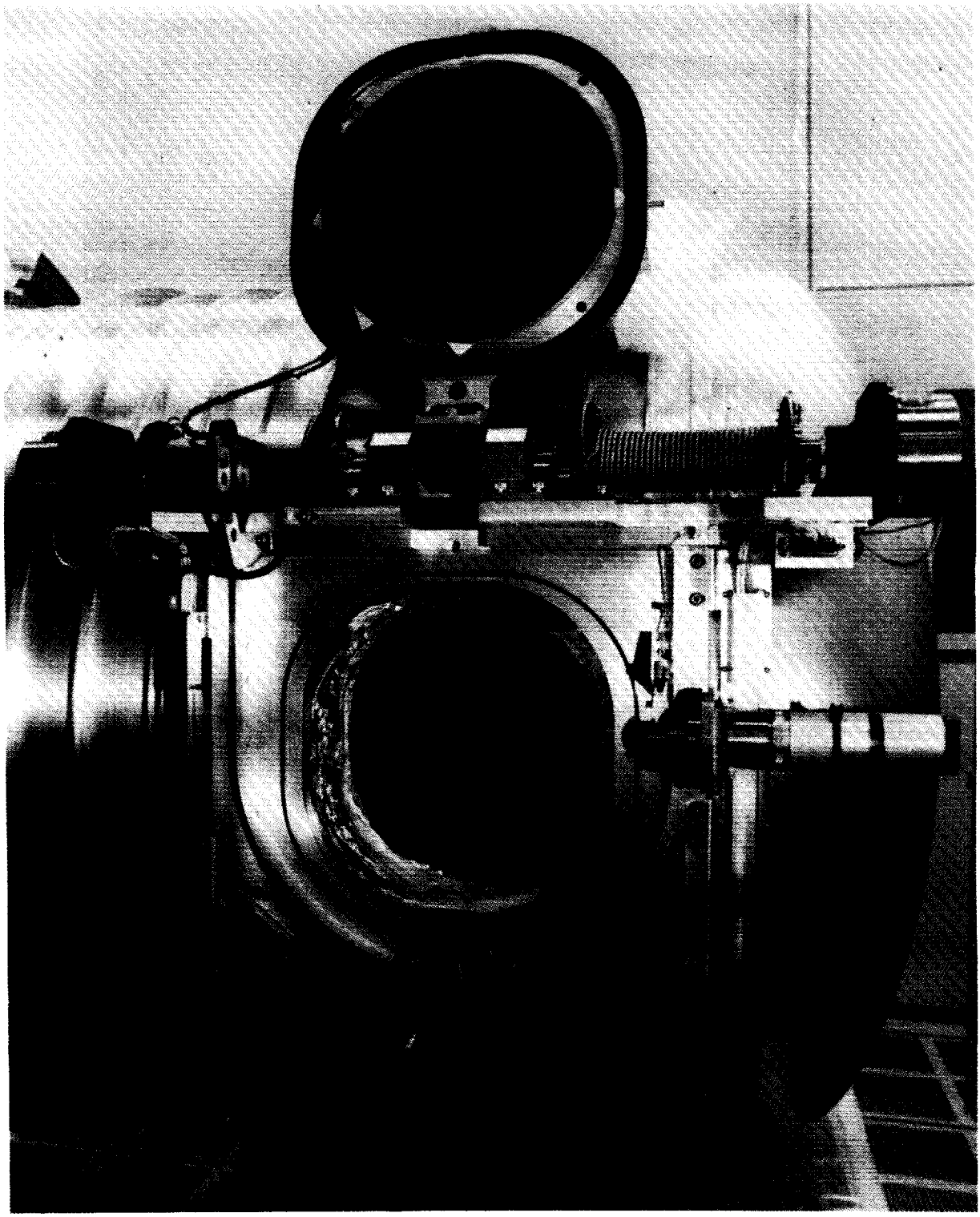

Fig. 2 Door System Assembled to CLAES Instrument

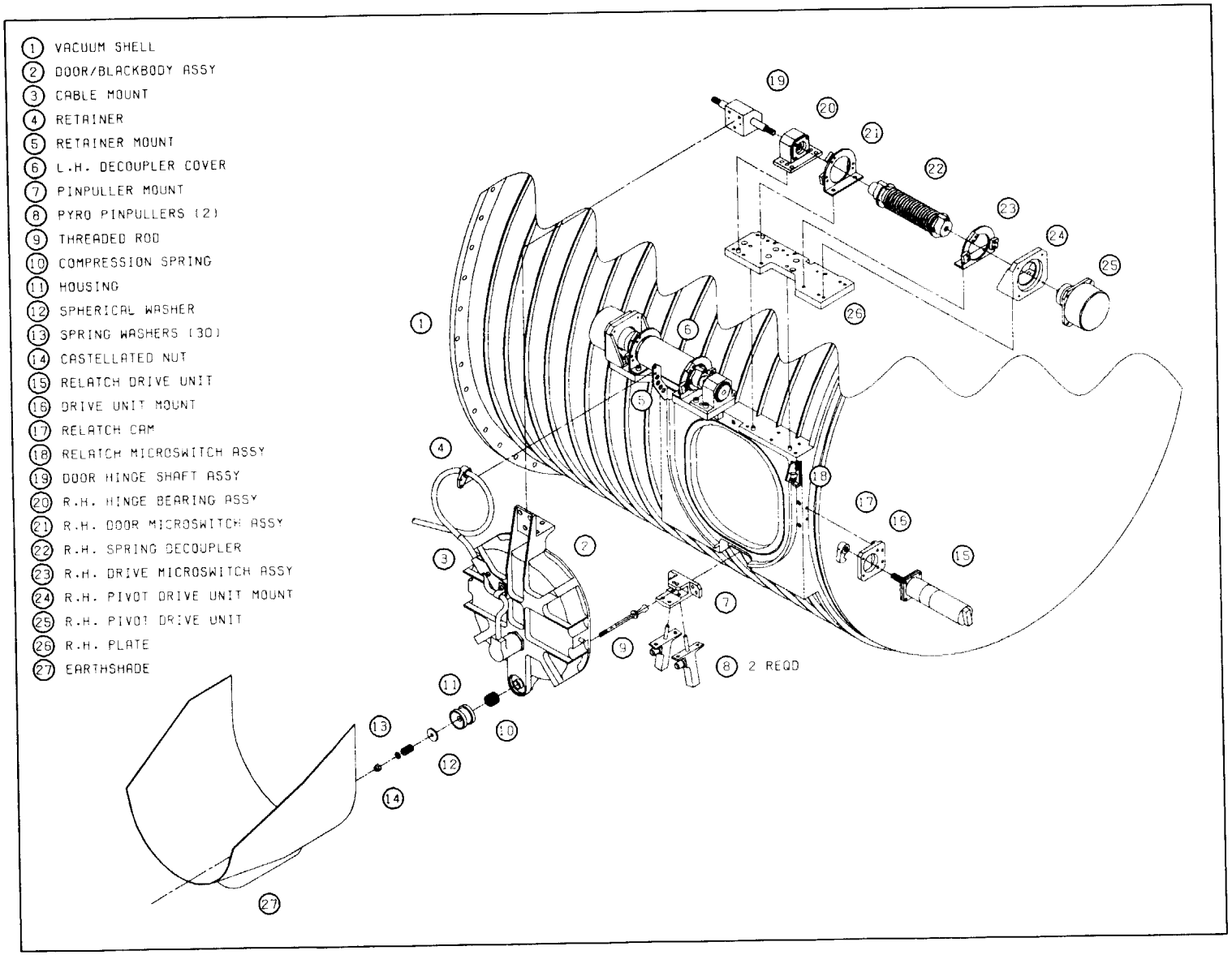

Fig. 3 Isometric Exploded View of Door System

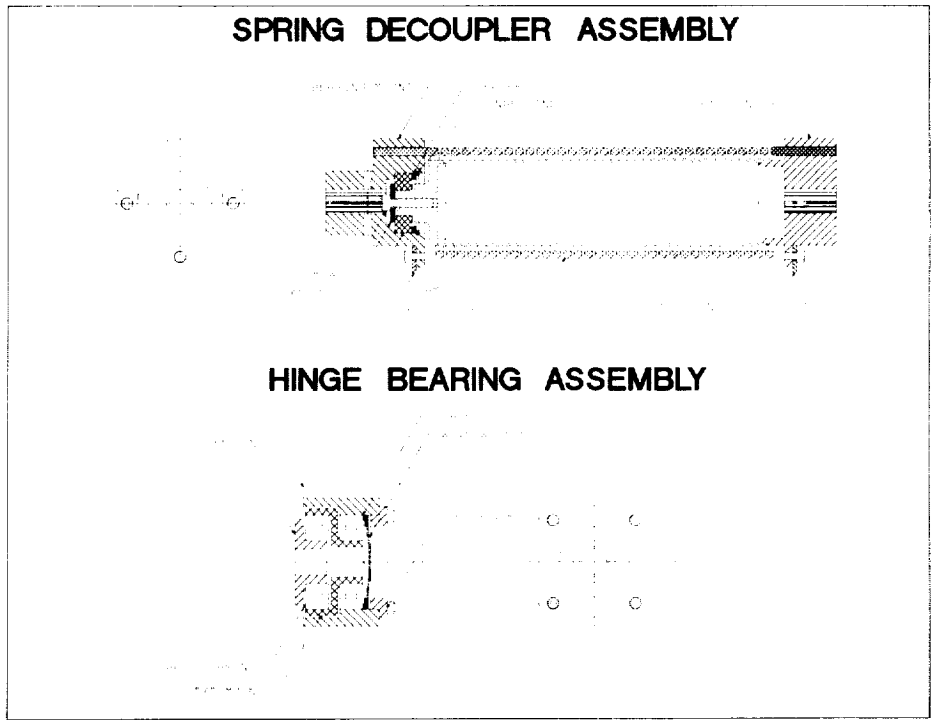

Fig. 4 Cutaway Views of Decoupler and Hinge Bearing Assemblies

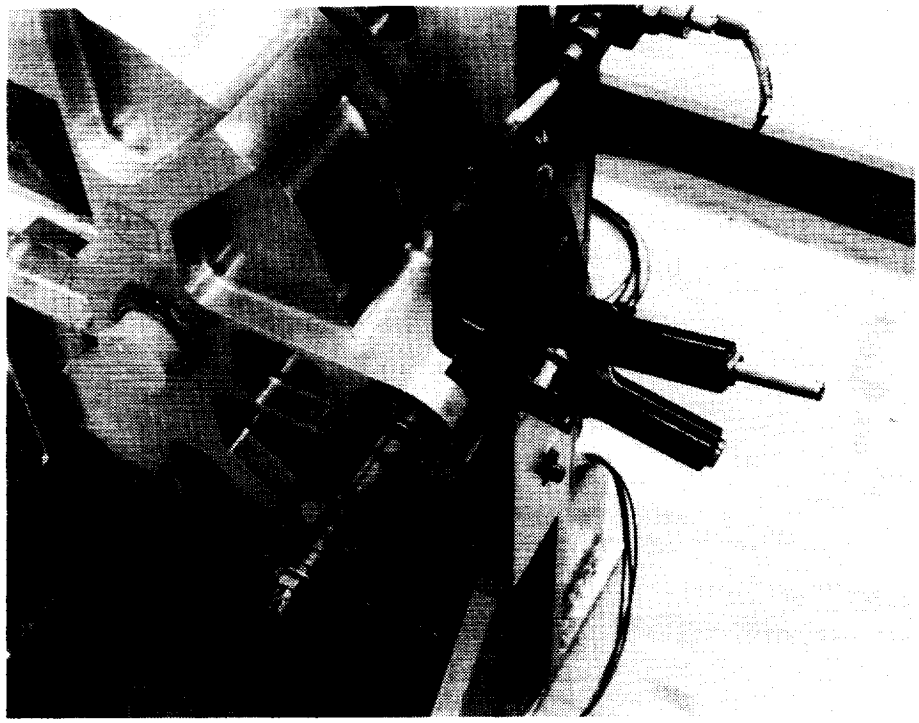

Fig. 5 Launch Latch With One Fired Pinpuller

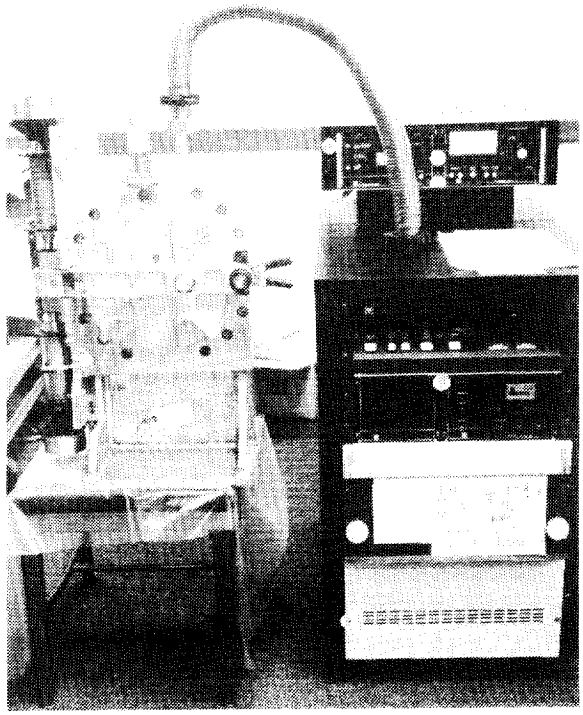

Fig. 6 Door Pressure Test Setup

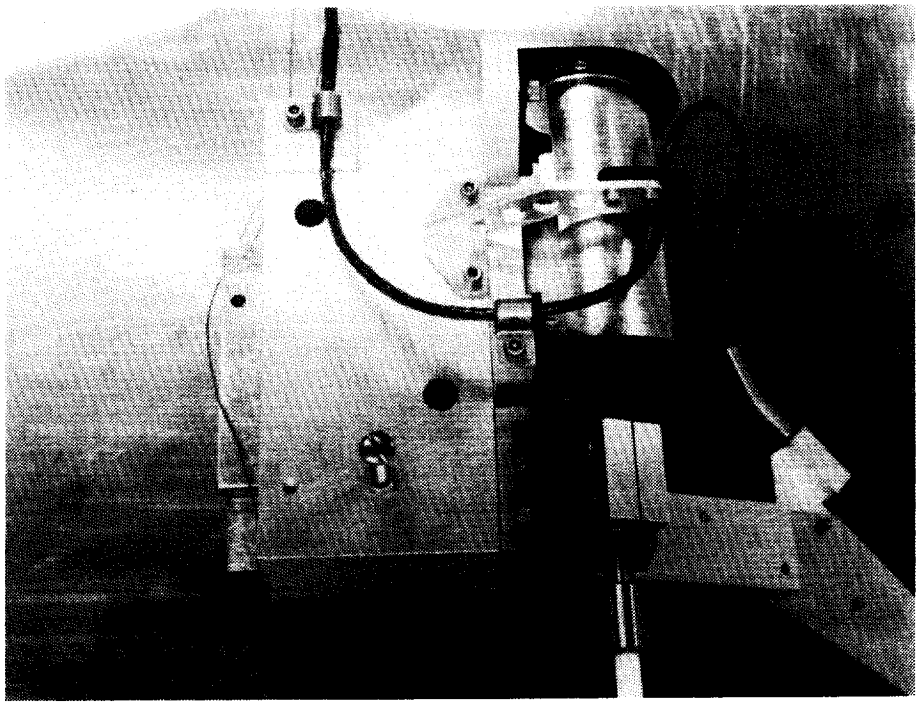

Fig. 7 Blackbody Electrical Harness Test Fixture

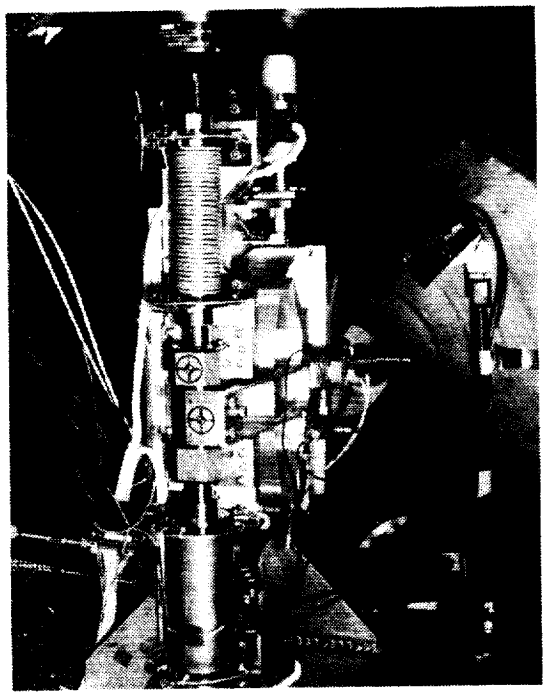

Fig. 8 Cold Functional Test

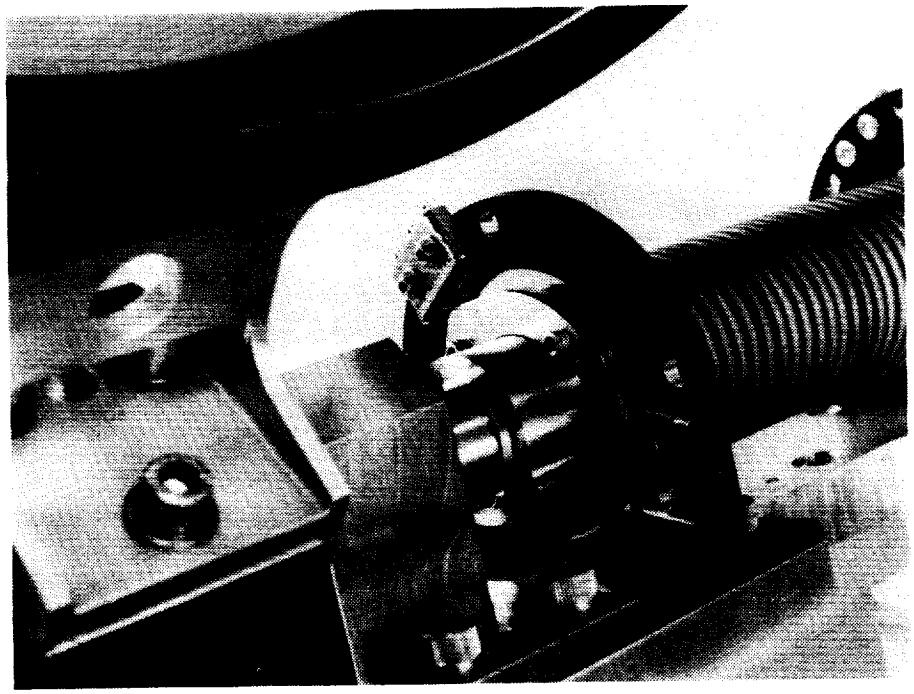

Fig. 9 Microswitch Assembly With Door at 135° Position

A SOFT ACTUATION SYSTEM FOR SEGMENTED REFLECTOR ARTICULATION AND ISOLATION

Michael L. Agronin and Louise Jandura*

ABSTRACT

Segmented reflectors have been proposed for space-based applications such as optical communication and large-diameter telescopes. An actuation system for mirrors in a space-based segmented mirror array has been developed as part of the National Aeronautics and Space Administration-sponsored Precision Segmented Reflector program. The actuation system, called the Articulated Panel Module (APM), provides 3 degrees of freedom mirror articulation, gives isolation from structural motion, and simplifies space assembly of the mirrors to the reflector backup truss. A breadboard of the APM has been built and is described.

INTRODUCTION

The National Aeronautics and Space Administration-sponsored Precision Segmented Reflector (PSR) program is an effort to develop generic technology for space-based wide-aperture segmented reflector arrays. Mirror fabrication technology and launch vehicle cargo volume limit the size of a single mirror. Constructing an array of mirror segments in space is one means of achieving large-diameter reflectors. Applications for this technology include relatively low-precision "light buckets" for optical communication systems as well as higher-precision primary reflectors for diffraction-limited telescopes. NASA's proposed Large Deployable Reflector (LDR), a space-based 20-m infrared telescope, is an example of such an application. A concept for the LDR spacecraft is shown in Figure 1.

The current phase of the PSR program is development and demonstration of component technologies, including lightweight mirror panels, truss structures to support the mirror array, and figure control systems. The control system technologies include sensors for measuring the shape of the array, algorithms for maintaining the shape, and an actuation system for articulating the panels. The PSR articulation system design concept was first reported by Mettler, et al. [1]. This paper discusses the subsequent breadboard implementation and testing.

* Members of Technical Staff, Guidance and Control Section, Jet Propulsion Laboratory, California Institute of Technology, Pasadena, California

Figure 1. Concept for the Large Deployable Reflector.

TASK REQUIREMENTS

Requirements for PSR component technology are derived from several proposed NASA missions that will utilize segmented reflectors. All of the missions involve infrared diffraction-limited telescopes. LDR is the primary source of requirements for space assembly and control system capabilities. The Sub-Millimeter Explorer (SMME) and the Sub-Millimeter Imaging Line Survey (SMILS), LDR pre-cursor missions, are the sources of requirements for mirror panel, sensor, and structure development. The requirements are listed below and quantified in Table 1.

- Each mirror panel must be articulated in 3 degrees of freedom: piston (motion normal to the plane of the mirror) and tilt (rotation about the two axes in the plane of the mirror). Lateral articulation is not required, since lateral panel misalignment can be optically corrected to the first order with piston and tilt articulation. Lateral truss vibration is assumed to be much smaller in amplitude than piston and tilt vibration because of high lateral truss stiffness.

Table 1. Actuation system requirements.

Category	Requirement
Range of motion	2 mm piston, 4 mrads tilt.
Position stability	<1 μm rms in a quasi-static (no truss vibration) environment. Stability under disturbances not yet defined.
Panel size	Hexagonal, 1 m corner-to-corner.
Truss thermal strain frequency range	dc to 2 x 10^{-4} Hz, based on 90 min orbit.
Truss vibration amplitude and frequency range	Specific disturbance spectrum undetermined pending spacecraft structural analysis. For development purposes, max. amplitude < 100 μm peak-to-peak, frequency range ≥ 1 Hz.
Temperature	Materials compatible with 100K. Testing at this temperature not required during development phase.
Power dissipation at the panel	< 5 mW for three actuators. Electronics may be remotely located.
Actuator position error update rate	1 Hz max. assumed for development purposes.

- The panels must be aligned in a paraboloid whose reference frame is the focal plane of the telescope. The truss cannot be used as a reference frame for positioning panels because it is flexible and subject to thermal strains and vibrations induced by other actuators (e.g., reaction wheels, cooler pumps, solar array drives) on the spacecraft.

- Each mirror panel is parabolic. The actuation system may not distort the panel shape.

- Final assembly of the telescope will be performed by an astronaut or robot in orbit.

- Mirror temperature must be maintained as low as 100K to avoid generating infrared noise. Power dissipation must be appropriately limited.

The figure control bandwidth also puts constraints on the actuation system design. The control concept is shown in Figure 2. A figure sensing

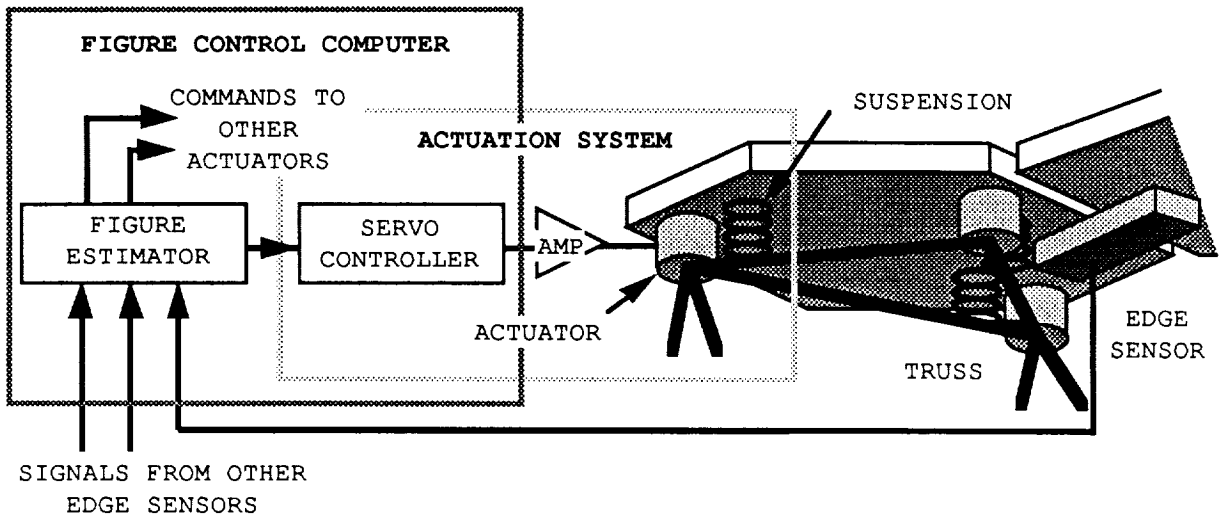

Figure 2. The figure control system.

system determines the position and orientation of each panel. Using this information, the central figure control computer calculates a position error for each actuator. The computer also processes the servo control law for each actuator. Several sensor concepts are under consideration. The edge sensor concept shown in Figure 2 uses interferometers to measure panel piston and tilt between adjacent panels, which the figure control computer transforms into an array shape. This concept is similar to the figure sensing scheme used by the Keck telescope, a 10-m segmented telescope under construction in Hawaii [2]. Whatever sensor is used, the actuator bandwidth is limited by the sensor update rate. That rate in turn depends on the number of mirrors in the array, sensor averaging time, and the computer processing speed. The update rate for the 90-panel LDR array is estimated to be as low as 0.67 Hz.

DESIGN CONCEPT: THE ARTICULATED PANEL MODULE

A design concept for the actuation scheme evolved based on the requirements described above. The biggest challenge was developing a control scheme that could isolate the panel from high-frequency truss motion with low-bandwidth feedback. The solution required complete integration of actuator, panel suspension, and control law design. Components were selected to achieve the desired system dynamic behavior.

To get around the low figure sensing update rate, we wanted to use an additional, more accessible reference frame for panel control. The moving truss cannot be used as a reference frame. However, since the panel does not have to move once the array shape is achieved, it made sense to use an inertial reference frame. Initially, we considered attaching inertial sensors to each panel, but this idea was abandoned because of the expense. Instead, we decided to use the panel's own inertia to passively isolate it from high-frequency disturbances and to use active control only for initial alignment and compensation for slow thermal truss strains. In space, the only forces acting on the panel come through the actuator and the suspension. Therefore, if the actuator and suspension are as mechanically compliant as possible, the actuation system acts as a passive low-pass filter. The design goal then is

to place the passband within the actuator's active control bandwidth. This soft actuation concept differs from the mechanically stiff systems used in other segmented reflectors such as the Keck telescope [3] or Lockheed's Advanced Structures/Controls Integrated Experiment [4], which must support mirror panels in gravity.

Actuator Selection

The electrodynamic or voice coil actuator, shown in Figure 3, was selected after an extensive actuator trade. It is ideal for a high-compliance actuation system because it produces force independent of displacement and it has zero mechanical stiffness. The electrodynamic actuator has other advantages as well. It is relatively inexpensive. Unlike a lead screw, it requires no lubrication, which eliminates the problems of contamination of optical surfaces and low viscosity at cryogenic temperatures. It also requires less complicated drive electronics than other options.

The electrodynamic actuators could have been sized to support the weight of the panel, but this would have significantly altered the design and packaging of the ground test actuators versus the flight-like versions. Instead, we decided to develop a separate gravity off-load device to support the panel's weight. With gravity off-loading (and in orbit), the actuator needs to generate only enough force to extend the suspension (0.003 N in the breadboard). At this force level, the power dissipated to a mirror by three actuators is only ~2 μW, well below the requirement.

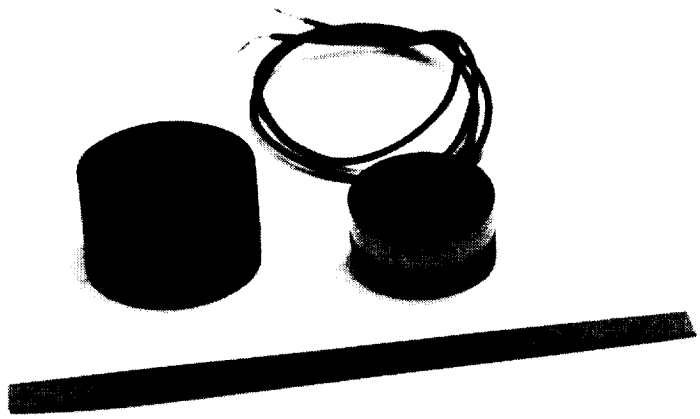

Figure 3. The electrodynamic actuator.

Suspension Design

The suspension design integrates the functions of isolation, kinematic attachment, and simplification of space assembly. The suspension assembly, including the mirror panel, is called the Articulated Panel Module (APM). An exploded view of the APM is shown in Figure 4. The panel is attached to three struts that are attached to a triangular subplane. The actuators act kinematically in parallel with the struts. The subplane is in turn attached to three truss nodes.

The struts perform two tasks. First, they stiffly restrain the panel from lateral motion, which is necessary since lateral motion is uncontrolled. However, they are extremely compliant in the controlled degrees of freedom which is consistent with the passive isolation goal. Second, they act as a kinematic mount between the panel and the subplane, allowing independent thermal growth of the panel and subplane without distorting either. The strut length and the flexure bending stiffness determine the piston and tilt suspension frequencies. The tilt stiffness can be controlled independently of the piston stiffness by selecting the radius R (shown in Figure 4) where the strut is attached to the panel. We matched the breadboard piston and tilt frequencies to within 9% of each other so the controller would have to contend with only one resonance.

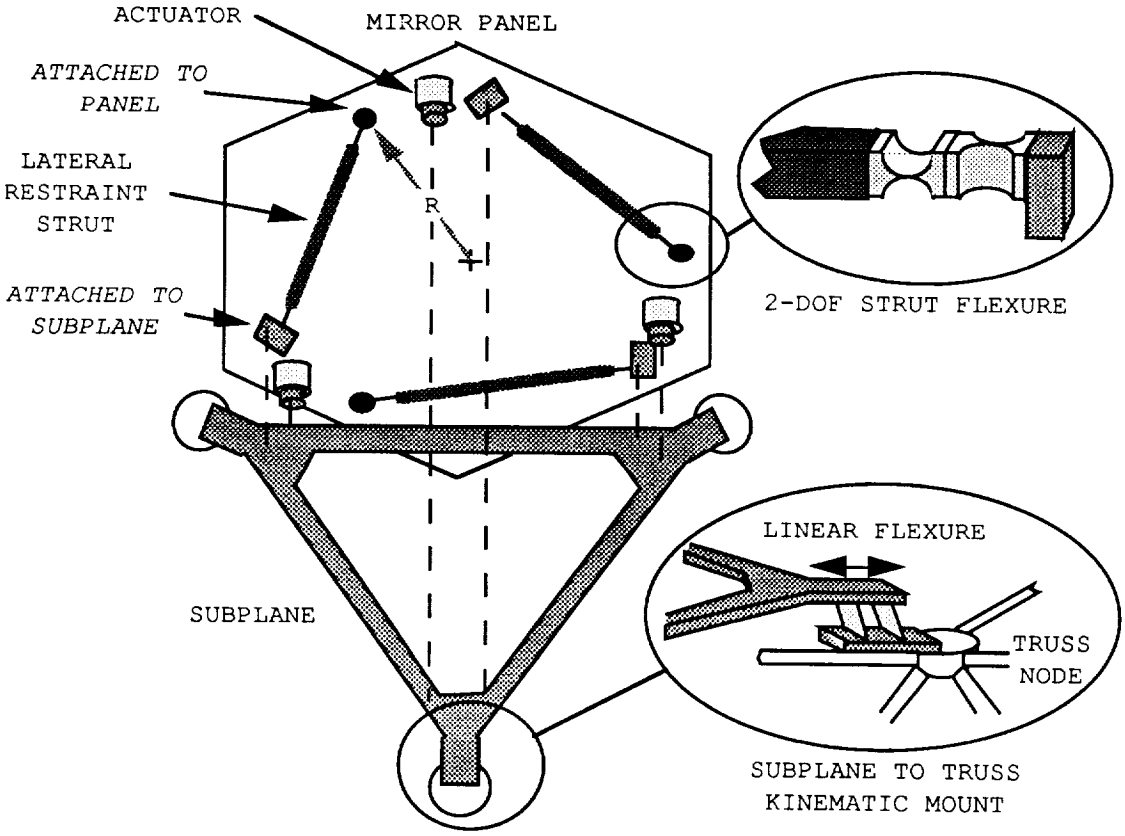

Figure 4. The articulated panel module.

The panel and actuators are attached to a subplane rather than directly to the truss, so that the suspension can be assembled, aligned, and tested before launch. The APM is a mechanically robust subassembly that can easily be attached to the truss during space assembly. The subplane has its own kinematic attachment to the truss, consisting of three linear flexures that point toward the center of the panel, as shown in Figure 4. This ensures that the subplane is not structurally redundant with the truss. The attachment is stiff to rigid body truss motion, but it allows for initial misalignments and independent thermal growth of the two structures without distortion.

Control Law Design

Taking advantage of symmetry, we used a 1-axis model of the APM for parameter selection and control law development. The model, shown in Figure 5, includes only one actuator, one strut, one-third of the panel mass, and one off-load mechanism. It is equivalent to the panel moving only in piston. We considered this model adequate for parameter selection since the piston and tilt natural frequencies are close together.

We selected a proportional-integral (P-I) control law for zero steady state error. Derivative control cannot be used because of the low (1 Hz) feedback update rate. Instead, we took advantage of the actuator's eddy current damping to provide derivative control. Eddy currents are induced in the housing of the actuator's coil piece when the actuator moves. Resistance to the eddy current is reflected back as a damping force. There is no damping from back-EMF because of a voltage feedback loop in the actuator driver.

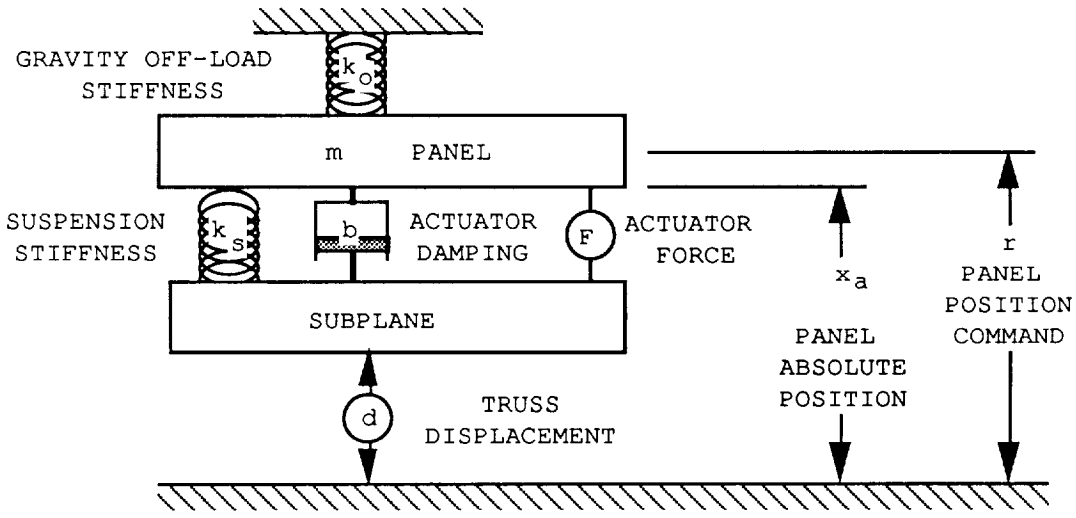

Figure 5. One-axis piston-motion model of the APM.

The closed-loop transfer function for the panel's response to a position command is:

$$\frac{x_a}{r} = \frac{\frac{p}{m}s + \frac{i}{m}}{s^3 + \frac{b}{m}s^2 + \frac{(k_o+k_s+p)}{m}s + \frac{i}{m}} \quad (1)$$

The closed-loop transfer function for the panel's response to a truss position disturbance is:

$$\frac{x_a}{d} = \frac{\frac{b}{m}s^2 + \frac{k_s}{m}s}{s^3 + \frac{b}{m}s^2 + \frac{(k_o+k_s+p)}{m}s + \frac{i}{m}} \quad (2)$$

P, the proportional gain and i, the integral gain are both normalized for sensor, actuator, and actuator driver gains in the equations above. The other model parameters are characteristics of the hardware and are defined visually in Figure 5. Parameter values, confirmed by experimentation, are listed in Table 2.

We used pole placement to select parameter values and controller gains to achieve desired dynamic performance. Pole-zero plots and their corresponding frequency responses are shown in Figures 6a and 6b. We want the damped natural frequency, labeled "C" in the figures, to be as low as possible because disturbances from the truss at frequencies above the damped natural frequency are attenuated. Truss disturbances are expected to be as low as 1 Hz. The suspension, the off-load mechanism, and the proportional gain act as springs in series which determine the damped natural frequency. The off-load mechanism should be fractionally as stiff as the suspension because we do not want its dynamics to dominate the system dynamics. We selected these parameters to put the natural frequency at ~0.2 Hz. Although it was mechanically possible to achieve a lower natural frequency, we could not accurately measure panel frequencies below 0.1 Hz.

The actuator eddy current damping controls the position of the zero labeled "D" in Figure 6b. Damping reduces the resonance peak, but it also reduces high-frequency isolation. Ideally, damping should be less than the value used in the breadboard, but the value was fixed by our actuator selection. In future implementations, the damping could be reduced by using non-conducting material in the actuator spool. The damping could also be increased, if desired, by changing the actuator driver to increase back-EMF.

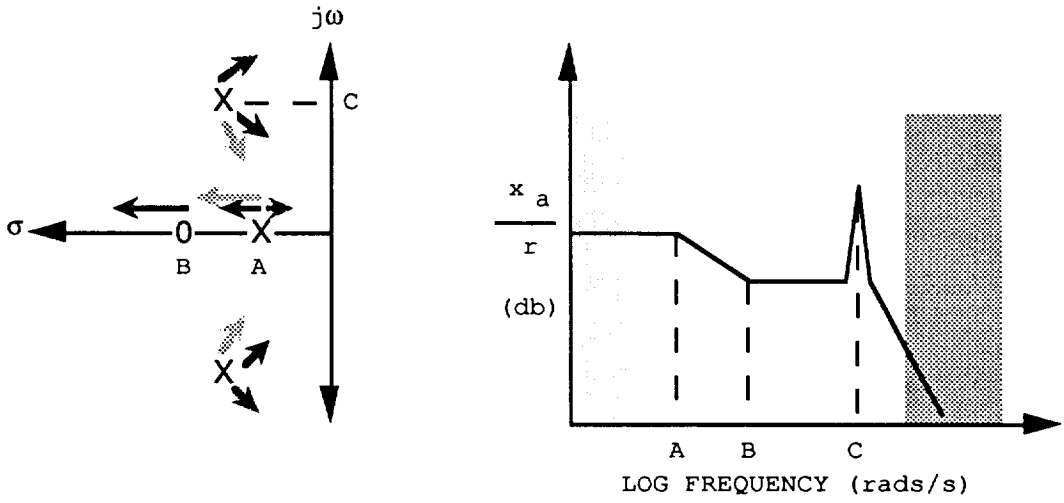

Figure 6a. Pole-Zero diagram and corresponding frequency response to position commands.

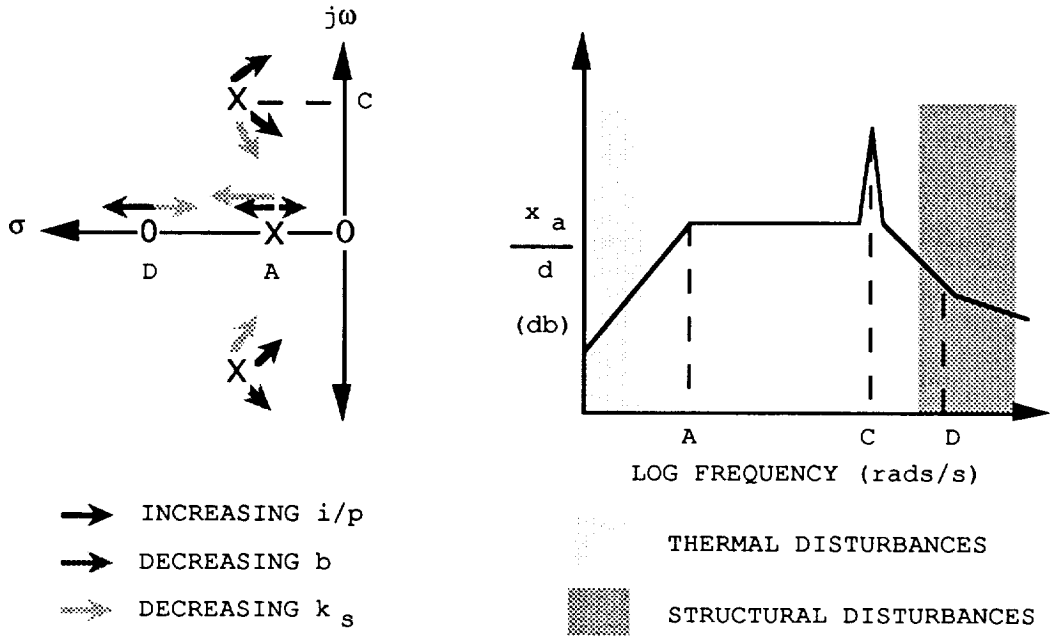

Figure 6b. Pole-Zero diagram and corresponding frequency response to truss disturbance motion.

The integral gain controls the lowest frequency pole, labeled "A" in Figures 6a and 6b, and therefore sets the command response bandwidth. The highest thermal strain frequency we have to actively compensate for is 2×10^{-4} Hz. We set the bandwidth at 0.06 Hz to achieve a reasonable step-response settling time.

Table 2. Dynamic model parameters.

Parameter	Value in 1-axis piston system (as modeled)	Value in 1-axis rotational system (as tested)
Panel mass/inertia m	2.01 kg	0.59 kg-m^2
Suspension stiffness k_s	3.68 N/m	1.24 N-m/rad
Off-load stiffness k_o	0.52 N/m	0.16 N-m/rad
Actuator eddy current damping b	3.02 N-s/m	0.91 N-m-s/rad
Proportional gain p	0.36 N/m	0.14 N-m/rad
Integral gain i	1.32 N/m-s	0.52 N-m/rad-s
System natural frequency w_n	0.24 Hz	0.26 Hz

PROOF OF CONCEPT: BREADBOARD DEVELOPMENT

We built a breadboard of the APM to test the feasibility of the design concepts as well as to explore more general control and isolation problems. In order to demonstrate feasibility, we had to emulate the APM dynamic plant, control system, and disturbance environment. We also wanted to maintain the flexibility to alter parameters and optimize the design rather than be constrained by a point design. Figures 7-9 contain photographs of the breadboard and an annotated diagram of its components.

A triangular aluminum frame, sized to approximate the mass and inertia of a mirror panel, substitutes for an actual panel. There are some differences: the triangular frame has slightly different moments of inertia in the two tilt axes, unlike the symmetrical hexagonal panel. Also, high-frequency (>20 Hz) structural resonances in the dummy panel do not coincide with actual panel modes.

The strut flexures are lengths of piano wire clamped at each end; the suspension stiffness can easily be altered by exchanging the installed wire with one of a different thickness.

The subplane is also a triangular aluminum frame. It is attached to a shaker, representing a truss node, at each corner. Closed-loop shaker control simulates truss disturbances. The shakers alone cannot support the weight of the subplane so we suspended the subplane from springs. Neither the shakers nor the springs laterally constrain the subplane, so lateral restraint struts, as in the panel suspension, tie the subplane laterally to ground.

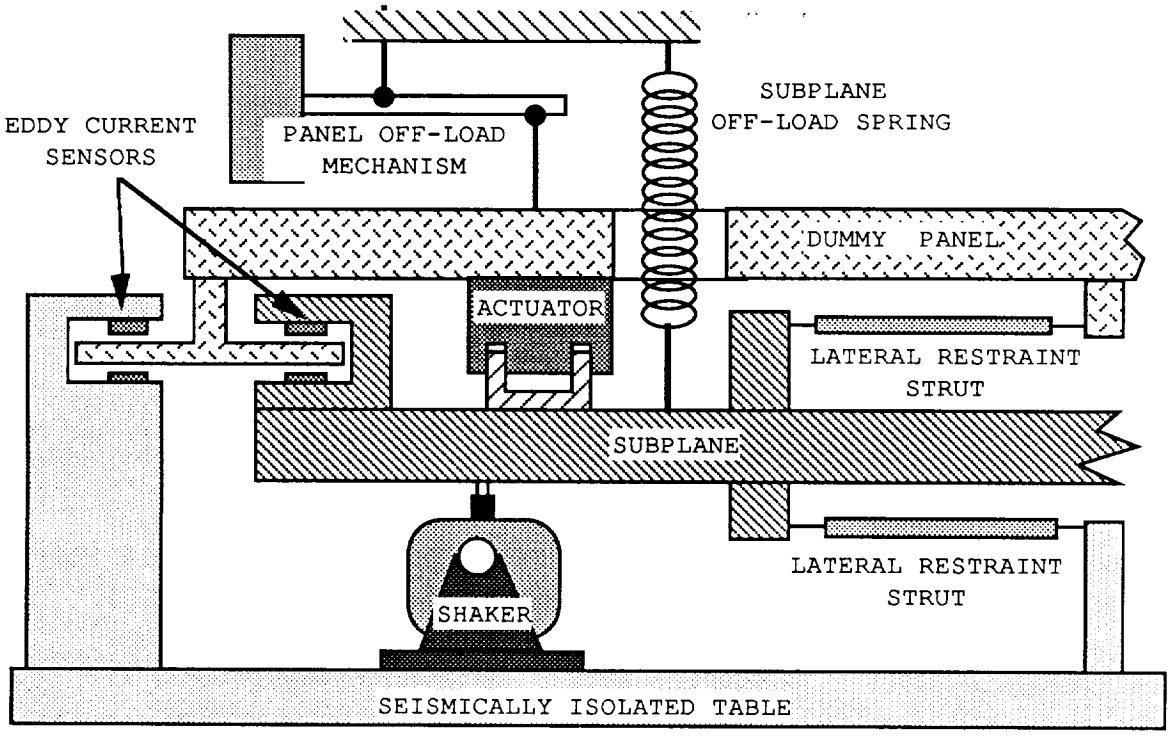

Figure 7. Schematic diagram of one corner of the APM breadboard.

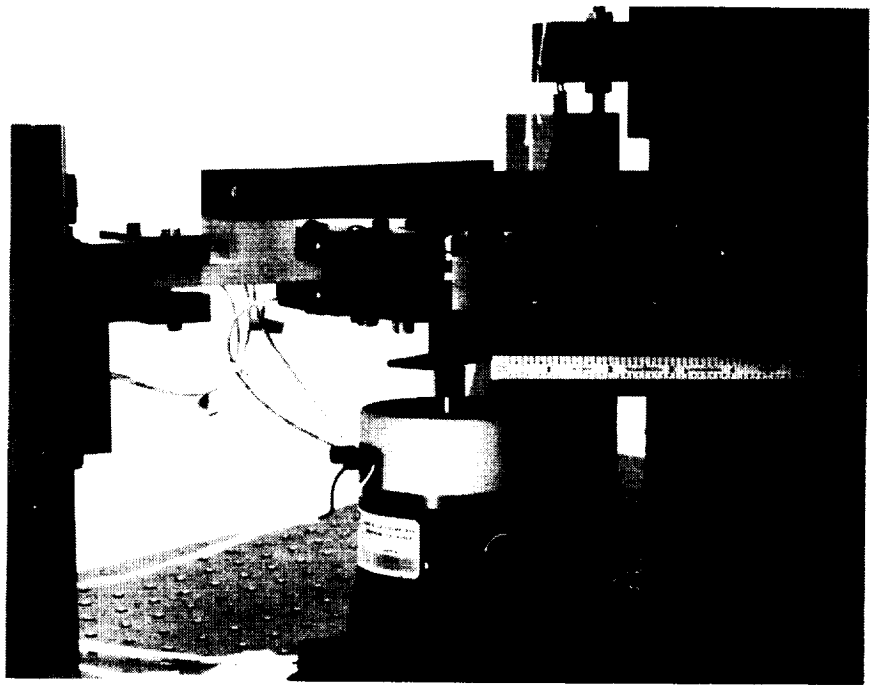

Figure 8. Photograph of one corner of the APM breadboard.

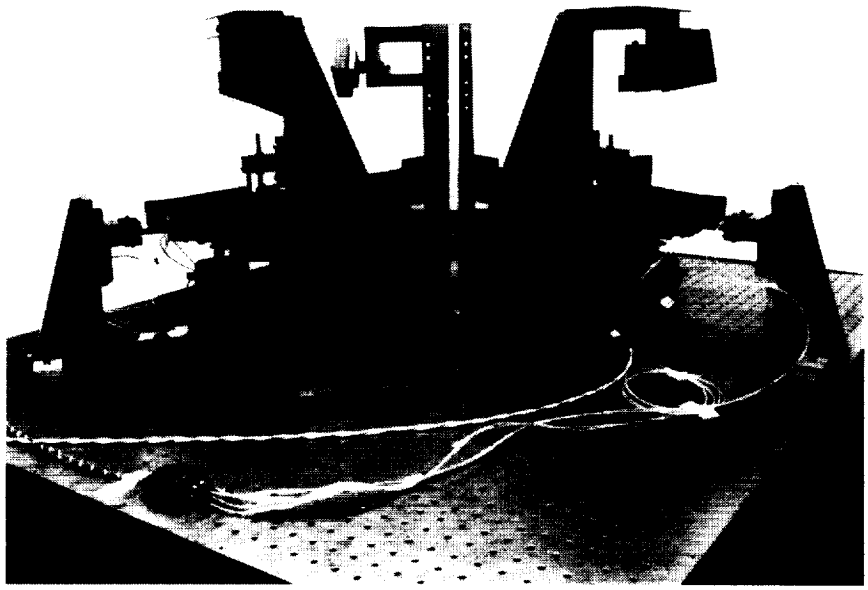

Figure 9. Photograph of the complete APM breadboard.

Eddy current sensors substitute for the figure sensor, which is still under development. The eddy current sensors measure panel-to-subplane vertical displacement and panel-to-ground vertical displacement at three points, from which piston and tilt can be determined. Subtracting the signals provides subplane-to-ground displacement for shaker control. The analog differential sensors have a 2.5-mm range and ~10-nm resolution. Sample and hold circuits added to the sensor output simulate different figure sensor update rates.

Analog circuitry emulates the servo control function of the central figure control computer. The analog boards are less expensive and easier to implement than a digital controller for the simple P-I control law.

The gravity off-load mechanism was particularly challenging because it must be fractionally as stiff as the panel suspension. We considered several options. An active off-load system was not considered because it would have been more expensive and complex than the breadboard itself. Linear springs were rejected because a spring with low enough stiffness and high enough load capacity was too long to fit in the laboratory. An overcenter mechanism, which uses a linkage to alter a linear spring's rate to near zero for small motion, was also rejected because of its mechanical complexity. A simple design using constant force coil springs was tested, but spring hysteresis prohibited its use. We finally selected a counterweight mechanism because of its mechanical simplicity and high probability of successful performance. The counterweight adds an effective mass to the panel, but that is acceptable because it is easy to account for in the system model.

The counterweight mechanism is shown in Figure 10. Three mechanisms, one at each corner, support the panel. The mechanism consists of a pivot arm with an adjustable lead weight at one end. The panel is suspended from a cord at the other end of the arm. The arm pivots on a cross flexure attached to a pylon mounted on the table. The cross flexure is designed for extremely low bending stiffness. Two lengths of cord, spaced a few inches apart, support the arm vertically. Two lengths of thin piano wire provide enough horizontal stiffness to eliminate yawing and horizontal motion.

The cross flexure adds negligible stiffness to the counterweight, but proper kinematic design is necessary to avoid pendulum stiffness. For zero pendulum stiffness, the pivot arm's center of gravity, the cross flexure pivot point, and the point from which the panel is suspended must be collinear. Stiffness is controlled by the equation:

$$k_o = \frac{-W\,h}{l^2} \tag{3}$$

where W is the weight of the panel and l and h refer to the horizontal and vertical distances, respectively, from the pivot point to the suspension point, as shown in Figure 10. The exact location of the pivot arm's center of gravity cannot be measured, especially since it moves when the lead weight is adjusted to balance the panel weight. In order to control the stiffness, h is adjustable. Notice from the equation that if h is positive (above the centerline in Figure 10), the spring constant is negative.

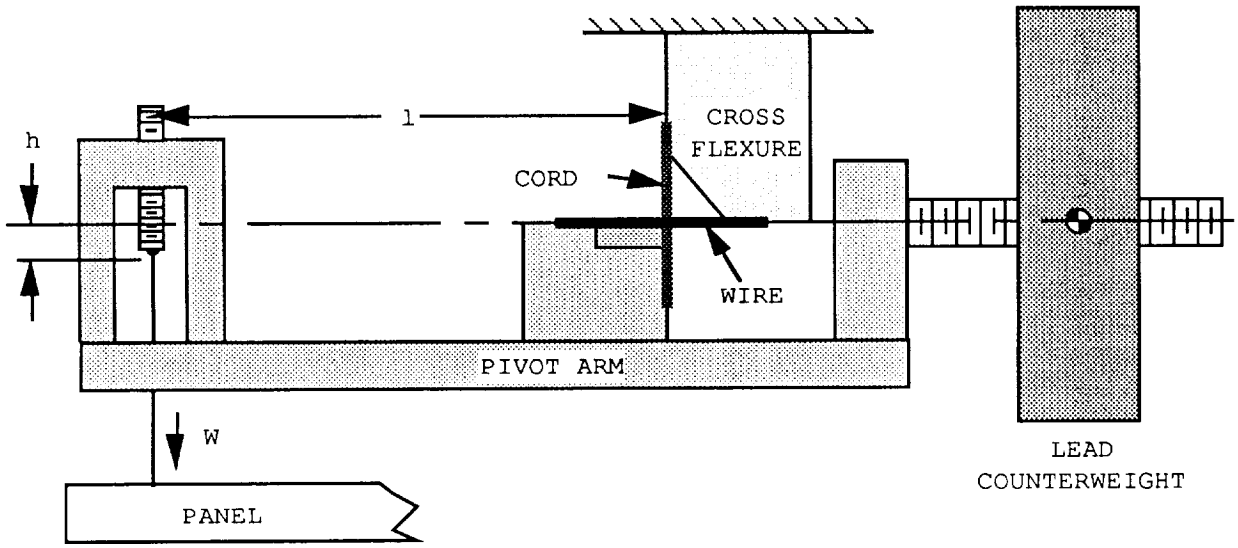

Figure 10. The counterweight off-load mechanism.

It is important to isolate the breadboard from seismic disturbances during testing; with the panel so well isolated, seismic disturbances cause the sensors to move indicating apparent panel motion. The breadboard is mounted on an optical table attached to a seismic pier. The pier is sunk in the earth through a hole in the floor of the lab and thus isolated from vibration of personnel walking down the hall, etc. Nonetheless, it was necessary to turn off the building's air handler during tests because of its seismic disturbances. We also built a "tent" over the breadboard to isolate it from air gusts; an enthusiastic gesture by one of the experimenters could drive the panel against its stops.

TEST RESULTS

The initial series of breadboard tests were intended to measure actual parameter values and validate the system model. We constrained the panel to 1 degree of freedom, as in our model, by locking the position of two of the counterweight mechanisms. The panel was free to tilt about the axis defined by the two attachment points of the locked counterweights, reducing the panel dynamics to a rotary system analogous to the linear motion system described in the model. Only one actuator and one shaker were operated for these tests. Individual parameter values measured from this rotary system are listed in Table 2. Values for the linear motion system were derived from the rotary system measurements.

The panel frequency response to position commands was measured by driving the actuator with white noise and recording the response with a spectrum analyzer. In Figure 11, the actual response is compared with the transfer function from Equation 1. Similarly, isolation from truss motion was measured by driving the shaker with white noise while the panel was commanded to hold a constant position. In Figure 12, experimental result is compared to that predicted by the transfer function from Equation 2. This figure shows that the optical table resonance as well as panel structural resonances were excited, results not considered in our model. Although the breadboard does not correspond structurally to a flight-like APM, the APM may share this problem if large-amplitude truss disturbances occur at its structural resonance frequencies.

Position stability and step response under no disturbance is shown in Figures 13 and 14. The system achieved 0.07 μm rms position stability over 15 s, well below the 1 μm rms stability requirement. Settling time to a step command is approximately 20 s.

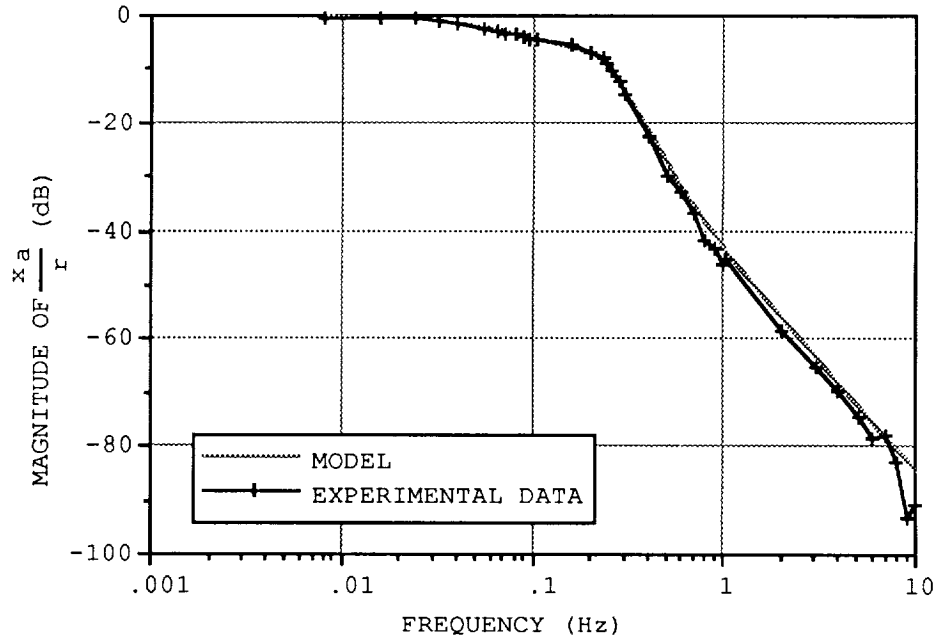

Figure 11. Predicted and experimental frequency response to position commands.

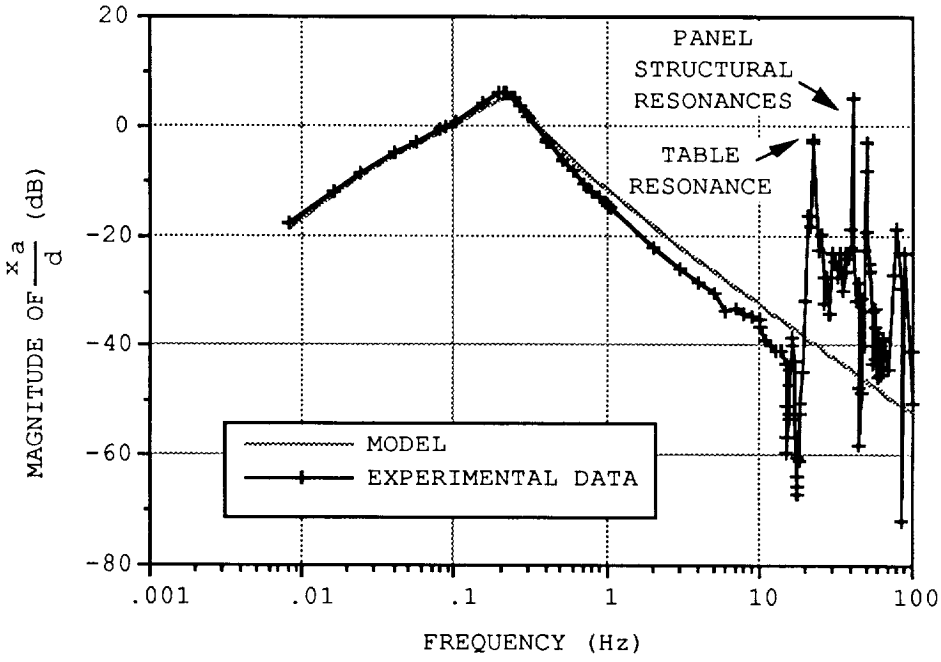

Figure 12. Predicted and experimental frequency response to truss disturbance motion.

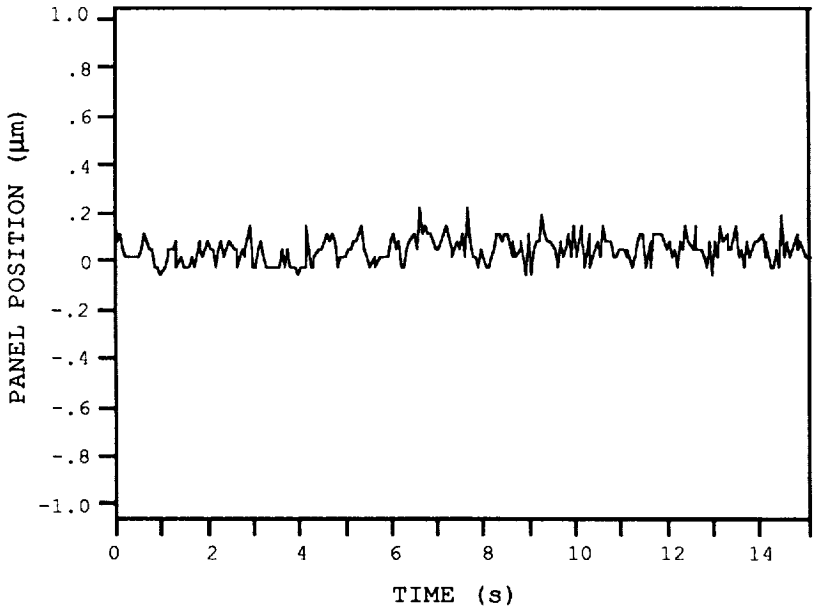

Figure 13. Panel position stability.

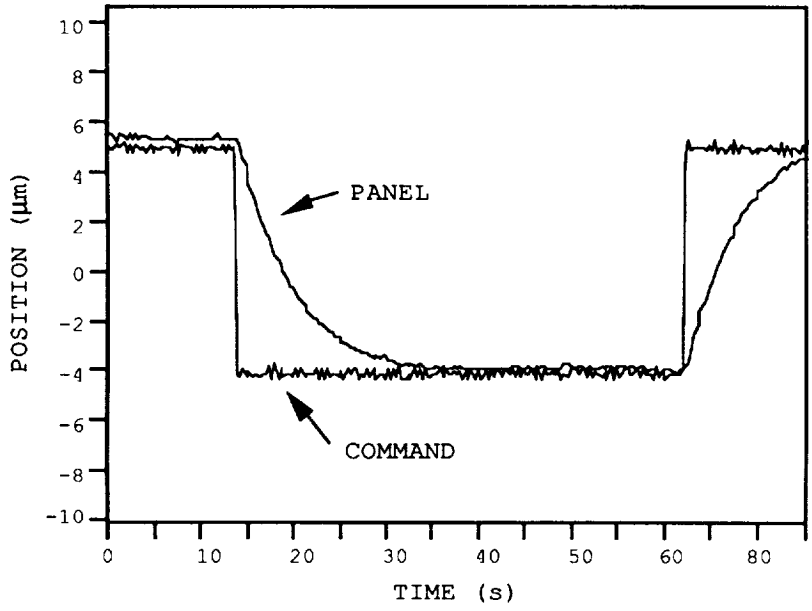

Figure 14. Panel step response to a position command.

FUTURE WORK

The next phase of breadboard testing will be to operate all three axes and compare performance to a three-axis model. After modeling the disturbance environment of a spacecraft in the focus missions, disturbance rejection requirements will be better defined, and design of an engineering model of an APM will proceed. Eventually, the PSR program hopes to demonstrate the complete figure control system with an array of APMs.

CONCLUSIONS

Thus far, all of the APM performance requirements have been met or exceeded. The APM shows great promise as a means of controlling and isolating mirrors or other optical components in limited degrees of freedom, with considerably less expense and complexity than a magnetic suspension. The authors hope that the design concepts used in the APM can be extended to other precision articulation and isolation applications.

REFERENCES

[1] Mettler, E., et al.: "Precision Segmented Reflector Figure Control System Architecture," presented at the S.P.I.E. Conference on Active Telescope Systems, Orlando, FL, March 1989.

[2] Gabor, G.: "Position Sensors and Actuators For Figure Control Of A Segmented Mirror Telescope," S.P.I.E., Vol. 172, p. 39, Instrumentation in Astronomy III, 1979.

[3] Gabor, G.: "Actuators For A Segmented Mirror Control System," S.P.I.E., Vol. 444, p. 287, Advanced Technology Optical Telescopes II, 1983.

[4] Lorell, K. R., et al.: "Development Of A Precision, Wide-Dynamic-Range Actuator For Use In Active Optical Systems," Proceedings of the 23rd Aerospace Mechanisms Symposium, p. 139, 1989.

ACKNOWLEDGMENTS

The PSR control system architecture was conceived by Edward Mettler, Daniel Eldred, Hugh C. Briggs, Taras Kiceniuk, and Michael Agronin. The authors wish to acknowledge the substantial contributions to this research by other members of the PSR Figure Control Team: Russ Allen, Dhemitrious Boussalis, and George Sevaston.

This work was performed at the Jet Propulsion Laboratory, California Institute of Technology, under contract for the National Aeronautics and Space Administration.

A DYNAMIC MOTION SIMULATOR FOR FUTURE EUROPEAN DOCKING SYSTEMS

G. Brondino and Ph. Marchal*
D. Grimbert and P. Noirault**

ABSTRACT

Europe's first confrontation with docking in space will require extensive testing to verify design and performance and to qualify hardware. For this purpose a Docking Dynamics Test Facility (DDTF) has been developed by MATRA under a CNES contract. It allows reproduction on the ground of the same impact loads and relative motion dynamics which would occur in space during docking. It uses a nine-degree-of-freedom, servo-motion system, controlled by a real-time computer, which simulates the docking spacecraft in a zero-g environment.

The test technique involves an active loop based on six-axis force and torque detection, a mathematical simulation of individual spacecraft dynamics, and a nine-degree-of-freedom servo-motion of which three DOF's allow extension of the kinematic range to five meters.

The configuration has been checked out by closed-loop tests involving spacecraft control models and real sensor hardware. The test facility at present has an extensive configuration that allows evaluation of both proximity control and docking systems. It provides a versatile tool to verify system design, hardware items and performance capabilities in the ongoing HERMES and COLUMBUS programs.

The paper describes the test system and summarizes its capabilities.

INTRODUCTION

The HERMES spaceplane will develop on-orbit servicing capabilities in Europe, which will open new horizons for European space system designs and operations. In this context, rendezvous and docking represents a major step in expansion of European orbital operations, and is typical of HERMES mission requirements.

---

* Centre National d'Etudes Spatiales, Toulouse, France
** MATRA, Velizy, France

Because mission success for HERMES will be dependent on the docking function, which must be performed reliably and safely, docking must first be verified by extensive ground tests tailored to qualify the system hardware for flight. A research and technology program has been sponsored by CNES at MATRA, to develop a motion-simulation facility to evaluate the relative control of closing spacecraft, and the contact dynamics of docking systems. This test facility is proposed for design, integration/verification and operational support in the development and operation of the HERMES proximity and docking system. Currently, it is planned to utilize this facility to define the requirements, to explore the technology and to assess the dynamic performance of HERMES-baselined soft docking.

TEST FACILITY OVERVIEW

Different concepts may be considered for ground simulation of two spacecraft docking in a zero-g environment. The concept selected consists of a real-time, active loop based on a six-degree-of freedom servo-motion with six-axis force and torque detection and mathematical modeling of the docking spacecraft dynamics. The docking hardware under test is physically installed in the motion-generating device (Fig. 1).

At a high sampling frequency (125 Hz), the forces and torques exchanged during contact of the docking interfaces are sensed and transmitted to the computer as input data to the spacecraft dynamics model. Compensation for gravity effects is concurrently made in the computer. The derived relative kinematics are then transformed into real motion.

This simulation technique is adaptive enough to accommodate any change in the docking spacecraft dynamics to be evaluated with a given set of docking hardware.

The docking is provided by a relative motion in all six degrees of freedom between two structural rings representing the docking interfaces. The motion is produced by a six-axis table, driven by six electrical screw jacks. One of the rings is fixed in the laboratory coordinate reference axes.

To represent the final approach (the last five meters), three degrees of freedom have been added, consisting of large amplitude translation along the docking line, and two rotations serving to simulate the angular misalignments about the transverse axes.

At the end of the final approach simulation, the test facility must achieve a reference docking test configuration. Thus the three additional degrees of freedom must be nullified, and the test system

must have no residual structural flexibility or backlash. During the final approach there is no contact, so the rotations and lateral translations can be represented by moving the rendezvous sensor (two rotations, using a two-axis, dedicated rotation device). For arresting the translational motion, a clamping system utilizing air brakes is employed for hardlocking the mobile mount, with emphasis on eliminating flexibilities and backlash.

The algorithms which are used for handling the nine degrees of freedom are based on optimization within the constraints on the motion axes.

The facility design offers a high structural stiffness and a high motion resolution. The geometrical configuration is optimized to reach the best compromise between kinematic stroke and dynamic loads in the docking hardware.

The screw jacks used on the six-axis table use precision ball screws (3 mm per revolution) driven by stepper motors (3200 steps per revolution). They provide a motion resolution of 1 μm and a load capability of 1500 N at low speed (<2 cm/sec). The measured backlash is 50 μm, and the maximum speed is 10 cm/sec. The load sensors are mono-axis piezoelectric force transducers, selected for their stiffness (10^8 N/m), their high linearity and their low noise (0.5 N over a 1000 N range).

The test facility involves a real-time computer architecture (Fig. 2), based on a 68020 work station for test operation and monitoring, a 12 Mflop array processor for simulated dynamics computation, and a GOULD 32/67 for data recording and output.

The software of the DDFT includes, in addition to the orbital dynamics, the simulation of structural flexibilities (first combined mode of the deployed solar panels and antenna) and liquid sloshing (one tank in each vehicle). Plume effects are computed off line, and their influence memorized to be used in real-time software.

In order to calibrate the facility and to verify validity of its performance, an extensive series of open- and closed-loop runs were made under a full range of operating conditions. The checkout culminated in testing functional docking hardware.

During these checkout operations, some limitations on the testing capabilities were identified:

1. The bandwidth is limited to 6 Hz, which is a limitation in the range of spacecraft mass and docking hardware stiffness characteristics that can be evaluated (Fig. 3).
2. The load and speed capabilities of the six-axis table make no provision for accommodating "impact docking" hardware.

3. Vibrations associated with screw-jack activation cause degradation of the contact force measurements.
4. Backlash and absolute accuracy need improvement to be more representative of real motion.

PERFORMANCE VALIDATION

A one-axis testbed evaluation has been performed to derive characteristics of the screw jacks and to validate the hardware and software configurations. The measured backlash of the screw jacks is now less than 5 μm.

The vibration level has been lowered, but it is still important because of stepper motor resonance at some drive frequencies.

Closed-loop tests have been conducted to validate the computer architecture and the management of software. The computing time has been optimized with the sampling frequency at 125 Hz, so that the simulator bandwidth attains 6 Hz.

A screw jack prototype based on a satellite roller screw has been developed. It is used for the six-axis table and is characterized by:

- Low noise level (no balls in the screw)
- Manufacturing accuracy of the screw at 10 μm
- No backlash
- Additional guidance of the screw jack (no collapse)
- Good motor-screw coupling
- Rotation lock for the linear part
- Stop pin for initial positioning

Limitations still exist. The most important one is the excessive vibration level during operation, which can be effectively reduced by substituting a DC motor/encoder assembly for the screw-jack actuation.

This solution is being studied at present and will provide further advantages (increased load and speed capabilities), so that the DDTF will allow evaluation of impact docking dynamics involving initial velocities to 10 cm/sec, forces to 5000 N and a lower noise level.

Validation

The introduction of simplified approach-control laws referenced to real test rendezvous sensor information is currently underway. This will allow validation of the closed-loop operation of the test facility through the full range of its testing capabilities.

The Imaging Rendezvous Sensor (IRS) uses a new process mode called Flash During Transfer (FDT), developed by MATRA, which allows work under marginal lighting conditions (even with the sun in the sensor field of view). The sensor uses a special target pattern, composed of five optical retro-reflectors (fig. 5), illuminated by a pulsed laser source. This equipment can measure with high accuracy the relative attitude and position of the two bodies(three rotations to 20 meters and three translations from 250 m to contact).

The Telemetry Rendezvous Sensor (TRS), which is used for distances from 1000 meters to 2 meters, measures the phase difference between the emitted and the retro-reflected wave, of an amplitude modulated laser source. This sensor can use the same target pattern as the IRS.

The characteristics of the sensors are as follows:

	IRS	TRS
Field of view	10°	10°
Attitude range	±2°	±2°
Distance range	0-250 m	2-1000 m
Attitude resolution	0.25°	0.25°
Line of sight precision	0.05°	0.05°
Distance resolution	1%	1-3%
Pulse	100W	100mW
Duration	200 nsec	-
Modulation rate	1 Hz	15 MHz
Measurement rate	1 Hz	1-10 Hz
Target	2-3 Kg	1 Kg
	0.1-1.5 m	0.1 m

Functional Synthesis:

The DDTF can perform docking tests from the last five meters of the controlled final approach (based on real sensor measurements) down to linkup of the docking interfaces (by use of simplified docking mechanisms) (Fig. 4).

Within the computer, rigid-body mass properties from 4000 kg to 60,000 kg and inertia properties from 10^4 kg.m^2 to 10^7 kg.m^2 can be simulated, providing significant margins over today's known mission needs.

The testbed bandwidth is about 6 Hz, so that the test hardware stiffness may vary between 10^3 N/m and $3x10^6$ N/m in translation, and 10^4 Nm/rad and $3x10^6$ Nm/rad in rotation.

The attainable performance is subject to the testbed operating capabilities as follows:

Final Approach (emphasis on motion)

	Translation	Rotation
Position Range	5cm inside a 10° conical envelope	±5°
Velocity Range	axial 10 cm/sec radial 2 cm/sec	5°/sec
Resolution	0.1 mm	0.001°
Accuracy	1 mm	0.01°
Acceleration range	5.10^{-3} m/sec^2	10^{-3} rad/sec^2

Docking (emphasis on contact loads)

	Translation	Rotation
Position Range	±7.5 cm	±2.5
Velocity Range	1.5 cm/sec axial 0.5 cm/sec radial	0.2°/sec
Resolution	1 μm	-
Accuracy	1 mm	-
Acceleration range	0.1 m/sec^2	10^{-2} rad/sec^2
Load range	1.500 N axial 900N radial	- 500 Nm

The basic architecture of the testbed facility is shown in fig. 5, with hardware items separated from computer software. A computerized graphic display allows visualization in real time of the individual spacecraft response motion during a test run, in either spacecraft or orbital coordinate reference axes. In addition, provision is included in the facility to accommodate enhanced spacecraft dynamic models and pilot interfaces so that manual proximity control and docking can be evaluated.

CONCLUDING REMARKS

A dynamic testing capability for docking systems has been described. The technology, based on current off-the-shelf components, has been optimized to eliminate backlash and to minimize vibrations (which produce the most significant limitations on the testing performance). Computations and computers in the control loop incorporate complete motion generation and spacecraft dynamics simulation, so that the facility acquires a potential for implementing both spacecraft proximity control and docking systems (sequentially or independently) without limitation on the testing requirements.

This unique concept provides a versatile test tool to validate system design, to demonstrate hardware items, and to verify dynamic performance capability and reliability.

Currently, application of this facility is being planned for testing HERMES docking model hardware in a joint CNES-ESA program, and evaluating the required manual control performance for docking. Because of use in HERMES missions of the FREEDOM space station docking system, this testing is primarily intended to evaluate the design revisions of the system in order to accommodate the HERMES soft-docking requirements.

REFERENCE

G. Brondino and Ph. Marchal, Centre National d'Etudes Spatiales, Toulouse, France; D. Grimbert and P. Noirault, MATRA, Velizy, France, "DDTF Improvements for More Accurate Space Docking Simulation", EIOOTS, September 1989.

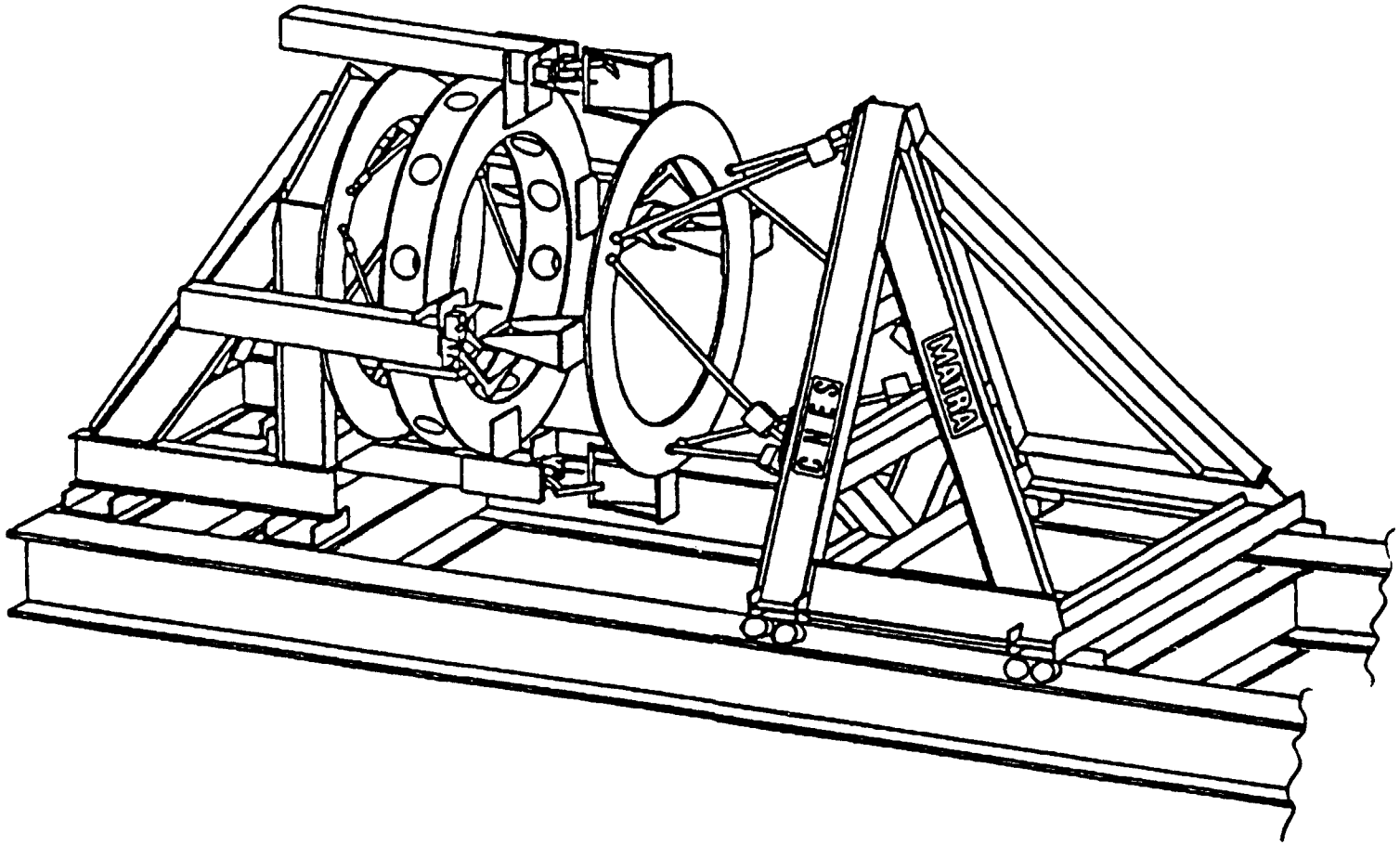

Fig. 1 : Representation of the actual DDTF

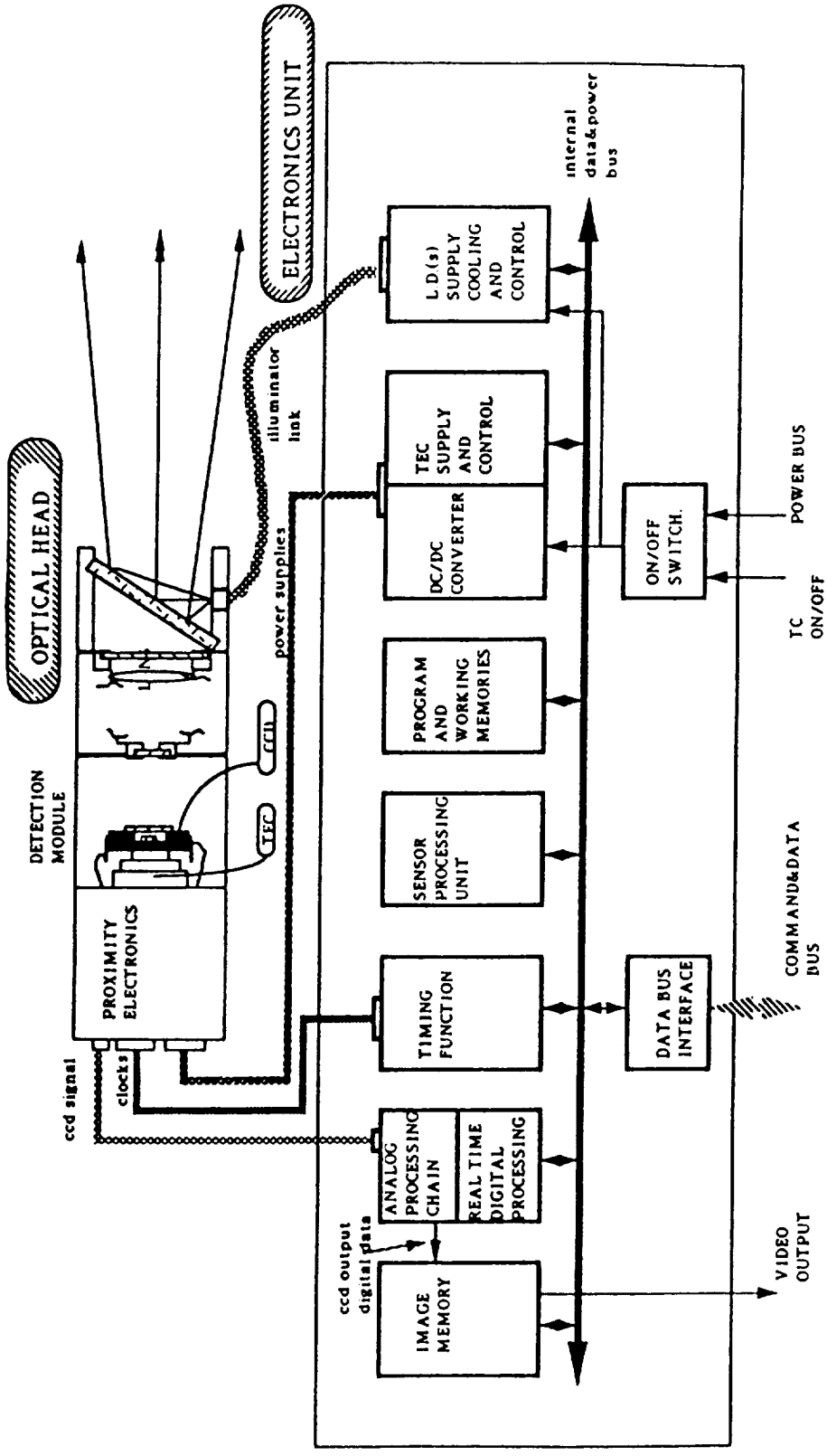

Fig. 2 : Real time computer architecture

C-2

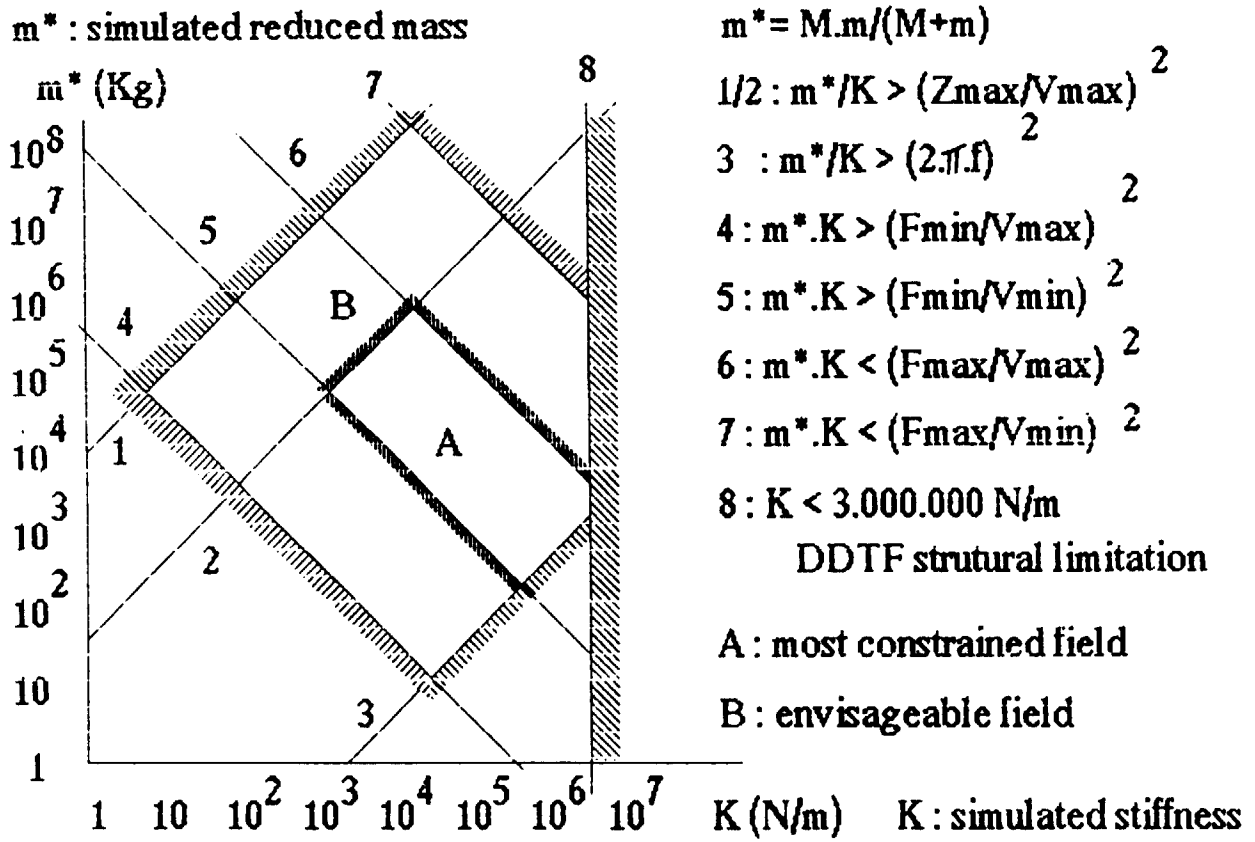

Fig. 3 : Field of DDTF limitations

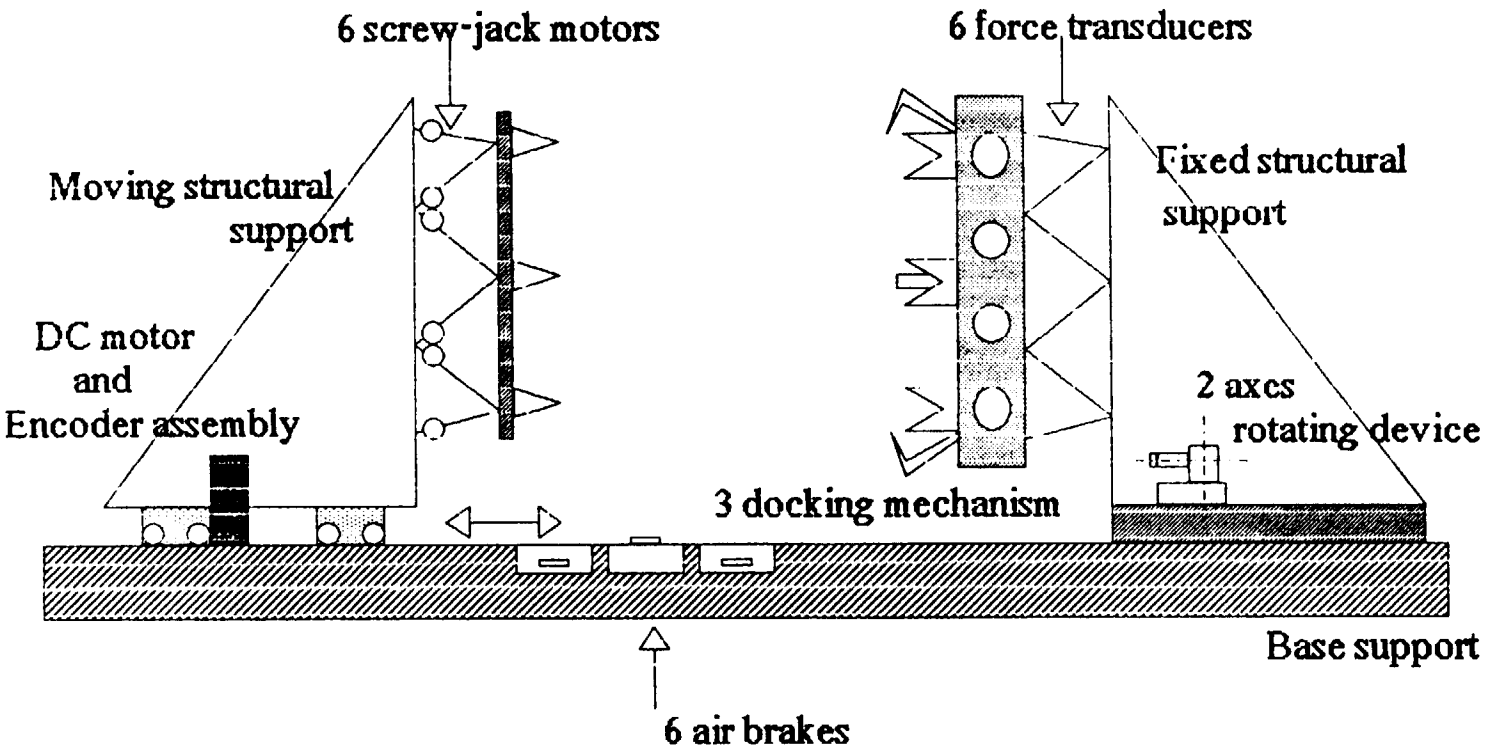

Fig.4 : Testbed hardware configuration

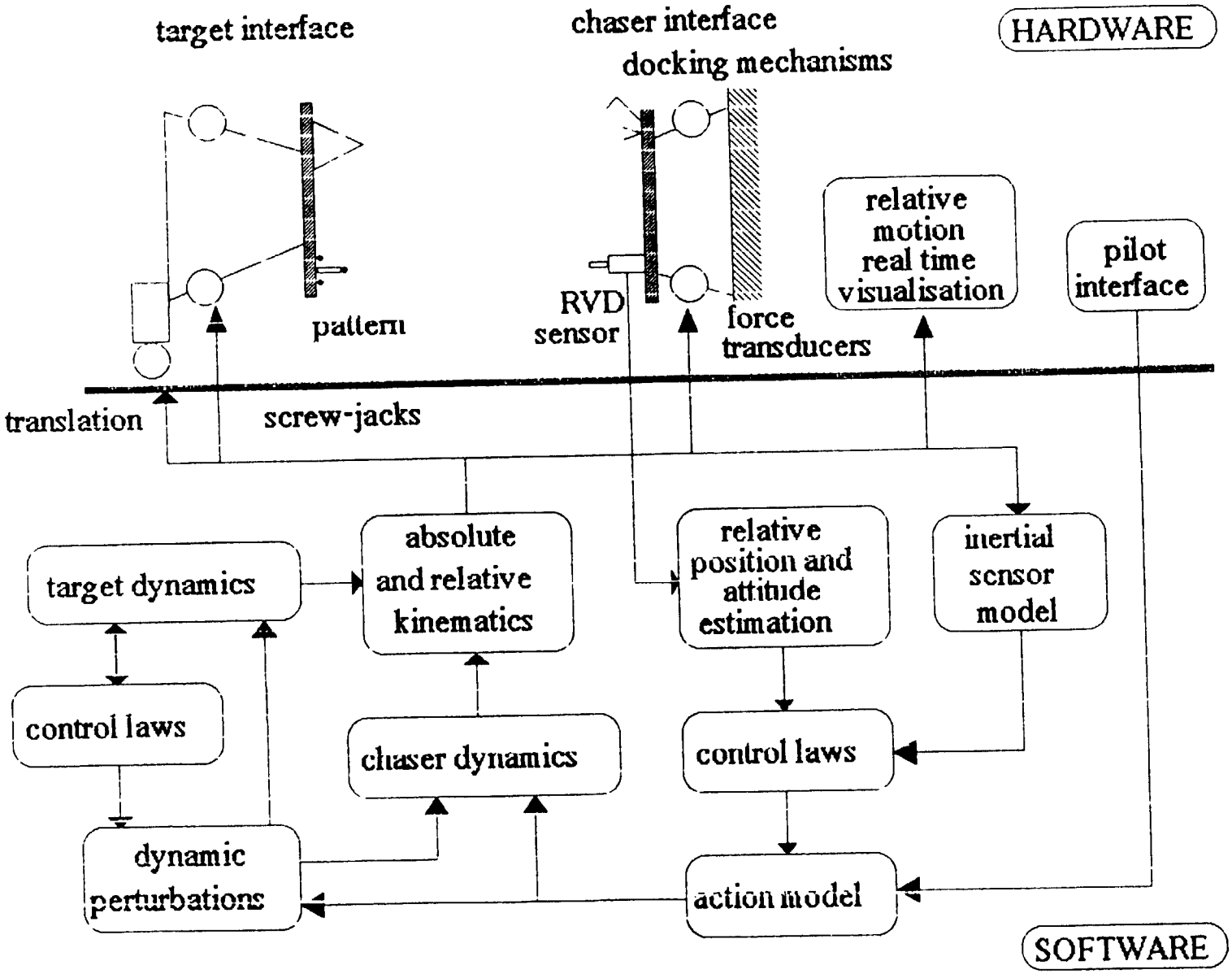

Fig. 5 : Global architecture

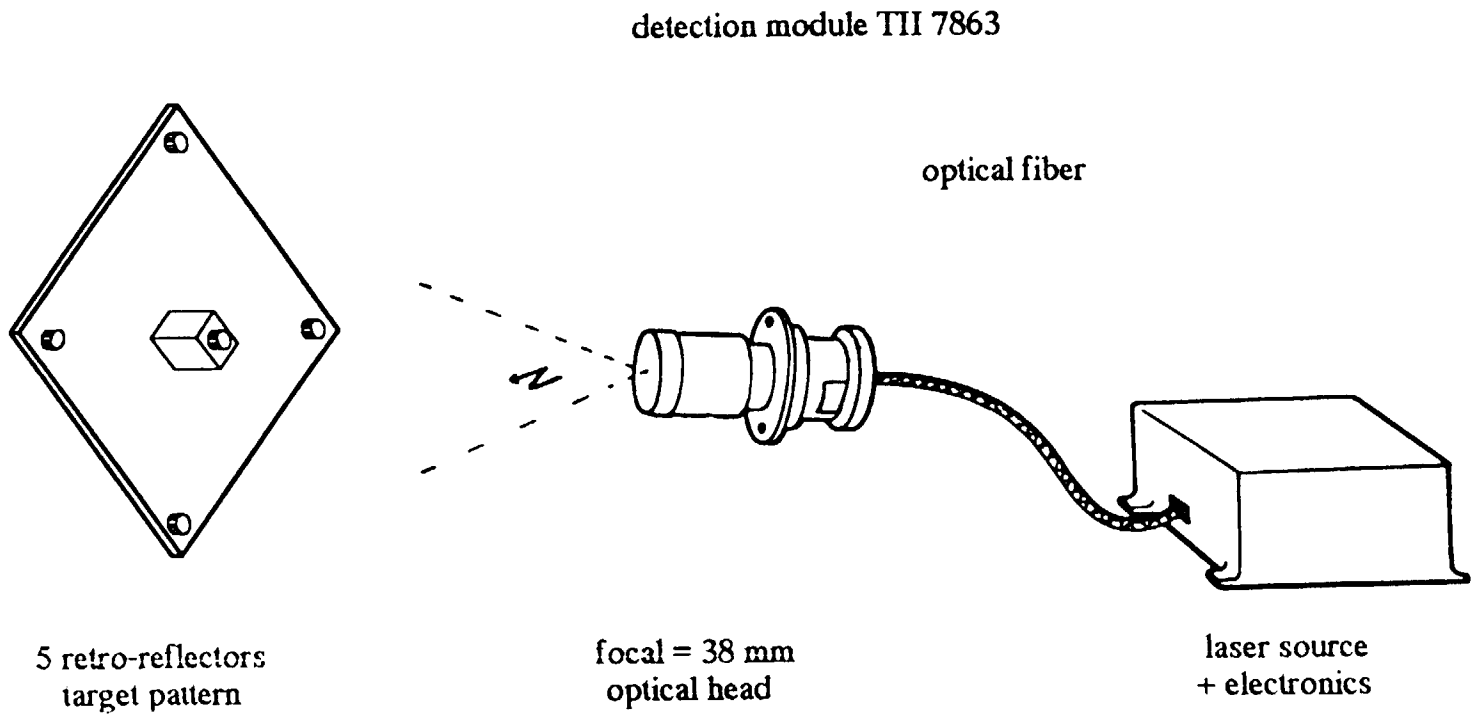

Fig.6 : Imaging Rendez-vous Sensor and target pattern

N90-22086

THE DEVELOPMENT OF A COMPLEMENTARY EXPENDABLE LAUNCH VEHICLE INTERFACE FOR AN STS DEPLOYABLE PAYLOAD

Ed Eubanks* and John Gibb*

ABSTRACT

This paper describes the development of a unique interface, the Titan Payload Adapter (TPA), between a Space Transportation System (STS) deployable payload and an expendable launch vehicle (ELV). Separate ascent and separation constraint systems allow a payload with integral trunnions to retain its originally designed, boost-phase load structure, yet also allow the expendable booster vehicle to separate from the payload via retro-rockets. We discuss design requirements as well as development problems and their resolutions.

INTRODUCTION

The Challenger accident and the subsequent STS redesign and upgrade period created an immediate need for an ELV capable of boosting a shuttle-class payload into orbit, with a minimum of design changes to the payload. Lockheed Missiles and Space Co. (LMSC) developed an interface to address this need which adapts such a payload to the Titan IV booster (Fig. 1).

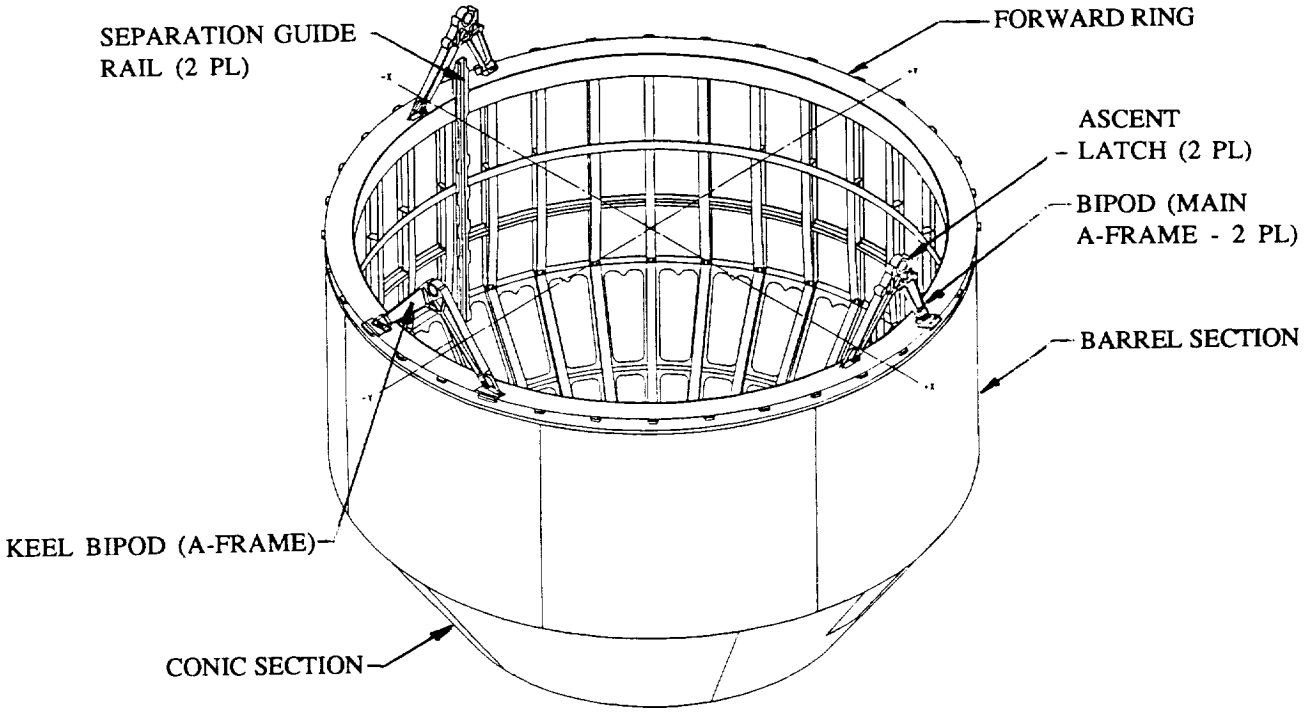

FIGURE 1: Titan Payload Adapter

* Lockheed Missiles & Space Company, Inc., Sunnyvale, California

REQUIREMENTS

Several groundrules directly influenced TPA design. Specific requirements for the adapter design were that the interface must:

1) Cause no significant structural change to the payload (i.e., retain four-point payload trunnion system);

2) Attach to the ELV mounting interface (Titan IV, Stage II);

3) Accommodate dynamic and thermal distortion during ascent and residual distortion during separation;

4) Separate from the payload via existing booster retro-rockets;

5) Prevent contact between the booster and payload structure during separation;

6) Meet the above separation requirements with only three out of four retro-rockets functioning (this is actually a goal, not a requirement).

Additional derived requirements also affect mechanism design for the adapter. These requirements address concerns of redundancy, reliability, flexibility, manufacturability, and weight minimization. All mechanisms are required to have redundant activation paths for reliability. We found that the separation mechanisms must be flexible enough to minimize impact loads, yet stiff enough to prevent undue motion leading to Booster Vehicle/Satellite Vehicle (BV/SV) contact. This somewhat unique flexibility requirement is a direct consequence of the separation guidance system deadband, which results in impact loading during separation. Weight minimization of components is a goal, but no specific requirements exist.

DESIGN EVOLUTION

The TPA engineering team faced a challenging design task. This problem, reduced to its essential kinematic description, was to provide a six-degree-of-freedom (DOF) constraint between the BV and the SV during ascent, and five-DOF constraint during separation (Fig. 2). The TPA engineering team, a small group consisting of a broad range of disciplines, worked together to produce a system which meets all requirements.

The predominant TPA structural design problem is the absence of a planar boundary typically existing between the spacecraft and the booster. Preliminary work done by the engineering team, using the booster and payload structural interface requirements as constraints, indicated that the most efficient TPA structural design would consist of a cylindrical "barrel" mated to a diameter-reducing conical section. The adapter barrel envelopes the aft two meters of the payload, while the conic section attaches to the booster. Hardpoints on the barrel are required to transfer high trunnion loads into a ring-longeron system, eventually leading to an evenly stressed skin at the conic portion. The engineering team desired that the adapter fit within a standard "hammerhead" 5-meter-diameter payload fairing (PLF) for structural weight efficiency. However, the space available for the adapter structure between the payload and the PLF is insufficient when dynamic deflections are accounted for. The solution of this problem resulted in a 5-meter-diameter barrel structure with a modified PLF attached to the forward end of the barrel. The aft portion of the PLF (the hammerhead conic) is removed and the

TPA doubles as a fairing for the payload in this region, carrying both payload inertia and aerodynamic loads.

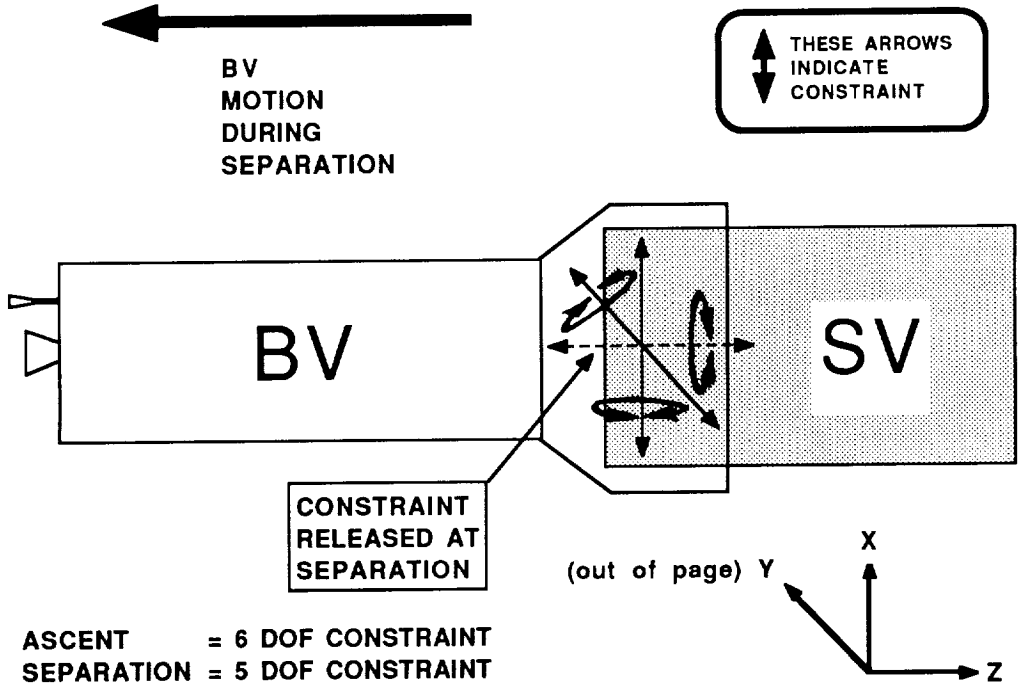

FIGURE 2: Ascent and Separation Constraints

The TPA's designers decided to divide the ascent and separation constraint tasks after developing the preliminary structural design. We believed that separating the tasks would produce a more optimal solution than one system designed to constrain the payload during both ascent and separation. The ascent constraint design task, then, was to react loads kinematically, as is done with the shuttle trunnion system, and then release this constraint at separation.

Ascent Constraint System

TPA designers produced numerous iterations of the BV/SV ascent constraint system in the course of developing the final configuration. We considered one early system using three latch mechanisms bolted to a forward ring structure on the TPA cylinder, one latch at each main trunnion and one at the keel trunnion. This design did not receive serious consideration because of high predicted loads and the requirement to preclude structural redesign of the payload, which virtually mandates retention of the four-trunnion concept. Additionally, stress analysts predicted large bending moments in the TPA forward ring due to the distance between the latch points and the skin of the adapter (0.25 m). Large ring bending moments were also predicted for the earliest four-trunnion constraint concept. This concept used two latches at the main trunnions and slotted bearing plates at the keel and aft trunnion locations to react loads in a similar fashion to the original shuttle latch system. Other proposed designs allowed the ring to support high moments, but were ultimately eliminated due to a payload access requirement which forced the payload adapter forward ring to be about 0.5 meters aft of the plane containing the main and keel trunnions.

To accommodate the aft placement of the ring, TPA designers considered a four-trunnion configuration wherein the supports mating with the main and keel trunnions increased in height, but remained bolted to the forward ring. The stress engineers once again predicted excessive bending moments applied to the ring. The design team eliminated the moments by adding bipod supports between the forward ring and the trunnion latches and keel bearing plate with spherical bearings at each ring attachment point. Likewise, the aft slotted bearing plate was attached to the TPA structure with a bipod, but lesser loads (and consequent distortion) allowed using a pin joint attachment. The spherical bearings and pin joints are incapable of transferring moments to the TPA structure (except as may develop as a result of friction in either a bearing or pin). The legs of the main and keel trunnion support bipods are designed to establish a path that brings the trunnion loads into the barrel main longerons and forward ring as close as possible to the skin at two points for each trunnion. This halves the point loads applied to the longerons and greatly minimizes the moment applied to the ring.

Ascent Latch

TPA engineering considered many concepts during latch development, with the aim of achieving a configuration satisfying several requirements. These include rapid unlatching, redundancy, the capability to withstand loads up to 220 kN, using an existing flight-qualified initiating device, and compatibility with the kinematic ascent support system. The rapid unlatching requirement led us to eliminate the STS trunnion latch mechanism from consideration. The concepts we did consider further used either pin pullers, explosive bolts or separation nuts for quick initiation. We studied several latch configurations gaining mechanical advantage through links or levers to minimize loading on the initiating device. Yet we also wanted both simplicity of design and minimal components for high reliability. Because of concerns about high latch loads, pinpullers were eliminated from consideration. The pinpuller-actuated designs required numerous linkages designed to reduce the load at the actuator, which resulted in uncertainty about reliability and stiffness due to the number of components. After much consideration, the design team proposed a final concept of actuation by a separation nut without a bolt ejector (Fig. 3). The

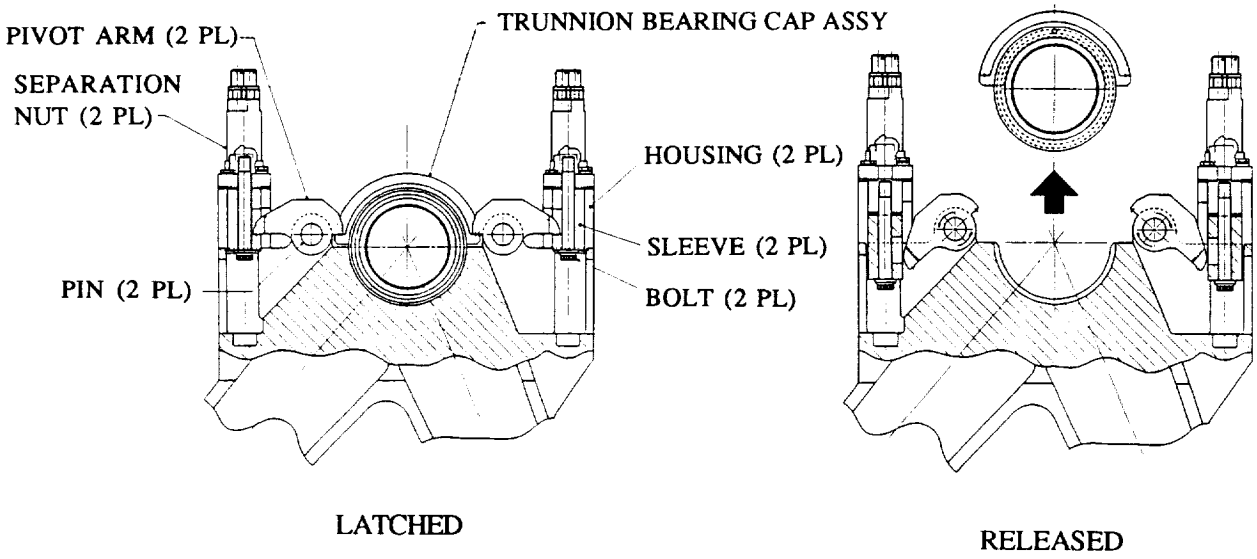

FIGURE 3: Ascent Latch

principal advantages of this design are simplicity, strength, and reduced shock, due to the elimination of the bolt ejector. Development testing proved that the latch's stored strain energy was sufficient to rapidly eject the bolt without assistance.

Separation Guide System

Preliminary studies by the separation analysis group showed that avoiding contact between the adapter and the spacecraft required a guidance system; an unguided system resulted in contact, even under nominal conditions. This conclusion was fairly obvious given the two-meter overlap of the two structures and the minimal clearances between them. The engineering team proposed several guidance concepts, based on rails and rollers.

The rail/roller separation guidance concept was previously used by the Lockheed Agena spacecraft and its adapter. The Agena system originally used three rails with two planes of rollers (Fig. 4). A fourth rail was added to the Standard Agena to reduce loads. The rollers acted upon the rails in compression only for both of these systems. Furthermore, the nominal rail/roller clearance was one-eighth of a millimeter, and rail/roller loads were likely induced by dynamic and thermal distortion during ascent (distortion predictions were beyond the state of the art at this time).

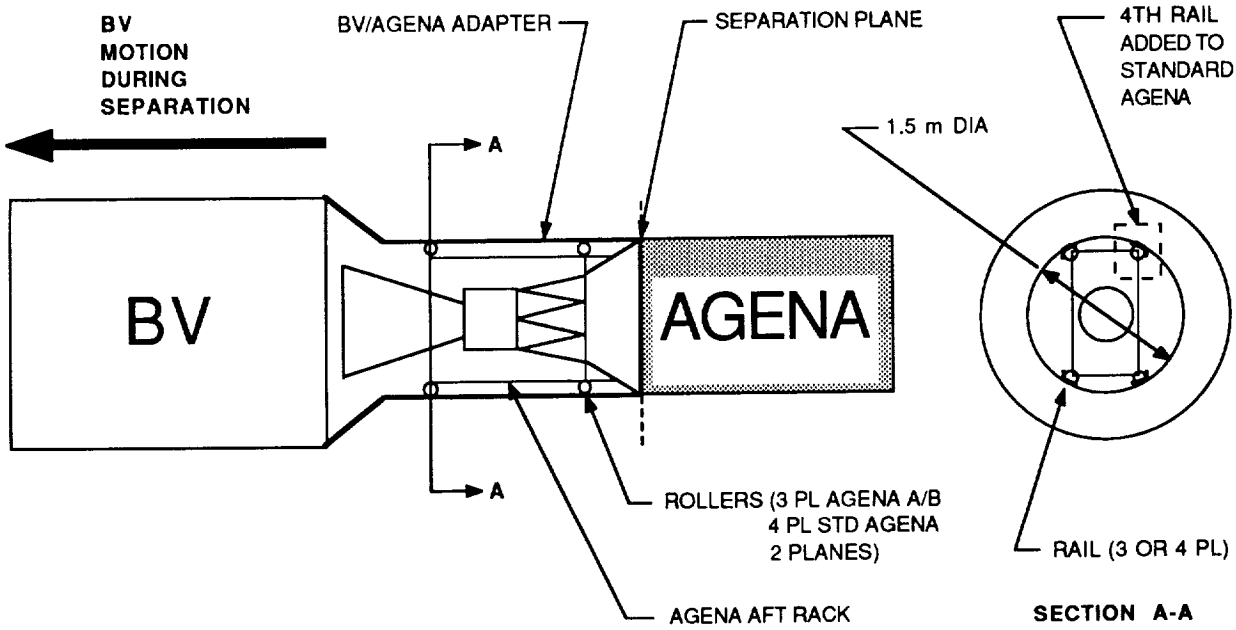

FIGURE 4: Agena Rail/Roller System

Initially, the design team proposed a three-rail system mounted to either the adapter for the payload, with two planes of compressively loaded guide rollers, similar to the original Agena but on a larger scale. The rail/roller interfaces between the payload and booster adapter are approximately at a 1.5-meter diameter for the Agena system, and this is increased by 230% to 5 meters on the Titan Payload Adapter. However, the payload's design precluded a three-rail system, and, moreover, kinematics prevented mounting the rails on the payload (relative pitch or yaw increases effective rail diameter, causing high compressive loads). Faced with these limitations, the design team proposed a two-rail system with rollers attached to the payload and rails affixed to the adapter. The designers realized that in addition to

radial loads (as in the Agena), tangential loads would also be reacted with a two-rail system. Several rail/roller concepts were examined to address this problem. We chose a C-shaped rail cross section because it has low local distortion under load and it encloses the rollers, preventing jamming or mislocation caused by ascent distortions.

Ascent Distortion

The most unusual and difficult problem the engineering team faced was accommodating BV/SV dynamic and thermal ascent distortions in the separation system to prevent it from becoming a secondary load path. Structural dynamic analysis predicted relative motion of plus or minus three centimeters between rails and roller locations on the payload. We knew a separation system similar to the Agena's, with its minimal rail/roller clearance, would undoubtedly react high loads during ascent at these distortion levels. The design team suggested expanding the rail/roller deadband to accommodate the dynamic motion, but analysis showed that this would result in large impact loads during the separation phase. Increasing the rail/roller freeplay locally, at the ascent positions of the rollers, was next considered (Fig. 5). Analysis of this concept, dubbed the "rail pocket" design, determined that it also could produce unacceptably high loads for most separation cases. This design is analogous to a bicycle hitting a pothole. The design team proposed using three planes of rollers, staggering the pockets so that two rollers remained on the rail when one was over a pocket. Unfortunately, manufacturing tolerances, residual ascent distortions, or rail flexibility could always permit a roller to contact a pocket.

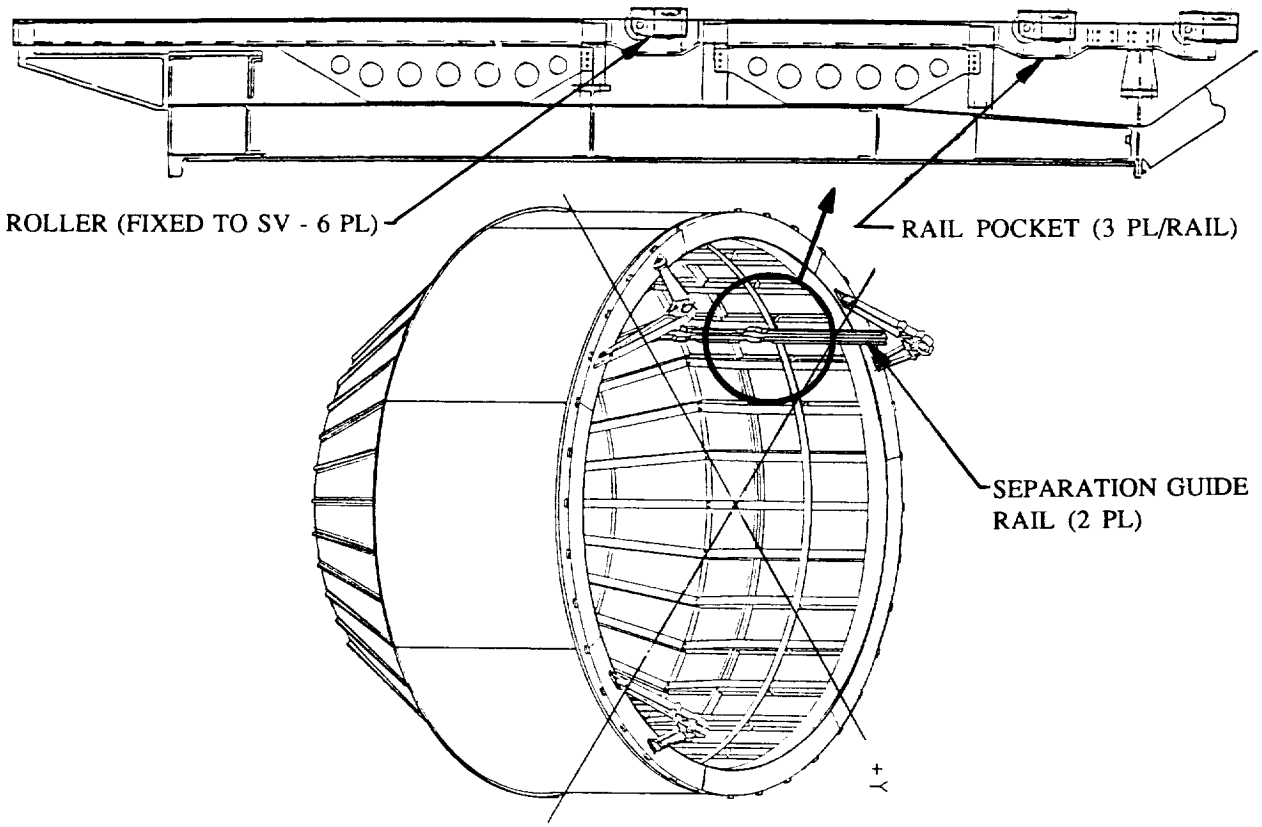

FIGURE 5: Rail Pocket Concept

TPA engineering began investigation of active solutions to the ascent motion problem after analysis of the rail pocket design failed to produce acceptable loads. Two basic concepts were proposed, rail "trap doors" and "active rollers." The trap door concept was based on the guide rail having a movable portion which accommodated rail/roller ascent motion. At separation, the movable portion of the rail would lock into place, giving the effect of a continuous rail. We became concerned about a roller becoming jammed when the trap door was open during ascent, and also about a trap door failing to close against a residually displaced roller at separation. These concerns caused us to focus on the active roller concept.

Residual Distortion

The active roller concept allowed the rollers to be free to move during ascent and locked them into position during separation (Fig. 6). The separation analysts determined that this concept could produce acceptable loads if proper control of the rail/roller deadband and total system flexibility was maintained. Additionally, we used kinematic analysis to determine that three roller locations on the payload would be sufficient for guidance. All three rollers are required to take tangential loads, but only two are required to react radial loads for a kinematic separation constraint system (Fig. 7). Thus constrained in five DOF, the payload is unaffected by residual distortions of the TPA. Residual distortions can result from thermal strain, PLF (aero) loads during ascent, and inertial ascent loads. A three-roller separation system is also unaffected by manufacturing tolerances of the TPA or payload.

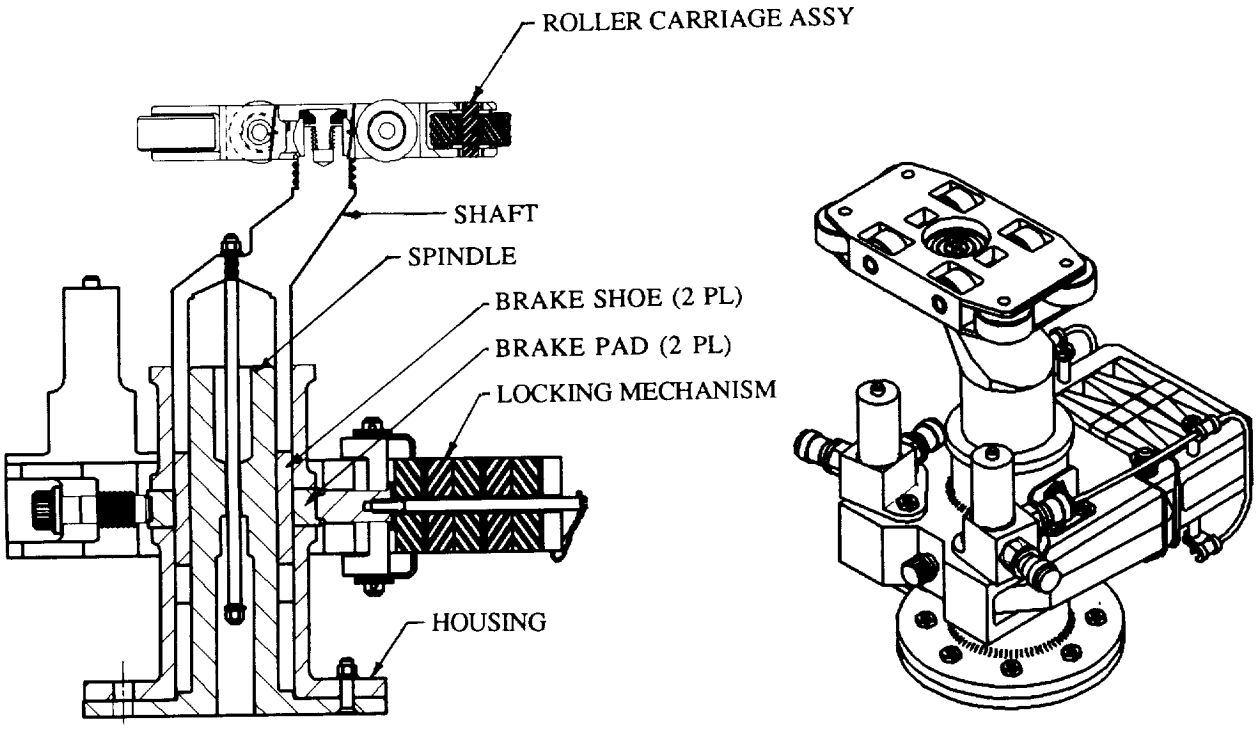

FIGURE 6: Active Roller Mechanism

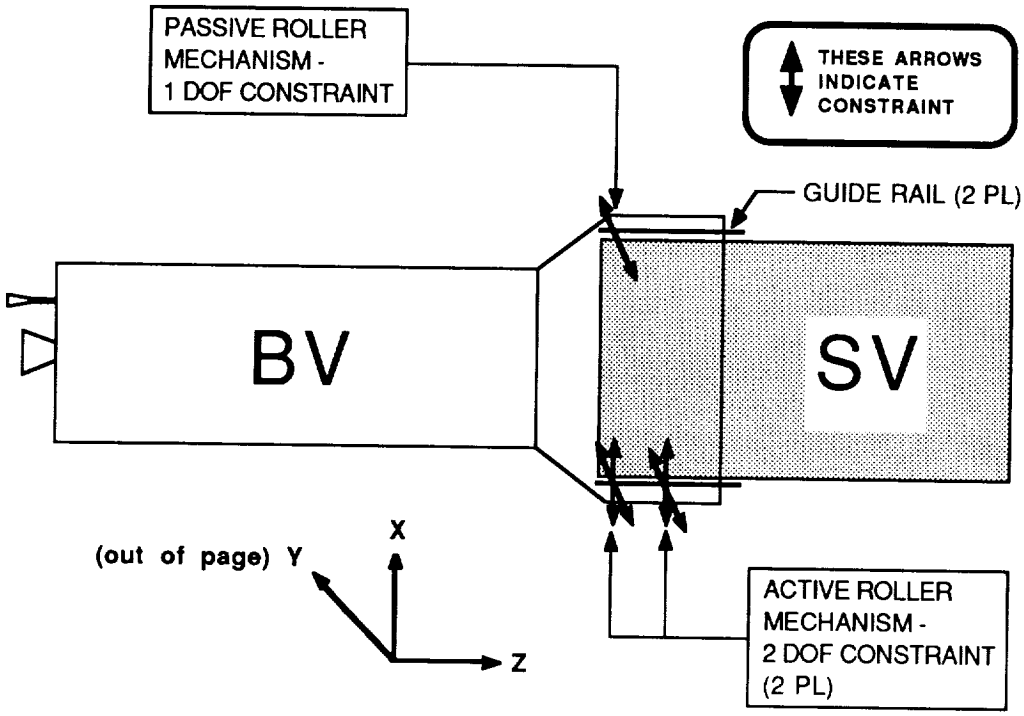

FIGURE 7: Three Roller Separation Constraint System

The engineering team decided to make the rollers reacting both radial and tangential loads active mechanisms (with lock-up). However, a requirement to limit the number of pyrotechnic circuits led us to design the roller taking only tangential loads as a passive mechanism (no lock-up). The separation analysts showed that a plus or minus three centimeter tangential deadband at the passive roller location exclusively would produce acceptable loads with anticipated flexibilities. Predicted flexibility values were later verified by testing end-item hardware.

Active Roller Mechanism

The primary requirements for the active separation guidance mechanism are that it accommodate relative rail/roller deflections of up to plus or minus three centimeters in both the radial and tangential directions during ascent, and that it support loads predicted to be as high as 20 kN and 9 kN in the radial and tangential directions, respectively, once activated at separation. The engineering team created a mechanism comprising a cylindrical housing with an inner telescoping shaft to accommodate the radial deflections (Fig. 6). We felt that a device based on a linkage arrangement could have allowed the required deflections but would have had unacceptably high deflections under the predicted loads. The inner shaft has an integral offset arm ("dogleg") at the outboard end near the rail. This dogleg accommodates tangential deflections as the inner shaft rotates in its housing. The dogleg offset is sized so that it is longer than the greatest tangential deflection. We accounted for friction effects to ensure that shaft rotation can never hang up in a fully deflected condition.

The TPA team next needed to solve the problem of locking the inner shaft to the housing with sufficient force to withstand the predicted separation loads. We preferred pinpuller activation to meet redundancy and rapid actuation requirements. We studied one design that used spring-loaded levers to engage splined locking surfaces, but eliminated it due to concerns over immediate engagement of the splines. Up to two millimeters of motion might have been required to lock the splined shafts, and analysis showed that this had undesirable effects on separation. A design that provided for immediate positive lock-up was required. TPA designers revised the spline mechanism, replacing the coarse mechanical spline grip with a friction grip (Fig. 8). An inner spindle was also added to the outer housing to provide additional friction braking surface for the lock-up brake pads. The two pads, when clamped by the lock-up springs, provide four friction surfaces (inner and outer) to react separation loads from the telescoping/rotating shaft to the cylindrical housing. The lock-up springs are a stack of five high-rate leaf springs, which can be applied by either of two pinpullers. TPA engineering gave high priority to a development program to investigate high-coefficient-of-friction materials for braking surfaces, which is discussed in a subsequent section.

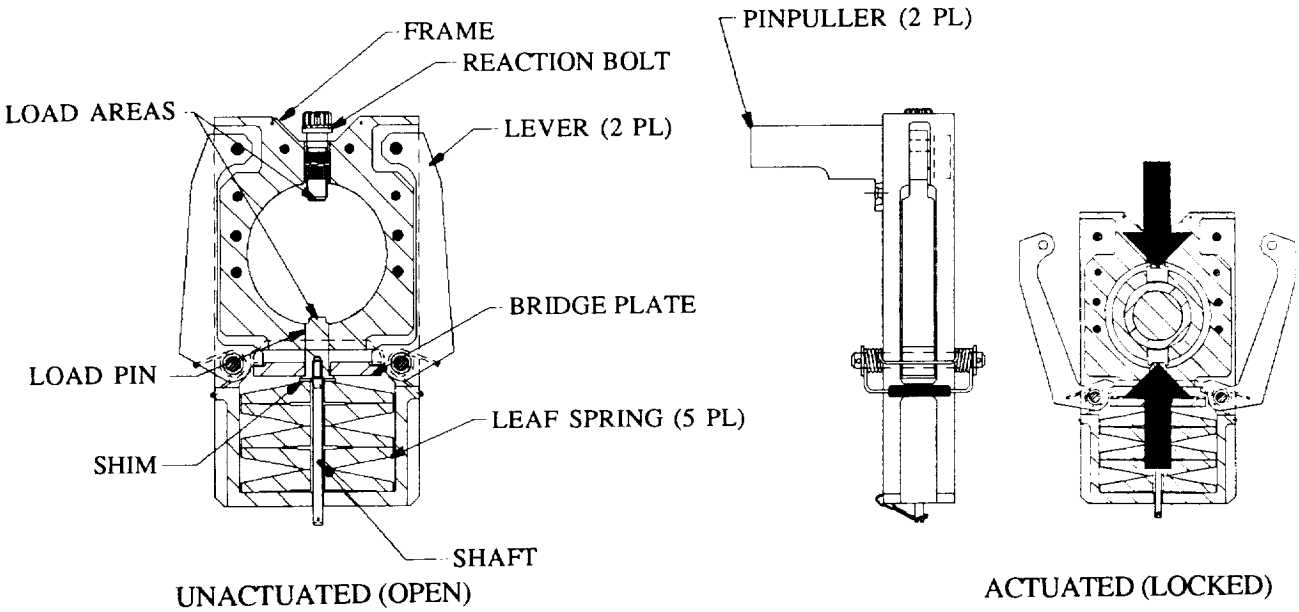

FIGURE 8: Active Lock-up Mechanism

Passive Roller Mechanism

The two primary requirements for the passive roller mechanism are to accommodate plus or minus three centimeters of relative tangential rail/roller deflection during ascent and to withstand loads of up to 9 kN in the same direction during separation. The implied design requirement, of course, is to allow unrestricted radial motion during both ascent and separation. The TPA designers were easily able to meet the relative ascent motion requirement by increasing rail/roller freeplay to plus or minus three centimeters, thanks to the separation sensitivity study proving acceptable loads. We decided to account for radial motion with a telescoping device similar to the active roller mechanism. An outer housing mounts to the payload, and the inner shaft, attached to the roller, is free to move

radially relative to the payload. Initially, the design team proposed coating the sliding surfaces of the mechanism with a teflon-impregnated anodic finish. However, analysis proved that binding of the telescoping action could result if the mechanism was under tangential load, since the coefficient of friction of the coating was not sufficiently low enough. To rectify the potential problem, the inner shaft was redesigned with rollers which transfer tangential loads to track surfaces attached to the outer housing (Fig. 9). The rollers provide an effective friction coefficient an order of magnitude below the teflon-anodic coating.

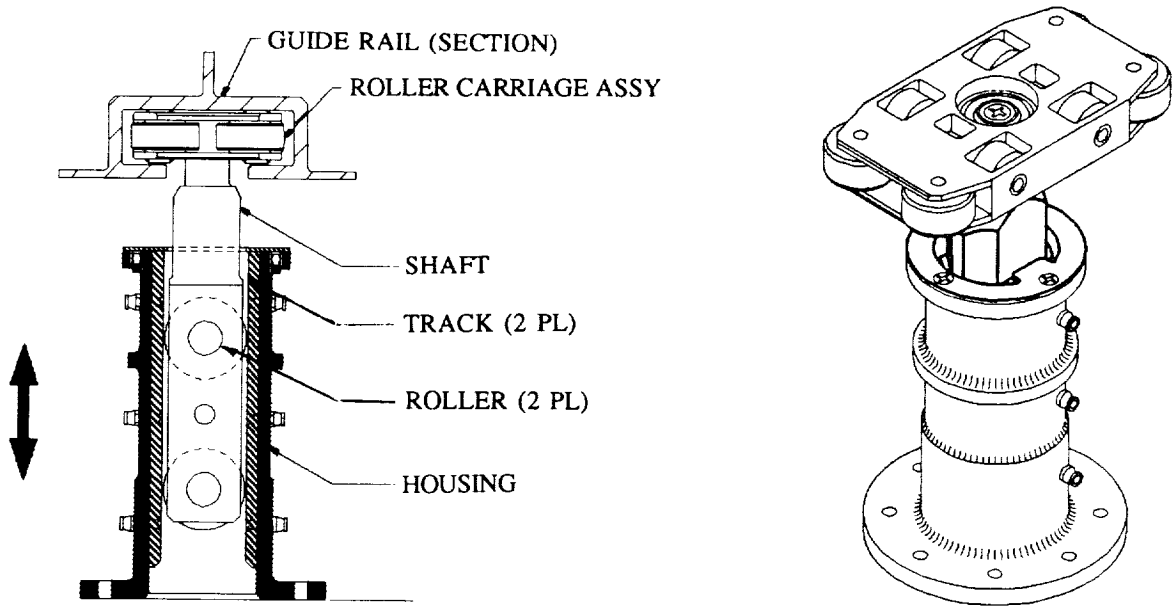

FIGURE 9: Passive Roller Mechanism

Roller Carriage Assembly

The TPA designers, in the early stages of the separation system design process, planned on using rollers to react loads against the rails. This concept was proven in the Agena program to cause minimal loss of separation impulse due to friction. Later, however, for simplicity in the TPA separation system, the design team proposed using low-friction sliders. Additionally, sliders are advantageous for reducing contact bearing stresses, which initially were high for the roller systems considered. Testing later proved sliders to be unworkable, although initially promising.

The engineering team revisited the roller concept and proposed some modifications to reduce bearing stresses, such as increasing the crown radius of the rollers and increasing the number of rollers in contact with the rail. We used an aggressive development test program to identify the most promising bearing method and validate the predictions of the stress group regarding load capability. The final design of the separation roller system is based on an eight-roller "carriage" (Fig. 6). A monoball pivot at the center of the carriage prevents the transmission of moment at each guide constraint, to allow a kinematic system. The rollers have low-friction teflon bushing inserts. The bearing shafts are also mounted in teflon bushings in the carriage structure. Thus, redundant bearing paths are provided. Snap rings retain the bearing shafts in the carriage.

TEST PROGRAM

The TPA engineering team used extensive development testing early in the design phase to assist the decision-making process, as well as to refine design details. The most critical testing involved friction surfaces, in an effort to find both low and high friction combinations for the rail/roller and active lock-up mechanisms, respectively. Unfortunately, the results of early coupon (sample) testing did not always correlate to later component-level testing.

Rail/Slider Testing

The rail/roller coefficient of friction greatly influenced separation performance, as shown by analysis. Failure to achieve separation could be caused by friction dissipation of retro-rocket impulse, especially in the One Retro Misfire (ORM) cases, which had 25% less impulse combined with high guide loads due to retro imbalance. Early separation analysis assumed the effective Coulomb friction coefficient to be 0.048, from previous Agena experience. Later parametric study showed that coefficients as high as 0.15 were tolerable, which, in combination with other factors, caused design to investigate sliders in place of rollers.

We used coupon testing of various materials, both lubricated and unlubricated, to select a candidate slider/rail material combination with suitable characteristics. All tests were done at ambient temperature and pressure. Low-load static tests (inclined plane) identified Anatef I, Anatef II, and Kahrlon as promising coatings for aluminum surfaces. Anatef (either type I or II) was selected after high-load testing with vendor-supplied samples of these coatings.

Unfortunately, trouble developed during a dynamic simulated system test of two sliders in a rail fixture some time later. We recorded coefficients of friction of up to 0.4 as well as visible and audible evidence of gouging and scuffing. TPA management directed the design team to reinvestigate roller concepts while the cause of the high slider friction was determined, to provide a back-up precluding schedule impact. Engineering found that the Anatef coating's friction coefficient was very sensitive to surface finish, and the production finish on the rails and sliders was not smooth enough. The coupon samples were buffed to a finish at least four times smoother than production rail/slider hardware by the vendor. Manufacturing of rails with the required surface finish would have been both difficult and expensive, so TPA management decided to return to rollers when full-scale development testing showed good results.

Rail/Roller Testing

The rail/roller development test program to evaluate materials and bearings for strength and effective coefficient of friction looked at two roller bearing and two journal bushing configurations. The first roller design had a 7075 aluminum outer sleeve ("tire") press fit on the outer bearing race, and the second used a stainless steel tire. The tires were machined with a 0.25 meter crown to minimize bearing stresses in the rail and roller. Some amount of crown is desirable to preclude tire edge contact (with resulting high stresses) caused by distortion. Under load, the aluminum tire yielded and loosened on the bearing. The steel-tire bearing test resulted in inconsistent (spiked) drag loads attributed to high compressive loads on the bearing due to the interference fit of the tire and bearing and the high tire/rail contact stress. The journal bushing rollers were built using a solid 7075 aluminum

wheel and a solid stainless steel wheel. The wheels were machined with the same crown radius as the roller bearing tires, and the journal bearings were press fit into the wheels. The steel wheels exhibited a coefficient of friction of less than 0.05 under a maximum load of 8 kN, but left permanent indentations in the rail. The aluminum wheel test also found that the coefficient of friction was less than 0.05, but with no observed anomalies.

Design selected the aluminum-wheeled journal bearing to incorporate into the roller carriage breadboard test, based on the results of the bearing and materials test. An eight-tired prototype roller carriage was built, with four tires capable of reacting radial loads (in both directions) and four tires capable of reacting tangential loads (two in each direction, see Fig. 6). The carriage was placed in a production rail section and attached to a load application and measurement test apparatus. We measured carriage drag force while applying radial loads up to 16 kN and tangential loads up to 11 kN simultaneously (resultant 19 kN), in increments of 1 kN. All measured coefficients of friction were less than or equal to 0.05, including parasitic test apparatus forces.

Lock-up Device Friction Testing

Design conducted a development test program to evaluate material combinations with the object of finding a high friction coefficient to be used in the active roller mechanism lock-up device. Prototype lock-up mechanism components were created from four candidate materials, corrosion resistant steel (CRES), 6061 and 7075 aluminum, and titanium. The components built included the inner braking surface (spindle), the brake shoes, and the outer friction reaction surface, termed brake pads. The various spindle-shoe-pad combinations were tested for their effective coefficient of friction, with the titanium spindle, 6061 aluminum shoes, and titanium pads exhibiting consistently higher values than the other combinations for applied loads ranging between 4 kN to 22 kN.

ANALYSIS PROGRAM

The engineering team used analysis throughout the TPA mechanism design and development process, greatly influencing the design of the separation system.

Constraint Analysis

The separation engineering group used analysis to prove that the ascent constraint system was kinematic and to investigate potential "binding" (axial drag) of the payload in the adapter caused by transition from the ascent to the separation constraint system. Redundant constraint exists for the first two centimeters of separation (axial) motion, until the trunnions clear their respective latches and guide plates sufficiently. TPA management originally proposed a full-scale test program to evaluate binding effects. When difficulties in designing a zero gravity test apparatus which would provide meaningful results arose, the separation analysts were directed to look at the problem to determine what could be done. An Automatic Dynamic Analysis of Mechanical Systems (ADAMS) model of the ascent constraint system was built and used to confirm that it was kinematic by displacing the payload relative to the adapter and observing the resulting loads. Next, we investigated binding by adding separation constraint locations to the kinematic ADAMS model. By moving ascent/separation constraint locations relative to one another and assuming friction values at each interface, the worst-case separation drag force was found to

be 220 N. The separation analysts found that this force had negligible effect on overall BV/SV separation behavior when it was included in the detailed dynamic model.

Mechanism Analysis

Throughout the course of TPA design, analysis groups (i.e., stress, structural dynamics, thermal, and separation) worked in conjunction with design, materials and processes, and manufacturing engineers on mechanism development. The most significant recommendations analytical engineers made were regarding stress, friction requirements and loads. Stress analysts helped determine material choices and dimensions of each mechanism. Friction criteria were developed from binding analyses and lock-up margin analysis (in the case of the active roller mechanism) done by the separation engineers. The separation group also determined dynamic loads on the separation mechanisms. Finally, the analysts served an engineering audit function within the TPA design team itself.

Separation Analysis

The separation analysts modeled the BV/SV system with a digital computer simulation program called SEParation STudY (SEPSTY). The equations of motion used by this code assume the BV and the SV are rigid bodies, each with six DOF. These bodies interact with one another through a flexible rail/roller separation guide system. Figure 10 shows a schematic representation of the separation model.

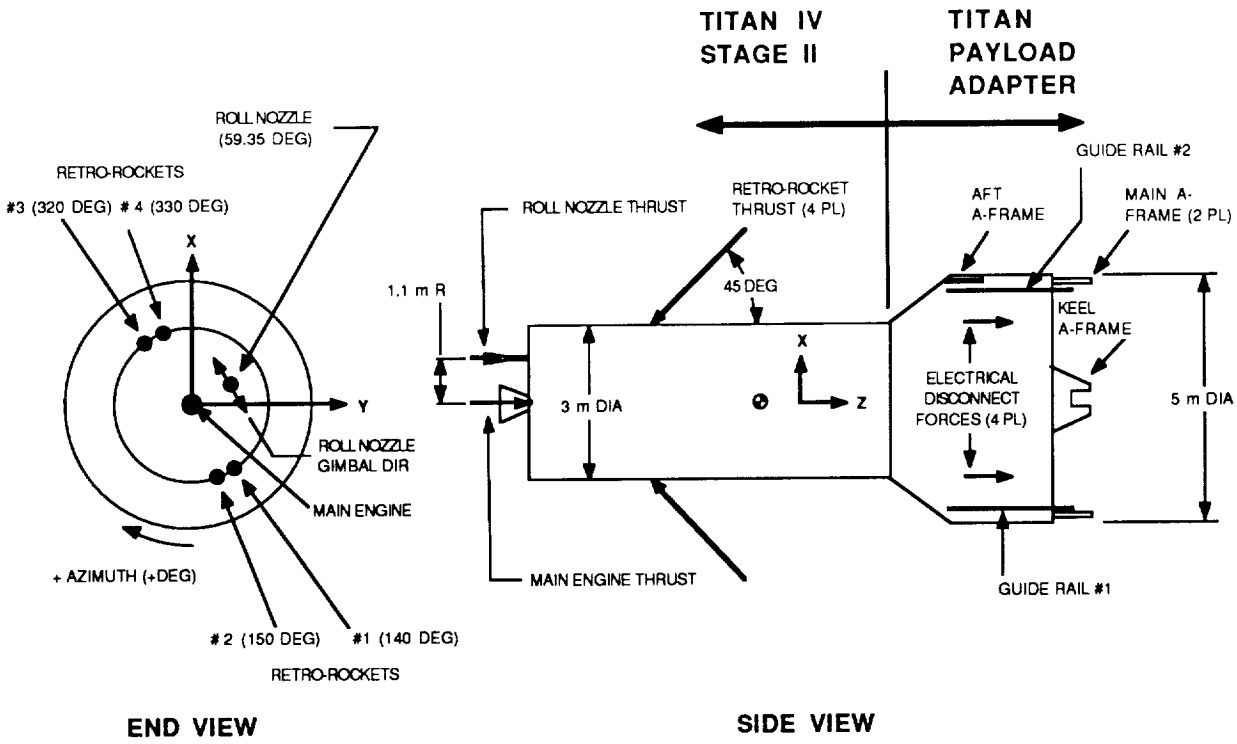

FIGURE 10: Separation Model Schematic

The SEPSTY TPA model has over 100 input parameters which all can be varied. The analysts determined that separation system performance was greatly influenced by three of these variables using a parametric study technique. The most significant parameters are friction coefficient and deadband (between rail and roller or slider), and flexibility of the overall rail/roller/mechanism structure. High friction and deadband values increase guide loads, as does low flexibility (high stiffness).

Table 1 lists the results of the separation analysis for nominal All Retros Firing (ARF) and One Retro Misfired (ORM) conditions. An ORM condition occurs if one of the four retro rockets fails to fire. In reality, an ORM condition is rare, but the condition is modeled to demonstrate separation system capability. The table shows the separation system performance over the evolution of the design. The most notable result is the decline in rail/roller guidance load as the separation system evolves from rail pockets to active mechanisms, and then from sliders to rollers.

		DESIGN					
PARAMETER	UNITS	Rail Pockets		Active Sliders		Active Rollers	
Retro State		ARF	ORM	ARF	ORM	ARF	ORM
SV Tipoff Rate	°/s	0.4	4.5	0.4	4.5	0.3	4.5
BV/SV Sep. Vel.	m/s	2.3	0.6	2.3	1.3	2.4	1.3
BV/SV Clearance	cm	4.3	2.3	4.3	3.0	4.3	3.6
Guide Loads -	kN						
Drag		5.0	17	0.4	1.9	0.2	1.2
Tangential		12	49	0.9	4.4	0.2	4.4
Radial		21	65	1.8	8.0	1.3	7.0

TABLE 1: Separation Analysis Results

SYSTEM OPERATION

Ascent Constraint System

The TPA ascent constraint system reacts loads in the same manner and direction, relative to the payload, as the four-point Shuttle latch system. Loads are transferred from the payload trunnion locations to the TPA structure via bipods in a kinematic arrangement which prevents moment transfer, allowing a lighter, more efficient TPA structure. Slotted bearing plates at the keel and aft trunnion locations react loads in the appropriate directions, but do not constrain separation motion. Latch mechanisms at the main trunnion locations are necessary to react loads along the separation axis during ascent and then to release this constraint at separation.

Each latch mechanism is attached to a main bipod structure (Fig. 1). The latch mechanism is composed of two identical subassemblies to provide redundancy. A subassembly comprises one separation nut, a sleeve, a bolt, and a pinned pivot arm with a two-to-one mechanical advantage (Fig. 3). Adequate load margin to use a thirteen-millimeter (half-inch) separation nut is ensured by this pivot ratio. The shorter leg of the pivot arm bears against a surface on a cap assembly. The assembly is mated to the payload trunnion and consists of a spherical bearing (which can also

slide on the trunnion) fixed to a bearing cap. The pivot arm's longer leg bears against a cutout in the sleeve. A bolt passes through the sleeve into the separation nut, which is fixed to the latch structure.

Redundant pyrotechnic devices activate the separation nut, initiated by primary and secondary electrical command signals. Prior to actuation, three 120-degree split nut segments (collets) are supported radially by a ring within the separation nut. The ring is driven away from the collets by gas pressure when the pyrotechnic devices fire, allowing the collets to translate radially, releasing the separation bolt. This action frees the sleeve, and thus the pivot arm, which rotates away from the bearing cap. The payload is no longer constrained to the TPA in the separation axis when both latch mechanisms have completed actuation. Redundant operation of each latch is provided by the two subassemblies. In the event that one subassembly fails to function, the bearing cap assembly rotates away from the unreleased subassembly's pivot arm. The designers provided for rotational redundancy in the cap assembly by allowing the cap to rotate relative to the bearing's outer race.

Separation Guidance System

Separation of the payload from the TPA is enabled when the ascent constraint system is released and the separation guidance system is locked-up. The active roller mechanisms are activated at virtually the same time as the ascent latches are released. Until lock-up of the active mechanisms, the separation guidance rollers are incapable of transferring loads from the payload to the TPA. The passive roller mechanism cannot react loads prior to separation because sufficient freeplay has been built into the rail/roller interface to accommodate ascent distortion. The active roller mechanisms accommodate ascent distortion due to their kinematic layout.

The active roller mechanism consists of a tubular housing, a spindle, a doglegged shaft, an external locking mechanism, and a roller carriage assembly (Fig. 6). The housing and spindle are fastened to the payload. The shaft, supporting the roller carriage, is mounted within the housing, but enveloping the spindle. Prior to the lock-up mechanism activation, the shaft is free to telescope and rotate, which in combination with the dogleg, accommodates large dynamic ascent motions of the payload relative to the TPA. The locking mechanism mounts to the housing and applies force to frictionally lock the shaft to the housing and spindle when activated. This force is applied through two openings in the housing, which contain load-reacting brake shoes. In turn, these shoes apply load to brake pads constrained by two similar openings in the shaft. The brake pads also react against the spindle, thereby providing a total of four lock-up friction surfaces. The centers of the windows, shoes, and pads are nominally coincident, and we chose dimensions and tolerances to allow lock-up over the predicted range of residual displacement.

The locking mechanism is made up of a frame, five leaf springs, a bridge plate, a load pin, a reaction bolt, two levers, and two pinpullers (Fig. 8). In the unactuated state, the preloaded spring stack is retained between the bridge plate and the frame, attached to the active roller mechanism housing. Preload is transferred via one lever arm to each pinpuller. When either pinpuller actuates, its corresponding lever rotates, allowing the bridge plate to apply spring force to the load pin. The bridge plate can rotate about an unactuated lever surface, providing redundancy. Locking force is thus applied to the brake shoe-pad-spindle combination of the active roller mechanism. This force is reacted against the bolt on the opposite side of the frame,

which "floats" on the housing much like a single-acting brake caliper on a bicycle. The bolt allows adjustment of the lock-up force and provides tolerance compensation.

One passive roller mechanism completes the separation guidance system. This mechanism has a telescoping shaft within a housing fixed to the payload (Fig. 9). Telescoping friction is reduced by rollers pinned to the shaft and running on tracks in the housing, which maintains the kinematic nature of the separation system. The roller carriage, running within the TPA rail, is bolted to the shaft.

Activation of the separation guidance system is also accomplished by primary and secondary electrical command signals, issued within milliseconds of the ascent latch activation signals. Redundant pyrotechnic devices are used for each lock-up mechanism pinpuller. When lock-up is achieved, by either one or both pinpullers actuating, each active roller mechanism provides constraint in two DOF. The passive roller mechanism provides one-DOF constraint outside of its deadband, for a total of five DOF (Fig. 7). The remaining, unconstrained DOF, is in the separation direction, which enables the TPA to retro away from the payload.

CONCLUSION

The TPA engineering team created an adapter which allows a payload, designed to launch on the STS shuttle, to be launched on an ELV with minimal changes to the payload. This adapter has mechanisms which allow retention of the four-trunnion payload mounting system (trunnion latches). Additionally, a separation guidance system consisting of active and passive mechanisms accommodates large dynamic and thermal ascent distortions between the payload and the adapter, as well as residual distortions at separation. Prior to actuation, the mechanisms constrain the payload to the adapter for ascent. When pyrotechnically activated, the mechanisms allow separation from the adapter using the existing booster retro-rockets.

The engineering team realized several lessons during the development of the TPA. One lesson is that design simplicity cannot always be pursued successfully. The early rail pocket concept is the most straightforward solution to the problem of large dynamic ascent deflections, but produces unacceptable impact loads. Similarly, sliders are certainly less complex than rollers, but materials and manufacturing problems forced transition to rollers. The slider problem illustrates the second and third lessons: the value of early development testing, and to be especially aware of surface finish when using low-friction coatings. However, perhaps the most important lesson provided by the TPA engineering effort is not strictly a design issue. The TPA program proved that a small, motivated team of designers and analysts, working in conjunction with manufacturing engineers, could operate in the bureaucratic environment of a large company and efficiently create a product in less than half the time typically required, within budget.

ACKNOWLEDGEMENTS

We thank Lockheed Missiles and Space Company for giving us permission to publish this paper, with special thanks to Wayne Proffitt and Bob Schroeder for their help in this regard. We are grateful for the information and technical assistance provided by Jim Desimpel, Tim Harrington, Dave Omori, and Gene Robbins, who all made significant contributions to the TPA engineering effort's success. Finally, we are indebted to Tom Huen and Russ Kackley of LMSC, and especially, Rich Horvath of Stanford University, for their help and encouragement towards writing this paper.

DEVELOPMENT OF A MULTIPURPOSE HAND CONTROLLER FOR JEMRMS

Nobuto Matsuhira*, Shoichi Iikura*
Makoto Asakura*, Yasuo Shinomiya**

ABSTRACT

A prototype multipurpose hand controller for the JEMRMS (Japanese Experiment Module Remote Manipulator System) has been developed. The hand controller (H/C) is an orthogonal type, with six degrees of freedom (DOF) and small size. The orthogonal type H/C is very simple for coordinate transformations and can easily control any type of manipulators. In fact, the JEMRMS is planned to have two manipulators controlled by a common H/C at this stage. The H/C was able to be used as a rate control joystick and a force-reflection master arm, using an experimental 6 DOF manipulator. Good maneuverability was confirmed in the verification test. The orthogonal type H/C is suitable for use as a common H/C for the two manipulators of the JEMRMS.

INTRODUCTION

The JEM (Japanese Experiment Module) consists of a pressurized module, an experiment logistics module, an exposed facility and a remote manipulator system (RMS). The JEMRMS has two manipulators, as shown in Figure 1 (Reference 1, 2). One is a large main arm (LMA) which is about 10 meters long, with 6 DOF for handling heavy payloads. The other is a small fine arm (SFA), which is about 2 meters long with 6 DOF and a gripper for carrying out sophisticated operations. It is attached to the LMA end effector. The two manipulators, LMA and SFA, are controlled by a single operator in the pressurized module.

Conventionally, the remote manipulators for unstructured work in hostile environments, such as space and nuclear power facilities, are manually controlled by a human operator. There are two main control methods. One is joystick rate control, such as used in the shuttle remote manipulator system (SRMS). The other is master-slave control, with a replica of the slave arm as the master arm. As master-slave control is often used in the nuclear field, sophisticated operations can be carried out easier than when using joystick control. However, the same number of master arms are needed as slave arms, because the master arm and the slave arm configurations are identical. On the other hand, joystick control is very simple.

The two control methods are desirable to be used appropriately, according to the required tasks for the manipulators. In space, the operation compartment is small and each equipment must be compact and lightweight. Consequently, a common hand controller for the two arms of the JEMRMS is needed.

Toshiba Corporation, Kawasaki, Japan
* Research and Development Center, Mechanical Engineering Laboratory
** Komukai Works, Space Programs Division

H/C DESIGN CONCEPT

The H/C equipped in a space station must be small size, lightweight and designed ergonomically as a man-machine interface. Furthermore, an ideal H/C can be used not only as a joystick but also as a master arm for any type of slave arm .

Thus, a 6 DOF orthogonal type H/C with force reflection was developed. It can be used as a common master arm for the JEMRMS. As the configuration of the LMA and the SFA is an articulated type and that of the H/C is an orthogonal type, it composes the master-slave manipulator system with different configurations (Reference 3, 4). The orthogonal type is very simple for coordinate transformations between the coordinate system of the master arm and that of the slave arm. It can easily control any type of slave arm merely by changing the coordinate transformation.

MECHANISM

The prototype H/C is about 35 x 35 x 35 cm in size, has a 15 x 15 x 15 cm motion area and is 15 kg in weight including the mechanical dead weight compensation system, which is not needed in space use. The configuration is shown in Figure 2.

The roll, pitch and yaw axes for the wrist joint are designed to cross at a center point of the grip handle. The 3 DOF for the translational axes are mechanically separated against the 3 DOF for the rotational axes. The drive units are commonly designed for the rotational axes and for the translational axes, respectively. Therefore, it becomes easier to control than any other structure in the H/C. The translational axes are driven by ballscrews, with an 8-mm lead. The three intersecting axes are driven by gears with a low gear ratio 1:4. Thus, the friction is very small for mechanical backdrivability and maneuverability.

A force or torque sensor using strain gauges is mounted in each joint. The gripper is controlled by a switch on the top of the grip handle. The optical sensor on the grip handle detects the operator's hand. When the operator removes his hand from the handle, the slave arm is servo held in position quickly.

The dead weight for the Z axis is compensated for by a constant force spring. Dead weights for the rotational axes are compensated for by a counterweight and a counterbalanced arrangement of drive units.

EXPERIMENTAL SYSTEM

The H/C was studied using a 1 meter long articulated type slave arm with 6 DOF and a gripper in place of the LMA and the SFA. The system configurations and specifications are shown in Figure 3, Figure 4 and Table 1. The specifications are not described for space use. The experimental slave arm has three intersecting rotational axes with a differential mechanism for easy control.

FUNCTIONS

The LMA and the SFA control methods are not always the same due to differences in structure, size and role. Control methods and auxiliary functions are required

to control these two arms, using a common H/C. The investigated functions are shown in Table 2. The H/C has three control modes, a position mode, a rate mode and a hybrid mode.

In the position mode, the system becomes a bilateral master-slave manipulator with force reflection. This control mode is used for dexterous manipulation by the SFA.

In the rate mode, the velocity of the slave arm end point is controlled proportional to the H/C displacement or force applied by the operator. This control mode is used for the LMA in long distance movement, such as joystick control with return to origin.

As the H/C has a small motion area compared to that for the SFA, the operator can change the position of the H/C origin or the motion ratio between the H/C and the SFA to use the SFA motion area effectively. The SFA is held in position when the H/C origin changes. The motion area coverage is shown in Figure 5.

In the hybrid mode, the translation is controlled by the rate mode and the rotation is controlled by the position mode. This mode is useful to operate the SFA without changing the H/C origin or the motion ratio.

The position and rotation for the H/C correspond to those for the slave arm with coordinate transformations. The transformation point for the position is changeable at any point, so that the rotation is determined for that point. To test the function, the point can be changed from the wrist joint to the grasping center point and the slave arm end point. For the wrist joint, the slave arm movement is very intuitive for the operator because of good spatial correspondence. For other points such as the grasping center or the end point, the slave arm configuration changes and the movement is not intuitive, but the operator can easily move the slave arm around a working point. When only the pitch axis for the H/C is moved, the slave arm configurations for the two cases are shown in Figure 6. The dotted line shows the configuration at the end of the movement.

These functions were able to be changed by keyboard operation in this experiment.

CONTROL

The position mode is bilateral master-slave control with a position servo loop and a force serve loop. The control block diagram is shown in Figure 7.

Both the H/C and the slave arm have a force sensor, a position sensor and a dc-servomotor mounted in each joint. The slave arm motors are driven by the rate control amplifiers and the H/C motors are driven by the current control amplifiers.

The joint coordinate system for the H/C and that for the slave arm are different, and servo control is accomplished in the Cartesian coordinate system for the H/C. The slave arm position, rate and force are transformed between the joint coordinate system and the Cartesian coordinate system. The dotted line in Figure 7 shows this coordinate transformation.

In the position servo loop, the position error between the H/C and the slave arm in the Cartesian coordinate system is transformed into the joint velocity for the slave arm. The transformation is expressed as:

$$\dot{\theta} = Js^{-1}\dot{\chi} \tag{1}$$

where:

$\dot{\theta}$ represents the joint angle vector, Js^{-1} is an inverse Jacobian matrix for the slave arm, and $\dot{\chi}$ is the Cartesian velocity vector.

This transformation is the same as that used for resolved motion rate control (RMRC). And the position of the slave arm in the Cartesian coordinate system is obtained by a homogeneous transformation matrix (Ts).

In the force servo loop, the slave arm joint torque, in which the dead weight is compensated for, is transformed into the force and torque in the Cartesian coordinate system. The transformation is expressed as:

$$f = (Js^{-1})^{T}\tau \tag{2}$$

where:

f represents the Cartesian force and torque vector, $(Js^{-1})^{T}$ is the transpose Js^{-1} matrix, and τ is the joint torque vector.

The force and torque error in the Cartesian coordinate system is fed back to the H/C. The torque in any part of the slave arm can be reflected, owing to the torque sensors mounted in each joint. In this control, the translational axes are force servocontrolled, but the rotational axes are controlled by only the slave arm force because of the low friction.

To change the transformation point, only exchange Js^{-1} for $Js^{-1}Jtp^{-1}$ in above equations. Jtp^{-1} is an inverse Jacobian matrix for the transformation between the slave arm wrist joint and the transformation point.

The rate mode is RMRC, which is used partially in the position mode, and it is easy to change from the position mode to the rate mode and the hybrid mode. The end point velocity for the slave arm is proportional to the H/C displacement or force applied by the operator, and the H/C is servo held in position at the origin. The two rate modes, displacement-use and force-use rate modes, can be easily realized by both H/C sensors. The input from the H/C is controlled with an insensitive range so that the slave arm cannot move by noises automatically.

Other types of slave arm can be easily controlled with the same H/C, by changing the coordinate transformation for the slave arm.

CONTROL SYSTEM

The H/C system is controlled by a 16-bit multi-CPU system (Intel 8086 and 8087) via Multibus interface, with a 10 millisecond sampling rate. The main calculation items are coordinate transformations, force feedback bilateral servo control, and slave arm dead weight compensation. To reduce the calculation time, an inverse

Jacobian matrix is induced by a computer algebra system REDUCE in advance, and a table look-up method for the trigonometrical function is employed. The main tasks for each CPU are as follows.

CPU1: system management and man-machine interface
CPU2: slave arm servo control
CPU3: H/C servo control
CPU4: inverse Jacobian calculation and dead weight compensation

BASIC EXPERIMENT

FUNCTIONAL TESTS

Functional tests were carried out using an experimental slave arm. The slave arm was able to be controlled by the H/C in the three control modes. The slave arm motion area was used effectively by the auxiliary functions.

In the two rate modes, force feedback was able to be realized in the displacement-use rate mode but not in the force-use rate mode. The slave arm movement when using force was smoother than when using displacement, because the inertia and friction for the translational axes of the H/C were not sufficiently compensated for. But, force feedback was effective in preventing the slave arm from an overload. Better rate mode selection requires more study and experiments, with the system improvement.

The hybrid mode was more useful than the rate mode, because the experimental slave arm was not as long as the LMA and it seemed to be difficult for the operator to control the six axes rates simultaneously by a H/C.

The most important function of the H/C system in the position mode is to feed back the force and to control the slave arm. As a result, an operator can feel the force acting on the slave arm correctly, and can move the slave arm freely.

Thus, the H/C was tested for the force reflection from the slave arm to the H/C, and the position trace accuracy using a geometrical pattern.

FORCE REFLECTION TEST

The slave arm was locked by brakes and the H/C was locked by stoppers mechanically. The force of the load cell acting on the slave arm and the generated force of the H/C force sensor were measured. The results are shown in Figure 8. Though the force hysteresis (dotted line) was large in PD control due to friction loss, a linear force relationship between the H/C and the slave arm was obtained in PID control, according to the force reflection ratio. However, the integral compensation in PID control was limited, because the H/C inertia effect was larger in operation, as the friction was smaller. The operation force for the H/C was less than 500 g in normal operation.

POSITION ACCURACY TEST

The operator watched a geometrical pattern directly in front of the slave arm, and traced the pattern with the slave arm holding a dry ink pen using the H/C. The

trajectories for the slave arm and the H/C are shown in Figure 9.

The H/C trajectory is the output from the Y, Z position sensor in the X-Y plotter. The motion ratio between the H/C and the slave arm was 1:2. Both trajectories corresponded even for detailed motions. The distortion seen in the H/C trajectory is due to the backlash from the wrist joint of the slave arm to the pen tip.

In this test, the working time when using the position mode was faster than when using the hybrid mode more than two times.

The position and the force between the H/C and the slave arm were found to be correctly transformed, with coordinate transformations from these data.

PERFORMANCE TESTS

Verification tests were carried out to investigate the work ability for the H/C system, such as inserting a peg into a hole and screwing a bolt. The two tasks needed force feeling. The force reflection ratio was less than 50 percent for stable operation. The operator watched the work situation directly in the following tests. The slave arm was controlled by the rate mode or the position mode with a large motion ratio, to approach the working place.

INSERTING A PEG INTO A HOLE

The H/C system was able to insert a peg (20 mm diameter) into a hole with 15μm clearance, for both horizontal and 45 degree inclined directions. The average working time was 10 seconds in the horizontal direction and 15 seconds in the inclined direction after short exercises. An experimental scene is shown in Figure 10. In such a fine task, a 1:1 motion ratio allowed better control for the slave arm than a 1:2 motion ratio.

SCREWING A BOLT

The H/C system was able to screw a bolt whose head design was large enough to grasp easily, standing in a vertical direction. The experimental data are shown in Figure 11. In this work, when the transformation point was selected at the grasping center (Figure 11b), the work was able to be carried out smoothly without vibration, and was easier than being selected at the wrist joint (Figure 11a). Only the yaw axis for the H/C could be controlled at the grasping center. On the other hand, the yaw axis and the Y translational axis had to be cooperatively controlled at the wrist joint. Changing the transformation point is effective, to allow moving the slave arm around a point.

CONCLUSIONS

A prototype multipurpose H/C with force reflection was developed. A basic study to control the JEM's LMA and SFA was carried out using a 6 DOF experimental slave arm. The verification test results showed that this orthogonal type H/C is suitable for use as a common H/C for the LMA and the SFA of the JEMRMS and can control them by selecting the control mode. Even when the controlled slave arm

configuration is changed, this H/C can easily control it by changing the coordinate transformation.

REFERENCES

1. K. Yamawaki et al., "Remote Manipulator System of Japanese Experiment Module", Proceedings of the 16th International Symposium on Space Technology and Science, Sapporo, 1988

2. K. Yamawaki et al., "Design and Evaluation of Man-in-the Loop Control System of Japanese Experimental Module Remote Manipulator System", 40th Congress of the International Astronautical Federation, MALAGA SPAIN, 1989

3. M. Handlykken et al., "Control system analysis and synthesis for a six degree-of-freedom universal force-reflecting hand controller", Proceedings of the 19th IEEE Conference on Decision and Control Symposium", Albuquerque, 1980

4. T. Arai et al., "Bilateral Control for Manipulators with Different Configurations", Proceedings of International Conference on Industrial Electronics, Control and Instrumentation, Tokyo, 1984

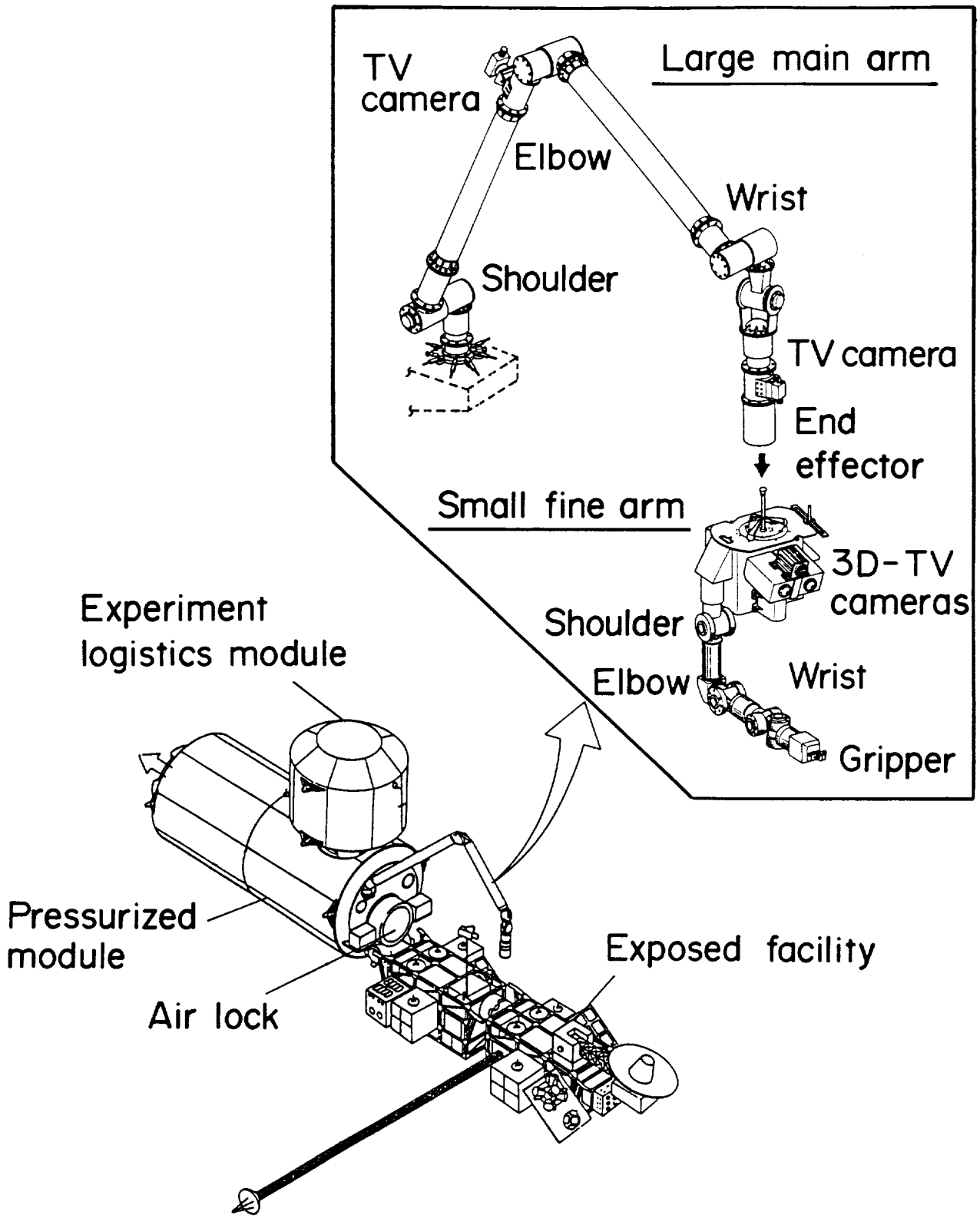

Figure 1. JEMRMS configuration (Initial)

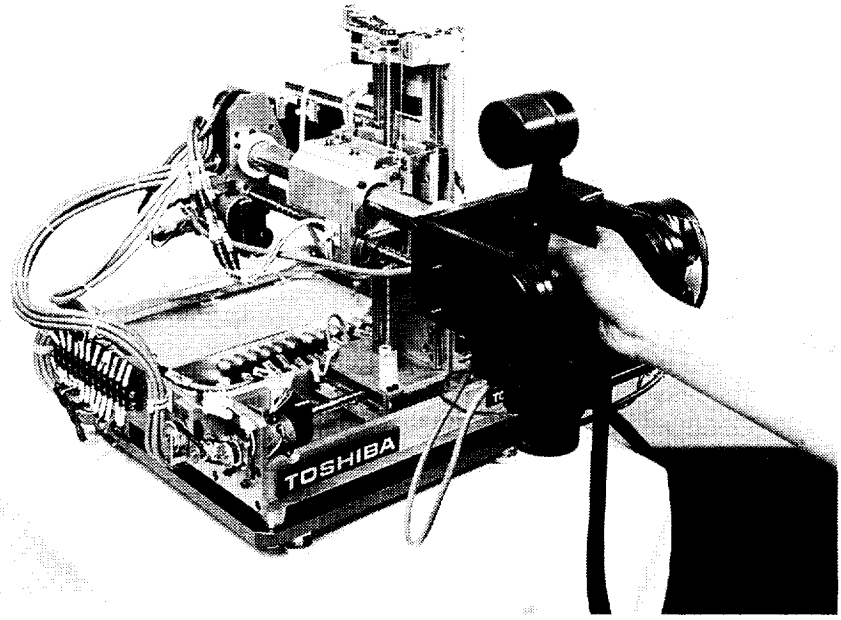

Figure 2. Multipurpose H/C prototype

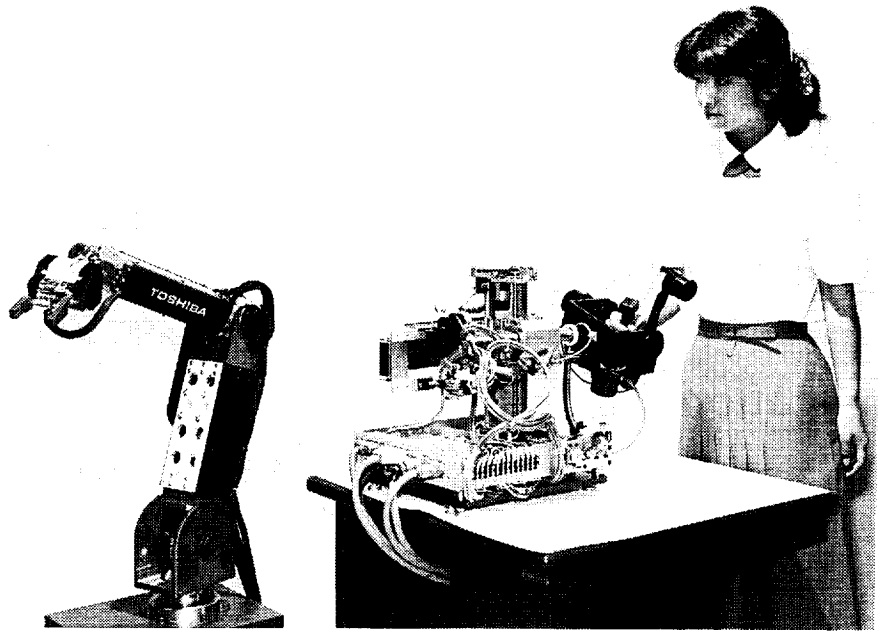

Figure 3. Experimental system

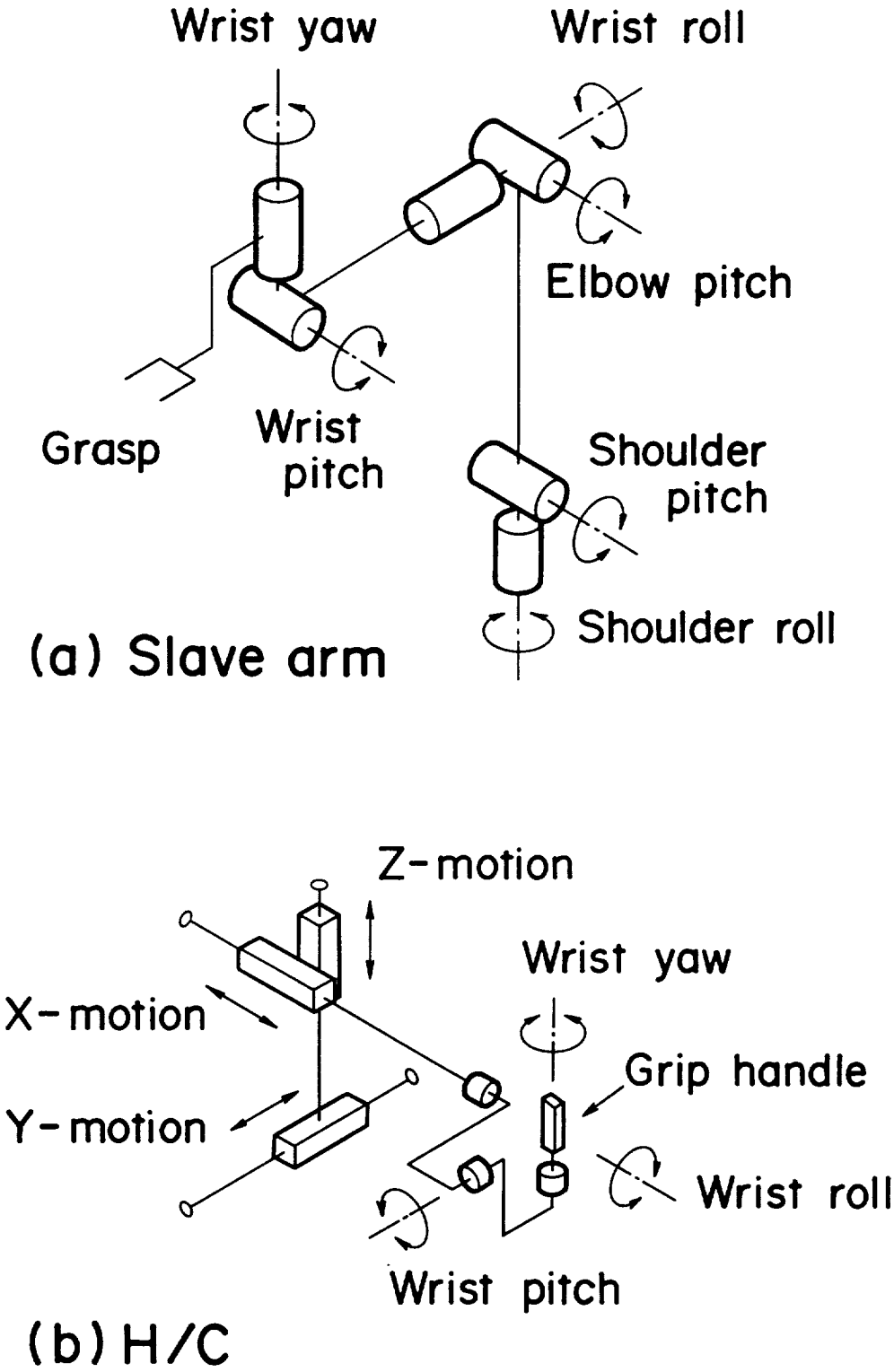

Figure 4. Slave arm and H/C configurations

Table 1. Specifications

	Slave	H/C
Type	Articulated	Orthogonal
DOF	6	6
Hand	Grasp	Switch
Length	1 m	0.15 m (in stroke)
Force	50 N	25 N / 0.45 Nm
Speed	60 cm/s	40 cm/s
Weight	50 kg	15 kg

Table 2. Functions

Position mode	Master-slave control with force reflection
Rate mode	Rate control (RMRC) displacement-use and force-use
Hybrid mode	Translation is rate mode and rotation is position mode
Changeable items Force reflection ratio Motion ratio (from H/C to slave) H/C's origin Transformation point (from H/C to slave)	

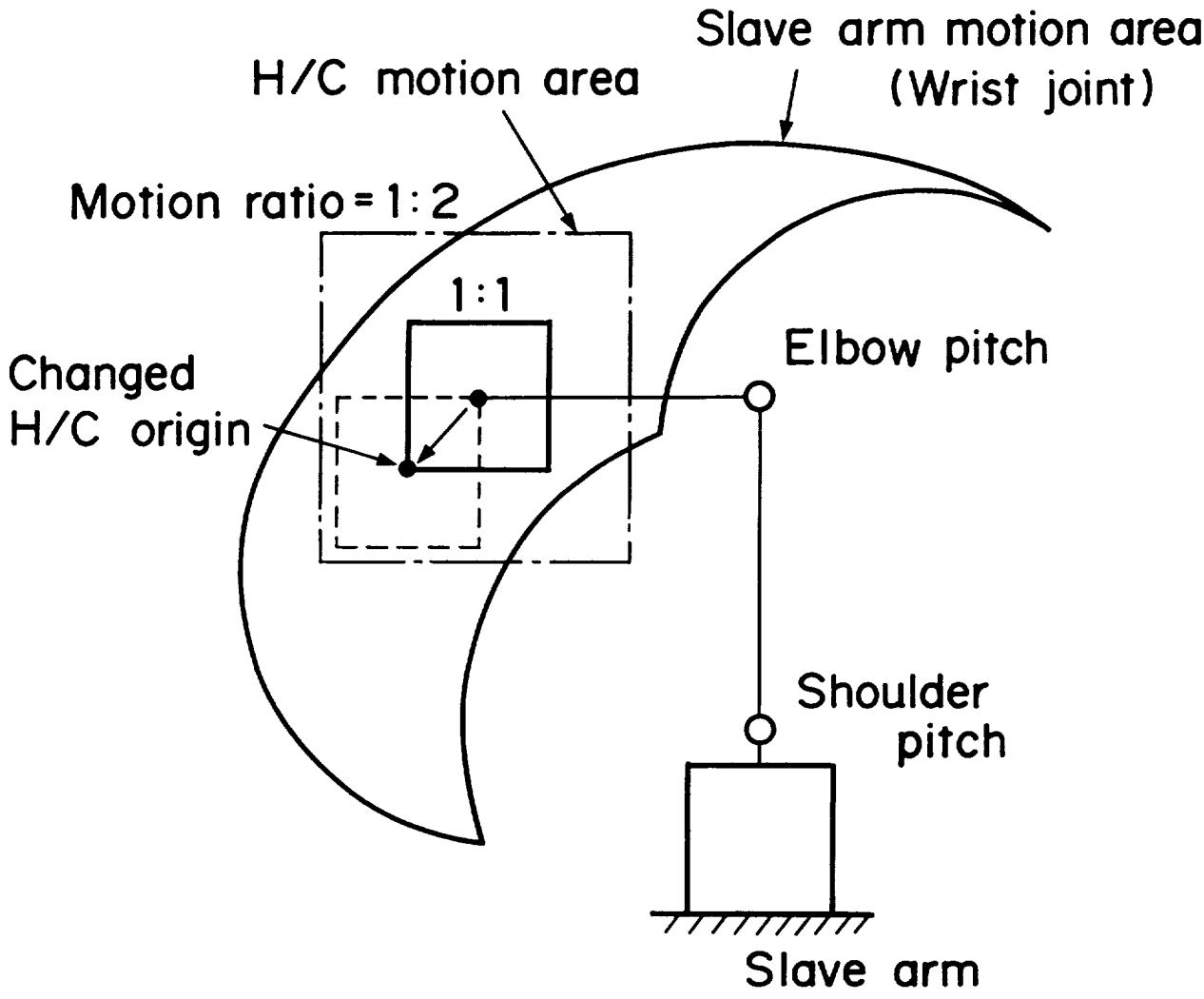

Figure 5. Motion area Coverage (Motion ratio/Origin change)

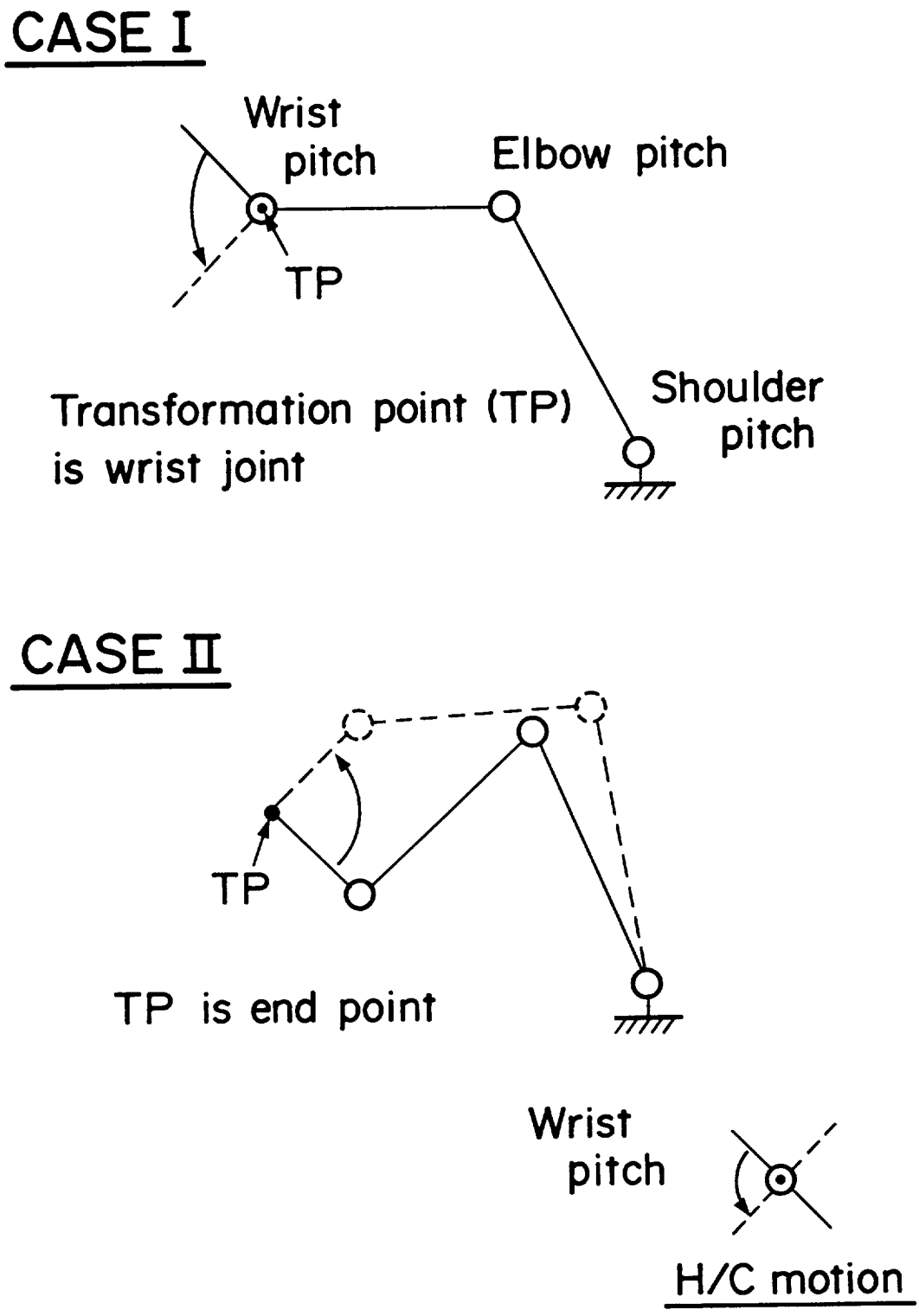

Figure 6. Differences in slave arm configuration

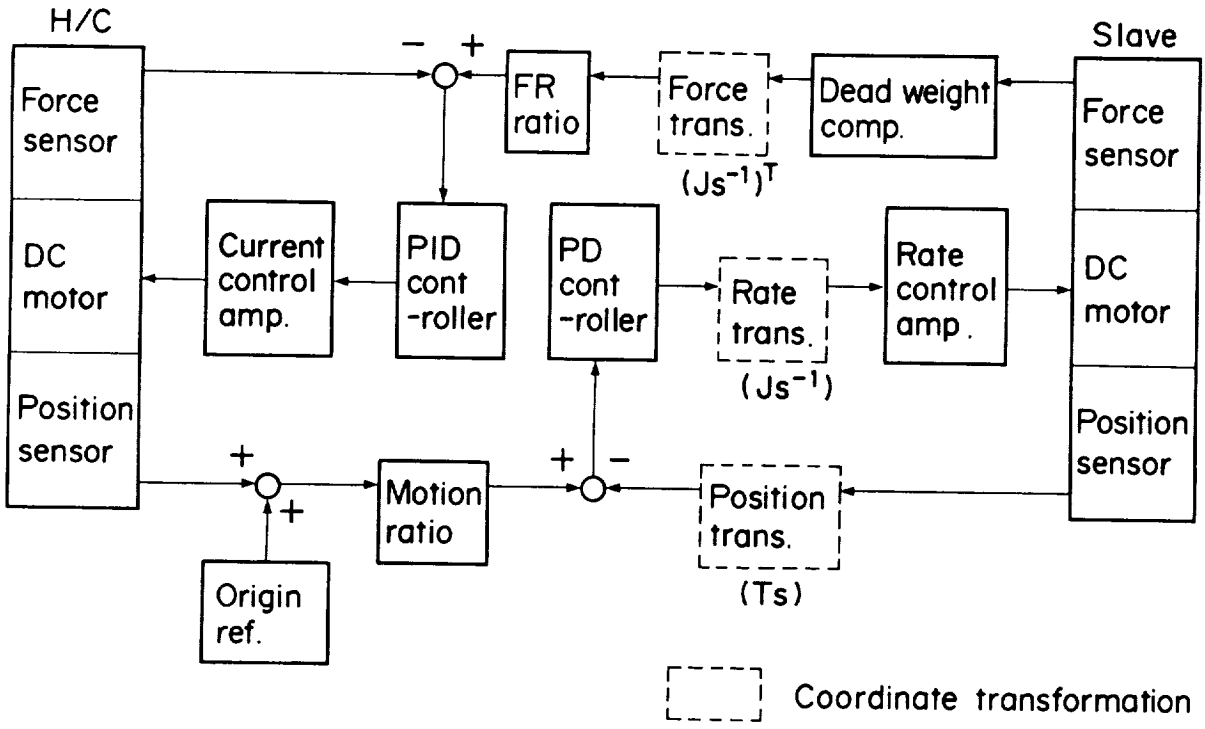

Figure 7. Control block diagram (Position mode)

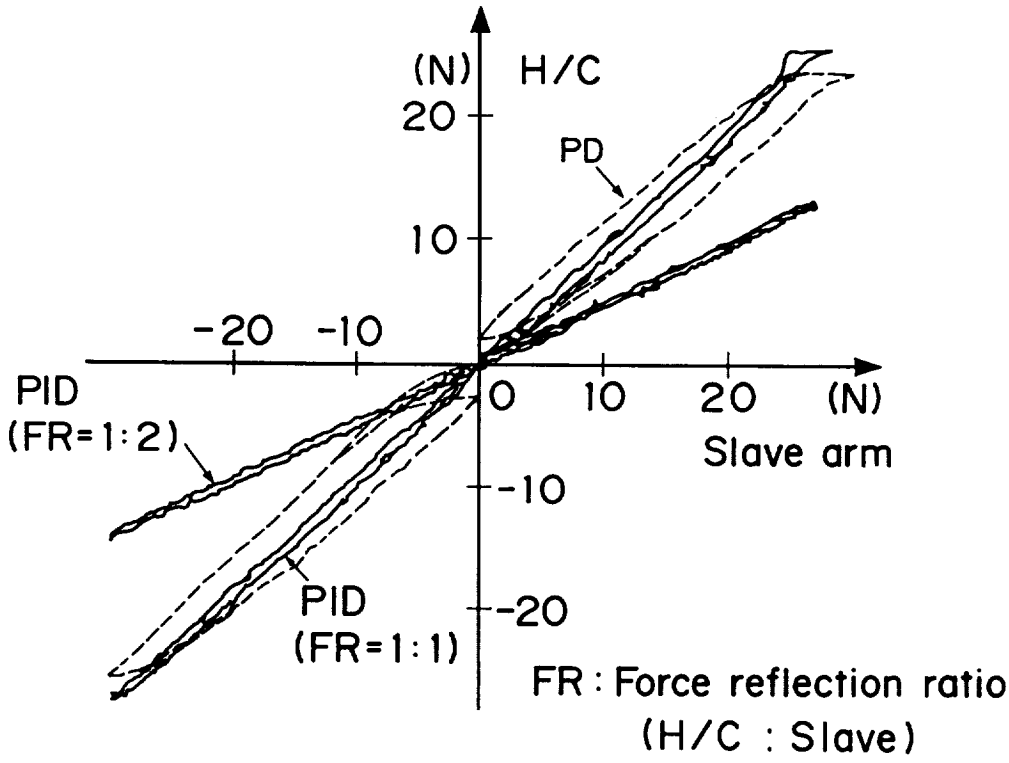

Figure 8. Force reflection test

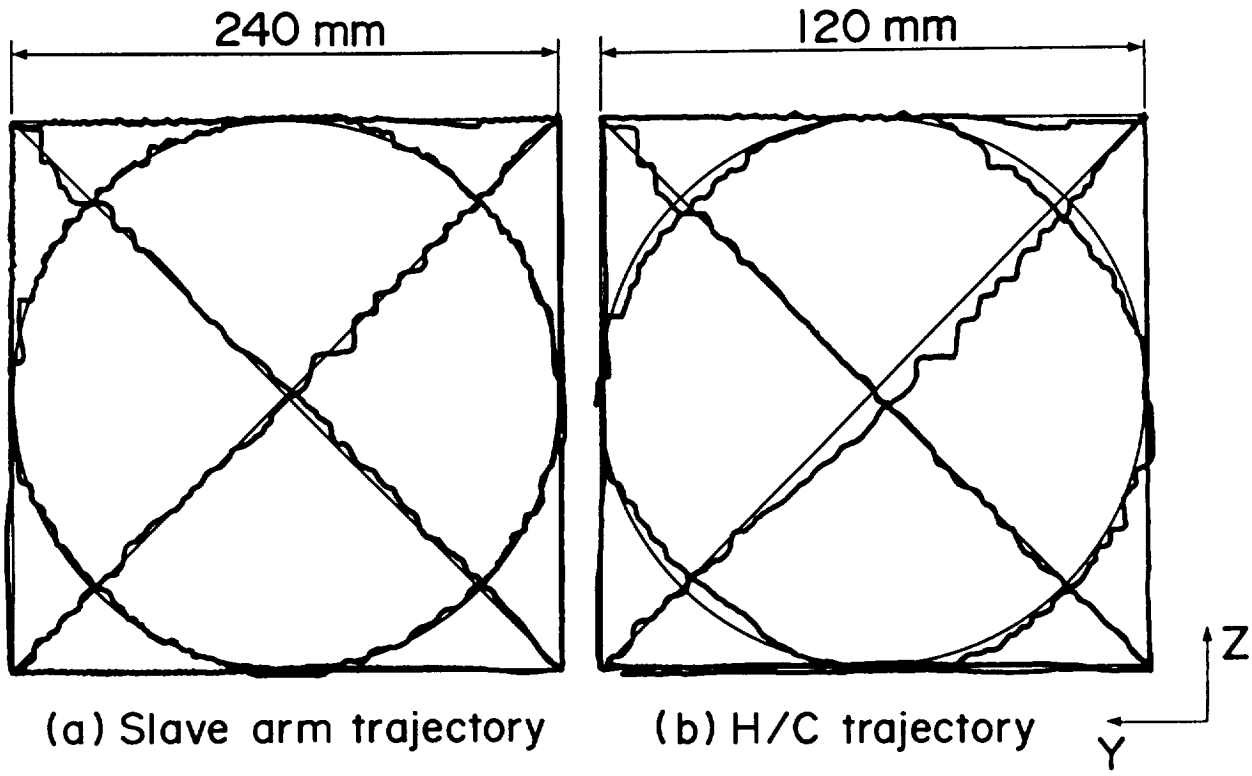

Figure 9. Position accuracy test in pattern trace

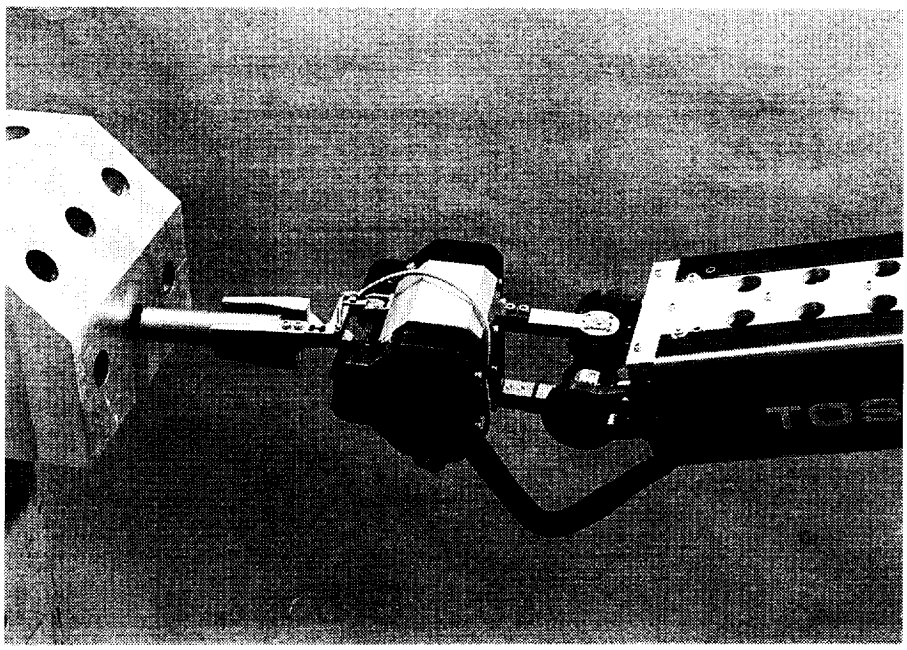

Figure 10. Peg-in-hole test

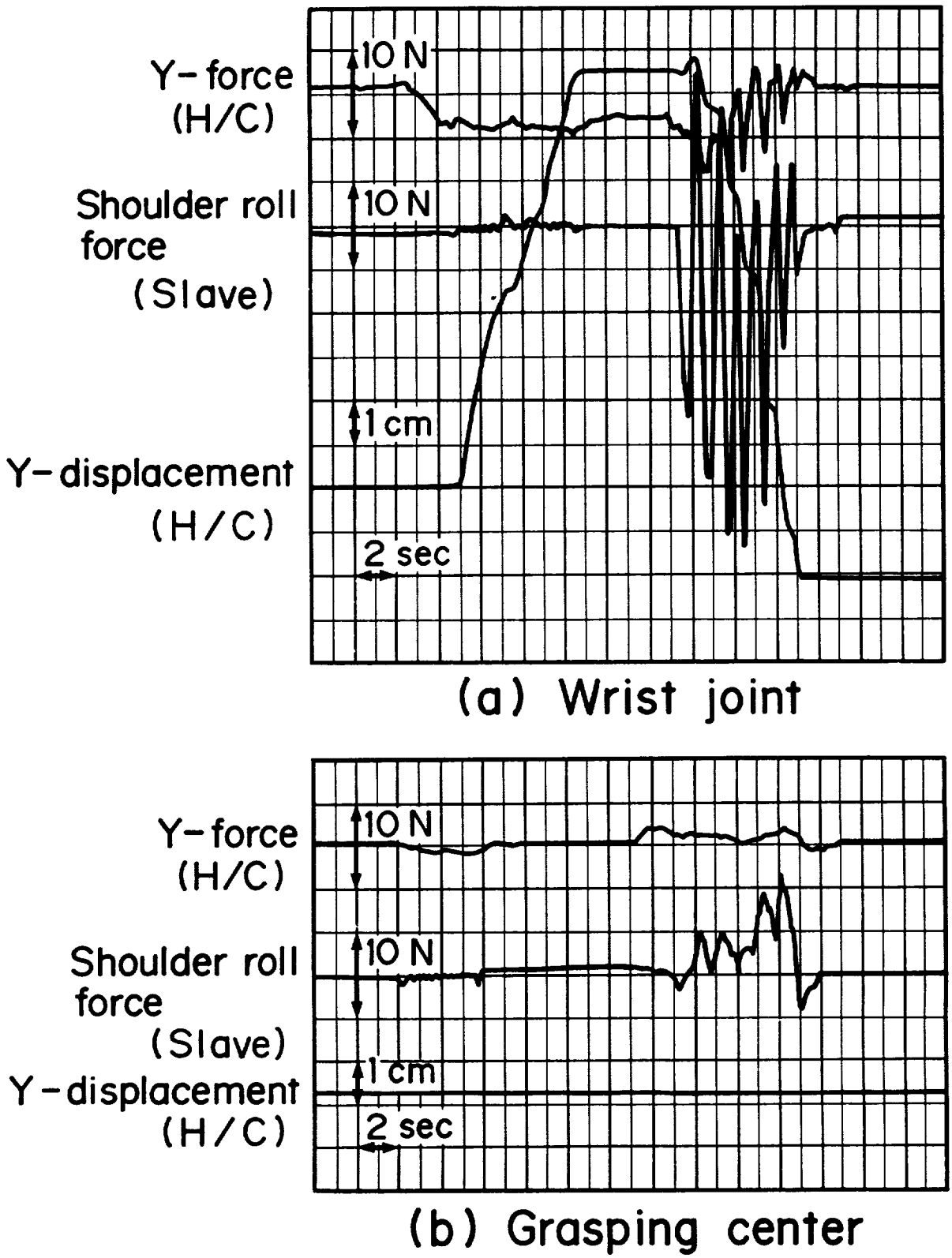

Figure 11. Change in transformation point (Screwing a bolt)

A ROBOT END EFFECTOR EXCHANGE MECHANISM FOR SPACE APPLICATIONS

Barney F. Gorin
Fairchild Space Company

Introduction

Efficient robot operation requires the use of specialized end effectors or tools for tasks. In many cases, multiple end effectors must be used, at different times, to complete a single complex job. These tools are normally stored on a simple rack fixture and attached to the manipulator as needed by the use of a simple grip mechanism. In most terrestrial applications, the tools are retained in the tool rack by the force of gravity. The grip mechanisms used to attach them to the manipulator are generally single acting, zero failure tolerant designs.

In spacecraft applications, the microgravity environment precludes the use of gravitational forces to retain the tools in the holding fixture. As a result of this, a retention mechanism which forms a part of the tool storage container is required. In addition to this obvious effect of the microgravity environment on-orbit, hazards are created which must be controlled for manned spaceflight applications. The safety requirements imposed for space operations near the National Space Transportation System Orbiter and the Space Station Freedom require multiple safety precautions which are not normally a part of ground operations.

One of the safety requirements imposed is that all items that could be "lost" in orbit, such as an end effector, must be held safely in place even in the event of two failures. This implies that the mechanisms used to attach the end effector to the manipulator and the tool storage container must incorporate not only a primary mechanism, but two redundant ones as well. Because a minimum of three catches must be active at all times, an interlock that prevents the release of one attachment before its opposite number on either the manipulator or the tool storage container is engaged is also required.

Because of these requirements, robot end effector exchange mechanisms for space applications tend to become large, heavy, and complex. They generally incorporate motor-driven actuators, a variety of sensors, and both electronic and mechanical interlocks.

A unique approach to this problem has resulted in the development of an end effector exchange mechanism that meets the requirements for spaceflight applications while avoiding the complexity usually involved. This mechanism uses multiple latching cams both on the manipulator and in the tool storage container, combined with a system of catch rings to provide retention in both locations and the required failure tolerance. Because of the cam configuration the mechanism operates passively, requiring no electrical commands except those needed to move the manipulator into position. Similarly, it inherently provides interlocks to prevent the release of one cam before its opposite number is engaged.

A working model of the latch cam system has demonstrated the operation of the mechanism. Extensive analyses and detailed models of a spaceflight design have shown that the proven concept can be manufactured without unusual difficulty.

Tool Exchange Requirements

For a robot manipulator to provide a wide variety of different capabilities, it must be capable of replacing the tools with which it works. This is an especially important capability for general-purpose space robots such as the Flight Telerobotic Servicer (FTS) because of the wide variety of tasks which are likely to be performed, the high cost of the robot, and the unique operating conditions associated with space flight. Since the full range of tooling that will be required over the life of the program has not been identified the ability to exchange one tool for another is especially critical.

For space applications, each tool must be thought of as an item to be firmly attached to the manipulator rather than a smaller part to be gripped by a general-purpose end effector. It must also be positively retained in a toolbox or tool storage container when it is not in use. In the microgravity environment of space, the tool storage container itself must contain mechanisms to grip and secure the tool.

The requirement for positive retention of the end effector both on the manipulator and in the tool storage container is made more complex by the safety requirements defined for manned space flight. These requirements categorize the loss of an end effector into space as a "catastrophic hazard",which must be controlled by not less than three independent inhibits.

To provide an effective method of removing and installing various end effectors on the manipulator, the mechanism used must provide the following functions:

a. The End Effector Exchange Mechanism (EEEM) must provide for tool pickup and release;
b. The EEEM must provide automated fail-safe latching with the tool on the manipulator, in the tool storage container, and at all times during the exchange;
c. The EEEM must provide automated tethering of the tool to the manipulator or a toolstorage container by incorporating sufficient interlocking inhibits to tool release;
d. The EEEM must provide sufficient preload between the end of the manipulator and the base of the end effector to react the loads applied by the manipulator without allowing a gap to form between the end effector and the manipulator;
e. The EEEM must provide an electrical/electronic interface between the manipulator wire harness and the end effector, which provides all of the power and signal leads necessary for tool function;
f. The EEEM must incorporate sufficient instrumentation to provide a positive indication that the end effector is properly latched in place on the manipulator or tool storage container;

g. The tool storage container box must provide launch and landing accommodations for the end effectors.

Exchange Mechanism

The Fairchild Space Company (FSC) developed an EEEM (called the Fairchild Exchange Mechanism or FEM) under an internal research and development effort. The emphasis of this program was to develop a highly reliable, simple EEEM which would meet all of the space application requirements.

The FEM is a part of an end effector system that incorporates the end of the manipulator, the EEEM, the end effector, and the tool storage container. This approach, illustrated in Figure 1, recognizes the interrelationships between the various requirements and the difficulty in meeting these requirements at all times in the exchange process with a series of independent mechanisms.

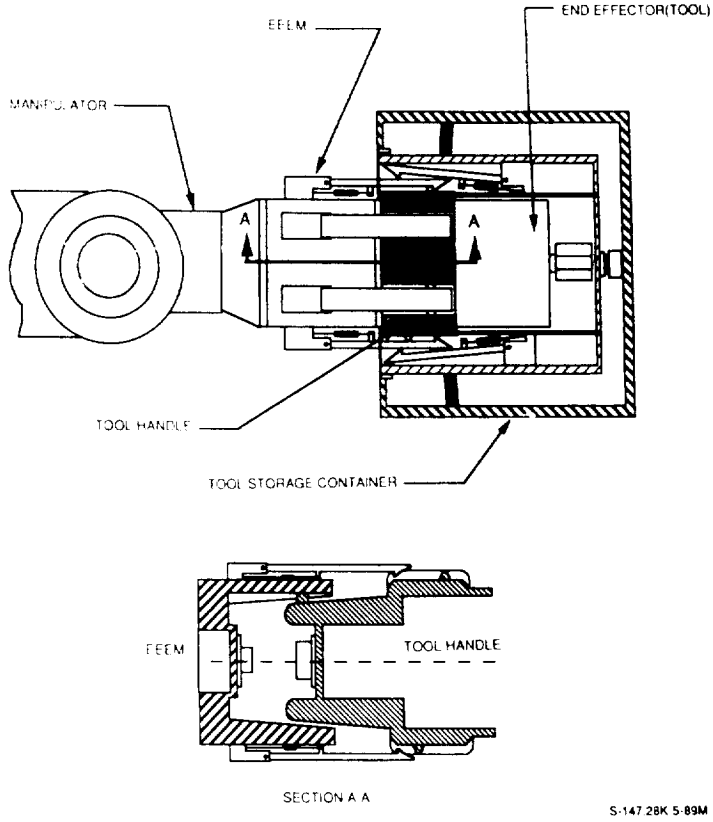

Figure 1. The FEM Provides Positive Retention of the Tool Both on the Arm and in the Tool Storage Container

The central part of this system, the FEM itself, operates using six spring actuated latching cams. These cams, and the retention ridges they engage, inherently operate in a reversing manner. This inherent reversal allows the simple mechanism shown to retain the end effector both on the arm and in the tool container storage while affecting the change of grip in both directions without using electrical commands.

The FEM is totally mechanical. The spring-powered latch cams, located on both the manipulator and in the tool storage container, latch onto the latch ramps, which are a part of the tool for tool pickup and replacement. Because of the location of the springs that provide the torque necessary to grip the end effector, the maximum clamping force is provided at the fully engaged position. As the latch cam lifts away from the latch ramp during the exchange operation, the resulting decrease in the lever arm associated with the spring serves to reduce the force necessary to lift the cam.

As illustrated, the FEM is integrated into all of the other three system components. One set of latching cams is associated with the end of the manipulator, the second set of latching cams is a part of the tool storage container, and the catch ramps are a part of the end effector itself. Because of the FEM integration into the overall system, effective service is provided during all phases of operation with a minimum of volume and complexity.

The FEM is adaptable to all end effector requirements. It is illustrated in Figure 2 for small tools such as a Nut Runner and in Figure 3 for large tools such as the Module Service Tool (MST).

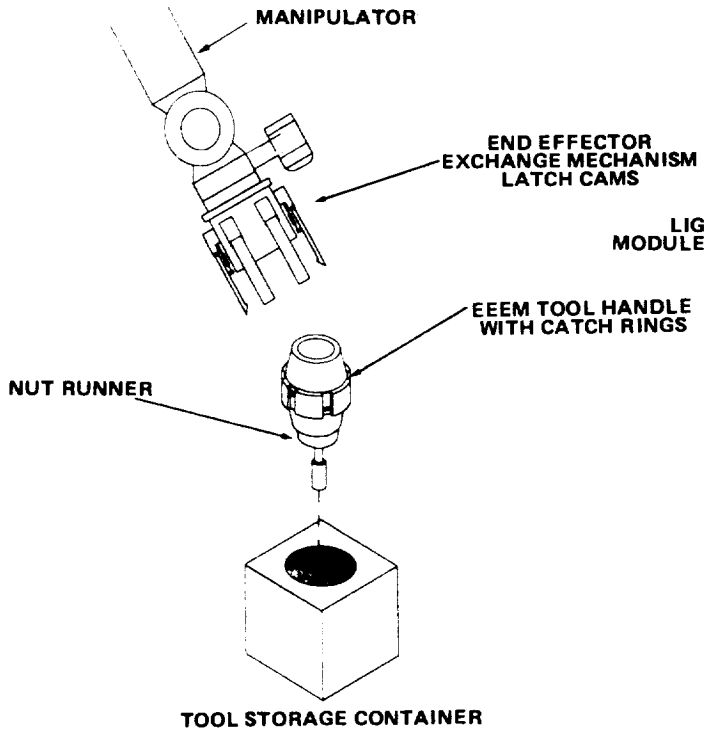

Figure 2. The FEM Incorporates the Manipulator Interface, the Tool and the Tool Storage Container into the End Effector Exchange System

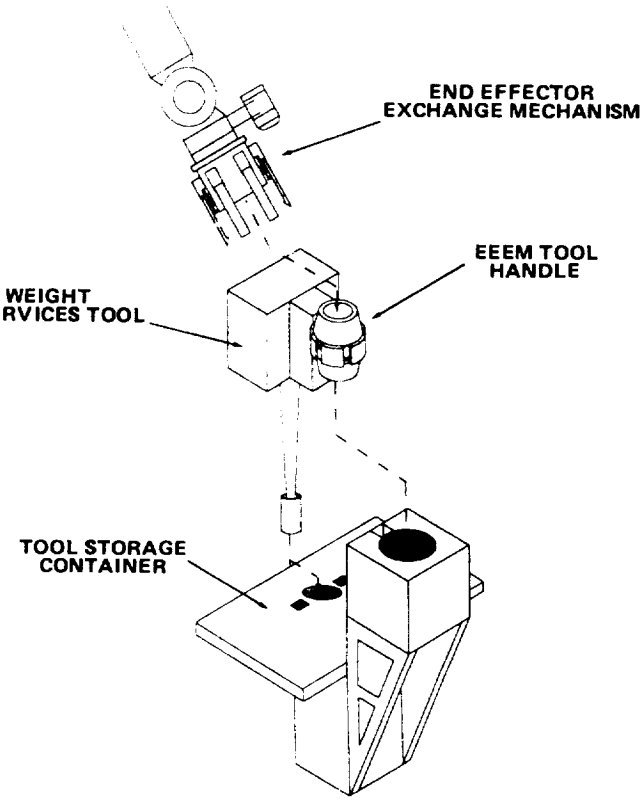

Figure 3. The FEM is Suitable for use with Large Tools Such as the Module Service Tool

The FEM is simple to operate. It uses an insertion motion in which the manipulator arm is moved linearly into the tool interface for tool pickup. A similar motion, moving the tool into the tool storage container, replaces the tool in the tool storage container. This movement requires only the push force the manipulator provides to actuate the latch cams attaching the tool to either the manipulator or the tool storage container and to interface the electrical connector.

Tolerance stackup analyses have been performed to verify that the FEM will be relatively straightforward to manufacture because the precision required is no greater than is normal for aerospace hardware. Similarly, analyses have been performed to verify that the insertion forces required will be within the range possible for general-purpose space manipulators. These same analyses show that the clamping forces the FEM provides will be sufficient to maintain positive contact between this tool base plate and the manipulator face.

The complete absence of motors and gears significantly reduces the complexity of the FEM. It also minimizes power requirements, thermal problems, command requirements, and the number of system parts.

The selection of the number of latching cams and the location of the latch ramps which form a part of the FEM is based on the failure tolerance requirement associated with manned space flight. The FEM incorporates six latch cam pairs and six latch ramps. These are arranged as three primary latches and three backup latches on both the manipulator and the tool storage container. The primary latch cams are aligned to latch onto the three primary latch ramps on the tool handle during the tool exchange operations. The three backup latch cams on both the manipulator and the tool storage container engage with the secondary ramps before the primary cams are lifted from the primary ramps. This provides the necessary interlocking architecture and redundancy for system safety.

The backup cams and ramps for retention on the manipulator are the primary cams and ramps for retention in the tool storage container and vice versa. During the exchange process, if for some reason the primary latches fail, the secondary latches will retain the tool in a safe position either on the manipulator or in the tool storage container. They will not, however, position it suitably for use. When the tool is held by the secondary latches, simply re-inserting the tool into the tool storage container will engage the tool into the primary latches.

As a result of its design, the FEM provides all of the primary services required for a flight system EEEM, retaining the tool on both the manipulator and in the tool storage container, and providing sufficient failure tolerance for manned spaceflight applications. In addition, the FEM offers several other advantages. It is a passive system which requires no electrical commands or complex interlocks for operation. It provides both the mechanical attachment of the end effector to the manipulator and the electrical interface as a part of a single, linear mechanical motion provided by the manipulator itself without additional motors or actuators. It is inherently failsafe.

Tool Storage Container

As with most hardware for space applications, the EEEM, tools, and tool storage container must survive both the launch and landing phases of the mission. The nature of the system is that the latch cams attached to the manipulator will be required only to survive this environment in an "unlatched" condition. Similarly, the tools will be required to simply survive the launch environment. The tool storage container, however, will be required to support the end effectors during launch and landing. As a result, it must incorporate all of the provisions necessary for it to do so. This will include sufficient preload on each tool to retain it positively in position and sufficient latching moment on the latching cams to retain their position.

In orbit, the tool storage container will continue to protect the end effectors, providing them with a controlled environment. This implies protection from viewing both the direct sun and deep space for long periods of time. To accomplish this, the tool storage container will be equipped with a container lid which will open when the tools are in use.

In addition to firm support during the launch environment, the tool storage container must also provide some compliance during tool exchange to

minimize the precision with which the manipulator must be positioned. This capability is also provided by using a spherical bearing scheme that allows the tool receptacle to rotate slightly to align with the tool during exchange.

Both the latch cam system and the tool storage container compliance design are based on an existing Fairchild spacecraft product, the Soft Umbilical Mechanism (SUM). While the appearance and purpose of the SUM are completely different from that of the EEEM and tool storage container, the principles of operation are identical. This design heritage provides a high level of confidence in the expectation that the FEM and tool storage container systems can be built and qualified for flight with a minimum level of risk.

A New Six-Degree-of-Freedom Force-Reflecting Hand Controller for Space Telerobotics

Douglas McAffee, Edward Snow, William Townsend*
Lee Robinson, and Joe Hanson

Robotic Hardware & Flight Experiments Group
Jet Propulsion Laboratory
California Institute of Technology
4800 Oak Grove Drive, 138-212
Pasadena, CA 91109

Abstract

A new six-degree-of-freedom universal Force-Reflecting Hand Controller (FRHC) was designed for use as the man-machine interface in teleoperated and telerobotic flight systems. The features of this new design include highly intuitive operation, excellent kinesthetic feedback, high-fidelity force/torque feedback, a kinematically simple structure, mechanically decoupled motion in all six degrees of freedom, good backdrivability, and zero backlash. In addition, the new design has a much larger work envelope, smaller stowage volume, greater stiffness and responsiveness, and better overlap of the human operator's range of motion than do previous designs.

This paper briefly describes the utility and basic operation of a new, flight prototype FRHC called the Model X. The design heritage, general design goals, and design implementation of this advanced new generation of FRHCs are presented, followed by a discussion of basic features and the results of initial testing.

Introduction

Many future space operations anticipate the extensive use of robot manipulators and servicers to assist astronauts and scientists in the exploration of space and development of a space-based infrastructure.

Although robotics is a rapidly developing field, for decades to come there will be many applications and tasks that are far too complex and unstructured to be performed completely by unsupervised autonomous robots. Therefore, the need for direct human supervision and control of these advanced robotic systems will continue in the foreseeable future. This is also true in terrestrial applications, such as undersea exploration, remote defense technologies, and various tasks in the nuclear industry. Often it is necessary to have the human operator physically removed from the actual worksite, remotely supervising and guiding the robot in the performance of a difficult or dangerous task. One of the key problems facing the designers of human-supervised robotic systems is how to make these sophisticated machines user friendly--how to facilitate human interfaces with these complex remotely operated (teleoperated) machines. To help solve this problem, JPL has developed a unique man-machine interface known as the Force-Reflecting Hand Controller.

---

*William Townsend is presently a private consultant with Barrett Design, Somerville, Mass.

The FRHC can be used by a human operator to reposition the mechanical arm of a remote robot (telerobot). This operation is performed by simply grasping the FRHC's handgrip and moving it in a desired direction and rate. The remote robotic arm will respond by mirroring the operator's every move. At the same time, if the remote arm comes in contact with, or applies forces to, objects in the remote worksite, then the FRHC mechanism is actuated and the human operator is able to physically feel scaled representations of forces and torques that the remote robot's arm is applying. Laboratory experiments have shown that this type of force feedback information significantly increases an operator's task performance and can prevent damage to the manipulator or worksite [1]. This paper describes an advanced new, flight prototype FRHC recently built at JPL called the Model X. (See Figure 1.)

ORIGINAL PAGE
BLACK AND WHITE PHOTOGRAPH

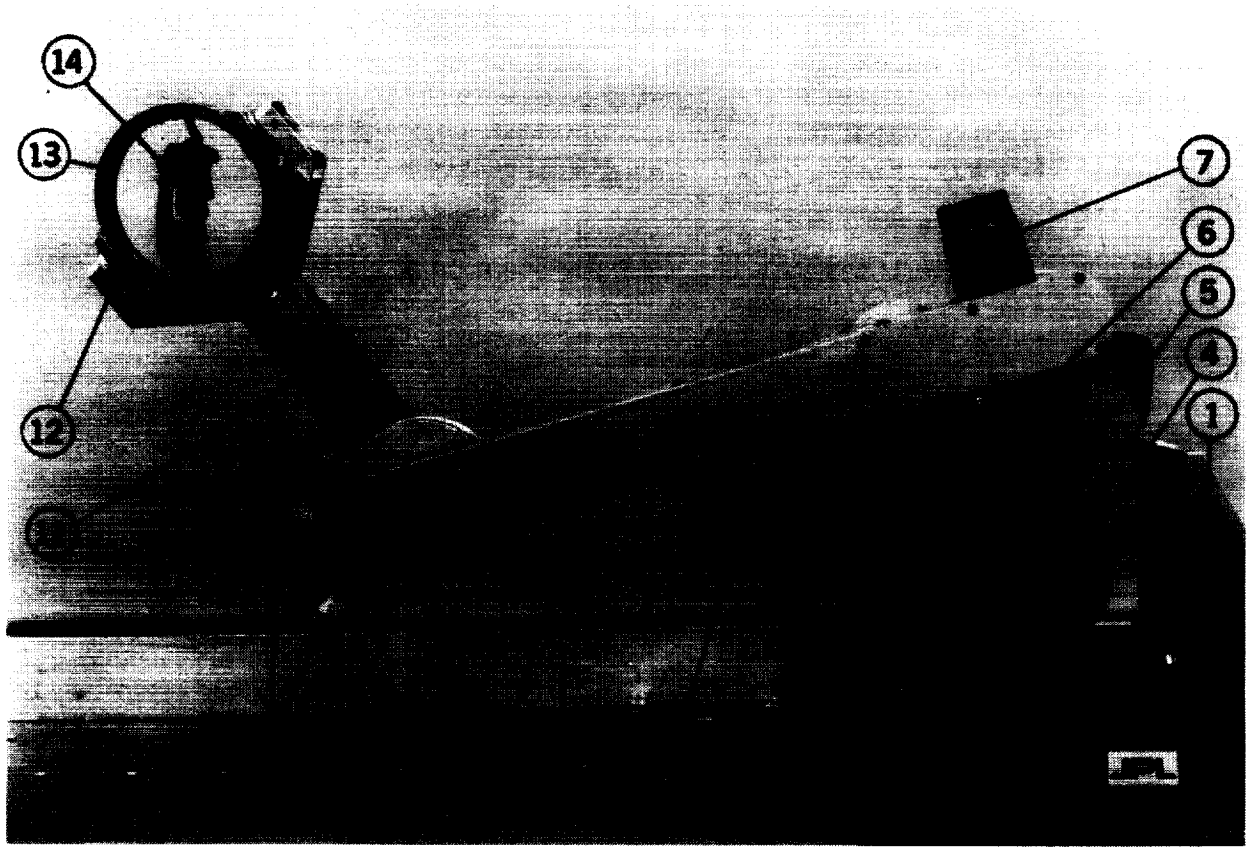

1. Mounting Stand
2. Base
3. Joint 1 Sector Pulley
4. Joint 2 Motor Shaft
5. Joint 2 Sector Pulley
6. Joint 4 Motor
7. Joint 5 Motor
8. Joint 6 Motor
9. Link 2
10. Joint 3 Assembly
11. Link 3
12. Joint 5 Pulley
13. Joint 6 Pulley
14. Handgrip

Figure 1. The Model X Force-Reflecting Hand Controller

Design Heritage

For many years, researchers have worked to develop a useful and intuitive human interface to teleoperated machines [2,3,4,5]. For more than a decade, JPL has pioneered work in the field of teleoperation and has contributed greatly to the general body of scientific and engineering knowledge about these systems.

In the late 1970s J.K. Salisbury (presently at MIT) in collaboration with A.K. Bejczy of JPL developed a new "universal" force-reflecting master for use in bilateral control of teleoperated systems [6,7]. Since then, three generations of this design have been built and integrated into various telerobotic research environments. The most recent edition is called the "Model C FRHC." Collectively, these hand controllers have undergone several years of testing [1,8].

In 1988, JPL began to look seriously at an opportunity to join a West German flight project called ROTEX (RObotic Technology EXperiment). The proposed venture would require JPL to supply a flight qualified force-reflecting hand controller complete with stand alone electronics and control software. The endeavor was short lived however, and was eventually canceled due primarily to international scheduling and budgetary conflicts. Nevertheless, the effort lasted long enough for the development of two significant operational prototype components: the flight hand controller and its control electronics [9].

This new force-reflecting hand controller was dubbed the "Model X FRHC". A conceptual design for the Model X began in 1986 under W.T. Townsend, who at the time was a post-graduate student of Salisbury and assigned to JPL. The goal of Townsend's work was to investigate alternative FRHC design concepts and suggest an improved version that could eventually be flight qualified [10]. The present design of the Model X was significantly influenced by both Townsend's work and that of Salisbury, inheriting many of their design features and incorporating several new ones.

General Design Goals

The Model X FRHC was developed to meet design requirements stemming from four basic sources.

First, the Model X began as a specific flight project with several functional requirements and constraints. These included a) sense positional changes in X, Y, Z directions, and roll, pitch, yaw orientations, b) apply up to a 17.8 N (4 lb) output force and a 0.452 N•m (64 in•oz) torque to an operator, c) provide a 0.254 x 0.254 x 0.254 m (10 x 10 x 10 in) work volume, which is relatively small due to the limited operating space of this particular flight experiment, d) use an upright, vertical, mounting configuration in order to utilize the one feasible mounting location available for this particular flight experiment, e) allow full operation in both zero-g and at a ground station, in one-g, without external modifications such as adding counter weights, f) stow within a Space Shuttle mid-deck storage locker, g) use a limited amount of power, and h) have a low overall mass.

Secondly, as an anticipated flight project there were several stringent flight qualification requirements. These included a) withstand launch and landing loads, b) use flight crew cabin

approved materials, c) no sharp edges on parts and minimize part count, and d) provide for quick emergency stowage.

The third basic source of design requirements came from the fact that there were several features of existing hand controllers that were to be incorporated into the new Model X design. These included a) highly intuitive operation, b) low friction, c) no backlash, d) high backdrivability, e) simple kinematics, f) low, semi-isotropic inertias, and g) mechanically decoupled degrees of freedom.

Finally, the fourth basic source of functional requirements came from the desire to incorporate a few enhancements over previous hand controller designs. These included a) higher structural stiffness, b) a larger work volume, and c) optimization of the joint/link configuration to allow better overlap of the human operator's range of motion without interfering with other operator control station functions.

General Design Implementation

During establishment of the flight experiment functional requirements and constraints several conceptual designs for a flight qualifiable force-reflecting hand controller were analyzed until a highly promising candidate was found.

One of the first activities in the detailed design process was to determine initial link lengths, based on operational and stowage requirements. A static load analysis was performed to estimate the joint torques necessary to satisfy the hand controller force/torque output requirements. Following this, the motor type and size, along with the corresponding transmission drive ratios, were selected by balancing several constraints, namely: produce the required joint torques, minimize friction, stay within power allocations, consider flight heritage, and delivery times. Brushless DC torque motors were selected with 1000 line, dual quadrature, incremental optical encoders mounted directly on their shafts. Some relevant design parameters are listed in Figure 2.

JOINT	Joint Range* (degrees)	Motor Stall Torque** N•m (in•oz)	Transmission Drive Ratio	Output Joint Torque N•m (in•oz)
1	± 25	0.821 (116.3)	16.0 : 1	13.120 (1858)
2	+ 37/ - 58	0.821 (116.3)	28.0 : 1	23.056 (3265)
3	± 80	0.606 (85.8)	18.3 : 1	13.784 (1952)
4	± 175	0.288 (40.8)	2.3 : 1	0.664 (94)
5	± 175	0.288 (40.8)	2.3 : 1	0.664 (94)
6	± 170	0.086 (12.3)	8.0 : 1	0.692 (98)

* Variations from the standard vertical mounting configuration with Links 1, 2, and 3 all at 90 degrees w.r.t. each other (as shown in Figure 4)

** Higher peak torques can be output for shorter periods of time.

Figure 2. Joint Actuator Parameters

Pulleys and steel-cables were used in the actuator transmission design. A novel new steel-cable routing scheme was implemented that allowed several significant design features. These features are discussed in the "Basic Features" section of this paper.

The overall hand controller mechanical stiffness was a primary concern during the design process. This is evident at several critical locations throughout the design. In the design of Joint 1 and Joint 4 a single preloaded, gothic-arch, x-type bearing was used. Joints 2 and 3 were designed with a matched pair of preloaded, back-to-back duplex bearings. Links 2 and 3 are made of aluminum tubing with a square cross-sectional shape which is significantly stiffer than round tubing of the same basic size and material. The steel transmission cables, used in all six joints, are pretensioned. Each joint steel-cable circuit can be accurately pretensioned which is an enhancement over previous designs. The transmission circuits for Joints 1 and 2 were designed with double spans of steel-cable in order to reach desired stiffness levels. Joint 3 required a 3-stage drive reduction design in order to meet stiffness goals. (The other five joints have only single stage transmissions.)

The design, fabrication and first complete assembly of the Model X Hand Controller was performed in seven months. A 3-D, solids-molding, mechanical CAD workstation was used for the entire design and some of the analysis work.

Basic Design Features

As indicated in the abstract to this paper, the Model X design has successfully incorporated many of the design goals stated above. Features of the Model X are further discussed here.

The Model X is considered a "universal" hand controller because it can be used with robot manipulators that are structurally dissimilar to one another and to the Model X. The fact that the Model X has "six degrees-of-freedom" (6 DOF) is important because this enables it be used to control robot arms, or other objects, in the six dimensions required to fully specify a unique position and orientation (i.e., X, Y, Z directions and roll, pitch, yaw orientations).

The Model X provides the human operator with "excellent kinesthetic feedback." The act of moving a telerobot's mechanical hand in the performance of a task is directly correlated to the physiological motor sensations that would occur if the operator were performing the task with his own hand. The intrinsic eye-hand coordination of the human operator is fully utilized, making the performance of the task, at the remote worksite, "highly intuitive" to the operator.

The Model X is capable of producing "high-fidelity force feedback" cues to the human operator. The forces and torques encountered by the telerobot at the remote worksite are faithfully reproduced by the hand controller mechanism allowing the operator to physically feel scaled representations of these remote interactions. The Model X has a good dynamic force output capability. Small feedback forces to the operator are not obscured by friction levels, and yet it can also output relatively large forces. Moreover, the forces and torques transmitted to the operator are crisp and distinguishable.

Minimizing friction in the mechanism was an important consideration during the Model X design. The Model X is run "open loop" (i.e., the actual output forces to the operator are not measured or fed back to the control algorithms), therefore the friction in the mechanism

becomes the limiting factor in determining the smallest commandable output force. This, of course affects the force resolution mentioned above. If the friction levels were too large they could deflect the operator from an intended input trajectory (path) or, in severe cases, they could degrade the backdrivability of the hand controller. The Model X has relatively low friction levels as shown in the "Initial Testing and Evaluation" section.

Using guide pulleys and steel-cables, as opposed to gear trains and drive shafts, made it possible to produce a mechanism with virtually no backlash. Having "zero joint backlash" (or play) is an important feature because it eliminates position deadband in the mechanism. This helps the stability of the control system.

The novel new steel-cable routing scheme used in the actuator transmission design allowed several very significant design features. For instance, it allowed all six joint motors, which make up almost half the Model X's overall mass, to be mounted near the base of the hand controller. This greatly reduced the inertial effects caused by the mass of these motors. The cabling design uses a minimum number of guide pulleys between the motor input and the joint output pulleys which helps to reduce mechanism friction.

The new steel-cable routing scheme also allowed the Model X to be designed with very "simple kinematics." This means that the Model X is relatively simple to describe mathematically. Computationally, a robot manipulator and a force-reflecting hand controller appear very similar. Many of the control techniques and approaches used in each system are identical. A standard notation for describing the geometric inter-relationships between one joint / link assembly and the next are provided in the Hartenberg/Denavit parameters. (Shown in Figure 3.) There are no joint offsets or link twists and the link lengths remain constant. In addition, five of the joint axes intersect orthogonally to one another and the sixth is parallel. This simplicity helps minimize the time required for a computer to calculate where the center of the Model X's handgrip is, relative to a fixed reference location (forward kinematics). In fact, of six-degree-of-freedom manipulators, the Model X has one of the simplest configurations possible.

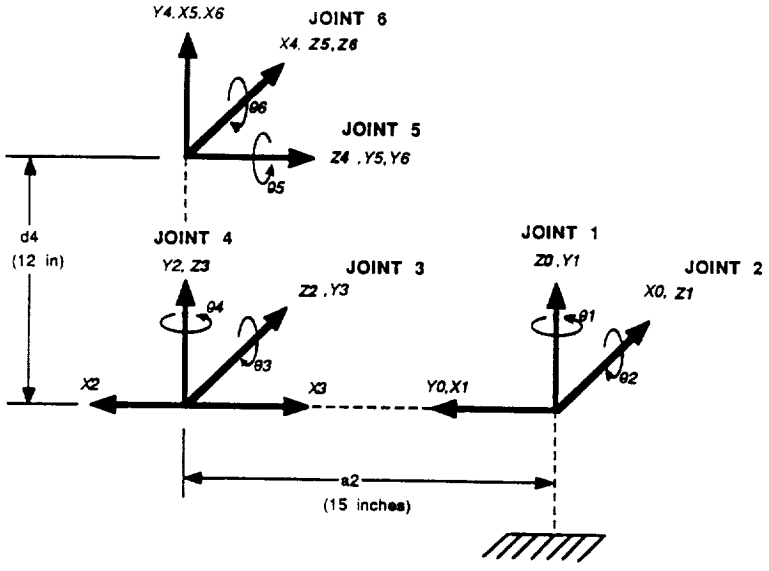

Denavit/Hartenberg Parameters

i	αi	di	θi	ai
1	90	0	θ1	0
2	0	0	θ2	a2
3	90	0	θ3	0
4	90	d4	θ4	0
5	90	0	θ5	0
6	0	0	θ6	0

INITIAL JOINT ANGLE VALUES FOR THE FIGURE SHOWN ABOVE	
θ1	90 degrees
θ2	0 "
θ3	180 "
θ4	90 "
θ5	90 "
θ6	0 "

NOTES

θi : is the angle from x(i-1) to x(i) positive CCW about z(i-1) and referred to as the "Joint Angle"

di : is the distance along z(i-1) from x(i-1) to x(i) and is referred to as the "Joint Offset"

αi : is the angle from z(i-1) to z(i) positive CCW about x(i) and is referred to as the "Link Twist"

ai : is the distance along x(i) from z(i-1) to z(i) and is referred to as the "Link Length"

Figure 3. Kinematic Coordinate Assignments and Hartenberg/Denavit Parameters

Even though the Model X has no kinematic offsets the new steel transmission cable routing technique allows the Link 2 assembly to be physically offset from Links 1 and 3. (See Figure 1.) This feature increases the mechanical dexterity and permits the hand controller to fold up into a "small stowage volume" when not in use.

Finally, the steel-cable routing design permits all six joints to be "mechanically decoupled" from one another, that is, each joint rotates completely independent of all others. This helps to simplify the software control algorithms required to activate the Model X.

While the Model X Hand Controller was being designed, great care was also taken to ensure it would have maximum "stiffness and responsiveness." This attention to structural stiffness improves the quality and clarity of the forces the operator feels because it shortens the response time of the mechanism. This also contributes to control system stability. (See stiffness evaluation in the following section.)

The "work envelope" of a hand controller refers to the three-dimensional space through which the operator is able to move the handgrip. A cross-sectional view of the work volume of the Model-X while in the vertical mounting configuration is shown in Figure 4. This cross-section would be rotated ± 25 degrees about the Joint 1 axis to obtain the 3-D work volume.

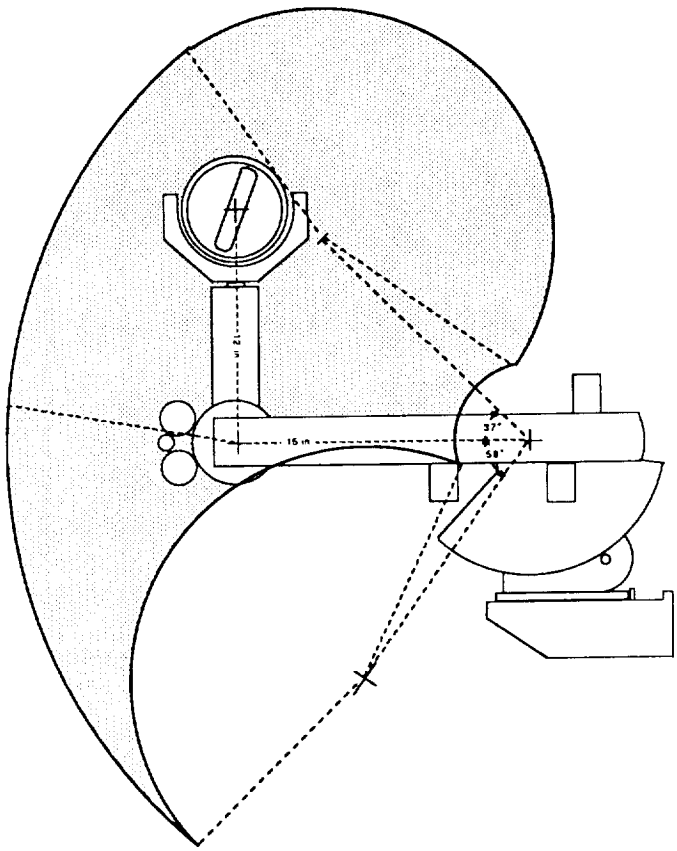

Figure 4. Model X Work Envelope

In special mounting configurations, this work envelope coincides directly with the range of motion for the human operator's arm. (See Figure 5.) This means that the Model X can follow almost any motion of the human operator's hand over its entire reach.

Figure 5. Model X Horizontal Mounting Configuration

Initial Testing and Evaluation

There are several key design parameters that are of particular interest when evaluating the utility and effectiveness of the Model X Hand Controller. These parameters include positional resolution, dynamic range of the force output, friction levels, inertia, backdrivability, backlash, stiffness, dynamic mechanical response, and natural (resonant) frequencies. Together these parameters provide a thorough characterization of the mechanism.

In order to quantify some of these parameters, the Model X has undergone several initial tests and measurements. Although these early test results are preliminary in nature, they provide an encouraging initial verification of the design goals.

The positional resolution (i.e., the smallest detectable motion at the handgrip) changes slightly across the work volume due to the geometry of the Model X. At near full extension, the Model X has its least resolution. In this configuration, the positional resolution is still better than 0.051 mm (0.002 in) and increases as the handgrip is moved closer to the Joint 1 axis.

The dynamic range of output forces and torques provides insight into the quality and clarity of the forces that are "reflected" back to the person operating the Model X. The dynamic range is defined as the maximum commandable output force divided by the minimum. The output forces in the X, Y, and Z directions are position dependent and are inversely proportional to the distance out from the Joint 1 axis. When the hand controller is fully outstretched and operating in gravity (worst case), the Model X can output feedback forces to the human operator ranging from about 0.8 N up to 18.7 N (3 to 67 oz). Larger forces are possible as the handgrip is moved closer to the Joint 1 axis. In space applications, the maximum output forces in the Link 2/Link 3 plane will be significantly higher since there are no gravitational forces to counteract. The orientation degrees of freedom, Joints 4, 5, and 6, can output torques up to 0.664 N•m (94 in•oz).

The Coulomb friction forces (also referred to as static friction) the operator feels at the handgrip will vary throughout the work volume depending again on the effective radius to the axis of rotation (i.e., how far the handgrip is from the Joint 1 axis). With the hand controller near full extension, these friction levels are about 0.8 N (3 oz) in any direction and slightly increase as the handgrip is moved closer to the Joint 1 axis. The friction levels for the three orientation degrees-of-freedom are constant because the effective radius to the joint axis of rotation never changes. These frictional torques are 0.04 N•m (6 in•oz) about Joints 4 and 5, and 0.09 N•m (13 in•oz) about Joint 6.

Since the Model X was designed for space flight, the overall mass was kept as small as possible without compromising structural ruggedness. It has a total mass of 14.5 kg (32 lb). The motors are mounted near the base of the hand controller, which greatly reduces their inertial effects. The four motors mounted on Link 2 are evenly distributed about the Joint 2 axis. This causes the center of gravity for Link 2 to be only 40.6 mm (1.6 in) from the Joint 2 axis of rotation which helps to reduce the moment of inertia for the link. The low overall inertia and friction levels result in the hand controller mechanism being very backdrivable.

At over 0.1133 m^3 (4 ft^3), the Model X has a work envelope that more than doubles that of previous hand controllers. (See Figure 4.) The actual work envelope is much larger than that specified in the functional requirements of the original flight project. This was done in order to maintain the applicability of the Model X design to a wide variety of tasks. Even with a much larger work volume the Model X can still be folded up and compactly stowed within a 0.051 m^3 (1.8 ft^3) volume, which is smaller than previous designs.

The Model X has a rugged structural design that is necessary for the rigorous demands of space flight. The mechanical stiffness of the device also plays a roll in establishing the fidelity and quality of feedback forces to the human operator. Measuring the compliance of a mechanism, which is the inverse of its stiffness, provides us with a good estimate of this important parameter. Initial tests were performed to determine the radial compliance for critical joints. These measurements were made by positioning the hand controller in a desired configuration and rigidly locking the motor shafts. A precision dial indicator was placed in contact with the mechanism at a known radius from the joint axis. A known static load was applied to the hand controller and the corresponding deflection was measured. (See Figure 6.)

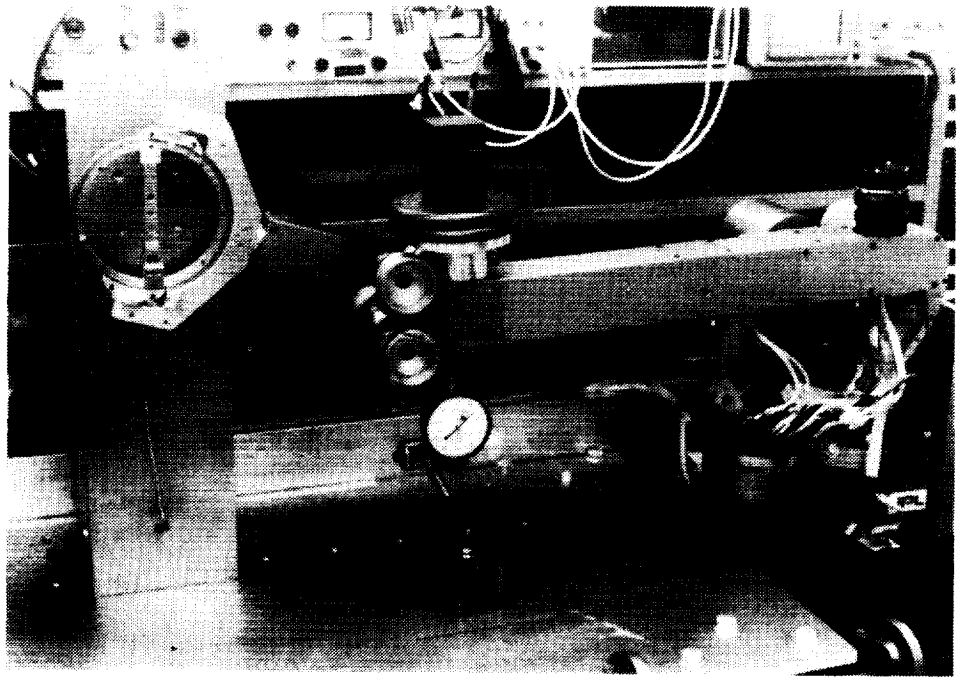

Figure 6. Joint 2 Radial Compliance Measurement

This measurement of the overall radial compliance of the joint combines several sources of structural compliance found in the mechanical system (e.g., actuators, transmissions, bearings, and link bending) and assumes them to be concentrated along the joint axis.

From these data an approximate torsional spring constant for the joint was determined. For example, under a 41.8 N (9.4 lb) static test load, there was a 0.81 mm (0.032 in) deflection at the end of Link 2. This represents a torsional spring constant (k_t) about the Joint 2 axis of more than 222.6 N•m/deg (1970 in•lb/deg). The natural frequency (f_n) can be approximated by evaluating the following equation:

$$f_n = \frac{1}{2*\pi} \sqrt{\frac{K_t}{I}}$$

where I is the combined moment of inertia for Links 2 and 3 about the Joint 2 axis. Evaluating this equation yields an initial estimate of the structural natural frequency, about the Joint 2 axis, of over 21 Hz.

A different set of tests were performed in order to more directly examine the mechanical response dynamics and resonant frequencies of the Model X. The Model X is a fairly complex multi-degree-of-freedom mechanism and it inherently behaves in a complex and nonlinear way to traditional frequency response testing methods. An initial estimate, however, can be inferred by examining the output force dynamics of individual joints when subjected to a step change in input.

Joint 1, for example, was tested in the following manner. The hand controller was positioned in its fully outstretched (worst case) configuration. This configuration was maintained by locking the motor shafts of Joints 2 and 3. Only Joint 1 was free to move. The Joint 1 motor was connected to a single-axis motor driver box. This driver box generated a 212 Hz PWM signal that could be adjusted from about 0.2% duty cycle up to 99.8% full power. It also provided a motor direction change toggle line. To measure the output force of the Model X the handgrip was replaced with a single-axis force sensor. This force sensor was then rigidly mounted to a restraint fixture which provided a rigid surface to push against when the Joint 1 motor was energized. (See Figure 7, but note that it does not show the hand controller fully extended.) Switching the motor direction toggle line from low to high caused a step change in motor output torque from cw to ccw and resulted in a step change in the state of the mechanical system. The dynamic output force signal, read by the force sensor, and the motor direction toggle line were displayed on a digital oscilloscope. (See Figure 8.)

Joint 2 was tested in a similar manner and its dynamic mechanical response is depicted in Figure 9. Joint 3 was further isolated for testing by physically removing the entire Link 2/ Link 3 and Handgrip Gimbal Assembly from the rest of the mechanism and rigidly mounting Link 2 to a metal table top. The dynamic mechanical response for Joint 3 is shown in Figure 10.

These frequency response tests confirmed our expectation that the mechanical system would behave in a complex and non-linear way. However, by assuming only moderate simplification, an initial estimate of the damped natural frequency for Joints 1, 2 and 3 can be approximated using various standard approaches [11]. For example the damped natural frequency (Ω_d) can be simply estimated by determining the peak time (t_p), which is the time required for the response to reach the first peak of overshoot, and dividing it into pi (π).

$$\Omega_d = \frac{\pi}{t_p}$$

The natural frequency about a joint can also be initially estimated by measuring the elapse time for several successive peaks and then finding an average peak to peak period. The reciprocal of this value would be an approximate measure of the natural frequency.

These methods indicate natural frequency values, for the Model X, within the following ranges:

Joint 1 = 27 to 29 Hz
Joint 2 = 27 to 33 Hz
Joint 3 = 37 to 40 Hz

These values are approximately two to three times higher than those found in previous hand controller designs.

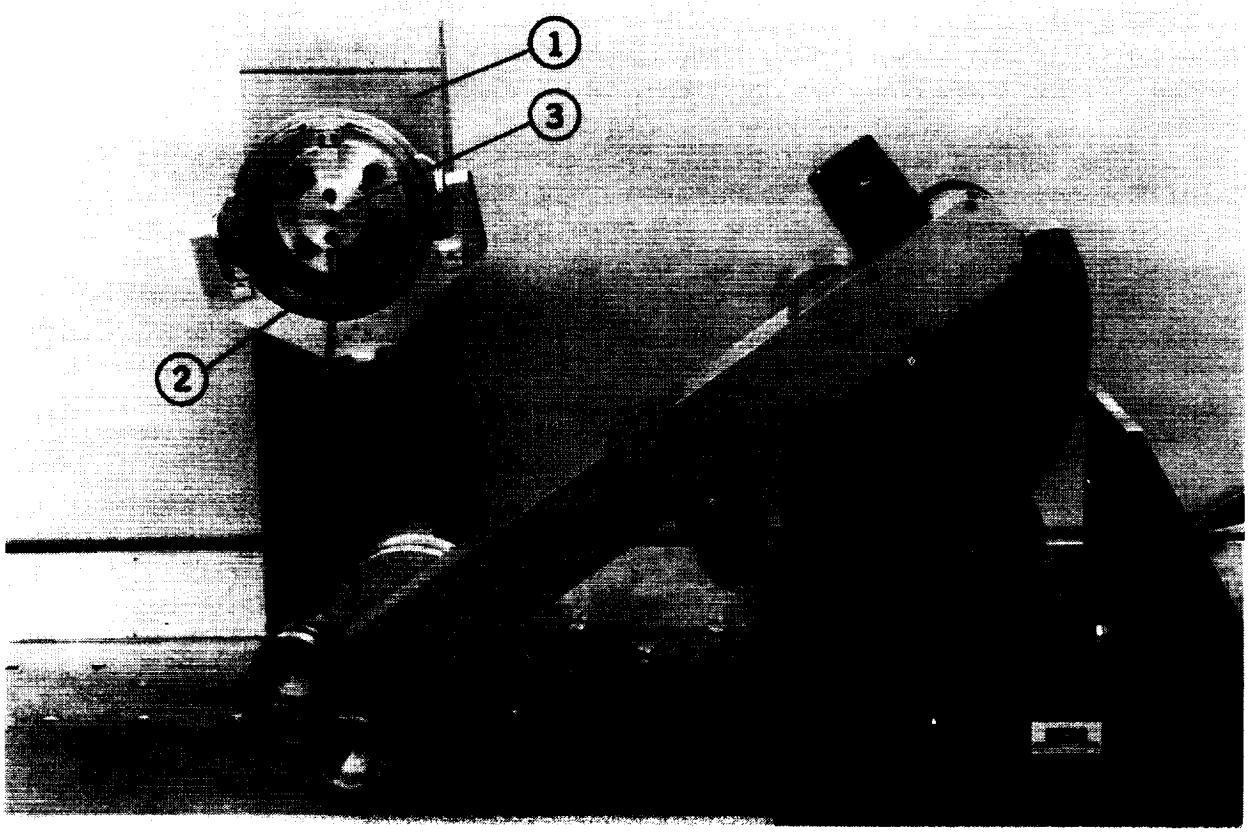

1. Vertical Restraint Fixture 2. Single-Axis Force Sensor 3. Force Sensor Mounting Bracket

Figure 7. Joint 1 Dynamic Mechanical Response Test Apparatus

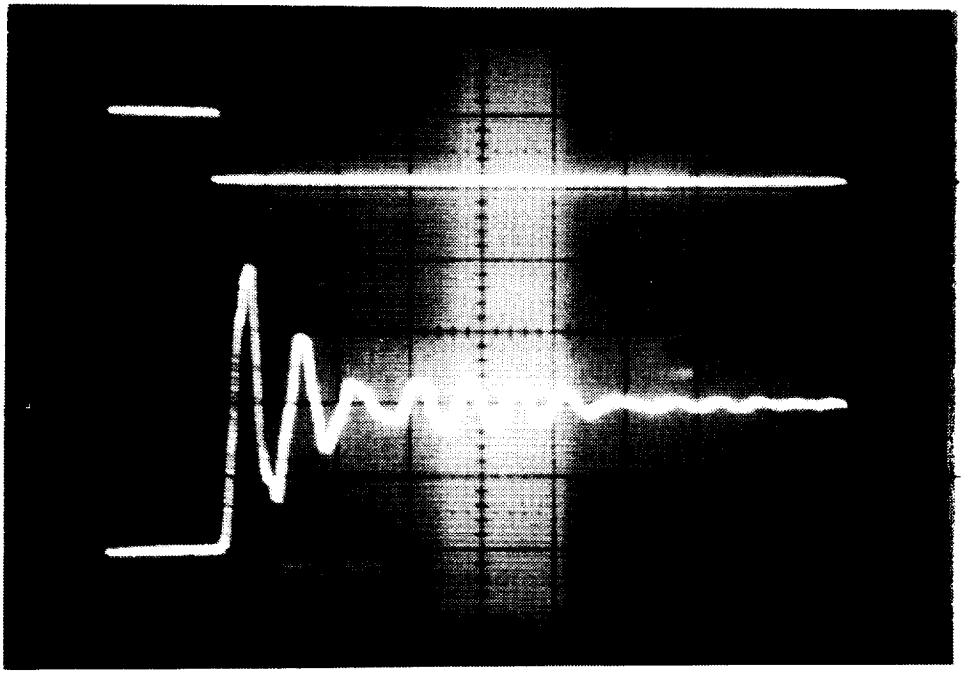

Motor Direction
Toggle Line
5 volts/div
(High= cw
Low= ccw)

Model X
Force Ouput
At the Handgrip
2 volts/div
(1v = 1.7 lbs.)

Timebase:
50 msec/div

Figure 8. Joint 1 Dynamic Response to a Step Input

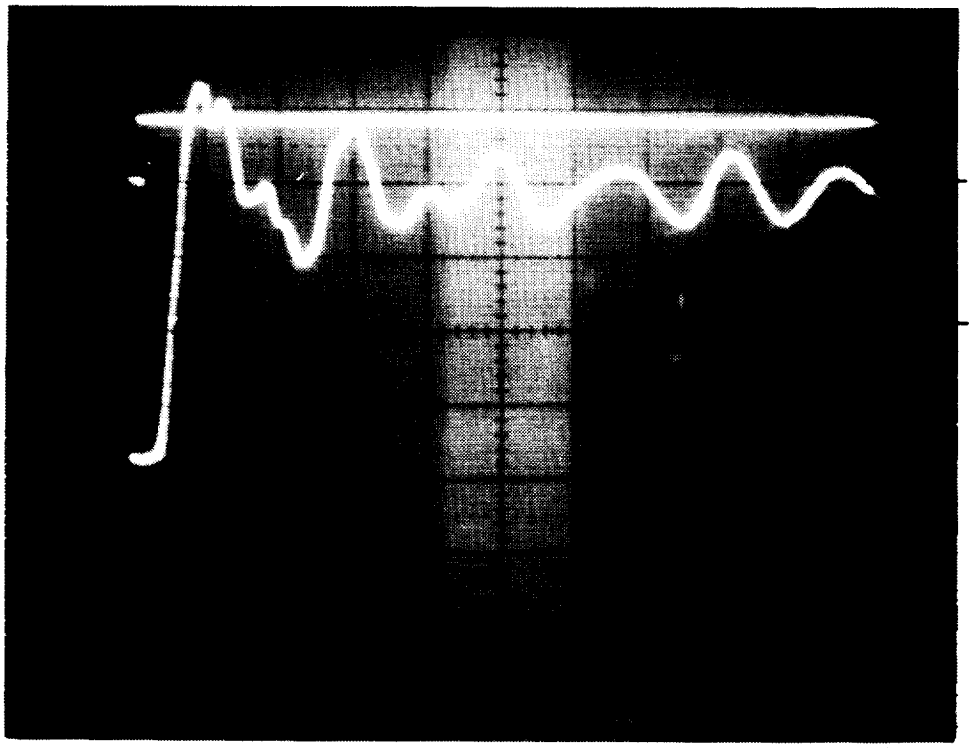

Figure 9. Joint 2 Dynamic Response to a Step Input

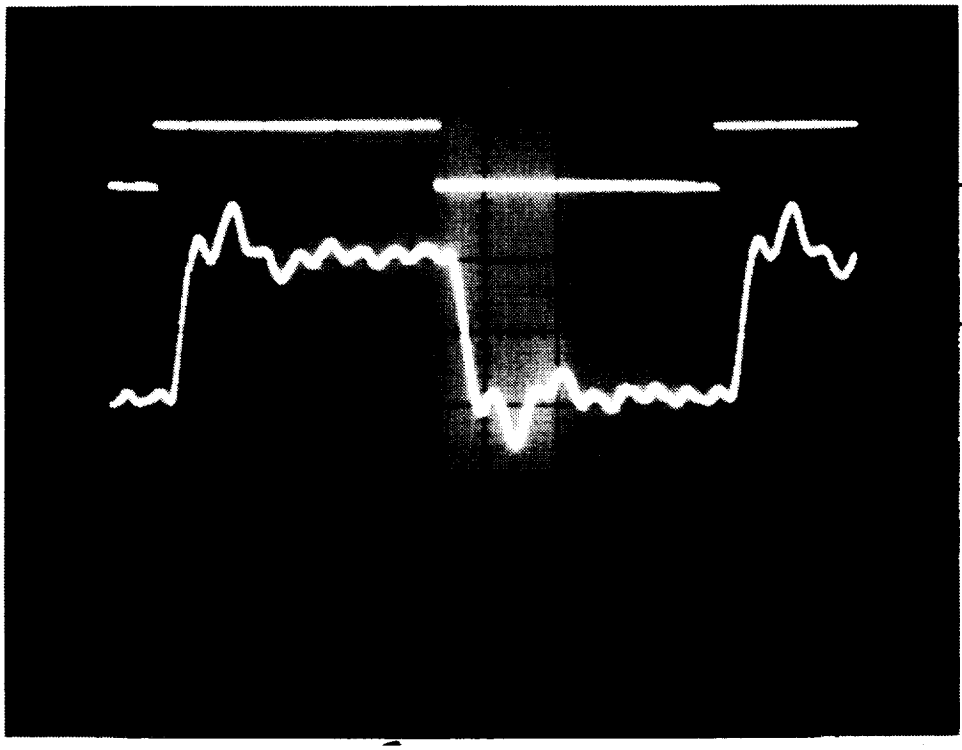

Figure 10. Joint 3 Dynamic Response to a Step Input

Summary

The Model X FRHC meets or exceeds many of the original design goals. It is a unique step forward in universal force-reflecting hand controller design. It combines many of the intrinsically desirable features of previous designs such as highly intuitive operation, low friction, low inertia, high backdrivability, no backlash, simple kinematics, and mechanically decoupled joint rotation. In addition, it is a rugged, flight-worthy device, with high stiffness and structural natural frequencies in excess of 25 Hz, allowing the Model X to generate high-fidelity force feedback cues to the human operator. It has an overall mass of only 14.5 kg (32 lb). The mechanical transmission incorporates a unique steel cable routing design that provides many beneficial features including the capability of folding the Model X for compact stowage in less than 0.051 m^3 (1.8 ft^3). With a fully usable work volume of over 0.1133 m^3 (4 ft^3) i t more than doubles the range of motion than that of previous hand controllers especially since it is optimized to coincide with nearly the full range of motion of the human operator's arm.

Other Potential Areas of Application

The Model X Hand Controller is a very intuitive, highly versatile, human interface to complex multi-degree-of-freedom dynamic machines.

As a position input device with force output capabilities, the Model X has been optimized to be the fundamental and natural interface a human operator needs in order to manipulate multi-dimensional spacial relationships where force cues can help associate a coordinated response. As such, the Model X may prove to be a useful human interface in applications other than the control of teleoperated robotic arms.

Areas of possible application of Model X design technologies might include a) new seven, or more, degree-of-freedom redundant robot manipulator design that would have good force control capabilities, b) new pilot interfaces for underwater exploration robots, c) a new helicopter pilot flight control interface, d) nuclear industry applications, e) an RPV ground based flight controller, and f) computer image manipulation.

Acknowledgements

The research described in this paper was carried out by the Jet Propulsion Laboratory, California Institute of Technology under contract with the National Aeronautics and Space Administration. The authors would also like to thank Dr. Antal Bejczy who was the impetus for the initial flight experiment and served as the Principal-Investigator during the flight development stage of this effort, along with Dr. Blake Hannaford who was the Co-Investigator. Dan Kerrisk who served as the Task Manager. Brad Gibson, Brad Swenson, Brian Okerlund, and Richard Fleischner of the JPL CAD Services Group for their invaluable finishing touches to the design.

References

[1] "Performance Evaluation of a Six-Axis Generalized Force- Reflecting Teleoperator", B. Hannaford et.al., JPL Publication 89-18 (Internal Document), June 1989.

[2] "A Force Reflecting Positional Servo-mechanism", Nucleonics, vol. 10 pp. 43-45, November 1952.

[3] "Force-Reflecting Electrohydraulic Servomanipulator", R.S. Mosher and W. Berthold, Electro-Technology, vol. 66 pp. 138-141, December 1960.

[4] "Some Work on Manipulator Systems at ANL; Past, Present, and a Look to the Future", Ray C. Goertz, Proceedings of the 1964 Seminars on Remotely Operated Special Equipment, vol. 1 AEC CONF-640508, pp. 27-69.

[5] "Teleoperators and Human Augmentation", An AEC-NASA Technology Survey, by Edwin G. Johnson and William R. Corliss, NASA SP-5047, Dec 1967.

[6] "Study of Modeling and Evaluation of Remote Manipulator Tasks with Force Feedback", J.W. Hill, Report 5 & 6, JPL Contract 95-5718 Stanford Research Institute, Menlo Park, CA., 1979.

[7] "Kinesthetic Coupling Between Operator and Remote Manipulator", A. Bejczy and J.K. Salisbury, Proceedings of the International Computer Technology Conference, ASME, August 1980.

[8] "Teleoperator Subsystem/ Telerobot Demonstrator: Force Reflecting Hand Controller Equipment Manual", D.A. McAffee and Tim Ohm, JPL D-5172 (Internal Document), January 1988.

[9] "TRIIFEX Final Report", R.L. Robinson, JPL D-6541 (Internal Document), June 1989

[10] "Initial Development of the Model X: An Alternative, Compact, Force-Reflecting Hand Controller", W.T. Townsend, Internal JPL Memorandum 347-87-764 (Internal Document), August 1987.

[11] "Modern Control Engineering", K. Ogata, Prentice-Hall Publishing, pg. 235, 1970.

[12] "Mechanical Design of Robots", Eugene I. Rivin, McGraw-Hill Book Co., 1988.

THE RESUPPLY INTERFACE MECHANISM RMS COMPATIBILITY TEST

Stewart W. Jackson,* Frank G. Gallo*

ABSTRACT

Spacecraft on-orbit servicing consists of exchanging components such as payloads, orbital replacement units (ORUs), and consumables. To accomplish the exchange of consumables, the receiving vehicle must mate to the supplier vehicle. Mating can be accomplished by a variety of docking procedures. However, these docking schemes are mission dependent and can vary from shuttle bay berthing to autonomous rendezvous and docking. Satisfying the many docking conditions will require use of an innovative docking device. The device must provide fluid, electrical, pneumatic and data transfer between vehicles. Also, the proper stiffness must be obtained and sustained between the vehicles. Fairchild Space Company has developed a device to accomplish this, the resupply interface mechanism (RIM). The RIM is a unique device because it grasps the mating vehicle, draws the two vehicles together, simultaneously mates all connectors, and rigidizes the mating devices.

Johnson Space Center (JSC) Manipulator Development Facility (MDF) was used to study how compatible the RIM is to on orbit docking/berthing. The MDF contains a shuttle cargo bay mockup with a remote manipulator system (RMS). This RMS is used to prepare crew members for shuttle missions involving spacecraft berthing operations. The MDF proved to be an excellent system for testing the RIM/RMS compatibility. The elements examined during the RIM JSC test were:

- RIM gross and fine alignment
- Berthing method sequence
- Visual cuing aids
- Utility connections
- RIM overall performance

The results showed that the RIM is a good device for spacecraft berthing operation. Mating was accomplished during every test run and all test operators (crew members) felt that the RIM is an effective device.

This paper will discuss the purpose of the JSC RIM test and its results.

* Fairchild Space Company Germantown, Maryland

INTRODUCTION

The recovery of LDEF in late January 1990 has once again demonstrated that on-orbit retrieval of spacecraft is a routine operation for the shuttle. Perfecting the process of spacecraft retrieval would lead to the enhancement of on-orbit spacecraft servicing. To facilitate on-orbit servicing a spacecraft must be designed for maintainability. Maintainable spacecraft provide easy access for exchange of various components using Extra Vehicular Activity (EVA) or a robotic manipulator such as the RMS. The various components are ORUs, payloads, and consumables. Consumables maintain the spacecraft functional integrity. These consumables consist of propellant, coolant, water, waste, etc. With replenishing capability, the spacecraft operational life can be extended. Replenishing can be accomplished using two scenarios. The first would involve rendezvous and docking of a spacecraft and refueling tanker. The second would require retrieval of a spacecraft using the RMS, and then berthing it to a refueling tanker in the shuttle cargo bay. The interface used to mate the two vehicles has to provide transfer of utilities across the separation plane. The type of utilities requiring transfer are electrical, pneumatic, and fluid. Additionally, the mating interfaces must be brought together to their specified rigidization. The Fairchild Space Company (FSC) realizes the important role that the interface must play in spacecraft servicing. Therefore, FSC initiated an Internal Research and Development (IR&D) program to define, design, build, and test an interface system for generalized spacecraft. The RIM illustrated in figure 1 is the result of this program. The RIM functions are:

1. To provide mating guidance during the docking/berthing process.
2. To capture and draw the two vehicles together.
3. To connect simultaneously all utility connectors.
4. To rigidize the interface.

The unique aspect of the RIM is that it accomplishes the above docking tasks in a single action.

The RIM was tested at JSC MDF to determine its compatibility to the RMS.

RIM DESIGN DESCRIPTION

The RIM illustrated in figure 2 consists of two parts: an active half and a passive half. The cylindrical shape of the RIM is designed such that the passive half fits internally into the

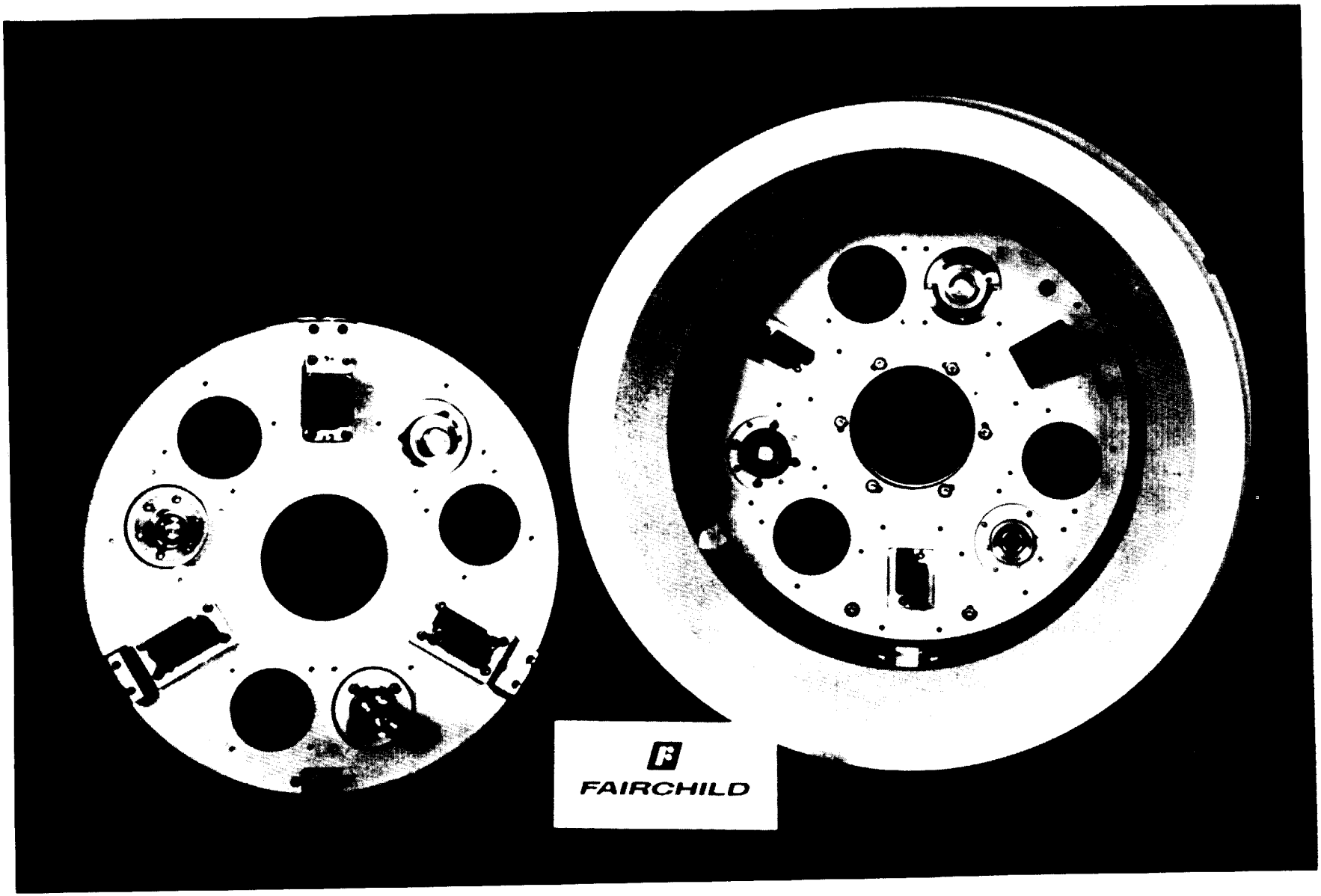

FIGURE 1: THE RIM

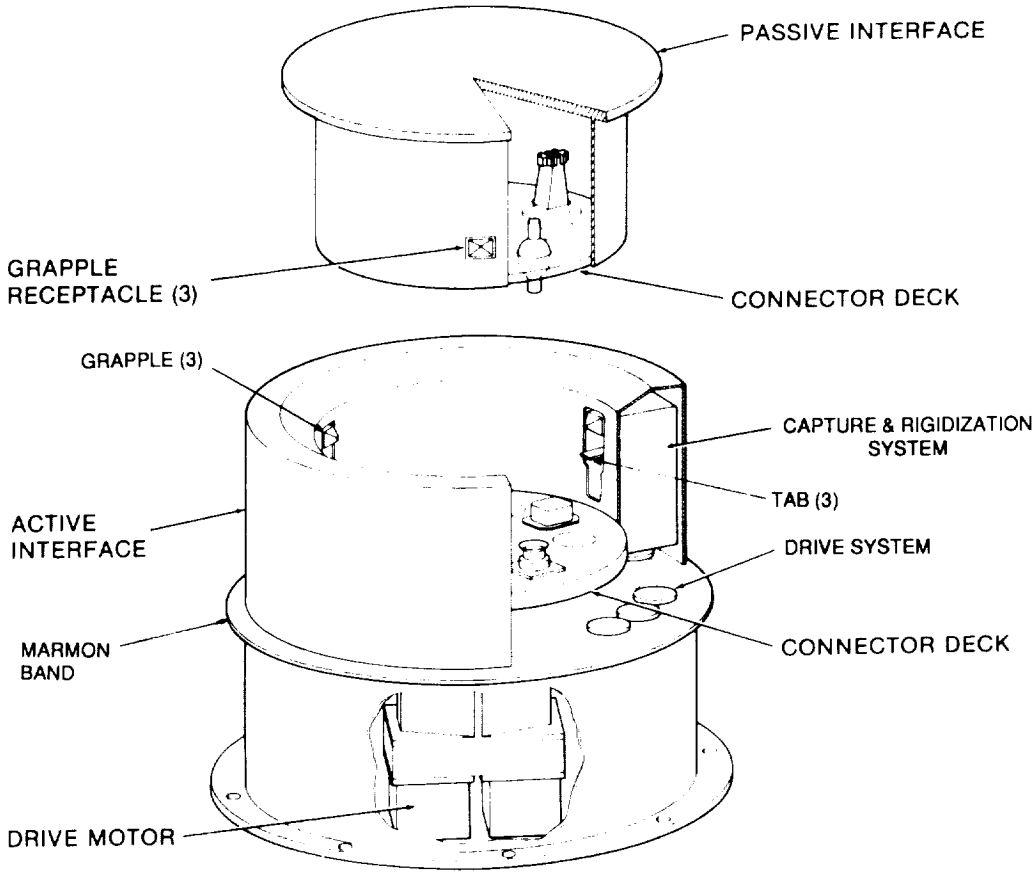

Figure 2: RIM, EXPLODED VIEW

active half. The active half is normally mounted to the refueling tanker. It contains the proprietary capture/rigidization mechanisms, sensors, a controller system, a safety system and the female halves of the electrical connectors and fluid couples. Also, the active half has an opening with a conical rim. The conical rim accepts gross positioning and alignment tolerance of $\pm$ 2.0 inches and $\pm$ 10°. This opening is gradually tapered at a 45° angle providing for a passive RIM final alignment of $\pm$ .200 inches. Fine alignment and positioning of the passive half is provided by the active half inner wall and capture/rigidization system. A radial keyway on the active RIM inner wall corrects for rotational alignment. This keyway is designed to accept a passive RIM final positioning alignment within the connectors' and fluid couplings' mating tolerance. The proprietary capture/rigidization system (see illustration in figure 2) consists of three grapples and tab devices. The grapples and tabs are located two inches below the conical

section and 120° apart. These grapples are actuated simultaneously via a chain drive system that is driven by one motor. The grapples travel radially toward the RIM center. The grapples protrude a maximum of one inch beyond the active half inner wall before driving downward. The grapples are used to grasp the RIM passive half and drive the two halves together. The grapples maintained coupler and connector mating during servicing operations and provided the required rigidization.

The passive half is normally mounted to the servicing vehicle. The RIM passive half contains the receptacles for the grapple system and the male half of the electrical connectors and fluid couplings.

All connectors and fluid couplings are mounted on the RIM connector decks (illustrated in Figure 2) that are utilized in each half of the RIM. One deck is located inside of the RIM active half. The connectors on this deck are mounted on floating interface plates which provide 6 degrees of freedom for each connector and coupling. Also, the active RIM connector deck contains load bearing pads. The loads that are produced from berthing and rigidization are transferred by the load-bearing pads, into the RIM structure. The other connector deck forms the interface surface of the passive half. Each connector on the passive connector deck is rigidly mounted.

The RIM is also equipped with an emergency release system. This system consists of three jettison spring assemblies mounted on the periphery of the active half of the RIM at 120° apart. A marmon clamp (illustrated in Figure 2) with explosive bolts is used to secure the two halves of the active RIM system. Firing the bolts releases the marmon clamp, enabling the outer portion of the active half of the mechanism to be jettisoned, demating the connectors in their normal fashion.

The fluid couplings used in this test were supplied by Fairchild Control System Company (FCSC), Moog, and Futurecraft. Electrical connectors have been supplied by both G&H Technologies and AMP.

RIM TWO-PART TESTING

A two-part proof-of-concept RIM test was performed. The first test was conducted in-house to verify mechanism operation and berthing alignment range. The second test verified the compatibility of the RIM mating scenarios with the RMS controls. The RMS test was performed as part of the JSC satellite resupply demonstration/test held in the MDF. In addition to the RIM test JSC also demonstrated the capability of their Magnetic End-Effector (MEE), Force Torque Sensor (FTS) and Tracking and Reflecting Alignment Concept (TRAC). The results of testing these systems will not be presented in this paper.

TEST CONFIGURATION

RIM JSC test setup

All testing was performed in the JSC MDF. The MDF consists of a full-scale shuttle cargo bay mock-up with a 50-foot hydraulically activated manipulator arm. This manipulator arm is geometrically similar to the shuttle RMS but is designed to operate in a 1-g environment. The arm is operated from a replica of a flight control console located in the same coordinates, from the cargo bay, as a flight unit would be on the shuttle. The MDF closed circuit television (CCTV) system can operate an either an MDF configuration or flight configuration. To produce as much realism in this test as possible, the flight configuration was chosen. The flight system CCTV consists of two split-screen TV monitors, a maximum of five TV cameras in the cargo bay and two cameras on the manipulator.

For the RIM test setup illustrated in figure 3, we decided to simulate in the shuttle cargo bay a spacecraft consumable replenishing scheme. This scheme required that a refueling tanker be place stationary in the cargo bay. Then the servicing vehicle was maneuvered by the manipulator arm and berthed to the tanker. The servicing vehicle used was a spacecraft mockup designed by JSC. The passive RIM was mounted to the bottom of the spacecraft mockup using the mounting bolt pattern provided. The MDF arm is capable of lifting 35 lbs. maximum in a 1-g environment. However, the spacecraft mock-up and the passive RIM exceeded this weight. JSC provided a Counter Weight System (CWS) that created the means to simulate a weightless spacecraft and enable the MDF arm to manipulate the spacecraft. This setup provides the arm operator with complete attitude control of the spacecraft/RIM berthing axes. The simulated refueling tanker was a trigon-shaped truss structure that sat in the payload bay with the active RIM attached.

NASA JSC systems

In addition to testing the RIM, three JSC systems were evaluated: TRAC, FTS, and MEE. Each system complemented the success of the test.

The TRAC consists of a CCTV camera placed under the active rim looking up through an access hole at a target mirror on the passive RIM. TRAC uses cross marks on the mirror and aft deck monitor to correct the docking vehicle translation, pitch, yaw and roll (P,Y,R). Correct translation alignment between the passive and active RIM is established when the black cross marks on the mirror are coincident with the white cross marks on the aft deck monitor. Furthermore, attitude alignment is achieved by centering the cross marks in the reflection of the CCTV camera lens, as viewed from the monitor. The mating success is obtained

by the operator maintaining the above alignment during the vehicle berthing approach.

The FTS is placed between the MEE and RMS to measure the force and torque produced during docking operations and felt by the RMS. Graphically and numerically the force and torque are displayed on the aft flight deck monitor.

The MEE was used instead of the standard RMS snare end-effector. It worked well and did not hinder test operations.

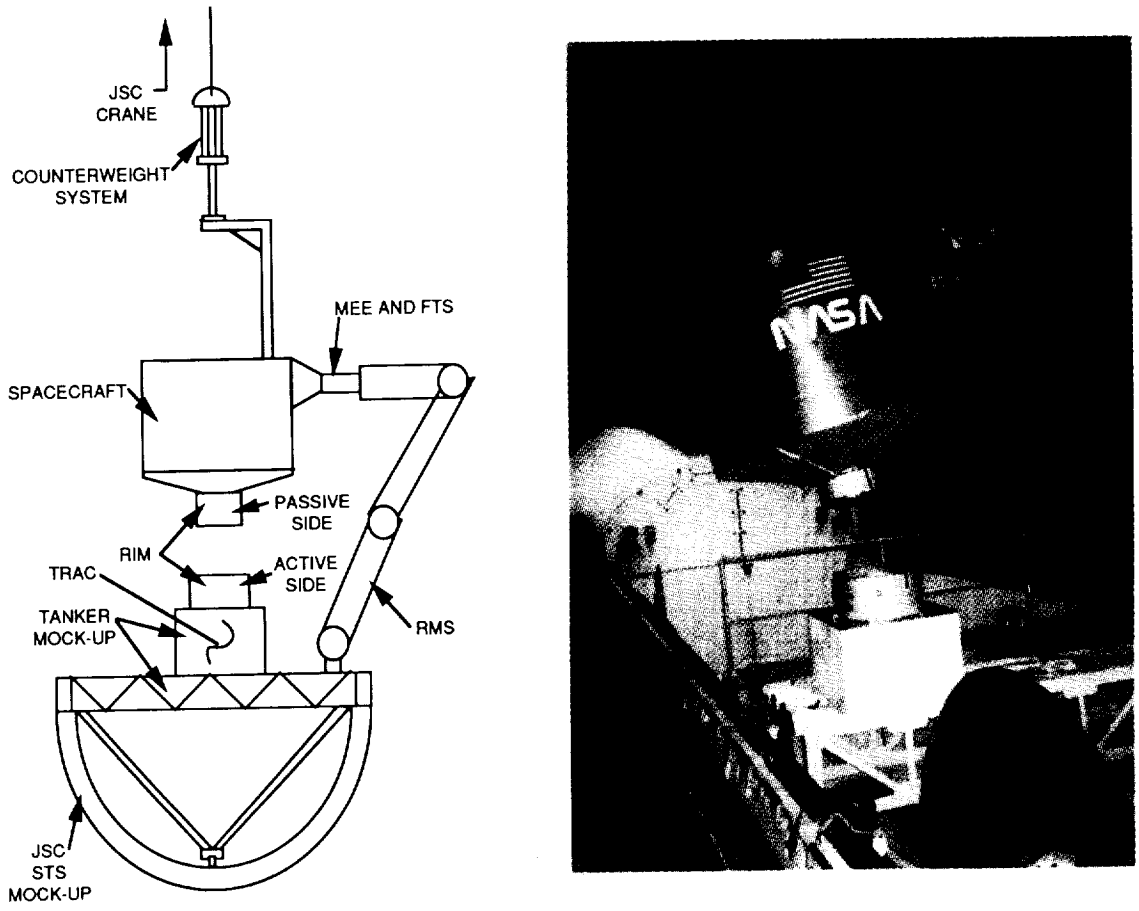

FIGURE 3: RIM JSC TEST SETUP

RIM cuing marks

Two sets of black vertical cuing marks were placed on the RIM to enhance visual sighting, from the cargo bay camera positions, of the spacecraft during berthing. The RIM aft contained one mark on the passive and two on the active RIM, as illustrated in figure 4a. The parallax created by the two aft bay cameras when

sighting the cuing marks made it necessary to add two vertical cuing marks on the active RIM. The cuing marks on the active RIM were collimated with the one vertical cuing mark on the passive RIM. When viewed from either camera, the cuing marks were aligned as illustrated in figure 4b. The front of the RIM (the part facing the orbiter aft deck window) had one cuing mark on the passive and one on the active RIM, as illustrated in figure 5a. These cuing marks were arranged to be collimated viewed from the aft flight deck window as illustrated in figure 5b.

To obtain a successful berth, the RIM front and aft cuing marks must be simultaneously aligned before driving the passive and active RIM together.

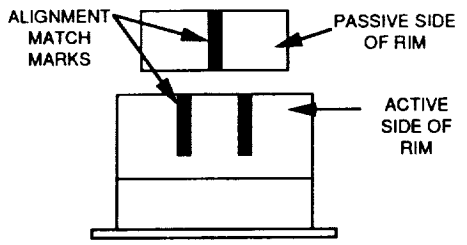

a: RIM AFT VISUAL CUEING MARKS

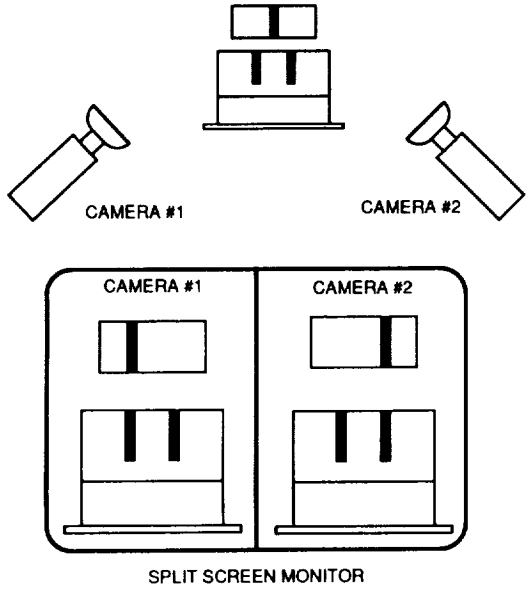

b: OPERATORS VIEW OF ALIGNMENT MARKS

FIGURE 4: AFT RIM CUEING MARKS

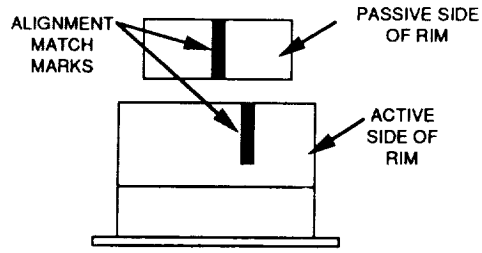

a: RIM FRONT CUEING MARKS

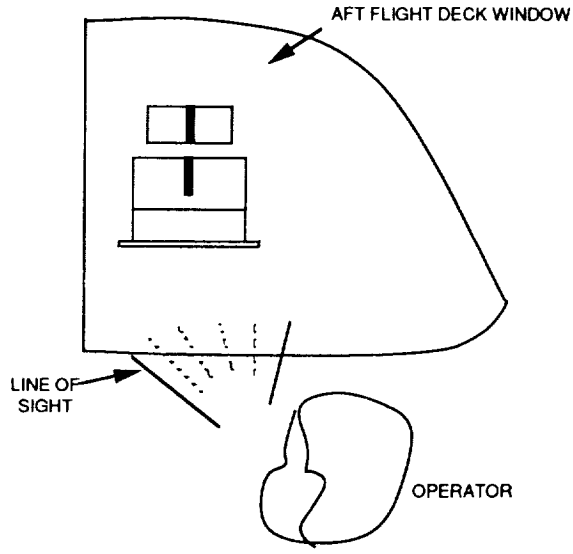

b: OPERATORS VIEW OF ALIGNMENT MARKS

FIGURE 5: RIM FRONT CUEING MARKS

TESTING PLAN

After completing the test setup procedures, the test plan required that the manipulator with the MEE attached grasp spacecraft mock-up. The spacecraft is then maneuvering to a position approximately five to six feet above the active RIM on the tanker. From this hovering position the spacecraft was skewed and placed out of the TRAC camera line of site. This procedure was performed at the beginning of each test run by a different manipulator operator than the one performing the test. The test operator had no prior knowledge of the spacecraft mock-up position at the berthing sequence initiation. Using the FTS, TRAC, and various visual aids, the operator aligned the RIMs and maneuvered them together. When the passive RIM engaged the active RIM, the capture/rigidization mechanism pulled the RIMs together and simultaneously mated all connectors and couplings. For the berthing schemes, we used five different test conditions:

1. Normal mode with FTS and TRAC
2. Normal mode with TRAC
3. Visual mode with cargo bay cameras
4. Visual mode and FTS
5. TRAC and FTS mode

The above test conditions were accomplished by reducing the number of berthing aids available to the operator for each mode. Varying the berthing modes created testing conditions that provided data on the RIM functional operation. The five test conditions are described below.

Normal mode with FTS and TRAC

For the normal mode, the operator had five berthing aids available to assist in the berthing process. These aids are:

1. Visual inspection out of the aft flight deck window.
2. Camera view of the cuing marks on the RIM from the four cargo bay cameras.
3. RMS control coordinate display. This is a digital display that describes the location of the active RIM center point by cartesian (X,Y,Z) and attitude control (P,Y,R) coordinates. This coordinate system is not orbit defined but it is spacecraft (shuttle) fixed, as illustrated in figure 6.
4. FTS
5. TRAC

These berthing aids were used at the operator's discretion.

Normal mode with TRAC

This mode is the same as the normal mode with FTS and TRAC,

except FTS is not used.

Visual mode with cargo bay cameras

In the visual mode with cargo bay cameras, the RIM cuing marks (black vertical hash marks) are permitted to be viewed only from the aft flight deck windows and/or cargo bay cameras.

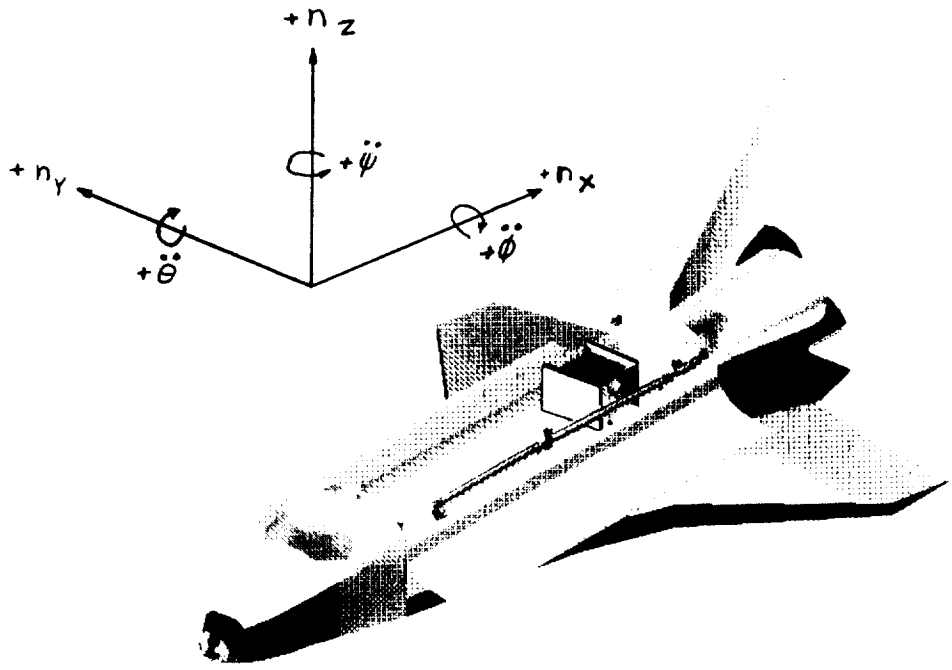

FIGURE 6: SHUTTLE COORDINATE SYSTEM

Visual mode with FTS

The RIM cuing marks are viewed only from the aft flight deck and the FTS can be used.

TRAC and FTS mode

For the TRAC and FTS mode, the aft flight deck window was blocked. This prevented the operator from observing the berthing process through the window and provided a more difficult berthing task. Only the TRAC and FTS could be used; no other cuing aid was permitted.

Optional runs

After the completion of the schedule test runs, each test operator was given the opportunity to perform an option run using the berthing aids of his/her choice. The option runs established if there are berthing aids more favorable than others. Six

option runs were conducted, these are:

1. Visual mode, FTS and TRAC
2. Normal mode with FTS and TRAC
3. Visual mode and cargo bay cameras
4. Visual mode and FTS
5. Visual mode
6. Normal mode with FTS

Test operators

Different RMS operators were used during this test. The MDF technicians were used for the initial setup and checkout runs. The preliminary manipulator arm checkout was performed by the chief MDF operator, Owen August. Then six crew members conducted the test sequence:

Franklin Chang
Greg Harbaugh
Jerry Ross
Carle Meade
Jan Davis
Lacy Veach

None of the crew members were introduced to the hardware prior to the test. At the time of the test, each crew member was individually briefed on the test plan and setup. Each crew member was allowed one to two system checkout runs before performing the test runs. The reason for limiting prior familiarization of the test was to increase the difficulty of accomplishing a successful berth.

TEST RESULTS

Normal mode with FTS and TRAC

The normal mode with FTS and TRAC produced no test difficulty for the operators. Each crew member had positive feelings about the effectiveness of this mode of operation. After the first run, some of the crew members developed a systematic approach to achieve berth. They used the following steps:

1. Fly the spacecraft over the tanker using visual sighting out the aft cockpit window.
2. Place the spacecraft approximately 6 to 12 inches over the passive RIM within the TRAC camera sights.
3. Adjust attitude using the TRAC camera.
4. Use TRAC to adjust translation during vertical fly-in.
5. Use FTS to accomplish smooth insertion of the passive RIM into the active RIM.

Normal mode with TRAC

Normal mode with TRAC did not create any additional challenges for the test operators. The fly-in portion of the berthing process does not require the FTS. In this case, the FTS is only used during the RIM insertion. However, the crew members had no adversities in successfully completing a smooth berth without the FTS. What was interesting was that all the crew members used sighting out of the aft flight deck window to adjust the flying spacecraft attitude and translation coordinate. Then approximately 6 inches above the tanker, they switched to the TRAC for the fly-in and mate.

Visual mode with cargo bay cameras

The visual mode with cargo bay cameras presented several challenges for the crew members. It was difficult to determine the spacecraft depth perception (x position along the shuttle velocity axis). Also, pitch adjustment within 1.5 degrees was hard to obtain. The pitch degree of 1.5 was required to ensure a smooth insertion of the passive RIM into the active RIM during the second alignment stage. Furthermore, the pitch adjustment reduces the probability of binding by preventing any sliding wall act. Some wall sliding is permissible during mating, but, if a perfect engagement is to be obtained, the walls of the RIMs should not touch. These difficulties were solved by first sighting the RIM's visual cuing marks from the aft flight deck window and aft cargo bay cameras, and then adjusting attitude and translational coordinates. Using the split screen mode of the monitor allowed viewing both images of the aft cameras on the same screen, which facilitated adjustments. Pitch was adjusted by using the manipulator digital coordinate display. The digital display was programed to give coordinate location of the passive RIM during fly-in. After making the adjustments, the operators had to only fly the spacecraft into the tanker RIM within the tolerance of the first alignment stage (+/- 2 inches and +/- 10 degrees). The flying RIM was permitted to slide down the RIM conical section and position itself to be grasped by the proprietary capture/rigidizing mechanism. Most of the berths achieved were jerky but doable.

Visual mode and FTS

Without the cargo bay cameras, the aft vertical cuing lines on the RIM could not be used. It became extremely difficult to determine depth perception. Several times the operators had to back the passive RIM out of the active RIM to avoid binding. All the crew members decided to use the digital display and follow similar steps as in the visual mode with cargo bay cameras. Berthing was achieved successfully.

TRAC and FTS mode

Although this mode is unrealistic for RMS berthing operation, it did give us an opportunity to study the RIM compliance to the TRAC and FTS. The TRAC and FTS case require that the aft flight deck window be blocked and the operator have no knowledge about the position of the spacecraft. The crew members' first step was to locate the spacecraft. This was accomplished by raising the spacecraft high enough for it to be observed through the TRAC camera. The spacecraft was then brought close enough (about 4 feet) to the tanker RIM to see the target mirror for attitude adjustment. Translational adjustments were performed continuously during the fly-in. All runs in this case were smoother than the previous mode.

Optional

The optional runs were similar to the test mode, except for one case. One crew member decided to use visual mode only. This involved berthing the spacecraft by viewing the RIM cuing marks from the aft flight deck window. Berthing was successful without using any other cuing aid.

TEST CONCLUSION

The test successfully validated the RIM design and demonstrated the compatibility of the hardware with the RMS. The RIM gross alignment tolerance worked well. The crew members were able to successfully berth the RIM during visual mode with cargo bay cameras scenario by sliding the passive RIM down the conical wall of the active RIM. This action proved that the RIM gross positioning alignment tolerance was adequate even though some jerky motion occurred. The jerky motions produced in some runs can be alleviated by increasing the active RIM inner diameter and rounding the edge where the conical ring meets the inner RIM wall. This would provide smooth transition along the surfaces. Furthermore, adding horizontal hash lines on the passive RIM can give the arm operator insertion depth information when the TRAC and FTS are not available. It was shown when using the TRAC that high mating tolerance accuracy can be accomplished, whereas the visual mode only permits low tolerance. Therefore, the test expressed the importance of determining the proper visual cues for the docking task. We found that the better the visual cues, the tighter the berthing tolerance could be. The type of visual cues to use is a function of the docking vehicle geometry, visibility, lighting, line of sight, viewing equipment, and operator's experience. This test was conducted with one vehicle in the cargo bay. If a second spacecraft was present, the cuing aid scheme would change. It is important to evaluate the condition in which the berthing is going to be performed. This scrutiny will lead to choosing the best cuing aid for the

berthing configuration.

ACKNOWLEDGEMENT

The authors wish to thank NASA Johnson Space Center for extending an invitation to Fairchild Space Company to participate in their satellite resupply demonstration. We would like to give special thanks to JSC Propulsion and Power Division, the New Initiatives Office, and the Manipulator Development Facility.

REFERENCES

1. Gallo, F. G; Jackson, S. W; Pullen, J. L.; and Gorin, B. F.; "Resupply Interface Mechanism," AIAA-89-2732, July 10-12, 1989.

RELATCHABLE LAUNCH RESTRAINT MECHANISM FOR DEPLOYABLE BOOMS

by Robert M. Warden*

ABSTRACT

A new Relatchable Launch Restraint Mechanism has been developed which enables a deployable system to be restrained and released repeatedly rather than the normal "one-shot" release systems of the past. The deployable systems are of the "self-extending" type which rely on a lanyard attached to a drive motor to control the deployment and retraction. The Relatch Mechanism uses the existing drive motor to also actuate the latch. The design and kinematics of the Relatch Mechanism as used on two flight programs are herein described.

BACKGROUND

Deployable systems are used for many aerospace applications in which a payload must be held close to the spacecraft for support during launch to prevent damage but must extend out away from the spacecraft to function properly in space. Antennas, magnetometers and solar arrays are examples of such payloads.

Most deployable booms which have been used in space have relied on two separate mechanisms for operation: one for securing the unit for launch and another for deploying and retracting the unit in space. In the past, this launch restraint has been released using one-time-only actuated devices such as explosive bolts or cable cutters.

With the advent of the space shuttle, new requirements are now generally imposed: those of retracting and resecuring the unit in preparation for re-entry and landing.

The mechanism described in this paper not only secures the unit for launch, releases the unit and controls the deployment, but also retracts and relatches the unit using only one motor or drive system. This unlatch-deploy-retract-relatch sequence can be repeated many times thus allowing reliability testing of the system by using the actual flight components.

LATCH DESIGN REQUIREMENTS

The purpose of the Relatch Mechanism is to avoid pyrotechnic release of launch restraint devises on aerospace systems. The Relatch Mechanism is a reliable alternative to cable cutters or explosive bolts especially in applications which must be operated repeatedly in order to show reliability or be relatchable in preparation for retrieval and re-entry. Also, the hazards associated with the use of pyrotechnics are completely avoided; and, since the unlatch process is nondestructive, there is no need to replace any components between cycles.

---

* AEC-Able Engineering Co., Goleta, California

Another disadvantage of pyrotechnic actuators is that to justify reliability, many samples must be tested and accurate batch control maintained. After each deployment cycle, the pyrotechnic device must be replaced. The Relatch Mechanism, however, has proved its reliability and repeatability by successful operation for many repetitions at high and low temperatures and at various motor voltages using the same components which will be used for flight.

The Relatch Mechanism was specifically designed to secure a self-deploying lattice structure of the type used to extend sensitive instruments away from the spacecraft. When the boom is fully retracted and latched, it is capable of withstanding the loads induced by the vibration of launch. Once the boom is in space, it is required to unlatch and deploy. The latch is designed so that the axial forces from the center post due to the preload in the boom do not act in a way to unlatch or release the system. The launch loads, therefore, are taken by the center post and latch assembly and not by the lanyard and motor which are, in fact, unloaded when the latch is engaged.

The motor-drive system is used here to restrain the mast from deploying too fast and also to facilitate retraction. The Relatch Mechanism uses this existing drive system to also actuate the latch so that there are fewer active components in the system. Although a specific drive was used in this system, a wide variety of motor-drive combinations would work equally well to actuate the mechanism.

SYSTEM DESCRIPTION

The complete system consists of the self-extending boom, motor-drive assembly, restraining lanyard, and the latch mechanism (Figure 1.). When fully deployed, the mast straightens out to form a very strong and stiff triangular lattice structure. When retracted, however, it is a loose coil which must be constrained somehow in order to survive the vibration of launch. The most effective way to do this is by confining the retracted mast in a thin cylindrical shell (or canister) with end plates. This constrains the mast in the radial and axial directions.

The bottom of the mast is attached to the base plate which is in turn attached to the spacecraft. In this way, the mast has a fairly direct load path to the spacecraft which gives good root support.

The top of the mast is attached to the top plate onto which the payload is mounted. When the mast deploys, the top plate, along with the payload, moves away from the canister/bottom-plate assembly.

The cylinder and base plate, therefore, form a cup or "canister" and the top plate is the lid. To secure this enclosure for vibration, the lid must be fastened down and then released when the mast is ready to be deployed. This can be done either "externally" in the way of clamps or bands or "internally" by means of a central rod or post down the middle of the canister through the retracted mast. There is, in fact, adequate clearance down the middle of a retracted mast which is usually reserved for the lanyard that restrains the mast during deployment. This second method of internally securing the top plate was chosen for the Relatch Mechanism because it uses a single, centrally located probe on to which a latching device could be engaged.

Figure 1. The Relatch Mechanism was designed to work with a self-deploying triangular lattice column that is capable of retracting to a small fraction of its deployed length. The mast must be restrained during deployment to prevent damage to the boom or payload. The lanyard is a metal ribbon, used as a tether, which runs down the middle of the mast.

The top end of the lanyard is attached to a bridle system which controls the last bit of deployment and makes it possible to retract the mast by simply pulling on the lanyard. When the mast is fully deployed, the lanyard is slack so as not to affect the mast properties. The other end of the lanyard is attached to the motor drive system. When the motor is driven one way, the mast deploys. When polarity to the motor is reversed, the mast retracts.

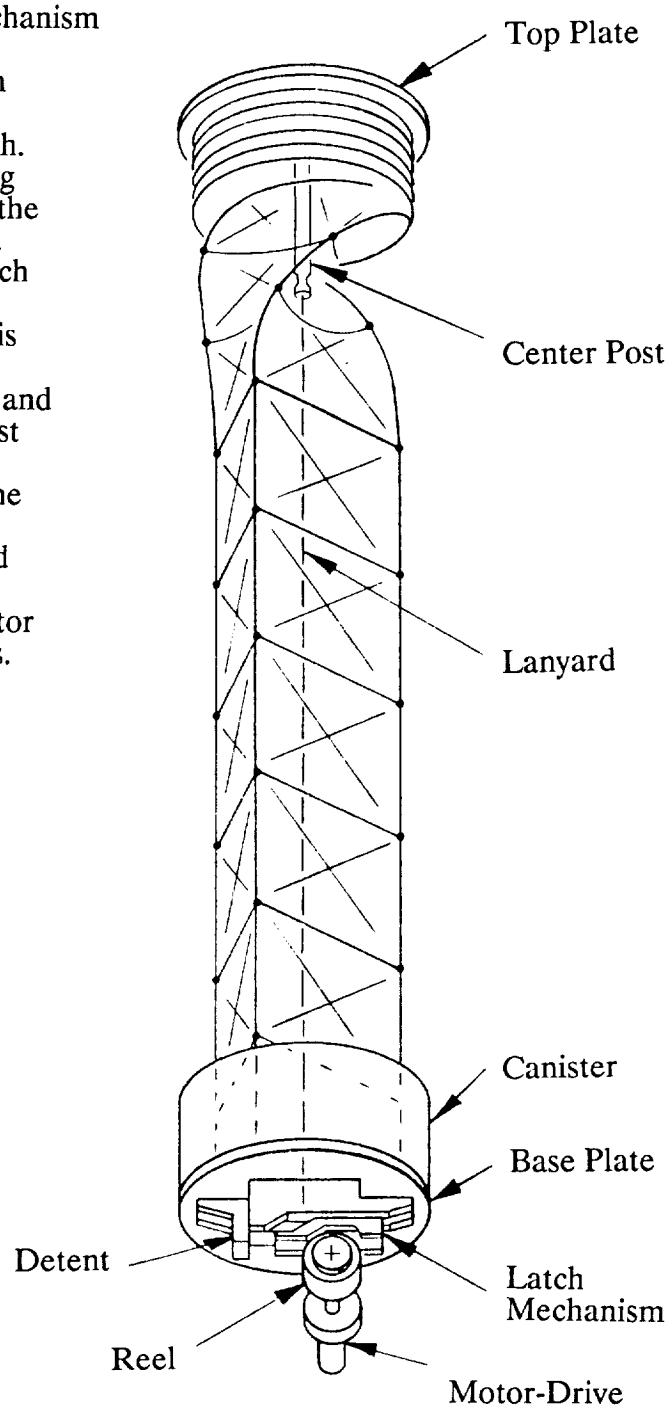

Figure 1. SYSTEM COMPONENTS

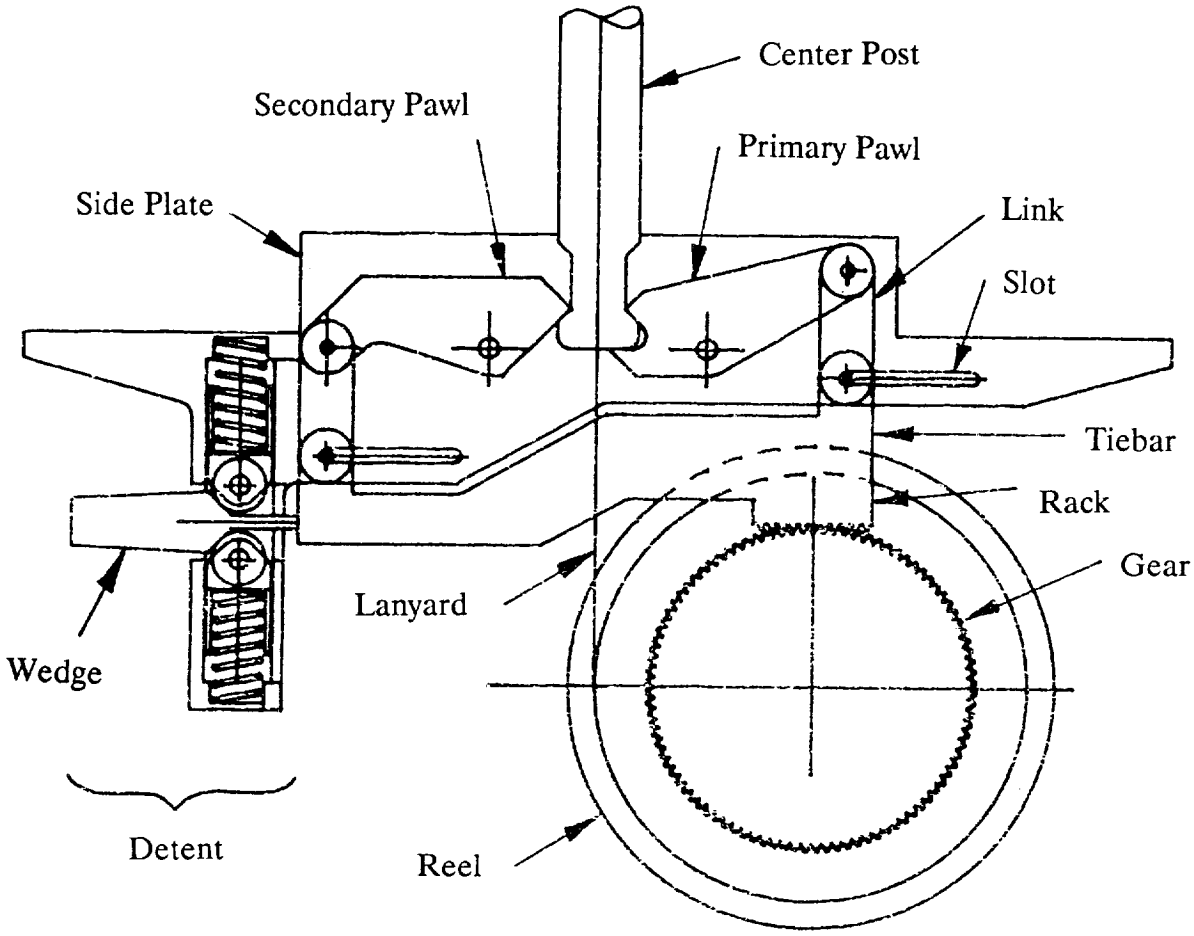

Figure 2. LATCH COMPONENTS

Figure 2. The Relatch Mechanism, together with the center post, holds the deployable boom together during vibration. The center post is attached to the top plate, the latch is mounted to the bottom plate, and the mast is captured in between. The Relatch Mechanism is designed so that the axial forces from the center post as a result of the preload on the boom do not act in a way to unlatch or release the system. The center post is captured by two pawls which are supported in turn by twin links to the tiebar. Since the links are parallel to the main direction of force and are in compression, the mechanism is able to restrain large forces as long as the tiebar constrains the ends of the links. The axial forces in the links are transferred to the side plate or chassis through dowel pins which are able to slide in the slots in the side plate. The slots also limit the travel of the tiebar.

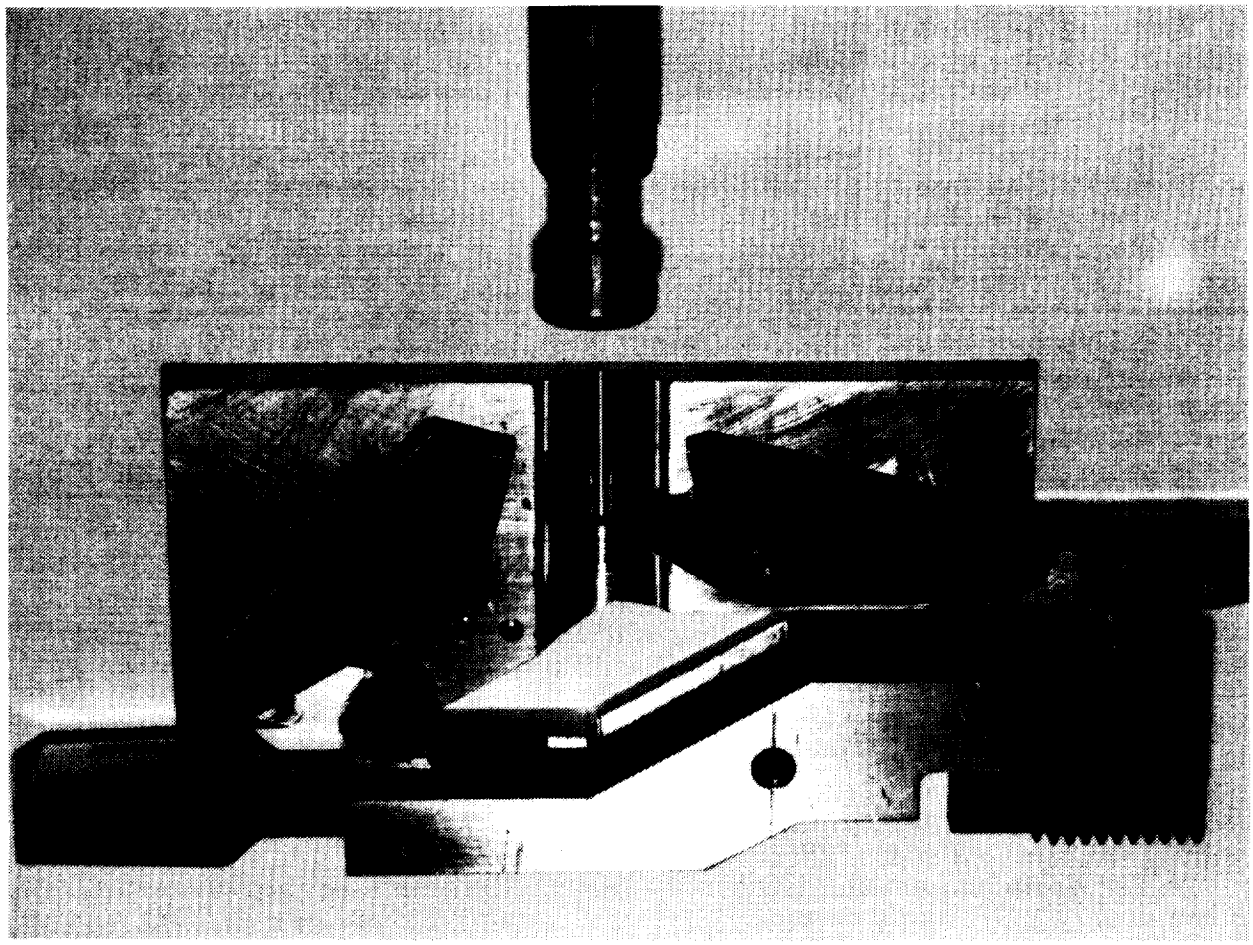

Figure 3. UNLATCHED POSITION

Figure 3. This photograph of the development unit shows the Relatch Mechanism in the unlatched position. This unit has been cycled over 300 times in the engineering mast.

LATCH FUNCTION

Power applied to the motor-drive system rotates the reel assembly, thus moving the tiebar. This pulls the wedge through the detent and at the same time positions the latch pawls to release the center post. If the center post is restrained for some reason, the tongue on the primary latch pawl pushes on the center post to initiate deployment. After the rack clears the gear, the slight taper on the wedge causes the tiebar to travel to the end of the slot (called the unlatched position). Limit switches indicate the latched or unlatched position.

The motor-drive system continues to rotate the reel assembly which pays out the lanyard thus controlling the deployment of the mast. This continues until the mast is fully deployed and the limit switches cut off power to the motor.

Retraction of the unit is the most important action performed by this mechanism and best illustrates the function of the system. The drive motor pulls on the lanyard which initiates retraction. Continued operation of the motor retracts the mast until it is fully stowed. The objective of the design is to allow the motor to decouple from the retract process in order to actuate the latch. This is achieved by using a spring loaded reel (Figure 4.) which allows the drive to continue to rotate and thus actuate the latch while continuing to hold the lanyard and therefore the mast. At the same time, the center post contacts and pushes the tongue on the primary latch pawl, which causes the tiebar to move and the rack to engage into the gear. To prevent any possibility of jamming, the first tooth on the rack is spring-loaded to synchronize the rack and gear.

Once the rack is engaged in the gear, the lanyard and center post can no longer retract. The cam, therefore, stops rotating and the hub (which is attached to the drive gear) continues to rotate. The gear drives the rack to move the tiebar which causes the latch pawls to grab the center post and pull on it to preload the system. At the same time, the wedge is driven through the detent which now holds the latch in place. In this way, the launch loads are taken by the center post and latch assembly and not by the lanyard and motor. In the latched position, the connecting links are parallel to the center post so that launch loads do not unlatch the system. The motor can actually be removed when the unit is fully retracted and latched.

The Relatch Mechanism requires a drive unit which could be any combination of a.c. or d.c. electric motor or motors coupled to a gear box to reduce speed and increase torque. The motor-drive system used on both flight booms is called a "Dual-Drive" which is a reliable, redundant drive mechanism developed for space applications. In this mechanism, two independent motors are used to drive opposite sides of a harmonic gear set, which converge at the output shaft to provide low speed and high torque. In this way, either of two separate drive trains may be used to power the unit.

This mechanism is referred to here as a follow-up on previous design work. The Dual Drive was presented in a paper at the 16th AMS in 1982.

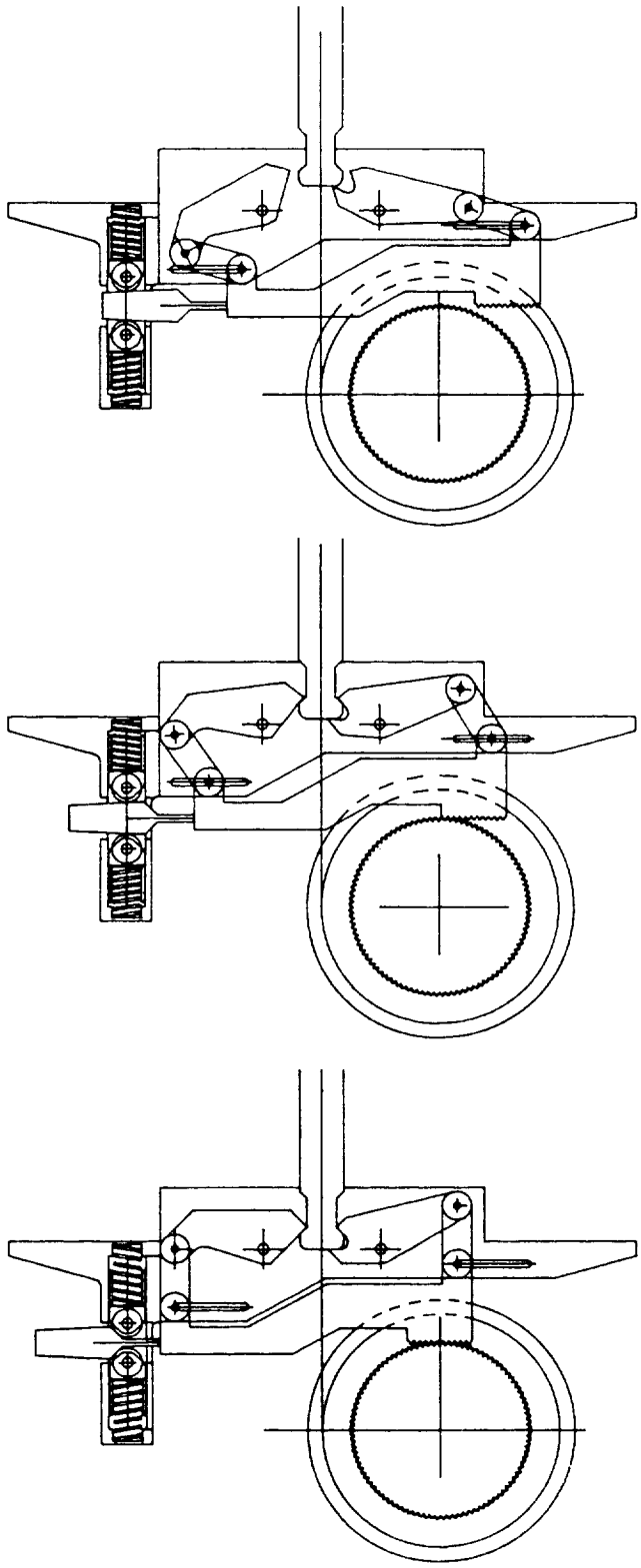

Figure 3a. LATCH SEQUENCE

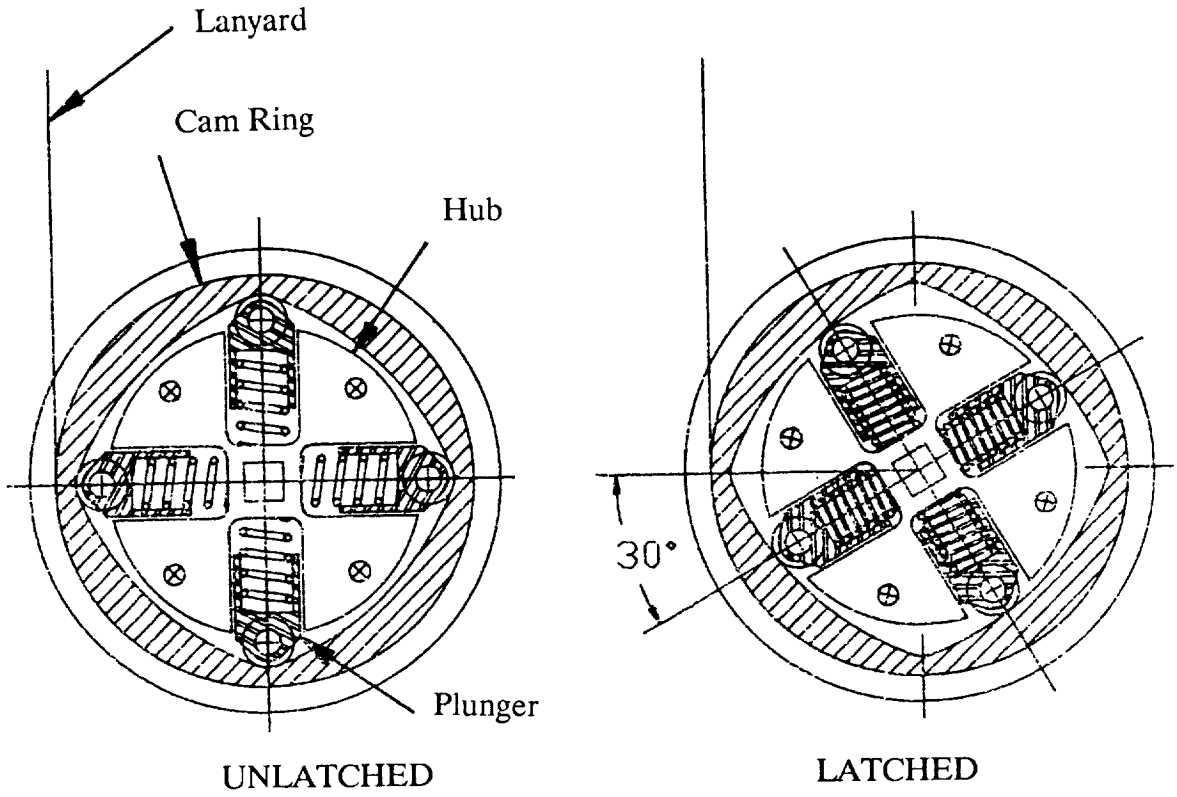

Figure 4. REEL ASSEMBLY

Figure 4. The reel is attached to the motor and to the lanyard. When the motor is driven one way, the mast deploys; when polarity to the motor is reversed, the mast retracts. The reel assembly allows the required differential travel between the lanyard, which stops at full retract, and the gear, which must continue to rotate in order to actuate the latch. When the center post contacts the primary latch pawl, the cam ring is prevented from rotating but the hub is able to continue to rotate.

The reel assembly contains four spring-loaded plungers which roll on a specially shaped cam ring. The cam is shaped to reduce tension on the lanyard as the latch is actuated. The hub of the reel is directly attached to the motor-drive and also to the drive gear. The cam is rotationally positioned by the spring plungers which compress when torque is applied to the cam thus allowing the hub to continue to rotate for another 30 degrees.

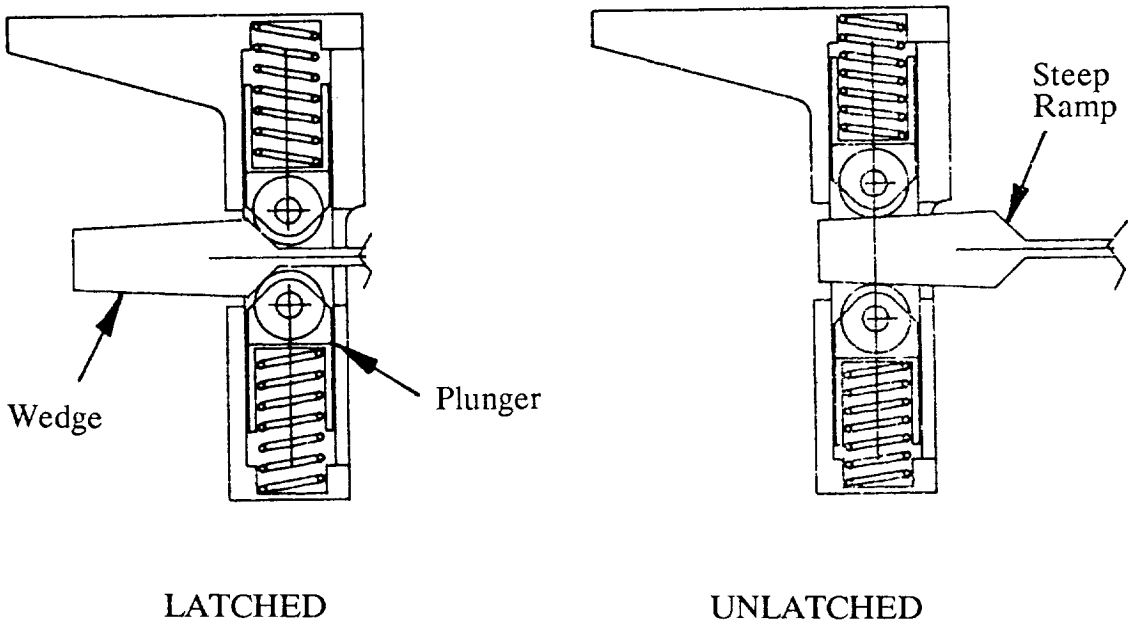

Figure 5. DETENT

Figure 5. The detent holds the tiebar in the fully latched position during vibration. By incorporating a detent mechanism into the latch, the drive motor is not subject to the vibration loads of launch. When the Relatch Mechanism is actuated, the wedge is pulled through the plungers and is then pushed out of the way. The steep ramp on the wedge was designed to assist the motor to preload the boom.

Figure 6. The self-deployable booms thus far used have been of the triangular lattice type which are made up of unidirectional fiberglass rods, bonded aluminum fittings and various fasteners. This type of mast has been used for the past 25 years because it is lightweight, strong and stiff, and retracts to a fraction of its length. Two flight units have used the relatch mechanism to reduce overall system complexity and weight.

The first program was the ZEPS (Zenith Energetic Particle Spectrometer) boom for the UARS (Upper Atmosphere Research Satellite) which was built for General Electric. The ZEPS boom uses a 12.5 inch diameter mast which extends to 15 feet. The second program was the MDRA (Mast Deployment Retraction Assembly) for the Explorer Platform which was built for Honeywell. The MDRA boom uses a 17.5 inch diameter mast which extends to 5 feet. The two programs are similar in that both are based on lanyard-restrained, coilable retractable lattice columns.

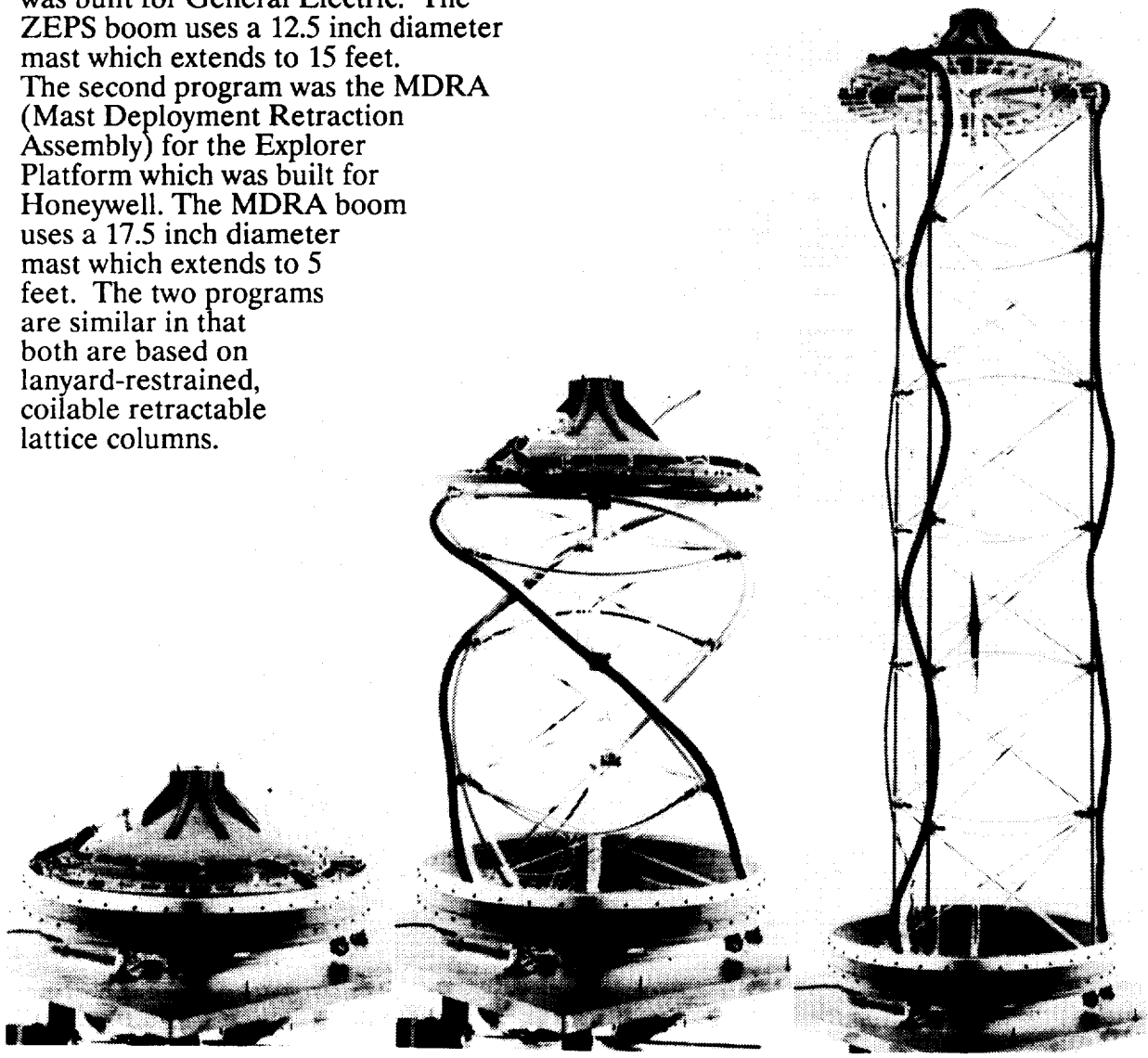

Figure 6. DEPLOYABLE MAST

TEST DATA

Two years of development and testing have gone into the design and manufacture of the Relatch Mechanism. The first part of the development involved designing and redesigning the mechanism to satisfy the requirements of the functional kinematics. In other words, making it work. After the basic configuration was defined, an engineering development unit was manufactured and tested. This unit functioned without problems, successfully latching and unlatching under various conditions.

The flight units were designed and manufactured based on the configuration of the development unit. These units also performed well except that the initial chart-recorder traces from the first flight unit showed higher than expected latching torque values. The Relatch Mechanism was analyzed to determine the source and components of the forces with the hope that one component could be easily modified to bring down the peak force. The actual relatch/unlatch profile was determined to be the sum of the force curves from four main components:

A. REEL ASSEMBLY spring force and friction
B. DETENT - spring force and friction
C. PRELOAD - linkage force, neglecting friction
D. TIEBAR - sliding and rolling force of latch

Latching occurs when the mast is retracted; unlatching occurs when the mast is deployed. As shown in the graphs on the following pages, some forces add to the total and some subtract. The latching and unlatching functions were both analyzed because by modifying one component to improve the latch function, the unlatch function could be made worse. The detent was the most obvious choice to be modified, and the force traces show the final results

The test data is presented as Torque versus Angle at the gearbox output shaft. The theoretical total is the sum of the above force components which operate in different directions: the preload force acts in the Z axis, the latch friction and detent act in the X axis, and the reel and drive system act in an angular axis. To more easily understand and analyze the various force components of the system, the force diagrams were converted into units of 0 to 30 degrees motion at the reel which corresponds to the fully unlatched to fully latched position. Although the reel is capable of 30 degrees of travel, the Latch Mechanism only requires 28 degrees.

The actual force trace was taken from the motor leads at 28 volts d.c. and is presented as Current versus Time.

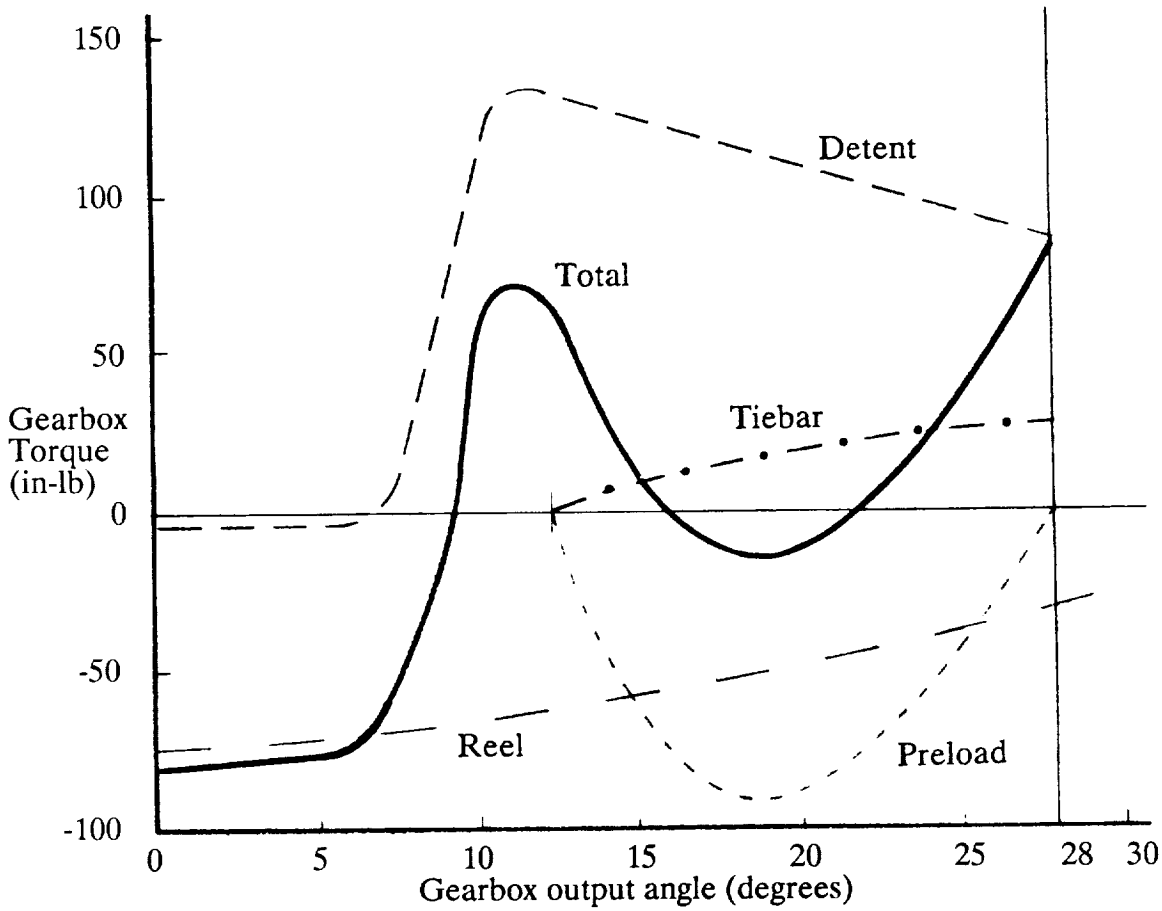

TOTAL FORCE, Deploy (Unlatching)

ACTUAL FORCE TRACE, Deploy

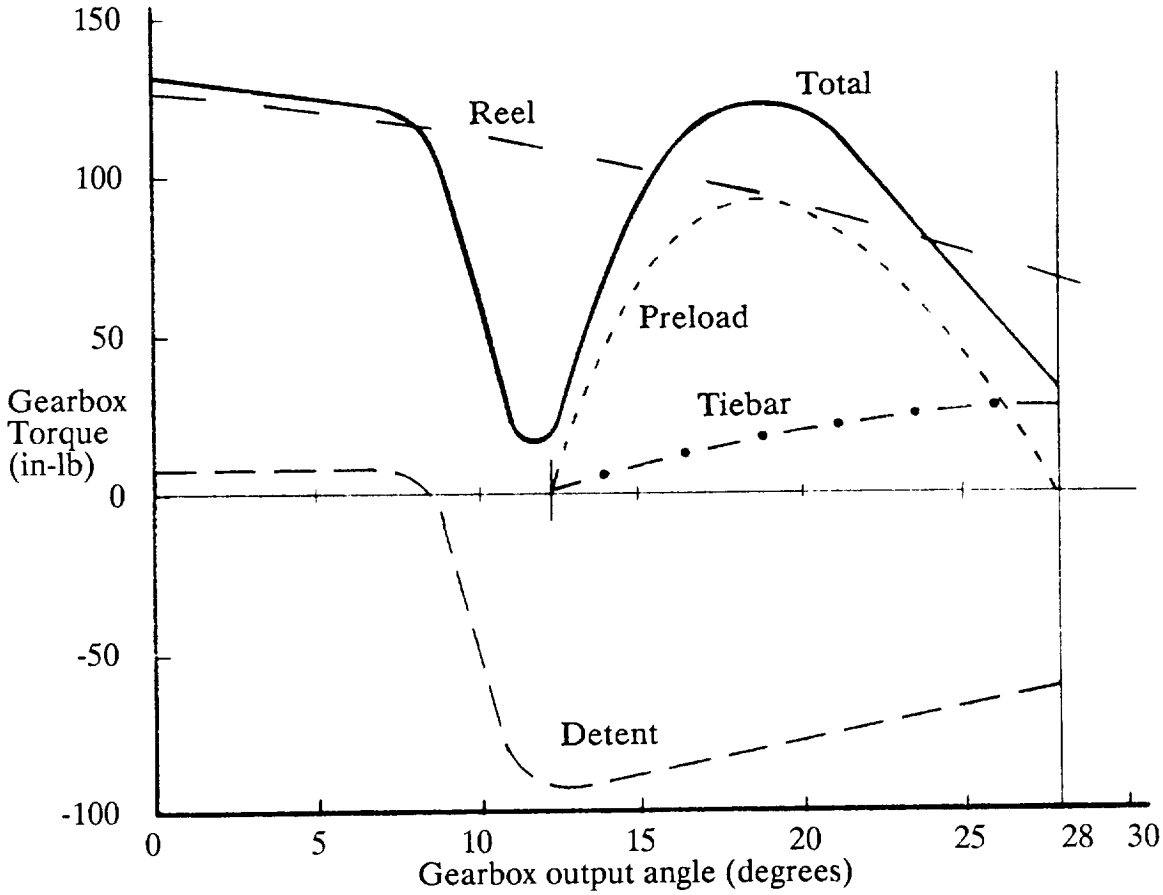

TOTAL FORCE, Retract (Latching)

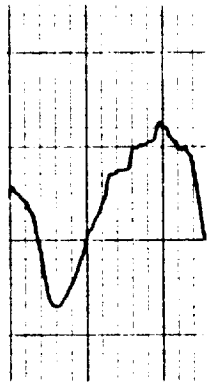

ACTUAL FORCE TRACE, Retract

TEST RESULTS

Three latch mechanisms have been integrated and tested in deployable booms. The first was the engineering development unit which was built essentially as conceived and went through extensive testing.

Two problems, however, occurred in the flight versions which were not experienced in the engineering development unit. The preload for the flight units was much higher than the development unit and the flight motor was not as powerful as the development motor. To get more work out of a smaller power source, some creative engineering was needed to solve the problems which were generated by these changes.

The first problem was an increased latching force as indicated on the chart recording of the motor current. The first few cycles were within specification but, on subsequent cycles, the motor current was much higher. The cause of the increased motor torque was difficult to isolate because when the system is assembled, it operates as a unit with many forces acting at once. A decision was made to disassemble the system and examine the components for abnormalities. After careful examination, the slot in the side plate of the latch mechanism was found to have some galling on the loaded surface caused by the dowel pin sliding under the increased preload. To handle the increased sliding force, the slot was enlarged and a small roller was added which could handle the load while reducing the sliding force. This change was tested and proven on a modified development unit and incorporated into the flight units.

The second problem was that the motor did not have a large enough margin of safety. To assist the motor, the wedge in the detent was re-shaped to help the motor in the final part of latching where the preload is achieved. Although this change sounds simple, detailed analysis was required to properly shape the wedge and size the detent springs.

CONCLUSION

The Relatch Mechanism has been demonstrated to be a reliable alternative to releasing devices such as cable cutters or explosive bolts, especially in applications which must be operated repeatedly to show reliability or be relatchable in preparation for retrieval and re-entry.

In addition to the vibration requirements, the Relatch Mechanism also functioned repeatably and reliably at high and low temperatures and various motor voltages.

ACKNOWLEDGEMENT

The author wishes to thank all the engineers, designers and technicians who helped in the evolution and refinement of the Relatch Mechanism, specifically Jim Axtell and Mike Cathcart who had the patience, intelligence and persistence to make the system work right.

The Connector Space Reduction Mechanism

by M. Bruce Milam
NASA/GSFC
Code 716

INTRODUCTION:

In the summer of 1987 the Telerobotic Engineering Office initiated an effort to review the current Space Station Work Package 3 hardware concepts and fabricate mockups for the Robotics laboratory (NASA/GSFC Building 11). The particular hardware selected for the mockup effort was the Station Interface Adapter (SIA), Payload Interface Adapter (PIA), Deck Carrier (DC) and the box-type Orbital Replacement Unit (ORU) (see figure 1). At that time only a rough design concept existed for the hardware, allowing the opportunity to fill in vague areas in the design as necessary to allow the mockups to function. A decision was made to generate and select concepts that were reasonable for upgrade to space flight.

One vague area was the utility connection at the PIA/SIA interface. The PIA/SIA interface consists of two devices with three legs. Each leg includes provision for coarse alignment, fine alignment and a utility connection (see figure 2). The utility connection consists of electrical data, electrical power, fibre optics and fluid couplings. The interface is held together with a single mechanism. The mechanism has the capability to pull the interface together, preload the interface and eject the interface halves. Only one electromechanical device is required to mate the system.

BACKGROUND:

A review of current NASA and industry concepts was initiated. The concepts fell into two general categories, connector mating orthogonal to the PIA/SIA interface and connector mating parallel to the PIA/SIA interface (see figure 3). In each category some concepts use the mechanical power of the single structural attachment mechanism while others have independent motors. A decision was made to use a concept that did not require a dedicated electrical motor. This would reduce the interface total number of electromechanical devices from four to one. This is a tremendous reduction in system complexity, providing schedule and cost savings with no affect on the function of the utility connections.

The next choice was the direction of connector motion with respect to the PIA/SIA interface desired to mate connectors. The connectors can be mated parallel or orthogonal to the PIA/SIA interface (see figure 3). The motorless parallel concepts require provisions to ensure that the interface is structurally together prior to connector mating. This adds complexity to the system levers, pivots, etc. This also introduces the possibility of the utility connection mechanism preventing structural attachment of the payload. The motorless orthogonal concepts are the simplest. A decision was made to pursue the motorless orthogonal concept where the connectors are mated as the structural mating of the PIA/SIA occurs. This is the simplest possible approach using only the mechanical power of the structural mating mechanism for the utility connection.

The next step was to plot the mating trajectory of the PIA/SIA alignment system and select suitable connectors. The mating trajectory is determined by the fine and coarse alignment provisions in the system. The system has trajectory plots for each degree of freedom but only the most critical translation plots are shown. To make a trajectory plot of the PIA/SIA system, one must plot the worst-case misalignment vs. the interface height. Misalignment is the linear or angular measure from perfect alignment at the location in the system where the connectors are located (see figure 4). Then one simply compares these plots with connector-required trajectory plots from the manufacturer's drawings and specifications.

THE PROBLEM:

The connector evaluated for our application was the G & H Technologies shell #1 type connector. These have many desirable features and have flight history on the Modular Multimission Spacecraft ORUs. The housings are tough and have forgiving geometry; it is unlikely pins will be bent during operation. The connector-required trajectory plot was compared with the system plot and it was found that in the worst case connectors could not be mated (see figure 5).

THE SOLUTION:

To resolve this problem two avenues exist. The interface alignment system can be changed or the connectors can be modified. Improving the alignment system must be done with care since fine alignment over long interface heights will cause system binding (see figure 6). This is a problem on the PIA/SIA interface with its central attachment mechanism. When mating or demating the interface, the alignment pins and cones will not separate or mate in unison. This problem forced modifications to the mockup hardware to eliminate

binding. With this in mind a decision was made to leave the mating system as it is and modify the connector trajectories instead.

The connector translational and rotational requirements can be relieved with the addition of guides and gimbals, but these do not change the travel required. The guides must be long and protrude above the interface. This could be a safety hazard. The problem could be eliminated with the addition of an alignment cusp with a feature that when depressed an amount the connector halves move together twice that amount. This device eliminates the requirement for tight tolerances over large distances for the connectors. If the device is designed carefully, blind mate connectors of all types could be used. The only problem with the system is with the 1-to-2 motion ratio, the force to mate connectors doubles. The structural mating mechanism has ample force margins to overcome this problem. G & H Technologies has been working on connectors that require significantly lower mating force. Other companies have successfully accomplished this with different styles of connectors. This imminent marriage of connector technology will eliminate the mating force problem. Several design concepts were generated, ranging from a mechanism using levers and cams to one with racks and gears. The latter was chosen for the first cut since it appeared more robust.

The device has some design features that are essential and others that are arbitrary. The device has two halves an active half and a passive half (see figure 7). The active half contains the mechanism that provides the mating motion. Both halves can rotate about an axis and translate along that axis. When mounted into position, these axis are orthogonal to one another. This allows for misalignment of mating interfaces in rotation and translation about two axis. The halves can gimbal about only one axis each or binding and pin bending will occur upon demating of connectors.

The sequence of operation is as follows(see figure 8):

1. and 2. The PIA and SIA are brought into close proximity in the worst-case alignment situation.

3. The interface height is reduced until the cusp makes contact. Each half of the mechanism is gimbaled until each half is parallel.

4. and 5. As the interface height is reduced, the connector moves twice as fast, cutting the distance or space with the fine alignment requirement by 50%. For this reason the device is called the Connector Space Reduction Mechanism (CSRM).

The amounts of translation and rotation can be chosen to match the application. For our application and geometry, +/- 0.635 cm (0.25") translation and +/- 6 degrees rotation were allowed on the passive half and +/- 0.635 cm (0.25") translation and +/- 1.5 degrees rotation for the active half. These values allow ample margins for our specific application. Translational and rotational misalignments about the axis orthogonal to the PIA/SIA interface are handled by the proven means of giving one connector half a compliant mounting.

A requirement is that malfunctioning or damaged connectors must not interfere with structural attachment. This is simply achieved by mounting one connector half on springs with a preload exceeding the normal connector force by 50%. If the connector is damaged, the connectors will simply push out of the way, allowing structural mating (see figure 9).

THE HARDWARE:

The prototype CSRM was designed for G & H Technologies shell #1 blind-mate connector. An adapter plate was fabricated for operation with 3 AMP, blind-mate connectors. The CSRM was designed for a 3109-N (700-pound) worst-case mating force. The mounting includes material that encloses the PIA and SIA 5.08-cm (4") square tube with through bolts. The motion of the device is provided by dual racks and pinion. These require good alignment and this is provided with four IKO linear roller bearings. The bearings provide smooth, precise motion between the cusp and the connector mounting plate. The device is made predominantly of aluminum with an anodized coating. The device has brass gimbal bushings that provide translation as well as rotation. The CSRM halves are held in neutral position in translation and rotation by compression and tension springs. The device consists primarily of milled-out pieces. This provided the strongest final product (see figure 10).

ASSEMBLY AND TEST:

The device was assembled and installed on the PIA/SIA mockup in the GSFC Telerobotics laboratory. The device halves were placed loosely on the PIA/SIA structure. Both halves were adjusted until, when perfectly aligned, both halves were in the neutral position with respect to translation and rotation. Then matching holes were drilled through the SIA and PIA square tube for permanent mounting.

The device was tested several cycles with the PIA/SIA mating normally. No problems were encountered. Then several mating cycles were accomplished with the PIA imbalanced to

force the worst-case misalignments to the system. The CSRM performed flawlessly. The CSRM has operated several cycles weekly since 3-24-89 without a single malfunction. The prototype CSRM has exceeded the number of life cycles for a flight unit by a factor of ten. The testing was accomplished with G & H connector shells and repeated with AMP blind-mate connectors on an adapter plate. The AMP connectors are excellent for the laboratory since they are low cost and readily available. AMP connectors are much more fragile than G & H connectors, and the CSRM has yet to damage a shell or bend a pin.

IMPROVEMENTS AND FUTURE WORK:

Since this was a prototype device, two areas for potential improvement came up. The first area is that one of the telescoping shells on the active half of the device can be eliminated (see figure 11). This would offer decreased weight and complexity. The second improvement would be to reduce the weight of the device. The prototype passive half weighs 14.5 kg (32 pound) and the active half weighs 25.8 kg (57 pounds). The weights are to high due to limited stress analysis and compound factors of safety. The device could be reduced in weight by 30% and possibly 50%.

CONCLUSION:

The CSRM is a simple device that can reduce the number of electromechanical devices on the PIA/SIA from 4 to 1. The device uses simplicity to attack the heart of the connector mating problem for large interfaces. The CSRM allows blind-mate connector mating with minimal alignment required over short distances. This eliminates potential interface binding problems and connector damage. The CSRM is compatible with G & H connectors and Moog Rotary Shutoff fluid couplings. The CSRM can be used also with less forgiving connectors, and this has been demonstrated in the laboratory. The CSRM is a NASA/GSFC exclusive design with patent applied for. The CSRM is the correct mechanism for the PIA/SIA interface as well as other similar berthing interfaces.

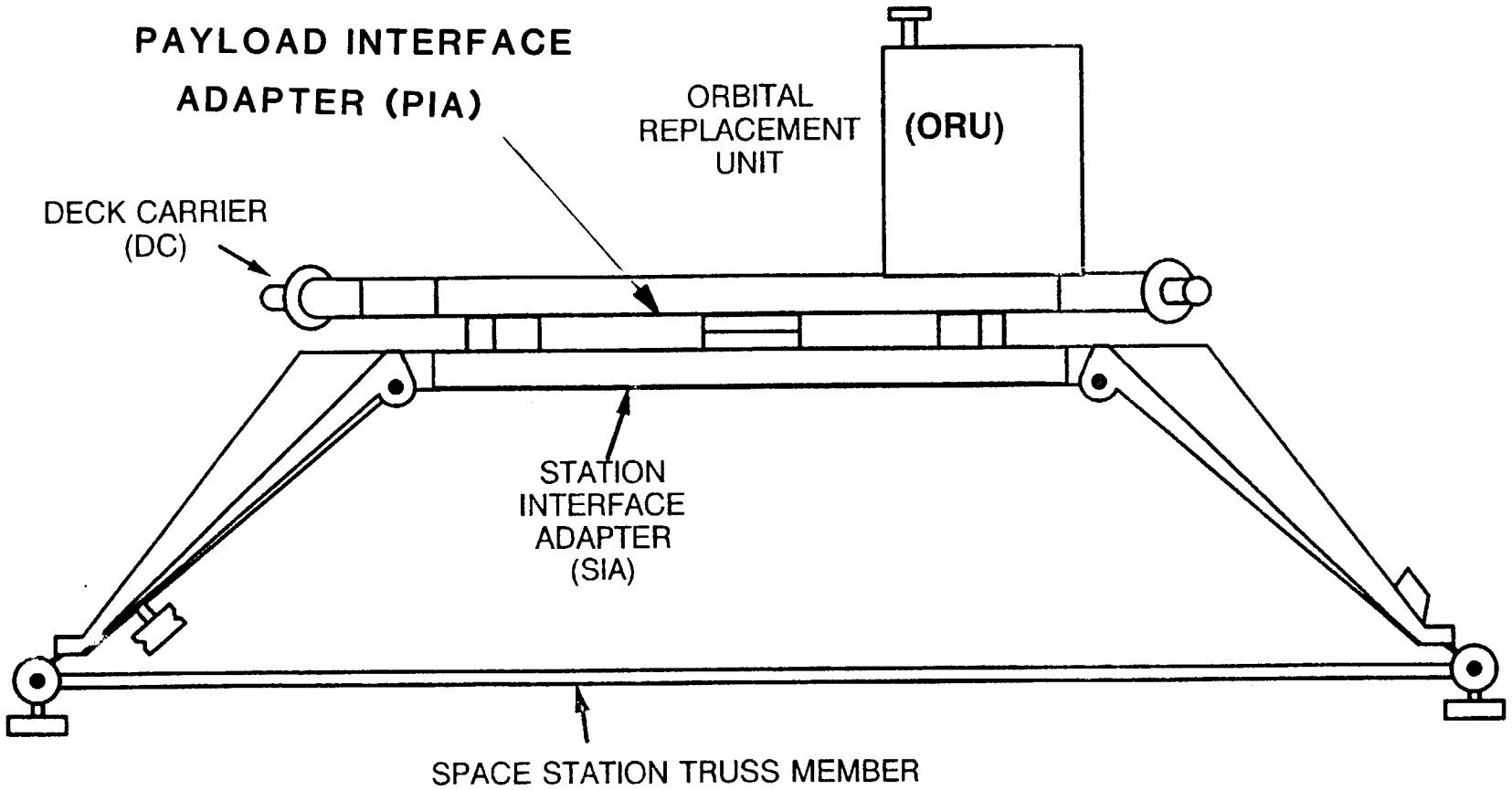

FIGURE 1

A365.005

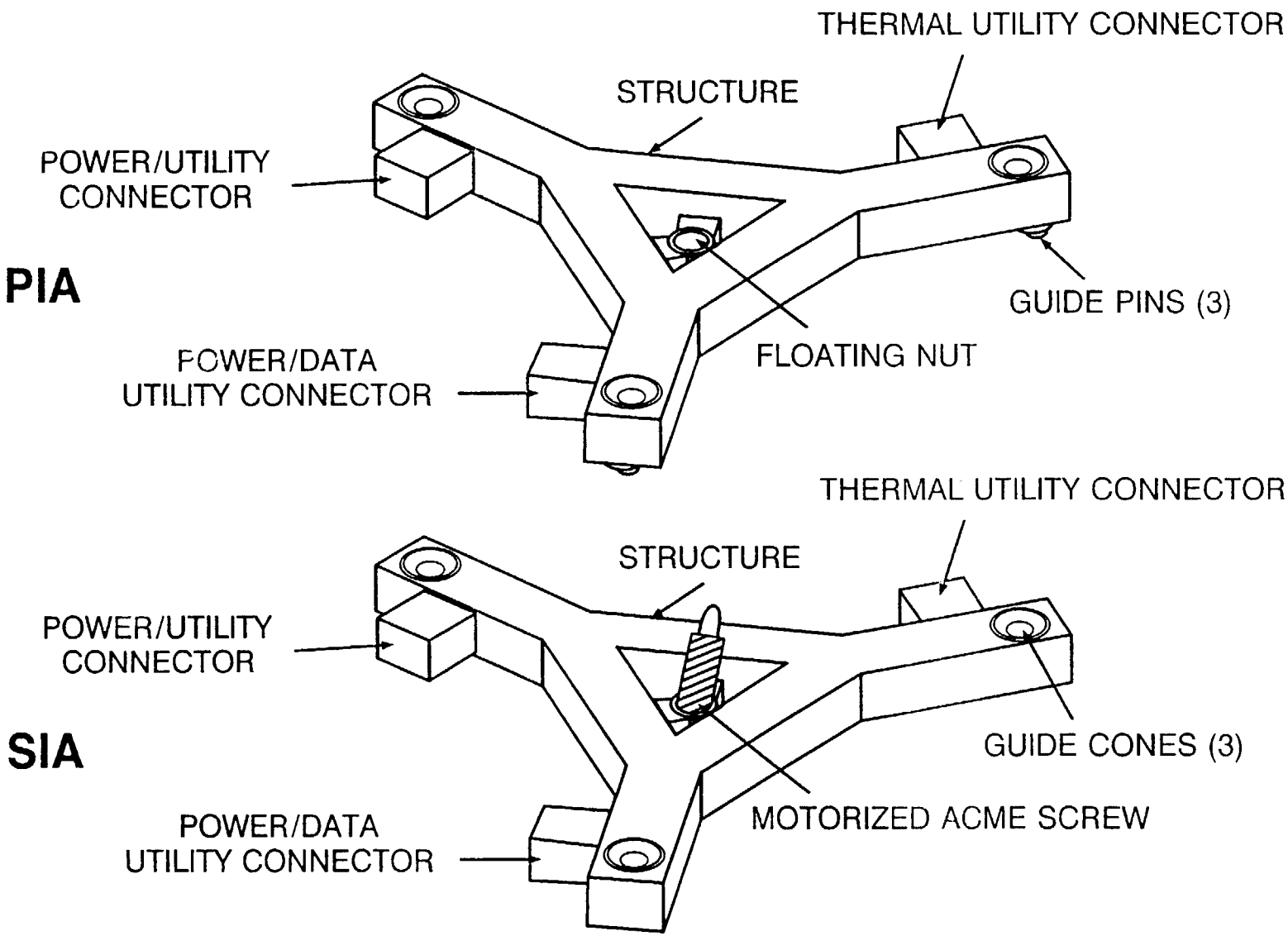

PIA/SIA INTERFACE

A365.010

FIGURE 2

PIA

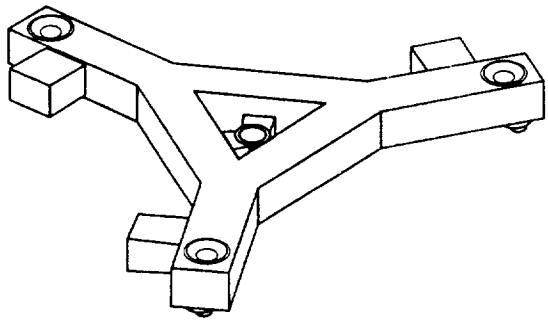

SIA

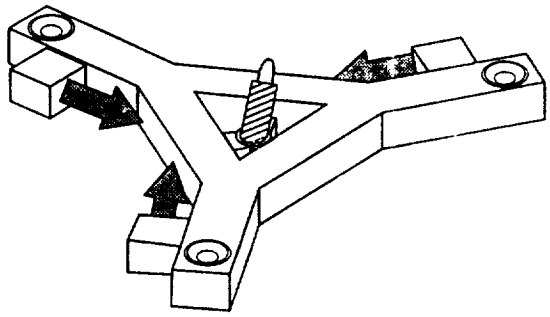

A365.008 CONNECTOR MATING PARALLEL TO PIA/SIA INTERFACE

PIA

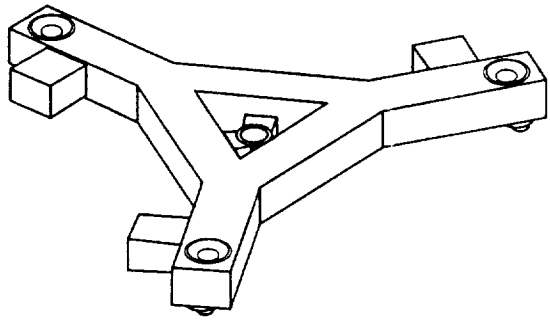

SIA

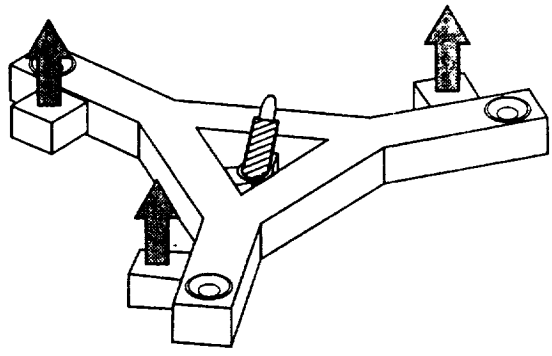

A365.009 CONNECTOR MATING ORTHOGONAL TO PIA/SIA INTERFACE

FIGURE 3

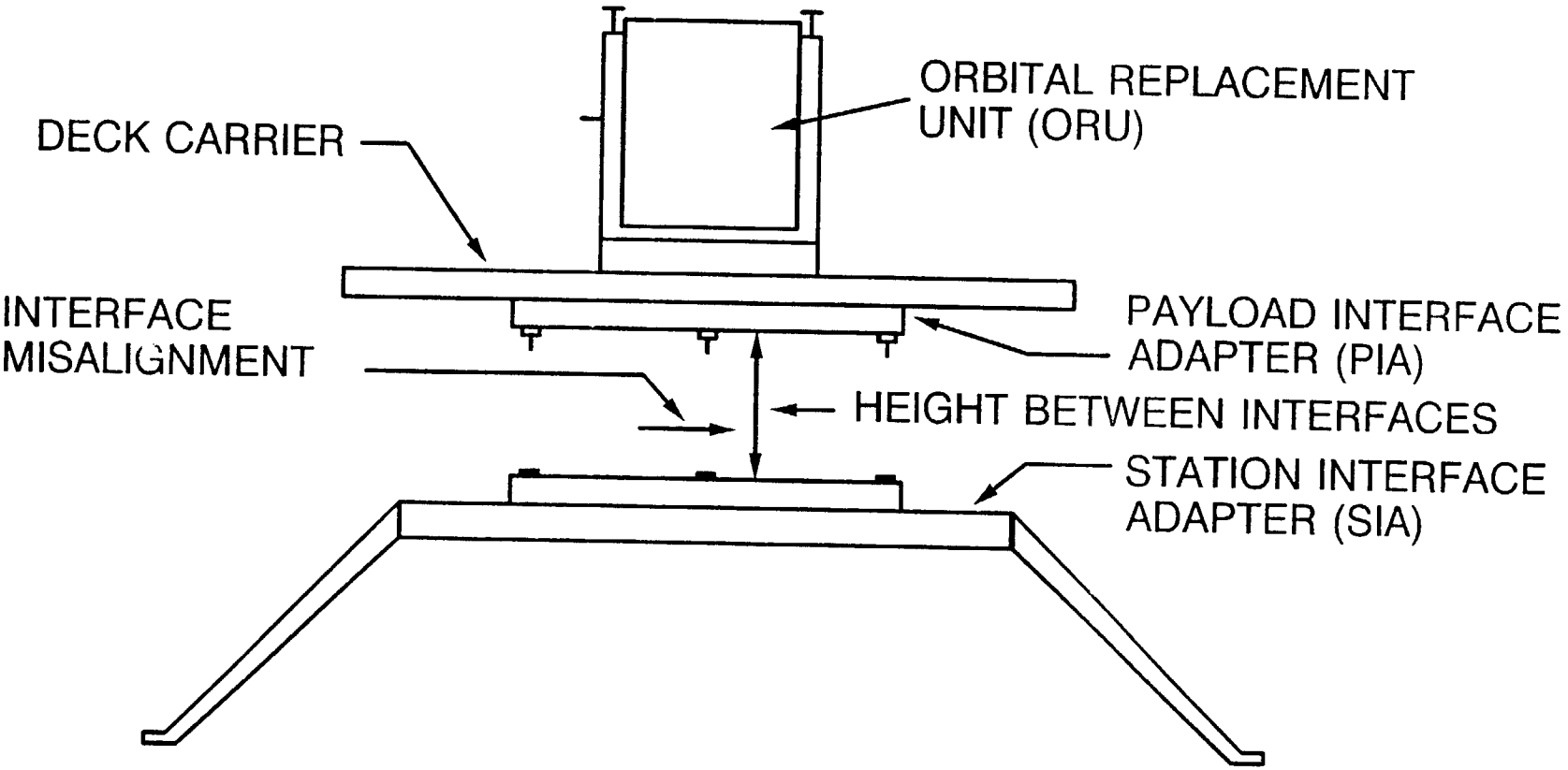

MATING TRAJECTORY PLOT

A365.006

FIGURE 4

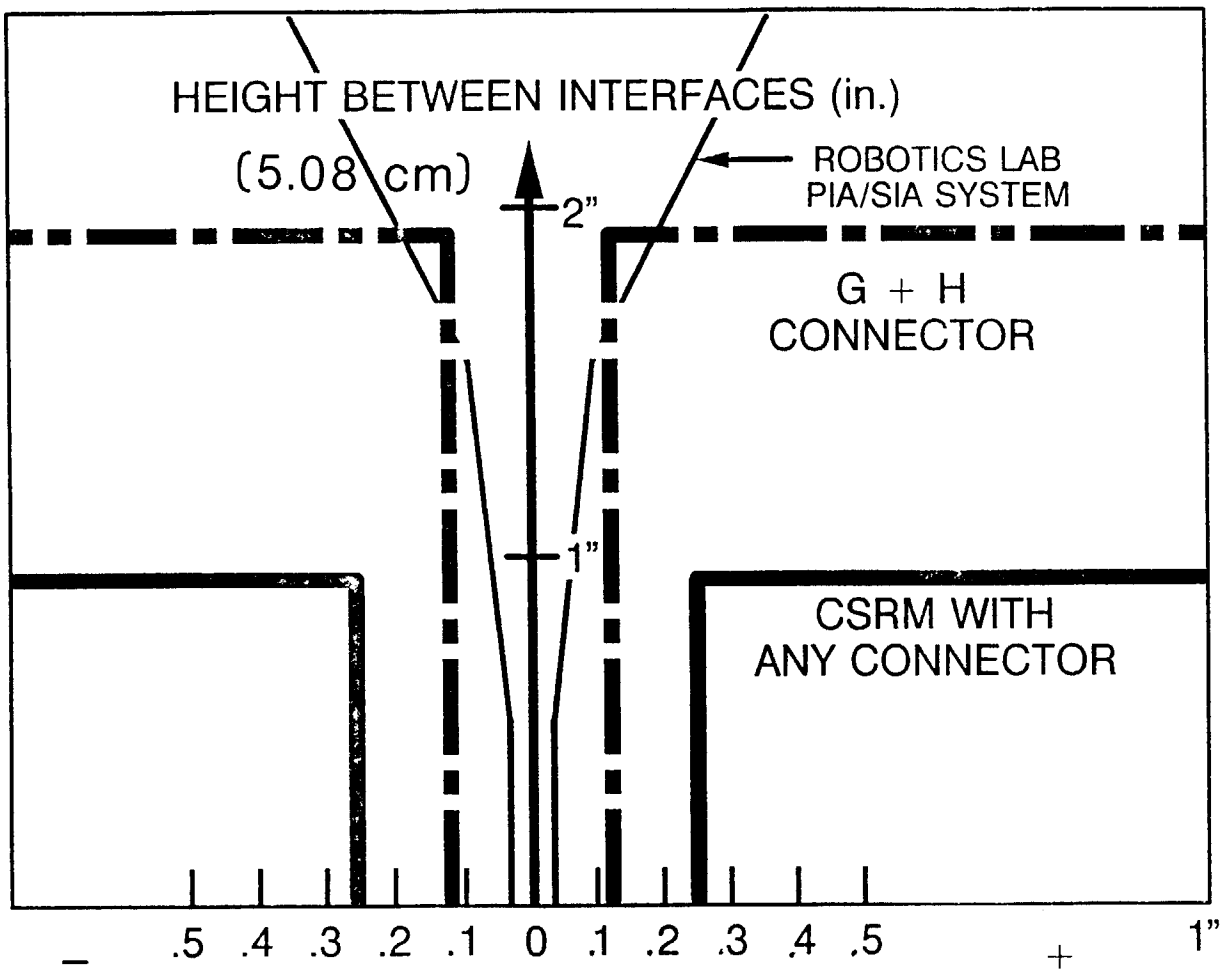

ALLOWABLE INTERFACE MISALIGNMENT

FIGURE 5

A365.007

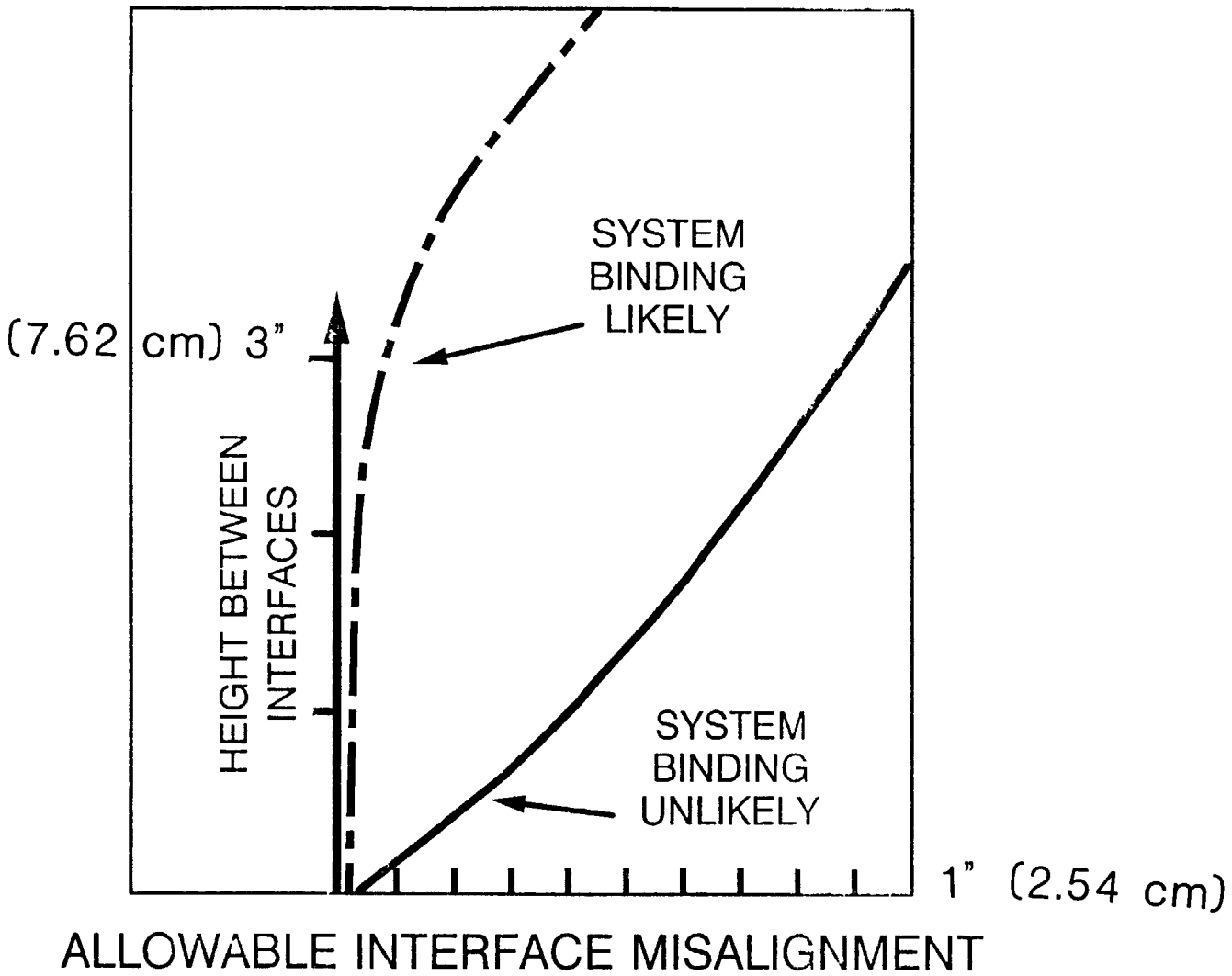

A365.001

FIGURE 6

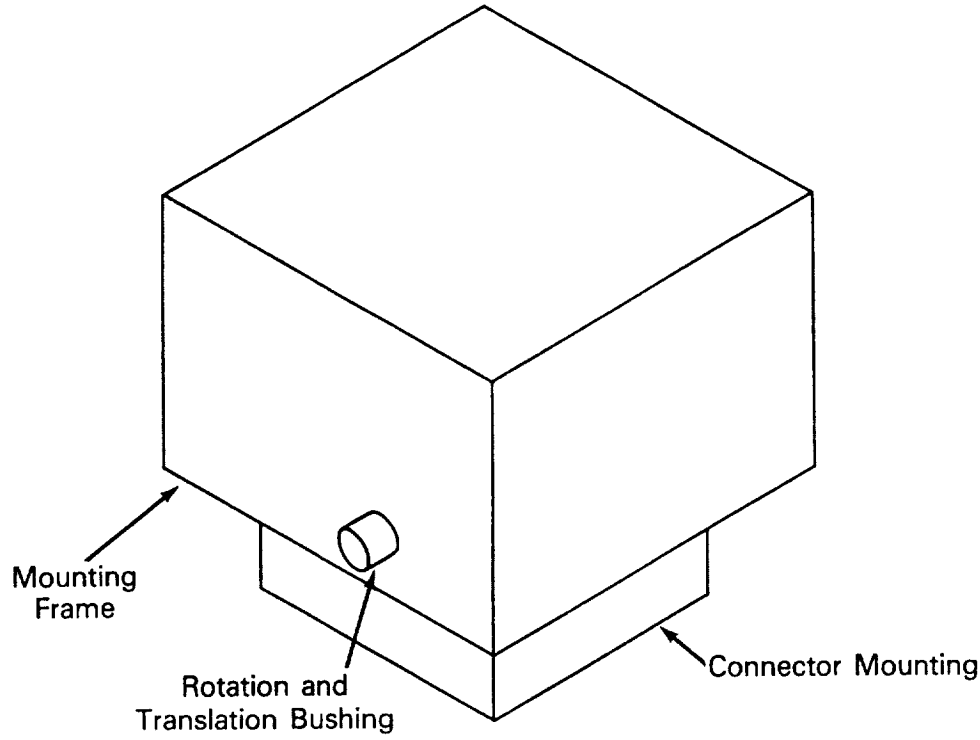

CSRM Passive Half

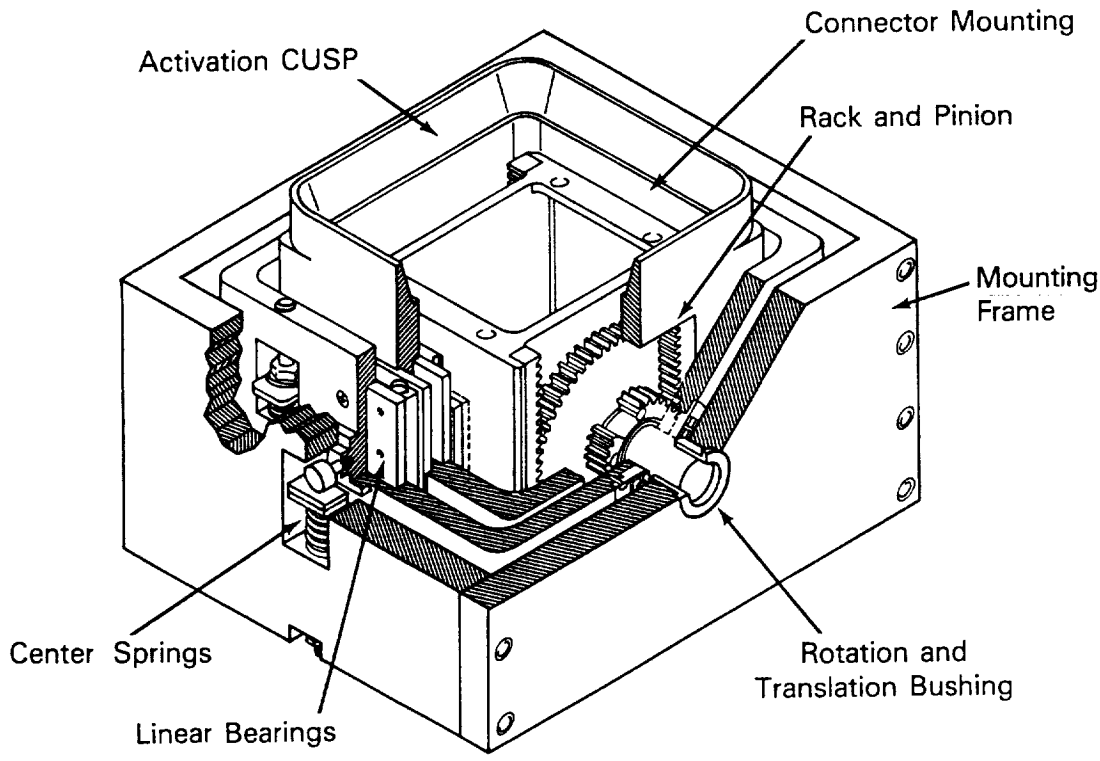

CSRM Active Half

FIGURE 7

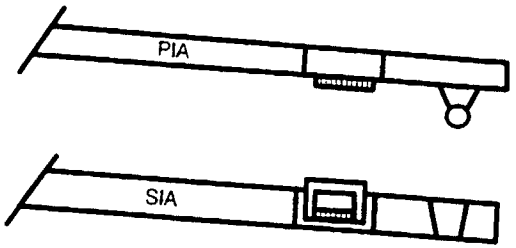

1. THE PIA/SIA ARE BROUGHT INTO CLOSE PROXIMITY.

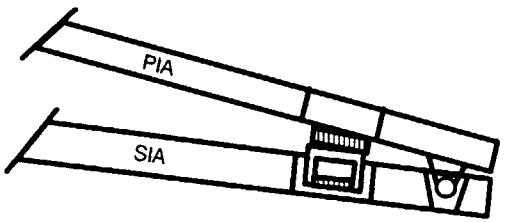

2. THE WORST CASE MISALIGNMENT.

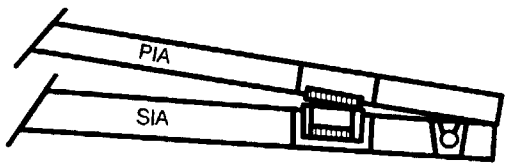

3. THE CRSM CUSP MAKES CONTACT AND DEVICE HALVES GIMBAL TO BECOME PARALLEL.

4. AS THE INTERFACE HEIGHT IS REDUCED THE CONNECTOR MOVES TWICE AS FAST AS THE INTERFACE.

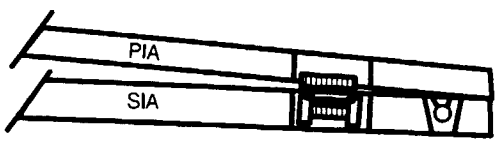

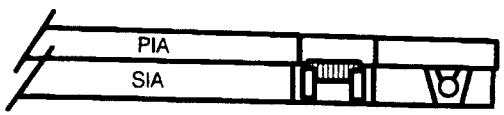

5. THE CONNECTORS ARE MATED.

CSRM SEQUENCE OF OPERATION

A365.002

FIGURE 8

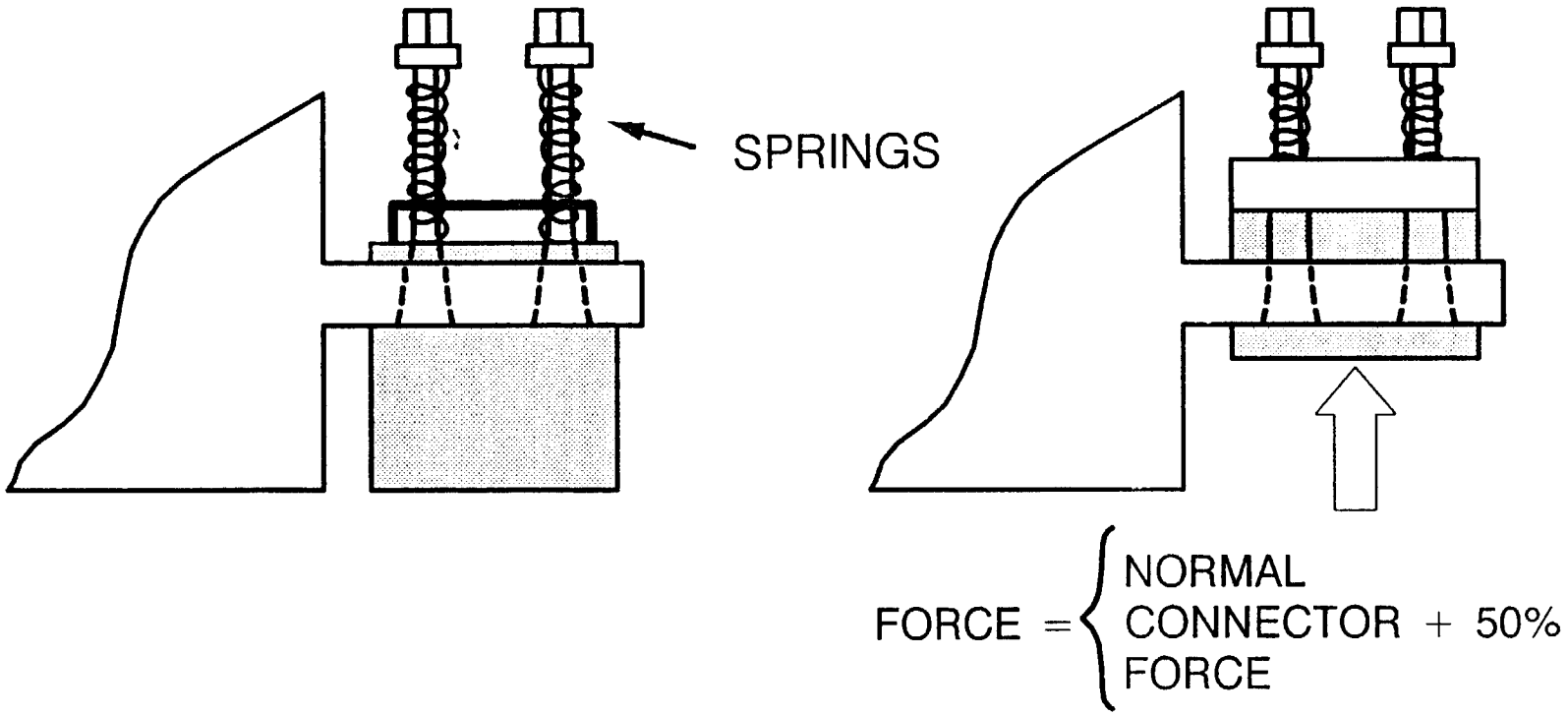

CONNECTOR MOUNTING

FIGURE 9

A365.004

STATION HALF

PAYLOAD HALF

The CSRM is a NASA/GSFC exclusive design

FIGURE 10

CSRM HARDWARE

IMPROVED CSRM
"ONE TELESCOPING CYLINDER ELIMINATED"

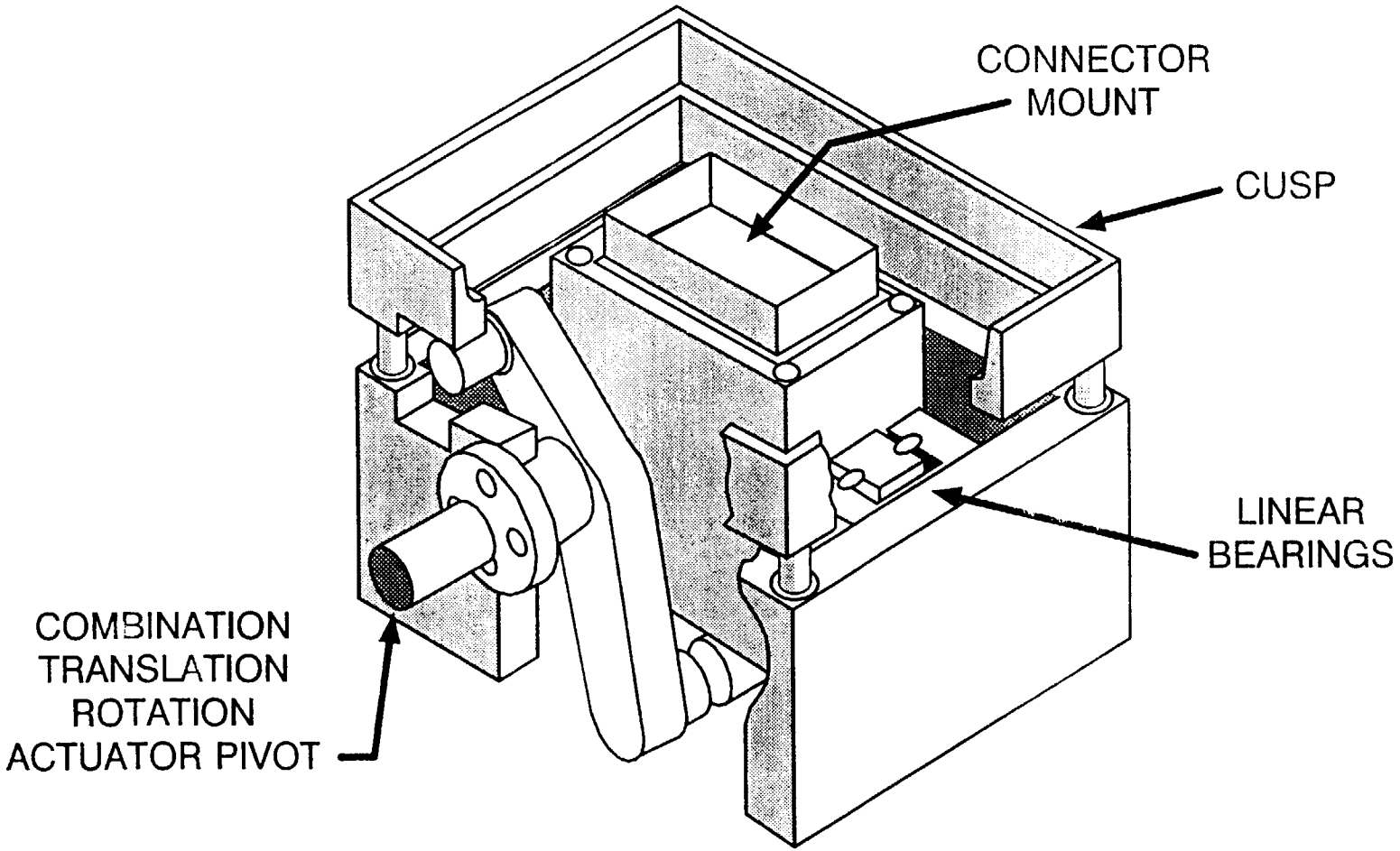

A365.003

FIGURE 11

DRIVING AND LATCHING OF THE STARLAB POINTING MIRROR DOORS

Herbert R. Beaven, Jr.* and Raymond R. Avina*

ABSTRACT

The Starlab Experiment, a major SDIO technology initiative, is an attached payload which will be delivered into Earth orbit aboard NASA's Space Shuttle in 1991. Starlab will generate and aim an eighty centimeter diameter laser beam into space through a large opening in the structure which houses the pointing mirror. Two doors, each somewhat larger than a desktop, cover the opening when the laser/optics system is non-operational. Latch Mechanism Assemblies hold the doors shut during liftoff/ascent and, again, during Orbiter reentry. Each door is powered by a Door Drive System during the many open/close cycles between various experiments. The design, testing and resultant failure modes of these mechanisms are the focus of this paper.

INTRODUCTION

Overall design and management of the Starlab Program is the responsibility of the Astronautics Division of Lockheed Missiles & Space Company, Inc. (LMSC). The U. S. Air Force's Space Systems Division (AFSSD) oversees all aspects of the program for the Strategic Defense Initiative Organization (SDIO). The Starlab Experiment physical equipment resides in two main entities: (1) the Module, a pressurized crew module similar in size and construction to Spacelab and mounted forward in the Orbiter cargo bay; (2) the Pallet, an unpressurized segment mounted on a standard ESA pallet and attached to the aft end of the Module. The Module's forward end is interconnected to the Orbiter cabin by a pressurized personnel access tunnel. Figure 1 shows the physical arrangement of major equipments.

The marker laser beam originates in the Module (which is manned during flight by astronauts) and is directed aft, through the main telescope mounted to the vertical optical bench of the Pallet (Figure 2). The beam is expanded to an 80 cm. diameter as it exits the telescope and is then aimed outside the Orbiter toward targets either in space or the Earth's atmosphere. The beam director, sometimes called the pointing flat, is a gimballed mirror which measures 1.47 meters across and is mounted to the horizontal optical bench in the extreme aft end of the Starlab Pallet. The pointing flat is shown in Figure 3.

*Astronautics Division, Lockheed Missiles & Space Company, Inc., Sunnyvale, CA 94088-3504

The Aft Protective Enclosure Assembly, simply referred to as the aft cover, is a large (8.63 ft. long, 7.26 ft. wide, 4.19 ft. high) aluminum honeycomb structure which completely encloses the Pallet's horizontal and vertical optical benches. The flight article is shown in Figure 4. Its sole function is to provide thermal and contamination protection for the telescope, pointing flat and other sensitive optical equipment located on the Pallet. In order for the marker laser beam (and other smaller ancillary beams) to safely exit through the aft cover opening without vignetting, each of two large doors is unlatched and rotated 90° to its full open position. This enables Starlab to optically acquire and track a variety of rapidly moving experimental targets with doors open, yet be fully protected from solar radiation with doors closed (Figure 5).

LATCHING OF THE DOORS

System Overview

The design of the Latch Mechanism Assembly was driven by two basic system considerations: (1) the device must be inherently reliable and (2) how many devices are needed to restrain both aft cover doors? The door latching system has a unique mission: restrain both doors, holding them in the closed position during the relatively high vibration levels of liftoff, ascent, and descent. Then, after Starlab is inserted into orbit and reaches a condition of operational readiness, the doors are unlatched. The latch mechanisms allow the doors to be rotated open and closed, when needed, by the Door Drive System. Reliability is the ability of the device to reach orbit intact, and then respond to the astronaut's "unlatch" (or "latch") command. Although both of these functions are important, the technical success of the mission is more dependent upon the unlatch function than it is on the relatch function. The reason for this is that the aft pallet cavity, with its key optical components, must be physically exposed to space and sky in order for the experiment to proceed.

One of the most intensely debated design issues was whether to have four door latch assemblies or two. Four latches equated to a fore and aft latch for each door. Just two latches required that one door overlap and restrain the other at the apex. This cap door would be the one which would be latched. The final decision was to choose the two-latch approach using the port door as the "capper". The main reason for the decision was to reduce the quantity of mechanism and moving parts to an absolute minimum, thereby maximizing system reliability.

Design Requirements and Alternatives

The Latch Mechanism Assembly detail design is the result of conformance to the following requirements:

1. Military Specification MIL-A-83577B (USAF) 01 Feb 1988. Assemblies, Moving Mechanical, for Space and Launch Vehicles, General Specification For.

2. Main actuating devices shall be space-proven hardware.

3. Main actuating devices shall be dual redundant, i.e., one device shall serve as the primary actuator while the other device shall serve as the secondary or backup actuator.

4. Assembly shall have long narrow footprint due to the scarcity of aft cover surface area on which to mount it.

5. Mechanism shall be non-backdriveable with electrical power off. When mechanism is locked with power off it will remain locked during worst case vibration/shock environment. When open it will remain open.

6. Mechanism shall be fully functional in a hard vacuum at +154°F and at -24°F. It shall be capable of withstanding 7.4 g(rms) between 20 Hz and 2000 Hz for 1 minute on each of major axes at lab ambient temperature and pressure.

7. The door pin holding (main load path) components such as the hook, pivot pin, bushings and baseplate shall be able to handle maximum door pin loads during the high acceleration stages (liftoff, ascent and insertion) without undergoing plastic deformation.

8. The design shall be kept "spartan" in its simplicity through the elimination of any extraneous part or feature.

The WHY of Our Final Design Decisions

Details of the Latch Mechanism Assembly final design are illustrated in Figure 6. The comparisons below indicate some of the major design alternatives and demonstrate that adherence to the foregoing list of design requirements led us to our final design decisions.

- Linear Actuators versus Linear Solenoids. The actuator had been previously flown and was space-qualified. We were unable to find a solenoid with the correct force-displacement characteristic which was certified for flight. (Design Requirement #2). Since the linear actuator uses the jackscrew principle it is

non-backdriveable. The linear solenoid is readily backdriveable. (Design Requirement #5). The selected linear actuator is capable of functioning over a temperature range from -65°F to +150°F. (Design Requirement #6). The linear actuator which was finally selected is shown in Figure 7.

- Single versus Dual Actuators. There was no debate on this issue because of Design Requirement #3. The use of redundant key components is a widely accepted method for substantially increasing aerospace mechanism reliability.

- Serial versus Parallel Interconnection. Again, the Design Requirement, #4 in this case, made clear the need for latch assembly geometry to conform to the long slim aspect ratio. Parallel ganging of linear actuators would have resulted in an overall assembly width which exceeded the available mounting area.

- Single Center Link versus Four Bar Linkage. The initial design of the connection between the tail end of the primary actuator and the front ball joint of the secondary actuator employed a four-bar linkage. Kinematic studies of an alternative single-link design indicated that, in the event of primary actuator failure, hook rotational displacement and the movements of both actuator bodies caused by secondary actuator ram retraction, were all acceptable. In keeping with Design Requirement #8 (Simplicity), the single center link was chosen over the four-bar linkage.

- In-line Pivots versus Random Pivot location. Figure 6 shows that the following centers of rotation (CR) are in-line: hook CR, center link CR and secondary actuator CR. The benefits of this CR alignment are a lower profile baseplate with minimum lip height, and ease of machining the six pivot holes associated with these CRs. (Design Requirement 8).

- Flag Feature.
  Examination of Figures 6 and/or 8 show an appendage on the head of the hook referred to as the flag. This feature serves as a redundant visual indicator of latch mechanism hook status (open vs. closed). Local TV cameras mounted aft in the Orbiter cargo bay can be trained on either Latch Mechanism Assembly in order to visually verify hook status in lieu of depending only on LED lamps at the control panel. The flag is painted a glossy reflective yellow to aid identification.

Test Program and Results

Acceptance testing of the three Latch Mechanism Assemblies consisted of a six-step sequence.

1. Initial Measurements and Adjustments.
   a. Insulation resistance measurement of all wiring using a megohmeter.
   b. Electrical bonding check by measurement of ground path resistance.
   c. Adjustment of hook and center link positions by setting of extend microswitches on each linear actuator.

2. Functional Test at Lab Ambient Conditions.
   a. Retract and extend primary actuator without simulated door pin. Monitor voltage and current.
   b. Retract and extend secondary actuator. Monitor voltage and current.
   c. Repeat above procedure with simulated door pin. Figure 8 shows the latch assembly functional test setup.

3. Thermal/Vacuum Cycling
   a. Test chamber is evacuated to a hard vacuum.
   b. Temperature is cycled between -24°F and +154°F 8 times with a 2 hour soak at each extreme.
   c. Each linear actuator performs one retract/extend cycle after soaking at each temperature limit.

4. Functional Test at Lab Ambient Conditions.
   a. Same as Step 2, above.

5. Random Vibration.
   a. 7.4 g(rms) over a frequency range of 20 to 2000 Hz for one minute on each of 3 major axes.
   b. Each linear actuator performs one retract/extend cycle after vibration on each axis.

6. Final Functional Test at Voltage Limits.
   a. Same as Step 2, above, with nominal voltage (28 VDC) applied.
   b. Same as Step 2, above, with maximum voltage (32 VDC) applied.
   c. Same as Step 2, above, with minimum voltage (24 VDC) applied.

Two of the three Latch Mechanism assemblies successfully passed all tests in the above test series. A third unit exhibited a retract microswitch failure during thermal/vacuum cycling at the cold temperature limit (-24°F). Microswitch failure analysis was underway but not complete at the time this paper was written. The plan is to replace the microswitch and completely repeat the six-step acceptance test sequence. Figure 9 shows the location of the failed microswitch.

Systems Overview

Starlab will orbit the Earth approximately every 90 minutes. During the total mission Starlab will complete approximately 112 Earth orbits with an experiment planned during each of up to 100 orbits. This plan will require 100 open/close cycles of each aft cover door. If either door were to stay in the closed position, or even partially closed, the experiment objectives would be placed in considerable jeopardy. Manual intervention by an astronaut would necessitate an extra vehicular activity (EVA). However, no EVAs are currently planned. For these reasons the reliability of the mechanisms which latch and drive the doors is a primary design goal.

In contrast to the latch mechanisms, both of which must unlatch only once, the Door Drive Systems, one to open/close the port door and one for the starboard door, MUST WORK during 100 full cycles (maximum). Couple that fact with another: the Door Drive Systems are much more complex in terms of function and parts count, thus system reliability is at greater risk. Examination of Figure 10, a Cadam layout of the Port Door Drive System, underscores the point made above regarding the complexity and parts count of the Door Drive System. The Dual Drive Actuator (DDA) is the prime mover whose output is transmitted to the single-pass spur gearset through a detent-type clutch. The spur gear is pinned to the main drive shaft which is coupled at each end to a moving hinge shaft via Oldham couplings. The Door Drive System can be perceived as being composed of a DDA/clutch assembly containing most of the super-precision components (tolerances in the ten-thousandths of an inch) and a driveline made up of larger precision parts (tolerances in the thousandths or coarser). A full section view of the DDA is shown in Figure 11. This drawing further demonstrates the complexity of the Door Drive System.

Design Requirements and Alternatives

The Door Drive System detail design is the result of conformance to the following requirements. Note that Requirements #1 through #4, below, are identical to Latch Mechanism Assembly Requirements #1, #2, #3 and #6.

1. Military Specification MIL-A-83577B (USAF) 01 Feb 1988. Often referred to as the MMA Spec (Moving Mechanical Assemblies).

2. Main actuating devices shall be space-proven hardware.

3. Main actuating devices shall be dual redundant, i.e., DDA (Dual Drive Actuator) System 1 shall serve as the primary torque transmission path while System 2 shall serve as the secondary or backup

torque path. Each DDA "System" includes its own dedicated brushless DC motor.

4. Mechanism and driveline (entire Door Drive System) shall be fully functional in a hard vacuum at +154°F and at -24°F. They shall be capable of withstanding 7.4 g(rms) between 20 Hz and 2000 Hz for 1 minute on each of 3 major axes at lab ambient temperature and pressure.

5. Total elapsed time for opening both doors from full closed to full open position shall not exceed 3.5 minutes. Total elapsed time for closing doors shall not exceed 3.5 minutes.

6. The DDA shall exhibit sufficient torque margin to drive a simulated door assembly cyclically through a full 90° arc with hinge line vertical in ground tests. Thrust loads due to door weight are sustained at the forward roller bearing of each hinge shaft assembly. Torque resistance at each of these bearings is greater during this ground test than it will be on orbit because door weight is zero on orbit.

7. Door hinge/shaft assemblies shall be of robust construction capable of carrying combined shear and torsional loads from each door assembly during the high acceleration stages (liftoff, ascent and insertion) without undergoing plastic deformation.

8. Limit switches, a pair mounted at each of the 4 hinge assemblies, shall stop rotation (Auto Mode only) at the full open and full closed positions and switch LEDs on the control panel to signal door status to the astronauts.

9. The design, though not "spartan", shall be kept as simple as possible.

The WHY of Our Final Decisions

The final design layout of the Door Drive System is shown in Figure 10. Details of the Dual Drive Actuator appear in Figure 11. Adherence to the design requirements list (above) was a major factor in arriving at the design decisions described below.

- Rotary versus Linear Door Motion for Opening and Closing. Although the first concept called for linear door motion, it later became clear that rotating the doors was the only viable approach. The only spatial clearance issue with rotating doors was: when the doors are rotated full open, do their tips clear the big closed doors of the Orbiter cargo bay? Kinematic studies done in scale on Cadam indicated several inches of clearance assuming worst case tolerances throughout. By comparison, the

angled top faces of the aft cover precluded linear doors since, when sliding open, they would have collided with a variety of equipments mounted near the outside perimeter of the aft cover. A more easily debated reason for rotary instead of linear was our strong preference for a completely rotational door system allowing the use of a variety of inexpensive yet high quality off-the-shelf rotary-type bearings and the avoidance of long guide-rails, linear bearings and routing of aircraft cable most likely required in the linear motion approach. Rotary door motion more readily conformed to Design Requirement #9.

- Selection of the Dual Drive Actuator (DDA).
  Without question, the DDA is the cornerstone of the Door Drive System design. Therefore, the choosing of available dual drives was a key hardware selection decision. The field was immediately narrowed by Design Requirement #2 requiring space-proven hardware. The DDA finally selected was developed some years ago at Caltech's Jet Propulsion Laboratory and, with various design nuances, was the actuator of choice in a number of space-related programs. It has passed several full-blown Flight Qualification Test Series and had flown once, functioning successfully in the space environment. The DDA has many attractive features such as: dual redundancy (Design Requirement #3), huge torque multiplication in a small package, rugged yet lightweight and pre-qualified for space use on prior programs. Of course, all of these fine features do not come free. The fabrication, finishing and inspection of many intricate parts, plus the complicated assembly procedure followed by a series of environmental acceptance tests result in a very costly final assembly.

- Spur Gears versus Worm & Wheel in the Driveline.
  Trade studies of the torque/speed characteristics of various methods for linking the DDA output to the main driveline boiled down to two approaches: spur gears versus worm/wheel. Parameters which differentiate the two types of gearing are ratios, parasitic torque and backdriveability. Worm ratios are generally higher per gear pass which meant lower driveline speed and longer door cycle times. The mesh efficiency of the spur involute profile is hard to beat and results in lower torque resistance. A close watch has been kept on all parasitic torques because of limited available torque output from the DDA. Worm non-backdriveability, sometimes a very useful feature, was perceived as a disadvantage for the case of door mass and acceleration perturbations causing high stress and potential wear at the worm and wheel contact spot. This was a non-problem for the spur gears which when backdriven to torques higher than 100 lb-in., cause the detent clutch to ratchet, thus limiting tooth stress. Spur gears were selected as the best method for meeting Design Requirement #5.

- Tapered roller bearings versus Deep Groove Radials for the hinges. Although deep groove radial bearings are miserly consumers of torque, the deciding feature for the hinges was bearing thrust capacity; measured in thousands of pounds for tapered rollers and tens of pounds for radials. If a door assembly weighs 30 lb. at 1 g it will "weigh" well over 200 lb. during liftoff/ascent. And this is not a steady load but a pounding load due to superimposed random shock input. High Hertzian contact stress in radial bearings can result in brinelling (raceway indentation) because the ball to race contact area is essentially a point contact. Tapered rollers make line contact with their raceways thus reducing contact stress. The price to be paid for the superior thrust capacity of tapered roller bearings is their inherently greater torque resistance which, for this application, is about 2 lb-in. per bearing. With 4 roller bearings per driveline, their total torque resistance will be approximately 8 lb-in., a figure which is high enough to merit attention but low enough to be acceptable. These bearings will perform in accordance with Design Requirement #6.

- Independent Hinge Shafts versus A Single Driveline Shaft. The initial concept for shafting to drive the doors was a single .500 inch diameter stainless steel shaft driven near the center of its length by the spur gear and pinned to a moving hinge at each end. The major flaw in this concept was differential thermal expansion/contraction between the aluminum honeycomb structure to which the fixed hinges are attached and the one-piece stainless steel shaft. Differential expansion had the potential to cause severe binding between the fixed and moving hinges which, in turn, could result in higher than acceptable torque resistance. The 3-shaft idea, i.e., a main drive shaft driving 2 independent hinge shafts through couplers which act like expansion joints, was selected because it disallows axial force buildup as a function of differential thermal expansion or contraction. Reference Design Requirement #7.

- Redundant Door Control Electronics. From the very beginning of our dialogue regarding the door control system, Systems Engineering insisted upon a redundant approach. That is, door opening and closing would be done semi-automatically, which means an "open" or "close" command would be manually initiated with the remainder of the sequence being automatic. If, for any reason, the semi-automatic system should fail, the doors could still be opened and closed by the astronauts' switching to "Manual" operation. This redundant systems approach requires the use of a pair of microswitches at each of 4 hinge assemblies, one switch for Auto mode and one for Manual mode. Figure 12 indicates the method employed for switch mounting and actuation. Note that only one switch is seen because the pair is stacked side-by-side with one hiding the other from view. This scheme is in consonance with Design Requirement #8.

Test Program Plans

Acceptance testing of the three Dual Drive Actuators will consist of a six-step sequence almost identical to that performed on the Latch Mechanism Assemblies.

1. Initial Measurements and Adjustments.
2. Functional Test at Lab Ambient Conditions.
3. Thermal/Vacuum Cycling. Test DDA at Combined Limits of Temperature and Voltage.
4. Functional Test at Lab Ambient Conditions.
5. Random Vibration.
6. Final Functional Test at Voltage Limits.

Note: The sole deviation of the DDA test sequence from that of the latch mechanisms is Step 3. The DDAs are run with full load at each high temperature plateau and each of 3 voltage levels. Also the DDAs are run with full load at each low temperature plateau and each of 3 voltage levels.

Two additional major tests are planned: (1) Driveline Torque Margin Verification wherein a simulated port door is rotated full open and full closed at the high voltage limit then at the low voltage limit. Test measurements will include times required for full opening and full closing in addition to DDA motor temperatures. Present plans call for this to be done at lab ambient temperature and pressure. Figure 13 illustrates the driveline mounted to special test equipment. (2) Full-Up Aft Cover Thermal/Vacuum Tests will be done in a large environmental test chamber. The full-up aft cover assembly (flight hardware) will be fastened to a large handling dolly and suspended, with thrust axis and hinge drivelines vertical, inside the thermal/vacuum test chamber. The chamber will be pumped down to a hard vacuum and then temperature cycled between +154°F and -24°F for at least 8 full cycles. At each temperature plateau the real flight door system will, for the first time, be exposed to combined worst case temperature and voltage in a vacuum. It is this door cycle test of the full-up aft cover assembly that will finally prove or disprove the flight readiness of the aerospace mechanisms which do the driving and latching of the Starlab pointing mirror doors.

LESSONS LEARNED AND CONCLUSIONS

Several valuable technical lessons were learned during the engineering development of these moving mechanical assemblies. This information came to us from two sources: (1) our own design, fabrication, assembly and testing efforts and (2) other projects working on similar devices, such as the DDA.

- Failed Microswitch on Starlab Latch Mechanism Assembly.
  The function of this sub-subminiature microswitch, one of 3 used in each of 2 linear actuators per latch assembly, is to interrupt

current to the actuator motor when the ram reaches full retract position. The microswitch failed to function with the temperature at or near -24°F. The linear actuator is rated to perform down to -65°F which is substantially colder (41°F) than the failure temperature.

The first part of the analysis on the faulty actuator was to verify that the circuit was open across the retract microswitch by performing a continuity check. The results indicated that the circuit was open, when in fact it should have been closed due to the fact that the actuator was in the full mechanical retract position. This verified the failure encountered during the initial thermal cycle test. At this point, the actuator case was removed to investigate the reason for the failure. During removal of this case, the microswitch contacts closed.

The actual activation of the microswitch is accomplished by a cam, traveling on a linear path, pushing up on a triggering device which, in turn, compresses the microswitch plunger. It was determined that the triggering device was not adjusted properly and therefore the microswitch plunger could not be compressed a sufficient distance to cause activation at a cold temperature. The trigger was then adjusted so as to compress the plunger when the cam made contact. After the rework, the unit was tested for 20 cycles at both -24°F and +145°F with no failures. This verified that the failure was due to the trigger. This was typical of an "infant mortality" type of failure of a tiny mechanism composed of intricate precision parts. One question which arises, is this failure mode impending on the latch mechanism assemblies which have already successfully passed these same acceptance tests?

- DDA Motor Stalled at Low Temperature/Low Voltage.
  This acceptance test failure (not Starlab) points to the wisdom of thoroughly testing a flight assembly in an environment which faithfully simulates real operating conditions. In this case the motor stall occurred at -40°F and was caused by a seized universal joint. The U-joint ball was defective due to a design error allowing too large a tolerance on ball diameter. The replacement ball was a better fit with the mating part and the DDA performed well in the repeat test.

- DDA Incapable of Producing Output Torque.
  This, also, was an acceptance test failure (not Starlab) wherein the DDA output shaft was unable to drive the load even though the motor was turning. Failure analysis indicated that a major subassembly in the transmission path, the harmonic drive, was experiencing gear disengagement and tooth skipping. This was the result of incorrect hardware selection, i.e., the commercial grade (loose gear fitup) harmonic drive was selected instead of the aerospace quality unit with tighter gear fitup. The replacement harmonic drive was installed and the DDA successfully passed the repeat acceptance test.

Some Lessons Learned

1. Always ground test flight hardware at the anticipated worst case combination of conditions. For example: test at lowest temperature combined with lowest pressure combined with lowest voltage combined with longest time duration.

2. It pays to pay attention to detail. The fine design details, such as the correct mounting and actuation schemes for microswitches, are too often thought of as mundane issues, deserving of only minimal attention by the design engineer. If any item has the potential for crippling the mission then it warrants engineering attention.

3. Selection of off-the-shelf precision components and devices is fraught with danger. The design engineer is at risk, usually because he assumes he understands what he needs to, about the workings of the device. Complex devices are frequently full of surprises regarding their functional limitations. Contact the vendor; he is the real expert on his particular device.

4. Study the successes and failures of devices used on other projects which are similar to what you are developing. Gathering the necessary information is an activity well worth the effort. Keep in mind that design engineering is very much a business of collecting, filtering and applying good technical information.

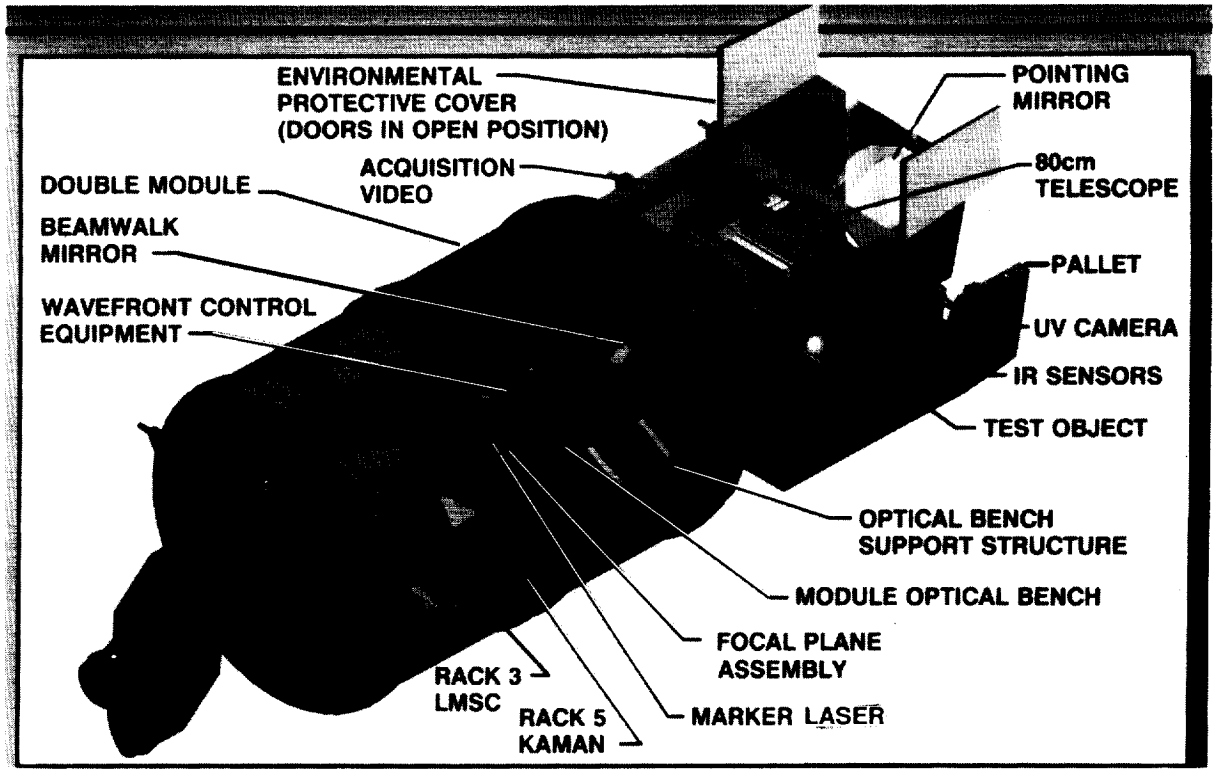

Figure 1. Starlab Experiment Hardware Layout

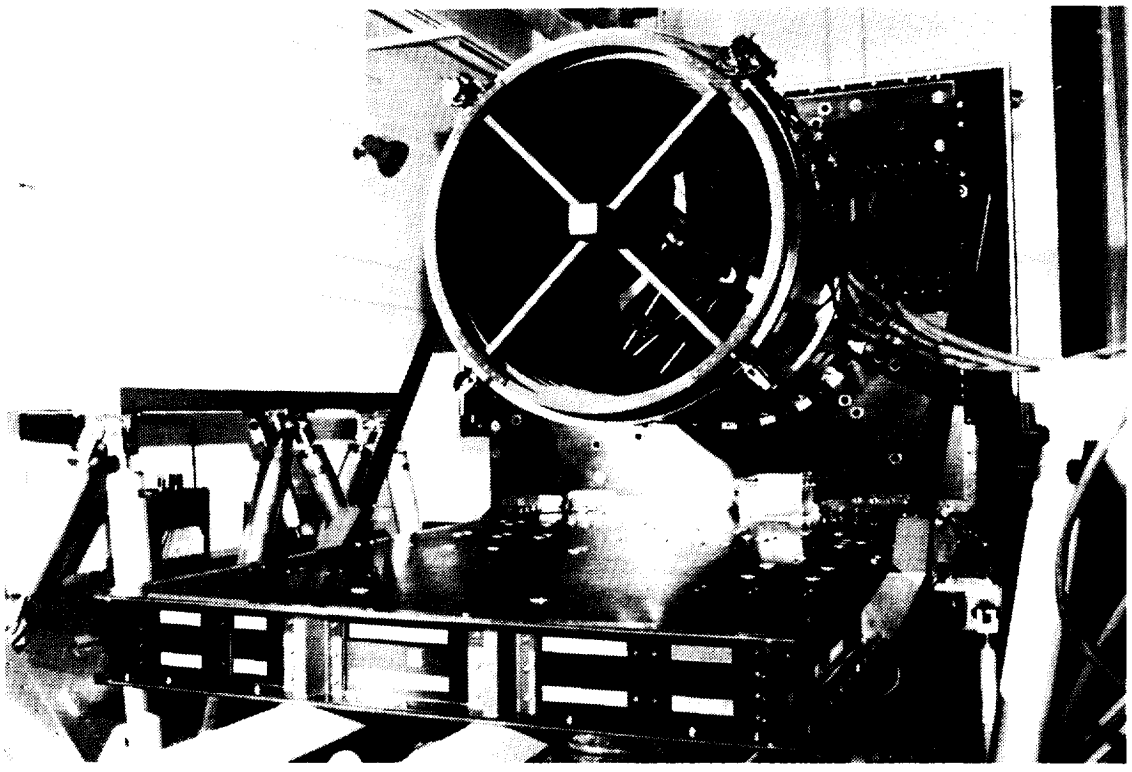

H0-4001/001

Figure 2. Aft Pallet Optical Benches and 80 cm Telescope

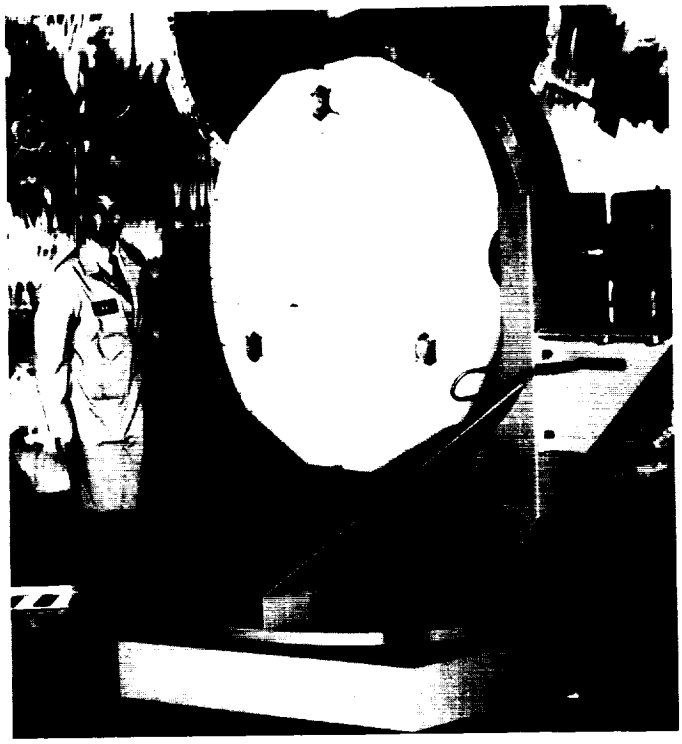

Figure 3. Pointing Mirror Mounted on Test Stand

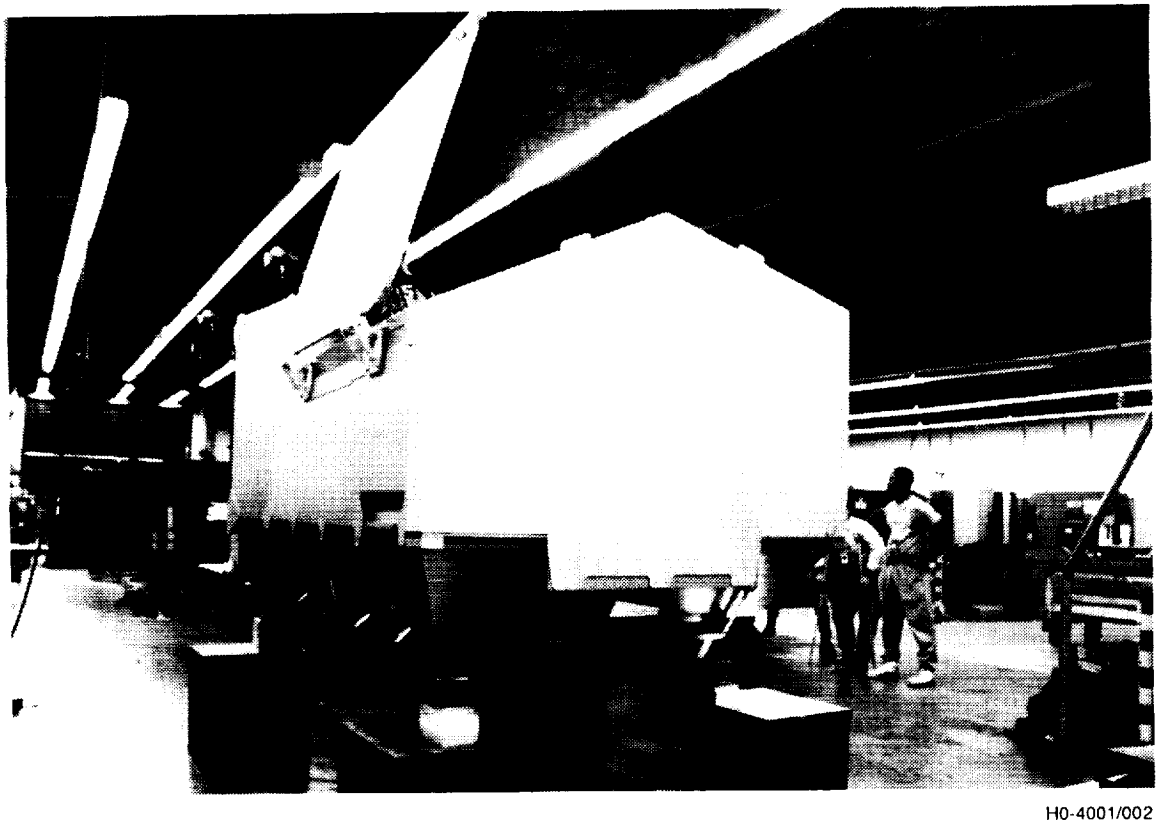

H0-4001/002

Figure 4. Aft Protective Enclosure Assembly, Port Door Partially Open

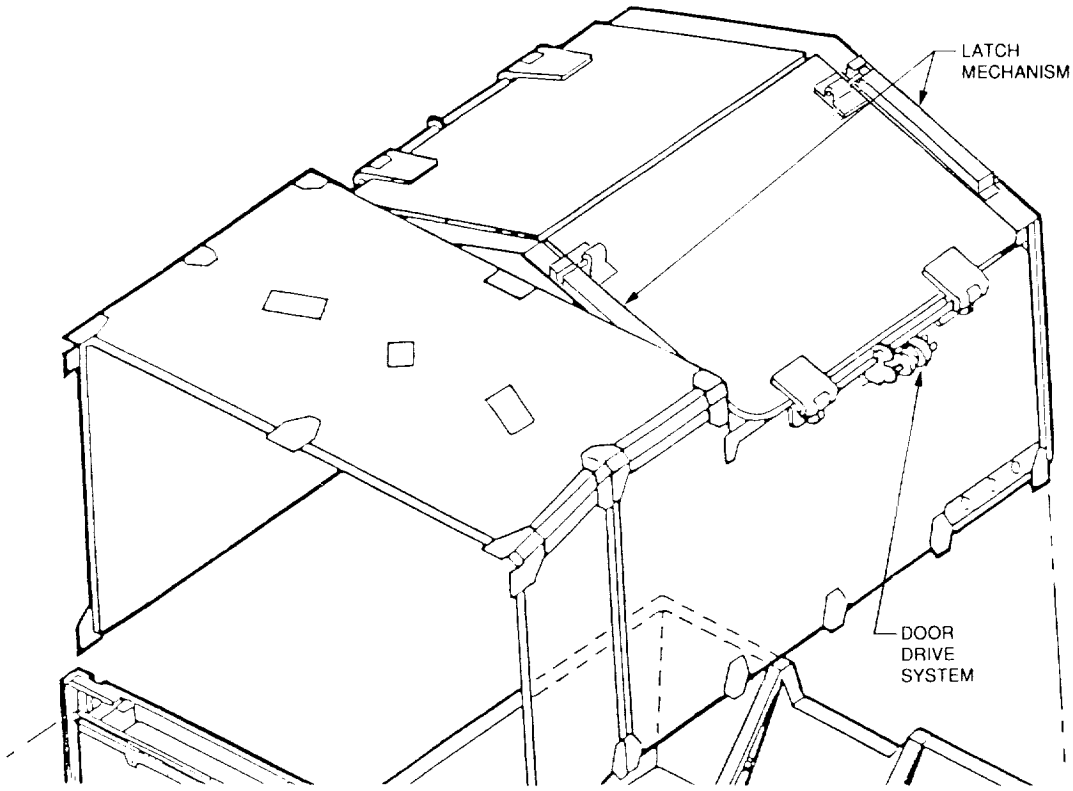

Figure 5. Aft protective Enclosure Assembly, Doors Closed

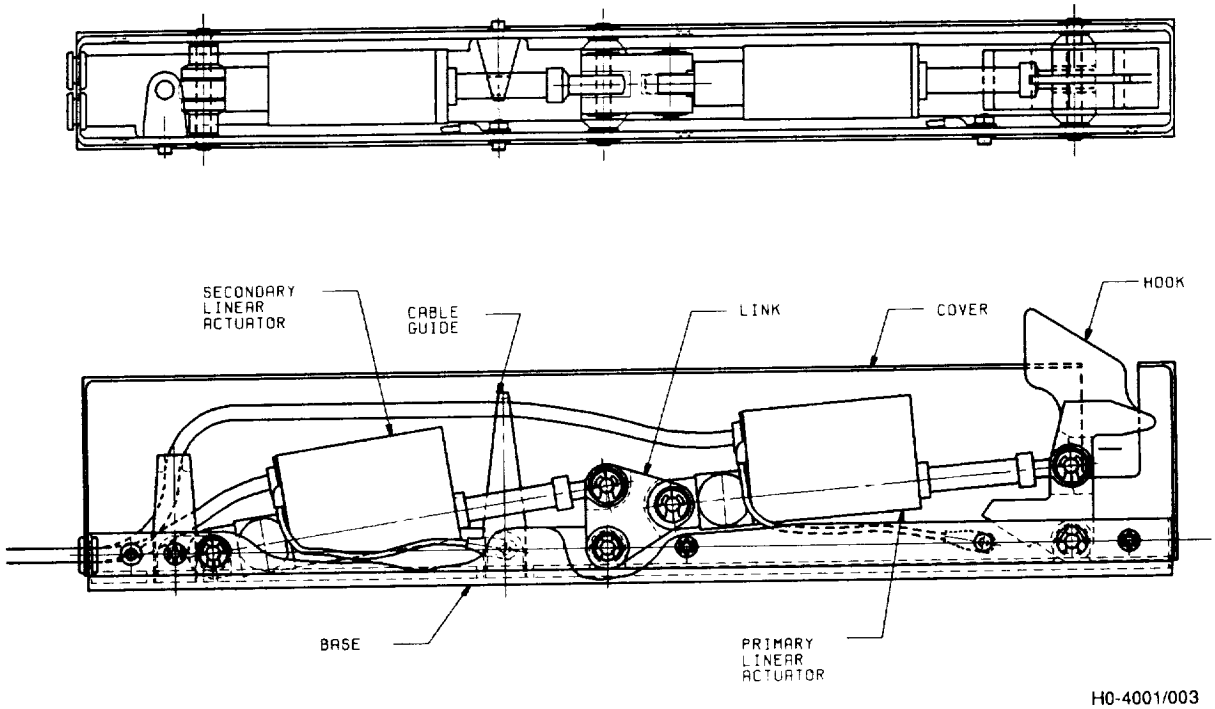

Figure 6. Latch Mechanism Assembly

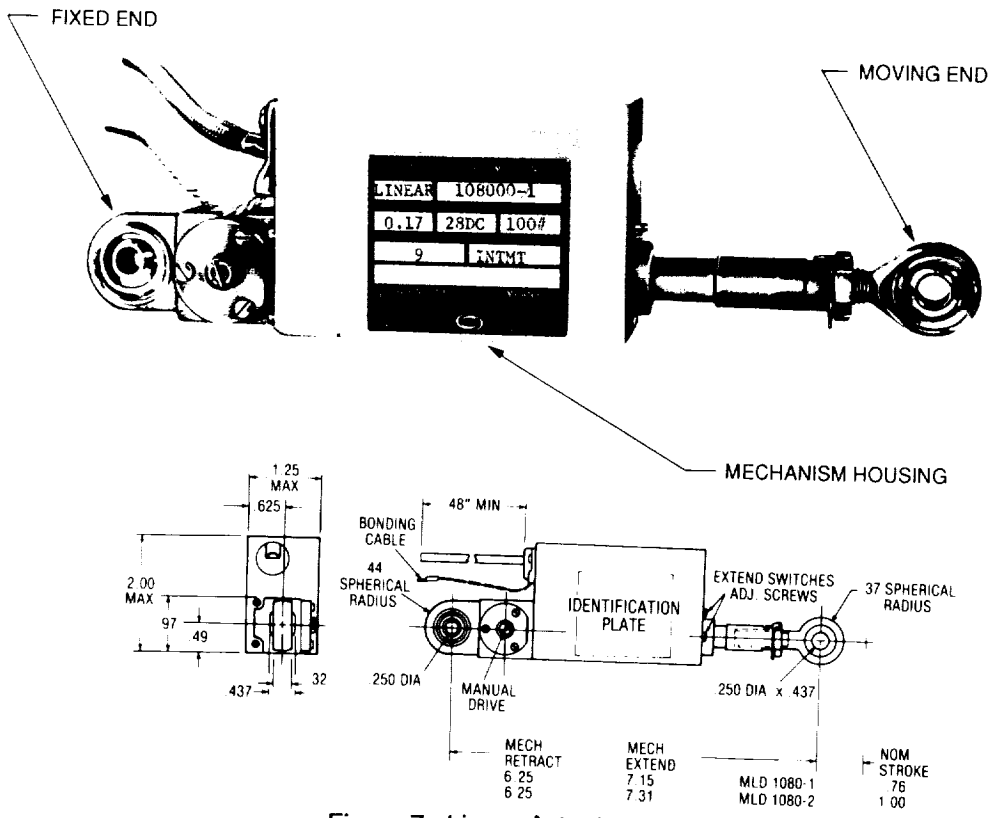

Figure 7. Linear Actuator

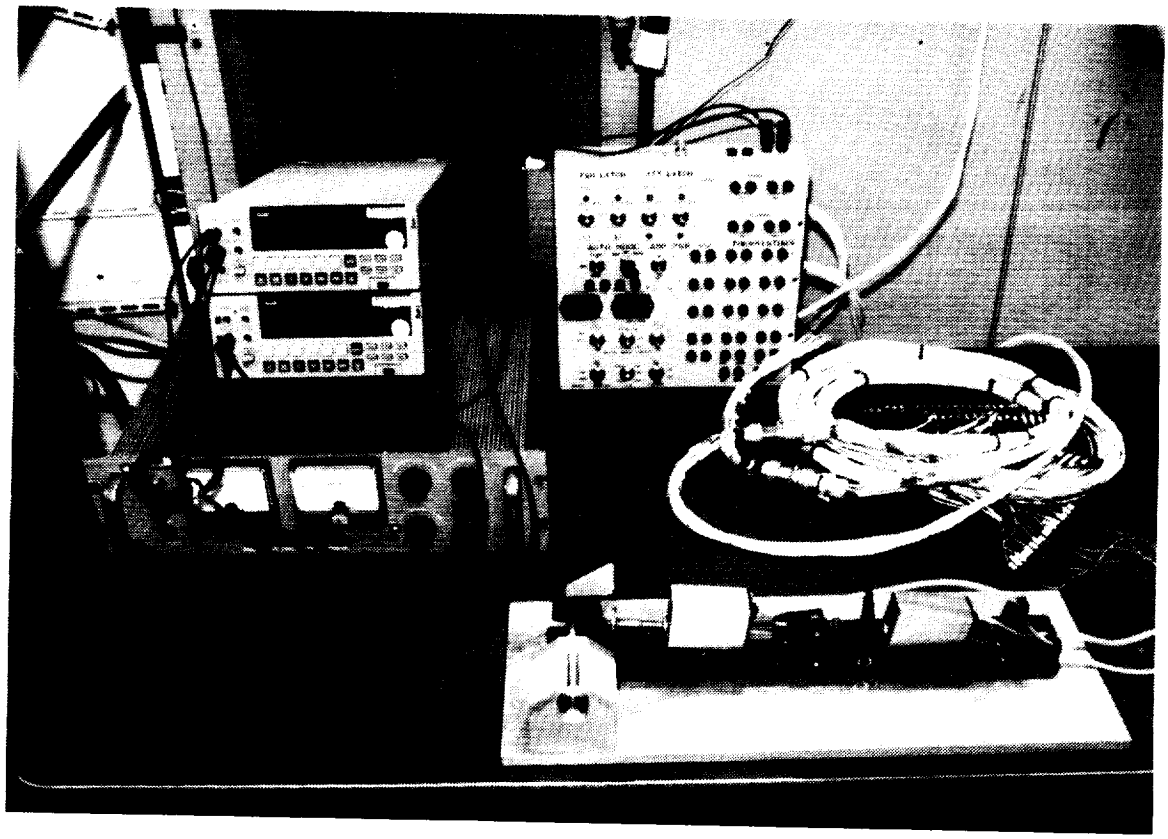

H0-4001/004

Figure 8. Latch Mechanism Assembly Under Test

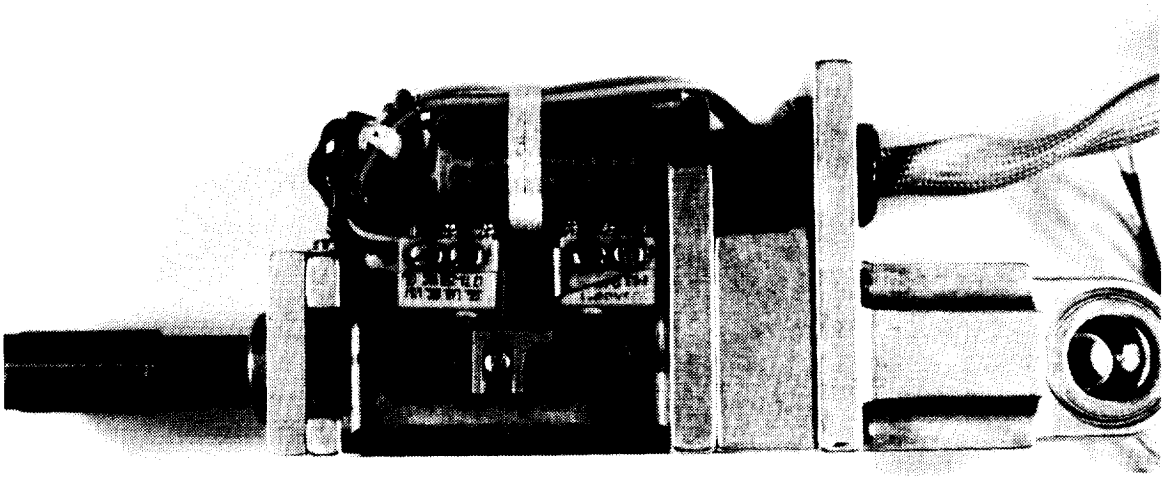

Figure 9. Linear Actuator Showing Cam and Microswitches

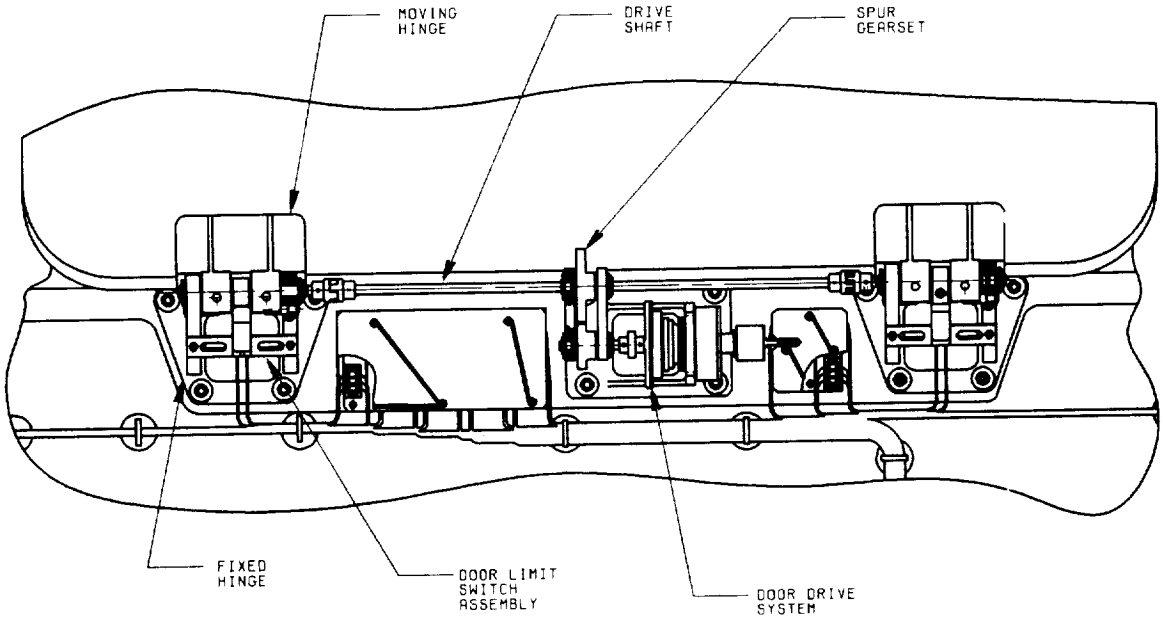

H0-4001/005

Figure 10. Door Drive System. Portside Shown

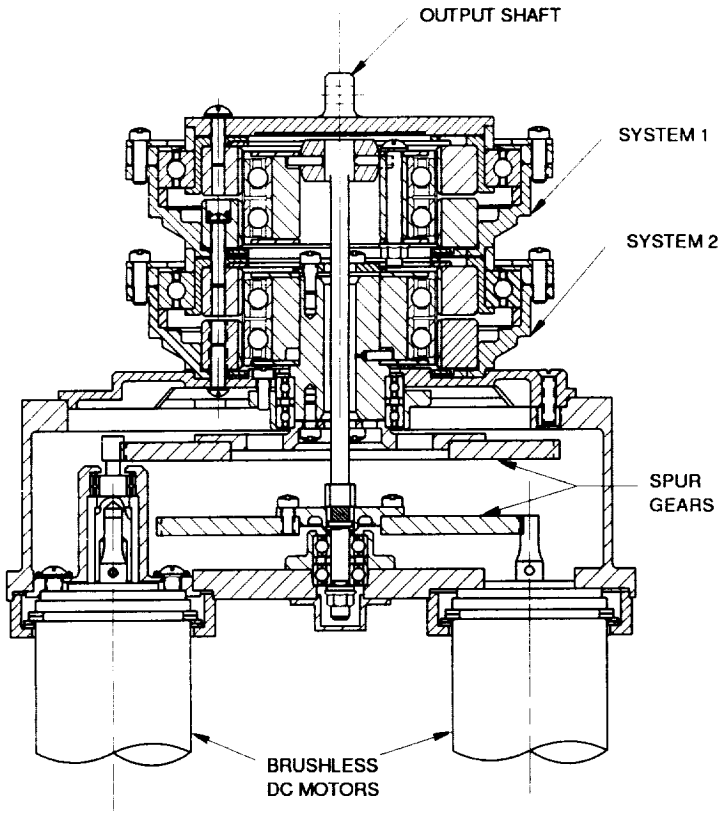

Figure 11. Dual Drive Assembly Cross-Section

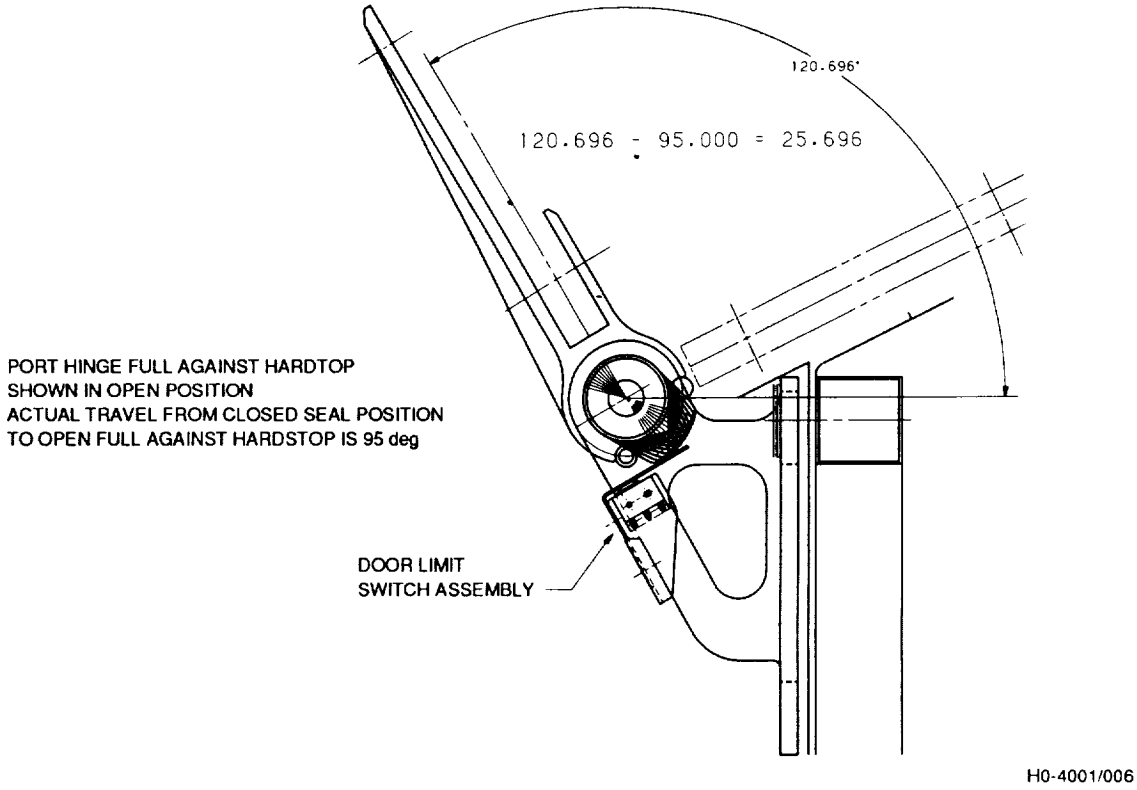

Figure 12. Door Limit Switch Arrangement

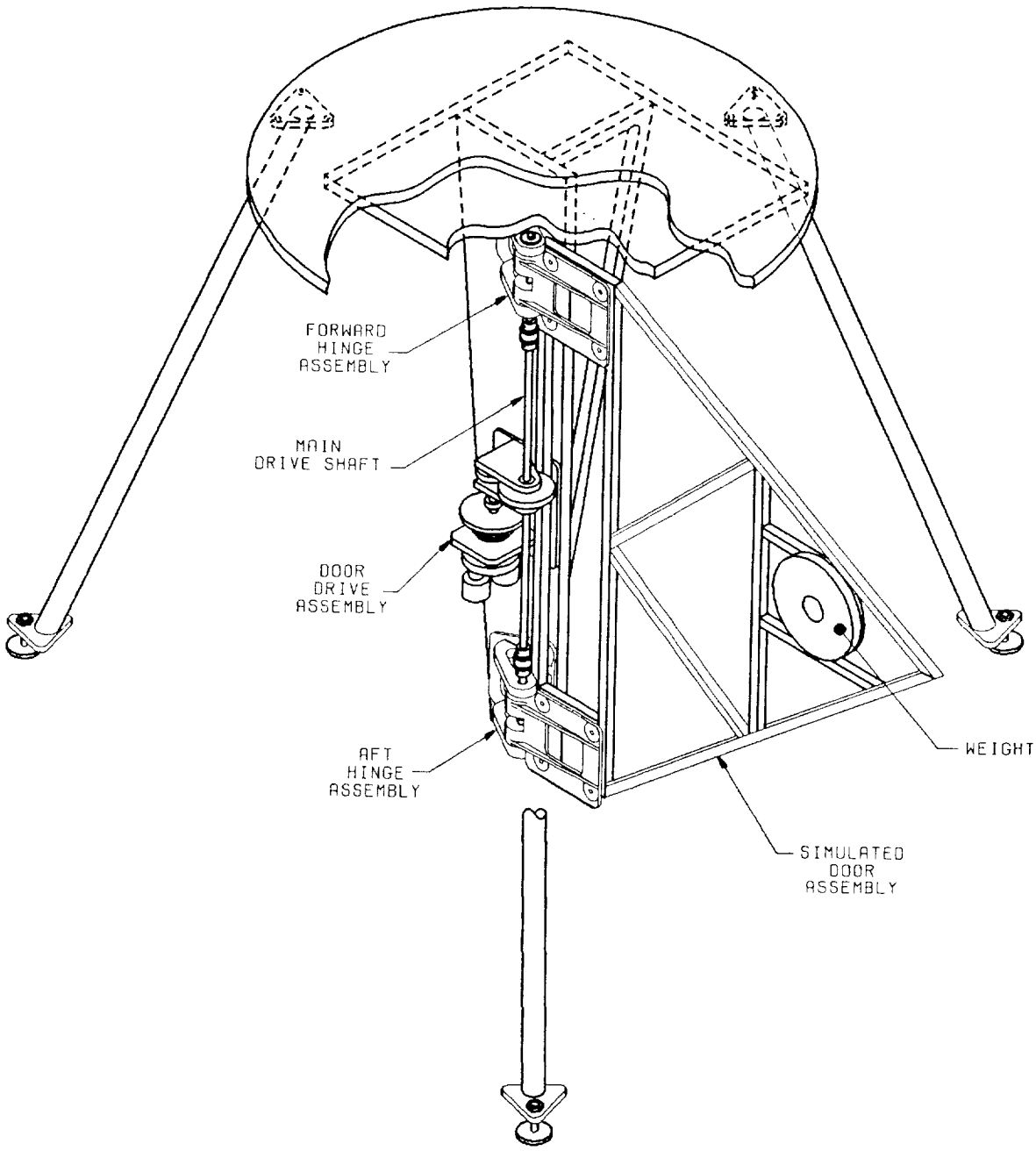

H0-4001/007

Figure 13 . Driveline Special Test Equipment

ORBITAL MANEUVERING VEHICLE (OMV) THREE-POINT DOCKING LATCH

W. Neill Myers, John C. Forbes, and Wayne L. Barnes*

ABSTRACT

The primary purpose of the OMV is to dock with orbiting payloads and then either transfer them to a different orbit or return them to the Space Shuttle for servicing. Some such missions will involve docking with payloads equipped with a Flight Support System (FSS) type of interface; an example is the Hubble Space Telescope (HST). This paper describes the design and development of a mechanism to be used for testing this docking concept on the MSFC test beds. The test results to date are also presented.

HISTORY

The FSS interface was developed as a standard means of supporting payloads while in the Shuttle cargo bay, and, with the aid of the Shuttle Remote Manipulator System, it was intended for berthing operations only. However, the OMV is required to dock with payloads equipped with this interface. While these docking conditions can be computer simulated, testing is required to verify this model and discover any potential design problems. Therefore, beginning early in the OMV program, MSFC developed the hardware required for this testing.

DESIGN AND OPERATION

The test hardware consists of three latches and mounting structure which simulates the OMV Three-Point Docking Mechanism (TPDM; See Figure 1). The HST FSS trunnions were used in sizing the latch. The "three-point docking" interface consists of three 1.5 inch diameter trunnion rails equally spaced on the payload at a six foot diameter mounting circle.

The latch mechanism design has several unique features in relation to existing mechanisms of its type. These are:

- Trunnion rail sensing and automatic operation
- A relatively large capture envelope
- Speed control for relatively quick trunnion containment and slow trunnion pulling/latching
- A large pulling force capability
- The ability to capture a rail without precise alignment

* NASA, Marshall Space Flight Center, Huntsville, Alabama

- o After capture, the ability to lock the trunnion onto the supporting structure, thereby removing the handling loads from the drive mechanism, and
- o The ability to release the latches to free the trunnion rail.

The latch mechanism (See Figures 2 and 3) includes three intermeshing rotatable fingers which are located between two faceplates. The V-shaped cutout in these plates defines the capture envelope for a trunnion (+/- 3.5 inches wide by 4.0 inches deep). The power for the fingers is supplied by a one foot-pound torque motor acting through a harmonic drive with a speed reduction of 160:1.

The operation of a single latch begins with the fingers fully open and clear of the capture envelope. When a trunnion rail enters the envelope, this action is detected by the breaking of an infrared beam which spans the upper section of the V-shape. Through electronics, the fingers are commanded to close at a set rate controlled by tachometer feedback. A second infrared beam is used to detect any escape of the trunnion prior to its containment by the fingers. When this containment position is reached, as determined by a rotary potentiometer, latch closure ceases.

At this point, the fingers would contain the trunnion until the other two trunnions have been contained by their respective latches. All three latches will then be commanded to close at a slow rate (to limit the accelerations imparted to the captured payload).

As a trunnion is pulled into the latch recess, it moves past four locking pawls and deflects a spring loaded pad. When the pad deflection reaches a given point, the spring loaded locking pawls open to contain the trunnion. A linear variable displacement transducer (LVDT) under the pad signals that this point has been reached, and power to the latch motor is cutoff. The trunnion is thus locked between the locking pawls and the spring loaded pad.

The faceplate/finger assembly is mounted on a base by a pivot pin. This allows the assembly to cock (+/- 5^{o}) until stop surfaces are reached. A leaf spring, which is attached to the pivot pin and retained in the base by pins, provides centering. The ability of the mechanism to cock about the pivot allows the trunnion crossbar to fully enter the recess and engage all four pawls, even if the crossbar was not originally parallel to the recess.

When the captured payload is to be released, the latches are commanded to open. As the fingers of a latch reach the fully open position, they actuate cam mechanisms which retract the locking pawls via links and free the trunnion. This is indicated by the LVDT position and the latch opening is stopped.

TESTING

Phase one of testing involved the use of a single latch mechanism to verify that both MSFC test facilities, the Flat Floor and the Six Degree-of-Freedom (6-DOF) Test Bed, give consistent results. The Flat Floor facility tests involved attaching the mechanism to an air bearing vehicle which was propelled at various speeds (up to 0.1 ft/sec) and trajectories across a flat epoxy floor. Latch operation began when a trunnion rail, which was fixed to a massive stationary structure, entered the capture envelope. The contact of the two simulated vehicles was much more dynamic than had been predicted. Some test cases, which were within the requirement ranges for OMV, nearly resulted in trunnion escape. These cases reinforced MSFC's argument that the OMV TPDM should have automatic closure due to the three second OMV to ground time delay.

About half of the fifty Flat Floor tests were repeated at the 6-DOF facility. This test bed uses computer controlled hydraulic actuators to move a large table to which the test mechanism is mounted. The payload docking interface is attached to the ceiling. The test parameters were setup to simulate the Flat Floor vehicle and a 3-DOF system. Kinematic data from these tests compared extremely well with the data from the earlier tests. The 6-DOF facility, having been calibrated and validated, could now be used for Phase two testing.

The objective of Phase two is to measure, analyze and document TPDM contact dynamics with the 6-DOF facility. Docking of the OMV with various payloads (from about 3000 to 78000 pounds) will be simulated by using three of the latch mechanisms. The 25000 pound HST will be given special emphasis. Issues to be investigated include latch closing profile and sequence, docking loads, and optimum infrared sensor location. This test phase is scheduled to begin in February 1990.

Phase three will involve piloted control of the docking process and will verify man-in-the-loop operations with the TPDM. This series of tests is to be performed later in 1990.

CONCLUSIONS

The tests performed to date have resulted in several changes to the OMV TPDM latch design. These include the change to a V-shaped capture envelope which is very similar to MSFC's design. This change provides for more predictable contact dynamics as well as the added material required for mounting the infrared sensors. The other design modifications include provisions for automatic closure and two step/two speed operation. Hopefully, the results of test phases two and three will determine if the latch design needs further refinement.

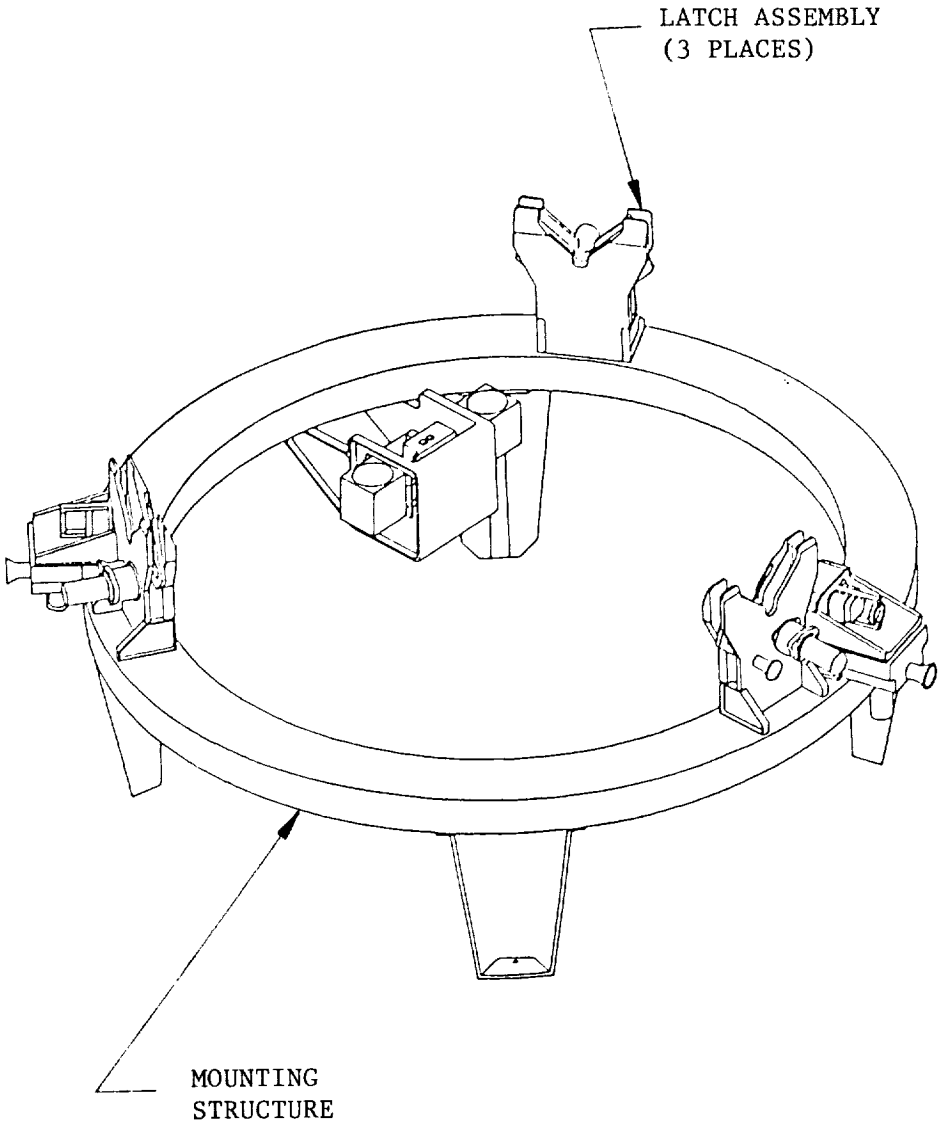

OMV TPDM

FIGURE 1

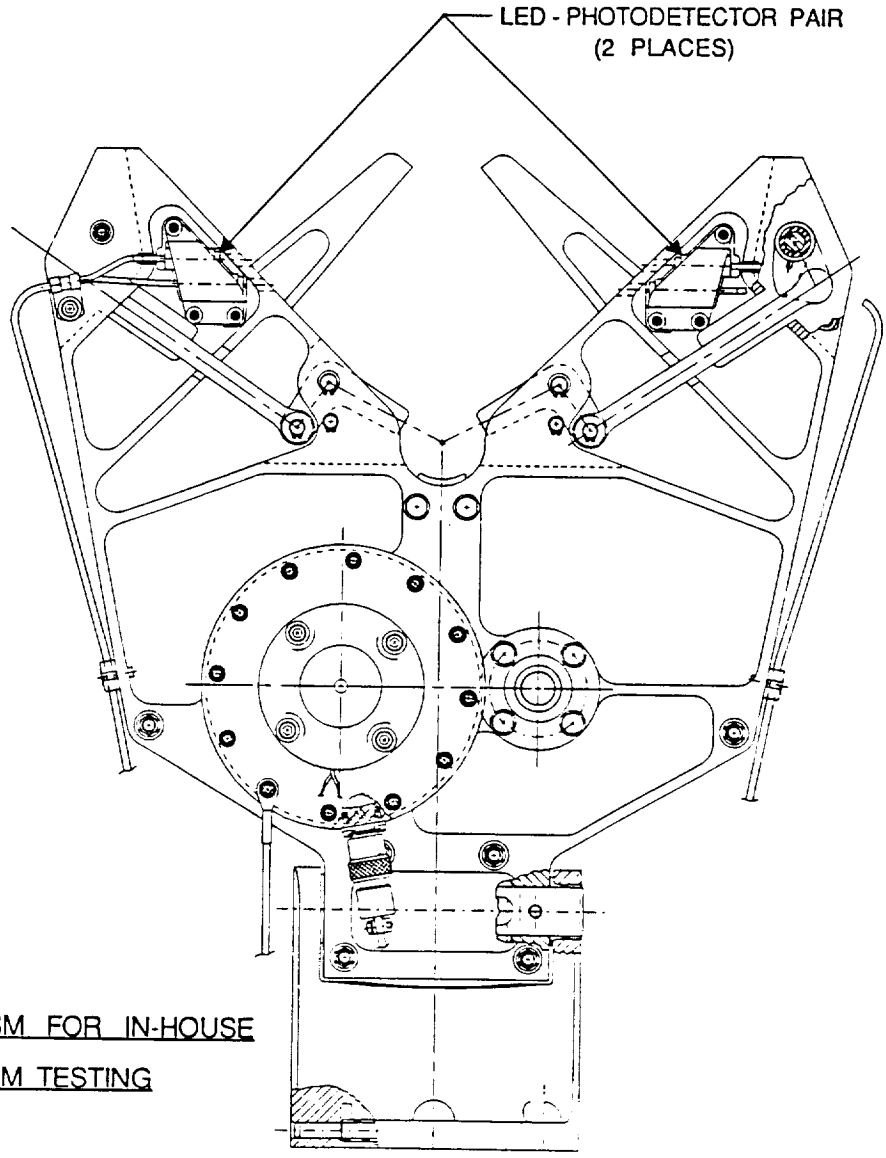
LED - PHOTODETECTOR PAIR
(2 PLACES)
MECHANISM FOR IN-HOUSE
TPDM TESTING

FIGURE 2

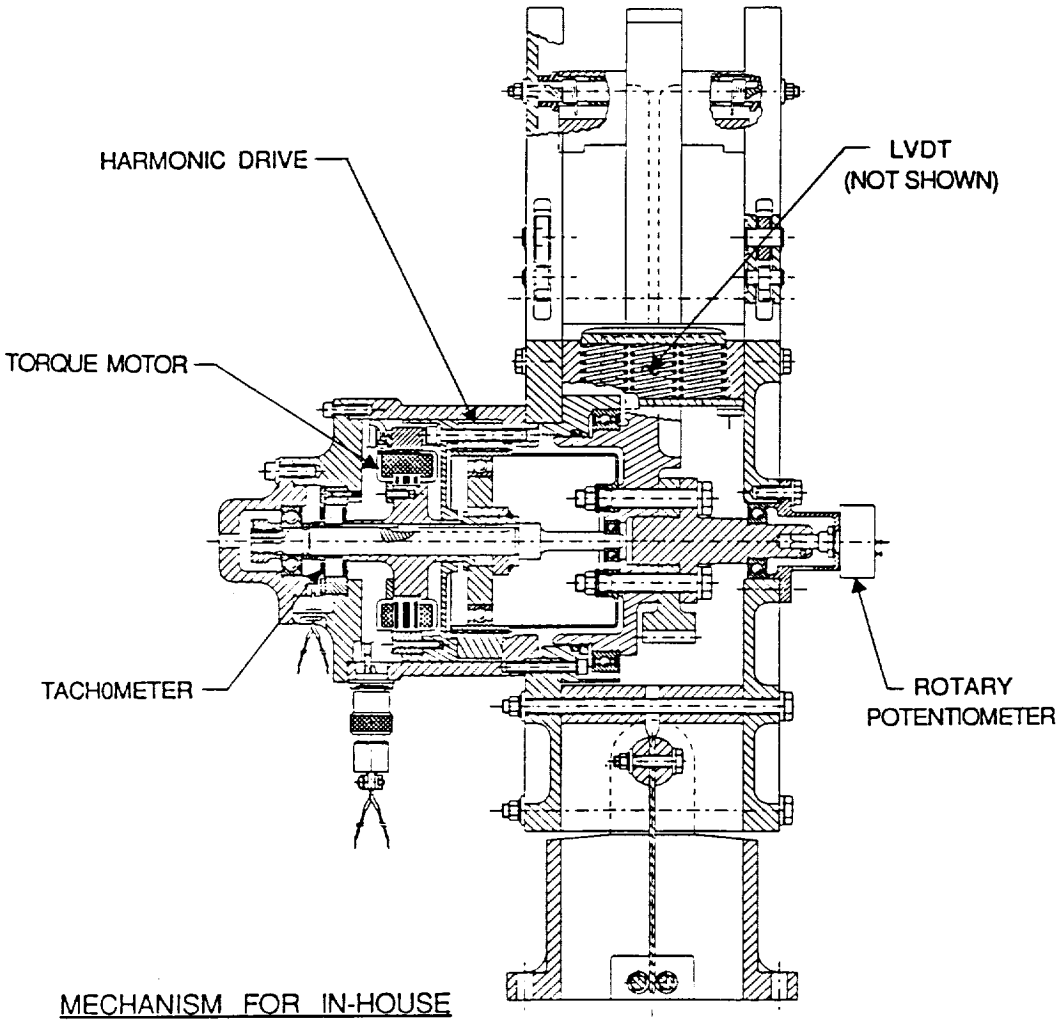

MECHANISM FOR IN-HOUSE TPDM TESTING

FIGURE 3

N90-22095

Experience With Synthetic Fluorinated Fluid Lubricants

Peter L. Conley and John J. Bohner*

Abstract

Since the late 1970's, the wet lubricant of choice for space mechanisms has been one of the family of synthetic perfluoropolyalkyl-ether (PFPE) compounds, namely Fomblin Z-25 (Bray-815Z) or Dupont's Krytox 143xx series. While offering the advantages of extremely low vapor pressures and wide temperature ranges, these oils and derived greases have a complex chemistry compared to the more familiar natural and synthetic hydrocarbons. Many aerospace companies have conducted test programs to characterize the behavior of these compounds in a space environment, resulting in a large body of hard knowledge as well as considerable "space lore" concerning the suitability of the lubricants for particular applications and techniques for successful application. This paper summarizes the facts and dispels a few myths about the compounds, and provides some performance guidelines for the mechanism design engineer.

Background

Most mechanism designers have been confronted with the difficulties of effectively lubricating mechanisms for a space environment. A wet lubricant offers major advantages over a solid lubricant: the liquid will flow and replenish used lubricant, a liquid will not form unpredictable solid debris, and a liquid offers the potential for elastohydrodynamic (EHD) lubrication if speeds are great enough. However, the central problems of a deep space vacuum, long unattended operation, and severe thermal environments preclude the use of most liquids without resort to cumbersome seals or heaters.

In the early 1970's, two series of synthetic fluorinated fluids became available. One series is based on Monte Edison's Fomblin Z-25 oil and includes Bray (now Burma-Castrol) -815Z oil, along with 3L-38, 3L-38RP, 600, 601, and 602 greases. A slightly different base oil chemistry was used to formulate the Dupont Krytox 143xx series of

* Hughes Aircraft Company, Space & Communications Group
El Segundo, California

fluids. These fluids are generally known as perfluoropolyalkylether (PFPE or PFAE) compounds: they are synthetic fluorocarbons.

Examples of typical oil types that have been used effectively in space are listed in Table 1, along with room temperature vapor pressure and viscosity data. Figures 1 and 2 illustrate the difficulties of a space environment in a simplified fashion. Figure 1, calculated using the Langmuir equation[1], illustrates the rapid loss of oil from a mechanism at even moderate temperatures. It is interesting to note that the natural super-refined hydrocarbon outperforms all but the synthetic fluorocarbons. Figure 2 shows the approximate pour points of the same oils, illustrating the principal disadvantage of the natural material.

It is clear that the synthetic fluorocarbons, and in particular the Bray-815Z oil, offer very clear advantages over any other available lubricant.

Drawbacks

With such an obvious advantage regarding the space environment, the synthetic fluorocarbons appeared initially to be something of a panacea for space lubrication problems. However, early testing revealed surprises regarding performance of the oils in boundary (non-EHD) lubrication situations. A few cases are listed below.

- 1980: Hughes tested several of the Bray compounds for use in a large precision oscillating gimbal application. The results were unacceptable, shown in Figure 3. At the conclusion of the test, the oil had been polymerized, resembling brown sugar.

- 1983: the European Space Tribology Lab reported[2] on a similar phenomenon, and equally unacceptable results at various speeds. The same report contains an account of severe wear, substrate damage, and lubricant polymerization using the Fomblin Z-25 oil in a relatively short-lived gear drive.

- 1984: NASA completed long-term vacuum testing[3] of a large number of lubricants in small bearings at relatively high speed as well as start/stop operation, and concluded that the PFPE lubricants performed well under these conditions.

- 1984: the authors tested bearing performance for a 10-degree scanning mirror design. Our results were extremely interesting, as shown in Figure 4. The oil was not substantially polymerized. However, grooves approximately 1.25 microns deep had been milled into the inner race along each ball path.

- 1984-1988: Aerospace Corporation published[4-6] a series of papers describing oil polymerization and the chemistry of iron fluoride formation with ball bearing steels.

- 1985: Hughes Electro-Optical Data Systems Group conducted tests[7] with PFPE oils and greases under both boundary and EHD conditions, using both steel (AISI 440C) and ceramic (Norton Noralide silicon nitride) balls and 440C races. The results confirmed those published earlier. With steel balls, the grease polymerized quickly under boundary conditions, while oil polymerized slowly and repeatably in EHD. Contaminated grease outlasted the non-contaminated sample. Most importantly, for the duration of this test, the ceramic balls prevented the now-familiar polymerization under boundary conditions.

Similar data has been reported from many sources. It has become quite apparent that the PFPE oils and greases cannot be used without a careful assessment of the real tribological conditions of an application. Applications should be reviewed in light of the conditions which are known to result in oil breakdown. With this knowledge, new applications can be evaluated quantitatively and steps taken prior to test failures.

Chemical Behavior

The unique chemistry which imparts the marvelous physical properties to the PFPEs is also responsible for their strange behavior in metal-to-metal contacts of various applications. While the PFPEs are quite similar, the Fomblin Z-25 fluid is a less branched, more linear fluid than the Dupont Krytox fluids. The two structures are shown in Figure 5. The basic repeating units of the Fomblin contain more ether linkages than the Dupont product: the ether bonds are believed to be the weak points of these molecules. As a result of these differences, the Z-25 fluids have better physical properties, but are slightly more susceptible to chemical attack.

While chemically inert to almost everything, including hot hydrofluoric acid, oxygen, and strong bases, all of the PFPEs are subject to catalytic attack by Lewis acids. Table 2 lists some of the common metals which will form fluorides that are Lewis acids. The "Achilles' heel" of these fluids is a tendency to break just a few molecules under severe mechanical stress. When used in mechanisms, this severe stress will tend to occur under boundary lubrication as shown in Figure 6. At the asperity contacts, metal flourides are formed which then go on to catalytically decompose much more of the fluid.

Contact Analysis

It is important to recognize that an exact analysis of the contact conditions in a real mechanism is problematic. In order to produce useful data, a mechanism test must instead be well characterized. To extrapolate results from one test to another, or from a wear test rig to a mechanism, the data must be grouped according to some basic rules. Using these rules, we can outline wear regimes corresponding to predictable success or failure.

1 - Determine the real speeds, loads, and life. Simple estimates of mechanism life are usually incorrect. There are several important considerations to include in a life profile.

- Many mechanisms are used within a control loop which results in a complicated tracking profile, which may include dither life about a single point.
- Payload oscillations should be calculated: these frequently contribute significantly to the worst case requirements.
- Stepping dynamics should be estimated via simulation or observation.
- Geartrain windup loads will be important for a large payload and a stiff geartrain.
- Motor rotor oscillations should be calculated for the early stages of a geartrain.

2 - Calculate lubricant stress cycles. Under the conditions found above, the actual lubricant stress cycles should be calculated. Ex-

amples are ball crossings over a given race location and the number of times an individual gear tooth moves through contact.

The catalytic reactions described in the preceding sections all require a certain number of lubricant stress cycles to develop significant products. Using stress cycles as a criterion will predict the failure of a bearing due to dither or control system noise: total degrees traveled or equivalent revolutions will not. In addition, oscillating applications can be compared directly to continuously rotating applications using the stress cycles criterion.

3 - Calculate maximum contact (Hertzian) stresses during each lubricant stress cycle. Higher loads will mean a greater amount of fresh metal exposed in the contact for catalysis, and will result in shorter lives for a given material combination. Reference 5 indicates a life dependence on contact stress, but at loads higher than would be found in a well designed mechanism. We have also found some slight correlation between loads and life: unloaded motor bearings tend to have long life expectancies.

4 - Check for EHD conditions. It has been shown[2,7] that PFPE oils will decompose under calculated EHD conditions as well as boundary, although at a much slower rate. In our experience, few space mechanisms ever get into EHD. Gear teeth are particularly unlikely to ever get out of boundary conditions.

Chemical Prevention

The key to chemically preventing the oil decomposition is to prevent the catalytic action of strong Lewis acids on the functional surfaces. The easiest way to do this is to prevent acid formation by not imparting high stress to the oil, i.e., stay in full EHD. As this is not possible, passivation of the functional surfaces is necessary. This can be accomplished by using surface materials which either don't form Lewis acids such as ceramics, or other materials which form weak acids in thin films. Curiously, normally inert gold is a moderate Lewis acid former and has been found[8] to be unacceptable when used with PFPEs in slip ring applications. The use of ceramics, in the form of hardcoatings like TiN or TiC or as a bulk like Si_3N_4, is an excellent way to reduce or eliminate catalytic breakdown. Conventional nitride hardcoatings, which result in inert "white layers", have also proved to be effective.

Based on the contact calculations, we suggest that life data be broken down into plots for each material system and lubrication regime. The next sections summarize some data which can be used to evaluate new designs.

Geartrain Data

Figure 7 summarizes years of data on the small geartrains typical of space mechanism design. Since we moved away from dry lubricants in the early 1980's, Hughes has successfully flown or qualified hundreds of gearhead designs using Bray 600 grease. All of these are stepper motor driven and use a martensitic steel base material, typically PH 13-8 Mo. Gear sizes run from 120 DP to 32 DP.

Several methods have been used to avoid grease degradation, depending on the severity of the application. We have selected material systems which will delay the polymerization reactions described earlier. Demonstrated performance for several material systems is shown in the figure.

It should be emphasized that none of the reported data represent a failure. However, the indicated bare steel data point is shown in Figure 8. Some evidence of tooth wear is obvious, and analysis of the grease showed steel wear particles. Even the more resistant systems begin to show evidence of wear as we move beyond a life of 1×10^8 stress cycles.

As more demanding applications come along, we intend to push the proven performance envelopes out further in all directions. With forethought about the materials system and the oil supply, the PFPE lubricants will satisfy almost any space gearing application. The environmental advantages of the PFPEs essentially demand their use.

Ball Bearing Data

Ball bearing applications will tend to be much more critical than gearing applications. Traditionally ball bearing applications have been divided into two classes: EHD conditions and boundary lubrication conditions. Our data indicates that with the synthetic fluorocarbons, one must consider oil starvation[9] as a subset of each of these conditions.

Figures 9, 11, and 12 show demonstrated life data for these classes. Taken together, the three figures show a continuous spectrum of the life which can be expected from PFPE lubricants in ball bearing applications.

EHD Data

Figure 9 shows several data points for EHD applications. Based on the information from reference 2, the erratic torque behavior found in the high-speed application could have been predicted and avoided. Instead we have more data confirming the earlier work, where it was suggested that oil breakdown gradually results in a starvation phenomenon and increased breakdown. Figure 10 shows the degraded oil following the test.

Boundary Data - Starved Conditions

Figure 11 indicates the rapid onset of bearing failure under boundary conditions if there is inadequate oil available. The result of the lubricant breakdown is a rapid increase in bearing friction torque (see Figure 3). In one of the tests shown, replacement of the 440C balls with Si_3N_4 balls eliminated the breakdown for the duration of this test.

The chemical breakdown of the oil results in a consumption of the available supply. Thus, rapid starvation of a bearing can occur with these lubricants. A bearing design used successfully with a different lubricant may seem to exhibit anomalous behavior with a synthetic fluorocarbon. Comparison of Figures 11 and 12 shows that life under starved conditions will be predictably shorter than under normal boundary conditions.

Starvation will result whenever an excess supply of oil is not available at the contact. A few situations which will cause this are:

- Grease-plating or a similar thin film deposition of oil. The original rationale for using these techniques is that only a few molecules in the contact are needed to do the lubrication. This does not allow for oil breakdown or loss.

- A non-porous ball retainer. The retainer should be designed to function as a reservoir. This will renew the oil supply in the contact and dilute the breakdown products.

- Insufficient renewal of the contacting surfaces. In 1980, our 4 degree oscillation test demonstrated this dramatically. The rocking motion did not supply fresh oil to the contact, and the foam retainer was an ineffective reservoir as a result.

Boundary Data - Flooded Conditions

Even with adequate oil available at the contact, breakdown will still occur and some chemical side effects begin to appear: great care should be exercised as we get beyond 10^6 stress cycles. Noticeable changes in bearing torque will not show up until much later, as the entire oil supply becomes affected. Figure 12 indicates the lives demonstrated for well-lubricated bearings under a variety of conditions.

On the far right of the figure are a few examples of very small (approximately 1 cm outside diameter) stepper motor bearings. They are not preloaded and are insensitive to small dimensional changes as well as torque noise. These bearings proved to be entirely satisfactory for the lives indicated, although the oil had been virtually used up, as shown in Figures 13. A reasonable upper bound for this type of application without using ceramic coatings or balls would be $5x10^8$ crossings.

The other bearings in the figure showed minor (<100%) torque increases. This will often not be significant, and the lives indicated can be realized for deployment and most positioning mechanisms. However, we find that the oil breakdown products result in a chemical wear phenomenon which could be very significant for precision gimbal applications.

Wear Rate Data

Post-test disassembly and profilometry of some of the test bearings shows that the action of the oil decomposition removes significant amounts of metal from the active race surfaces, as shown in Figure 4. The amount of material removed will most likely not be significant for bearings preloaded with a spring, or in applications which are not preload-sensitive. For rigid duplex pairs, the preload changes may result in stiffness losses which are unacceptable.

Figure 14 summarizes our available data. Note that the ordinate is the total material lost from both races. We have found that while the inner and outer races do not wear evenly, the total wear is consistent. Two types of bearing preload are represented. We have measured material lost from a bearing with a constant preload, for example that

provided with a constant force spring. In the same test, we measured material lost from a rigid duplex pair of the same design.

For a bearing under constant load, we would expect that the wear rate would decrease as the surfaces become smoother and conform better, but never go to zero. We suggest that an estimate of loss rate can be obtained using an expression of the form:

$$\text{Wear} = K1 * \ln[L/Lo],$$

where L is the life in stress cycles, Lo is selected as the initiation of wear at cycle 1, and K1 is a constant which depends on the application. This line is shown in the figure. The two data points indicated seem to lie roughly on the same line (K = 0.133), although they are from different bearings. The two had identical material systems and similar contact stresses and oil supply.

For the duplex pair, we would expect that the wear rate would decrease rapidly as the preload is reduced, reaching zero when the preload stickout is eliminated. This suggests an expression of the form:

$$\text{Wear} = Wo * \{1 - e^{-C * \ln[L/Lo]}\},$$

where Wo is the total approach of the two races under preload, and C is chosen to match the data.

These formulas are simplified fits to a complex situation. The physics dictate that the initial wear rates would be the same regardless of loading. The form of the first equation could be altered to provide for this, but we do not feel that the data are adequate to support a more complex model.

Closure

Traditional techniques to impart enhanced boundary performance to the PFPEs by using chemical additives have also been attempted. Those efforts have been thwarted by the lack of solubility of appropriate additives in the base oils. Reports continue to circulate of new and successful compounds which will work but the published literature (and indeed the availability of such compounds) is sparse. The approach does hold merit if the chemistry can be solved.

In our experience various methods to mitigate the oil breakdown, be it deliberate contamination, surface layers, or ceramics, have extended the life of PFPE systems. The methods have widely different cost and an effectiveness that roughly parallels the increased costs. It is the responsibility of the designer to characterize a particular application and select appropriate protection from the ravages of chemistry. Instead of selecting a different lubricant, comparing the life requirements of a new application to the accumulated data may allow use of the PFPEs for their unequalled environmental properties.

References

1. Handbook of High Vacuum Engineering, Reinhold Publishing Co., H.A. Steinherz, editor.

2. Stevens, K.T., "Some Observations on the Performance of Fomblin Z-25 Oil and Braycote 3L-38RP Grease in Ball Bearings and Gear Boxes", Proc. of the 1st European Sym. on Space Mechanisms and Tribology, Oct. 1983, pp 109-117.

3. McMurtrey, E.L., "An Evaluation of Grease-type Ball Bearing Lubricants Operating in Various Environments", N85-11239 (NASA TM-86480), Oct. 1984.

4. Carre, D.J., "Perfluoropolyalkylether Oil Degradation: Inference of FeF_3 Formation on Steel Surfaces under Boundary Conditions", ASLE Preprint No. 85-AM-3H-1, Feb 1985

5. Carre, D.J., "The Performance of Perfluoropolyalkylether Oils Under Boundary Lubrication Conditions", AD-A191 057, Feb 1988

6. Carre, D.J., "Perfluoropolyalkylether Lubricants under Boundary Conditions: Iron Catalysis of Lubricant Degradation", Report No. SD-TR-88-27, Mar 1988.

7. Personal conversation with L.C. Lipp and K. Christopoulos of Hughes EDSG.

8. Personal conversation with J. Glosbrenner of Litton Polyscientific.

9. Brewe, D.E. and Hamrock, B.J., "Analysis of Starvation Effects on Hydrodynamic Lubrication in Nonconforming Contacts", Trans. ASME, V01. 104, July 1982, pp 410-420.

Table 1
Typical Oils for Space Use
20 C Properties

Type Designation	Trade Name	VaporPressure (torr)	Viscosity (CSt)	Pressure/Viscosity Coefficient (@400 MPa)
Natural Hydrocarbon	Apiezon C	3.5×10^{-9}	283	1.2×10^{-4}
Synthetic Hydrocarbon (PAO)	Nye 176A	6.6 x 10-9	1050	1.1×10^{-4}
Synthetic Fluorocarbon	Bray-815Z	8.7×10^{-12}	180	6.8×10^{-5}
	Krytox 143AC	1.2×10^{-9}	720	
Neopentyl-polyolester	Nye NPE UC-7	5.1×10^{-9}	75	N/A
	Nye NPE UC-4	2.1×10^{-8}	44	

Table 2
Representative Lewis-acid Forming Metals

Name	RelativeReactivity
Titanium	100
Aluminum	35
AISI 440C	22
Iron	12
Gold	6

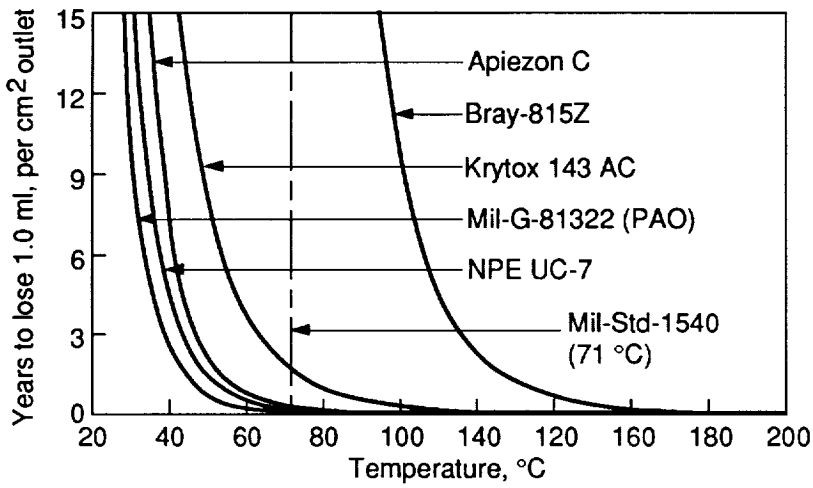

FIGURE 1. RELATIVE EVAPORATION OF REPRESENTATIVE AEROSPACE LUBRICANTS

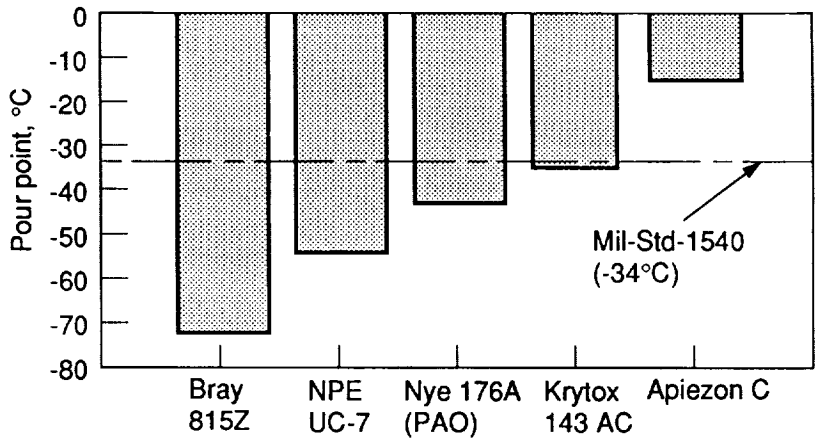

FIGURE 2. TYPICAL AEROSPACE LUBRICANT POUR POINTS

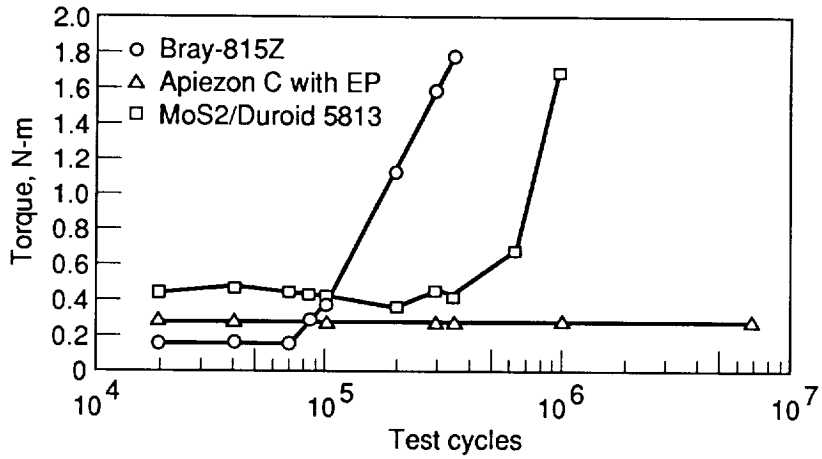

FIGURE 3. 1980 OSCILLATING GIMBAL TEST
Lubricant Comparison, 4 deg Peak-to-Peak

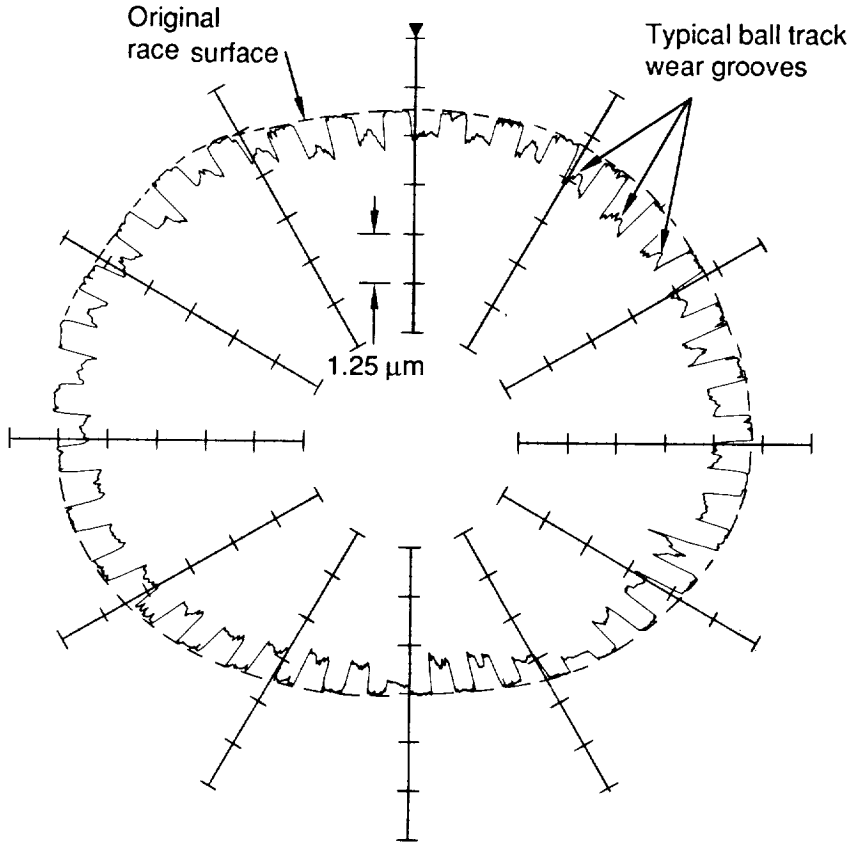

FIGURE 4. INNER RACE PROFILOMETER TRACE:
FOLLOWING 20 MILLION CROSSINGS

Bray-815Z

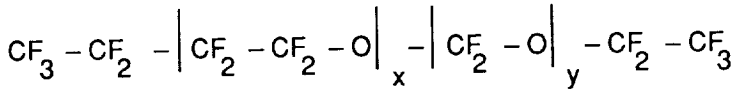

$x = y \simeq 50$

Krytox 143 xx

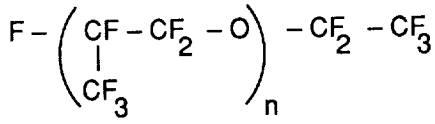

$n = 10$ to 60

FIGURE 5. APPROXIMATE CHEMICAL STRUCTURE FOR TWO TYPES OF PERFLUOROALKYLPOLYETHERS (PFAE, PFPE)

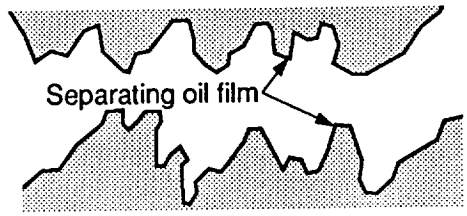

a) Elastohydrodynamic Lubrication (EHD)

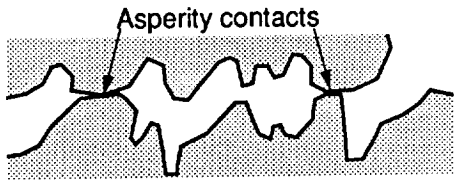

b) Boundary Lubrication

FIGURE 6. LUBRICATION REGIMES

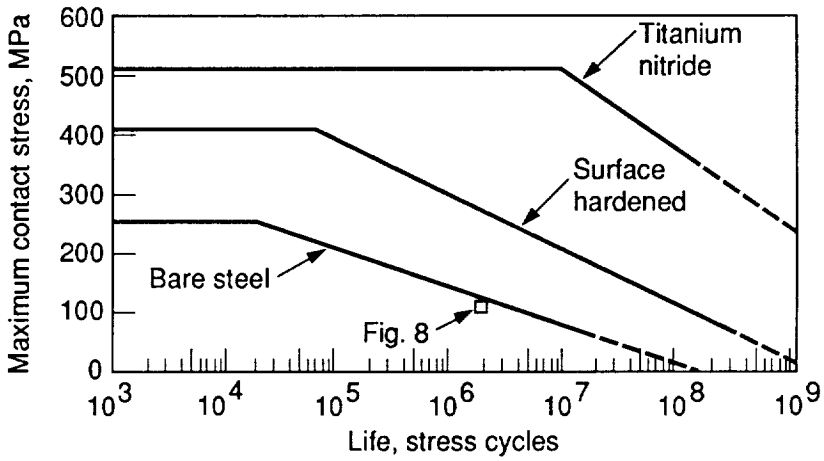

FIGURE 7. GEARTRAIN EXPERIENCE ENVELOPES
Contact Stress vs Stress Cycles
Bray-600 and Martensitic PH CRES

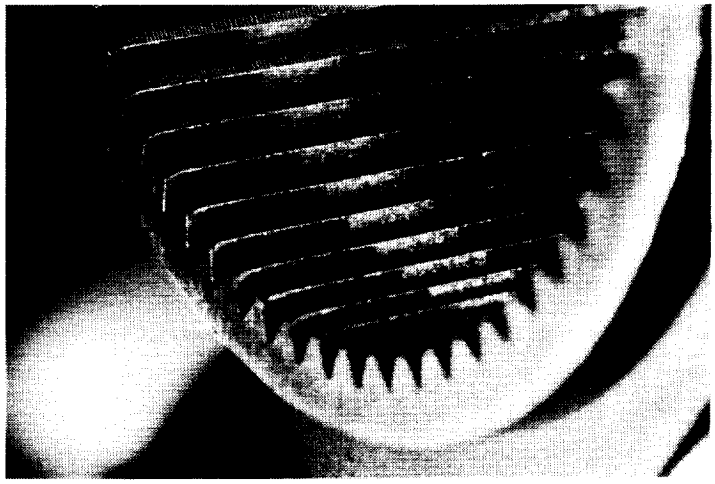

89SC-08417-15

FIGURE 8. DATA POINT FROM FIGURE 7

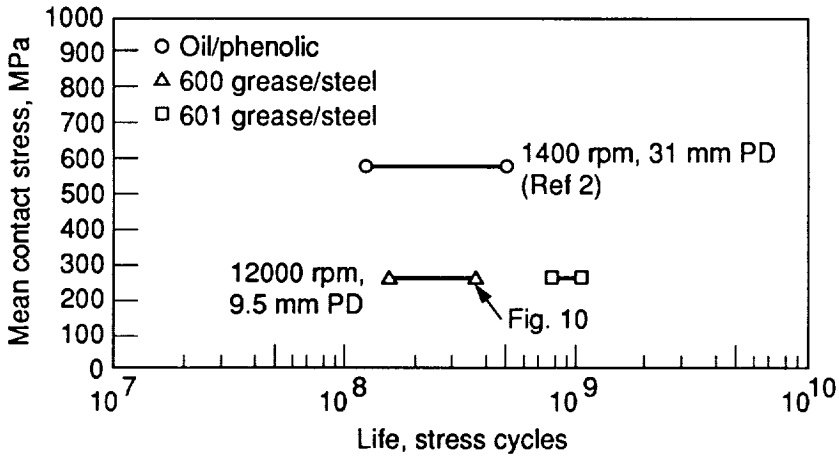

FIGURE 9. BALL BEARING DATA POINTS
Ranges of Observed Breakdown Despite EHD Prediction
Bray-815Z and Derivative Greases

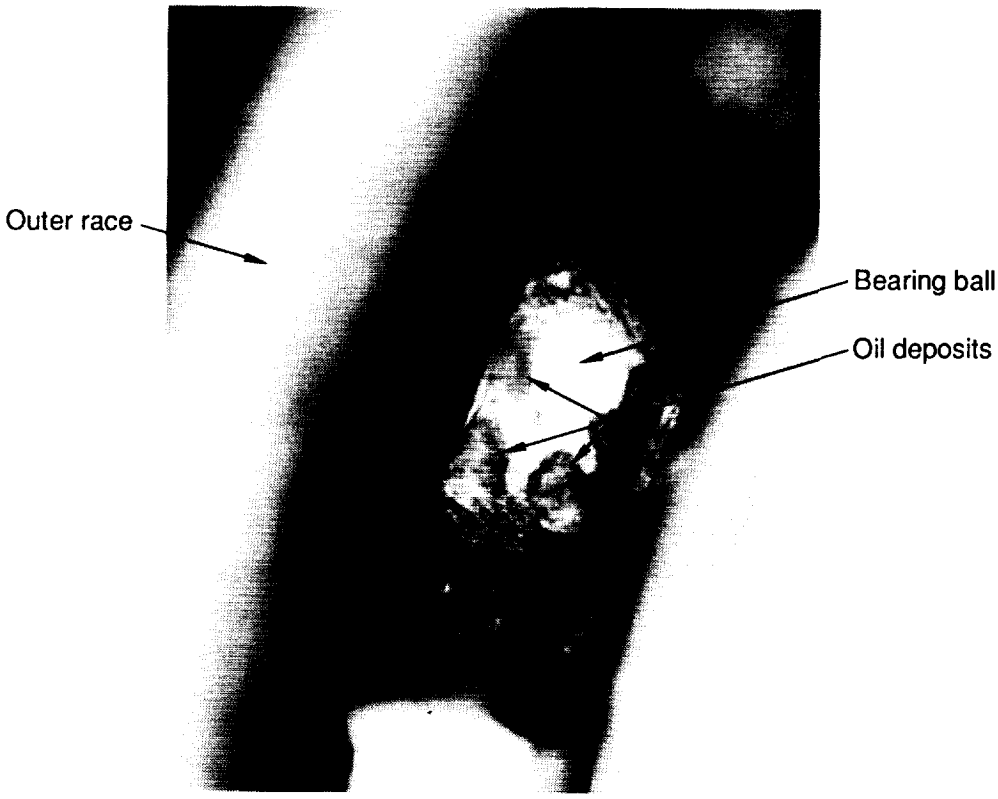

FIGURE 10. MACRO PHOTOGRAPH OF
9.5 mm BEARING FOLLOWING TEST

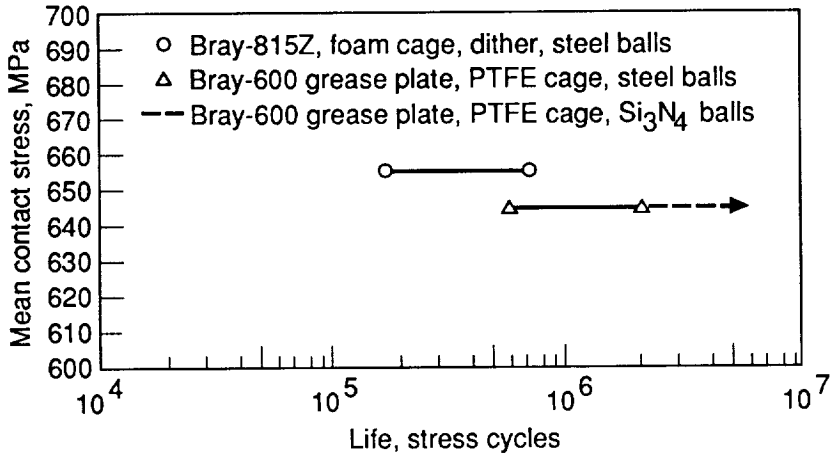

FIGURE 11. BALL BEARING DATA POINTS
Insufficient Oil Breakdown Ranges
Bray Oil and Grease, AISI 440C

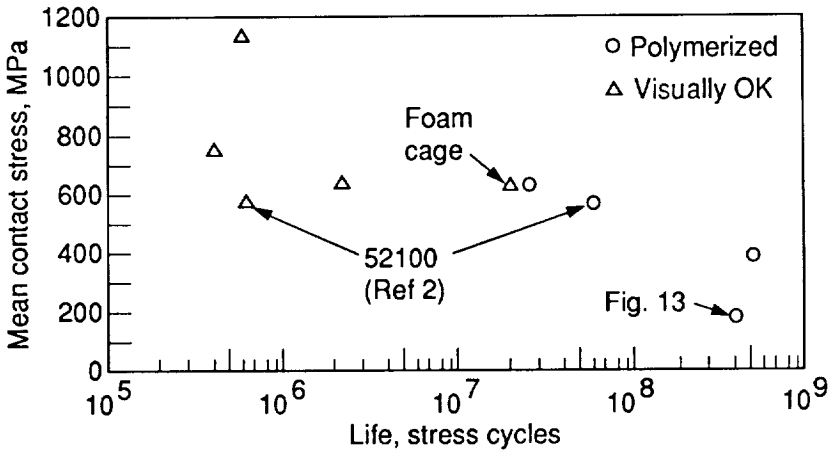

FIGURE 12. BALL BEARING DATA POINTS
Breakdown Under Boundary Lubrication
Bray-815Z, Phenolic Cage, AISI 440C

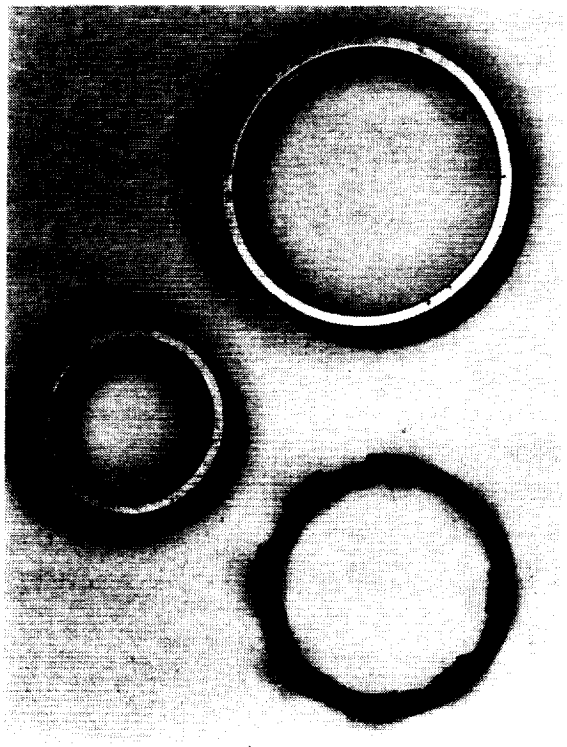

88-95915

FIGURE 13a. RACES AND RETAINER FOLLOWING TEST

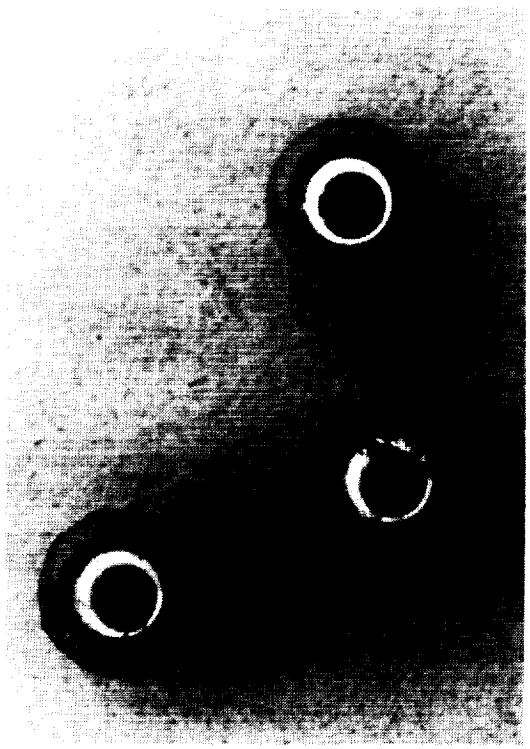

88-95914

FIGURE 13b. BALLS FOLLOWING TEST

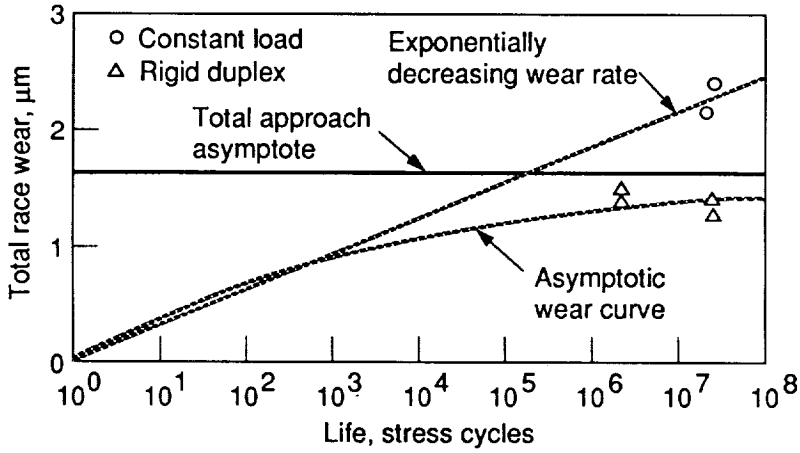

FIGURE 14. BALL BEARING DATA POINTS
Chemical Wear: Preload Loss
Bray-815Z, Foam/Phenolic, AISI 440C

N90-22096

TRIBOMATERIAL FACTORS IN SPACE MECHANISM BRAKE PERFORMANCE

H.M.Hawthorne*

ABSTRACT

The asbestos/phenolic pads of SRMS brakes are unsuitable for use in long-life space mechanisms because their friction decreases on extended sliding in high vacuum. Dehydration of the material and accumulation of wear debris in the conforming interface of this tribosystem induces the permanent friction changes. Other polymer and some ceramic based materials exhibit similar frictional torque behaviour due to the development of minimal contact patches by the interfacial debris. In contrast, high friction occurs when other ceramics form many small contacts throughout fine debris beds. Generating this latter interfacial structure during run-in ensures that the in-vacuo friction remains stable thereafter. Such materials with low wear rates are potential candidates for friction elements in SSRMS and similar mechanisms.

INTRODUCTION

The friction elements of Shuttle Remote Manipulator System (SRMS) brake and clutch assemblies are pairs of annular pads of an asbestos/phenolic composition. These components meet all the performance requirements, such as those of back-up arrest of arm motion or joint holding, anticipated for short duration Shuttle missions. However, when extensively slip tested under load, these pads can exhibit a greatly diminished friction output in-vacuo [1,2], which fully recovers on return to atmosphere. It was initially thought that this was an anomaly which occurred unpredictably when sliding in vacuum. However, it is now known [3] that a reduced friction torque is the normal output from this tribosystem after equilibrium in the vacuum environment has been attained. This torque variability means that asbestos/phenolic material is not suitable for friction elements in mechanisms subject to long exposure to space vacuum, such as those of the Space Station Remote Manipulator System (SSRMS).

Studies have been carried out to seek materials which will exhibit stable, high friction behaviour in this conforming contact in high vacuum. Simulation testing is described and the results for both SRMS brake, and these other, materials are presented and discussed in relation to the wear debris microstructure which develops at the sliding interfaces in this tribosystem.

EXPERIMENTAL

The materials investigated included polymeric and ceramic based composites, ceramic coatings and cermets. Ring specimens bonded to, or coatings sprayed on, backing discs were ground flat and test surfaces lapped with diamond slurry (ceramics) or SiC paper(polymerics).

*Tribology & Mechanics Laboratory, NRCC, Vancouver, Canada.

A high vacuum tribometer, Figure 1, was evolved to simulate both the chemical environmental aspects (air, vacuum and residual gas species) and mechanical ones such as load, sliding speed and, most importantly, the contact geometry, self-alignment and stiffnesses of the mechanism components. The friction and wear behaviour of materials was determined from tests involving continuous unidirectional, or bi-directional (60s CW/10s off/60s CCW), sliding of one specimen against the other at 100 r.p.m. under normal loads up to 70 N (bearing pressures to ≈ 0.14 MPa) for long periods. Although speed and loads were similar to those of SRMS operation and qualification slip testing [1], the present simulation was both more intensive, because of the higher rate of slip accumulation, and much more extensive.

Tests were performed under hydrocarbon-free conditions, below 1.3×10^{-4} Pa (10^{-6} Torr). Friction torque was monitored throughout all experiments and wear was measured by specimen weight loss. Specimen surfaces were examined by optical and scanning electron microscopy, and by stylus profilometry.

RESULTS AND DISCUSSION

SRMS Brake Material

Extended in-vacuo sliding friction trends for the asbestos/phenolic brake pad specimens (under SRMS loading of 43N) are shown in Figure 2. Whether from unidirectional or bi-directional sliding, these components typically exhibit a drastic reduction in friction torque to about 20% of the run-in value, followed by a slow but only partial, recovery to some value below the minimum allowable level. Even then, further small decreases can occur in frictional torque output, either spontaneously or after some event disturbing the tribosystem.

It has been shown previously [2] that the first stage of this friction torque characteristic, i.e. the drop to minimum levels, is initiated by a reduction in the water vapour concentration available to the sliding interface upon dehydration of the hygroscopic brake composition. The variable onset of the torque drops in Figure 2 reflects different degrees of moisture saturation of the brake material specimens. Although drying must precede it in SRMS material, the low slip torque regime develops as a result of microstructural changes at the sliding interface. Wear debris is generated at the rubbing surfaces and trapped in the conforming contact of this tribosystem, Figure 3, and it is the structure and properties of this dry debris layer which controls the system's in-vacuo properties [2,3]. The minimum and partly recovered friction torque levels result from variations in the extent of this "third-body" [4] debris layer in the interface.

Clearly, low and variable friction torque is inevitable from the extended use of SRMS brake pads in vacuum. Similar tests with several alternative types of materials sliding in this unique tribosystem gave the following results.

Other Polymeric Based Materials

Friction trends from the polymeric materials studied are illustrated in Figure 4. They all developed low friction output on sliding in the high vacuum, much earlier than the asbestos/phenolic composition. The low friction torque of these other polymeric based materials is related to the ready formation of localized wear debris features, Figure 5, on worn specimen surfaces. Microscopic and profilometric examination show these to be proud of the surfaces. It is inferred that such structures bridge the interface during sliding, separating the original sliding surfaces and confining the nominal load-bearing contact to a small fraction of the brake pad area. Although debris shear strength will also have an influence, the low torque output of the system is mainly due to this greatly restricted contact area.

Ceramic Based Materials

Ceramic based materials were found to exhibit widely different sliding friction trends in this high vacuum conforming contact system [5]. After run-in, friction either remained steady at high, moderate or low values over long sliding distances or it behaved in a very unstable manner, as shown in Figure 6. These friction trends were also related to the debris morphology found on worn surfaces. When specimen surfaces had a matte appearance, e.g. as in Figure 7a, friction torque was moderate to high. This was considered to be mainly due to the many, finely distributed, load-bearing debris features on such surfaces, Figure 7b, providing a large total contact footprint during sliding [3,4]. In contrast, low frictional output was obtained when the interface developed relatively few contacts at raised wear debris islands, Figure 8, similar to the polymeric materials. The variable friction of the SiC/TiB_2 material may reflect sliding locus changes from the periodic shedding of parts of these bridging streaks as debris flakes [5].

Engineering the Interface

The behaviour of some ceramic materials in this tribosystem is more complex than was originally reported [5]. Because friction trends were similar in repeat tests, they were thought to be characteristic of a particular material. However, different sliding friction torque trends have now been found with some ceramic specimens in separate tests, e.g. as shown in Figure 9. The correlation between friction trend and wear debris morphology still applies; high friction torque resulting from "full" interfacial contact via the matte debris structures, Figure 7, and low torque output from the system when contact is limited to debris streaks, as in Figure 10. The latter are only ≈ 1 μm thick, yet they can still separate the sliding surfaces.

Whether it is the dense, fine debris bed or the isolated streaks which begin to form during the earliest stages of sliding depends on initial conditions in some way not yet understood. This, and other aspects, including the study of model interfaces, need to be researched

further. However, from a practical perspective several important facts about this tribosystem have been established, viz.:

-- the desired matte textured surface, and hence interface debris morphology, is more readily achieved, using appropriate running-in procedures, with some ceramic materials than others

-- this type of beneficial debris morphology cannot be generated on the polymeric, and some of the ceramic, materials studied

-- once the matte debris bed has been established on run-in surfaces, friction remains stable thereafter, in either uni- or bi-directional sliding in high vacuum.

Thus, the interface between some ceramic-based brake material specimens can be tailored to provide stable high friction torque output from this conforming contact geometry tribosystem.

Wear of Candidate Materials

The sliding wear rates of various materials measured in the present in-vacuo sliding experiments are listed in Table 1. These reflect the wear debris eliminated from the conforming contact during sliding plus any loose debris air blown from specimen surfaces after the tests. Values range above and below those of the asbestos/phenolic composition. Although SSRMS brake slip requirements have not been defined, some of these wear rates should provide long life since the light loads used in space mechanisms ensure that large sliding distances can be sustained before the pads wear away. For example, a material with a specific wear rate of 10^{-4} mm^3/Nm would require two million slip revolutions under SRMS loads to wear through 1.5 mm thick pads. However, minimization of loose wear debris accumulation in brake housings favours use of the lowest wearing materials.

CONCLUSIONS

From these tribological studies of materials in conforming contacts in the vacuum environment, it is concluded that:

- the low friction anomaly of SRMS asbestos/phenolic brake material is an inevitable consequence of its extended use in-vacuo. The friction loss, though partly recoverable, is permanent in a dry environment.

- the in-vacuo friction behaviour of the asbestos/phenolic material is determined first by residual moisture level and then by the extent, structure and properties of a dry interfacial wear debris layer.

- all polymeric compositions studied also develop permanent, very low friction torque from this sliding system, through development of minimal contact patches of wear debris within the brake pad area.

- ceramic materials exhibit various frictional outputs from this tribosystem, depending on interfacial wear debris characteristics. Limited contact area at a few debris islands gives low friction torque while high friction results from more extensive contact at fine debris features distributed throughout the brake pad area.

- the sliding surfaces of some ceramic materials can be tailored, by appropriate run-in procedures, to give the finely distributed wear debris morphology which ensures a stable high friction torque.

- some ceramic-based compositions with stable in-vacuo high friction and low wear rate in the conforming contact brake configuration may be suitable candidates for use in mechanical brakes in long-life space mechanisms, e.g. in Space Station Remote Manipulator Systems.

ACKNOWLEDGMENTS

Thanks are expressed to Sing Yick for assistance with the experiments and to Spar Aerospace Ltd. for partial financial support of this work.

REFERENCES

(1) Trenouth, J.M. and MacKenzie, C.W.: Investigation of an Anomalous Canadarm Brake Behaviour. Can. Aeronautics and Space J., 32, 205-213, 1986.

(2) Hawthorne, H.M.: Wear Debris Induced Friction Anomalies of Organic Brake Materials In Vacuo. Proc. International Wear of Materials Conf., Houston, ASME, Vol.1, 381-387, 1987.

(3) Hawthorne, H.M. and Kavanagh, J.: The Tribology of Space Mechanism Friction Brake Materials. Presented at CASI Symp. on Space Station. Ottawa, Nov. 1989 (to be published in Can. Aeron. & Space J.)

(4) Godet, M.: Third-Bodies in Tribology. Proc. 5th International Congress on Tribology (Eurotrib 89). Helsinki, Vol. 1, 1-15, 1989.

(5) Hawthorne, H.M.: Tribological Aspects of Ceramic Composites in Conforming Contacts. Proc. International Symposium on Advances in Processing and Applications of Ceramic and Metal Matrix Composites, Halifax, Met. Soc. CIM., 452-463, 1989.

TABLE 1.

Wear of polymeric and ceramic based materials in high vacuum conforming contact sliding tests

Material	Specific Wear Rate* ($\times 10^{-5}$ $mm^3/N\ m$)
Polyimide (SP 1)	29
Asbestos/phenolic	1.5 (High μ)
"	1.0 (Mixed μ)
Non-asbestos/phenolic	1.1 (Mixed μ)
PEEK/Glass fibre	0.7
Al_2O_3/TiO_2	43
Si_3N_4/SiC	15 (High μ)
WC/Co	13
Al_2O_3/SiC	11 (High μ)
Al_2O_3	7.5
$Si_3N_4/SiC/TiN$	6.5
SiC/TiB_2	4.5
$Cr_3C_2/NiCr$	0.8
$MoS_2/Nb/Mo/Cu$	0.6
Cr_2O_3	0.6
Si_3N_4/SiC	0.5 (Low μ)
(Cr_2O_3 vs. 440C steel	0.4)
(Al_2O_3 vs. 440C steel	0.2)

*Mean value of two sliding specimen discs

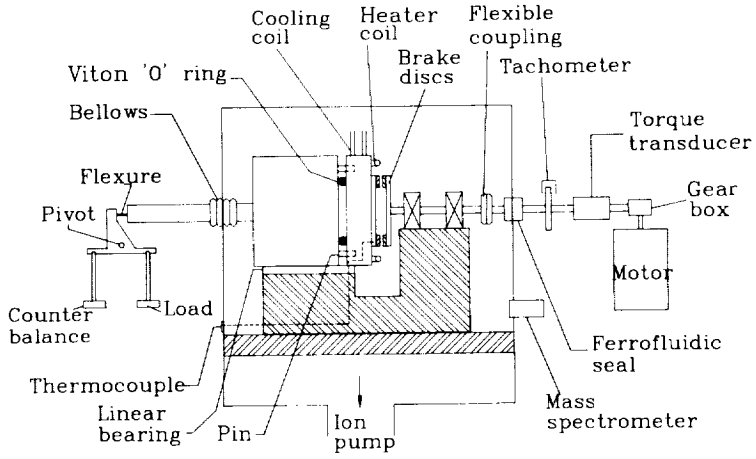

Figure 1. Schematic of the high vacuum tribometer.

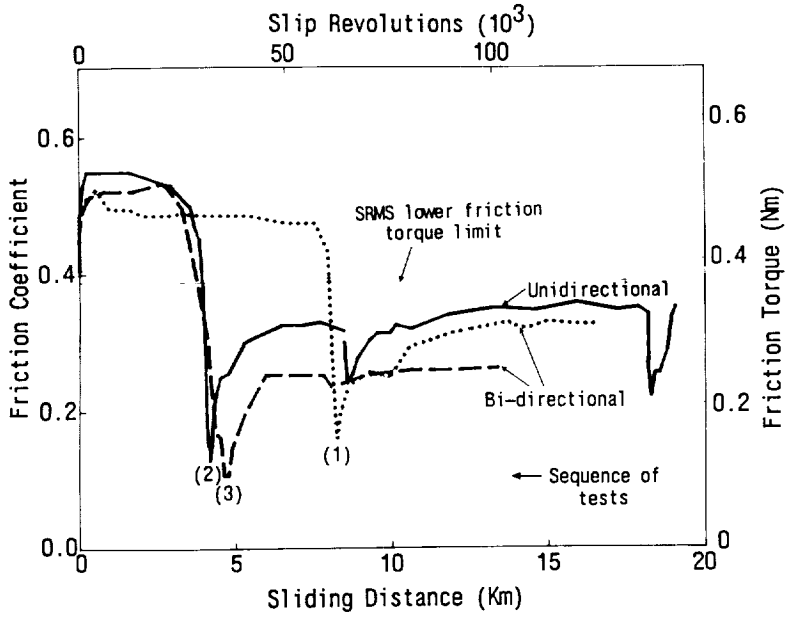

Figure 2. Friction trends from slipping of SRMS brake material in vacuum. First 2 Km (test 1) and 0.2 Km (test 3) were unidirectional run-in.

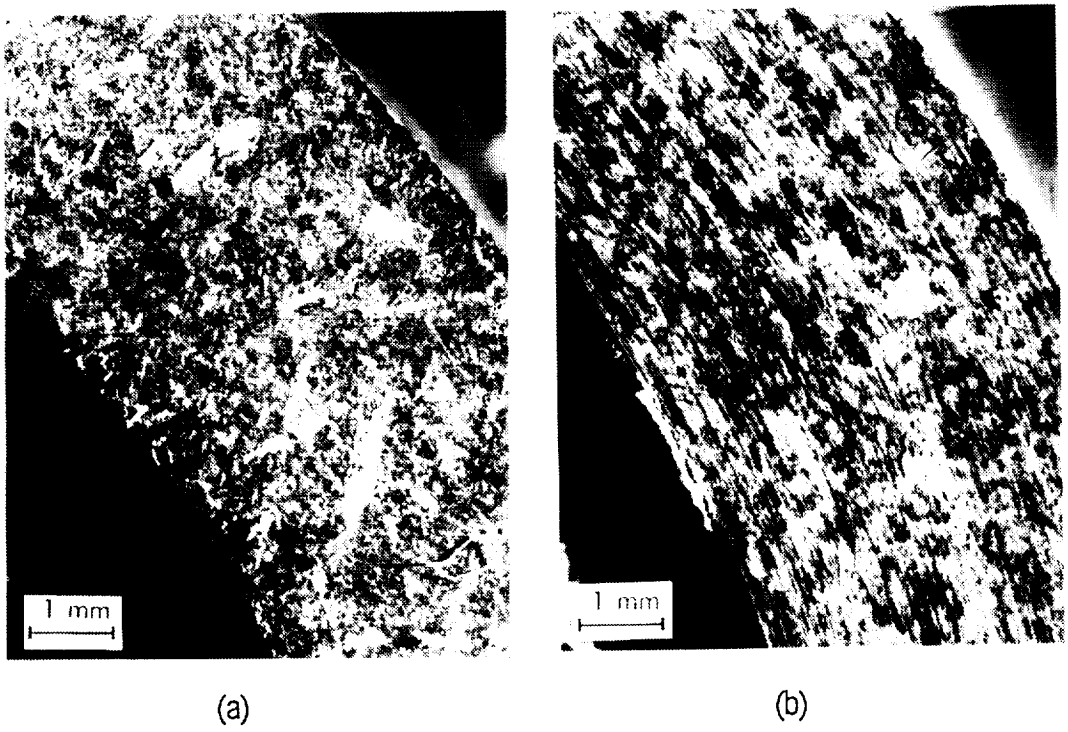

Figure 3. Asbestos/phenolic specimen surfaces before (a) and after (b) bi-directional sliding at low friction in vacuum.

ORIGINAL PAGE
BLACK AND WHITE PHOTOGRAPH

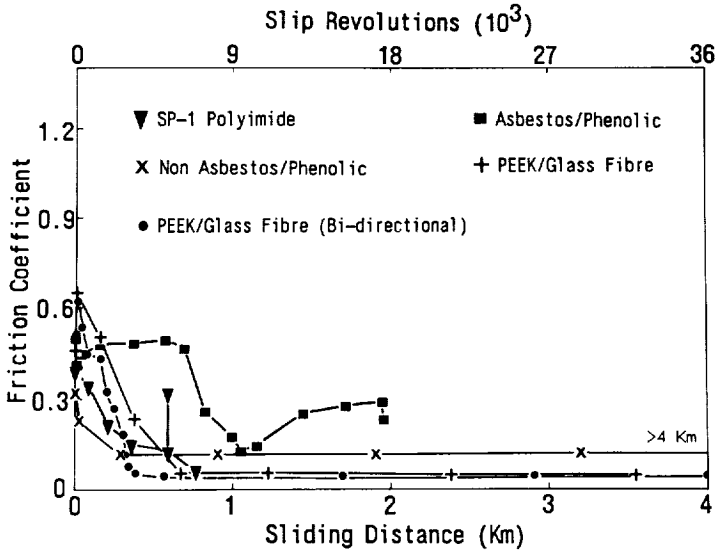

Figure 4. Friction trends from sliding of various polymeric compositions in vacuum.

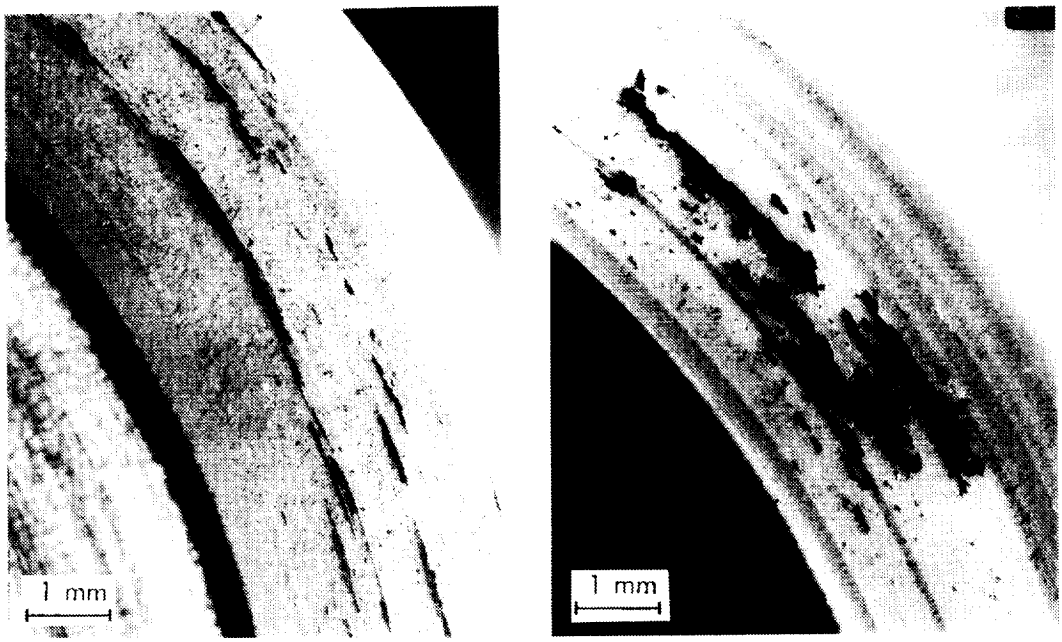

Figure 5. Wear debris structures on PEEK/glass fibre specimen surfaces after (a) uni- and (b) bi-directional sliding at low friction in vacuum.

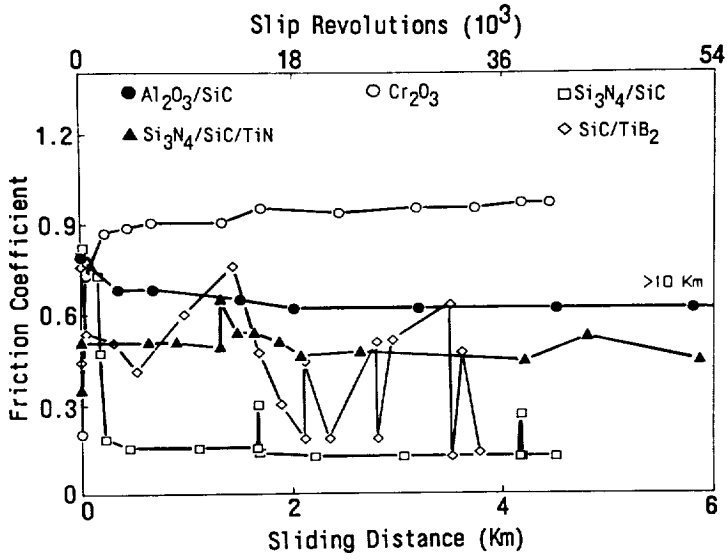

Figure 6. Friction trends of ceramic-based materials from sliding in vacuum.

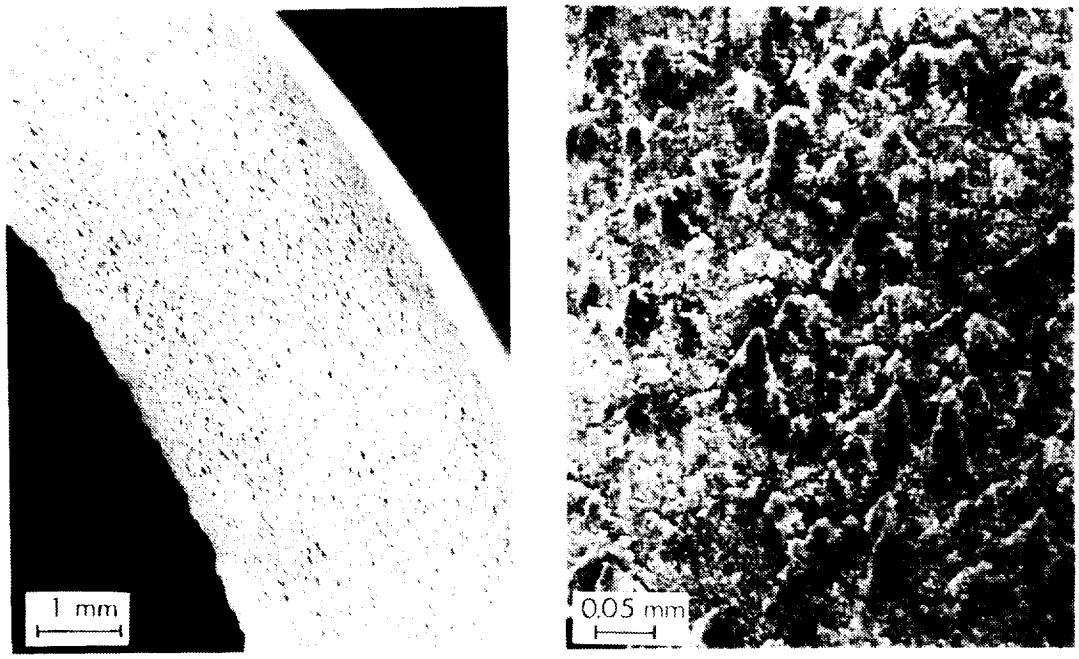

Figure 7. Finely dispersed wear debris texture on Al_2O_3/SiC specimen surfaces after sliding at high friction in vacuum.

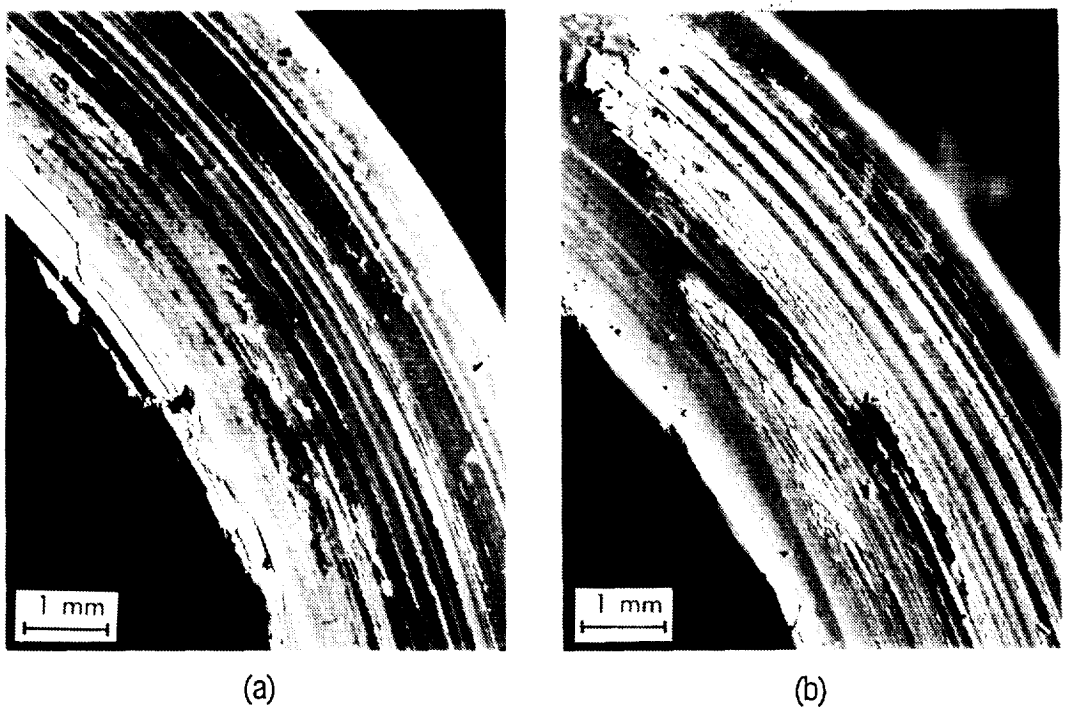

Figure 8. Worn static (a) and rotating (b) specimens of Si_3N_4/SiC after sliding together at low friction in vacuum.

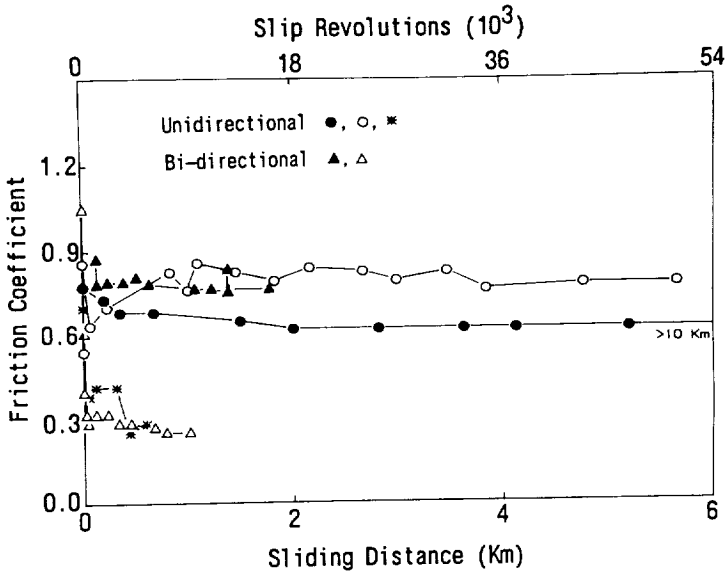

Figure 9. Different in-vacuo friction trends from separate tests of the same pair of Al_2O_3/SiC specimens.

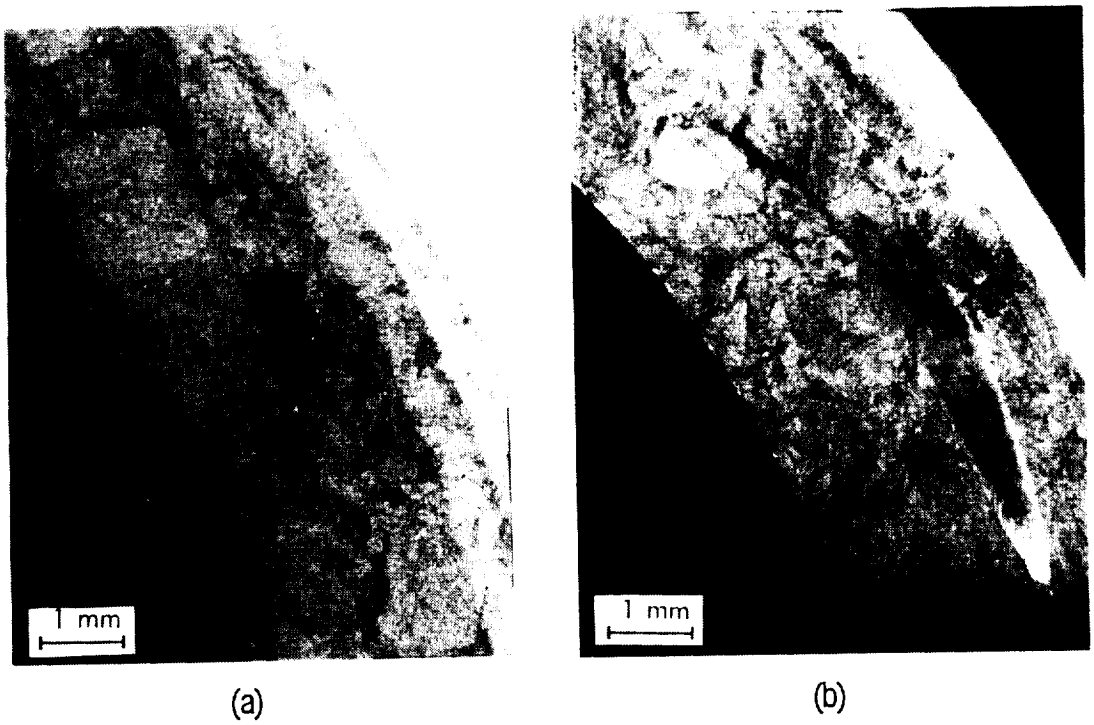

Figure 10. Wear debris patterns on Al_2O_3/SiC specimen surfaces after sliding at low friction in (a) uni- and (b) bi-directional tests in-vacuo.

POSITIVE LUBRICATION SYSTEM

N90-22097

by

Dennis W. Smith and Fred L. Hooper*

ABSTRACT

As part of the development of an autonomous lubrication system for spin bearings, a system was developed to deliver oil to grease-lubricated bearings upon demand. This positive oil delivery system (PLUS) consists of a pressurized reservoir with a built-in solenoid valve that delivers a predictable quantity of oil to the spin bearing through a system of stainless steel tubes. Considerable testing has been performed on the PLUS to characterize its performance and verify its effectiveness, along with qualifying it for flight. Additional development is underway that will lead to the fully autonomous active lubrication system.

INTRODUCTION

The useful life of a control moment gyroscope (CMG), reaction wheels, and momentum wheels is strongly dependent upon the spin bearing lubrication system. Current lubrication systems are passive in nature and consist of either a grease system or a controlled-leak-type oil system. The grease system has proven effective for lifetimes of up to three years for CMGs and up to 11 years in momentum wheels; systems have been designed for up to eight years in small CMGs. The controlled-leak-type, oil-only system has demonstrated encouraging performance in life tests but has had little experience in space and none on very active CMGs.

Future requirements for CMGs, reaction wheels, and momentum wheels include longer life and more rigorous service. Current data indicate that these increased demands are likely to stress the grease system beyond its endurance, and the passive controlled-leak oil system has questionable performance even for current demands. An alternative is an active oil system. Such a system would supply oil based on bearing requirements. The ultimate system would sense the oil requirement of the bearing and supply just enough oil to meet this need. This system would use a film of grease as a buffer, effectively storing any excess oil added to the bearing and metering the oil out to the running track when conditions demand it. Such a system could also reduce drag torque and unusual low-temperature runup behavior associated with excess lubricant within the bearing, while providing adequate lubrication for good reliability.

Progress toward an active autonomous oil lubrication system was initiated in 1983 when design was completed and testing started on a sensor that detects the ratio of cage rotational speed to shaft speed, which is a function of oil film thickness. In 1986, work was initiated on the oil pump and insertion system. This activity culminated in a positive lubrication system (PLUS) that will be used to supplement the life of the grease system by manually injecting oil at prescribed intervals. The PLUS will be available if needed because of unexpected circumstances.

OBJECTIVE

The objective of the PLUS is to, on demand, inject Coray 100® lubricating oil into the spin bearings of a CMG, reaction wheel, or momentum wheel. This will supplement the present passive Andok C® grease lubrication system, increasing the life of the system.

SUMMARY

The lubrication system currently being used consists of Andok C grease, which is initially packed between the balls but forms a channel as the bearing is run. The significant lubrication of the bearing is accomplished by the oil, which is supplied by the grease to the ball-race interface. In addition to grease along the ball track, some grease attaches itself to the cage and supplies oil to the ball-cage interface.

---

*Honeywell Corporation, Satellite Systems Operations, Glendale, Arizona

There are two major mechanisms for loss of lubrication from the ball tracks. The first is through migration of the oil away from the bearing and the other loss is evaporation. Eventually in the life of any bearing system, the supply of oil available to the ball-race interface becomes inadequate. When this occurs, the drag torque and subsequently bearing temperature increase, which accelerates the lubricant loss and degrades the lubricant. This can cause cage instability, which accelerates the degradation process. Such behavior is an indication of the end of life (defined as excessive drag torque). A passive lubrication system (greased-packed, controlled-leak, etc) cannot correct these conditions when they occur. The PLUS allows periodic bearing relubrication to extend the life of the system or intervention to correct premature (prior to normal end of life) lubricant-related problems as they occur. The PLUS has the capability to replenish the oil in the bearing (on command) by directly inserting the oil onto the balls for immediate restoration of EHD film thickness and return to normal operation.

PLUS DESIGN CONFIGURATION

The PLUS design consists of a pressurized reservoir with a solenoid valve, supplying oil through feed tubes to the bearings upon manual command.

PRESSURIZED RESERVOIR

The main component of the PLUS is a reservoir/solenoid valve, shown in Figures 1 and 2. The reservoir is mechanically pressurized by a spring compressed between the bellows and the outer housing. A number of pump designs were initially considered for the PLUS during the development period. The most significant of these were peristaltic, piezoelectric, and pressurized reservoir designs. The peristaltic design was abandoned because of material concerns, and the peizoelectric design proved too sensitive to lubricant properties and environmental conditions. The following is a description of the pressurized reservoir valve design that was eventually adopted.

The amount of spring compression (i.e., reservoir pressure) is adjusted by the initial position of the outer housing, which is threaded onto the valve housing. The bellows is extended during the oil-fill process and provides additional mechanical pressure. The installed dimensions of the spring and bellows provide an initial reservoir pressure of 80 psia with a 25-to-35-psia pressure drop from full to empty. In the event of spring failure, the bellows alone can provide enough pressure to deliver oil. The reservoir is designed for a deliverable volume of three milliliters but more or less is easily accommodated with simple design changes. Oil is discharged by opening the valve for 125 milliseconds at 10-second intervals. The amount of oil discharged per pulse can vary from 0.2 to 5.0 milligrams per pulse depending on reservoir pressure, operating temperature, and plumbing flow resistance.

The 28-V dc solenoid valve (Kaiser Eckel), Figure 3, has an operating pressure of 100 psig and a maximum leakage rate of 5.0×10^{-6} standard cubic centimeters per second (SCCS) GHe. The valve is constructed of 316 CRES and has a Viton seat. The valve and the bellows are electron-beam welded into position and then helium leak tested.

The oil volume requirement for the pressurized reservoir was based on adding 20 to 30 milligrams/month for three years plus approximately 200 milligrams for initial system fill. The volume of three milliliters (2.8 grams) is more than a factor of two greater than the estimated oil required.

FEED TUBE/BEARINGS

The testing and selection of the oil injection method is discussed in detail in the Oil Insertion/Transfer Design Section. A typical flight installation is shown in Figure 4. Oil is transferred from the valve to the delivery port in the bearing cartridge through a 0.063-inch outer diameter (OD) seamless CRES tube with a 0.016-inch inner diameter (ID). The actual design of the feed tube will vary considerably depending on the application and the oil insertion options. However, this size was selected because it was small enough to minimize the tube volume but large enough that small amounts of contaminates in the oil would not obstruct flow. Also, testing showed that this size feed tube functioned well over a wide range of operating conditions.

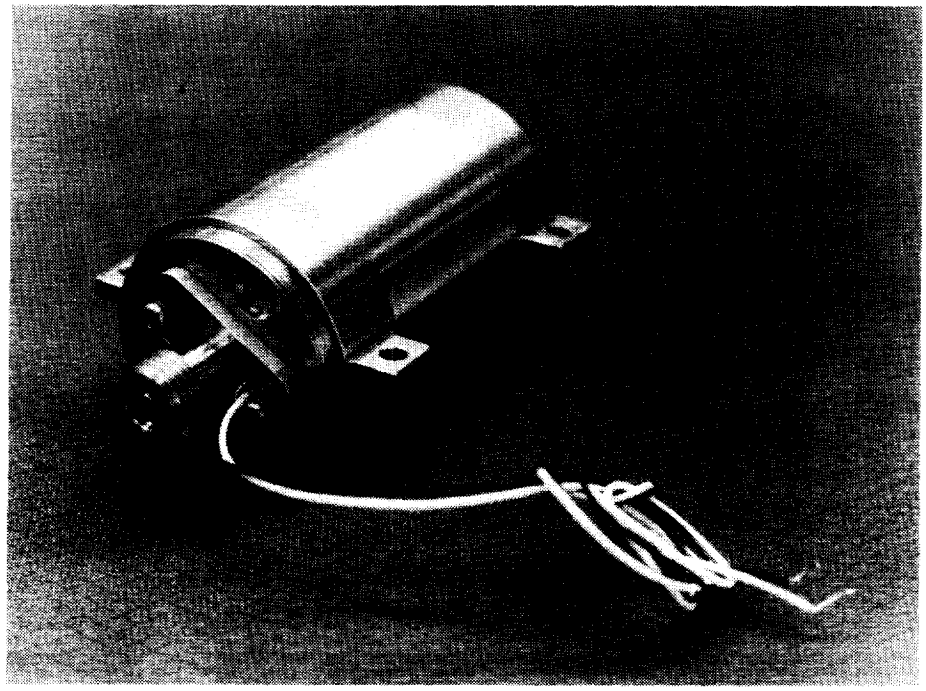

Figure 1. Reservoir Valve Assembly

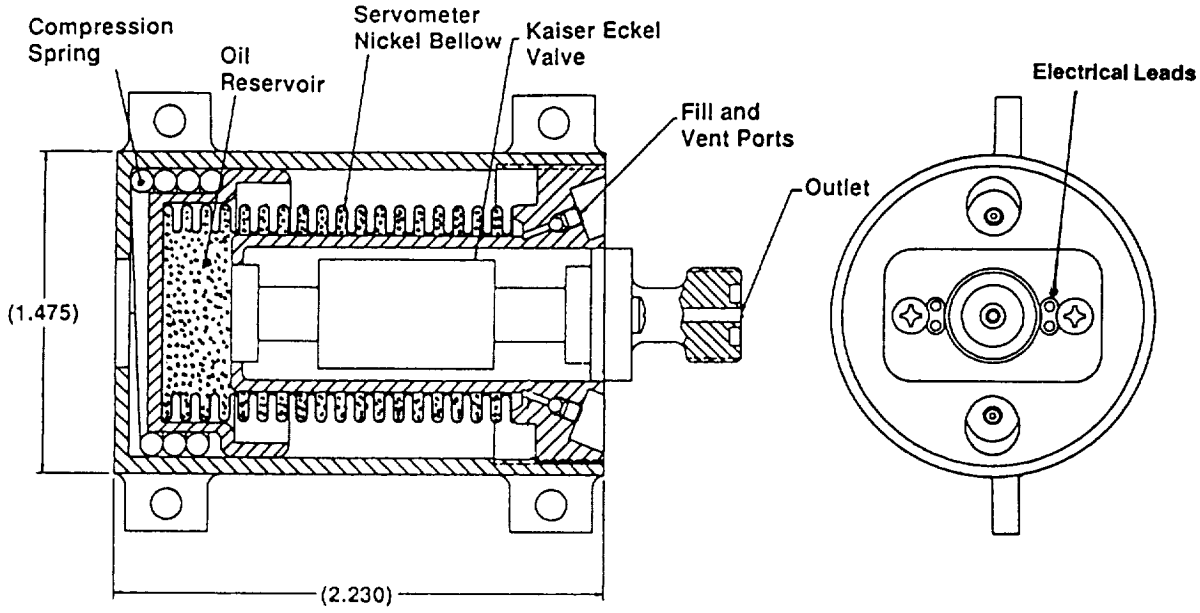

Figure 2. Pressurized Reservoir/Valve

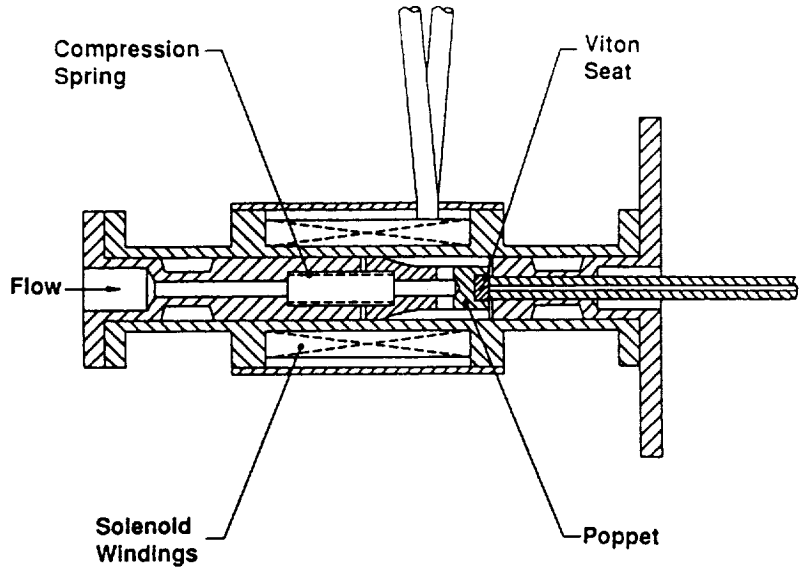

Figure 3. Kaiser-Eckel Solenoid Valve

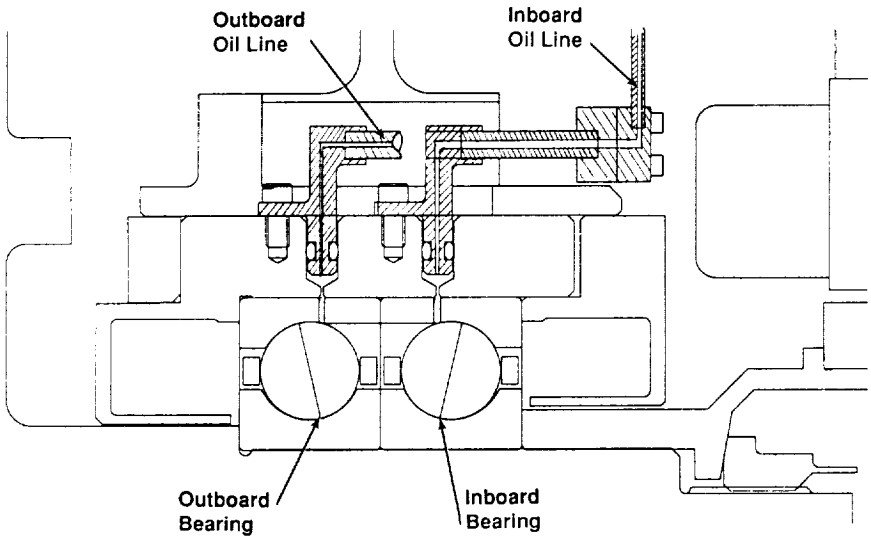

Figure 4. Typical Flight Installation

The bearing cartridge has two O-ring connector ports machined on the outer diameter to connect with the feed tubes. A 0.016-inch diameter hole connects these ports to the interior of the cartridge at a point that aligns with the center of a machined groove on the ID of the cartridge. This groove aligns with the four radial holes in the spin bearing outer races.

The spin bearings have four 0.016-inch OD radial holes in the each bearing 90 degrees apart. The holes go from the OD of the outer race to the interior of the bearing at a point within 0.004 inch of the balls.

CONTROL/TELEMETRY

Although normal operation of the PLUS is injecting a fixed amount of oil at predetermined intervals, it will also be used in the event of anomalous behavior. Current telemetry (spin motor current command and bearing cartridge thermistor) is monitored to detect abnormal bearing behavior. Abnormal bearing behavior is generally characterized by an increase in drag torque (proportional to the spin motor current command) and a corresponding increase in bearing temperature. At the onset of these abnormal conditions, a signal would be sent to the PLUS to inject 20 to 40 milligrams of oil per bearing. Previous testing has shown that this quantity of oil will reduce the drag torque to normal levels.

In the present system, there is no direct measurement to determine the exact amount discharged from the PLUS after the system has been activated (pulsed). The amount discharged is calculated based on component test data, in-flight usage history, and operating temperature. An indicator is presently being developed (i.e., linear potentiometer) that will monitor bellows position and, with telemetry, will give a direct measurement of the amount of oil discharged as well as the amount of oil remaining in the reservoir.

SYSTEM DESIGN DESCRIPTION

The present PLUS has two pressurized reservoir/solenoid valve assemblies per bearing for redundancy. When the command to inject oil into either the fixed or floating end is received, one solenoid valve per bearing opens and oil flows through the feed tubes into the small annulus between the outer races of the bearings and the cartridge (Figure 4). The oil then flows through the four small holes in the outer ring of each bearing from the annulus to the interior of the bearing near the balls. The PLUS design provides redundancy for both the oil supply and the oil paths.

SUMMARY OF TESTS

CHARACTERIZATION BENCH TESTING

Numerous tests were performed on the pressurized reservoirs to determine their operational characteristics. These tests determine the unit's output as a function of valve open/close time, temperature, and amount of oil previously discharged (i.e., reservoir pressure). This information is used during actual operation to determine the number of pulses required for a desired oil output.

TEST SETUP – The pressurized reservoirs used for the initial bench testing were flight-sized prototype units almost identical to the flight units shown in Figures 1 and 2, with pressure transducers installed to monitor oil pressure. These units were connected to various length/diameter feed tubes. The method of testing was to cycle the solenoid valve at various on/off times for a number of pulses while collecting and weighing the oil discharged and monitoring reservoir pressure. Testing was performed in both vacuum (bell jar) and atmospheric environments at various temperatures. The reservoir would be set at some initial pressure, which would slowly decrease as oil was removed from the reservoir.

OBJECTIVES – The objectives of this initial feed-tube/reservoir characterization testing using the prototype flight units were to determine the effects of various lengths and diameter of feed tubes/orifices, reservoir pressure, and temperature on oil delivery performance. Additional objectives were to define the performance and interface requirements of a flight PLUS.

FEED-TUBE CHARACTERIZATION – Numerous tests were performed on the pressurized reservoir with a variety of feed-tube configurations. The basic approach was to test

various length (3 to 12 inches) and ID (0.007 to 0.053 inch) feed tubes. Testing was conducted at temperatures between 20° to 120°F. Solenoid activation (pulse) time was varied between 25 and 5000 milliseconds; intervals between pulses were varied to determine the effects, if any, on output and to collect data required to optimize actual operation.

An example of the results of the testing is shown in Figure 5. The effects of reservoir pressure and temperature on oil delivery is shown on the upper plot. There is an increasing relationship between oil output and temperature that is due to an increase in pressure and a decrease in oil viscosity. The bottom plot shows the increased output as a function of pulse (valve open) time and temperature. The difference in oil output, shown on the top and bottom plots, is due to the difference in ID and length of the output feed tubes.

After the first-application flight design was selected, additional testing was performed with the prototype units to determine the performance with an even longer (>20 inches) feed tube. Although the calculated pressure drop showed adequate performance, a test was performed using the baseline-sized feed tube formed into a 2-inch diameter coil using about 20 inches of tubing. The testing was performed using a 2-milliliter capacity reservoir pressurized to 80 psia. The unit was pulsed 1700 times using 125-msec pulses at 10-second intervals. This test was conducted at temperatures from 20 to 75°F. The results of these tests are shown on Table 1. Although the output dropped considerably at 20°F (as expected), the pump/coil combination successfully delivered oil over a large range of temperature and reservoir pressure.

SUMMARY OF RESULTS – The performance testing demonstrated the ability of the units to perform under a variety of conditions. The performance of all units tested was uniform with consistent output. The testing also determined the performance characteristics of the system that are needed for actual operation during flight or future life simulation test.

BEARING TEST FIXTURE TESTING

OBJECTIVES – There were two primary goals of the testing: to develop a method of transferring oil from the pressurized reservoir to the bearings and to determine if oil injected into the outboard bearing would transfer to the inboard bearing.

TEST SETUP – The test fixture used is shown in Figure 6. The drive system consists of a 65-in.-oz Kollemorgan Brush Motor/Tachometer with feedback control to maintain continuous 6000 rpm. A bellows coupling connected the Kollemorgan drive motor to a ferrofluidic feedthrough (made by Ferrofluidics Corp), which maintains the vacuum chamber's integrity. These components are external to the vacuum chamber.

The bearing cartridges and clamp rings for the tests are duplicates of flight design cartridges. The bearing cartridge was attached to a 50-in.-oz Lebow torque transducer to measure the drag torque. The cartridge is also equipped with a flight thermistor. Both the temperature and the drag torque are continuously monitored on a strip-chart recorder.

OIL INSERTION/TRANSFER DESIGN – Two areas of concern were how to insert oil into the bearings and whether a PLUS was needed for each bearing or just for the outboard bearing. For PLUS installation, the effort would be minimized if oil inserted into the outboard bearing would transfer to the inboard bearing. There were several methods tested for injecting oil into the bearings. The design of each method is described in the following sections.

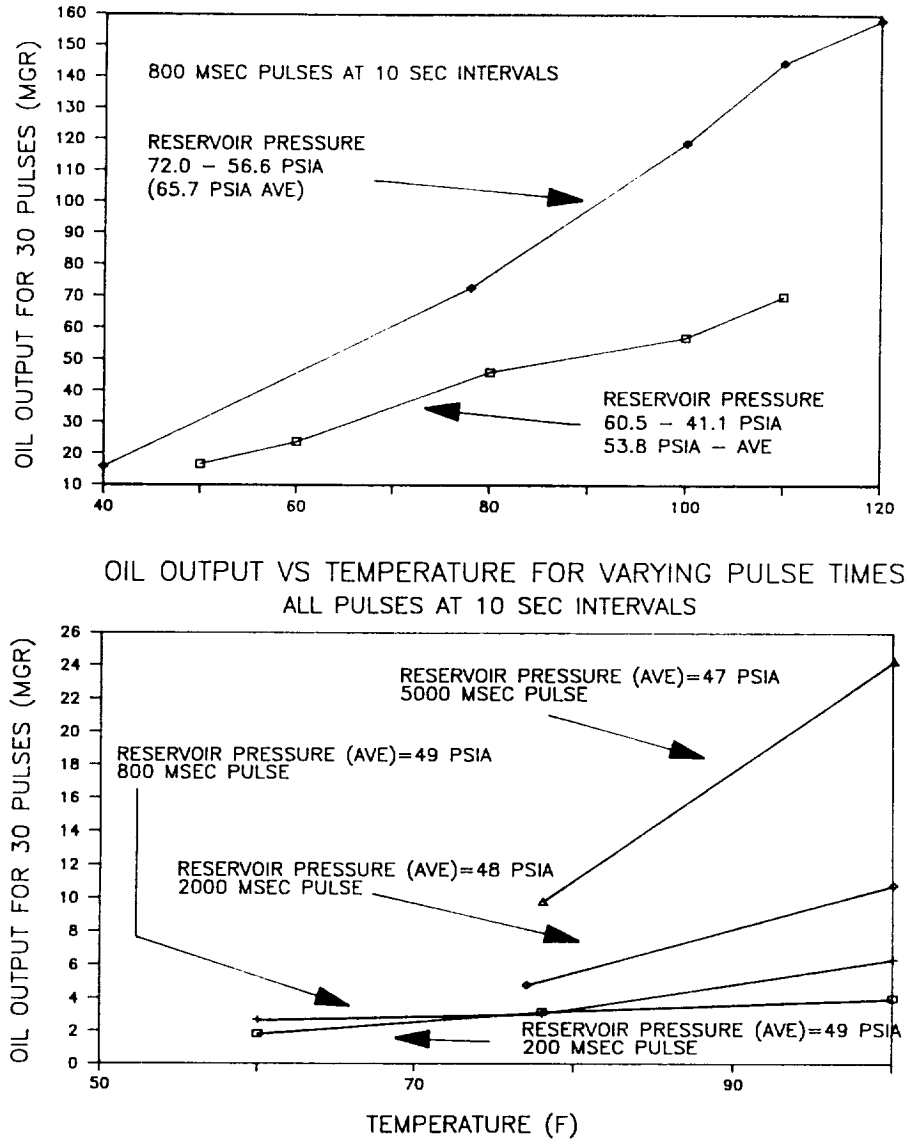

Figure 5. Oil Output versus Temperature

Table 1. Pump/Coil Performance Testing

Temp (°F)	No. of Pulses to Fill Coil (95 Mgrams)	Starting Pressure (psia)	Pressure Drop During Fill (psia)	Total Performance (Mgram/ Stroke)	Total Pressure Drop (psia)	Average Pressure (psia)
75	35	80	7	1619/1700 = 0.95	35	62
60	40–45	76	3	601/443 = 1.36	10	71
40	60–70	64	4	408/465 = 0.88	10	59
20	200	62	1	102/600 = 0.17	9	57

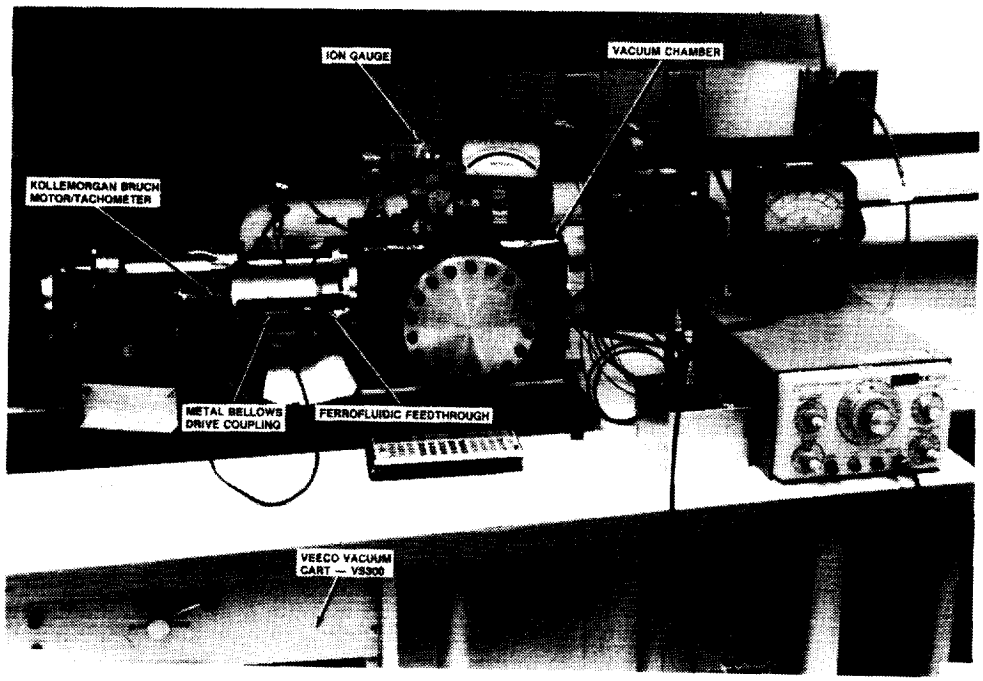

Figure 6. Oil Insertion Test Fixture

INNER-RACE-TO-CAGE TRANSFER (OPTION 1) – Option 1 inserted oil from a feed tube directly onto the spinning bearing inner race where the centrifugal force moved the oil to the underside of a lip on the bearing cage that protruded axially from the bearing (Figure 7). This cage with the designed lip was tested extensively with the PLUS in bench spindle testings but was never flight qualified. Oil insertion using this cage was demonstrated sucessfully, but the performance characteristics of this new cage were unproven. Due to the qualification time and departure from flight heritage, additional design and testing efforts were undertaken to develop a new method for inserting oil using existing flight-qualified cages.

INNER-RACE/OUTER-RACE DEFLECTION RING (OPTION 2) – Option 2 (Figure 8) used a feed tube to insert oil onto the spinning inner race. The oil would be centrifugally transferred to an oil deflection ring that would direct the oil into the outer race and balls. During the testing of Option 2, the cage (retainer) occasionally contacted the oil deflection ring. Based on this data and the unknown long-term effects that the ring could have on grease-cage coupling, the decision was made to eliminate this option.

DIRECT-TO-BALLS/CAGE-OUTER-RACE INSERTION (OPTION 3) – Option 3 (Figure 9) used a feed tube inserted between the cage and the bearing outer race to deliver oil directly onto the balls. The feed tube extending into the bearing was 0.025 inch thick. The cage-to-outer-land radial clearance was calculated to be 0.020 to 0.025 inch. With this tight clearance, there was concern that the cage might contact the lip if there was wear on the cage ID. It was decided that the flight design feed-tube lip would be made into a complete ring to provide a smooth surface identical to the outer land. A detailed analysis was performed to determine the actual cage-to-outer-race clearance. If this option was to be used, the bearings would have to have 0.025 inch of material removed from the ID of the outer land in order to maintain the existing cage radial clearance. An analysis showed that this material removal would not prevent the outer land from supporting design loads.

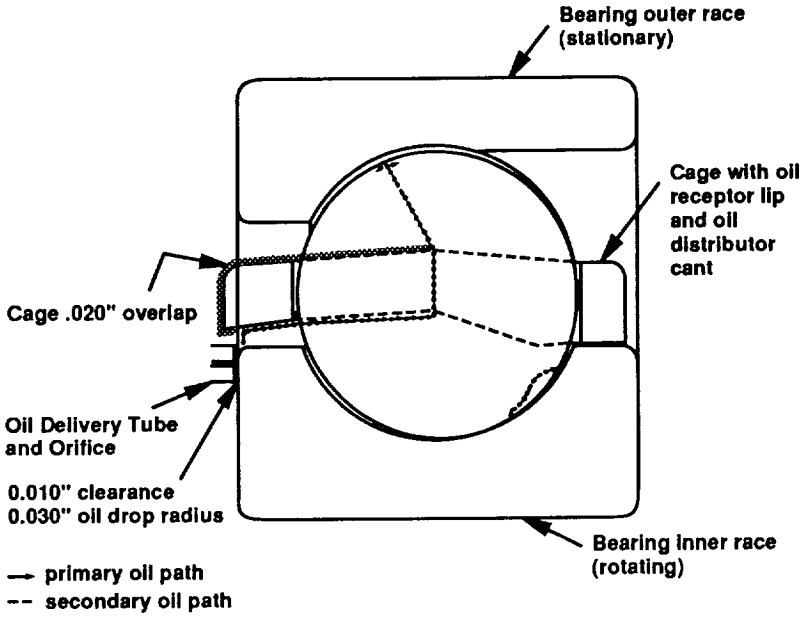

Figure 7. Previously-Developed Cage-Bearing Oil Distribution System (Option 1)

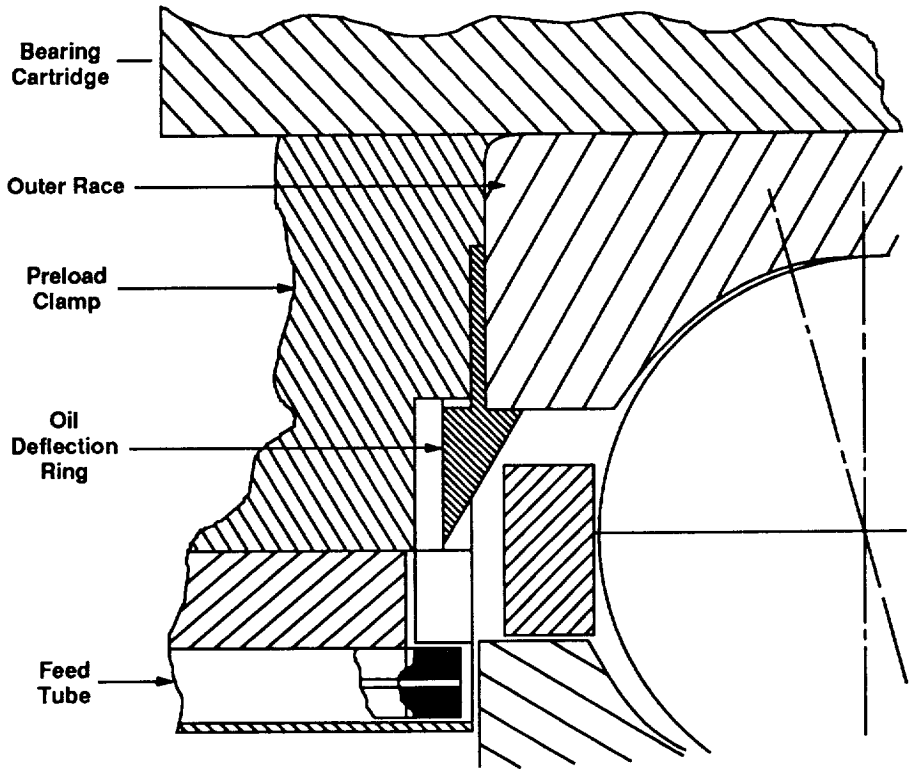

Figure 8. Oil Transfer (Option 2)

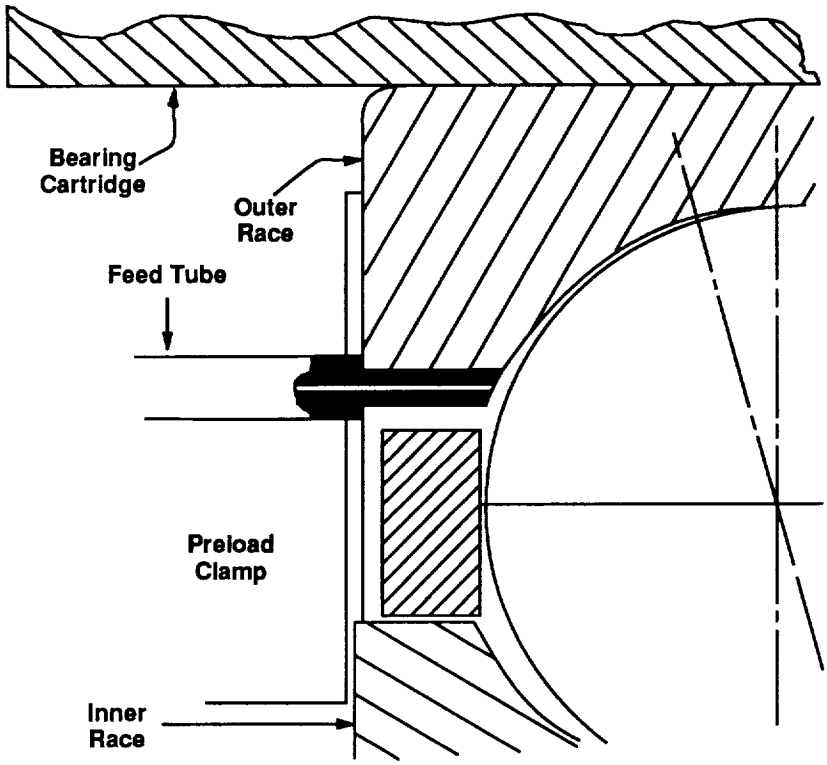

Figure 9. Oil Transfer (Option 3)

DIRECT TO BALLS/HOLE IN OUTER RACE (OPTION 4) – With Option 4 (Figure 10), oil flows through the feed tubes into the small annulus between the outer races of the bearings and the cartridge. The oil then flows through four 0.010-inch diameter holes in the outer race of each bearing from the annulus to the interior of the bearing at a point 0.002 to 0.004 inch from the ball.

This option would have two pressurized reservoirs for each bearing pair and provide redundancy for both the oil supply and the oil paths. Using this option, existing bearings and cartridges would have to be modified, but no new long-lead-time parts would have to be fabricated. The outer races of the bearings would have to have four diagonal holes added, as shown in Figure 10. The bearing cartridges would require the addition of an attachment hole to accept the feedtube from the pressurized reservoir and a small radial through hole to connect the attachment hole to the ID of the cartridge. This hole would coincide with the annulus at the interface between the bearings.

An analysis determined that the addition of these four holes would not compromise outer race load capacity. This was later confirmed by testing the modified bearings in an operational CMG.

DUAL-PATH INSERTION TO RADIAL BEARING HOLES (OPTION 5) – Option 5, shown in Figure 11, is identical to Option 4 except that the oil is injected through four radial (instead of diagonal) holes in the outer race of each bearing to the interior of the bearing.

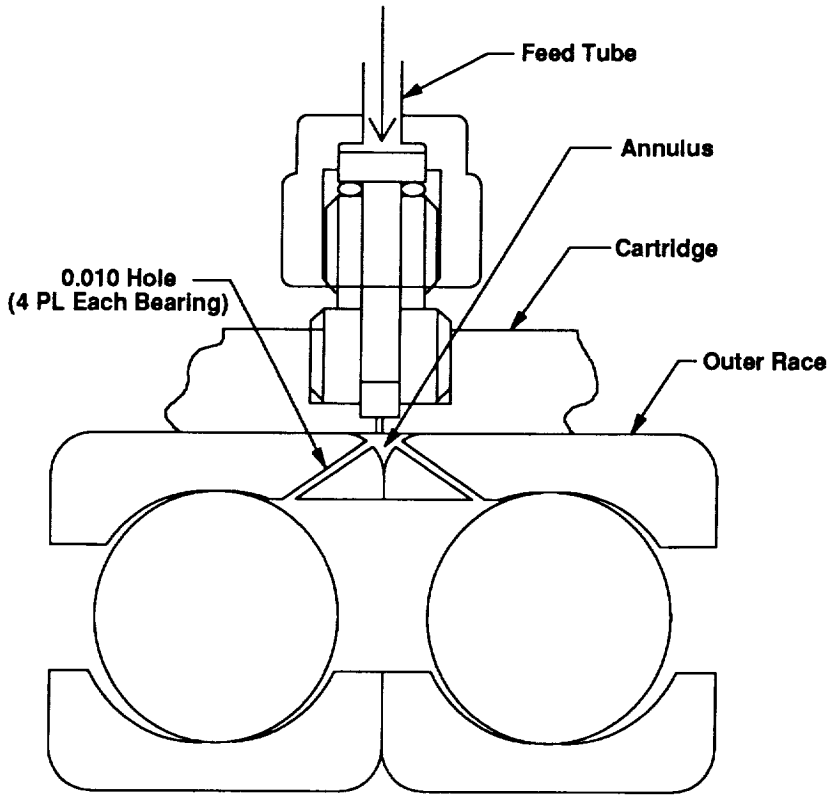

Figure 10. Oil Insertion (Option 4)

Using this design, one pressurized reservoir would supply oil to only one bearing. Option 5, like Option 4, would only require part modification instead of new long-lead-time parts. A machined groove was added to the ID of the bearing cartridge in two places. As with Option 4, an attachment hole was added to accept the feed tube from the pressurized reservoir, and a small radial through hole was electrodischarge-machined (EDMed) from the attachment hole to the ID of the cartridge. This hole intersected the annulus between the bearing OD and the machined groove on the ID of the bearing cartridge.

OIL INSERTION/TRANSFER OPTION TESTING/SELECTION – All tests were conducted using flight-designed 305 bearings and cages in the spindle test fixture (Figure 6). Oil was injected from the pressurized reservoir, using 125-second pulses at 5- to 10-second intervals. For all tests, the bearings and pressurized reservoirs were weighed before and after testing to determine the amount of oil transferred.

OIL TRANSFER TESTING – Options 2 and 3 (Figures 8 and 9) were the two methods initially considered for injecting oil into the bearings. These two methods were used for the transfer testing. Although a feed tube was used for the testing of Option 3, for a flight installation, a new preload bearing clamp would be designed to incorporate this oil injection feature.

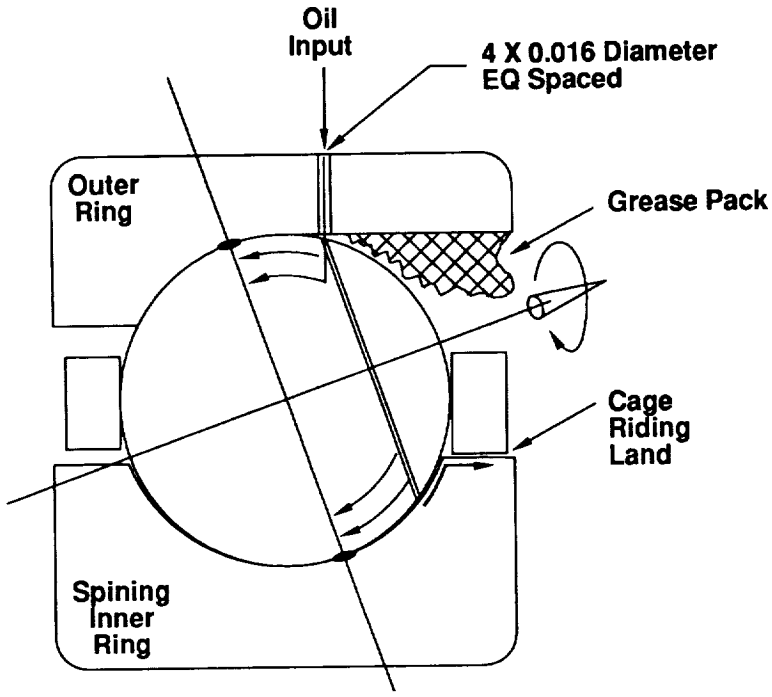

Figure 11. Nominal Bearing Geometry With Oil Holes (Option 5)

Numerous tests were run using both greased bearings and oil-only bearings. During the first five tests the bearings were injected with various quantities of oil while running in the test fixture. The bearings were weighed before and after testing to determine the amount of oil injected and the amount of transfer. Table 2 summarizes the results of the tests. The first four tests demonstrated consistent oil delivery to the outboard bearing but inconsistent transfer to the inboard bearing. Observations in earlier PLUS development tests indicated that oil would transfer from one bearing to the other; however, earlier tests were done using bearings with extended-lip cages (Figure 7). To determine if the type of cage was indeed a factor in oil transfer, two tests were run (No. 3 and No. 8) with an extended-lip cage. After the first five tests were performed there was concern that the weighing method, particularly with the greased bearings, was not an accurate enough determination of transfer because of the possibility of grease transfer between the bearings when they are separated. Since the testing needed to conclusively demonstrate transfer, the last three tests were done with greased bearing and the injected oil was impregnated with blue dye (Nitrofast Blue-2B®, manufactured by Sandoz Chemical). The blue dye demonstrated excellent delivery from the pressurized reservoir into the outboard bearing with all options, but practically no transfer from the outboard to inboard bearing. At this point the decision was made that each bearing would have to have its own direct oil injection to ensure proper bearing lubrication. During the testing of Option 2, the cage occasionally contacted the oil deflection ring. Based on this data and the unknown long-term effects that the ring could have on grease-cage coupling, this option was eliminated.

Table 2. PLUS Transfer Test Results

Test No.	Option No.	Oil/ Grease	Oil Delivered (mg)	Δ O/B (mg)	Δ I/B (mg)	Transfer
1	3	Grease	88	Unknown	Unknown	Unlikely
2	3	Grease	200	+63	-104	Unlikely
3	2	Oil only	1115	+152	+39	Yes
4	3	Oil only	200	+46	+21	Yes
5	3	Oil only	127	+15.2	+22.2	Yes
6	3	Grease	188 (blue dye)	+95	-146	No
7	2	Grease	262 (blue dye)	-125	-204	No
8	3	Grease	500 (blue dye)	+153	-215	Some (visual indication)

OIL INSERTION TESTING – Oil insertion testing was performed using Options 3, 4, and 5.

The primary goal was to test the capability of the various options to transfer oil from the pressurized reservoir to the bearings and to select the best option for flight design.

Oil Insertion Tests (Option 3) – To simulate Option 3 oil insertion for testing, a feed tube machined to 0.025 inch thick was fabricated and installed between the cage and the bearing outer race to insert oil directly onto the balls. The feedtube was secured in the setup to hold it hard against the outer bearing race.

Four tests were run, three with greased bearings and one with oil-only bearings. During the first test the weight gain of the bearing was undetermined although there was visual evidence of oil insertion. During the second test 63 milligrams out of 200 were injected. The third test was conducted using an oil-only lubricated bearing. During the test, 46 out of 200 milligrams were injected onto the bearings. The final test was run with greased bearings, and the injected oil was impregnated with blue dye. The blue dye showed an excellent visual indication of delivery from the pressurized reservoir into the outboard bearing, with 95 out of 188 milligrams delivered to the bearing. As stated earlier, bearing weights were not accurate due to grease transfer between bearings.

All four tests demonstrated consistent oil delivery into the bearings. Because of the results of the other testing and analysis as well as manufacturing considerations, the decision was made to eliminate this option.

Oil Insertion Tests (Option 4) – The test-cartridge was modified to accept a feed tube similar to the flight concept, and a set of test bearings was modified as shown in Figure 10. For these tests, one pressurized reservoir was used to supply both bearings.

Six tests were conducted using this option with oil-only bearings. For the tests, the bearings were run in a vacuum test fixture until the drag torque increased. At that time oil was injected into the bearing. In all of the tests, the drag torque immediately decreased.

Four tests were run using grease-lubricated bearings. The tests were run for four to six hours and then injected with 50 to 100 milligrams of oil (with blue dye). After the first test, the visual inspection indicated that oil flowed through only one of the eight holes (four holes in each bearing) in the two bearings. During the other three tests, various combinations of holes were manually plugged with grease, and oil quantities from 56 to 106 milligrams were injected. The results of the post-test visual inspections always showed that the

oil followed the lowest resistance path, which resulted in only one of the bearings receiving the oil.

The blue dye proved to be an excellent visual indication of oil insertion. It was observed that grease covered the oil outlet holes during every test, though the oil could readily unplug a grease-filled hole. Once one hole was unplugged, the others would not unplug, and oil would go into only one bearing.

The conclusion of this testing was that each pressurized reservoir could inject oil into only one of the two bearings. Because of this result and the manufacturing difficulties associated with the diagonal holes, Option 4 was abandoned.

Oil Insertion Test (Option 5) – The test bearings and cartridge were modified as described in the Dual-Path Insertion to Radial Bearing Holes (Option 5) paragraph. Three tests were run using greased bearings. For all of the Option 5 tests, the injected oil was impregnated with blue dye.

During the first test, 129 milligrams of oil were injected into the outboard bearings and 93 milligrams into the inboard bearings. After the test, the visual inspection indicated excellent oil transfer into both bearings and excellent distribution of the injected oil. During the second test, 74 milligrams of oil were injected into the outboard bearing and 39 milligrams into the inboard bearing. After the test, the visual inspection indicated excellent oil transfer and distribution in the outboard bearing but very little in the inboard bearing; this was due to the small amount injected. It takes 25 to 30 milligrams of oil to fill the annulus in the bearing cartridge before any oil can flow into the holes in the bearings.

The third test was designated the long-term test. For this test, the bearings were run for 14 days prior to oil injection. The purpose of this test was to determine if dry grease would effect the oil injection. The test cartridge used had no internal oil reservoirs and an open-labyrinth seal to allow the grease to dry out quickly. After the long run time, 108 milligrams of oil were injected into the outboard bearing and 84 milligrams into the inboard bearing. After the test, the visual inspection indicated excellent oil transfer and distribution in both bearings.

Several oil insertion tests had been performed on oil-only lubricated bearings to determine the system's ability to reduce drag torque. During these tests, the bearings were run until the drag torque and temperature increased and then various quantities of oil were injected. In all the tests, the drag torque, temperature, and observed cage instability decreased immediately after oil injection. These tests determined that 20 to 40 milligrams of oil injected per bearing were usually all that was required to restore drag torques to normal.

All the tests using this option demonstrated very consistent oil transfer into the bearings. Because of the results of these tests, the earlier testing, analysis, and manufacturing considerations, the decision was made to select Option 5 for the PLUS oil insertion technique.

OIL DISTRIBUTION – DYED OIL INJECTION – Other tests were conducted using the same test setup to determine the effects of injecting oil into a bearing with oil-depleted grease. Another objective was to determine the amount of oil that can be added to a set of bearings without causing an increase in the drag torque.

A set of greased bearings was starved by operating them at elevated temperatures in an open cartridge to evaporate 40 to 60 percent of the original oil. They were then installed

in the test setup and various quantities of oil were injected into the bearings. No significant changes in drag torque were noted following oil injection.

After the tests, a visual examination showed that the grease was wetted throughout, all surfaces showed good oil distribution, cages went from dry (before injection) to well oiled (after injection), and up to 40 milligrams could be added to a bearing without measurable change in drag torque.

FLOODING – Another test was conducted using the same test setup to determine the effects of injecting an entire reservoir full of oil (~2 grams) into a set of fresh bearings. This will simulate a worse-case failure of the PLUS (valve-open failure) early in the bearing life.

After running the bearings for about 40 hours the drag torque had stabilized at 2.30 to 2.50 oz-in. The reservoir valve was opened and remained open until all of the oil was discharged. The torque increased immediately but then slowly decreased until it returned to normal levels. This test showed that a valve-open failure will not cause long-term, high drag torques or other observable problems.

FIXTURE TEST CONCLUSION – The conclusions of these tests are: oil added to greased bearing will successfully migrate to the bearing critical areas; oil can be added to the bearings in small quantities without increasing drag torque; and oil added in large quantities does not cause long-lasting effects on bearing performance. Option 5 is the best method for injecting oil into bearings.

LIFE TESTS

Oil added to distressed bearings results in recovery of performance. This was demonstrated many times with the bearing spindle test fixture and has also been demonstrated in life tests. An RWA life test stopped after one year due to high bearing drag torques. After an addition of 40 to 50 mg of oil, the test was restarted and ran for three years. The unit was still operating normally when the test was terminated due to program consideration.

An accelerated life test on a momentum device was stopped at 67 percent of expected life because of abnormal bearing behavior (high drag torques and temperatures). The bearing had 50 mg of oil added to each bearing. The test was restarted and has run normally for an additional 17 percent of life. The current plan is to continue to add oil at fixed intervals to extend the life of the test well beyond its original planned duration.

PRESENT/FUTURE DEVELOPMENT

The current PLUS has been designed, built, and flight qualified.

The design of the next generation PLUS is in progress (Figure 12). Some of the features of the new design is a size-optimized design with full mechanical and electrical redundancy and constant output (not dependent on pressure, temperature, etc). The new design will have timed injection combined with manual override capability to provide a degree of autonomy.

Currently, there are outstanding proposals to install the PLUS on a small CMG and an RWA flight program.

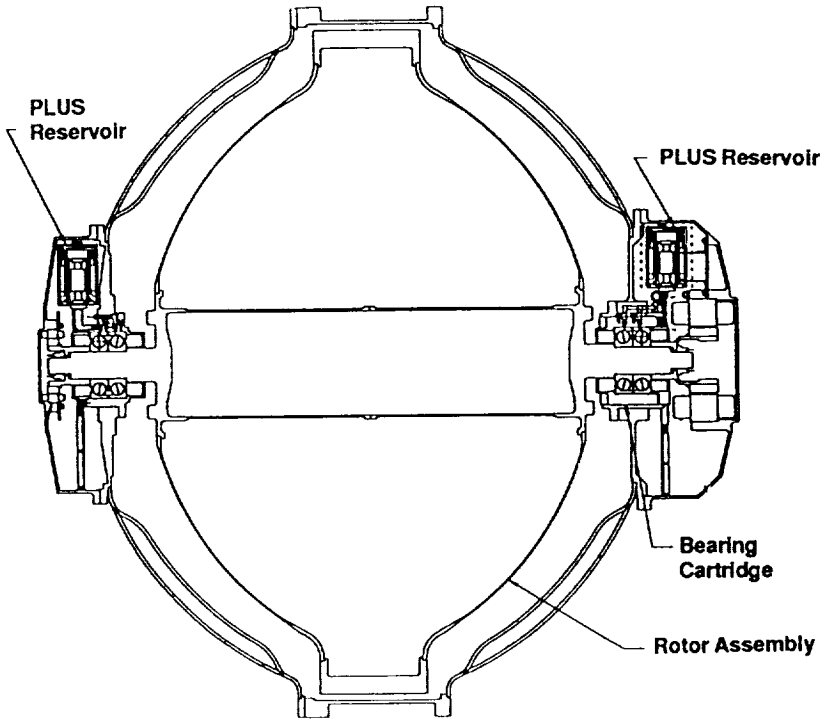

Figure 12. Typical Installation.

Also under development with IR&D funding is a lubricant monitor that senses the lubricant requirement and a control system that will command oil injection at the proper time, based on sensor output. This monitor and control system would be used with the present PLUS for an autonomous active lubrication system. (The present autonomous system will inject a fixed amount of oil at predetermined, but variable, intervals.)

SUMMARY AND CONCLUSIONS

The most significant observation in most bearing failures is lubricant degradation. Maintenance of adequate lubrication is the key to extended life. A well-lubricated bearing will run an extremely long time (fatigue life limited only).

The PLUS has shown to be an effective method of extending the life of grease-lubricated bearings well beyond passive system capabilities by adding oil. Tests have shown that the PLUS delivers oil to the critical bearing areas on demand. The PLUS is mission flexible with its full autonomy and has the capability to alter the lubrication cycle in response to unexpected demands. The PLUS can prevent anomalies or intervene if necessary to mitigate unexpected problems. It also has end-to-end ground test capability to verify operation before flight use. The PLUS provides lubrication life that is basically limited only by reservoir size.

N90-22098

ACTIVE CONTROL OF BEARING PRELOAD USING PIEZOELECTRIC TRANSLATORS

TED W. NYE*

ABSTRACT

In many spacecraft applications, mechanisms are required to perform precision pointing operations or to sometimes dither about or track a moving object. These mechanisms perform in a predictable and repeatable manner in benign temperature environments. Severe thermal gradients experienced in actual space applications however, cause assemblies to expand and contract around their bearings. This results in unpredictable changes in bearing preload, and hence bearing friction. This becomes a limitation for servos controlling pointing accuracy. Likewise, uncontrollable vibrations may couple into fixed preload (hence, fixed stiffness) mechanisms and limit pointing accuracy. Consequently, a complex problem we face today is how to design mechanisms that remain insensitive to changing thermal and vibrational spacecraft environments. Research presented in this paper involves the simplified modeling and test results of an actuator module that used piezoelectrically preload-controlled bearings. The feasibility of actively controlling bearing preload was demonstrated during this study. Because bearing friction is related to preload, a thermally active system designed with aluminum components and a 440C bearing, was friction tested at temperatures ranging from 0 to 70°C (32 to 158°F). Effectiveness of the translators were demonstrated by mapping a controllable friction range throughout tested temperatures. We learned that constant preload for this system could be maintained over an approximate 44°C (79°F) temperature span. From testing, it was also discovered that at the more deviate temperatures, expansions were so large that radial clearances were taken up and the duplex bearing became radially preloaded. Thus, active control of bearing preload is feasible but may be limited by inherent geometry constraints and materials used in the system.

INTRODUCTION

Mechanisms that can adapt to their environment are becoming more and more of a spacecraft necessity. High demands for gimbal performance and life are driven by future mission requirements as evidenced in Reference [1]**. No longer are passive systems able to meet requirements of the 1990's. Extremely tight pointing requirements dictate that actuators must not only operate reliably and predictably, but must be able to compensate

*TRW Space & Technology Group, Redondo Beach, California
**Numbers in square brackets refer to references at the end of this paper.

for environmental effects. This becomes particularly apparent when cryogenic payloads must be gimballed and actuator assemblies are operated at extremely low temperatures. Coefficients of thermal expansion for these housings and shafts generally differ to some extent with their bearings. The temperature changing precision fits can have a dramatic effect on the bearing preload, which will always manifest itself as a friction torque increase.

Rotary actuators are generally modeled as single degree-of-freedom (DOF) joints. They can be better represented, in a dynamic sense, as six DOF bodies. Assuming rigid housings and shafts, a duplex bearing will dictate constitutive relationships for at least five of the six DOF. Provided that sensible strain energy in the actuator is focused in the bearing, a robotic manipulator or gimbal assembly can be designed such that damping or vibration isolation is achievable in a variety of directions. Spacecraft mechanisms and their payloads are often susceptible to low frequency spacecraft vibrations during launch and in orbit. Typically we think of attenuating the disturbance functions by increasing damping or isolation of the driven payload. We may also "tune" the actuator in a modal stiffness sense so that it and its payload are uncoupled from high energy modes. This becomes a complex problem because designing to avoid modes that may occur in orbit may yield an actuator stiffness that is parametrically excited during launch. Actuators specifically engineered for one dynamic environment or operation may not be well suited for other environments. It would be a technology breakthrough if an actuator could exhibit adaptive compliance. Thus, an actuator would be actively stiffness-tuned to uncouple it and its payload from disturbances, or alternatively be used to damp-out vibrations entirely by acting as a soft, energy-absorbing joint.

The key parameter that makes for this adaptable actuator is controllable preload in a duplex bearing. This single parameter plays a crucial role in establishing frictional and transverse stiffness behavior. Although preload is controllable by using piezoelectric devices, it is unfortunately not directly observable and must be inferred by friction or stiffness measurements.

Piezoelectric materials exhibit crystalline lattice distortion when subject to an electric field. This distortion will manifest itself as an apparent strain that is repeatable and controllable. Piezoelectric wafers, arranged in a bonded stack, form a "pusher" or "translator." These translators have been employed in numerous applications [2,3] in commercial industry and at least one conceptual design in a bearing has been patented [4]. These translators can provide useful functions since expansion can be controlled precisely and significantly large forces can be generated. Thus, with bearing preload being extremely sensitive to raceway axial stickout, piezoelectrics are ideal devices for actively regulating this bearing parameter.

BEARING SENSITIVITIES

During the design of the active preload control module, a bearing parametric sensitivity study was performed. Many design cases were examined using software based upon theoretical relations presented in [5] and [6]. Relationships studied were temperature effect on preload, preload effect on friction, and preload effect on transverse stiffness. Observations were made on friction and stiffness relationships to ball size, raceway curvature, and contact angle.

Differential expansion between a bearing and its mounting assembly will always act to increase preload. Provided there is no significant change in axial dimensions, increasing temperature would, for example, cause a 440C bearing to expand faster than a titanium housing, thus increasing preload. Decreasing temperature would cause a 440C bearing to shrink faster than a titanium shaft, also increasing preload. For a typical 79 mm (3.125 in) bore, 440C stainless-steel thin race bearing mounted in a titanium housing/shaft, a change of 140°C (252°F) will double the preload from 34 to 68 N (75 to 150 lbs) as shown in Figure 1.

Increasing preload will always increase friction torque proportionally. Harris in [6] gives Palmgren's statistically based relationship between preload and friction.

$$M_i = f_1 F_B d_m \tag{1}$$

Where for a duplex pair,

$$f_1 = z \left(\frac{F_s}{C_s} \right)^y \tag{2}$$

and

z = .001, a constant for 30° contact angle
y = .33, a constant
F_s = static equivalent load
C_s = basic static load rating

F_B = preload
d_m = diametral pitch

For the 79 mm (3.125 in) bore bearing mentioned earlier, Figure 2 shows its theoretical friction-preload relation. Note that the friction torque more than doubles as preload is increased from 34 to 68 N.

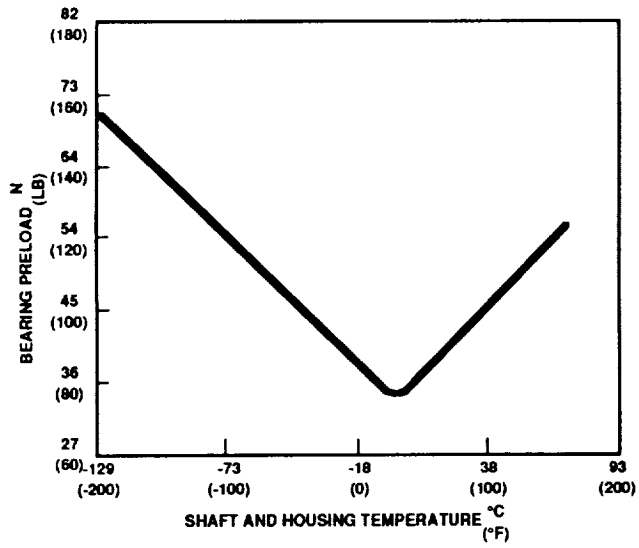

Figure 1. Theoretical Bearing Preload Versus Shaft and Housing Temperature

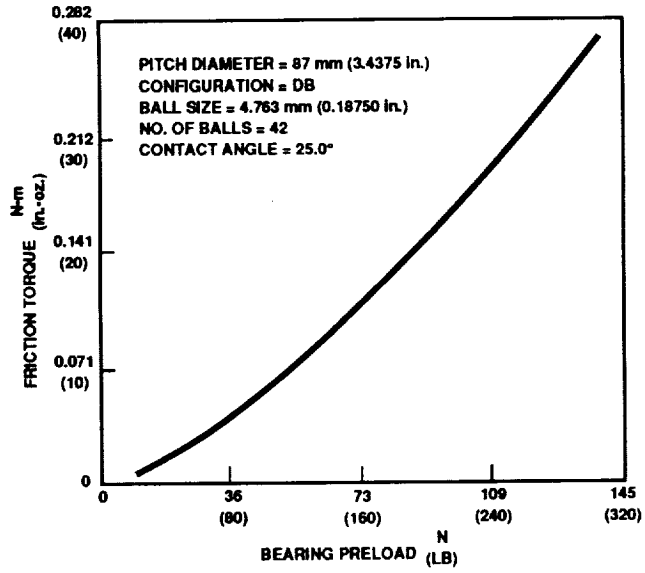

Figure 2. Bearing Friction from Preload

Preloading effects on bearing transverse stiffness is a complex phenomenon. Figure 3 shows some characteristic curves as theoretical stiffness changes with applied moment. Moment stiffnesses are typically the most crucial on electromechanical actuators since these assemblies tend to always cantilever their payloads and/or are subjected to bending type loads. For smaller moments, stiffness is highly dominated by preload. Conversely, preloading diminishes as external loads begin to increase in size and mask the small preload. Data in Figure 3 is relevant to a duplex pair with a 89 mm (3.5 in) axial spread between the races. For an adjacent duplex pair, doubling the preload can often times result in doubling the stiffness.

Ball size, raceway curvature, and contact angle all exhibit influences over stiffness as shown in Figures 4, 5, and 6. Minimum ball sizes, as a rule of thumb, tend to maximize stiffness but minimize load carry capability. Friction tends to decrease for bearings with larger balls primarily because the number of sliding interfaces against the retainer are less. Raceway curvatures approaching .500 will be stiffer since the raceway wrap-around the ball is increasing and the ball footprint or contact area increases. A larger footprint with decreased race curvature will cause more sliding at the race/ball contact zone and hence, friction would be expected to increase. Contact angle increasing for a double-back (DB) pair allows for better moment carrying capability as shown in Figure 6. Contact angle effects on friction behavior do not enter into the friction modeling function and are expected to be very slight for slow rotating systems.

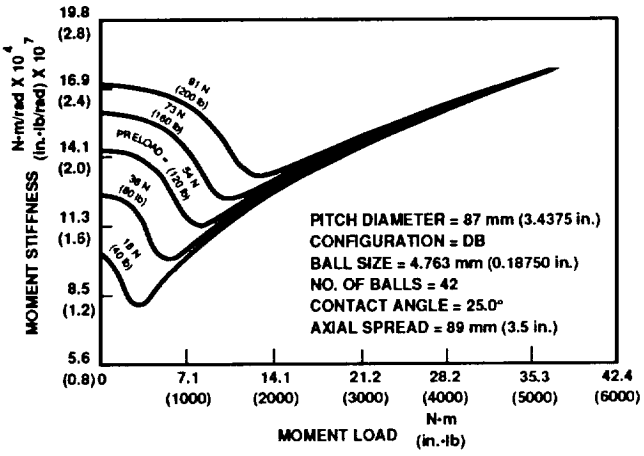

Figure 3. Effect of Preload on Bearing Moment Stiffness

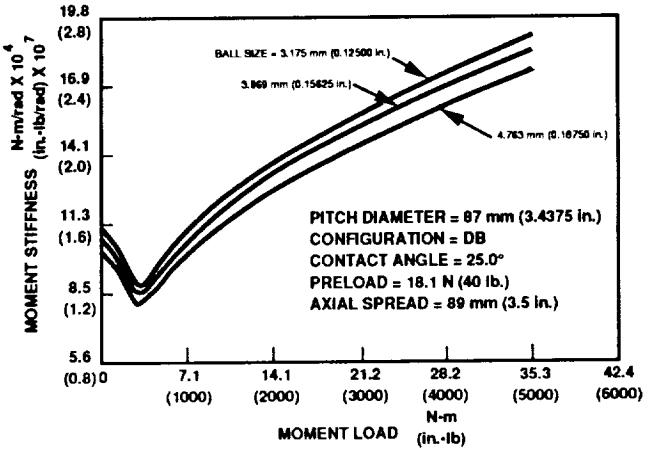

Figure 4. Effect of Ball Size on Bearing Moment Stiffness

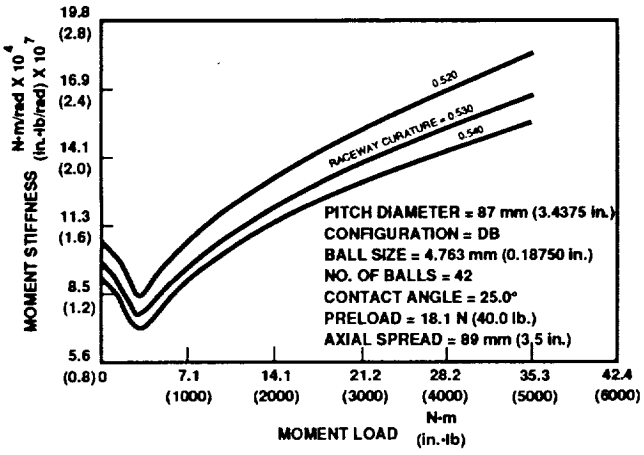

Figure 5. Effect of Raceway Curvatures on Bearing Moments Stiffness

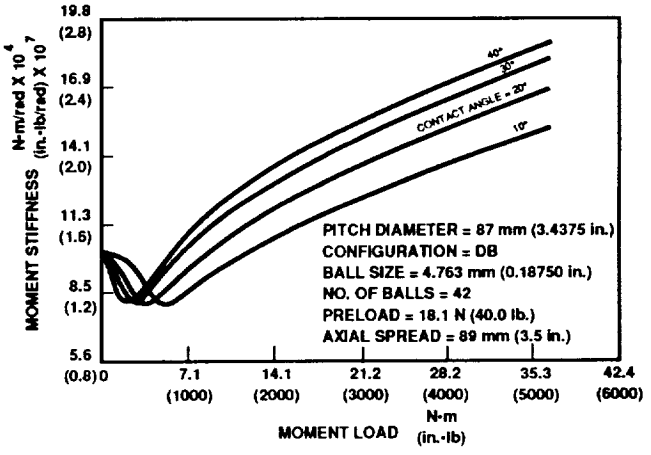

Figure 6. Effect of Contact Angle on Bearing Moment Stiffness

ACTIVE PRELOAD DESIGN CONSIDERATIONS

The active preload control scheme used for this study involved mounting piezoelectric translators on either side of one outer race of a duplex bearing pair. A section view of the test apparatus is shown in Figure 7. One major design concern was to insure that the piezoelectric translators could develop the required force after a substantial expansion for adjustment of the raceway stickout. The translators only work in compression. Thus, translators on the left hand side of Figure 7 were energized to push against the axial stiffness of the bearing. Translators on the right hand side of Figure 7 were included to reduce preload on the bearing for a scenario where the sliding bearing mount might stick or hang-up. Translators on both sides could also be preloaded against each other to reduce hysteresis and axial deadband.

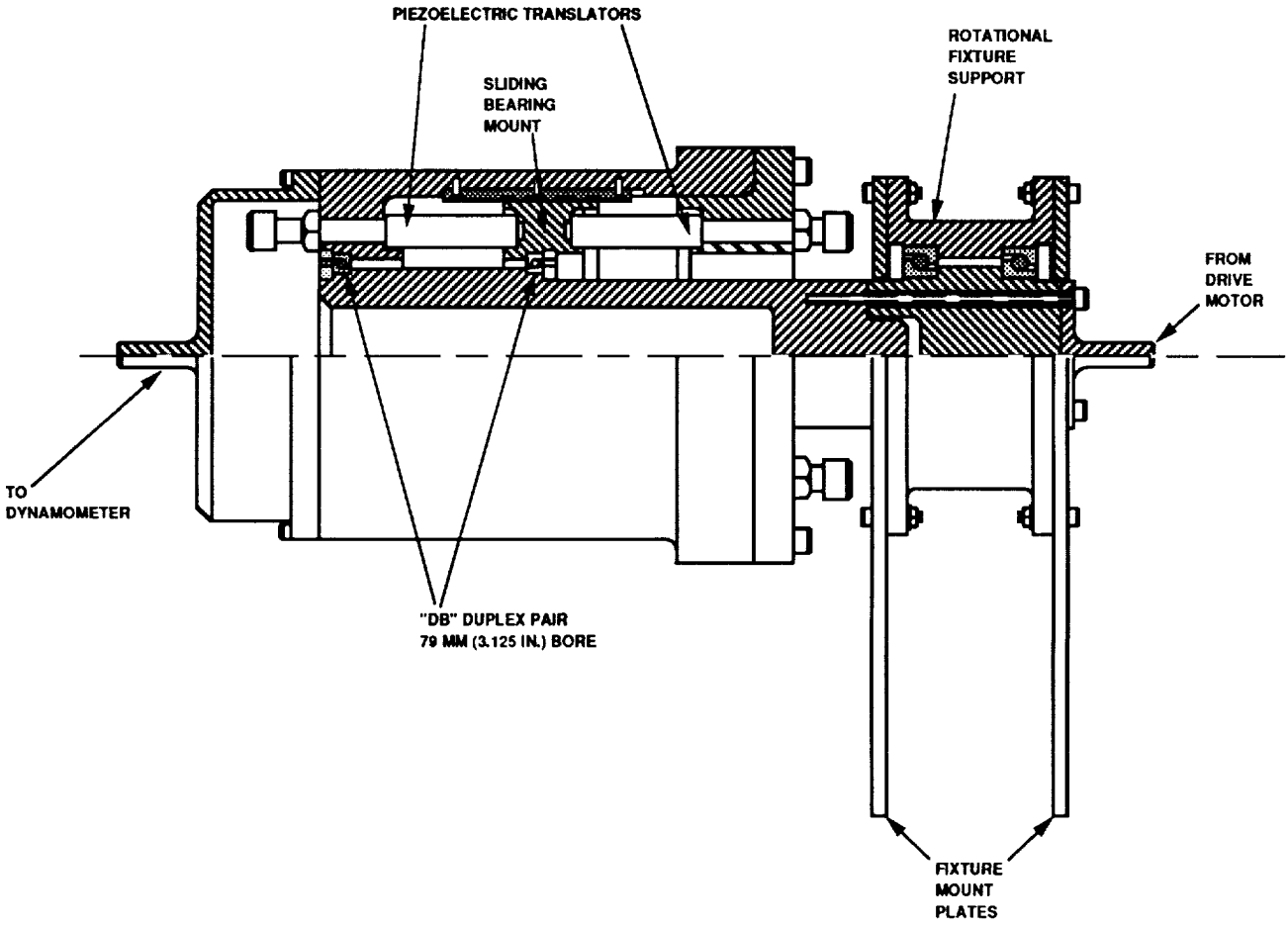

Figure 7. Section View of Test Module

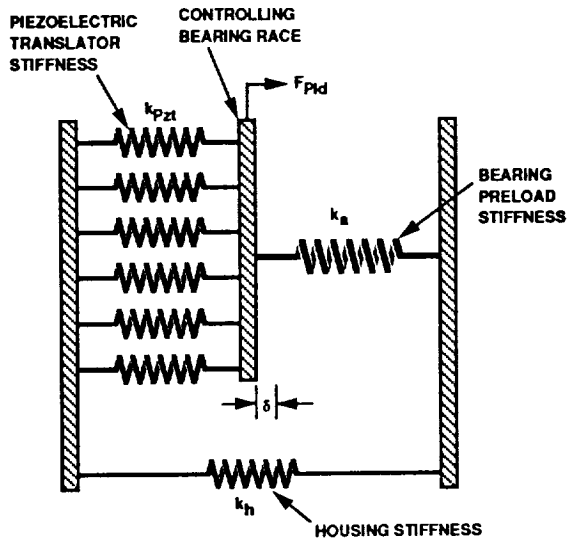

Figure 8. Mechanical Schematic of Preload Module

For this concept to work, it was important to study bearing forces and determine stiffness relationships necessary to control a wide range of preloads. Bearing stiffnesses, as shown earlier, are very nonlinear with load. This is a problem for picking a stiffness "constant" to put into finite element models or for doing bounding analyses. If we assume a lower bound for this stiffness, we can compare the deformations that will take place throughout the bearing system. Figure 8 shows such a system schematic used to formulate our modeling equations. To study how effectively we can control the bearing, we can first examine the deformation in a piezoelectric translator.

Let

$$\partial_n = \partial_f - \partial_c \tag{3}$$

Where: ∂_n = net translator expansion under load
∂_f = free state translator expansion
∂_c = translator compression

now,

$$\partial_c = \frac{F}{K} = \frac{FL}{AE} \tag{4}$$

Where: F = axial force
L = length
A = cross sectional area
E = Youngs modulus
K = axial stiffness

We also know that typical free strains for these translators are on the order of .1%

$$\epsilon = \frac{\Delta L}{L} = .001 \tag{5}$$

Combining (3) (4) and (5), we can solve for the free state translator length.

$$L = \frac{\partial_n}{\left(.001 - \frac{F}{AE}\right)} \tag{6}$$

Using this relation and referencing Figures 9 and 10 which show specific data for our module, we can analyze our preloading system. It was estimated that we needed .0216 mm (.00085 in) of expansion, against a load of 76 N (167 lbs). A translator of approximately 51 mm long by 1 cm diameter was then sized. For six translators on one side of the bearing, a net preload force of over 454 N (1000 lbs) was possible.

Deflection of the housing and mounting assemblies ideally should be at least ten times stiffer than the bearing being controlled. This insures that these extraneous compliances are kept to below 10% of the total system deformation. This was designed into the module housing with some additional margin because of uncertainties in the translator stiffnesses.

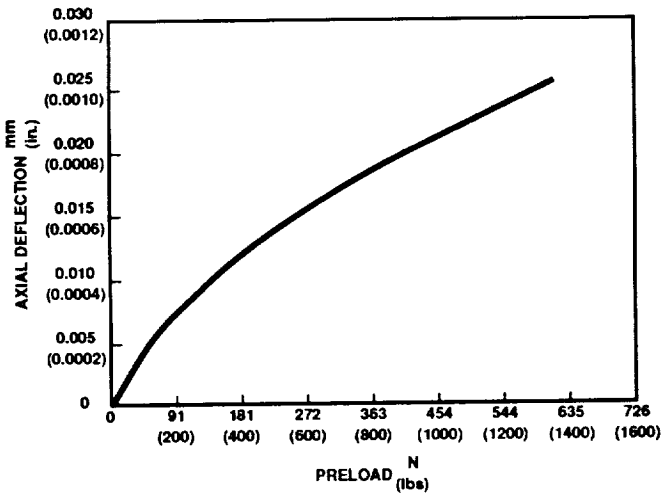

Figure 9. Axial Deflection of Bearing Race Due to Preloading

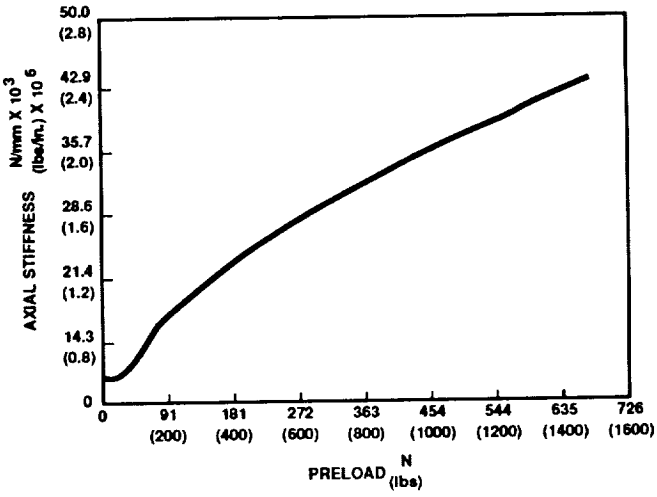

Figure 10. Axial Stiffness of Bearing Race from Preload

To test the effectiveness of the translators, expansion measurements were made as a function of voltage. Maximum applied voltage for these devices was 1000 volts per the manufacturers recommendations. By design, the translators averaged .0510 mm of free state expansion. After building and testing the module, the axial deflection of the outer race against bearing preload was measured and averaged approximately .0203 mm (.0008 in) as predicted. Voltage-expansion curves for the translators are shown in Figure 11.

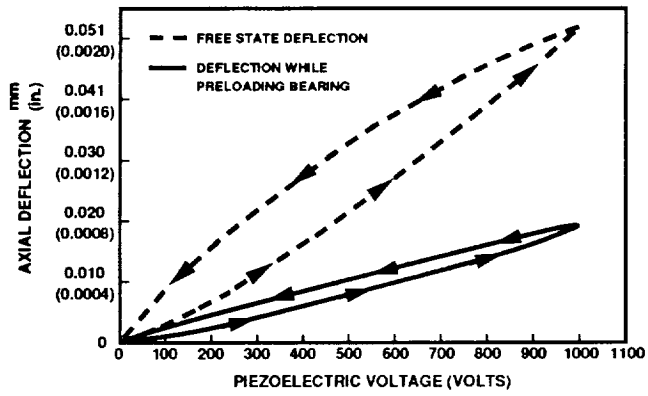

Figure 11. Axial Deflection of Piezoelectric Translators In Free State and Mounted

TEST SETUP

The intent of this project was to demonstrate that a constant friction device could be built that relied on piezoelectric translators for controlling preload. The bearing module test setup, shown in Figures 12 and 13, was subjected to temperatures ranging from 0 to 70°C while friction was being monitored (and controlled). Dry lubed bearings were used since wet lubricants would introduce error due to viscosity effects. An input drive motor rotated an internal shaft at about 1 RPM while frictional reaction torques were measured by a dynamometer attached to the module housing.

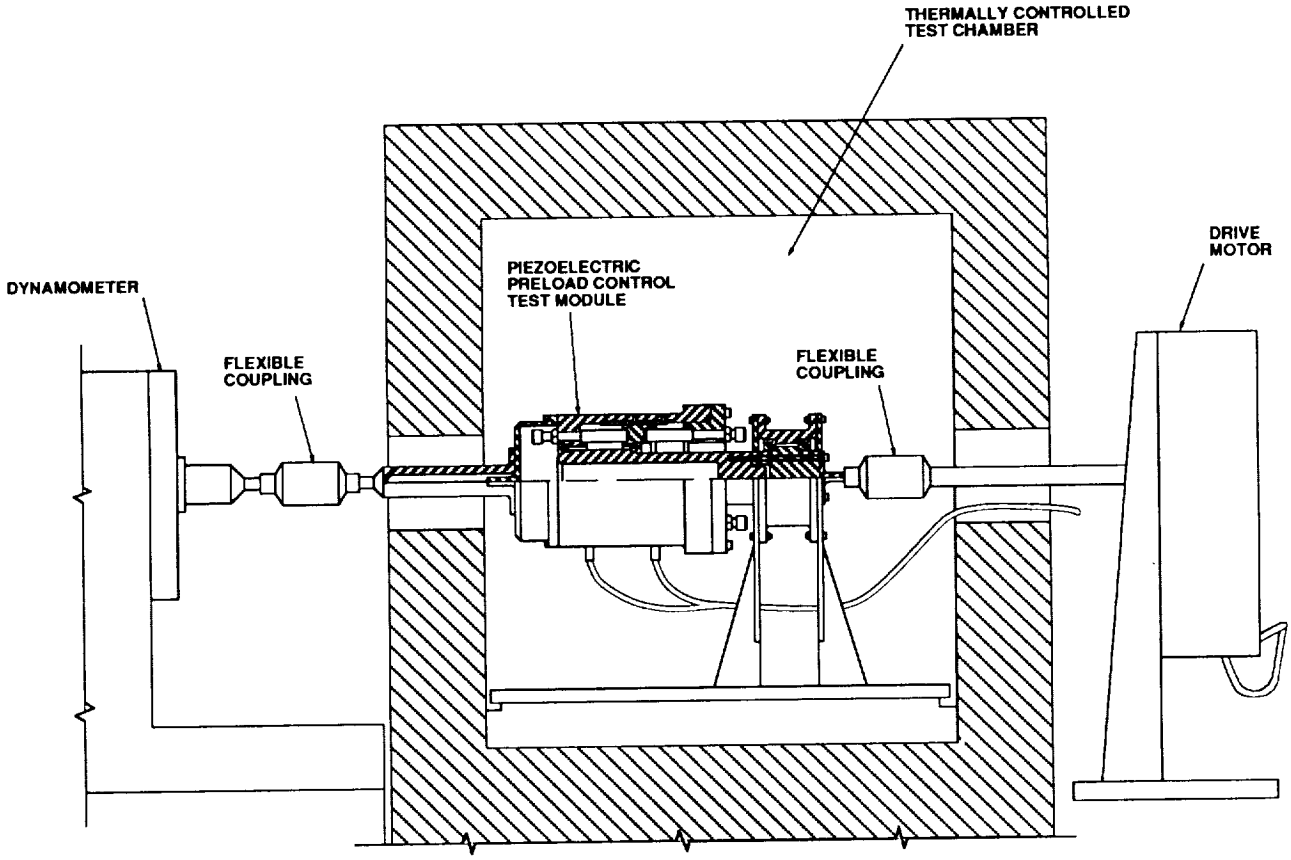

Figure 12. Test Module Setup

ORIGINAL PAGE
BLACK AND WHITE PHOTOGRAPH

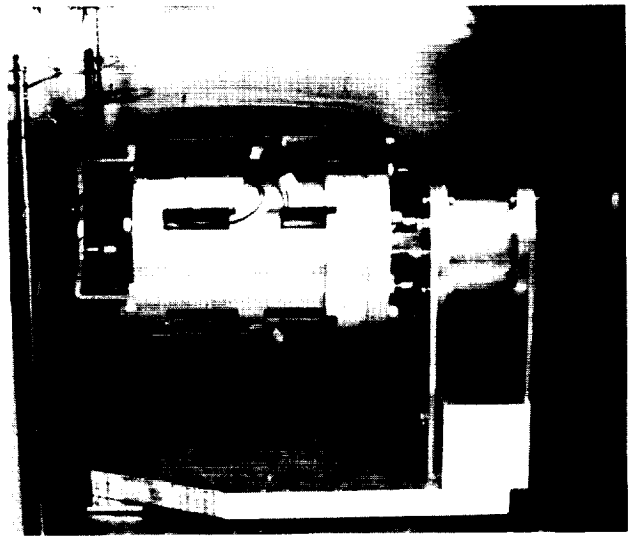

Figure 13. Bearing Preload Module Inside Environmental Chamber

The preload drive module consisted of a 6061 aluminum shaft and housing to produce a worst case thermal expansion mismatched system. Bearings consisted of a 79 mm (3.125 in) bore duplex pair, made from 440C stainless steel spaced 89 mm (3.5 in) apart. Bearings were mounted with line-to-line fits on both their bore and outside diameters. For this bearing module, unlike typical spacecraft products, little attention was paid to packaging, volume, or weight constraints to save on time and effort. Particular effort was focused on minimizing piezoelectric costs while ensuring that the translators would perform as expected.

EXPERIMENTAL RESULTS

As a first task, the module sensitivity to temperature, independent of compensation, was investigated. Dummy translators were made from aluminum rod stock and were used to replace the piezoelectric translators. Friction torque measurements at a variety of temperatures showed extreme inherent temperature sensitivity as shown in Figure 14. This data was in general agreement with theoretical results except that theoretical frictional magnitudes were much higher. An explanation for this follows in later discussion.

The compensated system behaved somewhat as expected showing very good control of friction (hence preload) throughout a 44°C temperature range. As shown in Figure 15, a friction-controlled envelope was measured as a function of temperature and translator energization. Controlling friction torque became limited by several unforeseen phenomena.

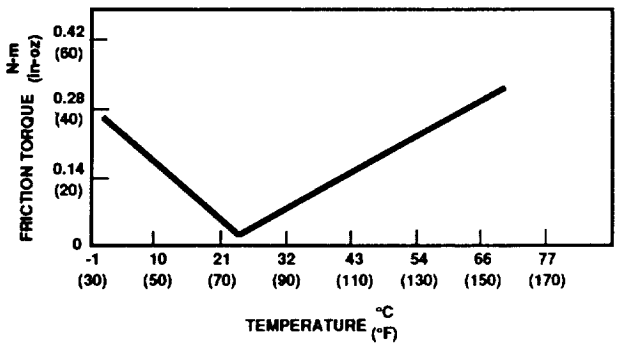

Figure 14. Inherent Friction Sensitivity of Tester Using Dummy Translators

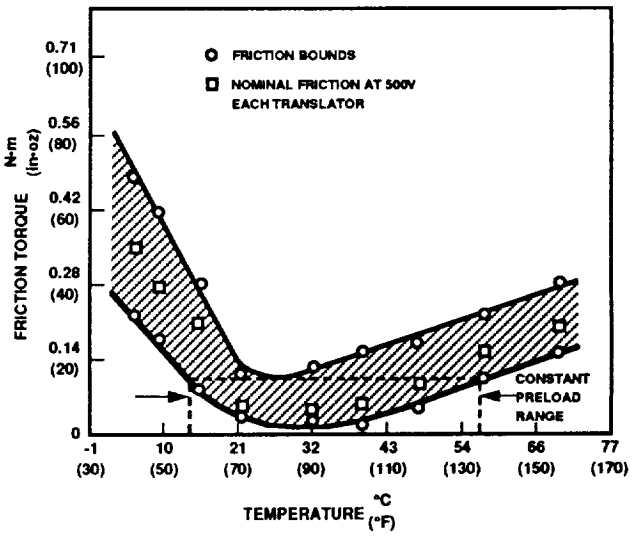

Figure 15. Controllable Friction Envelope for 440C Bearing and 6061 Aluminum Housing and Shaft

First, because of the severe mismatch of thermal expansion between aluminum and 440C stainless steel, radial interferences on the bearing fits at slightly deviate temperatures became overwhelming. Elastic deformations were so large that the thin race bearing became "radially" preloaded. Any attempts to slide races axially with the translators only served to increase preload. This behavior was thought to be responsible for the bounds of Figure 15.

Second, at room temperature, maximum friction torque measured was only .113 N.m (16 in.oz). If we look at Figure 2, based on the Palmgren friction relation, only 73 N (160 lbs) of preload was reached. It is believed much higher preloads were achieved however. Figure 11 shows the stickout was controlled properly with axial race displacement of approximately .0203 mm (.0008 in). Thus, the 454 N (1000 lbs) of preload was most likely achieved. Palmgren's frictional relationship is based on statistical measurements of many bearings, but without reference to lubricant. From various characterization tests, we have found the Palmgren relationship of equation (1) gives a good indication of relative bearing frictional behavior, but a rather poor indication of absolute frictional behavior. Thus, the theoretical friction relationship is very conservative.

Third, the piezoelectric devices themselves are not immune to temperature effects. Piezoelectrics have a large coefficient of thermal expansion of 5×10^{-6} (m/m)/°C. This most likely contributed to some of the preloading and must be taken into account for designs with severe temperature variation.

Lastly, hysteresis in piezoelectrics is usually present to about 20% of the maximum expansion in the free state. For this design, the translators pushing against each other cut this hysteresis in half. It was also discovered however, that as shown in Figure 11, when only energizing one side of the translators, measured hysteresis was not as large as expected. This suggests that a future design would work satisfactorily having only translators that preload, then allow the bearing axial force to "unload" the race.

SUMMARY AND CONCLUSIONS

The feasibility of actively controlling bearing preload was demonstrated by fabricating and testing a piezoelectrically controlled bearing module. Because bearing friction is related to preload, a thermally active system, designed with aluminum components and a 440C bearing, was friction tested at temperatures ranging from 0 to 70°C (32 to 158°F). Effectiveness of the translators was demonstrated by mapping a controllable friction range throughout tested temperatures. We learned that constant preload for this system could be maintained over a temperature span of approximately 44°C (79°F).

From testing, it was also discovered that at the more deviate temperatures, expansions were so large that radial clearances were taken up and the duplex bearing became radially preloaded. Thus, active control of bearing preload is feasible but may be limited by inherent geometry constraints and materials used in the system.

Although not tested, we learned by analysis that bearing moment stiffness corresponding to the controllable preload could have more than doubled. With moment stiffness being the most crucial for spacecraft applications, a large part of this stiffness for the test module was provided by the bearing axial spread. Thus, the inherent design desensitized the moment stiffness to preload, but still showed that stiffness could be controlled.

Controlling a structural joint for friction and stiffness behavior is both feasible and practical. To meet precision pointing applications of the future this technology will be necessary and will likely be incorporated into future state-of-the-art actuator designs.

REFERENCES

1. Estus, J.M.; Laskin, R.; Lin Y.H.; "Aiming Instruments on the Space Station," NASA Tech Brief, Vol. 13, No. 10, Item #22, October 1989.

2. Palazzolo, A.B.; Lin, R.R.; Alexander, R.M.; "Piezoelectric Pushers for Active Vibration Control of Rotating Machinery," ASME Journal of Vibration, Acoustics, Stress, and Reliability in Design, Vol III, pp. 298-305, July 1989.

3. O'Neill, C.G.; Randall, D.S.; Smiley, P.C.; "Piezomotors-Electromechanical Muscle, SAE 800512, 1980.

4. Mosley, J.; McLarty, D.; "Bearing with Adjustable Stiffness," United States Patent No. 4850719, July 25, 1989.

5. Jones, A.B., "Analysis of Stresses and Deflections," Vol 1, New Departure Division, General Motors Division, Bristol, Conn., 1946.

6. Harris, T.A., "Rolling Bearing Analysis," Second Edition, John Wiley and Sons, New York, 1984.

TEST RESULTS AND FLIGHT EXPERIENCE OF BALL BEARING MOMENTUM AND REACTION WHEELS

W. Auer*

ABSTRACT

The required satellite mission durations and levels of reliability have been considerably increased: While in the beginning of the 70's 3- to 5-year missions were planned, the standard is now 10 years with an expansion to 15 years and more for such programs as INTELSAT VII. Based on a 20-year test and flight experience with basically the same design, ball bearing momentum and reaction wheels with the required 15-year mission capability can be provided.

INTRODUCTION

The required satellite mission durations and levels of reliability have been considerably increased in the course of the last decade and so.

While for such programs as SYMPHONIE, APPLE, IRAS AND OTS, 2 to 5 years were planned, the specification for ECS, INTELSAT V, TV-SAT etc. called for a 7-year useful life. Presently, wheels are delivered for such programs as EUTELSAT 2 and DFS-KOPERNIKUS, calling for a 10-year operation capability.

For future missions, as for the INTELSAT VII satellites, a 15-year mission duration is required!

Besides design considerations and development efforts, the experience gained during testing and actual flight with wheels built essentially to the same procedures is of vital importance for providing that level of confidence necessary for the planning of such long missions.

WHEEL DESIGN

Design Description

A modular design was selected to cover a wide range of applications and specifications. With one ball bearing size three wheel diameter classes are provided which are given in Table 1 together with main parameters and/or parameter ranges:

Table 1. - Wheel Parameters

Wheel Diameter	Height	Angular Momentum	Mass
22 cm	7.5 cm	1.5 to 10 Nms	2.5 to 4 kg
26 cm	8.5 cm	5 to 20 Nms	3.5 to 6 kg
35 cm	12 cm	12 to 80 Nms	5 to 8.5 kg

* TELDIX GmbH, Heidelberg, Germany

In the following, the mostly utilized 35-cm diameter wheel (Fig.1) is discussed in some detail:

It consists of five subassemblies:

- Housing with Center Stud Bolt
- Flywheel Mass with Spokes, Damper Rings and Hub
- Ball Bearing Unit
- Motor Rotor
- Motor Stator with Commutation Electronics

These subassemblies are completely independent of each other and can be built and tested separately. Thus, performance deficiencies or unacceptable tolerances can be determined at the subassembly stage and, if necessary, corrected. After successful individual tests, the subassemblies can be "accepted" and assembled to the complete wheel.

This modular design approach allows also for relatively simple adaptations to different specifications without losing the heritage. For instance, the flywheel mass can be equipped with rings of different moments of inertia, or, the motor designed for lower or higher torque capability, or the bearing unit adapted to different speeds or speed ranges.

o Housing

The lightweight housing provides a defined environment for the delicate "interior". It consists of the upper and lower housing, both spun from sheet metal. In the latter, the base plate is fixed by electron beam welding. Both parts are soldered to each other via a tear strip.

The special curvature together with the center stud bolt is the reason for the capability to withstand easily the air pressure during and after evacuation.

o Flywheel Mass

To achieve a favorable inertia-to-mass ratio, the flywheel rim is linked to the hub by lightweight but stiff double-T-shaped spokes made of sheet metal. If this flywheel were excited by vibrations, introduced to the hub, resonance step-ups of 80 or so would result. Because no load relief is foreseen, these loads would lead to ball bearings of a size not acceptable with regard to mass and friction. Therefore, the flywheel mass is damped by two damper rings which are in friction contact with the spokes. The reasonance step-ups are now more than one order of magnitude lower.

o Ball Bearing Unit

This unit is decisive for life and reliability. Two ball bearings are rigidly preloaded to each other by spacer sleeves and nuts. The material

selection and geometrical properties assure a practical constant preload over temperature and temperature gradients.

The retainers are designed to operate stable under all speed, temperature and lubrication conditions. The initial amount of lubricant in the bearings is sufficient for providing an EHD-film for years of running. To assure a multi-year operation capability, a lubrication reservoir, activated by centrifugal force, is located between the outer rings. After a certain accumulated running time, this reservoir starts to bleed oil to the outer rings of the bearings.

o Motor Rotor

A brushless and ironless DC motor is used. Depending on the torque requirement, either one of the two cylindrical surfaces of the U-shaped rotor are covered with samarium cobalt permanent magnets.

o Motor Stator with Commutation Electronics

The stator coils are inserted into the holes of the cylindrical support of the armature. The stator is mounted between the above mentioned rotor surface. Thus, the permanent magnet flux is "cutting" the wires of the windings. To avoid eddy currents, stranded wire is employed in most applications.

The commutation sensors together with a shutter ring controls via electronics the currents in the coils of the motor. The sequence of switching provides also tachometer signals, and if necessary, also a speed direction indication.

For wheels which must be able to operate cw and ccw, two sets of sensors with adequate electronics are used.

Life Prediction

For the life prediction, the ISO/R281/1 is used. It takes into account newer research results. The traditionel AFBMA formula

$$L_{10} = \left(\frac{C}{P}\right)^3 \text{ million revolutions}$$

is extended to

$$L_{na} = a_1 \cdot a_2 \cdot a_3 \left(\frac{C}{P}\right)^3 \text{ million revolutions,}$$

where

L_{na} = modified nominal life with the probability n in percent that a ball bearing fails before L_{na} is reached,

a_1 = life adjustment factor for achieving or exceeding a life time with a probability other than 90 percent,

a_2 = life adjustment factor for bearing material

a_3 = life adjustment factor for nonconvential operating conditions,

C = dynamic load rating and

P = equivalent load.

The essential message is that even a non-failure life L_{NF} can be expected, provided there is "sufficient" lubrication.

For the utilized bearing size ISO 04 (20x42x12 mm^3), an equivalent load of 85 N, the load rating of 7800 N, the defined $a_1 = 0.05$ for achieving L_{NF} and a factor $a_2 \cdot a_3 = 2.5$ (resulting from material, cleanliness, surface asperity relative to lubrication film thickness), an L_{NF} of about 18 years results, when a speed of 6000 rpm is assumed. This life potential is beyond the present requirements of 15 years and valid for the fatigue life aspects.

Other failure mechanisms are:

1. Corrosion: Avoided by employing stainless steel and sealing of the housing.

2. Wear: Good surfaces, extreme cleanliness and a sealed housing are provided.

3. Retainer damage: A well proven material is used which is able to bear loads equivalent to 40,000 rpm for this bearing size continuously and a stable retainer movement.

4. Inadequate lubrication: A high-viscosity lubricant is used; surfaces wettability checked; a failsafe lubrication system is implemented.

TEST RESULTS

Lubrication Tests

After a theoretical and an experimental trade-off, an oil lubrication was favored; the generally employed grease lubrication for long life applications has some disadvantages: Excessive friction torque changes and spikes, especially over the temperature range and while employing temperature gradients. Furthermore, no simple mechanism for the replenishment of grease - without too much influence on the friction torque behavior - could be defined.

To assure a low friction torque over temperature and time, an oil film lubrication with the mineral oils SRG-60 and KG-80 was developed - similar to that employed in high performance gyro bearings. This task led to intensive investigations concerning materials, cleanliness, wettability, retainer dynamics, migration control, molecular seals, and oil distribution.

One test series was devoted to the determination of the minimum lubricant quantity for the generation of a full EHD-film. A main criterion for the quality of such a film was the electrical resistance as a function of time at different speeds. Because two bearings were mounted in an original bearing unit, one of the bearings was equipped with balls made from ceramics.

The retainers were vacuum impregnated and subsequently centrifuged to such an extent that no additional oil should come out during running. The oil amount, distributed to the steel parts was sequentially decreased from about 9 mg in steps down to about 2 mg and finally to about 1 mg. The torque over speed and time was recorded, together with a monitoring of the electrical resistance. It turned out that 2 mg are still sufficient for flawless operation while at 1 mg signs of starvation were evident: The resistance over time showed more breakdown spikes.

Therefore, it was concluded that the minimum amount of lubricant is 2 mg. At this lubrication condition, the constant friction torque level was reached shortly after switch-on. Also over temperature ranges (-10 °C to +55 °C), the torque values only changed some 10%.

With higher amounts of lubricant the run-in time increased accordingly from an hour to some ten hours but the finally achieved torque levels were practically the same as those got for minimum lubrication.

With a bearing unit, equipped with molecular seals and anticreep barriers, and with an initial amount of oil in the bearings of about 10 mg, years of flawless running are possible.

In the course of the initial development phase for wheels, due to schedule reasons, no testing for mission duration (at that time 5 years) could be planned. Therefore, a lubrication reservoir was conceived which starts to bleed oil to the bearings after some delay time. The working principle of this device is explained in the following to a certain extent.

The reservoir, situated between the two outer rings of the ball bearings on the outer spacer sleeve, is subjected to the centrifugal force during running. The lubricant - the base oil, stored as grease in a ring type chamber - can be centrifuged out through some orifices. The rate is limited by the thickener of the grease which forms a microporous filter in and in the vicinity of these orifices.

To avoid an early bleeding to the bearings, the centrifuged oil enters a coaxially situated oil reservoir, made from a porous material. This oil reservoir is vacuum impregnated with oil and afterwards centrifuged to an extent that in the nominal speed range no oil is bleeding to the bearings. Only after some operating time, when the oil from the grease chamber has re-saturated the oil reservoir, the bleeding to the bearing starts with a low rate.

Figure 2 shows the long-term bleed test of a grease chamber. At the beginning, a high bleeding rate is experienced which levels out after some thousand hours of centrifuging. The high rate of bleeding at the beginning allows for a good definition of the delay time of the lubrication reservoir. An overall bleed characteristic of the lubrication reservoir is indicated too. In this example, the delay time would be 7,500 hours, the oil amount for saturation of the porous oil reservoir 900 mg and the total supply of oil, fed to the bearings, 170 mg in 120,000 hours.

The bearing unit is designed in a way that "surplus oil" is not leaving the lubrication area "for ever" but is stored in the vicinity of the bearing. This could be also demonstrated by testing. The advantage is that this oil can creep back to the bearings. The disadvantage is that one may experience overlubrication with excessive friction torques.

To prove that no critical overlubrication can take place, an accelerated overlubrication test was performed. The test setup is shown in Figure 3. An original bearing unit operating with its spin axis in the horizontal position was modified. The grease chamber's inner cover was removed so that oil could be directly dropped into the open grease chamber. The results of this test are interpreted by using Figure 4. Over a time period of about 90 days, the maximum oil quantity, centrifuged out of a grease chamber in a mission, was added. The acceleration factor was therefore in the order of 40 for a 10 year mission.

The bearing unit was allowed to run in for 6 days. The current (a measure for the friction torque) decreased from 310 mA to 215 mA. Now oil was added in steps at a relatively high rate between day 7 and 15. Because this amount of oil was absorbed by the porous oil reservoir, no lubrication status change of the bearings had occurred.

The oil added afterwards led to a small increase of the current (day 22 to 31) with the beginning of more torque noise on day 32 and an increase of the current to 294 mA. During the days 33 to 41 no oil was applied to allow for stabilization and run in. In this period the current decreased to about 210 mA with heavy torque spiked (shaded areas).

The adding of oil was resumed on day 42. Two days later again signs of overlubrication appeared with increased torque noise and a subsequent

current increase to 320 mA on day 52. (The last oil increment was applied on day 48.) The following run-in period brought the current again down to about 210 mA on day 62.

To simulate a stop-start sequence, the bearing unit was stopped on day 77. Due to the high oil amount in the bearings, the current was 440 mA after the start on day 83; run-in occurred within about 3 days to a current between 210 and 218 mA. The oil amount of 100 % was reached on day 93.

A further addition of oil to about 108 % was performed on day 105 with a "response" of the torque on day 107 to about 330 mA. Now the bearing unit was stopped to simulate a stop-start sequence in an over-lubrication status. The switch-on (day 108) led to a longer run-in period but finally on day 122 the current was again down to 220 mA.

The test was the proof that a running bearing unit can distribute additional oil when applied in small quantities (actually continuously with a small rate) without excessive torques. Therefore,the feed rate of the lubrication reservoir is not so critical.

Storage Test

A wheel (SYMPHONIE qualification model) was qualified, integrated into the qualification model of a satellite and subjected to the qualification test of the satellite. After a storage period of five years it was possible to receive this wheel back for investigations. The only deterioration was an increase of the current which could be traced to a housing leakage. After reevacuation, the current was practically the same as during qualification.

Subsequently, the wheel was disassembled. The appearance of all sub-assemblies and parts was "as new". The bearings were well lubricated. The measurements of the roundness, surface parameters and so on confirmed that no degradation took place.

It was concluded that storage periods of a wheel, which could accumulate to say 15 to 20 years (integration + storage on ground + cold redundancy during a mission) should have no negative influence on the operational readiness of such a wheel.

Life Tests

A total of 103 years (status Nov. 1989) of testing were accumulated. Of special interest are two momentum wheels (3,000 rpm and 3,800 rpm) which have been in continuous operation - after full qualification - since October 1973. These wheels were also subjected to thermal cycling in half-year intervals to simulate eclipse periods. The currents/torque levels remained constant - within $\pm$ 10 % - after run in.

To increase the "torture" on the wheel, running at 3,800 rpm, it was mounted in a sunlight-shaft in March 1981. This was a cheap way to subject this wheel to seasonal and daily temperature cycling. As an example (Figure 5), the temperatures and currents over time are indicated for two days each in February, August and November 1985; the temperature was measured in the vicinity of one of the ball bearings. The temperature ranges from 3.5 °C to 30.5 °C. Daily changes occur with peak-to-peak values of 2.5 °C to 7 °C. The friction torques remain remarkably constant (0.012 Nm to 0.013 Nm).

Also a reaction wheel life test is performed with one daily triangular speed cycle between -3,500 rpm and +3,500 rpm. In this case, too, each half year temperature cycling takes place. Figure 6 shows the friction torque over speed at the start of the test (after run in) and after 10 years of testing. There is practically no change; this is also true for the results at lower and higher temperatures.

No ball bearing failure occurred during all life tests.

FLIGHT EXPERIENCE

Flight Programs

There are 19 satellite programs (40 satellites, 84 wheels) flying this basic wheel design. A total of 212 operating years was accumulated, not counting the cold redundant wheels.

The OTS wheel is that with the longest operation time of 11.5 years (status November 1989).

No ball bearing failures had been experienced. The two SYMPHONIE wheels showed signs of electronics degradation long after the planned mission duration of 5 years. The wheels served 9 years after the satellites were decommissioned, long after other failures (batteries, transponders etc.).

Due to the demonstrated reliability and long-life characteristics, 240 wheels were manufactured or are under contract.

Flight Operation Results

Because there were no failures reported, we found it rather difficult to get information concerning the performance of the wheels in orbit. However, it was possible to receive some results from the OTS, INTELSAT V, TV-SAT 2 and DFS-KOPERNIKUS Satellites. Data of the latter are presented at the Symposium only.

o OTS-B

This satellite has been 11.5 years in operation. In Table 2 some acceptance test and flight results are presented which show the motor current over speed, temperature and time.

Table 2 - Test and Flight Result OTS-B

	Acceptance Test Nov. 1976			Flight 18th Oct. 1989
Speed	22 °C	-5 °C	45 °C	4000 rpm 31 °C
3,600 rpm	220 mA	284 mA	186 mA	min 206 mA
4,000 rpm	230 mA	292 mA	192 mA	max 292 mA
4,400 rpm	234 mA	294 mA	198 mA	avge 248 mA

The attitude control utilizes an integrator in the loop. Therefore, a "massive" differential control component is necessary. This leads to a noisy current, as can be seen also in Figure 7 which shows the current over time on the 7th Sep. 1989 at a speed of 4,000 rpm and a temperature of 31 °C.

o INTELSAT V

Acceptance test, pre-launch and flight results can be compared in Table 3.

Table 3. - Test and Flight Results INTELSAT V

	Launch	Acc.Test (Amp)	Pre-Launch (Amp)	Post-Launch (Amp)	July 85 (Amp)	May 88 (Amp)
F 1	Dec 80	0.17	0.21	0.19	0.19	0.19
F 2	May 81	0.23	0.22	0.20	0.19	0.19
F 3	Dec 81	0.20	0.23	0.20	0.19	0.20
F 4	Mar 82	0.21	0.20	0.20	0.21	0.20
F 5	Sep 82	0.20	0.21	0.20	0.19	0.19
F 6	May 83	0.19	0.18	0.17	0.19	0.18
F 7	Oct 83	0.21	0.25	0.20	0.21	0.21
F 8	Mar 84	0.20	0.18	0.17	0.20	0.20
F10	Apr 85	0.17	0.21	0.20	0.20	0.17
F11	Jul 85	0.17	0.20	0.20	0.20	0.17

Temperatures were 20 °C to 35 °C, speeds in the nominal range.

o TV-SAT 2

In Figure 8 the wheel temperature, motor voltage (a measure for the speed) and motor current is plotted for the 28 of Sep. 1989, about at

maximum eclipse (launch: Aug. 1989). The satellite's position is 11° West which can be recognized in the temperature plot as a relatively high temperature gradient. The current, quantisized by TM, is not influenced by these moderate temperature changes. It compares favorably with the acceptance test result of 0.11 Amp at normal temperature and nominal speed.

CONCLUSION

A ball bearing momentum/reaction wheel of modular design with a special lubrication system has proved its ability of reliable long life operation during tests and in orbit. With this heritage, the specifications for a 15-year mission can be met with a high confidence level.

REFERENCES

1 International Standard ISO/R281/1, "Rolling Bearing Dynamic Load Ratings and Rating Life", 1977-03-15.

2 Dromgold, L.D. and Klaus, E.E., "The Physical and Chemical Characteristics of an Homologous Series of Instrument Oils", Bearing Conference Dartmouth College, Hanover, N.H., Sep. 5, 1968.

3 Auer, W., "Design and Lubrication of Ball Bearing Units for Flywheels", European Space Tribology Symposium, Frascati, Italy, April 1975.

4 Binge, D. and Treadwell, R., "The Design of a Solar Array Drive and Momentum Wheel for a Long Life Spacecraft", European Space Tribology Symposium, Frascati, Italy, April 1975.

5 Nieder, G., "Lubrication Test Program", Contract IS-659, COMSAT, 1978.

6 Auer, W. and Nieder, G., "Experiences with Shock Pulse Measuring Equipment gained during Verification and Life Testing of Space Ball Bearings", Second Tribology Workshop, ESTL, Risley,UK, Oct.15-17,1980.

7 Rapp, D., "The Influence of Five Years of Storage on the Operational Readiness of a Satellite Flywheel", Second Tribology Workshop, ESTL, Risley, UK, Oct. 15-17, 1980.

8 Auer, W., "Experiences with Start-Stop-Operation of Reaction Wheel Ball Bearings", ASLE/ASME Lubrication Conference, New Orleans, La., Oct 5-7, 1981.

9 Stevens, K.T. and Todd, M.J., "Cage Instabilities in a 42 mm OD/20 mm ID Angular Contact Bearing", esa trib 1, Sep. 1980.

10 Nieder, G., "Life Testing of TELDIX Ball Bearing Reaction Wheel Type RSR 2-O", ESA/ESTEC Yearly Reports 1979-1989.

11 Nieder, G., "Life Testing of a Ball Bearing Flywheel", ESA/ESTEC Yearly Reports 1973-1989.

12 Heimel, H., "Evolution of Large Momentum and Reaction Wheels", 3rd European Space Mechanisms and Tribology Symposium, Madrid, Spain, 30 Sep - 02 Oct, 1987.

13 Auer, W., "Ball Bearing versus Magnetic Bearing Reaction and Momentum Wheels as Momentum Actuators", AIAA International Meeting, Baltimore, Md., May 6-8 1980.

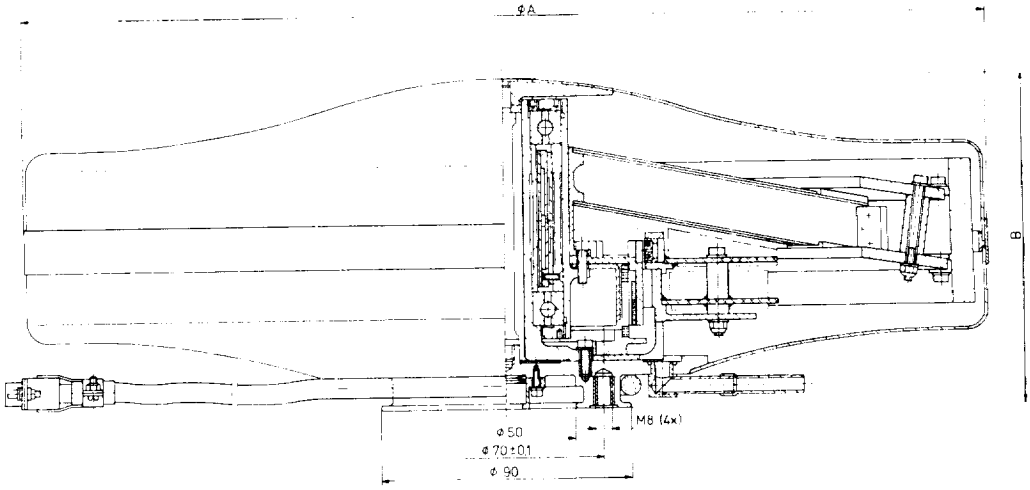

Figure 1. Wheel

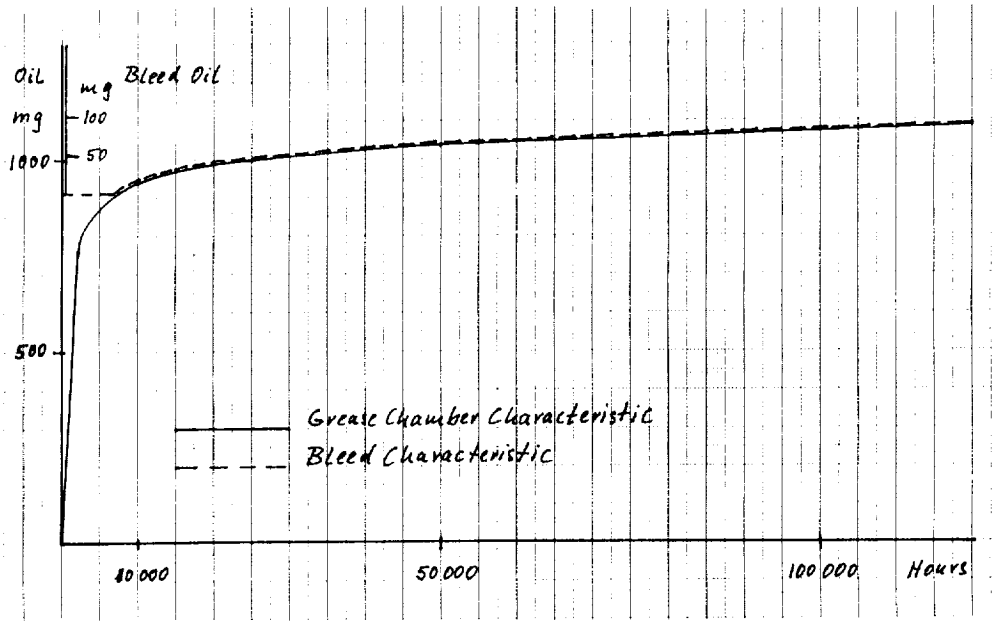

Figure 2. Grease Chamber Characteristic and Bleed Characteristic

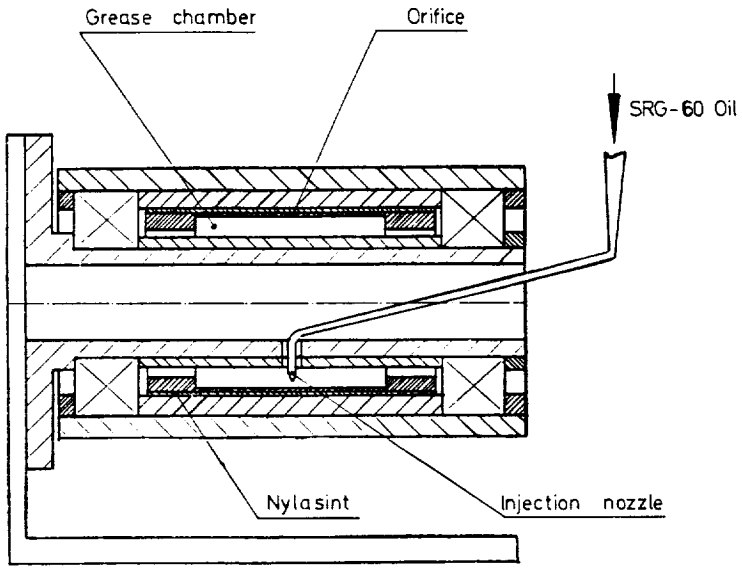

Figure 3. Test Setup for Overlubrication Test

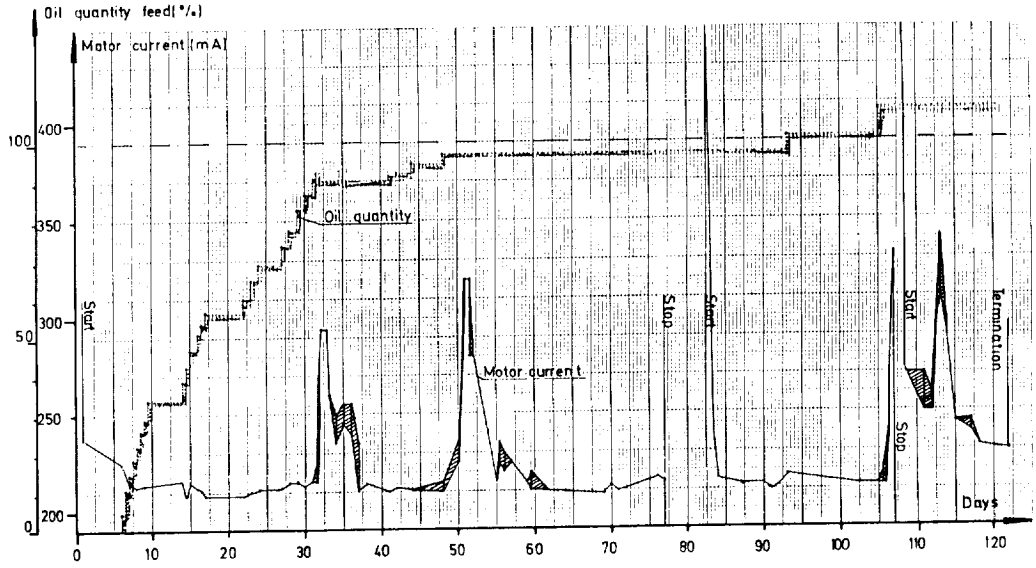

Figure 4. Results of the Overlubrication Test

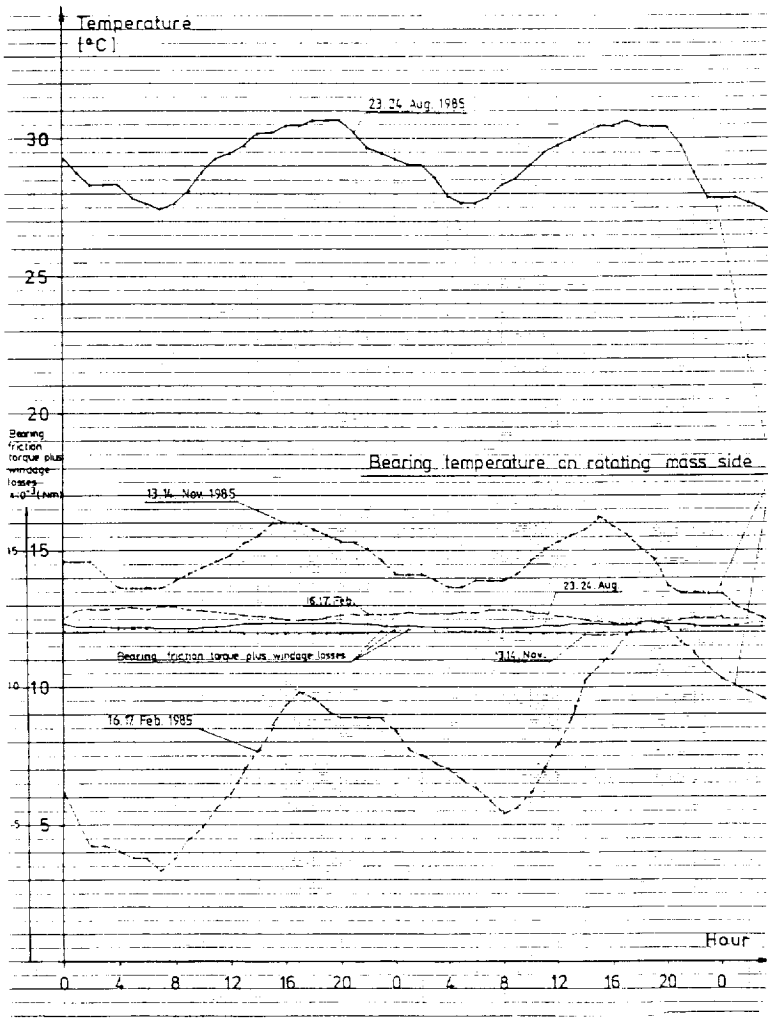

Figure 5. Life Test Results, Momentum Wheel

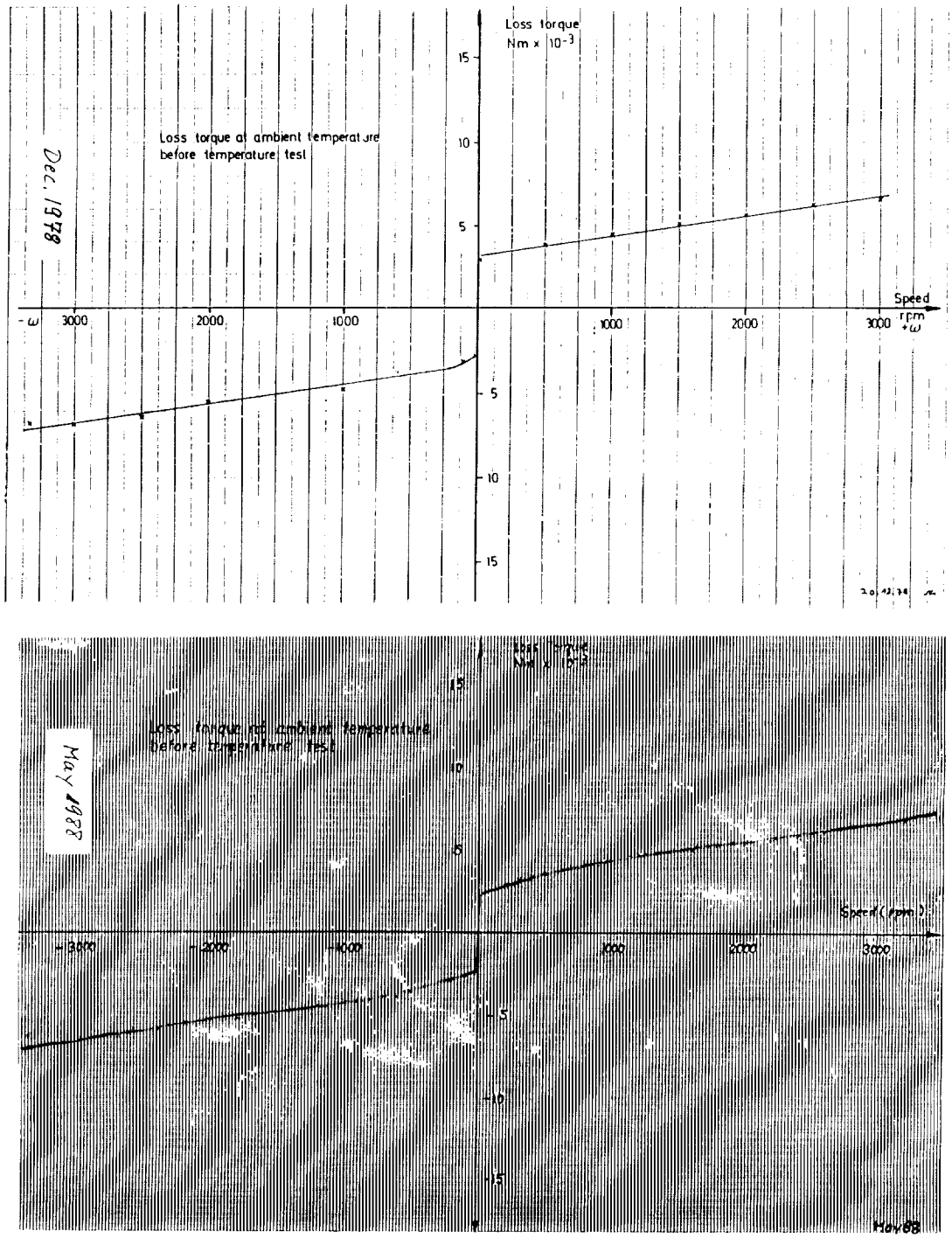

Figure 6. Life Test Results, Reaction Wheel

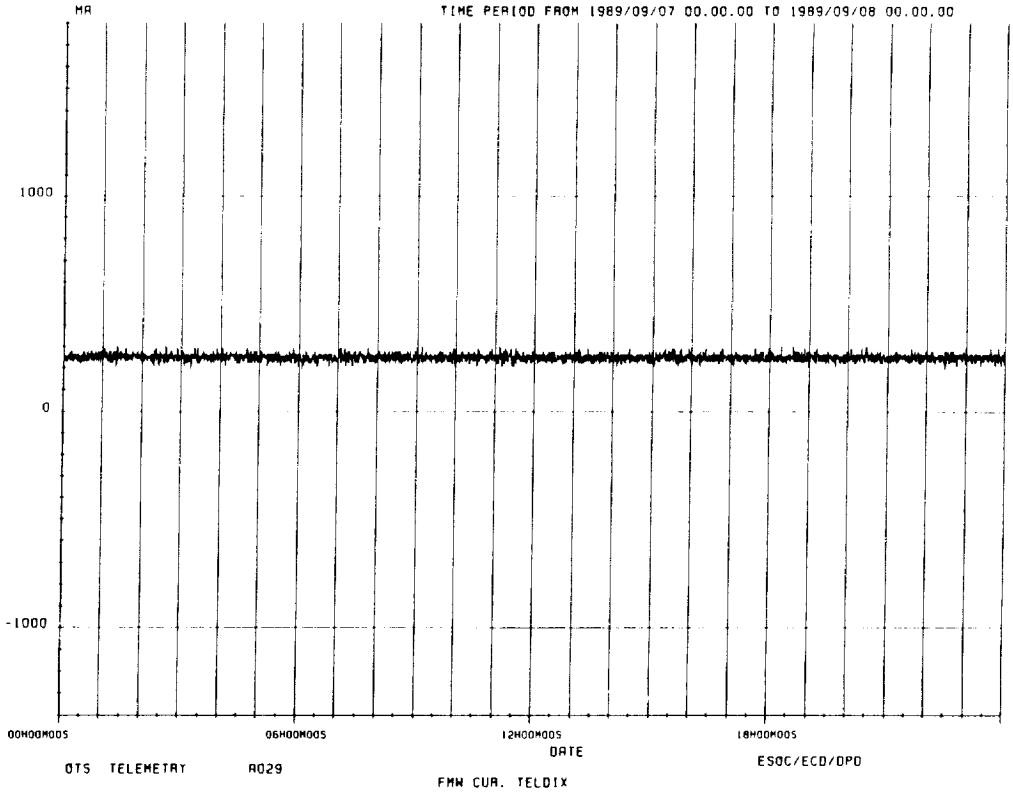

Figure 7. OTS-Current

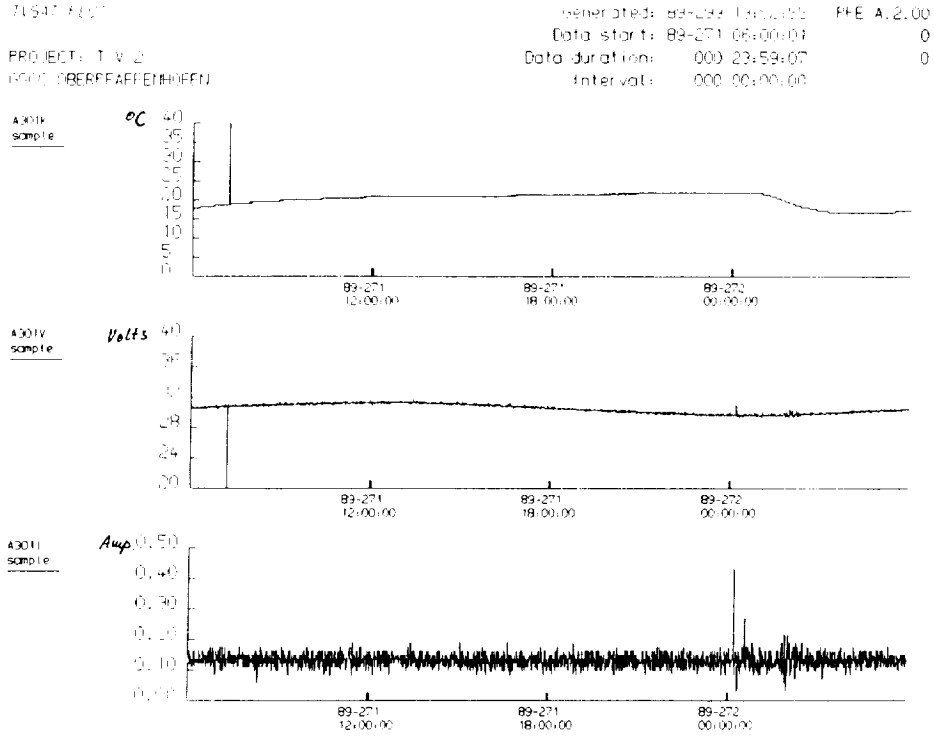

Figure 8. TV-SAT 2 - Current/Voltage/ Temperature

ON THE DESIGN AND DEVELOPMENT OF A MINIATURE CERAMIC GIMBAL BEARING

by Robert A. Hanson*, Barry O'Dwyer*, Keith M. Gordon*, and Edward W. Jarvis*

ABSTRACT

A review is made of a program to develop ceramic gimbal bearings for a miniaturized missile guidance system requiring nonmagnetic properties and higher load capacity than possible with conventional AISI 440C stainless steel bearings.

A new gimbal design concept is described which utilizes the compressive strength and nonmagnetic properties of silicon nitride (Si_3N_4) ceramics for the gimbal bearing. Considerable manufacturing development has occurred in the last five years making ceramic bearings a viable option in the gimbal design phase. Bearings with Si_3N_4 races and balls are now manufactured and available in several miniature sizes ranging from size 518, 3.2 mm bore x 7.9 mm OD (0.125 in x 0.3125 in), to size R8, 12.7 mm bore x 28.5 mm OD (0.500 in x 1.125 in). The design also utilizes a unique bearing design to overcome some of the inherent limitations of the ceramic material and adhesive assembly of the gimbal to simplify the manufacturing procedure.

This paper summarizes a preliminary study into the feasibility of the proposed design. Finite element analyses of the brittle ceramic bearing components under thermal stress and high acceleration loading were conducted to ensure the components will not fail catastrophically in service. Finite element analysis was also used to optimize the adhesive joint design. Strength tests on several candidate adhesives indicate that adhesives are available that provide adequate adhesive joint strength between the metal gimbal ring and the ceramic bearing rings. Bearing torque tests run at various axial loads indicate that the average running torque of ceramic bearings varies with load similarly to that of conventional steel bearings. Axial compliance (deflection vs load) tests indicate that the ceramic bearings are, not unexpectedly, somewhat stiffer than steel bearings. Preliminary results indicate the new design concept, utilizing ceramic gimbal bearings, is a viable option and further, more detailed study is warranted.

*Miniature Precision Bearings, Division of MPB Corp., Keene, NH

INTRODUCTION

The gimbal miniaturization program was initiated to develop an improved performance guidance system for an air-to-air missile which presents some serious gimbal bearing design problems. In particular, the design requires a nonmagnetic bearing material, high load capacity (necessary to survive the high acceleration forces of launch without Brinell damage to the raceways), and a tiny size 2.5 (1.2 mm bore) bearing is the largest that fits into the available space.

Table 1 - Required Load Capacity

Direction	N	lb
Radial	38.7	8.7
Axial	25.8	5.8

The miniaturization of the gimbal system reduced the diameter of the gyroscope drive motor magnet and coil, located outside the gimbal, making them closer to the gimbal bearings, thus exposing the current 440C stainless steel bearings to much stronger magnetic fields. The stronger fields result in significant magnetic attraction of the ferromagnetic bearings effecting the freedom of movement of the gimbal by magnetic drag. In tests, the traditional nonmagnetic bearing material, 2 % beryllium copper (copper alloy 172), eliminated this problem, but does not have adequate load capacity. The maximum acceptable Hertz contact stress for beryllium copper is much lower than 440C. In fact, the original 440C steel bearing had only marginal load capacity in the application.

Si_3N_4 bearings provide an interesting alternative since they are nonmagnetic and have higher load capacity than bearings made from either beryllium copper or 440C. Si_3N_4 has demonstrated superior bearing performance in many tests over the last 20 years. Its capabilities are well documented. Although the bearing is smaller than any monolithic all-ceramic ball bearing ever manufactured that we are aware of, it is a feasible project from a manufacturing standpoint, based on recent ceramic manufacturing developments.

A problem arises, however, with the design - conventional gimbal systems are designed with flanged outer ring gimbal bearings (never before attempted in ceramics and complicated by the tiny size of the components) and the gimbal bearing inner ring is mounted on the internally threaded trunnion of the inner gimbal and secured by a screw, as shown in Figure 1. Si_3N_4 has a low thermal expansion coefficient compared to the metals used for the gimbals, here Inconel 600, which would result in potentially damaging tensile hoop stresses on the inner ring at elevated temperatures. Si_3N_4 has a relatively low tensile strength and is subject to catastrophic brittle failure if the applied loads exceed the strength of the inner ring. A conventionally designed Si_3N_4 gimbal bearing, although it would be nonmagnetic and have improved load capacity, would be potentially very difficult to manufacture and subject to inner ring fracture at elevated temperatures. In addition, the bearing bore and OD and bearing mounting surfaces on the gimbals are precisely matched fits requiring ultra-precision machining which gets more difficult as the gimbals are miniaturized.

Table 2 - Thermal Expansion Coefficients		
Temperature Range: -54 to 123°C (-65 to 253°F)		
	/°C	(/°F)
Inconel 600[1]	12.6×10^{-6}	(7.0×10^{-6})
Si_3N_4[2]	0.97×10^{-6}	(0.54×10^{-6})

For many reasons it was desirable to develop a gimbal system design that allowed the use of ceramic bearings and also improved the manufacturability of the gimbals. A new design concept, Figure 2, was suggested that fixed the bearing rings to the gimbals with adhesives, rather than mechanically. This eliminated the need for the bearing outer ring flange and reduced the required precision of the gimbal mounting surfaces. The alignment of the proposed gimbal bearing can be adjusted during assembly of the gimbal, before the adhesive has cured.

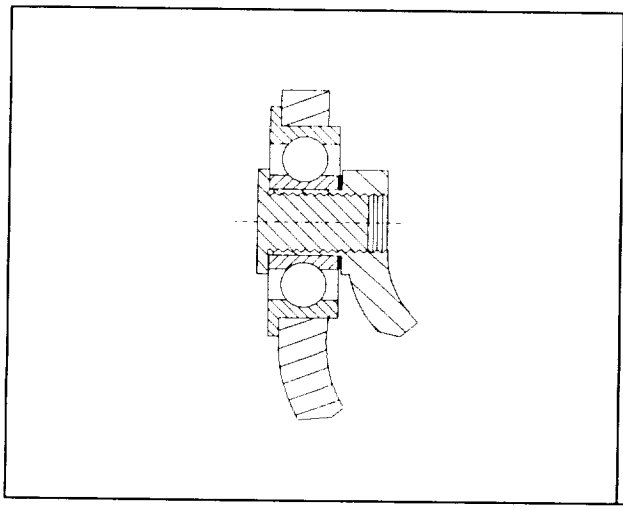

Figure 1: Conventional design

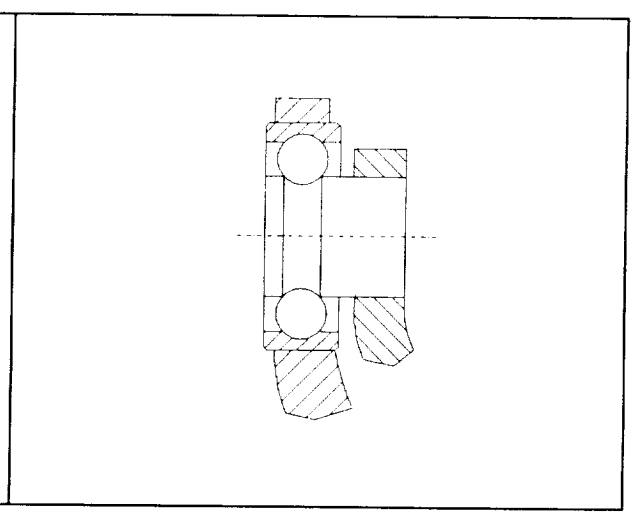

Figure 2: New concept

The bearing inner ring for the new concept design is a solid pin which is inserted in a mounting hole in the inner gimbal. This eliminates the risk of brittle tensile failure of the inner ring due to tensile stresses from a metal shaft that expands faster than the ceramic inner ring.

Another advantage of the new design is that, without the requirement for an outer ring flange for mounting, it allowed space for a somewhat larger bearing with additional load capacity.

CERAMIC MATERIALS

Cerbec NBD-100 (HIP) material was selected for the races and NC-132 (HP) for the balls based on extensive experience with the materials in the bearing industry as a whole and, more importantly, within MPB. Both materials have been well characterized by Cerbec

and others. Since the program is a rapidly evolving design with little time for prototype manufacturing, availability was also a crucial concern. NBD-100 race blanks and NC-132 balls were both readily available.

Ceramic materials do not significantly deform plastically under loads, as most metals do, but fail by brittle fracture at defects in the material. The probability of failure at a point is the combination of the calculated stress at that point and the probability of exposing a defect large enough to cause brittle failure at that stress. There is some finite chance that a defect in a low-stressed area may be large enough to initiate the failure there before it is initiated in a high-stressed zone. For this reason one must evaluate the probability of failure over the whole volume of the ceramic component, not only the highest stressed region, to determine the reliability of the component under load. Our preliminary study did not evaluate the probability of failure of each area of the component, only the highest stressed region. Further studies must be conducted to do this if the initial results are encouraging.

Furthermore, one must stress a large volume of material in strength tests on ceramics to get a good assessment of the probability of having damaging defects in a particular material lot. The reliability of the strength data depends directly on the volume of material stressed in the test and the number of samples tested. These two criteria define the sample size, that is the total volume of material tested. If the strength data does not have a high confidence level, the ceramic parts must be oversized or the loads reduced to give adequate reliability.

The Weibull plot representing the four point bending strength of the Cerbec NBD-100 done as a qualification test on a recent lot of material is shown in Figure 3. [2] There were 16 test specimens made in accordance with MIL-STD-1942B. The average failure load is 782 MPa (113 kpsi) and the Weibull modulus is 8.2. It should be pointed out that this is a conservative estimate for our use since the stressed area in this test is quite large, 4 mm x 20 mm, compared to the size of our components. It also should be noted that these tests, representing one lot only, may be somewhat different from other data that has been reported on this material.

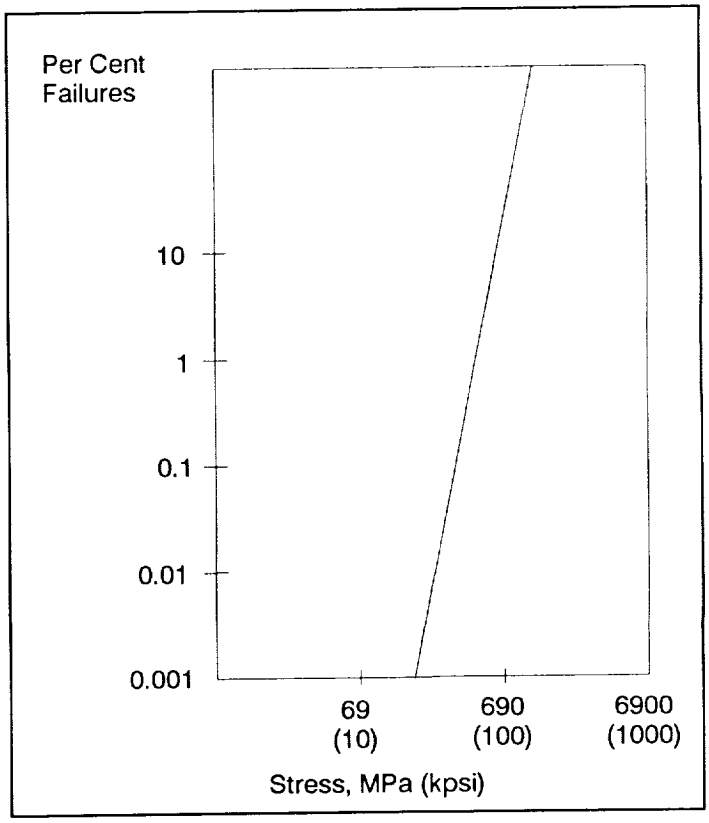

Figure 3: Four-point bending strength of NBD-100

LOAD CAPACITY

The conventional definition of bearing static load capacity of miniature and instrument bearings is the maximum load at which the maximum Hertz stress on the heaviest loaded raceway under the heaviest loaded ball will not cause significant permanent deformation, or fracture in the case of ceramics, or the maximum load at which the contact ellipse does not intersect the raceway/land corner. Generally radial load capacity is determined by the former criteria and axial load capacity by the latter.

The rating stress for 440C is specified by the AFBMA as 4,000 MPa (580 kpsi). [3] This value was determined by statically loading bearings at various levels and torque testing to find the point where the Brinells became apparent on the torque traces. The rating stress for BeCu can be estimated from the yield strength, 1,255 MPa (182 kpsi), by assuming the same relationship between yield strength and rating stress as was determined for 440C.

Si_3N_4, however, does not significantly plastically deform under load, it fractures once the stress limit is reached. The load capacity criteria for Si_3N_4 bearings must, therefore, be determined by a different method. No standard method has been established yet, but the general practice is to estimate the static load capacity from measured compressive fracture strength data. (In actuality the Si_3N_4 does not fail in the compressive stressed contact area, but in the tensile stressed zone immediately outside the contact zone.) Fujiwara et al. used acoustic emission to determine the fracture point in ball-on-plate tests and arrived at failure stresses of 11,000 - 13,800 MPa (1,600 - 2,000 kpsi). [4] Others have estimated the compressive fracture strength at 13,800 - 27,600 MPa (2,000 - 4,000 kpsi) using ball crush tests and ball-on-plate tests. [5,6] The rating stress of the Si_3N_4 for the purposes of this study was determined to be 6,900 MPa (1,000 ksi).

The calculated static load capacity of the bearings is given in Table 3. When compared with the required load capacity (Table 1), all three bearings have adequate axial load capacity, but only the Si_3N_4 bearing has adequate radial load capacity with some margin for safety.

Table 3 - Static Load Capacity

Bearing Description	Radial[a]	Axial[a]	Rating Stress[b]
Size 2.5 440C	39.1 (8.8)	105 (23.7)	4,000 (580)
Size 2.5 BeCu	30.2 (6.8)	82.7 (18.6)	2,650 (384)
Size 3 Si_3N_4	65.4 (14.7)	110 (24.8)	6,900 (1,000)

[a] Load capacity expressed as N/(lb)
[b] Rating stress expressed as MPa/(kpsi)

It should be noted that bearing design variables such as contact angle, the number and size of balls, and raceway curvature can significantly affect the load capacity. Some of these features are specified in table 4.

Table 4 - Bearing Design Features

Bearing Description	ID[a]	OD[a]	Width[a]	# Balls	d (ball)[a]
Size 2.5 440C	1.194 (0.047)	3.962 (0.156)	1.600 (0.063)	10	0.787 (0.031)
Size 2.5 BeCu	1.194 (0.047)	3.962 (0.156)	1.600 (0.063)	10	0.787 (0.031)
Size 3 Si_3N_4	none[b]	4.775 (0.188)	1.372 (0.054)	6	1.000 (0.039)

[a] Dimensions are mm/(in)
[b] There was no bore in the inner ring of this bearing. A standard size 3 bearing has an ID of 1.397 mm (0.055 in).

The radial load capacity of all the bearings in the table was enhanced by using tighter-than-normal race curvatures at the sacrifice of increased torque. The 440C and BeCu bearings listed in Tables 3 and 4 also were of full complement design (i.e., without retainers or ball separators), further enhancing the load capacity by providing more balls, therefore more ball contacts to carry the load, also at the expense of torque performance. The Si_3N_4 bearings, on the other hand, have a retainer and fewer balls which should reduce bearing torque.

ADHESIVE JOINTS

One of the primary concerns with the new design was the adequacy of the adhesive joints. The surfaces of the pins and gimbal bearing seats are very smooth, making adhesion more difficult. It was undesirable to roughen these precision, smooth surfaces to enhance adhesion since roughening operations might reduce the precision of the components, may reduce the bending strength of the Si_3N_4 pin, and cause damage to the inner raceway. The joints must withstand thermal excursions and severe vibration in service.

A pin/gimbal ring joint test piece consisting of a simulated section of the gimbal and a straight cylindrical pin, shown in Figure 4, was designed for adhesive strength tests. The test piece provides a relatively simple and inexpensive test bed that closely

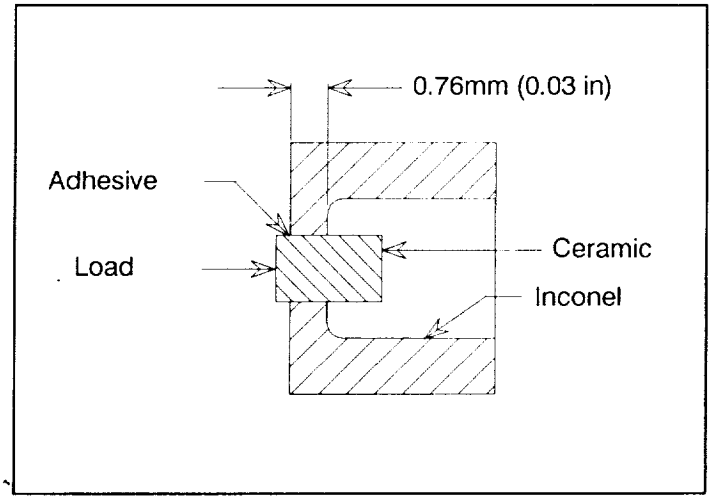

Figure 4: Adhesive strength test piece with applied loads

approximates the actual pin/gimbal joint for evaluation of adhesives, joint clearances, pin OD and gimbal seat surface finishes, etc. The gimbal test piece was thicker than the gimbal ring to make it strong enough to support the projected adhesive joint failure loads. The joint region was reduced in thickness to match the thickness of the gimbal ring.

Six candidate adhesives were selected based on recommendations of others with experience in the field, from adhesives manufacturers, and from manufacturers' data sheets.

Shear tests on the adhesive joint were conducted at room temperature to select the strongest adhesives for further development. The maximum shear load on the adhesive joint in service is estimated to be 122 N (27.5 lb). An initial diametral joint clearance of 0.0051 mm (0.0002 in) was used. A cross-head speed of 5 mm/min (0.200 in/min) was selected. Since the tests are time consuming and the components expensive and in short supply, it was decided to reduce the candidates to two or three as early as possible. The shear test results are given in Table 5. The results were clearcut with three adhesives performing well and three performing poorly. Adhesives A, B, and C, listed in Table 6, were selected for further tests, while adhesives D, E, and F were dropped from the program as being too weak to be suitable.

The smooth surfaces on the pin and gimbal seat did not reduce the adhesion strength of the joint to unacceptable levels. Further manufacturing operations to roughen the surfaces for improved adhesion are, therefore, unnecessary.

It is possible that different test conditions might have improved the performance of adhesives D, E, and F. Since our mission was to find a suitable adhesive for this application, not to study adhesives in general, we did not investigate this possibility.

Table 5 - Adhesive Joint Shear Failure Load[a]

Adhesive	Average	Range
A	331 (74.4)	279-363 (62.7-81.5)
B	328 (73.8)	306-365 (68.8-82.1)
C	282 (63.5)	266-299 (59.8-67.3)
D	66.3 (14.9)	61.8-70.7 (13.9-15.9)
E	29.4 (6.6)	14.7-68.5 (3.3-15.4)
F	18.7 (4.2)	11.6-28 (2.6-6.3)

[a] Failure load expressed as N/(lb)

Table 6 - Strongest Candidate Adhesives	
Aremco Bond 631	(Aremco Products,Inc)
Master Bond EP30	(Master Bond, Inc)
Hysol 956	(Dexter Adhesives and Structural Materials Div)

Further shear strength tests must be conducted at room temperature after cycling the joints to the temperature extremes, -54 and 123°C (-65 and 253°F), at the temperature extremes after long soaks at those temperatures, and after severe vibration. Preliminary temperature cycling tests on two of the three adhesives show the joint strength was reduced 10 - 20 % after five temperature cycles, retaining adequate strength. Longer exposures at the temperature extremes, more temperature cycles, and strength tests at the temperature extremes are necessary to properly test the design.

A finite element analysis of the joint was conducted assuming several diametral adhesive joint clearances from 0.0051 to 0.1270 mm (0.0002 to 0.0050 in) to evaluate the effect of the joint thickness on the tensile stresses on the ceramic pin, at cold temperatures. Since the metallic gimbal seat shrinks much faster than the ceramic pin, the encapsulated portion of the pin is subject to compressive stress, but the surface of the portion of the pin just outside the joint is subject to tensile stress. The polymer adhesive joint acts as a buffer between the two components, reducing the stress. Figure 5 shows the relationship between the diametral joint clearance and the resulting maximum principal stress on the ceramic pin at the highest stressed point at the low temperature extreme. The model assumes the pin is centered in the gimbal seat which, of course, may not be the case in actual gimbal assemblies.

The analysis indicates that joint diametral clearances of 0.01 mm (0.0004 in) and greater reduce the tensile stress at the highest stressed area to below 166 MPa (24 kpsi) and improves the reliability (considering only the highest stress region) to 99.999%. This clearance would also be considered a practical minimum to provide some alignment capability during the gimbal assembly.

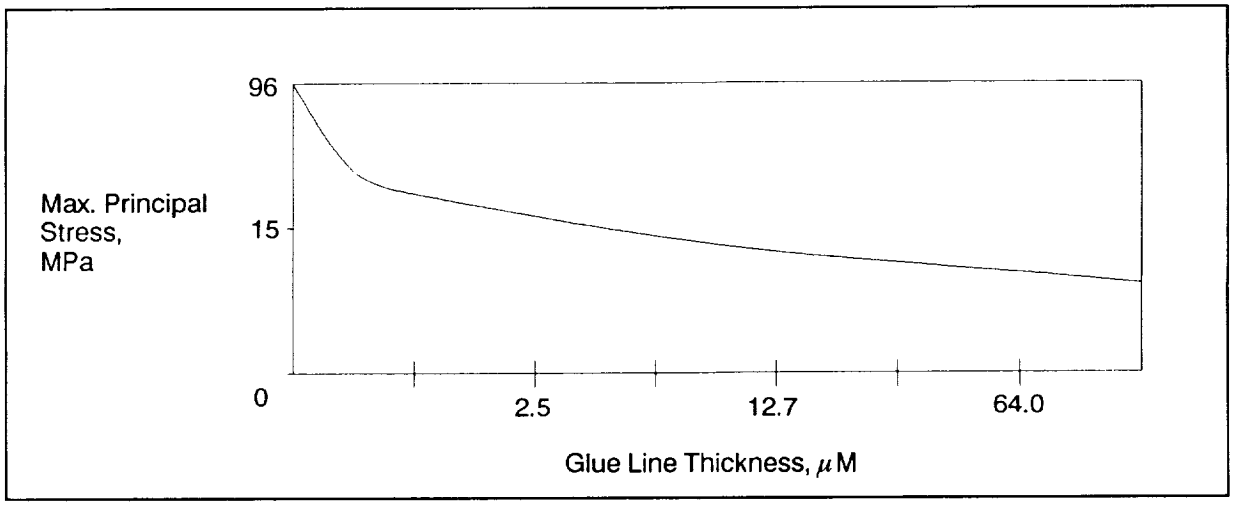

Figure 5: Maximum principal shear stress on pin vs. adhesive diametral joint clearance

PIN STRENGTH

The maximum estimated bending load on the inner ring/pin, seen during launch, is 122 N (27.5 lb). The ceramic pin must be designed to survive these loads. Although Si_3N_4 is very strong in compression, it is relatively weak in tension. Overstress leads to brittle fracture, and in this case catastrophic failure of the system. Finite element analysis of the pin/gimbal joint with the maximum design moment load results in a maximum principal stress on the pin OD near the joint of 173 MPa (25 kpsi).

The strength of the pin appears to be sufficient to support the large launch moment load without failure at least 99.999 % of the time, which is sufficient reliability for the preliminary design. Although this concern needs further study, the initial indications are that the design is adequate.

BEARING TORQUE

Low and consistent bearing torque is important to the proper performance of gimbal systems. Until actual test bearings of the new design are available the torque characteristics of the new bearing cannot be determined. However, the effect of axial load on bearing torque of 440C steel and Si_3N_4 bearings can be determined on other miniature bearings as a guideline.

Standard 440C and Si_3N_4 bearings of three common sizes were evaluated for running torque on an MPB RT2C torque tester at axial loads varying from 4.5 - 67 N (1 - 15 lb) on bearing sizes R2, R3, and R6.

Table 7 - Torque Test Bearing Dimensions[a]

Bearing Size	ID	OD	Width
R2	3.175 (0.125)	9.525 (0.375)	3.967 (0.156)
R3	4.763 (0.188)	12.700 (0.500)	3.967 (0.156)
R6	9.525 (0.375)	22.225 (0.875)	5.558 (0.219)

[a] Dimensions expressed in mm (in)

The average running torque vs axial load results for the R2 bearing size are shown graphically in Figure 6. The average running torque is defined in MIL-STD-206 as one half the average torque difference between consecutive clockwise and counter-clockwise torque traces on the same bearing. It can be seen that the slopes of the lines are approximately parallel, with the ceramic bearing torque being somewhat higher. The higher torque level of these ceramic bearings is probably related to the quality of the races, which are not as high in quality in terms of race finish and race curvature control as the comparable 440C races.

The finishing of ceramic bearing races has undergone significant advancement in the last year and the samples tested do not have the benefit of these improvements.

Of particular interest is the slope of the torque vs axial load lines, which are essentially the same for both 440C and Si_3N_4. This means as the bearings are loaded in service the torque response of the ceramic bearings will be similar to currently used 440C bearings.

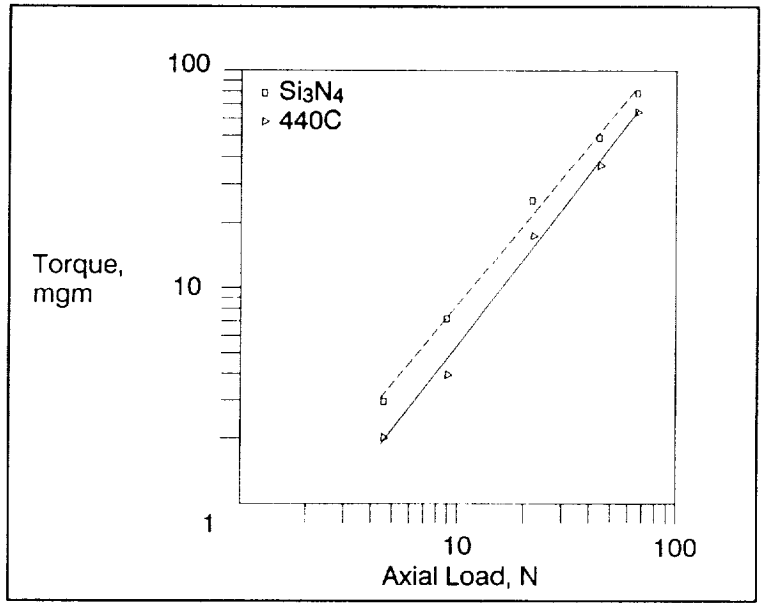

Figure 6: Average running torque vs. axial load for R2 bearings

In addition, the slopes of the logarithmic plots of all the torque vs axial load lines is reasonably close to 1.33. This has been the generally accepted relationship in the instrument bearing industry for many years. That is:

$$T \alpha F_a^x \quad [1]$$

where: T = Average running torque
F_a = Axial load
x = Torque / load exponent

In this case:

$$T \alpha F_a^{1.33} \quad [2]$$

Table 8 - Torque/Load Exponent (x)

Material	R2	R3	R6
440C	1.31	1.54	1.21
Si_3N_4	1.22	1.29	1.30

BEARING COMPLIANCE

Bearing compliance (displacement under force) is critical to gimbal design since the stiffer the gimbal the more resistant the system is to drift when exposed to acceleration. The bearings are the "softest" component in the gimbal, hence any improvement in stiffness or compliance of the bearings can have a significant effect on the gimbal system.

Axial deflection tests were run using the MPB axial deflection gage on the same three sets of bearings used for the torque tests. Table 9 gives the slope of the load/deflection curve at a load close to the rated load. The Si_3N_4 clearly provides a stiffer bearing than the standard 440C bearing.

Table 9 - Bearing Axial Compliance[a]

Material	R2	R3	R6
440C	0.095 (16.7)	0.091 (15.9)	0.028 (5.0)
Si_3N_4	0.081 (14.2)	0.066 (11.5)	0.022 (3.8)

[a] Compliance expressed as μm/N (μin/lb)

CONCLUSIONS

The use of Si_3N_4 gimbal bearings in this application appears worthy of further design study. The original magnetic and load capacity concerns are satisfactorily addressed using ceramic bearings and the preliminary study indicates the adhesive joint strength will be adequate, the compliance will be superior (stiffer), the bearing will react similarly to steel bearings as the load changes, and the Si_3N_4 pin will have adequate strength to survive the projected thermal stresses and moment loads. However, the concerns of pin strength, the strength of the thin outer ring when subjected to high bending loads, and the adhesive joint strength require further study, analysis, and test.

ACKNOWLEDGEMENTS

The authors wish to thank the Miniature Precision Bearing Division of MPB Corp. for support of the project and permission to publish the results. In addition the authors wish to thank John Lucek of Cerbec Ceramic Bearing Co. for providing useful data on the ceramic materials and several informative discussions. The authors also wish to thank Derek VanWyk and Adrian Wood of MPB for their assistance with the graphics and typesetting.

REFERENCES

1 Huntington Alloys (now Inco Alloys) data brochure "Inconel Alloy 600"

2 Courtesy of Cerbec Ceramic Bearing Company

3 American National Standard/Anti-friction Bearing Manufacturers Association Standard 9, Load Ratings and Fatigue Life for Ball Bearings, Section 3.8

4 Fujiwara, Yoshioka, Kitahara, Koizumi, Takabayashi, and Tada, Study on Load Rating Property of Silicon Nitride for Rolling Bearing Material, Journal of JSLE, Vol. 33, No. 4 (1988), P. 301

5 Private communication with John Lucek of Cerbec Ceramic Bearing Company

6 Komeya, K. and Kotani, H., Development of Ceramic Antifriction Bearing, JSAE Review, Vol. 7, No. 3, Page 72

N90-22101

AX-5 SPACE SUIT BEARING TORQUE INVESTIGATION

by Stuart Loewenthal*, Vic Vykukal**, Robert MacKendrick+
and Philip Culbertson Jr.++

ABSTRACT

This report describes the symptoms and eventual resolution of a torque increase problem occurring with ball bearings in the joints of the AX-5 space suit. Starting torques that rose 5 to 10 times initial levels were observed in crew evaluation tests of the suit in a zero-g water tank. This bearing problem was identified as a blocking torque anomaly, observed previously in oscillatory gimbal bearings. A large matrix of lubricants, ball separator designs and materials were evaluated. None of these combinations showed sufficient tolerance to lubricant washout when repeatedly cycled in water. The problem was resolved by retrofitting a pressure compensated, water-exclusion seal to the outboard side of the bearing cavity. The symptoms and possible remedies to blocking are discussed.

INTRODUCTION

The AX-5 space suit (Fig. 1), developed by the NASA Ames Research Center, exemplifies the next generation of space suit considered for use aboard Space Station Freedom. It s "hard" (aluminum) construction and bearing joints allows for significantly higher internal air pressures [57 kPa (8.3 psig)] than current fabric suit designs [30 kPa (4.3 psig)] without increasing crew work load. The higher internal pressure eliminates the need for extensive crew prebreathing of 100% oxygen prior to an EVA as required by the current shuttle suit. Mobility is achieved through joint rotation, thus suit performance is directly dependent on bearing performance.

Neutral buoyancy crew evaluation tests of the AX-5 suit were conducted in the Weightless Environment Test Facility (WETF) at the NASA Johnson Space Center (JSC). Some subjects noticed increase in joint torque after about 2 hours of immersion. The most notable joints were the elbows. However, the problem was not immediately apparent when the subject took off the suit (depressurized) and the empty suit was then repressurized. The initial investigation focused on lubricant washout from the bearings. The pressure retention lip seals, were located between the bearing and the interior of the suit to exclude crew perspiration from reaching the bearing during space operation. However, this location allowed WETF water to fill the bearing cavity during crew underwater evaluation.

Approach

Since consistently low torque at the joints was essential for astronaut acceptance of the hard suit concept, resolution of the bearing problem was of very high priority. The joints had to properly function both in a space environment as well as in the WETF at NASA JSC. Because water could reach the bearings, it was thought that the easiest fix was to find a lubricant that didn't washout. The baseline, perfluoropolyether (PFPE) 814Z space-qualified oil was quickly found to be unsuitable for water operation. It later became clear, after many tests with more than a dozen oils, that those which were viscous enough to resist washout were also too viscous to provide low breakaway or running torques. Therefore, it became necessary to explore possible bearing design changes. The goal was to

*Bearing Consultant, San Jose, CA
** NASA Ames Research Center, Mountain View, CA
+ Air-Lock, Inc., Milford, CT
++ Sterling Federal Systems, Inc., Palo Alto, CA

find a solution that caused a minimum amount of rework to the bearing joints since all of the joints had already been manufactured. The approach adopted consisted of the following points:

- Identify the mechanism responsible for rapid buildup in torque observed during underwater testing.

- Identify bearing design modifications which could eliminate the problem while evaluating the impact on the following constraints:
  - torque level
  - sensitivity to lubricant washout
  - design impact
  - cost & schedule

- Verify effectiveness of improvements through bench tests in water and in the NASA Ames Neutral Buoyancy Test Facility (NBTF)

Fig. 1 AX-5 Space Suit

BACKGROUND

There were 34 ball bearings incorporated into the primary joints on the AX-5 suit. The joints included shoulder, elbow, hip, knee and ankle. Each joint contained an interconnected pair of bearings which were oriented at an angle to provide the required joint rotation (see Fig. 1). These bearings ranged in

pitch diameter from about 145 mm (5.7 inch) for the lower shoulder joint to about 320 mm (12.6 inch) for the hip joint. The bearings were machined by Air-Lock, Inc. in a 4-point or "X" configuration as part of an integral joint complete with urethane lip seal as illustrated in Fig. 2. In the case of the shoulder joint, the primary load is 2240 N (504 lbs) of thrust due to the 57.2 kPa (8.3 psig) differential pressure acting across the joint. Desired operational lives were on the order of 17,000 and 107,000 cycles of oscillation for the shoulder and elbow, respectively.

Bearing Description

The bearings were machined from 17-4 PH stainless steel as part of a joint assembly complete with urethane lip seal. The bearing assembly was loosely fitted into the joint housing having o-ring seals and held by circumferential retaining cables on inner and outer races. The 17-4 PH stainless steel was selected for corrosion protection and machinability. The bearing was machined into a 4-point configuration with a nominal 45 degree contact angle. The high contact angle was selected to reduce contact stress from the pressure generated thrust load. Bearing maximum contact stresses were less than 1.4 GPa (200,000 psi) for the shoulder joint, which was comfortably below the allowable brinell stress limit for the stainless steel race at a Rockwell hardness of about 38. A disadvantage of the machining process was that the races were considerably rougher than commercially ground bearings.

Delrin idler balls were used as separators. They were slightly smaller than the 440-C main balls [4.8 mm diameter vs 4.9 mm (0.1875 in. diameter vs 0.193 in.)]. By keeping the diameters close in size, the resulting radial reaction force on the idler balls and thus drag could be kept low (see Fig. 3). Both main balls and idlers were inserted via a fill slot cut into the outer race.

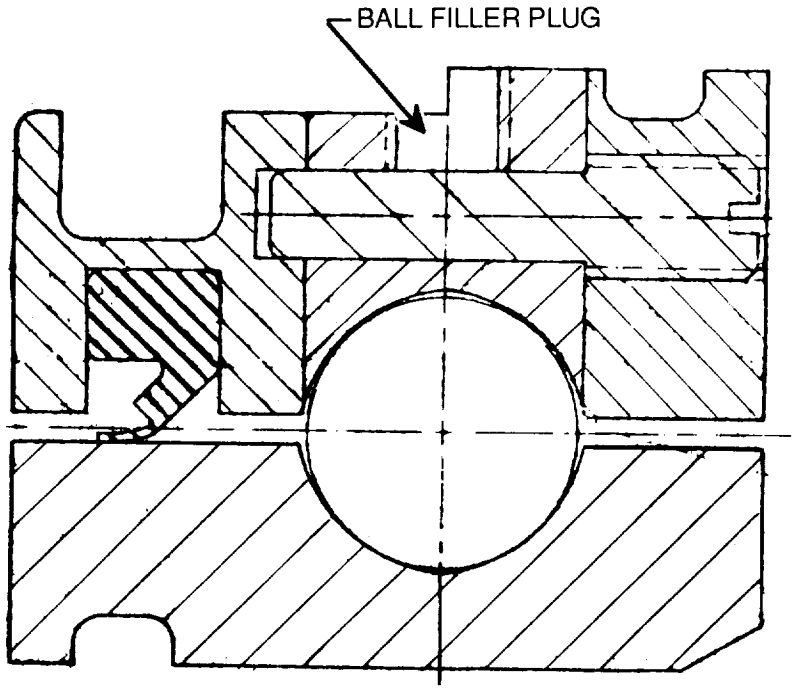

Fig. 2 Shoulder Joint Construction Showing Four-Point Bearing and Integral Seal

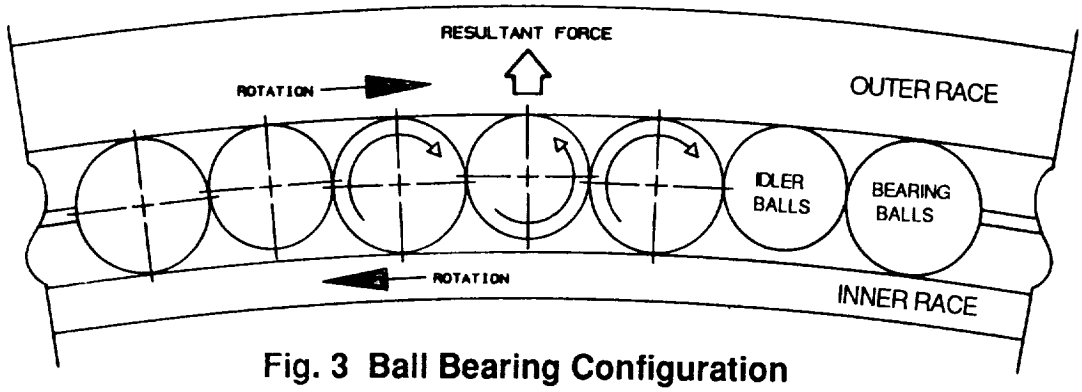

Fig. 3 Ball Bearing Configuration

Anomaly

Large torque increases were observed during oscillatory bearing life tests in bench tests with WETF water. An example of a test run on a shoulder joint bearing appears in Fig. 4. Normal breakaway torques were on the order of 0.23 to 0.34 N-m (2 to 3 in-lbs) and grew to more than 2.3 N-m (20 in-lbs) in the wet tests. 360 degree rotations tended to release or reduce the torque build up, as did ±10 degree cycles. In some cases cutoff torque limits occurred in only 40 cycles.

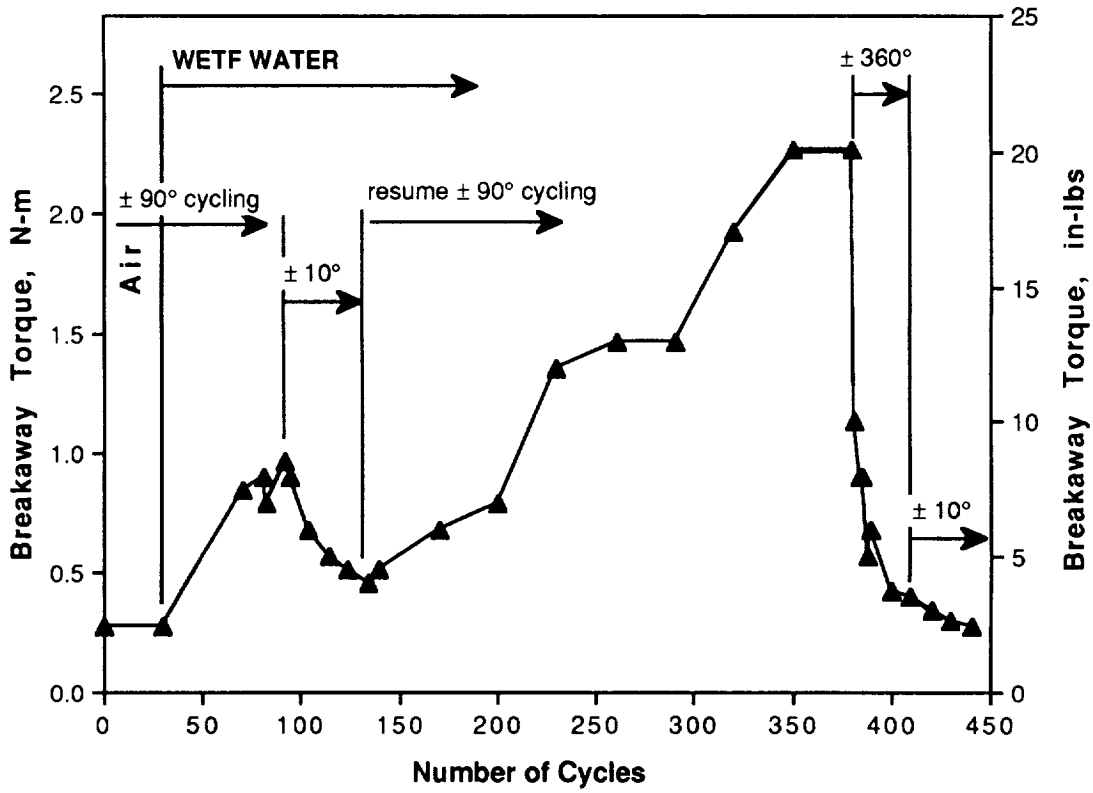

Fig. 4 Example of Bearing Torque Anomaly from Shoulder Joint Test

The observed large build up in breakaway torque with repeated oscillatory cycling appeared to be similar to the torque "blocking" observed by the authors in certain gimbals, see ref.[1], as well as by others, e.g. see refs. [2] and [3]. The term ***blocking***, first coined in ref. [2], is used broadly to describe a progressive torque build-up with time. While no one fully understands this mechanism, blocking is thought to be a consequence of excess friction from the balls pinching the cage. This phenomena, sometimes descriptively referred to as "cage wind up", can occur when individual balls are orbiting at different speeds due to small variations in contact angle, ball size or race geometry. These ball excursions or *ball speed variation* (BSV) cause some balls to advance and others to retard from the average speed, squeezing the cage's ball pockets and thus increasing drag. Direct evidence of this came from tests where the idler balls were removed and the bearing balls were equally spaced apart. No torque build up was observed for the first 300 cycles.

The adverse effects of BSV on cage loading for continuously rotating bearings have been known for some time, as discussed in detail by Barrish [4]. An estimate of the contact angle variation of balls as they orbit helps set minimum ball pocket clearances. However, the use of enlarged ball pockets or slots will not necessarily correct the potential torque problems associated with bearings which oscillate back and forth, as observed here. Furthermore unidirectional rotation usually releases or resets bearing torque close to original levels (as illustrated in Fig. 4) while constant stroke oscillations tend to aggravate blocking.

BLOCKING REMEDIES

Based on the initial assessment of the AX-5 bearing problem, a series of possible solutions were considered, along with their difficulty to implement. These included:

Looser Conformity

Transverse ball creep due to "spin" was identified in refs. [1] and [2] as a significant factor contributing to blocking. Spin is the circumferential slip which results when a ball tries to roll along a grooved race at some contact angle. The sideways motion that results is akin to the "hook" of a bowling ball which is rolling with spin down the alley. This sideways motion causes some of the balls to ride up the race, increasing the contact angle, the BSV and hence the tendency to jam.

Increasing the races' transverse radius of curvature can significantly reduce this spin component and thus the tendency to block. In Ref.[1], increasing conformity (race radius/ball diameter) from 51.7 % to 54 % , completely cured the blocking at the expense of increased contact stress. The AX-5 bearings were already at 54% conformity and although contact stresses could be increased, this change necessitated regrinding the races. This had negative schedule and cost impacts. It also required sacrificing one or more of the limited number of bearings for test purposes. For these reasons, it was put on hold until less drastic fixes were evaluated.

Smoother Races

Improving surface finish and reducing the waviness of the bearing races were expected to help reduce friction and reduce the contact angle variation associated with BSV. The race drawings called out a race surface finish of 0.4 μm (16 μ in.) rms and raceway diameter control to ± 0.025 mm (± 0.001 in.) in keeping with a machined surface. This is of lesser quality than standard commercial bearings having hardened and ground raceways. Since torque blocking problems were not encountered on previous joint designs containing commercial bearings, improved race surface quality could be important. However, this modification would also require that the joints be remanufactured. "Polishing" the races was later tried with no apparent success to alleviating blocking, possibly because surface polishing can't effectively correct imperfect race geometry.

Reduced Contact Angle

As mentioned earlier, ball/ race spin creates side forces which cause the bearing balls to climb up the bearing races. Spin is increased with an increase in contact angle so the effect of reducing contact angle was investigated.

Contact Angle Measurement - Before proceeding, it was necessary to know what the contact angle was under load, i.e. while operating. In the case of a 4-point bearing, there is a complicated relationship between free or manufactured contact angle and diametral play, race conformity and removed shim thickness. It was believed that the bearings were manufactured to a nominal 45 degree contact angle, although it was difficult to verify mathematically. A preferred method of determining contact angle, both free and loaded, is by rotating the inner race many revolutions and counting the number of revolutions of the orbiting ball group. This method is commonly referred to as the "turns" method. It is based on the well known kinematic relationships of epicyclic motion, such as those associated with planetary gears. In the case of a bearing with a fixed outer race, the contact angle ß is given by:

$$\cos ß = \frac{E}{d} \left(1 - \frac{2 Ø c}{Ø s} \right)$$

where: E = bearing ball pitch diameter
d = ball diameter
Øc = number of cage or ball group revs
Øs = number of shaft revs

Nominal contact angles under load for shoulder bearings S/N 101 and S/N 105 were measured to be 36.4 and 42.8 degrees, respectively, using the turns method. Each bearing inner race was rotated 100 revs and the ball group rotations were counted. The measurement was repeated 2 more times with close agreement.

Effect on Contact Load & Spin - Next the effect of smaller and larger contact angles on contact normal load and contact stress were calculated. The effect of reducing contact angle from 42 to 36 to 20 degrees, increased ball contact load from 46 to 52 to 82 N (10.3 to 11.8 to 18.4 lbs), respectively. This is due to the wedging effect with shallower angles under a pure thrust load. A spin analysis, similar to that conducted in Ref. [1], showed that the corresponding spin velocities for the above cases drop from 0.56 to 0.47 to 0.27 rads/sec. However, even though there was a 38% decrease in spin side force when the contact angle dropped from 45 to 20 degrees, the spin torque actually increased by 65% due to the increase in ball contact normal load. Thus the introduction of smaller contact angles would likely inhibit the blocking tendency at the expense of higher breakaway torques.

Reduced Friction Coefficient

Reducing the friction coefficient between the balls and races and between the balls and idler balls was the most obvious and easiest thing to try since no major bearing geometry change would be required. Unfortunately, finding the right combinations of idler ball material, cage design and lubricant which gave long term satisfactory performance both in and out of WETF water was anything but easy. The basic dilemma was that lubricants that were viscous enough not to be quickly washed out in water, gave relatively high breakaway torques. Those that provided low breakaway torques were too thin to last in water and quickly caused blocking.

Lubricants - The 814 Z oil, baselined for space use, was of very low viscosity (22 cS @ 100 °F) and had poor staying power in water. It was selected because its low viscosity would reduce the bearing running torque during joint rotation. However it was recognized that 814 Z oil because it is comprised of the lighter, hence more volatile, constituents has poorer outgassing characteristics than 815 Z type, the most common space mechanism oil. A total of about 20 different lubricants or greases diluted with freon were investigated. For example, a freon-diluted Mobil 28, mineral oil-based grease, that found prior success in the WETF tank showed improvement but also blocked in water. Exxon furnished several samples of water resistant lubricants with possible low breakaway torque capabilities. The two oils which appeared to have the most potential were Arox EP 46 and Teresstic 32. The Arox oil was specially formulated for rock-drilling machinery bathed in high pressure water. It contained a "tackiness" agent to inhibit wash off and an emulsifier agent to prevent the water from wetting the surface. Teresstic was designed to lubricate steam turbines and other precision machinery, such as those in paper mills. Unfortunately these oils had an inability to "wet" thus lubricate the urethane seal material, as evidenced by their "beading" on the seal surface and therefore received limited bearing testing.

Improved Ball Separator

The successful test with the idler balls removed gave hope that there was a way to keep the idler balls slippery or of finding a compliant material that wouldn't bind when pinched or a cage design that wouldn't allow the balls to jam.

Idler Ball Materials - A series of tests were conducted to identify the right idler ball material and lubricant combination. Fig. 5 synopsizes the breakaway torques of many of the test candidates. This data covered the first 500 cycles or until blocking torque stabilized, which ever came first. Black oxide-coated, stainless steel idler balls were tested with both 814Z and Mobil 28 grease, in and out of water. Breakaway torques in water generally started at about 0.3 N-m (2.5 in-lbs) and would climb to 0.8 to 1 N-m (7 to 9 in-lbs) inside of 300 cycles by hand rotation, occasionally drifting down to 0.6 N-m (5 in-lbs) at the end of 500 cycles. Krytox grease (a grease with a PFPE oil similar to 814 Z or 815 Z oils) gave similar results with the baseline Delrin idler balls. A full

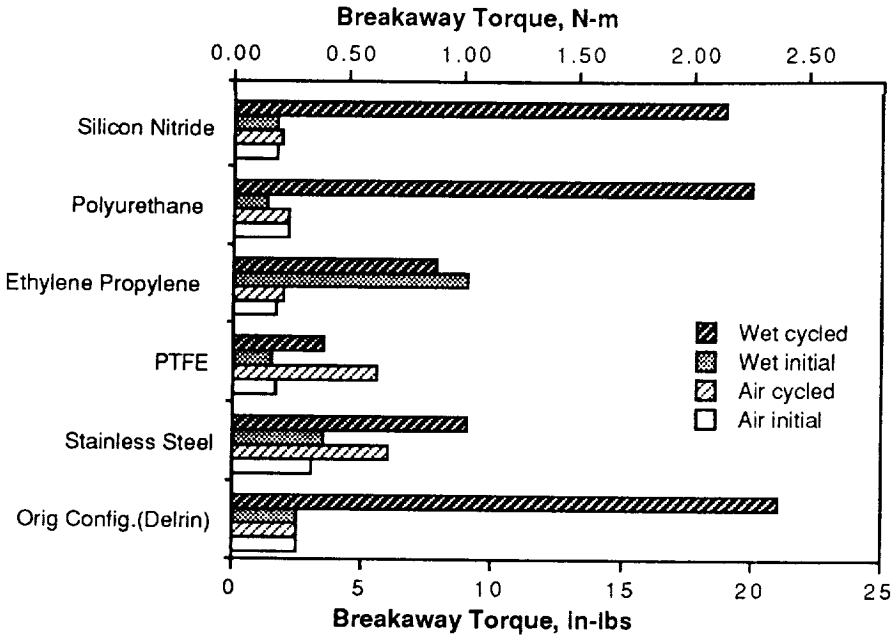

Fig. 5 Effect of Different Idler Ball Materials on Shoulder Joint Bearing Torque

complement of stainless steel bearing balls blocked almost immediately. Silicon nitride (Si_3N_4) idlers showed poor water performance, pointing out the importance of a compliant ball separator.

PTFE tube spacers, both large and small diameter, locked up in air in less than 200 cycles with 814 Z oil while PTFE idler balls gave relatively good results both in and out of water. Breakaway torques rose from 0.2 N-m (1.7 in-lbs) initially to 0.6 N-m (5.5 in-lbs) after 450 cycles out of water and 0.45 N-m (4.0 in-lbs) after 570 cycles in water. However, the PTFE balls showed some small dimples (1mm in diameter) under a microscope, indicating that the relatively soft PTFE was undergoing local brinelling.

A series of elastomeric idler balls of various shore hardnesses were investigated next. These included polyurethane/shore 60 to 90, ethelyene polypropolyene/shore 70 and Viton/shore 67 to 90. These materials gave good results up to 1300 cycles when lubricated but blocked badly when the lubricant washed out. This was an expected result considering the high coefficient of friction of these elastomers when unlubricated. Thus elastomeric idler balls were considered to be too risky with the ever present danger of lubricant migration or degradation. It became increasingly clear that finding a lubricant/material combination that would consistently work in water was getting more and more unlikely.

One Piece Cage - Kaydon manufactures a one piece, alternating slotted and circular pocket, snap over cage which it recommends for oscillatory bearings to inhibit torque anomalies. The theory is the slots will allow some free ball migration between back and forth oscillations. There was an interest in evaluating the effectiveness of such a retainer design in relation to other tests conducted, although an existing shoulder joint had to be reworked. The shoulder of the bearing was machined away to accept either a bronze, one piece slotted cage or an enlarged, circular ball pocket cage. Test results (see Fig. 6) showed that the slotted cage exhibited little torque buildup out of water but breakaway

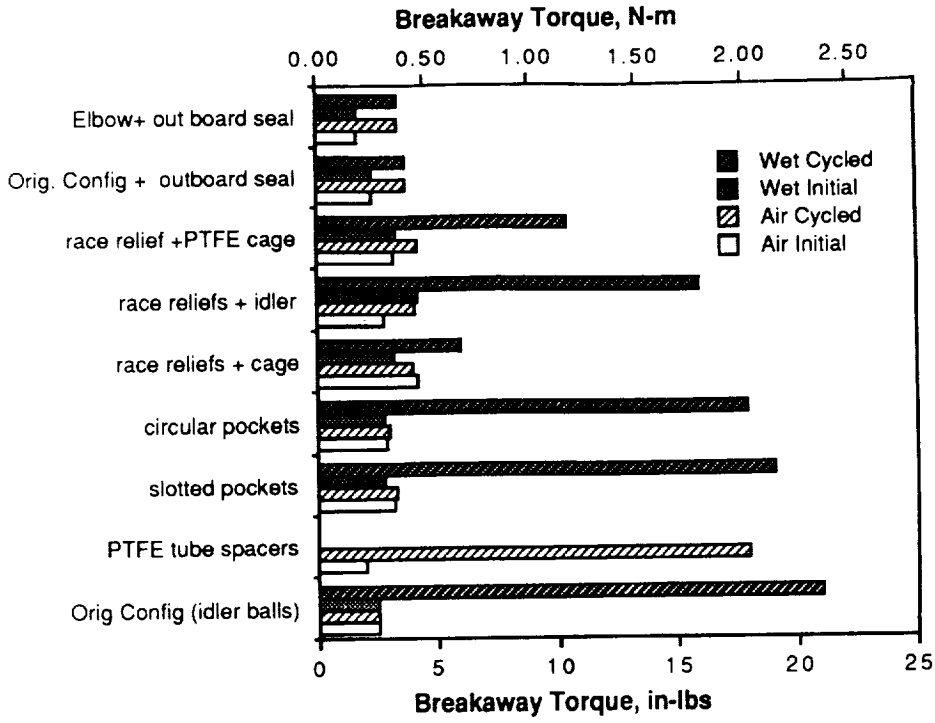

Fig. 6 Effect of Different Geometries, Race Reliefs and Outboard Seals on Shoulder Joint Bearing Torque

torques ranged from about 1.1 to 2.2 N-m (10 to 19 in-lbs) in water. The enlarged circular pocket cage exhibited similar behavior with torques to 2 N-m (18 in-lbs). Spray coating the cages with PTFE kept torques under 0.7 N-m (6 in-lbs) for the first 500 cycles in water. However, there was a persisting risk of PTFE wear through with this approach.

Race Reliefs - The balls are under an essentially constant load in a thrust loaded bearing, so if unequal ball spacing were to occur due to BSV, there is no opportunity to relieve the resulting wind-in torques. However, if a small region of the inner or outer race was recessed, then the ball passing over this relief would be momentarily unloaded and thereby given an opportunity to "release" its pinching load. (For this reason, radially loaded bearings are less apt to experience blocking since some balls can enter the unload zone opposite the radial load contact). Since the AX-5 joints can experience small angular motions, it was necessary to grind in multiple reliefs to be assured that each ball had an opportunity to pass over a relief during limited angular ball travel. Fig. 7 shows the geometry of the race reliefs cut a minimum of 0.002 inch along the nominal 45 degree contact at 18 locations. This depth was about 10 times the expected Hertzian deflection to guarantee ball unloading. Wet tests with a PTFE coated, one piece, circular pocketed, bronze cage exhibited some improvement but less so for a glass- reinforced PTFE cage (see Fig. 6). However, race relief tests with polyurethane idler balls show outstanding performance out of water, although torque once again rose dramatically in water.

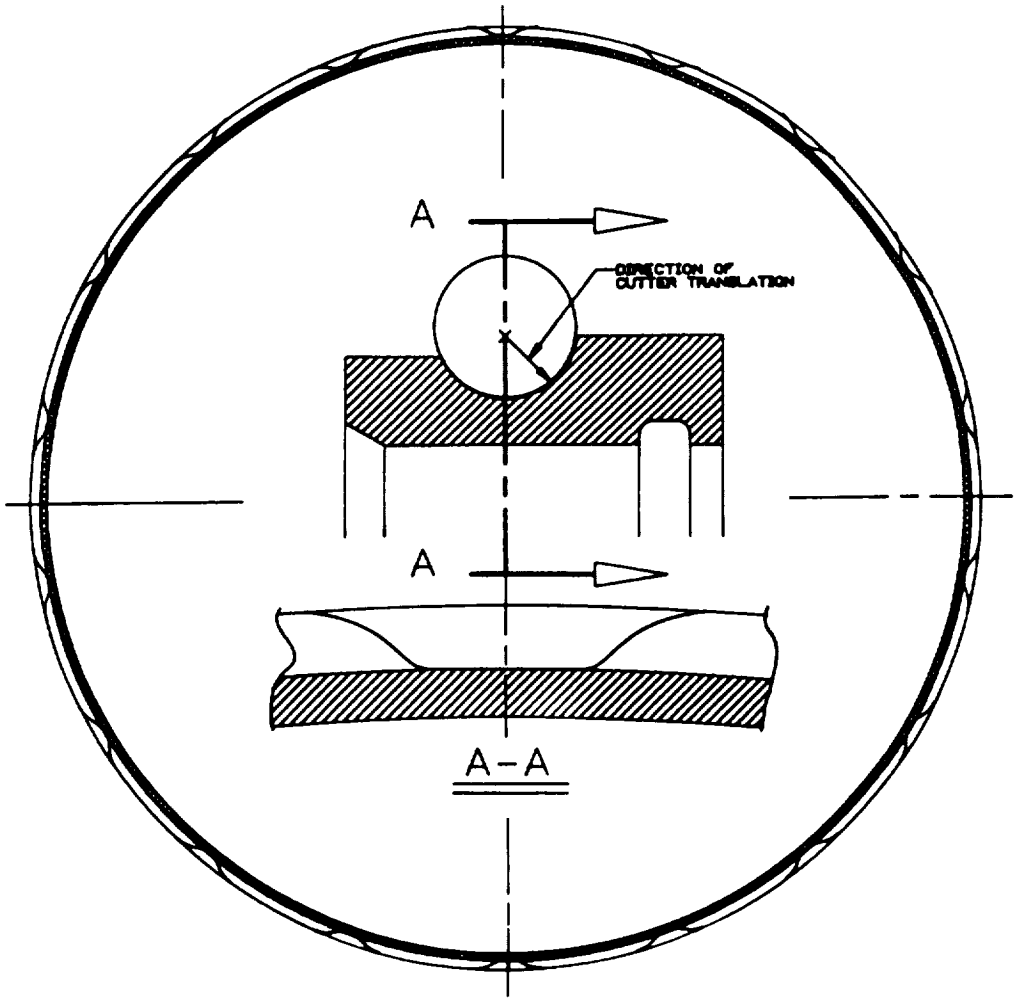

Fig. 7 Details of Race Reliefs

OUTBOARD SEAL REDESIGN

Based on the inconsistent results with all prior attempted solutions, the bearing joint assembly was modified to accept an outboard seal to exclude water from the bearing cavity. This meant that all of the suit joints would have to be remanufactured and a method found to alleviate the high hydraulic differential pressure acting across the seal in the WETF tests with resulting high seal drag forces. A solution was found that balanced the pressures across this seal by regulating the pressure within the bearing cavity at some intermediate level. This was accomplished by allowing a small, but controlled air flow leak between the pressurized interior and the bearing cavity through a ruby metering orifice designed for such leakage control. In this way, seal differential pressure could be limited and the bearing cavity would remain dry. A cross-section through the under water test version of this double-sealed joint appears in Fig. 8. The pressurized interior of the suit is to the left in this figure. Note that some air would leak past the circular retention cable and through the metering orifice to maintain bearing cavity pressure slightly below external water pressure. For space operation, the outboard seal is reversed against the external vacuum. The metering plug was relocated to the ball filler plug to reduce the differential pressure acting across the outboard seal.

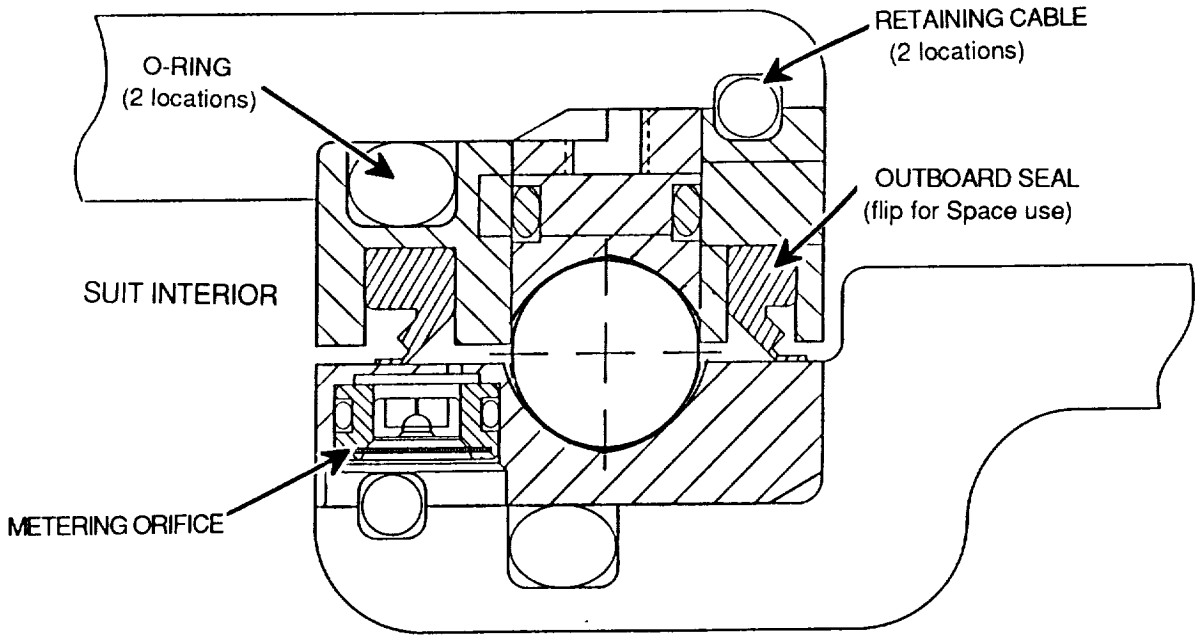

Fig. 8 AX-5 Bearing Joint Configuration for Underwater Tests

Although remanufacturing all the joint sub assemblies to accept this seal modification was not inexpensive, this approach positively eliminates lubricant wash out as a failure mode. Breakaway torques inside and outside of water remained nearly constant. An elbow joint torque trace covering 1000 oscillatory cycles appears in Fig. 9. Comparison of torque levels from shoulder and elbow joints with other designs is given in Fig. 6.

A modified shoulder bearing received 15,200 cycles or 43.5 hours of operation in water without torque buildup. Except for the outboard seal and metering plug, the bearing is the original configuration, lubricated with 814 Z oil and containing Delrin idler balls. Starting torque began at 0.3 N-m (2.4 in-lbs) rose to 0.5 N-m (4.2 in-lbs) at 9400 cycles and remained essentially constant until cutoff at 15,200 cycles. Running torques at 90 degs/sec were 0.85 N-m (7.5 in-lbs) initially, rose to 1.1 N-m (9.9 in-lbs) at 6100 cycles and then fell to 0.9 N-m (8.1 in-lbs) at 15,200 cycles.

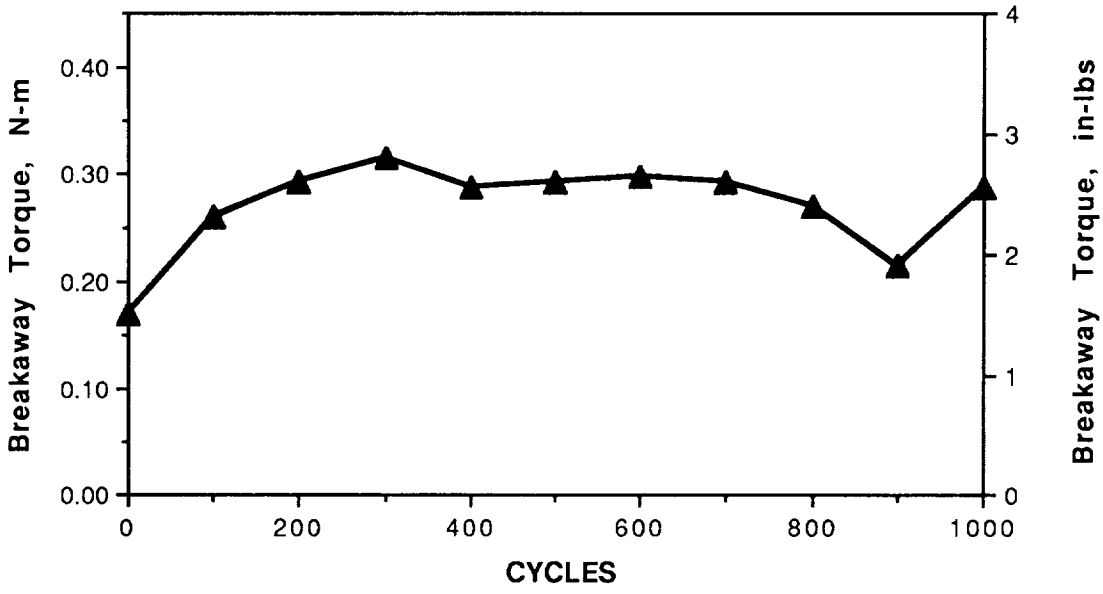

Fig. 9 Breakaway Torque Profile for Elbow Joint Bearings with Outboard Seals

The shoulder joint was depressurized at the end of each approximate 8 hour test day for a total of 6 times during the test. Depressurizing or unloading the bearing will generally reset the bearing torque if blocking is present. Although the totals achieved are not a single continuous run, the operational time per period greatly exceeds any of that anticipated for the suit in testing and or in service. Thus there is high confidence that torque blocking problems will not be observed. The effectiveness of this solution was later confirmed during successful crew evaluation tests of the AX-5 suit in the WETF at NASA JSC.

CONCLUSIONS

This investigation identified blocking to be responsible for the torque increases observed in the bearing joints of the AX-5 space suit. This torque anomaly was clearly aggravated by lubricant washout from the bearings during underwater tests which simulated crew evaluation in the NASA JSC WETF. The most telltale signs of blocking were the relatively rapid build-up of torque, the torque resetting upon unidirectional rotation and the absence of the problem when the bearing balls were freely spaced without separators. A large matrix of lubricants, idler ball material and ball separator designs were evaluated as possible solutions. None of these approaches worked consistently well in the water tests. The ultimate remedy was to provide a water-exclusion outboard, lip seal to the bearing joints, although this necessitated that all of the numerous joint assemblies had to be remachined. Some of the more general findings of this study are as follows:

(1) High ball/cage friction can cause blocking in oscillatory bearings no matter how well the cage may be designed.

(2) In difficult lubrication situations where blocking may occur, unidirectional rotation past the point of jamming will likely reset torque, at least temporarily.

(3) Constant stroke oscillations are more likely to cause blocking than a more random sequence of motion.

(4) Slightly undersized idler balls make effective ball separators, provided good lubrication can be maintained.

REFERENCES

[1] Loewenthal, Stuart H.: "Two Gimbal Bearing Case Studies: Some Lessons Learned" ; Proc. of 22nd Aerospace Mechanisms Symposium, NASA CP-2506, May 1988, pp. 253-269.

[2] Todd, Mike J.: "Investigation of Torque Anomaly in Oscillating PDM Bearings"' European Space Agency (ESTL) Report No. 49, May 1981.

[3] Phinney, D.D. ; Pollard, C.L. ; and Hinricks, J.T. : "Experience with Duplex Bearings in Narrow Angle Oscillating Applications"; Proc. of 22nd Aerospace Mechanisms Symposium, NASA CP-2506, May 1988, pp. 211-226.

[4] Barrish, Tom: "Ball Speed Variations in Ball Bearings", ASLE J. Lubrication Engineering, Mar. 1969, pp. 110-116.

DESIGN OF A TELESCOPING TUBE SYSTEM FOR ACCESS AND HANDLING EQUIPMENT

Alan C. Littlefield *

ABSTRACT

Spacecraft processing presents unique problems for the design of ground support equipment. Most access equipment must be fully self-supporting and completely independent of the spacecraft. Additionally, system reliability must be ensured to limit the risk of damage to critical hardware. Telescoping tubes are well suited to some of these unique requirements. A telescoping tube system consists of a number of nested structural tubes that can be extended and retracted (telescoped) while supporting a load. A typical telescoping tube system provides lateral, torsional, and vertical support for an access platform.

Following several incidents involving tube systems at the Kennedy Space Center (KSC), an effort was undertaken to develop improved telescoping tube designs. Several concepts were developed with emphasis placed on reliability, ease of maintenance, and cost effectiveness. The most promising concept was selected for detailed design and prototype development.

The prototype design utilizes adjustable rollers running on tracks bolted to the tube sections. A wire rope deployment system ensures that all tube sections are controlled during extension and retraction. Previous systems relied on gravity to extend the tubes. Track shimming and roller adjustment allow for fabrication of a high-precision tube assembly that does not require extensive machining or unusually large shop equipment. The use of rolling contact eliminates the contamination problems encountered with sliding tubes in previous designs. The prototype design is suitable for indoor or outdoor use. A prototype tube assembly has been fabricated and tested for strength, stiffness, maintainability, and endurance. The prototype tube assembly has met or exceeded all design requirements.

INTRODUCTION

Telescoping tube systems have been used to solve several unique access and handling problems at KSC. Tube systems have been or are currently in use in several areas including:

- Orbiter Processing Facility (OPF) Payload Bay Access Buckets.

*NASA, Kennedy Space Center, FL 32899

- Space Shuttle Orbiter Mate-Demate Device (MDD).
- Launch Pad 39B Line Replaceable Unit (LRU) Access Platform.

While the telescoping tube systems in use at KSC have generally worked well, there are a number of areas in each design that need improvement.

OPF Payload Bay Access Buckets

The OPF Payload Access Buckets (Figure 1) provide access to all areas of the Space Shuttle Orbiter payload bay for maintenance and inspection. The OPF buckets consist of a 0.8 m x 1.5 m (30 in. x 60 in.) work platform suspended from a four-section telescoping square tube assembly that allows 6.2 m (243 in.) of platform vertical motion. An electric hoist attached to the platform resists vertical loads, while the tube system resists lateral, torsional and eccentric (moment) loads. A bridge and trolley arrangement allows for horizontal motion of the platform.

Several problems exist with the current tube design. The primary problem is that the two intermediate tubes float freely between the inner and outer tubes and rely upon gravity for their deployment (the outer tube is attached to the trolley, and the inner tube is attached to the platform). Another problem with the OPF tubes is that the tubes slide on adjustable bronze bearings. Because of the sliding contact, the intermediate tubes sometimes bind and drop during extension. This can cause damaging impact loads on the structure. Also, the use of lubrication on the tubes is limited because of orbiter payload bay contamination concerns. This results in the generation of small bronze particles that create a contamination problem of their own. A more detailed account of problems with the OPF buckets and tubes may be found in reference 1.

Orbiter Mate-Demate Device

The Orbiter MDD is used to remove (or install) the Space Shuttle Orbiter from the Shuttle Carrier Aircraft (SCA). Telescoping tube systems are used to steady the orbiter and access platforms against wind loads. Three sets of similar tube assemblies are used. One set consisting of four tube assemblies provides lateral support for the orbiter lifting hardware. Each of these four-section square tube assemblies allows for 14 m (550 in.) of orbiter vertical motion while providing lateral support against wind load and allowing horizontal adjustment of the orbiter for mating operations. The remaining two sets of two tube assemblies provide lateral support for access platforms used during mating operations. Each four-section tube allows for 14.6 m (575 in.) of platform vertical motion while preventing the platforms from swaying and contacting the orbiter.

Like the tubes on the OPF buckets, the intermediate tubes on the MDD rely upon gravity for their deployment. This creates the risk of damage from free falling tubes. Also, the design of the MDD tubes required that the inside surfaces of the tubes be polished for the sliding bearings. This

requirement significantly increased the fabrication cost of the tubes. The inner sliding bearings, located between the tubes, cannot be removed for inspection or repair without completely disassembling the tubes. Finally, the sliding surfaces of the tubes require a significant effort to control corrosion.

Pad 39B LRU Access Platform

The LRU Access Platform (Figure 2) was designed to provide access to the Space Shuttle Orbiter payload bay at the launch pad. The 4.3 m x 6.1 m (168 in. x 240 in.) platform was suspended from two telescoping tube assemblies that provided lateral support. Each five-section telescoping tube assembly allowed for 16.2 m (637 in.) of vertical motion. The design of the LRU platform tubes was nearly identical to the OPF tubes. Operational testing of the tubes revealed severe binding within the tube assemblies. Several incidents of binding and falling tubes culminated in the failure of the mechanical stops that prevent the tubes from over-extending. The tube assemblies were removed from the pad, and a simplified design was implemented to meet the pad operational readiness date.

The primary cause of all the problems with the LRU Access Platform tubes was that they were simply an enlarged version of the tubes used in the OPF. Scaling up the marginal design of the OPF tubes increased the severity of the problems seen in the OPF to the point where the tubes would no longer function.

Summary

An investigation into all tube systems at KSC identified the above mentioned problems as well as other safety and maintenance concerns. A project was undertaken to improve telescoping tube assemblies at KSC. Specifically, the project tasks were to:

- Identify deficiencies in existing designs.
- Develop new design requirements.
- Design, fabricate, and test a prototype tube assembly.
- Develop design criteria or specifications for new tubes.

DESIGN DEFICIENCIES

As was previously discussed, design deficiencies and desired improvements were identified as follows:

- Unrestrained tube sections (gravity deployment).
- Contamination generation.

- Maintenance and inspection problems.
- Reliability.
- High fabrication costs and manufacturing problems.

PROTOTYPE DESIGN REQUIREMENTS

The prototype tube assembly size and loading approximates the system used for the OPF buckets. The specific design requirements were:

- Collapsed Length 4.3 m (168 in.)
- Deployed Length 10.4 m (408 in.)
- Lateral Stiffness (min.) 29 kN/m (167 lb/in.)
- Lateral Load (max.) 2.2 kN (500 lb)
- Redundant system for supporting intermediate tubes.
- Eliminate sliding bearings where possible.
- All lubricants sealed within assembly to minimize contamination. Grease preferred to oil.
- All moving parts easily accessible for removal or inspection.
- Three-section tube assembly expandable to at least four sections.
- Five thousand hour operating life on bearings.

TECHNICAL DESCRIPTION

Several design concepts were studied in an effort to fulfill all design requirements in a compact package at minimum costs. The prototype design (Figure 3) is fabricated from 300 series stainless steel. The two outermost tubes support rollers that engage on longitudinal tracks mounted to the two innermost tubes. A redundant system of wire ropes deploys and retracts the intermediate (middle) tube. The rollers and tracks and deployment ropes are designed to fit entirely between the tubes (Figure 4). This minimizes the collapsed length of the tubes and permits adding more tube sections to the assembly as desired. The number of tube sections is limited only by the strength and load capacity of the rollers and ropes. The tube assembly is designed such that no special or unusual equipment or material is required for fabrication. The prototype tube was fabricated under a fixed price contract with no significant difficulties.

Tube Sections

The three tube sections are 410 mm (16 in.), 330 mm (13 in.) and 250 mm (10 in.) square and 4.3 m (168 in.) long. Each tube is fabricated from two bent plates which are 6.3 mm thick and welded longitudinally. Each section also has a welded joint located 1.2 m (48 in.) from the top. The tubes were fabricated with the joints in order to demonstrate that unusual shapes and long tubes would not present problems for future designs.

The 410 mm (outer) tube has two angle brackets on one end for attachment to the test fixture. The 250 mm (inner) tube has a lug at the top for attachment of the hoist and provisions at the bottom for attachment of various loading fixtures.

Guide Track

The intermediate (330 mm) and inner tubes each have four tracks attached longitudinally, one bolted onto each side of the tube. Shims allow the tracks to be adjusted to the desired accuracy of the entire assembly. The track sections are 19 mm x 38 mm (.75 in. x 1.5 in.) cold-rolled stainless steel. The work hardening characteristics of the 303 stainless steel provide for a track surface of adequate hardness without requiring heat treatment or unusual materials. Each track section was provided with a joint at the location of highest load in order to demonstrate the effects of joints on longer tube sections.

Guide Rollers

The outer and intermediate tubes have four sets of guide roller assemblies on each side (16 total per tube). Each roller assembly contains two hardened rollers supported in a roller frame. A sealed ball bearing is press fitted into each roller. Teflon washers between the rollers and the roller frames prevent damage caused by inadvertent side loads on the rollers. The roller frame equalizes the roller loads and an adjustment bolt allows for roller alignment. The roller frames are easily removed to allow access to the rollers and bearings for inspection or replacement (Figure 5). The roller frames may be shimmed as required to eliminate inaccuracies or misalignment with the tubes. Removal of any one roller set does not compromise the adjustment of the tube assembly. The rolling contact of the roller and track arrangement and the sealed bearings minimize contamination problems.

Rope Deployment System

A redundant wire rope deployment system controls the intermediate tube. The outer tube is fixed and the inner tube is supported by a hoist. The deployment ropes maintain the intermediate tube centered between the outer and inner tubes (see Figure 6). Four sheaves are mounted to opposite corners of the intermediate tube (Figure 4). It should be noted that the

intermediate tube is positively driven both up and down. For normal operations, gravity will force the tube down and the upper ropes will remain unloaded. If there is any binding, the tube will be forced down to eliminate the possibility of the tube falling freely. This feature will also allow the tubes to be operated in any orientation desired. Wire rope terminations are provided on the outer and inner tubes. The rope terminations are adjustable to allow load equalization; however, the system is designed to function on a single rope system. Testing has shown that the rope loads remain equal within about ten percent. With a safety pin installed in the tubes, all sheaves and wire ropes may be easily removed for inspection or replacement (Figure 5). If the design requires more than three tubes, alternating corners of the tubes may be used for sheave mounts and rope terminations.

TESTING

Test requirements for the prototype tube assembly were developed to demonstrate tube operation, maintenance, and inspection based upon design requirements and projected user needs. The requirements were:

- No Load Functional Test
- Maintenance / Inspection Test
- Straightness / Side Play Test
- Stiffness Test
- Lateral Load Test
- Eccentric Load Test
- Torsional Stiffness Test
- Single Rope Operational Test
- Endurance Test

The tube assembly was installed and tested in a newly fabricated test stand at the KSC Launch Equipment Test Facility. Test loads are shown schematically in Figure 7. Most of these tests are self explanatory. Figure 8 shows the test fixture used to apply lateral loads to the tube assembly. This arrangement allowed the tube to be extended and retracted under constant lateral loads. The maintenance and inspection tests were used to demonstrate that the ropes, sheaves, and roller assemblies could be easily removed and installed. The lateral load test applied a 2.2 kN (500 lb) side load while the tube was extended and retracted. The eccentric load test applied a 9.3 kN-m (83 in. - kip) moment while the tube was extended and retracted. The endurance test was for 2000 extension and retraction cycles at full lateral load.

The prototype tube assembly met or exceeded all test requirements. The actual tube stiffness of 87 kN/m (500 lb/in.) was three times that specified in the design requirements. In addition to the above tests, the tube assembly has been subjected to two years of exposure to the KSC environment with no adverse effects (no maintenance has been required).

CONCLUSIONS

The prototype tube design eliminates all known deficiencies of existing systems and provides an economical and reliable solution to some of the unique problems of providing access to spacecraft. The prototype tube assembly has demonstrated that tube assemblies can be fabricated economically while providing improved maintainability and increased reliability. The prototype tube assembly can be used as a starting point for design of future systems or the modification of existing equipment. Design specifications for a telescoping tube assembly used on an X-Ray positioning system were developed based on the prototype tube assembly. The X-Ray system has been installed and has completed functional testing. A short design standard is being developed to ensure that the information learned from the prototype will be available to designers of new systems for use at KSC.

REFERENCES

1. Harris, J. L., Orbiter Processing Facility Service Platform Failure and Redesign, Proceedings of the 22nd Aerospace Mechanisms Symposium, May, 1988, NASA Conference Publication 2506.

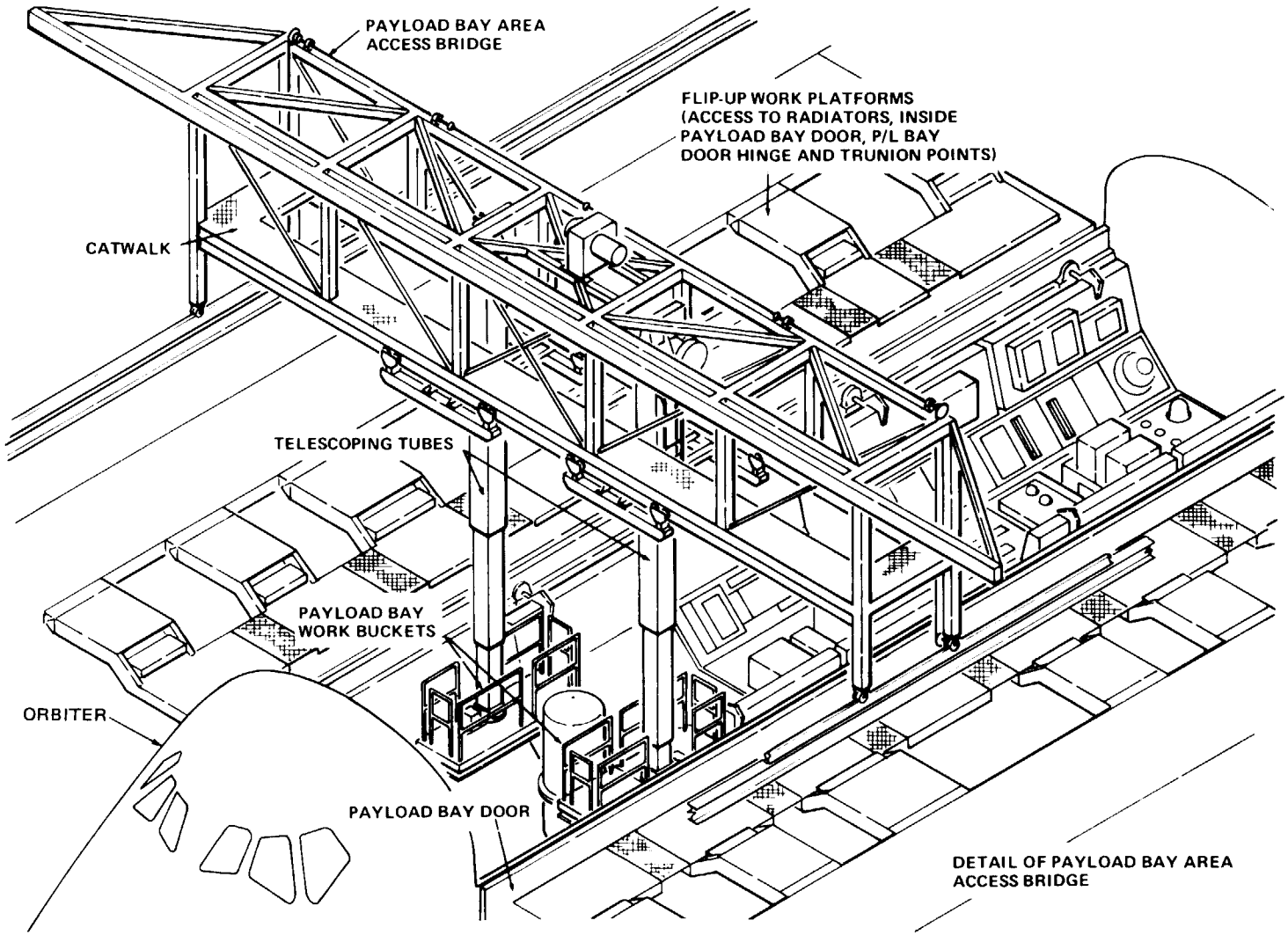

Figure 1. Orbiter Processing Facility payload bay access buckets.

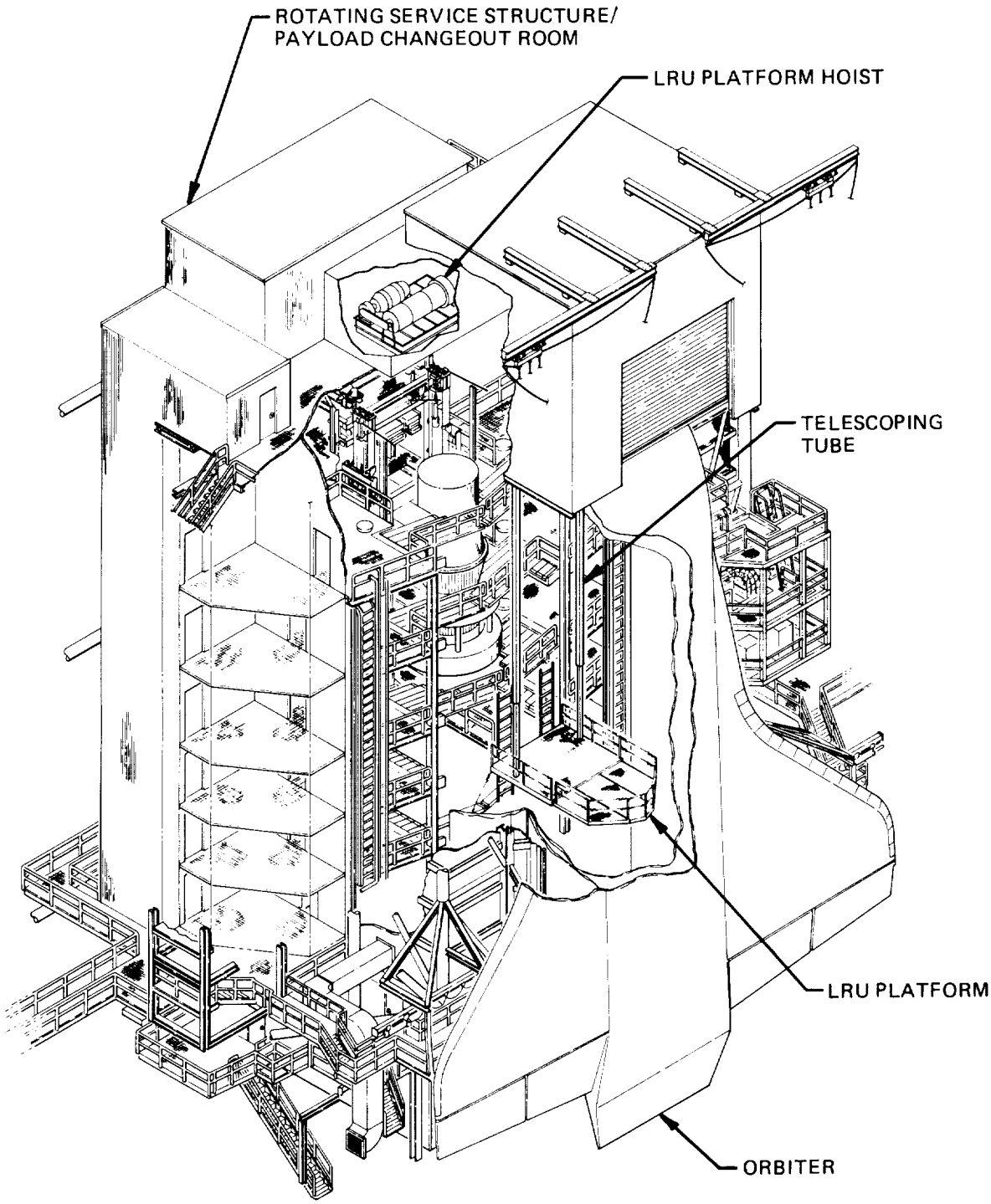

Figure 2. Launch Pad 39B LRU access platform.

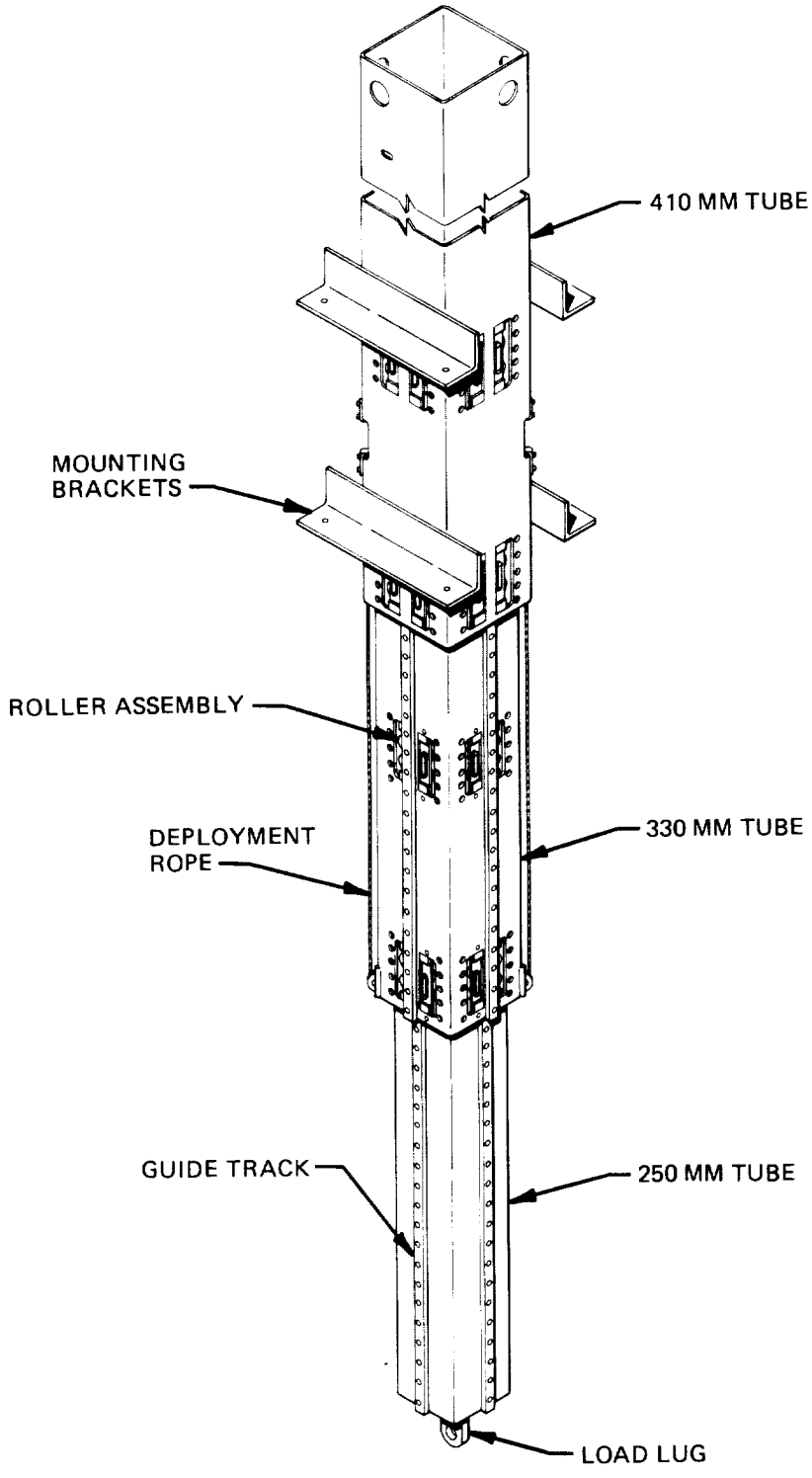

Figure 3. Prototype telescoping tube assembly.

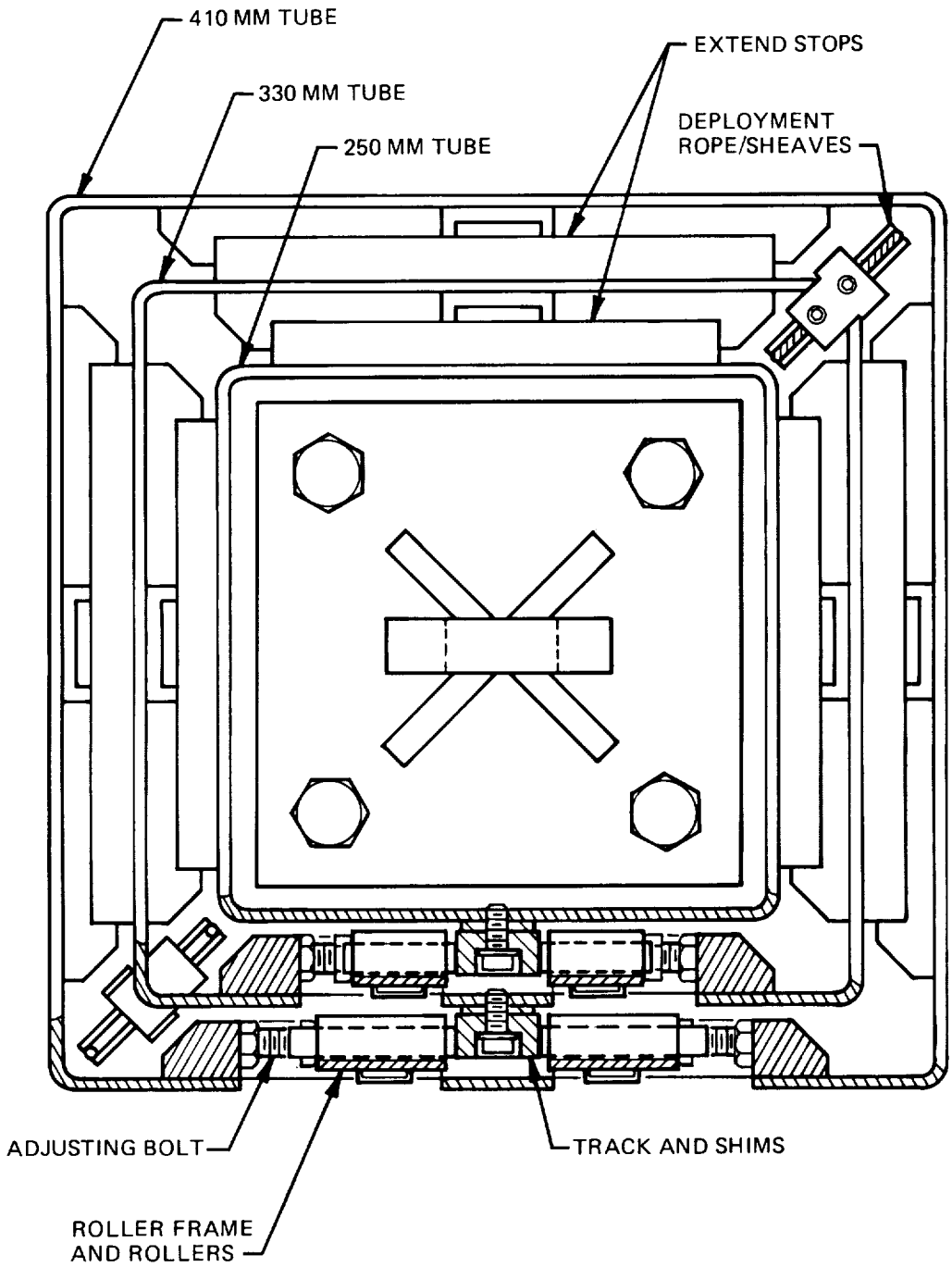

Figure 4. Top view of tube assembly sectioned at rollers.

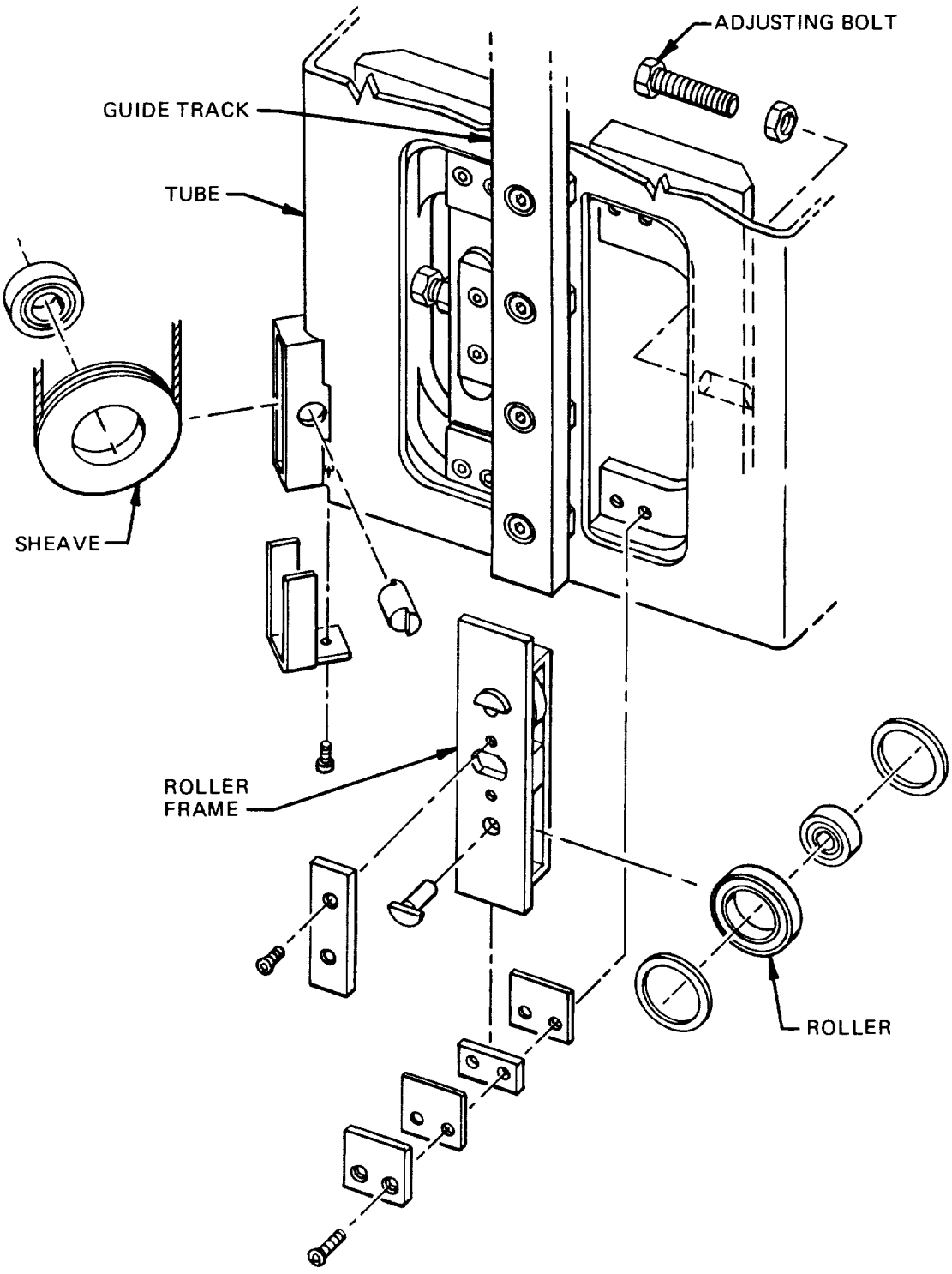

Figure 5. Detail of telescoping tube rollers and sheaves.

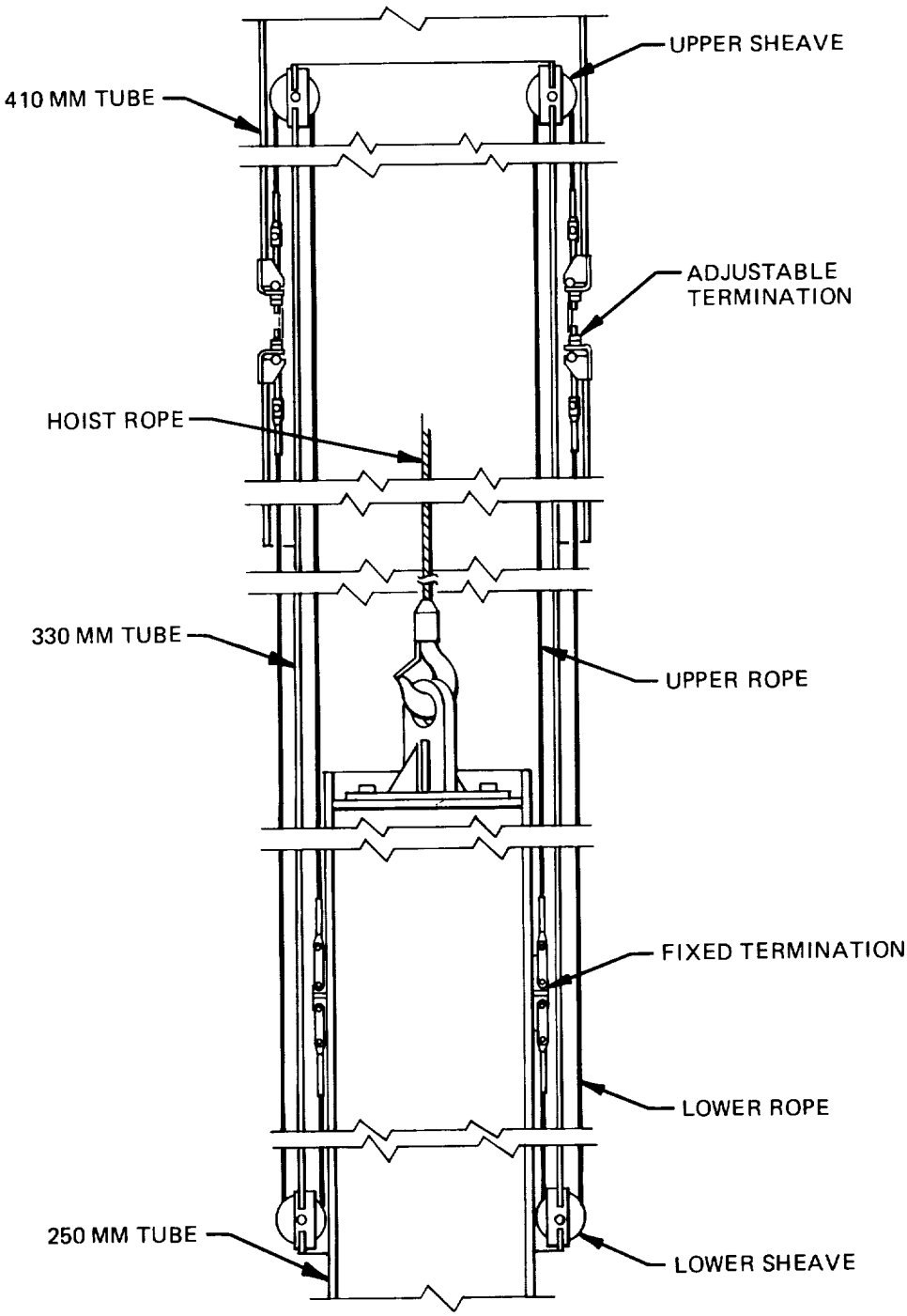

Figure 6. Deployment rope system.

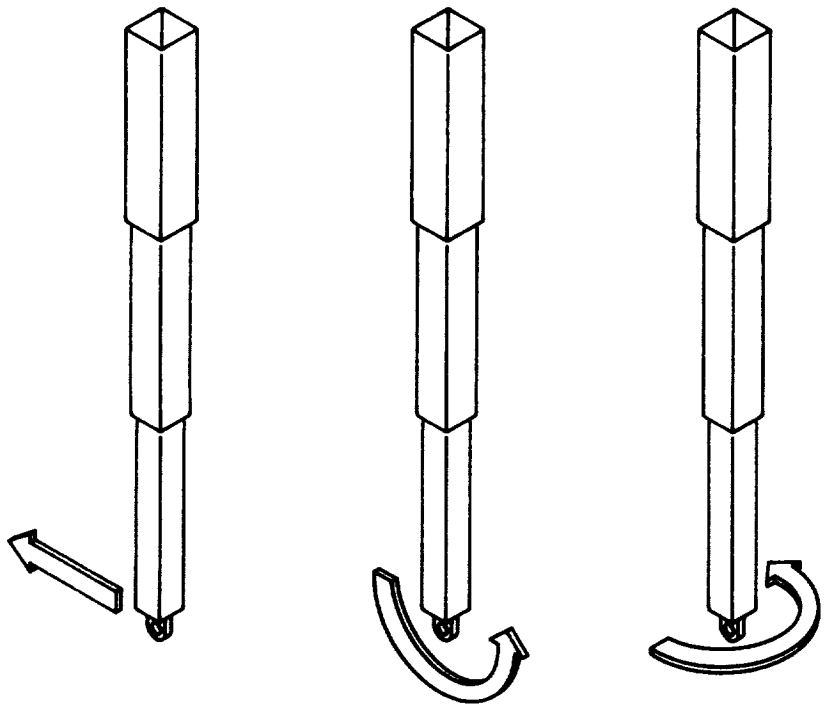

Figure 7. Telescoping tube assembly test loadings.

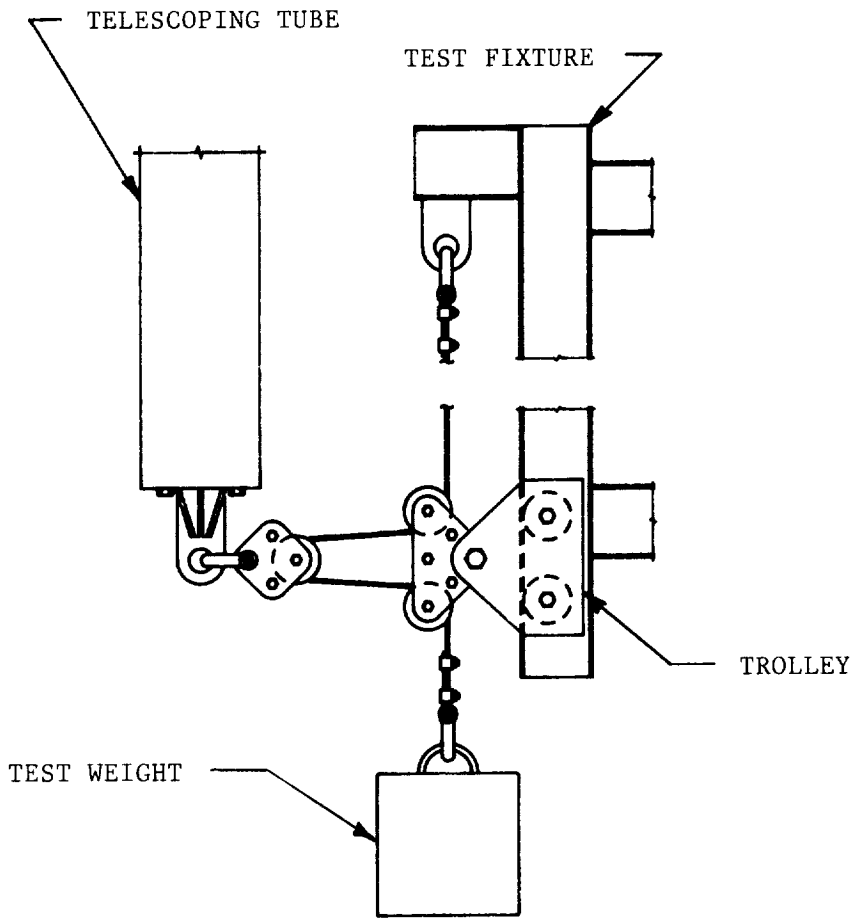

Figure 8. Lateral load test fixture.

CLEAN ACCESS PLATFORM FOR ORBITER

H. Morrison * and J. Harris *

ABSTRACT

This report describes the design of the Clean Access Platform at the John F. Kennedy Space Center (KSC), beginning with the design requirements and tracing the effort throughout development and manufacturing. It also contains:

a. A system description

b. Testing requirements and conclusions

c. Safety and reliability features

d. Major problems experienced during the project

e. Lessons learned, including features necessary for the effective design of mechanisms used in clean systems

INTRODUCTION

Due to upcoming sensitive scientific payloads, cleanliness has become an increasingly visible issue at KSC. The capabilities of intricate and expensive payloads can be impeded severely by even the slightest particulate contaminant. Designated as Class 100,000, the Payload Changeout Room (PCR) Clean Room, the facility used to clean the Orbiter payload bay, is governed by stringent National Aeronautics and Space Administration (NASA) specifications that dictate standards of cleanliness measurable in 0.5-micron units.

In response to the stringent demands for cleanliness, KSC has established a Contamination Control Program. As part of this effort, the Orbiter Payload Bay is cleaned immediately prior to payload installation. Cleaning occurs with the Orbiter in a vertical position at the launch pad, and the PCR mated to the Orbiter. However, in order to access all areas of the payload bay for cleaning, a vertically moving platform is necessary.

* Lockheed Space Operations Company, John F. Kennedy Space Center, Florida

In the past, a Line Replaceable Unit (LRU) platform was used to access the payload bay. However, the platform was designed prior to the current emphasis for strict cleanliness standards. As a result, the platform contributed greatly to particle contamination in the room. Specifically, the system had eight wire ropes and four sheaves entering the PCR, and had numerous exposed rollers. Moreover, the platform itself was fabricated of carbon steel. Cleanliness aside, the hoisting system was unstable and required labor-intensive manipulation to coordinate the pneumatically and electrically operated hoists.

Because of these inadequacies, the platform was determined to be unacceptable, and a new design was called for: The new design is called the Clean Access Platform or CAP. The CAP is a new vertically moving platform with extensible fingers and side-rotating extensions to provide access to all areas of the payload bay. Wherever possible, this new platform has been designed to incorporate not only safety features, but also cleanliness features. See figure 1 for a view of the CAP assembly.

Installation of the CAP at Pad 39A was completed in October 1989, and operation was initiated with STS-32R on November 29, 1989. Full operational capability was achieved for STS-36 in February 1990.

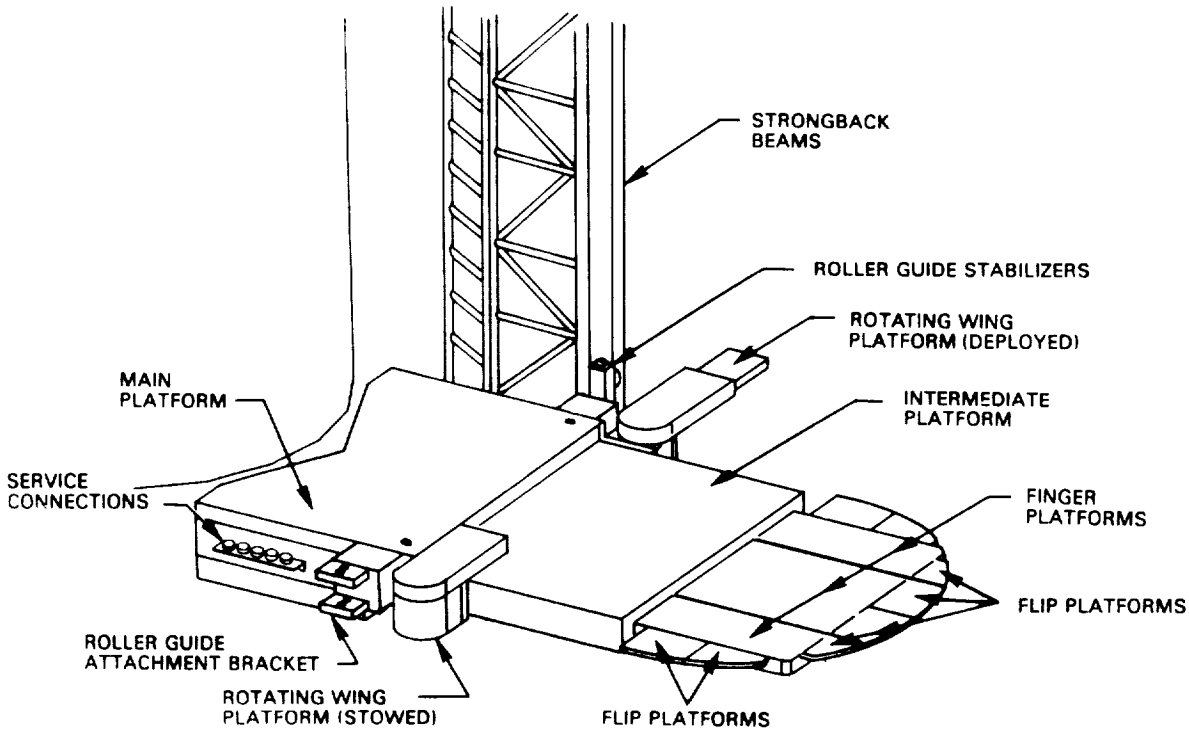

Figure 1. Clean Access Platform Assembly

REQUIREMENTS

After the payload has been installed in the Payload Ground Handling Mechanism (PGHM) in the PCR, and the Orbiter has been moved to the launch pad, the Rotating Service Structure (RSS) and the PCR are rotated to the Orbiter mate position. The PCR doors and the Orbiter Payload Bay Doors are then opened, enabling final cleaning of the Orbiter Payload Bay.

Access is required to the Orbiter Payload Bay inner mold line and to the Payload Bay Door inner surfaces from the Orbiter Payload Bay forward bulkhead to the aft bulkhead. The Clean Access Platform is designed to provide this access. Figure 2 illustrates the CAP in the deployed position.

To provide access to the Orbiter Payload Bay, the CAP must meet the following requirements:

a. The CAP must carry a live load of 680 kilograms (1500 pounds) (six technicians with tools).

b. Access must be to within 30 centimeters (12 inches) of the Orbiter Payload Bay inner mold line, but no closer than 15 centimeters (6 inches).

c. To meet time constraints, the CAP must be deployed and stowed in 2 hours maximum.

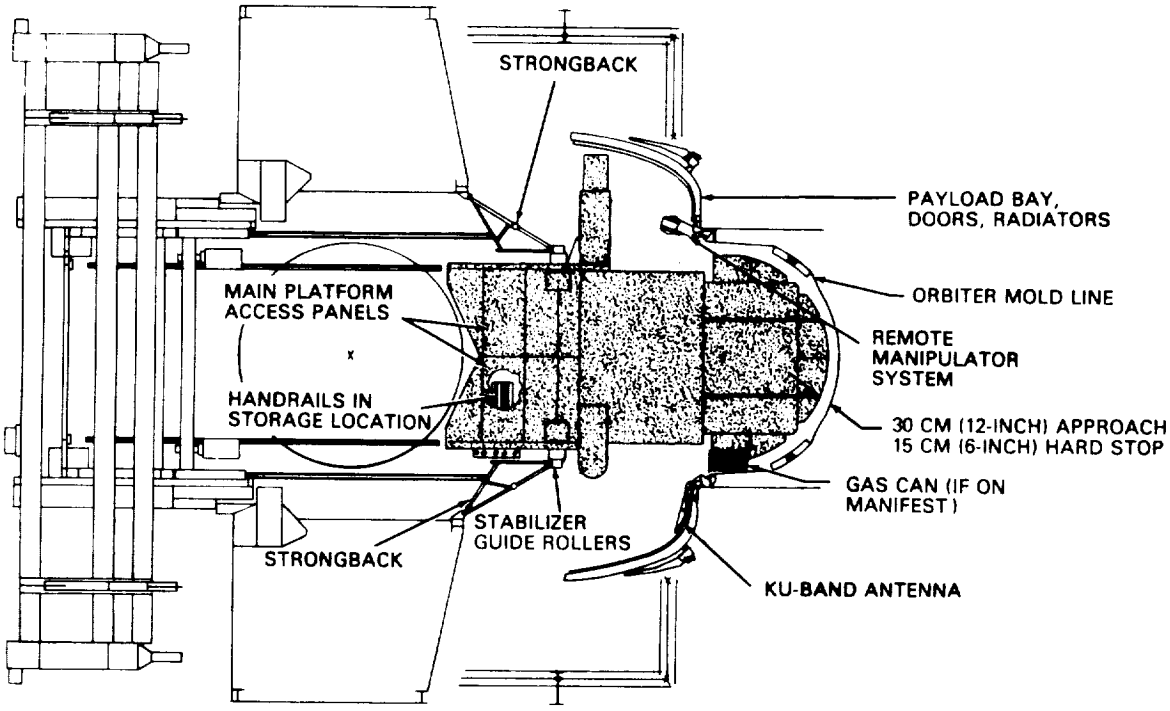

Figure 2. CAP (Deployed)

d. In operation, the CAP must reach any location in the Orbiter Payload Bay within 10 minutes.

e. Operation must be clean for both up-down movement and for extension-retraction of the platforms to ensure that the Class 100,000 Clean Room conditions in the PCR are not jeopardized.

f. When stowed, the CAP must not interfere with normal payload operations in the PCR.

g. The CAP Hoist System must meet NASA requirements for a man-rated platform so that technicians can ride on the main platform as the CAP is raised or lowered. Figure 3 illustrates the CAP and the safety features required.

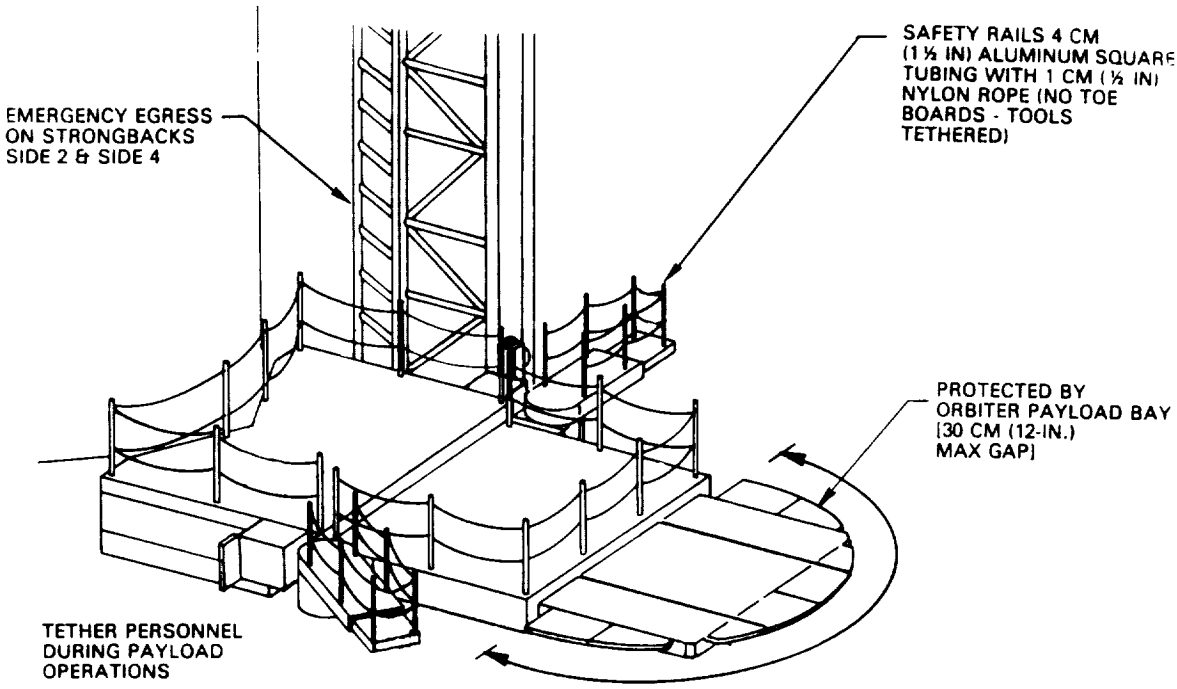

Figure 3. CAP Safety Features

h. The Clean Access Platform must be available for contingency access to the payload after installation in the Orbiter Payload Bay.

i. To accomplish contingency servicing, the CAP must be capable of handling the Line Replaceable Unit (LRU) Crane and other payload Ground Support Equipment (GSE).

DESIGN CONCEPT

After studies of alternate concepts, the design of a new moving platform similar to the existing LRU platform was chosen. However, that basic design was upgraded to provide additional access to the Orbiter Payload Bay Door inner surfaces, to permit technicians to ride the platform, and to operate in the PCR Clean Room environment.

The Clean Access Platform and Hoist System was designed by the Lockheed Mechanisms Design Section with support from Structures, Pneumatics/GN2, and Electrical Design groups. Design was accomplished using the Autotrol Computer Aided Design (CAD) system.

The final design consists of a main platform with intermediate and secondary extension platforms and rotating and extensible wing platforms on either side.

SYSTEM DESCRIPTION

The CAP consists of a hoist system, a control system, strongbacks and a stabilizer, rotating wing platforms, and extension platforms. All of these elements have unique functions and design characteristics.

Hoisting System

The hoisting system consists of two independent, commercial, off-the-shelf, 9100-kilogram (10-ton) hoist units, and was designed in accordance with NSS/GO 1740.9 and ANSI A120.1. The use of off-the-shelf hoists provides proven reliability and eliminates new system development problems. Dual hoists were chosen for safety reasons. Moreover, a total failure of any one hoist will not cause the loss of the platform system. Due to this feature, the hoisting system is unique at KSC. Figure 4 is an overview of the CAP hoist system.

Because of the long procurement lead time involved, the hoists were sized and selected early in the design phase. At that time, a large portion of the platform was anticipated to be stainless steel, and therefore much heavier than the current design. Consequently, the safety factors on the hoist system are greater than the required 8 to 1.

The hoists have single-part reeving with single-layer, dual, 2-centimeter (3/4-inch) wire ropes on their drums. The ropes are routed through sheaves from a remote hoist equipment room into the PCR Clean Room. Four wire ropes, two from each hoist, enter the PCR and attach directly to each side of the platform, eliminating the use of sheaves within the PCR.

The number of wire ropes entering the PCR is held to a minimum. The previous access system had eight wire ropes and four sheaves that were suspected to be major contributors to the particle contamination in the PCR.

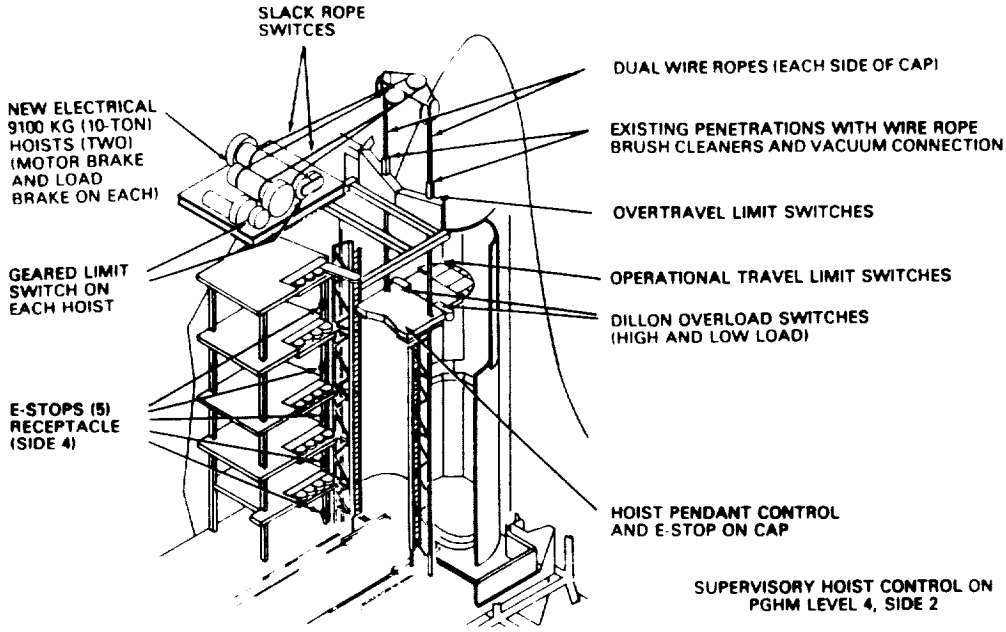

Figure 4. CAP Hoist System

Dual ropes are used to provide a rope to both sides of the platform from each hoist so that failure of a single hoist will not cause the platform to tilt. A single-layer grooved drum is used to limit the uneven rope take-up that is inherent in multi-layer rope drums. Single-part reeving minimizes the number of moving wire ropes in the Clean Room, thereby eliminating the requirement for wire rope sheaves at the platform.

Control System

The control system is 120 volts alternating current with dual contactors operating both hoists. A portable operating station is situated on the platform, along with a remote, fixed supervisory station. Remote emergency stop stations are located at various vertical travel intervals. Additional safety features include overload/underload sensors at each hoist attach point, slack rope switches at the hoists, operational travel limit switches, and overtravel limit switches.

The supervisory station has override capability to take control of the system from the operator's station on the platform. The emergency stop controls also are manned, and can stop the motion of the platform at any time.

The overload/underload sensors, slack rope switch, and overtravel limit switch are wired to a shunt trip circuit breaker located in a locked cabinet. Trip out of this circuit beaker shuts down the system. Further, the circuit breaker cannot be reset by Operations personnel. This feature ensures that serious problems will be resolved before resuming platform operations.

The control circuit conductors are routed through an umbilical which must be connected and disconnected each time the platform is used. This

arrangement created a problem early in the platform's use. Specifically, the control switches were normally open to accommodate the connect and disconnect operations; thus, the operators were able to disconnect the safety sensors and operate the platform. As a result, a circuit was added to detect when the umbilical is disconnected.

Strongbacks And Stabilizer

The 18-meter-long (60-foot-long) strongback is a truss structure fabricated from stainless steel with a structural rail guide assembly that guides the platform vertically and carries the overturning moments created when the platform is used. The strongback is foldable to meet clearance constraints, and to keep the guide rail as close as possible to the hoist attach point in order to limit hoist-induced moments.

The stabilizer is a roller assembly that rides in the strongback guide rail and has expandable latch pins to connect it to the platforms. Moment loads are transmitted from the platform, through the stabilizer rollers, and into the strongback.

Rotating Wing Platforms

The rotating wing platforms are attached to the side of the platform. The platforms not only have an air-tool operated rotating drive (see figure 5), but they also have an extensible element operated by an air tool that provides the motive force for the drive mechanism.

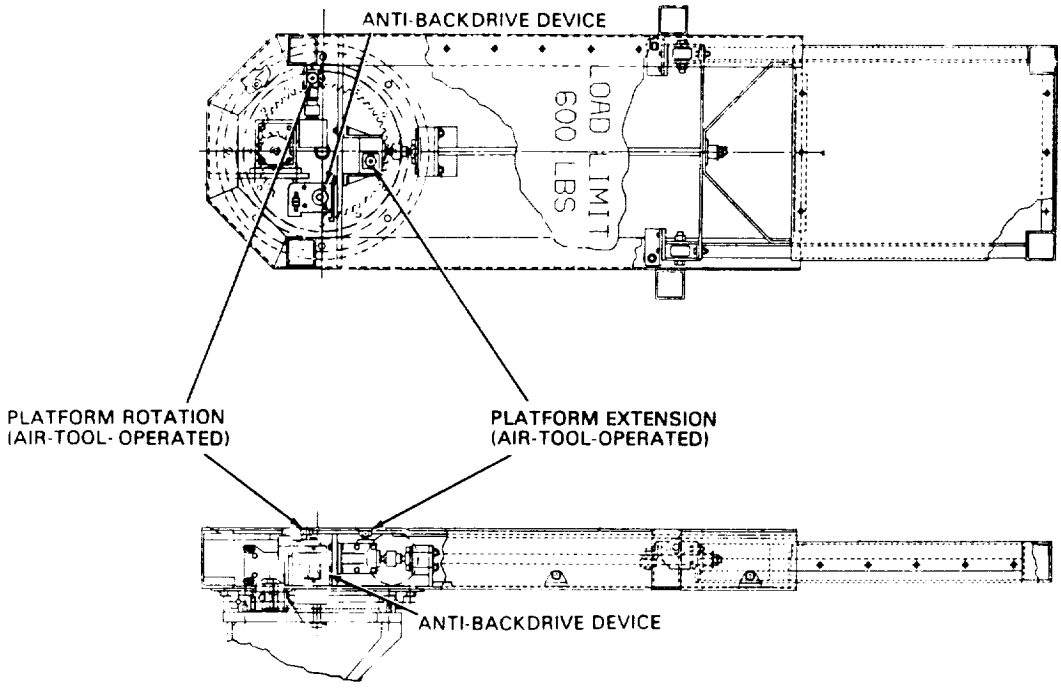

Figure 5. Rotating Wing Platform

A telescoping section was added within the rotating wing to provide clearance with the Remote Manipulator System (RMS). Both sections have hand-held, air-operated tools that provide the motive force.

One of the problems experienced with the platforms was backdriving of the rotating mechanism. Specifically, workers standing on the floor could push on the side of the wing with little effort and cause the platform to rotate. The drive mechanism gearbox was a 100-to-1 worm gear. Past experience with worm drives indicates that drives with ratios of greater than approximately 50 to 1 will not backdrive. Therefore, no problems were anticipated with backdriving. However, in actuality, the gearbox was a double-reduction worm gear with each reduction having a ratio of 10 to 1.

The problem was solved by installing a ratchet device on the wing ring gear to lock the wing in position when deployed. The ratchet device is independent of the drive mechanism.

Extension Platforms

The extension platforms consist of an intermediate platform that extends horizontally from the main platform and carries three side-by-side finger platforms that extend from it. In turn, the ends of the finger platforms have hand-deployed flip platforms to ensure complete access to the empty payload bay of the Space Shuttle Orbiter.

The drive mechanisms (see figures 6 and 7) for the intermediate and finger platforms are of the same design and, like the rotating wing platforms, use a hand-held air motor to provide the motive force. The mechanism is sophisticated, primarily due to the need for it to be self-supporting and to accommodate the relatively large angular and linear deflections of the aluminum platforms.

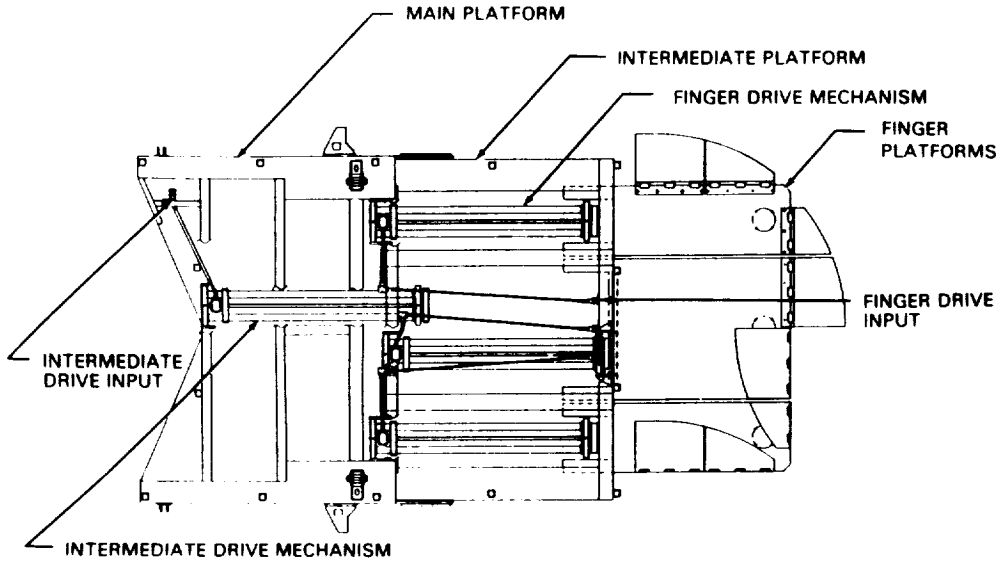

Figure 6. CAP Extension Drives

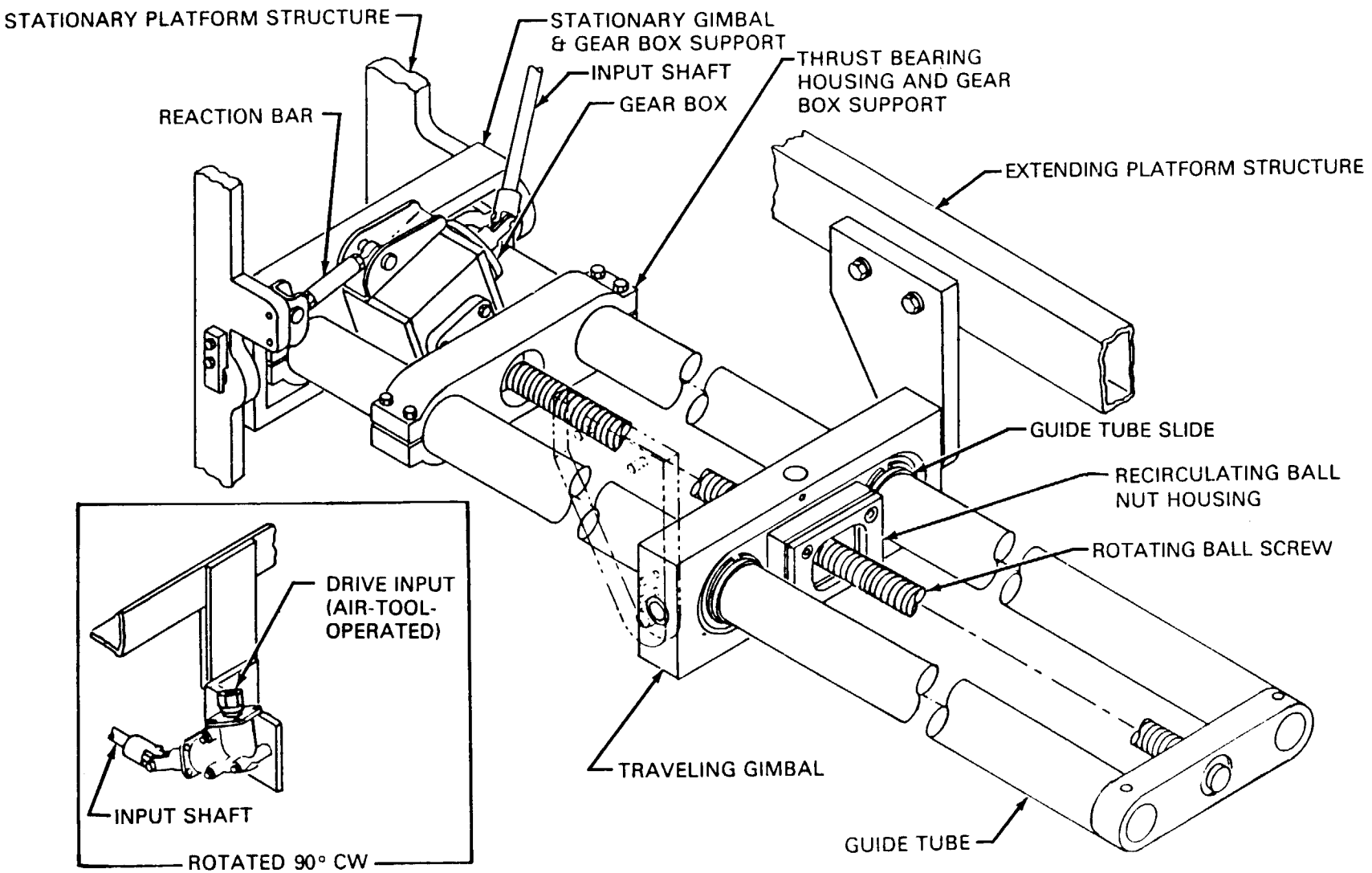

Figure 7. CAP Drive Assembly

The mechanism is a ball screw device with a traveling nut containing recirculating balls. The unit is gimballed on one end and free on the other, has a floating gearbox, and has independent thrust bearings for the rotating screw. The traveling ball nut is gimballed at its attach point on the extending platform, and slides on cantilevered guide tubes to provide support for the screw.

The ball screw is able to translate slightly in the guide tube fixture using thrust bearings configured to allow only tension loading of the screw. During platform extension, compressive loads in the drive are transferred to the guide tubes at the forward end of the screw. The elimination of column loading in the ball screw enabled the use of a significantly lighter screw, thereby reducing deflection at the end of the cantilever.

Slight backdriving problems also were encountered with the finger platform drive system, and were solved with a spring-actuated locking device that unlocks when depressed by the hand-held drive motor.

TESTING

In-plant testing consisted of simulated hoisting, load tests, and testing of the extensible drive mechanism assemblies. Load tests and hoisting tests were conducted at the vendor's plant so that the vendor's facilities would be readily available in case of any major problems.

Hoist system testing, including function tests and proofloading, was performed at KSC, as was proofloading of the strongback assemblies. Special test fixtures were designed to perform the load tests with the hardware inside the PCR.

Full-up system testing was conducted after all components were installed, and included a static proofload equal to 150 percent of the safe working load of the platform. Additionally, dynamic testing at 100-percent load was conducted.

Testing revealed that the system has a tendency to oscillate at approximately 1 hertz while being raised in slow speed. The problem was less pronounced in high speed and appeared to occur when the stabilizer rollers contacted joints in the wear plates on the strongback guide rails. The problem was resolved by smoothing the wear plate joints and could also be eliminated by retracting the platforms while raising the unit.

SAFETY AND RELIABILITY

In addition to a dual-hoist system with redundant load brakes, safety limit switches, and emergency stop stations, the CAP is equipped with removable handrails and emergency egress ladders. Associated operation instructions dictate that all tools on the platform be tethered, and that the number of passengers on the platform be limited to six. Moreover, CAP operators receive special training prior to certification.

A System Assurance Analysis (SAA) revealed a single failure point in the extensible platform drives, and corrective action has been taken.

PROBLEMS

Problem No. 1

The main problem encountered during the design phase of the project was due to startup complications associated with the use of the new CAD system. This project was the first one worked by the Mechanisms group that was accomplished exclusively with CAD. The original plan was to build 3D models and produce the drafted drawings from the models. However, the performance limitations of 3D soon became evident, and the plan was modified to use 2D layouts and drawings with 3D used only for envelope models of the structure and platform. File corruption due to new software was a major problem, and continued to plague efforts right up to the final drawing release.

Problem No. 2

A major problem during fabrication concerned weld failures and distortion due to poor selection of welding sequences. The fabricator was constrained by a stringent schedule, and thus did not always use balanced welding techniques. Therefore, some weld fractures occurred due to locked-in stresses. To compensate for possible unreliable welds, mechanical bolt-on brackets were designed for critical locations.

Problem No. 3

Major problems were experienced when deploying/stowing the CAP due to a minor misplacement [5 centimeters (2 inches)] of the strongbacks during installation. The CAP side attachment brackets were redesigned to correct this problem.

LESSONS LEARNED

The following lessons were learned from this design effort:

a. Cleanliness must be designed into clean systems. During the design phase, the following features should be incorporated wherever possible:

   (1) Use closed sections (for example, tubes) rather than I-beams.

   (2) Use rollers instead of slides.

   (3) Eliminate as many moving parts as possible.

   (4) If moving parts are unavoidable, enclose them if possible.

(5) Use corrosion-resistant materials.

(6) Use smooth surfaces for ease of cleaning.

(7) Grind welds smooth and eliminate any gaps or crevices.

b. When fabricating clean systems, cleanliness must be maintained starting with the fabrication process, and continuing throughout manufacturing.

c. The CAD system greatly increased the capabilities of the design engineers to perform tolerance build-up and clearance studies, thereby eliminating manufacturing and fabrication problems before they occurred.

d. The CAD system also allowed the design engineers to rapidly perform "what if" studies to deal with fabrication and installation errors.

e. Start-up CAD projects should have the most enthusiastic and competent engineers and designers assigned.

f. Major designer involvement is required in the fabrication testing and validation phases of a project to maintain high quality.

g. Installation requirements and tolerances must be documented clearly, and a new survey of the area must be completed to ensure the proper location of critical elements.

CIRCULARITY MEASURING SYSTEM
A Shape Gauge Designed Especially for Use on Large Objects

by
G. R. RohrKaste, P.E.
Systems Engineering Manager
Thiokol Corporation Space Services Division
Cape Canaveral Air Force Station, Florida 32899

Abstract. The Circularity Measuring System (CMS) was designed and is currently used to match the shapes of the redesigned Solid Rocket Motor's field joints during assembly in the Vehicle Assembly Building (VAB) at Kennedy Space Center, Florida. It is a fully developed mechanism used for the assembly of launch vehicles.

The CMS's development was unique for two reasons. First, it is an unusual solution to an original problem. The problem is to mate high-tolerance, large, flexible structures. The immediate (or obvious) solution is to measure radii from an approximate center. This proved to be operationally unfeasible, since the device to accomplish this required a complicated and lengthy setup and was sensitive to environmental change, especially temperature. A less obvious solution was to determine shape. Because the cases had been measured on a rotating table at the manufacturer's facility and again prior to casting propellant, they had already been matched to achieve the proper interference fit. Therefore, matching the shape is all that is required at final assembly. Determining shape could now be done with a bridge gauge, originally conceived as measuring arc heights and matching the corresponding points on each mating surface. This allowed the development of a highly portable, easily used device.

The second unique feature is the symbiosis of the bridge gauge with a personal computer. The data collected from the bridge gauge are used by the computer with a unique algorithm to piece together the arc segments generating the shape with a resolution of 30 ppm.

The bridge gauge (see Figure 1) has arms with two fixed end points, the distance between which is precisely 914.4mm (36 inches). An outwardly, spring-loaded probe slides along the perpendicular bisector of the line between the fixed points and measures small displacements within 0.0025mm (0.0001 inch). Roll and pitch sensors help the technician to level the gauge for maximum accuracy. Pins can be attached to the arms near the end points and to points near the probe, to mate with guide holes (if provided) in the object to be measured.

The technician measures the displacements at a sequence of positions around the circumference of the object. This could be done most conveniently by using the guide pins and indexing to a circumferential string of guide holes. The measured displacements are sent to the computer. For each

measurement, the portion of the measured surface between the end points can be approximated by the circular arc tangent to the end points and to the end of the probe. The computer calculates the arc for each measurement. It pieces together the arcs from the sequence of measurements to obtain a curve consisting of circular-arc segments that approximate the measured surface (see Figure 2).

Briefly, the algorithm works by smoothly joining circular arcs of specified curvature. Because the curvature data are approximate, a linear parametric deformation must be performed to generate a smoothly closed shape. A natural extension of the algorithm allows it to incorporate corners and be used to approximate unclosed curves in the plane. It is shown that the algorithm exhibits invariance under the Euclidean transformations, preserves convexity, and has convergence properties.

The shape gauge has been extensively tested against a radius-measuring device and photogrammetry, with the National Bureau of Standards in observance. It successfully demonstrated a repeatable accuracy of 0.10mm (0.004 inch) on a 3.7m (146 inches) diameter.

The bridge gauge and its associated computer constitute a system that measures the out of roundness of large cylinders. Currently the system is being developed to determine the shape of any continuously curved surface.

Intended originally for use on the Solid Rocket Motors of the Space Shuttle, the system has been demonstrated determining the preservation of circularity of submarine hulls. The system can also be used to measure the straightness or roundness of complex geometric shapes, such as aircraft or hulls of ships. Development of the device continues as a NASA "spin-off" for industrial and commercial use.

The requirement to measure the Redesigned Solid Rocket Motor (RSRM) field joint to a previously unnecessary accuracy precipitated the design of the Circularity Measuring System (CMS). The redesigned field joint has a modified tang, incorporating a capture feature; this also provides an interference fit (Figure 3). During the engagement of the joint, this capture feature must not be plasticly (permanently) deformed or the interference fit will not be preserved. To verify that the RSRM segments achieve the interference fit properly, the position of the o-ring sealing surfaces of the joint must be known relative to a common centerline within 0.076 mm (0.003 inch). This determination is made by Thiokol at the Wasatch facility. The Wasatch facility determines the selected fit of the segments in each rocket motor assembly. These measurements are made in the case of a new segment while on the turning machine (thus the center point of the radii is known with some assurance). In the case of a refurbished segment, the measurement is made on a massive rotating table with a linear displacement reading taken from an external known

position. In both cases the environment is controlled or at least stable and monitored so thermal expansion can be accounted for.

These measurements are completed prior to the cases being cast with propellant, turned on their side, transported by rail to Florida, removed from the transport, stored vertically, and then finally moved to the Vehicle Assembly Building for assembly. The case and propellant behave as a viscoelastic structure. The empty case having the same stiffness properties as a soft drink can with the ends cut off; the propellant having about the same density as the eraser on the end of a pencil. The propellant has properties similar to creep and appears to have a "memory." That is, it will return to a previous state, probably the state which caused the most internal stress. The point to be made is that while the circumference measurement has not changed, the casings certainly are not round.

In fact, our tests showed that they assume a tri-lobed shape sometimes referred to as "bread-loafing." Also, the cases have different properties: the forward and aft are stiffer because they have domes attached, and the two center segments are open at both ends. The aft segment has stiffener rings on its lower half increasing its stiffness, and the forward segment has the propellant star pattern for its core where the others are cylindrical. Thus each case has a different stiffness. To say that since the segments are all exposed to same environments they ought to deform the same is incorrect, since they all have different physical properties. The bottom line is that the segments must be measured prior to assembly in Florida after transit.

We determined that the segments were flexible enough, especially in the small displacements we were looking for, and that the handling and other associated equipment would cause deflections of sufficient magnitude to be unacceptable. We found the deflections inputted at the lower end of a segment were transmitted to the upper but inverted. The major axis at the bottom was now the minor axis at the top. This was attributed to the factory joint (a localized area of increased radial stiffness) in the center of each segment behaving as a fulcrum. It was also shown that this same phenomenon occurred when the segments were suspended from a lifting fixture; however, the loads then were imparted to the top, causing an inverted reaction at the bottom. A further complication occurs because the aft segment (the first in the assembly) is supported on four spherical bearings (a statically indeterminate load case), which are aligned on intersecting axes 60 and 120 degrees apart. Because of the four-point support, the loads into the structure need not be equal. The lifting beam which supports the suspended mating segment is also a four point fixture (again an indeterminent load case), but these four load points are on two axes, 90 degrees apart. Thus the perturbations in the radial shape caused by the handling and support equipment do not necessarily coincide.

To summarize, the goal is to determine the relative position of the tang and clevis at corresponding radial locations to within 0.076mm (0.003 inch). The segments have preserved their circumferential measurement. Thus the interference fit of the selected assemblies is conserved if the shapes can be made nearly identical. Transportation and handling alter the shape, and the physical properties of the segments vary.

There were various methods investigated to effect the field determination of shape. These will be discussed briefly. First was the process that was used prior to the RSRM design, that is to measure diameters. This process used a surveyors tape graduated in two (2) cm. increments, which was converted to British units for data recording and the data entered to the nearest 0.001 of an inch (0.025 mm). This technique was grossly flawed due to rounding errors, and was abandoned. Next a 3.7 m (146 inches) inside micrometer was used. Trying to determine shape by measuring diameters is not accurate because the assumptions that the end points and the center are in line, and the end points are equidistant from the center cannot be guaranteed. "Inspection & Gaging," Kennedy & Andrews, Industrial Press, pps. 272, 456-461, gives an excellent discussion of why this technique is wrong. An example is the Wankle rotor, where the measurement of points on the circumference 180 degrees apart are equal, which can give the appearance to be diameters. It is not until the realization that the center is not equidistant from the ends that the shape then becomes tri-lobed (which interestingly enough is the peculiar condition of the RSRM segments).

The obvious solution is to measure radially from a point that approximates the center. A tool was designed and tested; it has been referred to as the radius arm tool. Demonstrations of the radius arm tool showed an operational difficulty in that it is a complex assembly which must be installed on both the stationary and suspended sides of the joint. To effect this operation on the permanent scaffolding in the VAB required considerable time assembling and disassembling the tool. The sweep of the radius could not be manual, since varying angular velocity, axial, and tangential loads caused by human power created unacceptable errors. The device has a motor-driven sweep which is also indexed to relay angular position when the linear voltage displacement transducer (LVDT) is cued for a reading. To make the device such that it could be transported and assembled manually, it is primarily aluminum and therefore sensitive to temperature. The VAB is an unconditioned hangar. This inability to have a controlled environment in the VAB renders this tool useless in this assembly area. Additionally, the repeated assembly and disassembly of this tool as well as the relatively dirty work area would cause the bearings of the tool to wear, thus reducing the resolution of the tool.

Commercial techniques were canvassed, finding the most

suitable system to be photogrammetry. It has the resolution to achieve the 0.076 mm (0.003 inch) target. The flaw is that it takes a minimum of four (4) hours to process the data from the measurement. Because of the viscoelastic properties of the casing, in four (4) hours time the case shape will change.

The criteria for an operational tool were becoming evident: it must not require a controlled environment, it must minimize moving parts, it must be portable, and it must deliver immediate data results following the measurement (obviously some innovative thinking was in order here). Existing commercial systems of sufficient accuracy had a minimum of a four (4) hour wait to process data. The radius arm tool was not accurate in the VAB environs as well as being difficult operationally to use.

A purely mechanical device was tested (labeled the comparator). These devices were a block with two (2) dial indicators which simultaneously measured the tang and clevis while they were in close proximity (just prior to engagement). Six (6) or more units were used simultaneously about the circumference of the joint. These were unsuccessful at making the measurement because of the pendulum motion of the suspended segment. Also since the measurement had to be made with one segment suspended immediately above the other it was all but impossible operationally to alter the segment shape by a shaping device or redistribution of loads in the lifting beam cable drops.

From this tool another criteria was learned. The determination of clevis-to-tang gap cannot be made relative to one another in the VAB assembly environment.

Traditional or typical solutions to the measurement were not working. A completely different approach had to be taken since it did not appear sweeping a radius or determining run-out was workable. A feature independent of radii had to be found. The hypothesis presented was that instead of making a direct comparison of radial displacement we could compare arc heights from a fixed chord and extrapolate the displacement measurement from these readings. The tool could be a convenient length set by the chord. It would be portable and have only one moving part. Because of its compactness, thermal expansion and contraction would not significantly affect the measurement (so a controlled environment is not necessary). Data reduction would be immediate, especially if a personal computer is used as a data logger and processor. The tang and clevis can be measured independently. Thus all the criteria which caused the previous tools to be ineffective could be overcome.

The original hypothesis was expanded because the item intended to be measured, the curve, is continuous (approximates circular). Two adjoining arcs of different radius on a continuous curve share a common tangent at their adjoining point. With this geometric fundamental, the arc radius which can be calculated from the chord and arc

heights can be connected. With the circumference data (which has not changed since determined very accurately at the Wasatch facility), a very accurate approximation of the shape can be achieved. This approximation was shown to be repeatable to within 0.10mm (0.004 inch) under various conditions in numerous qualification tests.

The beauty of this tool is its sheer simplicity. It has already been described concisely in the abstract; further description for this paper's purpose does not seem warranted. The tool is completely documented by drawings, design manual, mathematical proof, operation and maintenance manual, as well as a compilation of tests performed.

Briefly, there were two major qualification tests preformed. The first was in the VAB at Kennedy Space Center where the micrometer and the CMS were tested using photogrammetry as a control. As stated previously with one independent measurement to scale upon a circumference or major chord (apparent diameter), the CMS determines absolute shape repeatable to 0.10mm (0.004 inch) on a 4m. (12 ft.) diameter. If all that is required is a shape comparison (as is the case of the RSRM assembly), then the independent measurement is unnecessary.

The fact that the CMS measurements can be used without a secondary independent measurement is key to its usefulness during SRM assembly. This ability has been demonstrated by test. The following logic exercise also demonstrates this ability.

> The selective fit of the mating segments has been previously determined very accurately with the fit defined as an interference fit. Therefore, if the two shapes are the same within a tolerance band, the segments will mate. Again this has been determined elsewhere and need not be repeated at final assembly. The SRB mate is a peculiar case in that the shape is very nearly circular and the center line of the segments nearly coexist. With these initial conditions, all we need to know is the deviation from circularity of the tang and clevis. CMS provides that set of data. Subtract the deviations from circularity for the tang and clevis at matching radial positions, and you get a distribution of delta circularity data. If the spread of this data does not exceed a quantity derived from the design tolerances of the interference fit, then the joint can be made. Please note this determination does not require that the circumference or radius be known at assembly. All that must be known is that the selective fit determination has been accomplished and you have the right segments to be mated. This argument has been presented for an interference fit but it also holds for a running fit or match fit.

The second series of tests occurred at Marshall Space Flight Center comparing the CMS with the radius arm tool

again using photogrammetry as a control. The National Bureau of Standards was in observance. Again CMS demonstrated its repeatability to 0.10mm (0.004 inch). This test was key in the CMS being accepted as the comparison gage for segment mating at KSC. Its ease of use, portability, and insensitivity to temperature all demonstrated its superiority over the other devices for this application.

The CMS has been demonstrated as an alternative device to determine hull circularity of a submarine at the Portsmouth Naval Shipyard. Here we learned how the maritime industry has wrestled with the problem of determining shape. The standard practice is to go to the lofting room and scribe an arc on a sheet of aluminum that exceeds the radius of the hull by a known distance. This template is then positioned against the hull with surveying equipment and using a small scale measure from the scribe line to the hull. This must be done at multiple frames along the hull. Each frame requires its own template. Each boat is different enough to require a dedicated set of templates. The Navy is acutely aware of the thermal distortion problems; so they attempt to make the measurements in the early morning, before sunrise when ambient temperature is most stable.

The CMS determination of deviation from circularity matched previous template trends, and its ease of use impressed the shipyard, but further development for the tool for this application has not occurred. However, this is going to be investigated as an area for future commercialization. The possible commercial applications seen today are assembly of large tankage, inspection of bulk storage tankage, lofting, flatness, and straightness determination.

Assembly of large tankage has problems very similar to the RSRM. Take the example of welding an end dome to the cylindrical section of a large tank. A standard practice is to start at one point and continue around until back at the beginning. Then any misalignment will be cumulative and concentrated at the point of closure. Normally, this misalignment is not great enough that the gap can not be drawn back together. But this causes residual stress which can be an undesirable situation. If better matching of the joint is possible so that the weld can be made in distributed beads, then the residual stress could be eliminated, reducing possible failure modes.

Since the CMS is portable, it could be used as an inspection device looking for local bulges or cavitation indicating weak areas of the walls. Periodic inspections of bulk storage tanks might mitigate the risk of repeating the accident occurring in the summer of 1989 when bulk storage ruptured in the northeast of the United States, spilling its contents into an adjoining waterway.

As a device to do or inspect lofting, the CMS is well suited. Previously discussed was our demonstration on a

submarine hull. From this it is possible to extend to surface vessel hulls as well as to any cross-sectional shape (e.g., aircraft fuselages and wing frames, etc.).

The tool can also be used in an inverse way from previously described applications to determine straightness or flatness (planarity). This would be useful in tooling or track alignment. All possible uses of the tool can not be fully defined. It can be used to determine convex, concave, or combined curvatures. With modest improvements, it can be enhanced for commercialization.

One of the areas which has been investigated as a product improvement is the elimination of the electrical umbilical between the instrument and its computer. The alternative is to use a small datalogger system employing Eprom's or similar devices. The datalogger would be programmed from the host computer, disconnected to make the measurement with the instrument, then reconnected to determine the shape. Another area of further development is the evolution of the algorithm to allow for nonclosure of the curve being measured. An algorithm has been developed for this purpose, but it needs revision for more general application.

Summary

The CMS was developed to make an in-situ determination of shape similarity for selected fit large cylinders (RSRM segments). It does this to a repeatable accuracy of 0.10mm (0.004 inch). This is less than goal of 0.07mm (0.003 inch) but was determined adequate because of the addition of an assembly aid that increased the entry chamfer of the clevis side of the joint. The usefulness of the CMS is demonstrated by the application to measurements other than its specific design purpose, such as submarine hull circularity, SRM mid-case circularity, as well as circularity of interfacing SRM tooling, specifically the rounding devices and horizontal disassembly devices.

Commercialization of the tool is being pursued, since it is an enhancement of metrology technology for circularity determination. The most accurate in-situ technology it replaces is determination from a template. The CMS is an improvement in accuracy and operation.

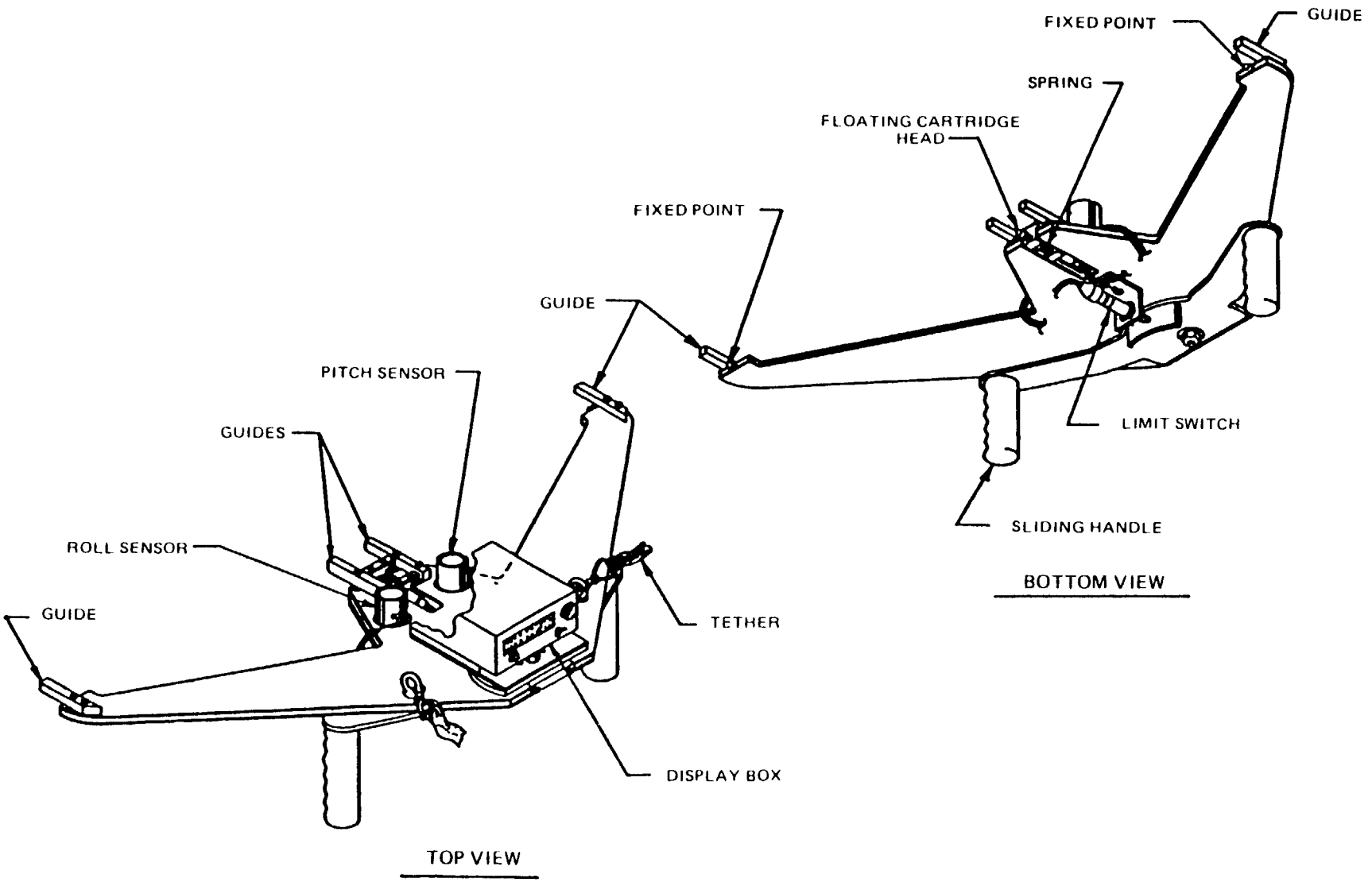

FIGURE 1. CIRCULARITY MEASURING DEVICE SYSTEM SHAPE GAUGE

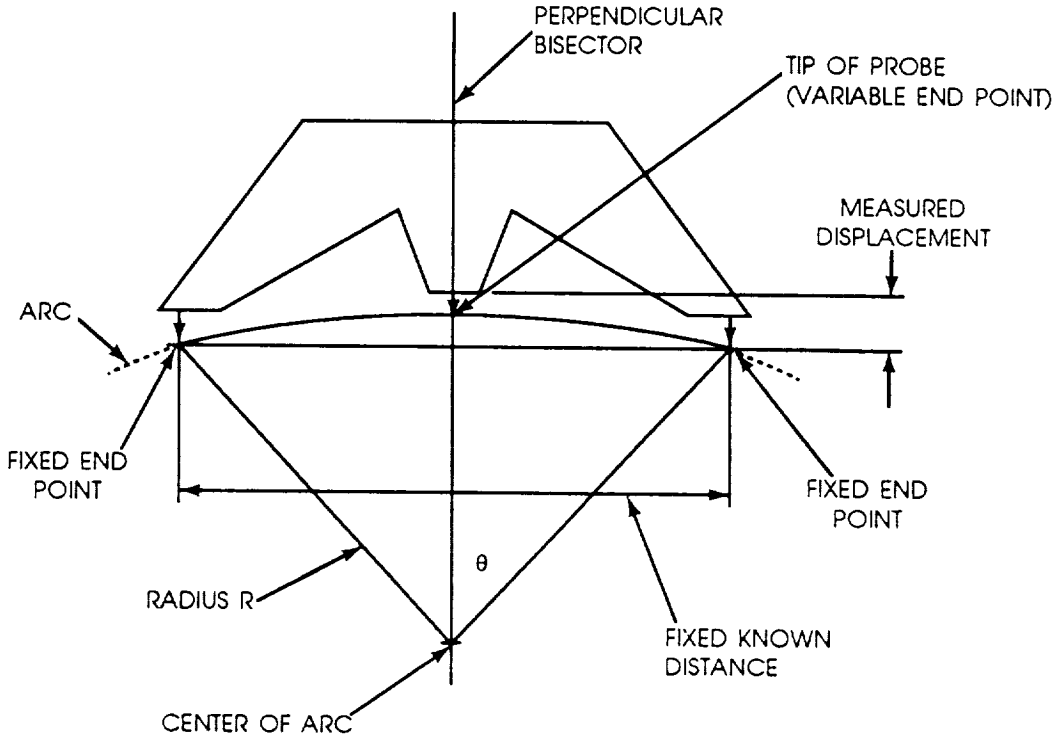

CONSTRUCTION OF ARC FROM MEASUREMENT

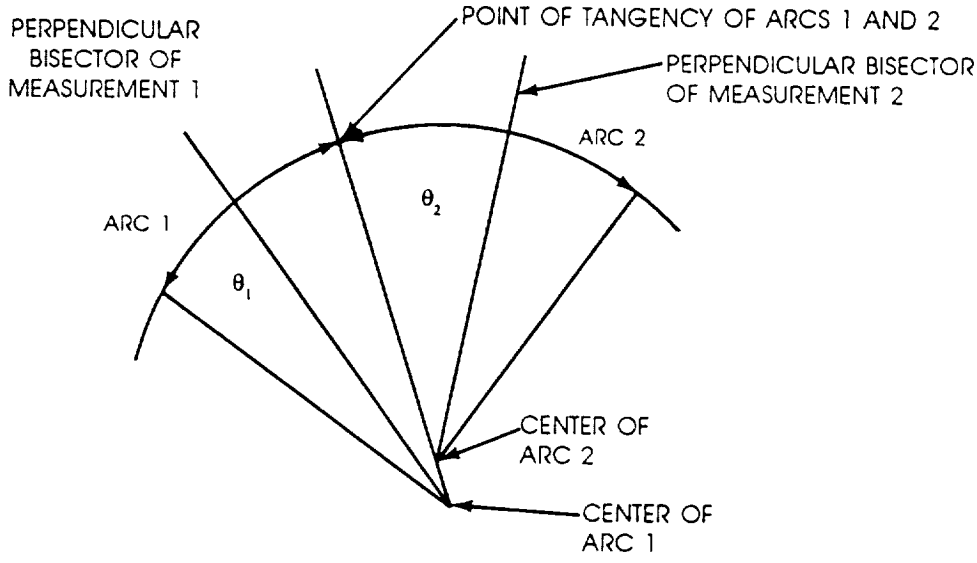

CONNECTION OF ARCS

FIGURE 2

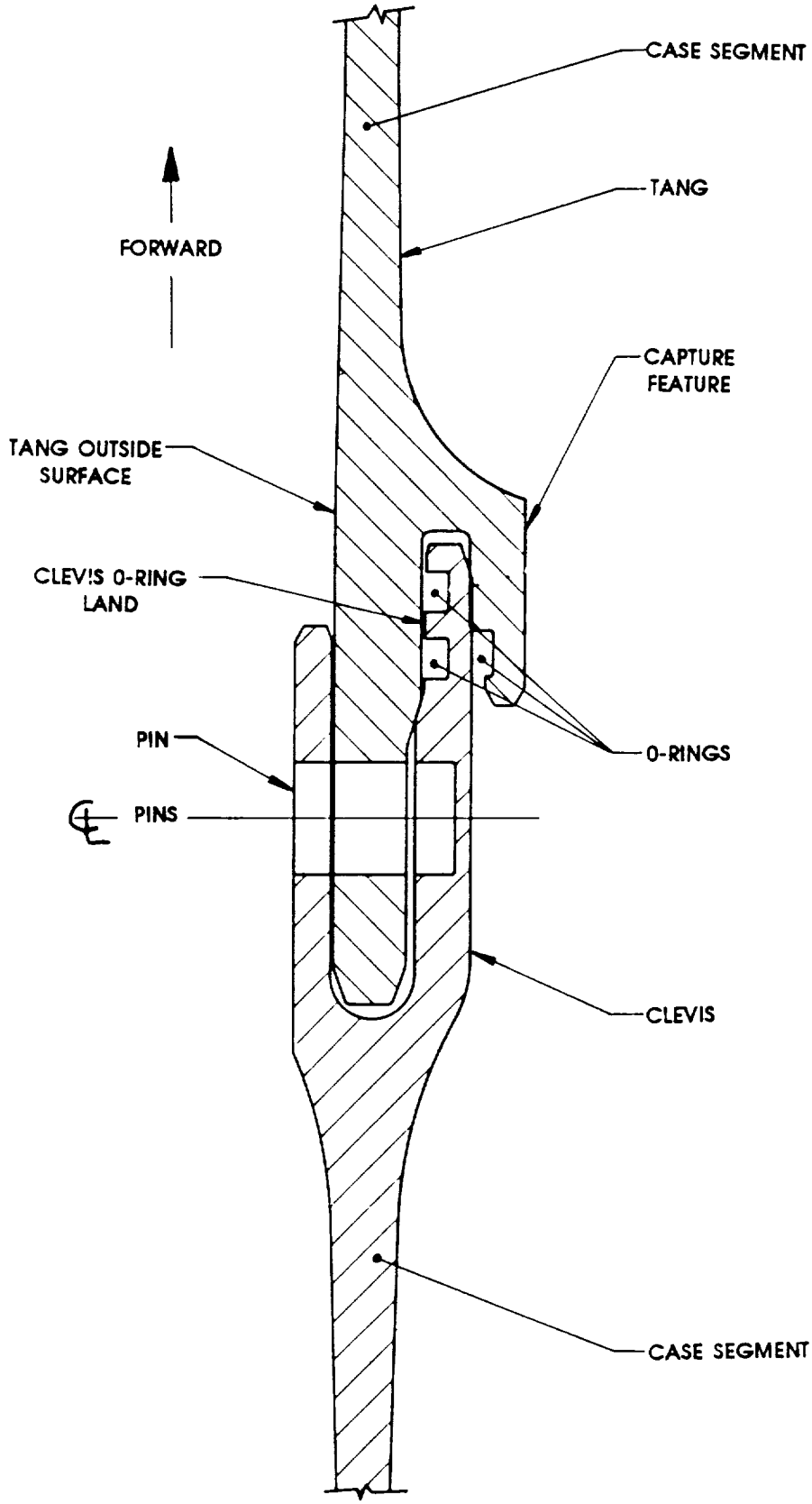

FIGURE 3. RSRM JOINT

DEVELOPMENT OF CABLE DRIVE SYSTEMS FOR AN AUTOMATED ASSEMBLY PROJECT

Charles A. Monroe, Jr.*

ABSTRACT

In a robotic assembly project, a method was needed to accurately position a robot and a structure which the robot was to assemble. The requirements for high precision and relatively long travel distances dictated the use of cable drive systems. This paper will discuss the design of the mechanisms used in translating the robot and in rotating the assembly under construction. The design criteria will be discussed, and the effect of particular requirements on the design will be noted. Finally, the measured performance of the completed mechanism will be compared with design requirements.

INTRODUCTION

The further exploration and utilization of space will include larger and more complex structures, requiring in-orbit assembly. This repetitive, time-consuming task is better suited for robots than astronauts. To develop the technology and experience necessary to carry out this endeavor, the Automated Structural Assembly Laboratory[1] was developed at NASA Langley Research Center (Fig. 1).

Completed in 1988, this facility involves a robotic arm that translates over a six- by six-meter area and a structural assembly support platform that rotates about its axis. The structure that the robot assembles is a tetrahedral truss. It consists of two-meter composite struts joined by aluminum nodes. The facility will accommodate trusses composed of three "rings" of tetrahedrons for a total diameter of 12 meters.

A design requirement for the equipment was that the robot must always "know" the position of its end effector in relation to the individual nodes of the structure it was assembling. For the mechanical components that convert the output from the motors to the desired translation or rotation, this requirement necessitated a very stiff system with essentially no backlash or slippage.

DESIGN CRITERIA

The assembly approach the research engineer chose required the robot to translate over a planar area and the assembly support turntable to rotate about its axis (Fig. 2). The specific requirements of the drive systems are as follows:

*NASA Langley Research Center, Hampton, Virginia

X and Y Translation Systems
Travel: 6 meters in X and Y directions
Speed: 150 mm/s
Acceleration: 610 mm/s^2
Accuracy: $\pm$ 0.25 mm

Turntable
Rotation: 6 revolutions
Speed: 1.45 degrees/s (150 mm/s at a node at the six-meter radius)
Acceleration: 5.8 $degrees/s^2$ (610 mm/s^2 at a node at the six-meter radius)
Accuracy: $\pm$ $.0024^o$ (+0.25 mm at a node at the six-meter radius)

X- AND Y-DRIVE SYSTEMS

Several drive systems were considered for the translation systems. A geared drive, such as a rack and pinion, would have an inherent backlash that would result in inaccuracies greater than the 0.25 mm allowed. The slippage in a traction system would also be greater than the allowable error. A ball screw arrangement would have sufficient positioning capability, but the need for a six-meter shaft would make this method impractical. A cable drive system was selected, which offers high accuracy over the required distance of travel.

This cable drive system must move 1400 kg in the X-direction, requiring an 854-N force to achieve the desired acceleration of 610 mm/s^2. The system consists of two parallel shafts, identified as the main drive shaft and the secondary shaft (Fig. 3). The output of a servomotor is increased via an 89:1 torque multiplier. This torque multiplier has a backlash no greater than one arc minute. This drives a 152-mm-diameter drum mounted on the secondary shaft. This drum drives the main drive shaft via an 8-mm cable that is wrapped around this drum and a 305-mm-diameter drum on the main shaft (Fig. 4). This shaft runs the length of the X-carriage and has 305-mm-diameter drums mounted on either end. The carriage is pulled along 9.5-mm cables that wrap around each end-mounted drum and terminate at either end of travel.

The Y-drive system (Fig. 5) must translate a 602-kg mass. Just as on the X-drive, a servomotor drives an 89:1 torque multiplier. However, rather than transmit this torque to another shaft, this shaft drives the lighter Y-carriage directly. Two cables are wrapped around a 203-mm-diameter drum once, and each is anchored at either end of travel.

The positioning requirements created a stringent deflection criteria which superseded stress considerations. On the X-drive system, the maximum angular deflection of the drive shaft between the center and end drums could not result in more than a 0.25-mm linear deflection at the 152-mm radius.

The primary reason for having a drum on each end of the drive shaft on the X-drive system instead of a single drum, as on the Y-drive, was to prevent "racking" of the X-carriage. The rails under the X-carriage are almost five meters apart, whereas the rails supporting the Y-carriage are slightly less than a meter apart. Also, while the center of mass of the Y-carriage remains fairly constant, the center of mass of the X-carriage varies with the position of the robot in the Y-direction. These two factors made "racking" a design consideration in the X-direction.

TURNTABLE

To give the truss and turntable (Fig. 6) the desired angular acceleration, a torque of approximately 4880 N-m was required. A system was needed to transmit and multiply the motor torque while maintaining the desired accuracy. As with the translation systems, other systems were considered and rejected because of the positioning criteria. A cable drive concept was judged to offer the best opportunity for meeting the accuracy requirement. Commercially designed systems[2] were unacceptable because of time and cost constraints.

A basic description of the system is as follows (Fig. 7). A 1.07-m-diameter drum is rigidly attached to the rotating portion of the turntable. Aligned parallel to the drum is a 51-mm-diameter shaft. Five cables were wrapped around the large drum seven times and the shaft once, with the cable ends attached at the top and bottom of the drum. A servomotor is attached to the shaft via an 89:1 torque multiplier that, along with the 21:1 gear reduction between the shaft and the drum, creates a 1869:1 reduction. This makes possible a large torque from a small motor and reduces the error in the already accurate servomotor.

A 760-N load is carried by the turntable's cables. A conservative design convention is to choose cables with a combined breaking strength of approximately 10 times this value. Also, to ensure that the cables were not damaged by too small of a bend radius, a safe practice is to have a bend-radius-to-cable-radius ratio of approximately 25:1. Considering the shaft's radius of 25 mm, the cable radius could not be larger than 1.0 mm. Five 1.6-mm-diameter cables were chosen with a breaking strength of 2200 N each for a total breaking strength of 11 kN.

DESIGN CONSIDERATIONS

Slippage on the drums is a function of the angle of contact of the cable on the cylinder (Fig. 8). The ratio of the taut side tension, T_1, to the slack side, T_2, must be less than shown in the equation[3]

$$T_1/T_2 < e^{(mu)(theta)} \qquad (1)$$

For this design, the critical angle of wrap, (theta), is 2(pi) and the coefficient of friction, (mu), is conservatively assumed to be 0.15. In this

case, the ratio T1/T2 must be less than 2.57. This was accomplished by designating a sufficiently large preload.

On the X-drive system, there was difficulty achieving sufficient preload on the cable connecting the drums between the two shafts. To solve this problem, the bearings supporting the secondary shaft and the housing of the torque multiplier were mounted on slotted plates (Fig. 9). Threaded rods that are attached to each bearing support plate are inserted through holes in blocks attached rigidly to the carriage. When bolts are tightened on the rods, the secondary shaft is pulled away from the main drive shaft, thus tightening the cable.

There are a few design differences worth noting between the turntable and the X- and Y-cable drive systems. On the turntable, the ends of each cable are attached to the large drum by a spring (Fig. 10). Since the spring constant is known, the preload can be determined by measuring the deflection of each spring. This ensures that the required preload is used and that the tension of each spring is equal. As long as a sufficient angle of wrap is maintained between the spring and the point that the cables separate from the drum, friction will prevent the springs from affecting the mechanism's performance.

On the X- and Y-systems, springs could not be used at the cable termination points because of transient expansions and compressions that would occur during acceleration and deceleration. Instead, the cables were tied to eye bolts at the termination points. The eye bolts were threaded so that the tension in the cables could be estimated by the number of turns used in tightening each eye bolt. Since the cables were oversized, they could be tightened to a point that is above the required tension to avoid slip on the drums, yet well below the cable breaking strength. A disadvantage of this procedure is that cables operating on the same drive system may have slightly different tensions. This has not proven to be a problem in the operation of the system. In applications where assurance of proper operation is critical, such as in-space construction, strain gauges or load cells on the cables would be advisable.

Another difference between the turntable and the X- and Y-drive systems involves using a grooved surface as opposed to a flat surface on the face of the drums. On the X- and Y-drive systems, each cable is wrapped around a flat-surfaced drum and terminated at either end of travel. The cable termination points are offset so that the cable will "walk" from one end of the drum to the other as it rotates along its length of travel (Fig. 11). This offset ensures that the cable will "walk" evenly without binding and that, on the Y-drive, the two cables will not tangle. The preload of the cables is great enough to ensure that no slippage on the drum occurs.

On the turntable, there are two factors that require a grooved shaft as opposed to the flat-surfaced drums in the translation system. First, the grooves are needed to guide the cables. The possibility of tangling or binding is increased by having five cables wrapped around a large drum rather than one or two cables extended linearly as on the translation systems.

Secondly, the grooves increase the friction between the shaft and the cables. As mentioned previously, 1.6-mm cables were selected to prevent damage due to the shaft's 25-mm bend radius. These small cables could not carry the excessive preload that is used in both the X- and Y-drives. With the shaft being grooved, a smaller preload could be used without bringing about slippage.

RESULTS

On the X-drive system, the position accuracy and repeatability is ±.05 mm, bettering the goal of ±.25 mm maximum. The speed is 124 mm/s, slightly less than the 152 mm/s design criterion, and the acceleration of 564 mm/s^2 is less than the desired 610 mm/s^2. The speed and acceleration are less than anticipated because a larger-than-expected force is required for motion. As the project evolved, unexpected items were added to the carriage's payload. Also, additional electrical wiring and air hoses in the cable carriers increased the carriers' resistance to motion. In retrospect, the sizing of the motor required to move the carriage could have allowed for these inevitable changes in an experimental project. These deficiencies do not have a significant effect on the facility's operation and could be easily corrected by providing a larger motor.

All of the design criteria have been surpassed with the Y-drive system. The positional accuracy and repeatability of the cable system is again ±.05 mm, bettering the ±.25-mm goal. The speed and acceleration achieved with the lighter Y-carriage are 223 mm/s and 743 mm/s^2 both surpassing the goals.

The rotational accuracy of the turntable is ± 0.0041^o, which is the minimum command step from the motor with the given gear ratio. This falls short of the design criteria of ± 0.0024^o, which was based on the goal of ±0.25-mm accuracy of a node at a six-meter radius. The achieved results have proven adequate. The maximum speed is 5.60 ^{o}/s and the acceleration is 19.32^o/s^2, both surpassing the requirements.

It is worth noting that all of the position accuracies were achieved running the motors open-loop. While the equipment does contain positioning sensors, no feedback from the sensors is necessary to obtain the above results.

CONCLUDING REMARKS

The purpose of the Automated Structural Assembly Laboratory is to prove that in-space robotic assembly is plausible and to develop the technology needed to carry this assembly out. The cable drive systems further this project in two ways. First, it is a fairly simple and inexpensive method for achieving the motion needed to conduct the robotic experimentation. Secondly, it offers a proven concept for accurate motion transmission that could ultimately be used for in-space assembly.

Similar drive systems could be used for other experimental and commercial applications. The design procedures could be essentially duplicated for even much larger systems to achieve similar accuracy.

REFERENCES

1. Rhodes, M.D.; Will, R.W.; Wise, M.A.: A Telerobotic System for Automated Assembly of Large Space Structures. NASA TM 101518, March 1989.

2. Roto-Lok^{R} Rotary Drive System, Trax Instrument Corporation, Albuquerque, New Mexico.

3. Fuller, D.D.: Marks' Standard Handbook for Mechanical Engineers, Eighth Edition. Chapter 3: "Friction" p. 3-32, 1978.

ORIGINAL PAGE
BLACK AND WHITE PHOTOGRAPH

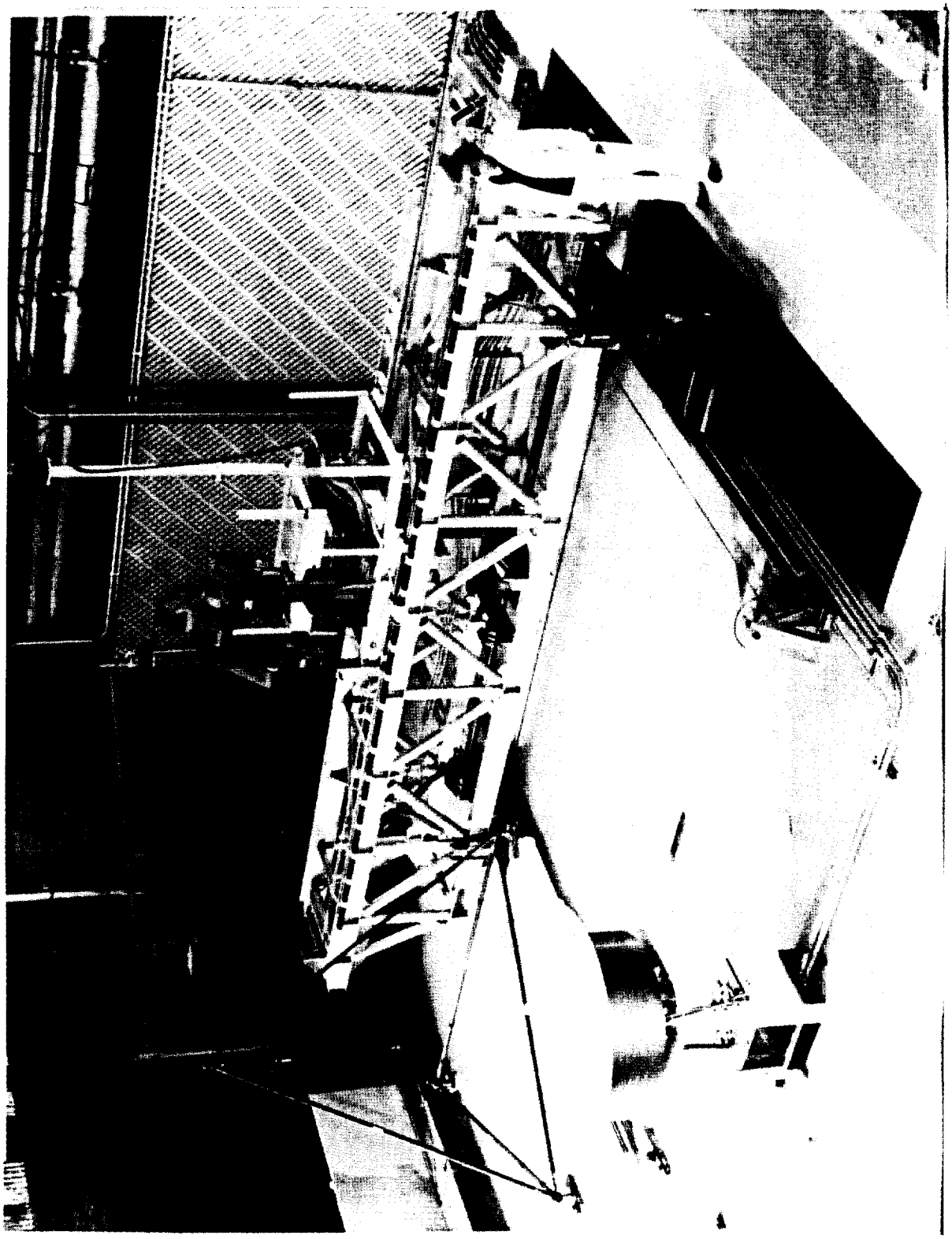

FIG. 1 -- AUTOMATED ASSEMBLY LAB

FIG. 2 – –

TELEROBOTIC ASSEMBLY FACILITY

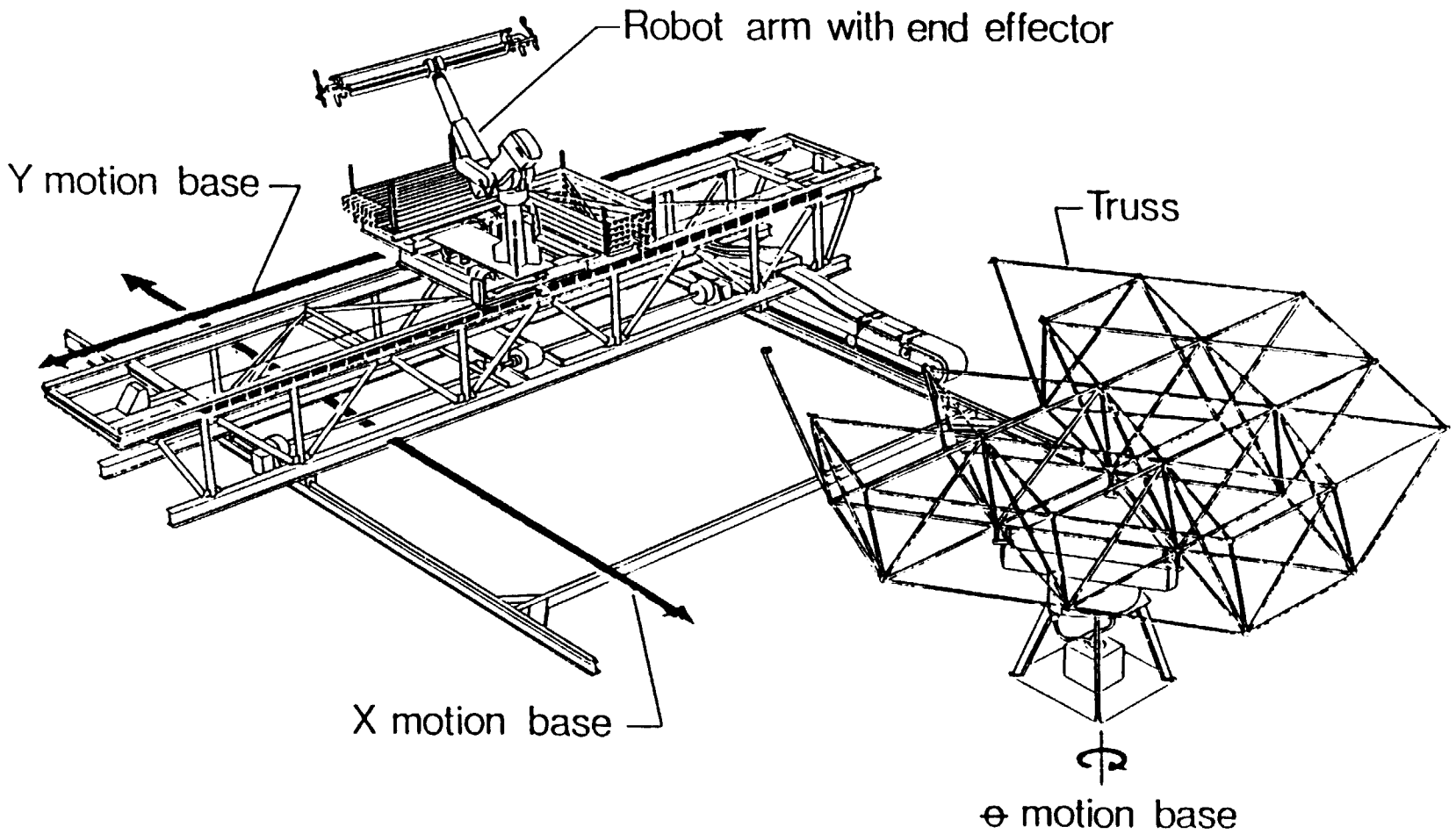

X-DRIVE SYSTEM
Fig. 3 - -

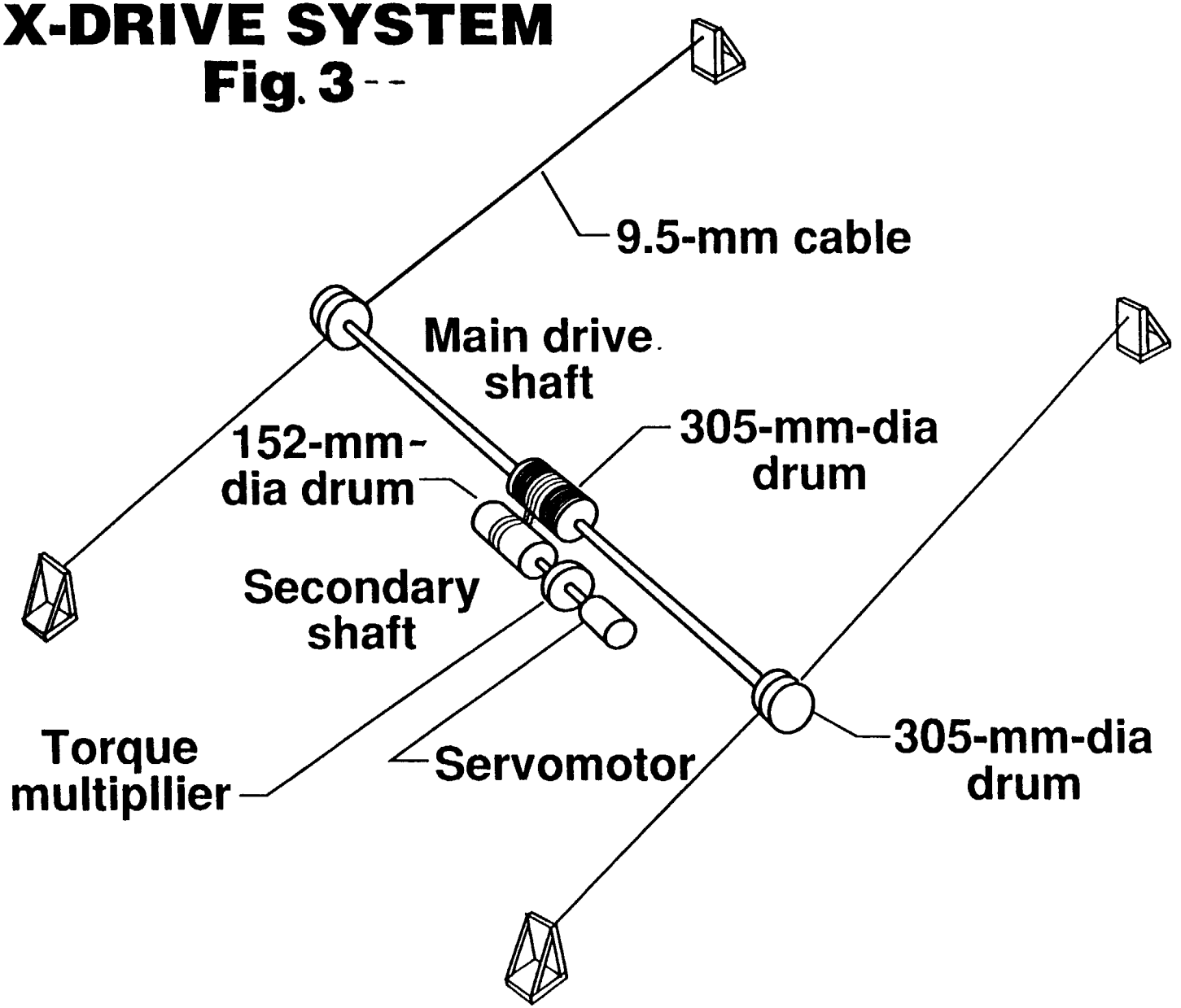

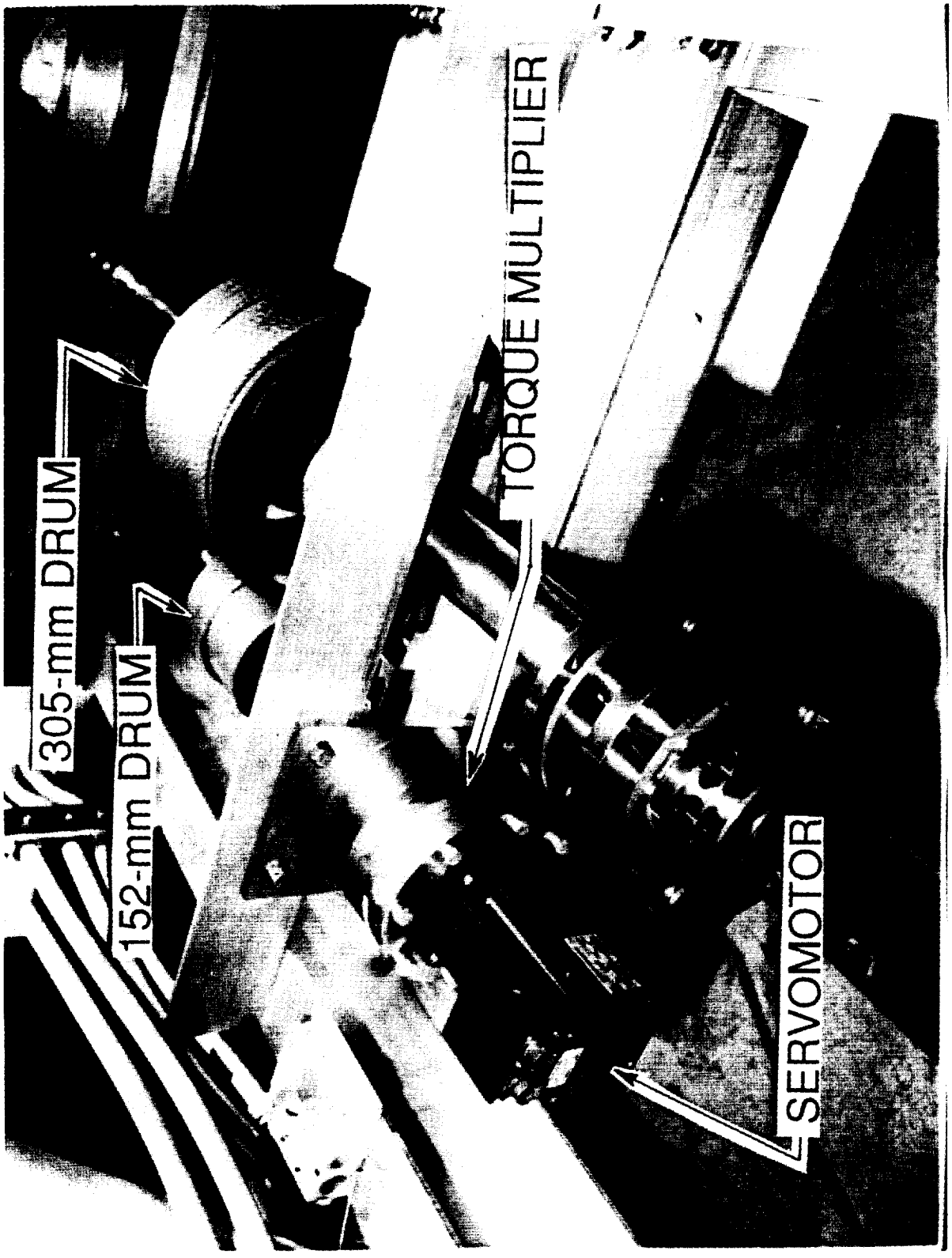

FIG. 4 -- X-DRIVE COMPONENTS

Y-DRIVE SYSTEM
Fig. 5 - -

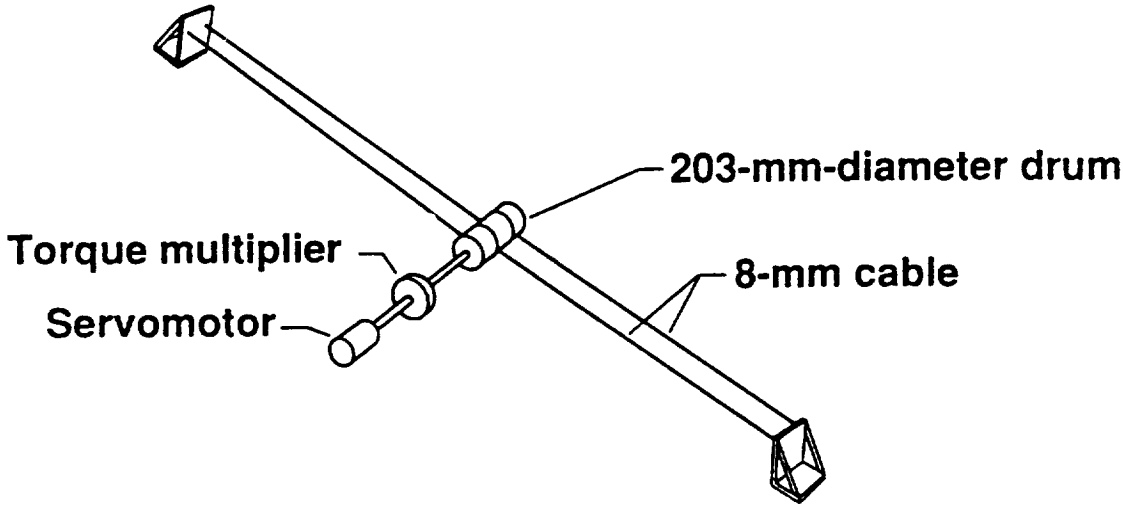

TURNTABLE
FIG. 6 - -

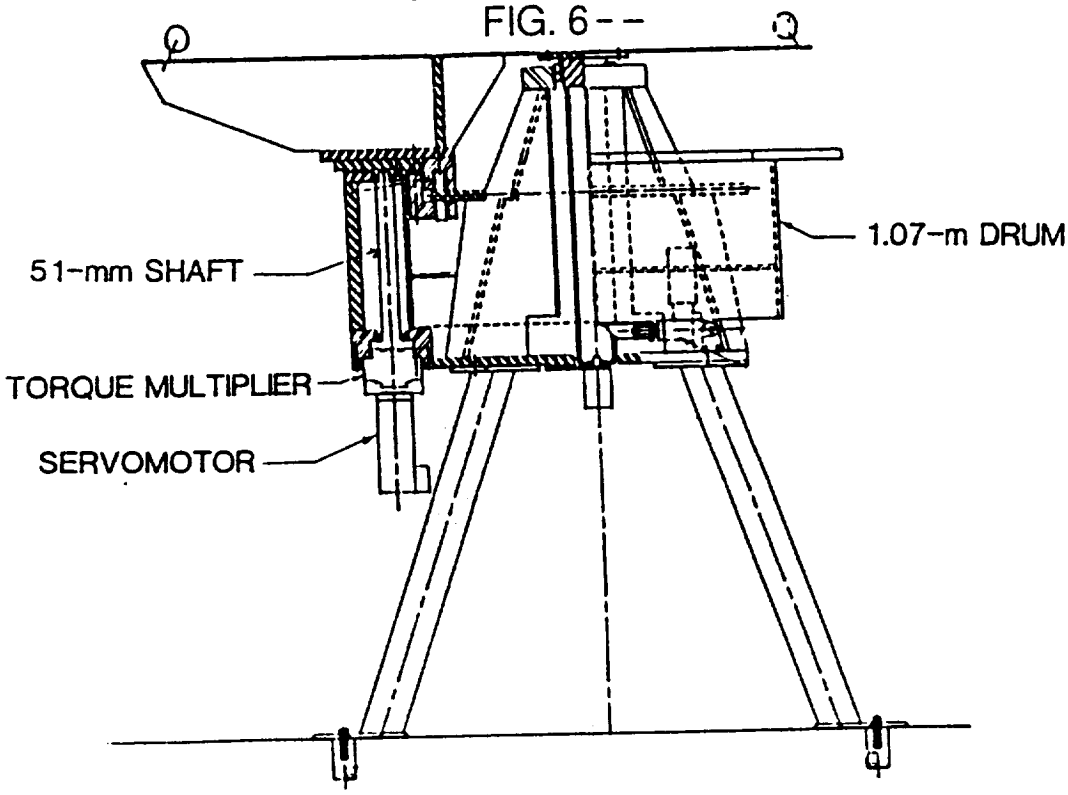

TURNTABLE DRIVE SYSTEM
Fig. 7--

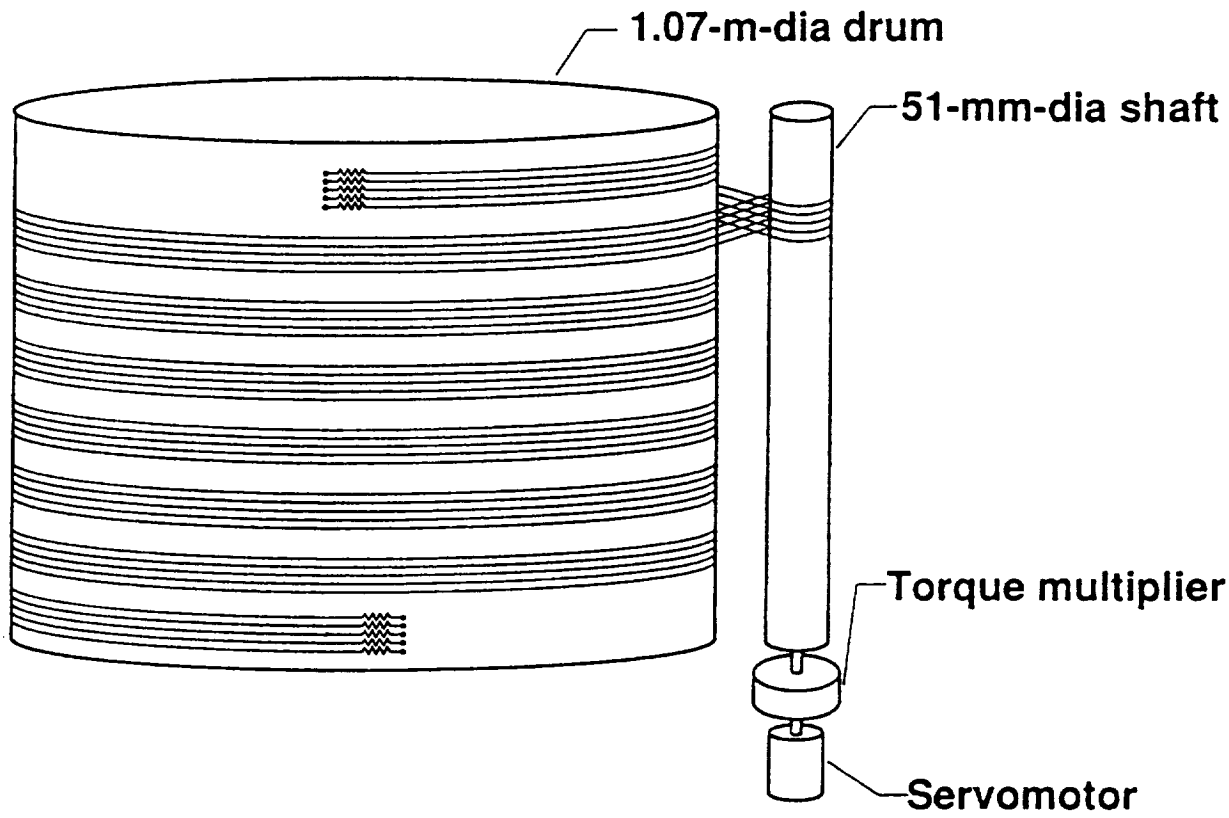

ANGLE OF CONTACT

FIG. 8--

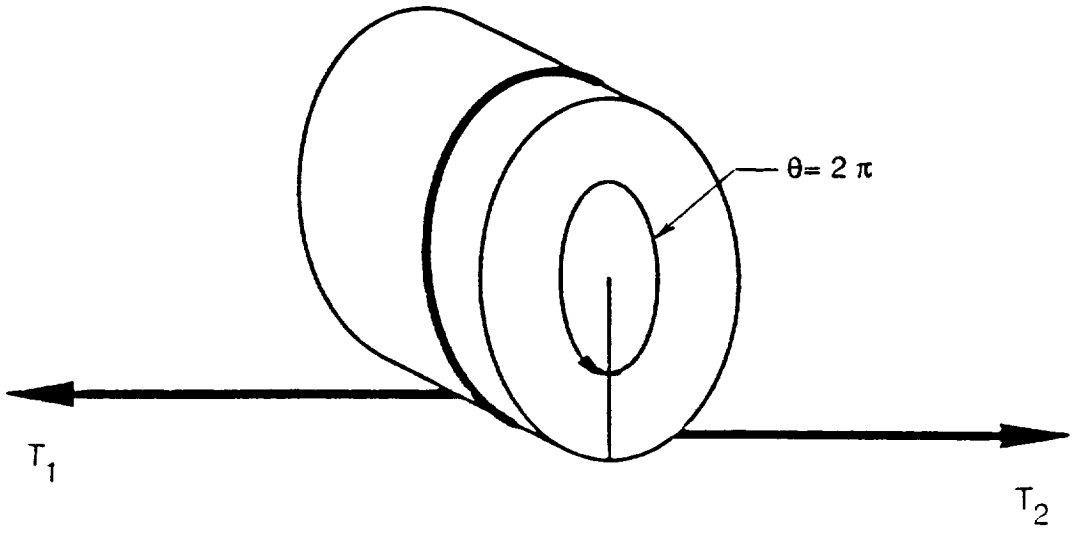

ORIGINAL PAGE
BLACK AND WHITE PHOTOGRAPH

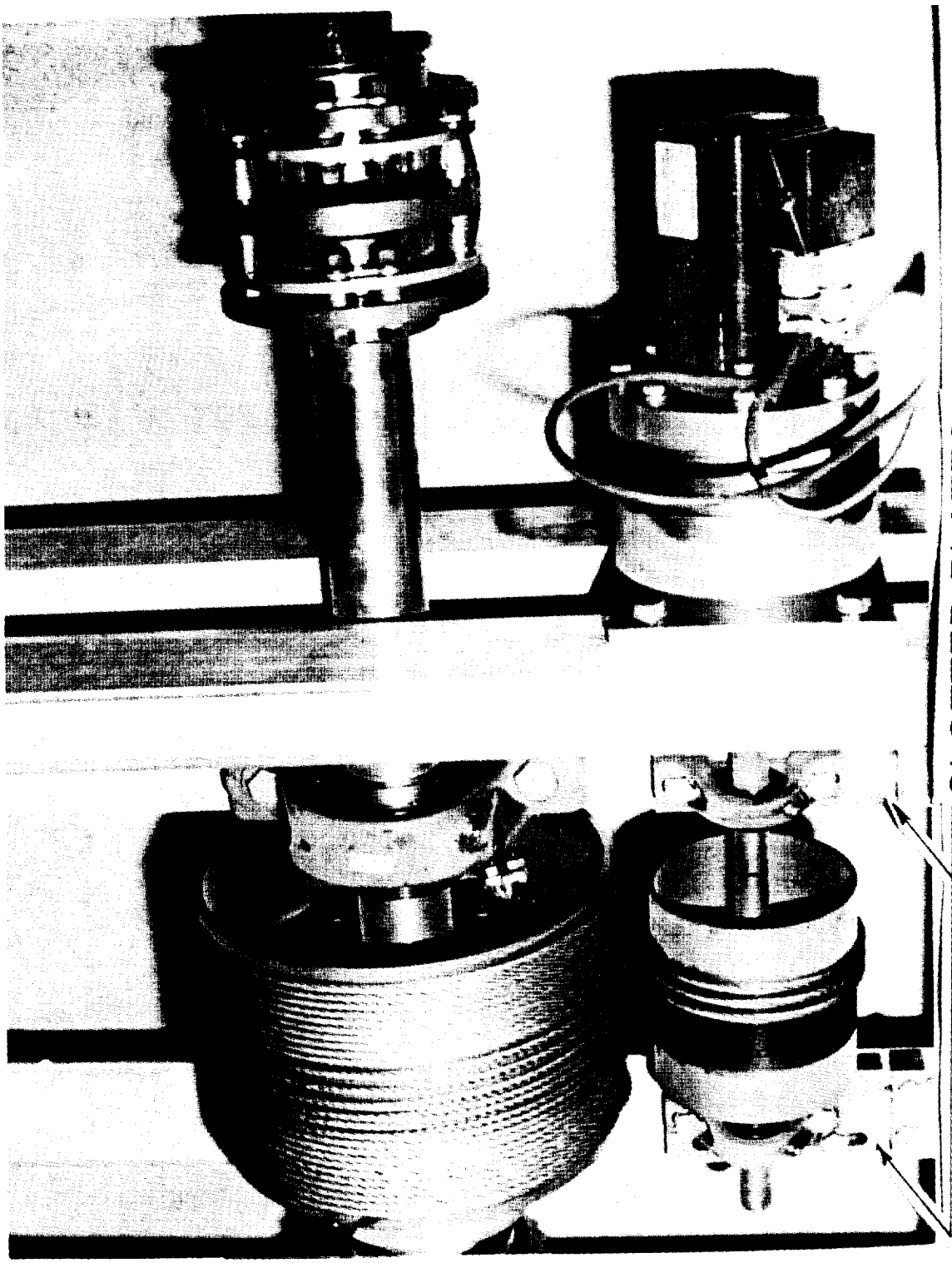

FIG. 9 -- X-DRIVE CABLE TENSION

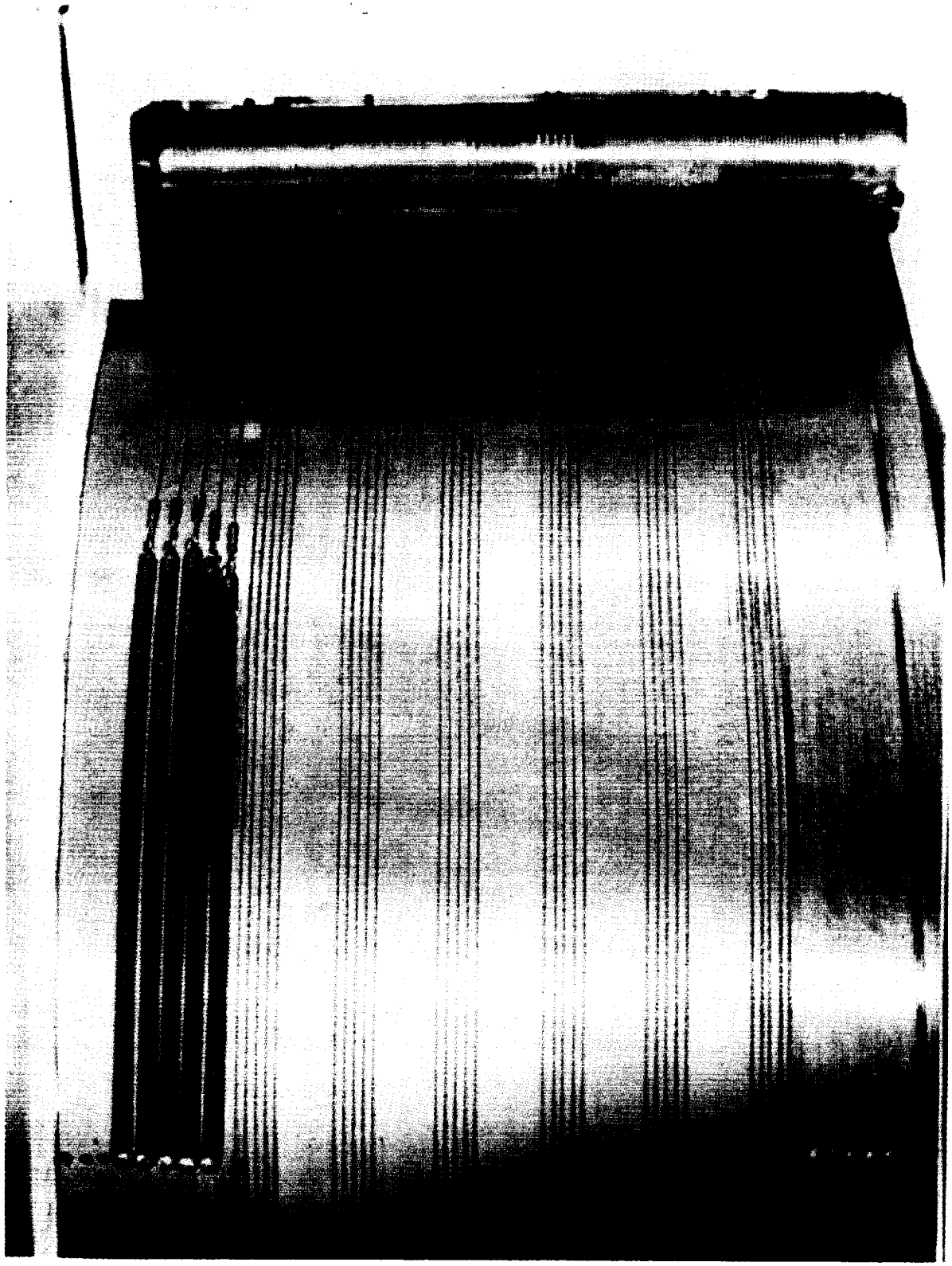

FIG. 10 -- TURNTABLE DRUM & SHAFT

CABLE TERMINATION OFFSET

FIG. 11 – –

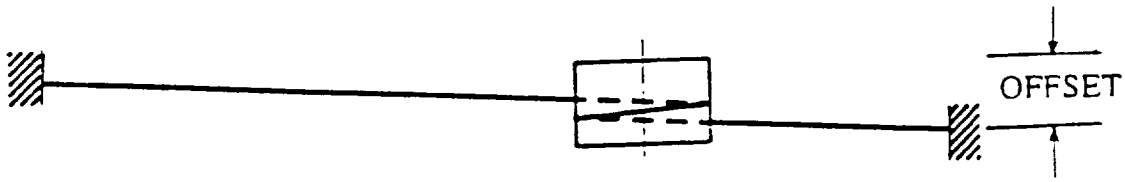

NASA

Report Documentation Page

1. Report No.	2. Government Accession No.	3. Recipient's Catalog No.
NASA CP-3062		

4. Title and Subtitle	5. Report Date
24th Aerospace Mechanisms Symposium	April 1990
	6. Performing Organization Code
7. Author(s)	8. Performing Organization Report No.
	10. Work Unit No.
9. Performing Organization Name and Address John F. Kennedy Space Center Kennedy Space Center, Florida 32899	11. Contract or Grant No.
	13. Type of Report and Period Covered Conference Publication
12. Sponsoring Agency Name and Address National Aeronautics and Space Administration Washington, D.C. 20546	14. Sponsoring Agency Code

15. Supplementary Notes

California Institute of Technology, Pasadena, CA 91109
Lockheed Missiles and Space Company, Inc., Sunnyvale, CA . 94088

16. Abstract

The proceedings of the 24th Aerospace Mechanisms Symposium, which was held at the John F. Kennedy Space Center, Kennedy Space Center, Florida, on April 18-20, 1990, are reported. Technological areas covered include actuators, aerospace mechanism applications for ground support equipment, lubricants, latches, connectors and other mechanisms for large space structures.

17. Key Words (Suggested by Author(s))		18. Distribution Statement
Circularity	End-Effector	Unclassified - Unlimited
Piezoelectrics	Satellite Attitude Cont.	Subject Category 39
Robotics	Bearings	
Hand Controller	Tribology	
Telescoping	Friction Brakes	

19. Security Classif. (of this report)	20. Security Classif. (of this page)	21. No. of pages	22. Price
Unclassified	Unclassified	448	A19

NASA FORM 1626 OCT 86

NASA-Langley, 1990